

# ***User's Short Reports***





You can jump to the top of the section by clicking titles.

## USER'S SHORT REPORTS

### CONTENTS OF USER'S PROGRESS REPORTS

Title	First Author	Proposal No.	Page
<b>A : EXAFS</b>			
The Structure Studies on the Thermal Stability of SiO <sub>2</sub> -supported V <sub>2</sub> O <sub>5</sub>	Asakura, K.	87-012	16
Photoemission Investigation of the Room Temperature Adsorption of TMG on GaAs Surface	Claverie, P.	87-134	17
Study on Solid Solution Strengthening of Austenitic Steels by EXAFS	Shibata, K.	86-082	18
Br and Ge EXAFS Studies of AgBr-Ag <sub>2</sub> O-GeO <sub>2</sub> Glasses	Morikawa, H.	86-084	19
An EXAFS Study of Co-Mn and Fe-Mn Bimetallic Solvated Metal Atom Dispersed Catalysts	Kanai, H.	86-085	20
Local Structure around Fe Atom in Bi-Zn-Fe-O Magnetic Glass	Sakurai, M.	87-005	21
Effects of Alloying Elements in Steels on EXAFS	Shibata, K.	87-017	22
EXAFS Study of Selenometallothionein Structure	Esaki, N.	87-019	23
An EXAFS Study of the Silica Supported Vanadium Oxide Catalysts Prepared by CVD Method	Sone, T.	87-116	24
Study of Al-Mn Quasi-crystal by EXAFS	Ino, H.	87-118	25
XANES Measurements for Ce Valence in Pd-Ce Ordering Alloys with a Basic Structure of FCC Lattice	Kuwano, N.	87-129	26
Studies on the Local Structures of the Iron Catalysts for Coal Gasification	Yamashita, H.	87-139	27
Structure Determination of Metal Complexes in Very Dilute Solutions by Fluorescent EXAFS Spectroscopy. Copper(II) Chloride Complexes in Acetonitrile	Yamaguchi, T.	87-144	28
EXAFS Measurements on the Copper Catalyst Prepared by the Novel Method	Yoshitake, H.	88-019	29
An X-Ray (1.7-14 keV) Beam Line for EXAFS Studies	Nakano, A.	88-006	30
The Local Structure of Iron-Tin Composite Oxides Studied by X-Ray	Yoshida, S.	86-086	31

## Absorption Spectroscopy

EXAFS Observation of Vapor Quenched Fe-Ag, Fe-Cu and Fe-Cu-Ag Alloys	Nakamura, Y.	86-087	32
Local Structure of Ni-Al Alloys in Connection with Premartensitic Phenomena and $\omega$ -Phase Character	Noda, Y.	86-088	33
Local Structure of the Perovskite-type $\text{SrCo}_{1-x}\text{Mn}_x\text{O}_3$ Solid-solution	Yoshiasa, A.	86-090	34
Local Crystal Structure of Exchanged Ions in Zeolite	Kuroda, Y.	86-093	35
Characterization of Supported RhFe and PtFe Bimetallic Carbonyl Clusters and Their Catalytic Functions	Ichikawa, M.	87-002	36
EXAFS and XANES Analysis of Selenium Compounds (II)	Kawashima, T.	87-008	37
Characteristics and Structure of NbC Films Fabricated by Ion Beam Sputtering	Tuneki, O.	87-009	38
Changes in Local Structure of Ultra-fine Rhodium Particles by Chemisorption	Fukushima, T.	87-010	39
In-situ EXAFS Studies on the Structure Change of $\text{Rh}_2$ Attached on $\text{SiO}_2$ During the CO Insertion Reaction	Asakura, K.	87-011	40
EXAFS Studies on the Structure of the Se-Rh/ $\text{SiO}_2$ and Its High CO Insertion Activity	Asakura, K.	87-013	41
Studies on the Structure of Bimetallic Colloidal Catalysts	Toshima, N.	87-016	42
An EXAFS Study of $\text{Ag}_3\text{SbS}_3$ - $\text{Ag}_3\text{AsS}_3$ Solid Solution	Sugaya, H.	87-020	43
An EXAFS Study of $\text{Ag}_3\text{AsS}_3$ Glass	Okuno, M.	87-020	44
Structure of Zinc(II) Iodide Complexes in Aqueous Liquid and Glassy Solutions	Yamaguchi, T.	87-023	45
Structure of Zinc(II) Chloride Complexes in Aqueous Liquid and Glassy Solutions	Yamaguchi, T.	87-023	46
Structure of Gallium(III) Chloride and Bromide Complexes in Aqueous Liquid and Glassy Solutions	Yamaguchi, T.	87-023	47
EXAFS Study on Active Sites for Hydrocracking and Hydrogenation Activities of Mo Supported Catalysts II. Effect of Mo Loading	Matsubayashi, N.	87-024	48
XANES and EXAFS of Nickel Thiolate Complexes ---in Terms of Nickel Containing Hydrogenases---	Yamamura, T.	87-120	49
The Structure of Intercalated Metal Particles in Layered $\text{K}_4\text{Nb}_6\text{O}_{17}$	Yoshimura, J.	87-121	50

A Study on the Correlation between the Local Structure and Photo-Catalytic Activity by Supported Niobium Oxides Catalysts	Nishimura, Y.	87-122	51
XAFS Studies on Local Structure of High $T_c$ Superconductors	Yamazaki, H.	87-123	52
Chemical Short Range Order in Liquid Rb-Se Alloys	Endo, H.	87-124	53
AsO <sub>4</sub> Molecule Distortion in KDA	Noda, Y.	87-126	54
A Study on the Ni <sup>2+</sup> Ions in Sodium Borate Glasses by EXAFS	Xu, Q.	87-127	55
Characterization of Zeolite-encapsulated Metal Phthalocyanin Catalysts	Ichikawa, M.	87-131	56
Temperature Dependence of the EXAFS Spectra for Silver and Palladium Small Metal Clusters: Dissimilarities of the Thermal Vibration and Thermal Expansion in Comparison with Bulk Metals	Yokoyama, T.	87-135	57
Structure of Germanium CVD Zeolite by EXAFS and XPS	Hibino, T.	87-136	58
XAFS Study of (Bi <sub>2</sub> O <sub>3</sub> ) <sub>1-x</sub> (Y <sub>2</sub> O <sub>3</sub> ) <sub>x</sub> System at High Temperatures	Kamijo, N.	87-140	59
Structural Studies on Precipitation Reactions in Qualitative Analysis by EXAFS and XANES Technique (I)	Nakai, I.	87-141	60
A XANES Study on Ni Zr Amorphous Alloys Prepared by Mechanical Alloying Method	Sakurai, M.	87-145	61
EXAFS Study on Fluoride Ion-conductive ZrF <sub>4</sub> -BaF <sub>2</sub> -CsF Glasses	Kawamoto, Y.	88-004	62
EXAFS Study on Active Intermediates of Cytochrome P-450 Models	Hirobe, M.	88-005	63
EXAFS Study on Thin Film of ZrO <sub>2</sub> on TiO <sub>2</sub>	Tanaka, T.	88-011	64
Rhodium-Niobia Interaction on Silica Formed by Air Calcination at High Temperature	Kunimori, K.	88-012	65
EXAFS Study on the Local Structure of Amorphous Te <sub>x</sub> C <sub>1-x</sub> Alloys	Tsunetomo, K.	88-013	66
Te-K EXAFS Study on the Structure of Amorphous Si <sub>x</sub> Te <sub>1-x</sub> Alloys	Tsunetomo, K.	88-013	67
XAFS Studies on Phase Transition in Iron and Iron Base Alloys	Yamazaki, H.	88-017	68
EXAFS Studies on the SiO <sub>2</sub> Attached Nb Dimer Catalyst	Kuwabara, R.	88-020	69
The Structure of the One-atomic Layer	Asakura, K.	88-021	70

## Rh Catalyst in the CO Oxidation Reaction

The Structure Studies on the Reversible Activity Change of the Noble Metal Catalysts	Asakura, K.	88-022	71
Elucidation of Structure of Catecholdioxygenase-model Complexes and Mechanism of Oxygenation of Aromatic Ring	Funabiki, T.	88-023	72
EXAFS and XANES Studies on Dynamic Behavior of Two-site Promotion of CO Catalyzed by Bimetal Clusters	Ichikawa, M.	88-027	73
Compact Fluorescence X-Ray Detector for Surface EXAFS and X-Ray Standing-wave Measurements	Funabashi, M.	87-142	74
La K-edge EXAFS Studies on the Structures of La Oxide Thin Layer Catalysts	Asakura, K.	87-015	75
Measurements of Spectra of Synchrotron Radiation in Soft X-Ray Region by Means of Helium Gas Scattering	Gotoh, S.	87-009	76
Study of Quarter-micron Pattern Replication by X-Ray Lithography	Ishiwari, H.	87-009	77
Radiation Durability of a-BNC:H for X-Ray Mask Membranes	Yamada, M.	87-009	78
Local Structure around Zn Atoms Diffused into GaAs Crystal	Kitano, T.	88-Y004	79
EXAFS Study of Rh/Al <sub>2</sub> O <sub>3</sub> Catalysts	Murofushi, Y.	87-Y017	80
Structure of Liquid State of Bi <sub>2</sub> O <sub>3</sub> by EXAFS	Koto, K.	87-130	81
EXAFS Studies of High Tc Superconductor Ca <sub>x</sub> Y <sub>1-x</sub> Ba <sub>2</sub> Cu <sub>3</sub> O <sub>7-y</sub>	Akai, T.	88-Y001	82
EXAFS Studies on Ca-Ni-Mo/Al <sub>2</sub> O <sub>3</sub> Catalyst for Hydrogenation of Coal Liquid Bottoms	Ushikubo, T.	88-Y001	83
Analysis of Modified Hopeite Films by Means of EXAFS	Sato, N.	88-Y005	84
XANES of Tb-L <sub>III</sub> in ZrO <sub>2</sub> -Tb <sub>4</sub> O <sub>7</sub> Mixed Conductors	Arashi, H.	88-Y025	85
EXAFS Studies of WSiN Films	Maeyama, S.	88-Y007	86
Copper K-edge Polarized EXAFS of High-Tc Superconducting Single-crystal YBa <sub>2</sub> Cu <sub>3</sub> O <sub>y</sub>	Maeyama, S.	87-Y012	87
YTTRIUM K-edge Polarized EXAFS of High-Tc Superconducting Single-crystal YBa <sub>2</sub> Cu <sub>3</sub> O <sub>y</sub>	Maeyama, S.	87-Y012	88
Barium K-edge Polarized EXAFS of High-Tc Superconducting Single-crystal YBa <sub>2</sub> Cu <sub>3</sub> O <sub>y</sub>	Maeyama, S.	87-Y012	89

## B : Biology

Killing on <u>E.Coli</u> and <u>Deinococcus Radiadurans</u> by Monochromatic X-Rays at Resonance Energy of Phosphorus K-absorption Edge	Maezawa, H.	86-101	90
Enhanced Killing on Cultured Mammalian Cells by Soft-X-Rays with Resonance Energy of Phosphorus K-absorption Edge	Maezawa, H.	88-039	91
X-Ray Contact Microscopy of Hydrated Human Nuclei	Shinohara, K.	88-033	92
NMR Study of the Irradiation Effect by SR Monochromatic X-Rays on BR-Deoxyuridine-monophosphate	Takakura, K.	86-100	93
Nondestructive X-Ray Fluorescence Spectroscopic Imaging of Trace Elements in Animal Tissues	Nakai, I.	88-034	94
Induction of Mutation and Chromosome Aberrations in Cultured Mammalian Cells by Synchrotron-produced Monochromatic X-Rays	Ejima, Y.	88-036	95
Detection of Damaged DNA Irradiated with Mono-X-Ray in the Presence of BrdU	Miyoshi, N.	88-037	96
Detection of the Damaged and Fragile Sites Irradiated with Mono-X-Ray on Chromosome	Miyoshi, N.	88-037	98
Studies on Auger Enhancement in Cultured Mammalian Cells with the Use of Radical Scavengers	Shinohara, K.	88-041	99
Crystallographic Studies on Intact Ribosomal Particles	von Bohlen, K.	87-028	100
Structural Studies of Lipoamide Dehydrogenase and 3-Isopropylmalate Dehydrogenase by Rapid Measurement of High Resolution X-Ray Diffraction Data	Takenaka, A.	88-043	102
High Resolution Data Collection for the Complex of Subtilisin BPN' with Streptomyces Subtilisin Inhibitor	Takeuchi, Y.	88-047	103
Crystal Structural Studies of Biological Macromolecular Assembly	Takeuchi, Y.	88-048	104
Diffraction Experiments of Hydrogenase at Two Wavelengths II	Higuchi, Y.	88-049	105
Phase Determination of Cytochrome c553 by Multi-wavelength Anomalous Dispersion Method	Nakagawa, A.	88-050	106
X-Ray Solution Scattering Studies on Solubilized Bacteriophodopsin III.	Kataoka, M.	86-028	107

Quarternary Structure Change of Tryptophanase Observed by Small-angle X-Ray Scattering	Kim, E.H.	86-103	108
Conformational Analysis of Broken Rodlike Chains; II. Conformational Analysis of Poly(D-Glutamic Acid) in Aqueous Solution by Small Angle X-Ray Scattering	Muroga, Y.	86-105	109
Molecular Shape of 114-kilodalton Pea Phytochrome Studied by X-Ray Solution Scattering	Tokutomi, S.	86-106	110
Improvement of "SAXES" and Development of Data Treatment Software	Ueki, T.	87-031	111
Structural Analysis of Oligomeric Proteins in Solution	Ueki, T.	87-032	112
Structural Behavior of Troponin-C upon Calcium Ion Binding	Fujisawa, T.	87-033	113
Inactivation of <i>Bacillus Subtilis</i> Spores by Monochromatic X Radiation with the Resonance Energy of Phosphorus K-shell Absorption	Munakata, N.	88-042	114
Analysis of Mutational Specificity in <i>lacZ</i> Gene on Plasmid pUC19	Yatagai, F.	88-053	115
Crystal Structural Analysis of a Ferredoxin from Mycobacterium Smegmatis by the Native Anomalous Dispersion Method	Tsukihara, T.	86-031	116
Intensity Measurements with Short Wave-length X-Rays; Structure Refinement of Ilmenite	Ohgaki, M.	88-054	117
Development of Specimen Chamber for Light Irradiation at Low Temperature and Its Application to Bacteriorhodopsin Photocycle IV	Tokunaga, F.	87-036	118
Effects of X-Ray Irradiation on Murine Heart Muscle	Matsubara, I.	87-037	119
Effects of 2,3-Butanedione-2-Monoxime on the Structural Changes of the Thin Filament during Activation of Frog Skeletal Muscles	Yagi, N.	87-038	120
Temperature Dependence of the Ripple Structure in DMPC-Cholesterol Multibilayer System	Matuoka, S.	87-039	121
Radial Movements of Myosin Heads in Murine Heart Muscle during Contraction	Saeki, Y.	87-043	122
Equatorial X-Ray Intensity Changes during Contraction of Frog Skeletal Muscles under the Inhibitory Action of 2,3-Butanedione-2-Monoxime	Takemori, S.	87-045	123
X-Ray Diffraction of the Live Squid Retina	Hamanaka, T.	87-040	124



Change in the Small-angle Diffuse Scattering from a Frog Skeletal Muscle during an Isometric Contraction	Wakabayashi, K.	87-041	125
Changes in Equatorial X-Ray Diffraction Intensities from Skeletal Muscle of the Frog Stretched at the Onset of Twitch	Iwamoto, H.	87-044	126
Time-resolved X-Ray Diffraction Studies of Equatorial Reflections from Frog Skeletal Muscle during Segmental Length Clamp	Kobayashi, T.	87-044	127
Effect of the Slow Sinusoidal Length Change (2Hz) on the Intensity of Myosin Meridional Reflections from Isometrically Tetanized Frog Skeletal Muscles	Wakabayashi, K.	88-056	128
X-Ray Diffraction Studies of the Modified Purple Membrane during Its Photocycle	Uruga, T.	88-057	129
Medium Angle X-Ray Diffraction of a Tonically Contracting Molluscan Smooth Muscle	Tajima, Y.	88-058	130
Dissociation and Association Kinetics of E. coli Ribosome. Stopped-flow X-Ray Scattering Study at Subzero Temperature	Tsuruta, H.	88-060	131
Structural Dynamics of Alpha-2-Macroglobulin and Fatty Acid Synthetase Studied by Time-resolved X-Ray Small Angle Scattering Experiment	Ikai, A.	88-060	132
Dissociation of Limulus Polyphemus (Horseshoe Crab) Hemocyanin Monitored by Stopped-flow X-Ray Scattering Method	Kimura, K.	88-060	133
Dissociation of Eisenia Foetida (Earthworm) Hemoglobin Monitored by Stopped-flow X-Ray Scattering Combined with Time-resolved Imaging Plate as Detector	Igarashi, Y.	88-060	134
Time Resolved Small-angle X-Ray Scattering Study of Aggregation Process of Cucumber Green Mottle Mosaic Virus Protein	Sano, Y.	86-107	135
Conformation Change of Amylose and Amylopectin Induced by Complexation with Iodine-Iodide	Hirai, T.	87-149	136

#### C : X-Ray Experiments

Detection Characteristics of Micro-channel Plates for Plasma X-Ray Diagnostics	Yamaguchi, N.	87-164	137
Quantum Efficiency of Gold Photocathodes (2-8 keV)	Cho, T.	87-164	138

X-Ray Diffractometric Determination of Lattice Misfit between $\gamma$ and $\gamma'$ Phases in Ni-base Superalloys	Ohno, K.	88-066	139
Powder Diffraction-profiles of the Monoclinic Superstructure of Tridymite	Kihara, K.	87-154	140
Chemical State Imaging of Rock Sample by X-Ray Fluorescence Spectroscopy Using Chemical Shift of Fe-K Absorption Edge	Nakai, I.	87-056	141
Application of Synchrotron Radiation to Archaeological Objects (III)d	Nakai, I.	87-056	142
Non-Destructive Chemical State Analysis of Cu Oxide Compounds	Saitoh, N.	87-057	143
Micro X-Ray Fluorescence Analysis Using Energy Tunable SR X-Ray Micro Analyzer	Hayakawa, S.	87-058	144
SR X-Ray Fluorescence Imaging by Image Reconstruction Technique	Takahashi, M.	87-155	145
Determination of Trace Siderophile and Lithophile Elements in Meteoritic Mineral Crystals by Microfocus X-Ray Fluorescence Spectrometer with Reference to Their Formation Conditions	Hidaka, O.	88-061	146
Fabrication and Characterization of Multilayer Zone Plate for Hard X-Rays	Saitoh, K.	88-063	147
Analysis of Ultra Trace Elements in Marine Ecological Samples by SR Monochromatized X-Ray	Ishikawa, M.	88-064	148
Photoacoustic EXAFS for the Analysis of Layered Materials	Masujima, T.	88-089	149
Applicability of Photoacoustic EXAFS Method to Various Samples	Shiwaku, H.	88-089	150
X-Ray Photoacoustic Imaging by Computer Tomographic Method	Masujima, T.	88-089	151
X-Ray Photoacoustic Absorption Spectra of CuInSe <sub>2</sub> and Phosphor Bronze	Toyoda, T.	88-089	152
Synchrotron X-Ray Rietveld Analysis of $\alpha$ -Hafnium Phosphate Hf(HPO <sub>4</sub> ) <sub>2</sub> · H <sub>2</sub> O, an Inorganic Ion Exchanger	Nakai, I.	85-148	153
Measurement of X-Ray Diffraction from Micrometer-size Sialon	Ohmasa, M.	87-060	154
Basic Characteristics of a Powder Diffractometer for the Photon Factory	Ozawa, H.	87-061	155
Kinetic Study Under High Pressure by Energy Dispersive Powder Diffraction Spectra	Yamanaka, T.	87-062	156
EXAFS and RDF Studies of Ge <sub>27</sub> S <sub>53</sub> I <sub>20</sub> Glass	Nasu, H.	87-064	157



The Structure Study of $\text{GeO}_2\cdot\text{P}_2\text{O}_5$ Glasses with the Anomalous X-Ray Scattering	Shimizugawa, Y.	88-065	158
Structure Analysis of Organic Compounds by X-Ray Powder Diffraction	Kurahashi, N.	88-067	159
Spatially Modulated Structures of $(\text{N}(\text{CH}_3)_4)_2\text{MnCl}_4$	Hamaya, N.	88-069	160
Diffraction Pattern of an Environmental Fibonacci Lattice	Terauchi, H.	88-072	161
Phase Transitions of Black Phosphorus and Black Phosphorus-arsenic Alloy at Very Low Temperatures and High Pressures	Shirotani, I.	86-114	162
Determination of the Environmental Structure around a Specific Atom in Crystalline Materials by the Anomalous X-Ray Scattering	Waseda, Y.	88-074	163
Spontaneous Distortion in Antiferro- magnetic $\text{TbCu}_5$ -type Compounds	Kamigaki, K.	85-125	164
Observation of Pendellösung Fringe Induced by X-Ray Resonant Scattering Using SR	Yoshizawa, M.	87-071	165
Magnetic Spontaneous Distortion of Lattice in Antiferromagnetic Compounds	Kamigaki, K.	87-158	166
Kinetics of Phase Transition in Graphite Intercalation Compounds	Metoki, N.	88-062	167
Determination of the Environmental Structure around a Specific Atom in Disordered Materials by the Anomalous X-Ray Scattering	Waseda, Y.	88-074	168
High Speed Iodine K-edge Subtraction Angiography in the Animal Experiment	Takeda, T.	87-189	169
Al-Mn Alloy ( $\phi$ Phase) Showing the Diffraction Patterns Similar to Decagonal Quasicrystals	Sasaki, S.	86-115	170
Anomalous Transmission of Thermally Scattered X-Rays in a Germanium Crystal	Kashiwase, Y.	87-067	171
Local Atomic Order in the Spin-glass System Au-Fe Alloys	Ohshima, K.	87-074	172
Studies on the Process of Reaction in Crystals by SR. --Dehydration of Alpha- $\text{AlOOH}$ .--	Ohmasa, M.	87-079	173
Study of Rubber-like Behavior in a Au-Cd Alloy by X-Ray Diffraction	Ohba, T.	87-080	174
Crystal-structure Determination of a Small Single-crystal Using Synchrotron X-Rays; $\phi$ Phase of Al-Mn Alloy	Sasaki, S.	87-081	175
The Detection of Localized Excited	Sawada, H.	88-078	176

States in Crystal Structures by the  
Single-crystal X-Ray Diffraction  
Method (I)

X-Ray Raman Scattering as a Substitute for Soft X-Ray Absorption	Udagawa, Y.	87-066	177
Tertiary Structure of Calmodulin in Solution	Izumi, Y.	87-082	178
Structural Study of Gelation of Branched Polyethylene in Solution	Izumi, Y.	87-083	179
Studies on Si(111) $\sqrt{3} \times \sqrt{3}$ -Bi and -Ag Surfaces by X-Ray Diffraction	Takahashi, T.	87-085	180
X-Ray Correlation Photoacoustic Measurement of Layered Materials	Sugitani, Y.	87-188	181
Crystallization of Poly(Vinyl Alcohol) on Heterogeneous Nuclei	Isoda, S.	88-083	182
Photoacoustic EXAFS Study at Beam Line 10C	Masujima, T.	88-089	183
Nuclear Excitation by Synchrotron Radiation -- Background --	Mukoyama, T.	87-093	184
Dynamical Diffraction of X-Ray in Perfect Crystals under Grazing- incidence Conditions	Hashizume, H.	86-076	185
Angle-dispersive X-Ray Diffraction by Water Molecules II.	Takeuchi, H.	86-125	186
The Bragg Case Phase Plate	Hirano, K.	87-090	187
X-Ray Standing Wave Analysis of GaAs/Si(100) Interface	Kawamura, T.	87-190	188
A Study of Solid-liquid Phase Transition for Lithium Metal by High Resolution Compton Scattering Measurements	Itoh, F.	86-124	189
High Resolution Compton Profiles on Al-Li-Cu Single Quasicrystal	Tanaka, Y.	86-124	190
Atomic Structure of Icosahedral Al-Mn-Ru-Si	Sakurai, Y.	86-127	191
Chemical Effects on X-Ray Intensity Ratios of Nuclei Excited by Synchrotron Orbital Radiation	Yoshihara, K.	87-088	192
A New Method for Determining Diffusion Coefficients of Point Defects by the Use of SR Topography	Hondoh, T.	87-095	193
X-Ray Photoacoustic Imaging for Depth Profiling	Masujima, T.	88-089	194
X-Ray Semi-pulse Photoacoustic Method for Depth Profiling	Masujima, T.	88-089	195
Focusing of Synchrotron Radiation by a Cylindrical Multilayer Bragg-reflector	Takenaka, H.	86-077	196

X-Ray Characterization of [1-x]InAs-xAlAs Alloy Films Grown on InP Substrates	Nittono, O.	86-129	197
Effects of Growth Interruption on Structure of MBE Grown GaAs/AlAs Hetero-interfaces Studied by X-Ray Diffraction	Koshiba, S.	86-130	198
Direct Observation of Dislocations in Solid Helium-4 by X-Ray Topography	Suzuki, H.	86-131	199
Section Topography Using a High-order Reflection and Its Application	Sugita, Y.	86-152	200
Dynamical Observation of Lattice Defects in Nearly Perfect Aluminum Single Crystals	Kino, T.	87-096	201
Orthorhombic to Tetragonal Phase Transition in High Tc Superconductor YBa <sub>2</sub> Cu <sub>3</sub> O <sub>7-y</sub> under High Pressure	Môri, N.	86-111 87-007	202
High Pressure and Temperature Generation with a Multiple Anvil System Using Sintered Diamond Anvils	Ohtani, E.	86-121	203
Search of Long-period Structures in Rare Earths	Hamaya, N.	86-122	204
Structure of Liquid Gallium under Pressure	Tsuji, K.	87-094	205
Structure of Liquid and Crystalline Bismuth under Pressure	Tsuji, K.	87-167	206
Accurate Powder Diffraction Measurements under Uniaxial Stress	Sorensen, Y.S.	87-169	207
High Pressure X-Ray Diffraction Study Using an Imaging Plate	Shimomura, O.	87-170	208
Observation of Antarctic Meteorites by Monochromatic X-Ray CT Based on Synchrotron Radiation	Funaki, M.	88-U003	209
Structural Behaviours of La <sub>2</sub> CuO <sub>4-y</sub> and La <sub>2-x</sub> Sr <sub>x</sub> CuO <sub>4</sub>	Hirosawa, I.	87-U006	210
Composition Dependence of Lattice Parameter for LEC Grown GaAs Crystals with Dislocations	Usuda, K.	87-C011	211
Phase Identification in Oxidized Hf/Fe Multilayer Films by Using Anomalous Scattering	Imafuku, M.	88-C022	212
Development of a Stepwise Temperature Control Device and Its Application to Time-resolved SAXS Measurements of Polymer Blends	Kojima, T.	88-C007	213
Time-resolved X-Ray Measurement of Surface and Bulk Strains in Silicon Irradiated by a Frequency-doubled Nd:YAG Laser	Kojima, S.	88-C013	214

X-Ray Fluorescence Analysis of Trace Metals in Polymer Using Synchrotron Radiation	Sato, E.	87-Y010 87-Y016	215
X-Ray Diffraction Study of Fe/MgO Multilayered Films	Koyano, T.	86-113	216
Synchrotron Radiation Lithography System in an Atmospheric Environment	Okada, K.	88-Y004	217
Computer-controlled Oscillating Mirror System for Synchrotron Radiation Lithography	Fujii, K.	88-Y004	218
Microstructure and Schottky Barrier Height of Yb/GaAs Interface	Hirose, K.	88-Y004	219
Interfacial Superstructures of AlN/GaAs and AlN/InP Systems Fabricated by Chemical Vapor Deposition with Surface Pretreatment of GaAs and InP Substrates	Fujieda, S.	88-Y004	220
MBE Apparatus for in Situ Grazing Incidence X-Ray Diffraction	Akimoto, K.	88-Y004	221
Analysis of Diffuse X-Ray Scattering from the Omega Phase in Titanium Alloys	Morinaga, M.	87-160	222
Imaging System with an Amorphous Silicon Linear Sensor	Hasegawa, K.	88-084	223
Real Time K-edge Subtraction X-Ray Imaging	Fukagawa, H.	87-046	224
In-situ Measurement of the Lattice Constant of Wustite Solid Solution under High Pressure	Sekine, T.	87-101	225
 <b>D : VUV and Soft X-Ray Experiments</b>			
The Electronic Properties of Ionic Insulators on Semiconductor Surfaces: Alkali Halides on GaAs	Klauser, R.	87-191	226
Optical Performance and Applications of a Soft X-Ray Microscope	Kagoshima, Y.	87-103	227
Soft-X-Ray $\pi$ -p $\pi$ Scattering by Light Element Solids	Suzuki, T.	88-110	228
Photon Energy Dependence of Desorbed Ions from H <sub>2</sub> O/Si(100) in the Valence Excitation Region	Namba, H.		229
Charge Distribution of Xe Ions Produced by Multiple-photoionization	Mukoyama, T.	86-134	230
Threshold Photoionization of Xe Subshell	Hayaishi, T.	86-073	231
Ionic Fragmentation Following the Sn:4d and 4p Photoionization of Sn(CH <sub>3</sub> ) <sub>4</sub>	Ueda, K.	87-105	232
Ionic Fragmentation Following	Ueda, K.	87-105	233

the C:1s and Sn:3d Photoionization  
of  $\text{Sn}(\text{CH}_3)_4$

Ionic Fragmentation Following the Ga:3p and 3s Photoionization of $\text{Ga}(\text{CH}_3)_3$	Ueda, K.	87-105	234
Optical Constants of Superthin Gold Films for Soft X-Rays	Yanagihara, M.	87-106	235
Re-examination of Soft X-Ray Reflectance of Multilayer Mirrors after Irradiation of SR	Yamamoto, M.	87-106	236
Multiple-photoionization of Rare-earth Atoms; Sm, Eu and Yb	Yoshino, M.	87-107	237
Polarized XANES Studies of Polyethylene and Fluorinated Polyethylenes	Ohta, T.	87-178	238
In Situ DC Oxygen-discharge Cleaning of Optical Elements	Koide, T.	87-179	239
Study of the Polymerization Process of Diacetylene Long-chain Compound by Inner Shell Polarized Absorption Spectra	Seki, K.	88-105	240
Surface EXAFS and X-Ray Standing-wave Profiles for $(\sqrt{3} \times \sqrt{3})\text{R}30^\circ \text{Cl}/\text{Ni}(111)$	Funabashi, M.	86-139	241
Structure Analysis of $c(2 \times 2)\text{Cl}/\text{Ni}(100)$ by Surface EXAFS and Soft X-Ray Standing Wave Methods	Funabashi, M.	86-139	242
Soft X-Ray Standing-wave Absorption Profiles of $c(2 \times 2)\text{S}/\text{Ni}(100)$ : Discussion on the Analysis Method and Comparison of the Detection Modes	Yokoyama, T.	86-139	243
Soft X-Ray Standing-wave Absorption Profiles of $p(2 \times 2)\text{S}/\text{Ni}(111)$ : Usefulness as a Surface Structure Analysis	Yokoyama, T.	86-139	244
Soft X-Ray Standing-wave Absorption Profiles of $(5\sqrt{3} \times 2)\text{S}/\text{Ni}(111)$ : Reconfirmation of Surface Reconstruction	Yokoyama, T.	86-139	245
Study on Local Structure around Sulfur of Iron Sulfide Catalyst	Matsubayashi, N.	86-141	246
Two-dimensional X-Ray Photoelectron Diffraction Measurements by Use of Retarding Field Type Analyzer	Kanayama, S.	87-108	247
The Optical Spectra of $\alpha\text{-Al}_2\text{O}_3$ Single Crystals in VUV Region II	Tomiki, T.	86-070	248
Photo-stimulated Desorption of $\text{H}^+$ Ions from Oxidized Silicon Surfaces	Takakuwa, Y.	87-180	249
Piezorefectivity of $\text{Na}^+2\text{p}$ Core Exciton in $\text{NaCl}$	Yuri, M.	87-181	250
Angle-resolved Photoemission Study	Aiura, Y.	86-145	251

of Oxygen Adsorption on W(110) at 300K			
Angle-resolved Photoemission Study of Hydrogen-adsorbed Cr(110)	Komeda, T.	86-150	252
Angle-resolved Photoemission Study of Oxygen-adsorbed Cr(110)	Komeda, T.	86-150	253
Electronic Structure of NbC(100) Surface: Angle-resolved Photoemission Study	Edamoto, K.	86-151	254
Angle-resolved Photoemission Study of O <sub>2</sub> Adsorption on NbC(100)	Edamoto, K.	86-151	255
Photoemission from SmRh <sub>3</sub> B <sub>2</sub>	Sugawara, H.	87-184	256
Photoionization Quantum Yield of Dimethylether in the Extreme-UV Region	Ukai, M.	87-113	257
Role on Molecular Superexcited States in the Photoionization Quantum Yields	Ukai, M.	87-113	258
Characteristics of Flat Field Spectrometers for Fusion Plasma Diagnostics	Kubo, H.	87-185	259
Threshold Electron-ion Coincidence Measurements of CO <sub>2</sub> <sup>+</sup>	Morioka, Y.	87-186	260
Non-ionizing Decay of Superexcited C <sub>2</sub> H <sub>2</sub> in the Vacuum Ultraviolet Region	Ukai, M.	88-100	261
Vacuum Ultraviolet Fluorescence in the Photodissociation of Superexcited N <sub>2</sub> and O <sub>2</sub>	Ukai, M.	88-100	262
High-resolution Absorption Spectrum of Calcium near the 4p <sup>2</sup> P <sub>1/2,3/2</sub> Edges	Ueda, K.	88-101	263
Absorption Cross Section of Krypton Atom in Its Photoionization Threshold Region	Maeda, K.	88-102	264
Test Operation of a VUV/Soft X-Ray Monochromator for Undulator Radiation at the Photon Factory	Muramatsu, Y.	87-104	265
Angle-resolved Photoemission Determination of the Band Structure of YBa <sub>2</sub> Cu <sub>3</sub> O <sub>7-x</sub> (001)	Sakisaka, Y.	88-U002	266
An Attempt at Pattern Demagnification by Asymmetric Bragg Reflection	Suzuki, S.	87-C008	267
Optical Constants for Coated Thin Films in the Soft X-Ray Region	Kihara, N.	88-C018	268
Photochemical Etching of GaAs at Low Temperature Using Synchrotron Radiation	Terakado, S.	87-C008	269
Synchrotron Radiation Excited Deposition of Silicon Film	Nara, Y.	87-C006	270
Radiation Damage in Silicon Nitride X-Ray Lithography Mask	Mori, I.	87-C006	271

Real Time Surface Analysis with Synchrotron Radiation Photoemission Spectroscopy	Maruo, Y.Y.	88-Y003	272
SRPES and RHEED Studies for the CaF <sub>2</sub> /GaAs(001) Interface	Maruo, Y.Y.	88-Y003	273
Bonding Properties at the CaF <sub>2</sub> /GaAs(111) Interface	Maruo, Y.Y.	88-Y003	274
First Observation of Synchrotron Radiation Post-Ionization Effect	Oshima, M.	88-Y003	275
SRPES Analysis of Interface Reactions between Si and YB <sub>2</sub> Cu <sub>3</sub> O <sub>y</sub>	Oshima, M.	88-Y003	276
Synchrotron Radiation Photoelectron Spectroscopy of Single Crystal Bi-Sr-Ca-CuO	Maeda, F.	88-Y003	277
SRPES Studies of High T <sub>c</sub> Superconductor Surfaces and Interfaces for Contact Formation	Oshima, M.	88-Y003	278
Reaction Mechanism Study with SR- Stimulated Etching of SiO <sub>2</sub>	Takahashi, J.	88-Y003	279
Photoemission and XANES Studies of Si(100) Surface Oxidation	Nakazawa, M.	87-Y002	280
Angle-resolved Photoemission Study of the Pd(110) Clean Surface	Yagi, K.	87-182	281



# THE STRUCTURE STUDIES ON THE THERMAL STABILITY OF $\text{SiO}_2$ -SUPPORTED $\text{V}_2\text{O}_5$

Kiyotaka Asakura, Masahiro Shirai, Junji Inukai and Yasuhiro Iwasawa

Department of Chemistry, Faculty of Science, the University of Tokyo, Hongo, Tokyo 113.

## Introduction

The Vanadium oxide is a catalyst for the partial oxidation of the hydrocarbon. To obtain the high surface vanadium oxide catalyst, the vanadium oxide is often supported on other oxide surfaces.  $\text{TiO}_2$ (anatase) is known as a most efficient support. It is explained as follows.  $\text{TiO}_2$  anatase lattice is crystallographically matched with  $\text{V}_2\text{O}_5$  lattice, hence the  $\text{V}_2\text{O}_5$  crystal epitaxially grows up on the  $\text{TiO}_2$  lattice. However, the mismatching between the support and supported oxide can produce the unexpected new catalyses as we have previously shown(1-3). To assure the contact between the support surface and  $\text{V}_2\text{O}_5$  and to produce the distortion owing to the mismatch we adopt the attached method for the preparation of the supported  $\text{V}_2\text{O}_5$ , using the reaction between the surface OH group and  $\text{VO}(\text{OC}_2\text{H}_5)_3$ .

In this work we prepared  $\text{SiO}_2$ -supported  $\text{V}_2\text{O}_5$  and examined the structure and thermal stability of the  $\text{V}_2\text{O}_5$  on the  $\text{SiO}_2$  by means of EXAFS.

## Experimental

The  $\text{V}_2\text{O}_5/\text{SiO}_2$  was prepared using the reaction between the  $\text{VO}(\text{OC}_2\text{H}_5)_3$  in hexane solution. The supported  $\text{V}_2\text{O}_5$  was then calcined at 673 K or 873 K. EXAFS spectra were measured at BL-10B of Photon Factory.

## Results and discussion

Fig.1 shows the Fourier transform of the  $\text{V}_2\text{O}_5$ . The first peak was directly attributed to the V-O bonding and the second one to the V-V. Fig.2 and Fig.3 show the Fourier transforms of the  $\text{SiO}_2$ -supported  $\text{V}_2\text{O}_5$  calcined at 673 K and 873 K. Only one prominent peak corresponding to V-O, indicating the amorphous structure. No aggregation to  $\text{V}_2\text{O}_5$  was observed even heated at 873 K. This is because of the strong V-O-Si bonding produced in the reaction between the  $\text{VO}(\text{OC}_2\text{H}_5)_3$  and OH groups of  $\text{SiO}_2$ . The Previous EXAFS studies on  $\text{TiO}_2$ -supported  $\text{V}_2\text{O}_5$  produced in a similar way reported that the thermal treatment at 773 K produced the large crystalline  $\text{V}_2\text{O}_5$ (4). Thus the thermal stability of the  $\text{SiO}_2$ -supported  $\text{V}_2\text{O}_5$  increased comparing to that of the  $\text{TiO}_2$ -supported  $\text{V}_2\text{O}_5$  and the amorphous structure was maintained at high temperature.

## References

- (1)A.Kase, K.Asakura, C.Egawa, Y.Iwasawa, Chem.Lett., 1986,855. (2)K.Asakura, Y.Iwasawa, Chem.Lett., 1986,859. (3)K.Asakura, Y.Iwasawa, Chem.Lett.,1988,633. (4)R.Kozlowski, R.F. Pettifer, J.M.Thomas, J.Phys.Chem,87,5176(1983)

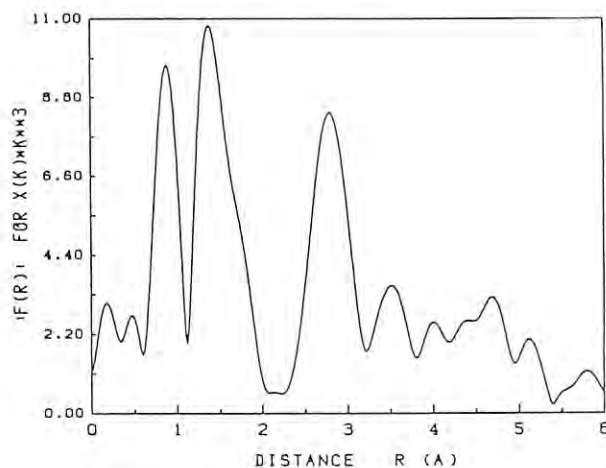


FIG.1 FT of  $\text{V}_2\text{O}_5$

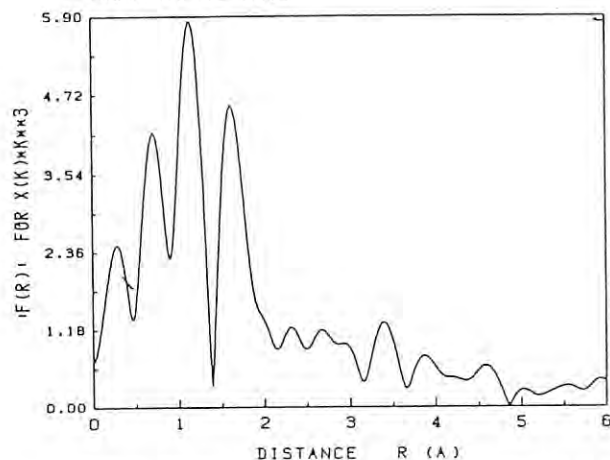


Fig.2 FT of  $\text{V}_2\text{O}_5/\text{SiO}_2$  calcined at 673 K

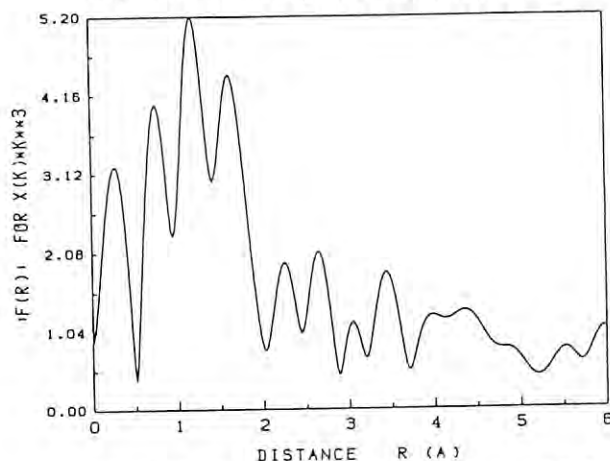


Fig.3 FT of  $\text{V}_2\text{O}_5/\text{SiO}_2$  calcined at 883 K



# PHOTOEMISSION INVESTIGATION OF THE ROOM TEMPERATURE ADSORPTION OF TMG ON GaAs SURFACE

Pierre CLAVERIE, Kousuke UYAMA, Shigeru MAEDA, Mitsuo KOIZUMI, Hidetoshi NAMBA<sup>1)</sup>, Haruo KURODA<sup>1)</sup> and Kenichiro TANAKA<sup>2)</sup>

Kuroda Solid Surface Project, JRDC, 5-9-9 Tokodai, Tsukuba, Ibaraki, 300-26, Japan

1) Research Center for Spectrochemistry and Department of Chemistry, Faculty of Science, University of Tokyo, Hongo, Bunkyo-ku, Tokyo 113, Japan

2) Photon Factory, National Laboratory for High Energy Physics, Oho-machi, Tsukuba, Ibaraki, 305, Japan

## Introduction

Recently, a great deal of interests has been focused on GaAs epitaxial growth by CBE resulting from developments in MBE and MOCVD. However, a number of aspects concerned with this process, such as the adsorbed states and sticking coefficients of source materials, are not yet well understood.

We report here the results of a preliminary study on the adsorption of trimethylgallium (TMG) on GaAs(110) surface at room temperature, which were carried out by means of the ultraviolet photoemission spectroscopy.

## Experimental

The experiments were conducted at the beam line 7B of Photon Factory. The UHV experimental apparatus has a double-pass CMA, LEED, quadrupole mass spectrometer, gas handling system and so on. The base pressure of UHV chamber is  $5 \times 10^{-11}$  torr. Ar ion sputtering (700eV, 30min.) and successive annealing at 350 °C were employed to obtain a clean reconstructed (1x1) GaAs(110) surface.

## Results and Discussion

We found that the TMG adsorption at room temperature reached saturation for an exposure to TMG as low as 3L. From the measurement of AES, the saturation coverage was estimated to be less than 0.1 monolayer. The stoichiometry of GaAs surface is known to vary depending on the condition taken in the cleaning procedures, but no direct correlation was found between the saturation coverage and the degree of As depletion from the surface.

The photoemission spectrum of a clean GaAs surface with 21eV stimulation, is shown in Figure 1, together with the spectra after 1L and 3L TMG exposures. The origin of the photoemission peaks of clean GaAs has been well established<sup>1)</sup>, according to which the first broad peaks in the 5-8eV region, which is associated with the p-like bonding states, is composed of two components (denoted 1 and 2 in fig.1(A)), among which the component 1 is attributable to the As associated p dangling bonds. The peaks 3 and 4 are due to the states mainly associated with Ga4s orbital with a small admixture of As4p orbitals. TMG molecule has two photoemission peaks in the 5-15eV region. From the comparison between the spectra (B) and (C) in fig.1, we can see that, on increasing TMG exposure, the intensity increases in the regions corresponding to the photoemission peaks of TMG (peak c: Ga-C, peak e: 1t2 orbital of methyl group<sup>2)</sup>). The intensity of the component which is mainly due to

As dangling bond (peak a), is expected to decrease to a great extent upon TMG adsorption. In fact, its intensity decreases a little after TMG exposure, but did not completely disappear. Although it is hard to extract a quantitative information, the results of deconvolution analysis clearly indicate that the spectra observed after TMG adsorption can be regarded as a simple superposition of the components due to TMG molecule and those of GaAs, indicating that TMG molecules are adsorbed on GaAs surface without decomposition and possibly most of them are just physically adsorbed.

In conclusion, we were able to elucidate, for the first time, some characteristic features concerned with TMG adsorption on GaAs surface at room temperature by using photoemission spectroscopy. The saturation occurs at the TMG exposure up to 3L, and the coverage at this state is less than 0.1 monolayer. All the observed data indicate that most TMG molecules are adsorbed without decomposition at least at room temperature.

## References

- 1) G.D.Davis, et al. J. Electron Spectrosc. Relat. Phenom. 23(1981)25
- 2) G.K.Barker, et al. J. Chem. Soc. Dalton Trans. (1975)1765

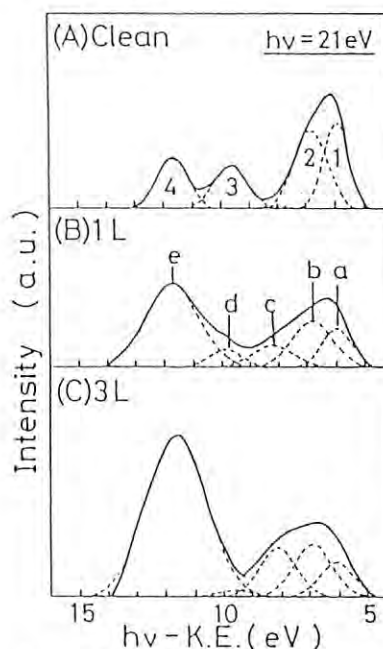


Figure 1 Photoemission spectra (A) clean surface (B) 1L TMG exposure, and (C) 3L exposure. The result of deconvolution is shown with broken line

## STUDY ON SOLID SOLUTION STRENGTHENING OF AUSTENITIC STEELS BY EXAFS

KOJI SHIBATA, NOBUHIKO KONDOH, KATSURO ODA, KOUZOU FUJITA AND MASAHARU NOMURA\*

Department of Metallurgy and Material Science, Faculty of Engineering,  
The University of Tokyo, Hongo, Bunkyo-ku, Tokyo 113\*Photon Factory, National Laboratory for High Energy Physics  
Oho-machi, Tsukuba-shi, Ibaraki 305Introduction

Carbon and nitrogen atoms strengthen steels remarkably. The mechanism, however, have remained unclarified. Shibata et al.<sup>1</sup> found that austenitic steels strengthened by nitrogen and carbon were noticeably softened by low cycle fatigue deformation. Such softening can be explained quantitatively by presuming an existing of short range ordering (I-S complex) between substitutional and interstitial atoms and its breakdown during cyclic deformation. Any direct evidence of the existence of such an I-S complex, however, has never been shown. The present authors<sup>2</sup> found that the existence of interstitial atoms around Cr atoms decreased the depth of the shoulder peak in absorption spectra of Cr K-edge. In the present work, the change in the shape of the shoulder peak were examined by using the other austenitic steels.

Experimental procedures

Fifteen steels with and without alloying interstitial atoms were melted in vacuum furnaces. Ingots were hot worked to plates. After solution treatment the plates were water quenched and machined to round bar specimens for cyclic and tensile deformations which were carried out with an Instron-type machine at ambient temperature. Thin plates were cut from as-solution treated and deformed specimens, and were polished mechanically and then electrolytically to foils of 20 to 40  $\mu\text{m}$  in thickness for XANES observations. The XANES observations were performed at room temperature by using synchrotron radiation at 7C beam line of the Photon Factory.

Results

In all the series of the investigated steels, the depth of the shoulder peak of the as-solution treated steels was decreased by carbon and nitrogen alloyings. It was found that Si decreased also the depth. The results were summarized and shown by Fig.1. In this figure, the depth was normalized. The effects of the deformation on the depth were not noticed. The results of 15Cr-15Ni-C and 15Cr-15Ni-N series steels were shown by Fig. 2.

Conclusion

It was found that the depth of the shoulder peak was decreased not only by nitrogen and carbon atoms but also by silicon atom in the austenitic stainless steels. The systematic effects of cyclic and tensile deformation on the depth were not observed.

References

- 1) K. Shibata et al.: Fatigue at Low Temperatures, ASTM STP 857(1985), Philadelphia, p.31
- 2) N. Kondoh et al.: Photon Factory Activity Report, KEK, 5(1987), p.173

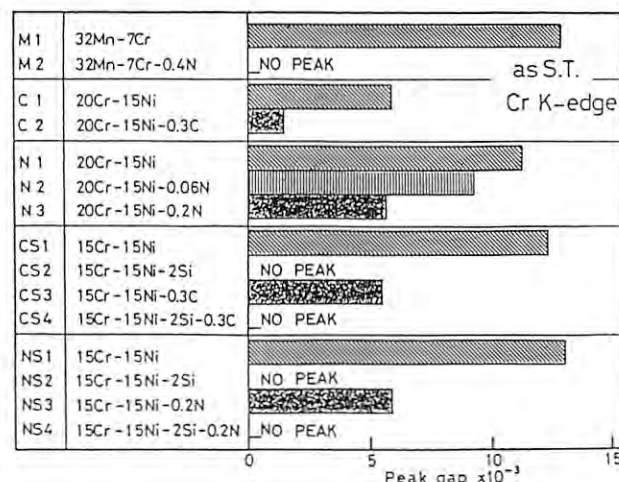


Fig.1 The effect of alloying element on the depth of the shoulder peak in Cr K-edge absorption spectra of various austenitic steels.

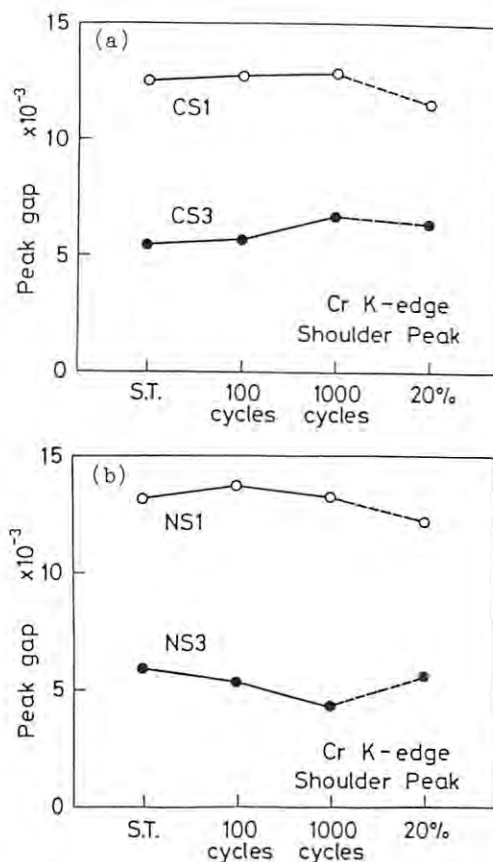


Fig.2 The effect of cyclic and tensile deformations on the depth of the shoulder peak of (a) 15Cr-15Ni-C and (b) 15Cr-15Ni-N series steels.

Br AND Ge EXAFS STUDIES OF AgBr-Ag<sub>2</sub>O-GeO<sub>2</sub> GLASSES

Hideki MORIKAWA, Yutaka SHIMIZUGAWA, Yasunori TABIRA, Satoru YAMAZAKI,  
Fumiyuki MARUMO and Masayuki YAMANE\*

Research Laboratory of Engineering Materials, Tokyo Institute of Technology,  
Nagatsuta 4259, Midoriku, Yokohama 227

\*Department of Inorganic Materials, Tokyo Institute of Technology, Oookayama, Tokyo 152

### Introduction

Glasses with high ionic conductivity have been prepared in the systems on silver halides.<sup>1,2</sup> Local structures around Ge and Ag atoms of the glasses in the system AgI-Ag<sub>2</sub>O-GeO<sub>2</sub> have been investigated by EXAFS method.<sup>2,3</sup> Ionic conductivity of the glasses containing AgI probably results from similar atomic configuration around Ag atoms between glasses and AgI crystals since AgI crystals show ionic conductivity. The glasses containing AgBr show ionic conductivity<sup>4</sup> although AgBr crystals do not show ionic conductivity. The present report describes Br and Ge EXAFS studies of AgBr-Ag<sub>2</sub>O-GeO<sub>2</sub> glasses.

### Experimental and Results

Mixtures of AgBr, Ag<sub>2</sub>O and GeO<sub>2</sub> were melted in a silica crucible and the melt was poured on to a copper plate to obtain glass. The table 1 listed the nominal compositions of the glasses prepared.

Table 1 Chemical compositions and results of EXAFS analysis.

Sample	Chemical composition(mol%)			O/Ge ratio	Bond distance(Å)	
	GeO <sub>2</sub>	Ag <sub>2</sub> O	AgBr		Br-Ag	Ge-O
G20	20	40	40	4.0	2.76	1.76
G30	30	30	40	3.0	2.76	1.77
G40	40	24	36	2.6	2.77	1.81
AgBr	-	-	100	-	2.89	-
GeO <sub>2</sub>	100	-	-	-	-	1.74

EXAFS spectra of the glasses in the neighborhood of the Br and Ge K absorption edges were measured by the normal absorption mode using a two crystal Si(111) monochromator. AgBr and GeO<sub>2</sub> crystals were used for reference samples. Powder sample was mixed with polyethylene powder and then pressed to a disc with a diameter of 12 mm, which was used for EXAFS measurements.

The  $k^3\chi(k)$  data were Fourier transformed to get  $|F(r)|$  curves which were shown in Fig.1(a) for Br EXAFS data and in Fig.1(b) for Ge EXAFS data. Atomic distances of the first coordination shell was analysed by the curve-fitting method using theoretical values of phase shifts and backscattering amplitudes. The values of atomic distances for Br-Ag and Ge-O were listed in Table 1.

Average Br-Ag distances for the glasses samples were obtained by the present EXAFS analysis to be

2.76-2.77 Å. These values clearly shorter than the Br-Ag distance of 2.89 Å in AgBr crystals where each Ag atom is octahedrally surrounded by six Br-atoms. Therefore, the average coordination number of Br atom in the glasses is less than six. It is probable that some of Br atoms are tetrahedrally surrounded by Ag atoms as found in AgI crystals and the structural similarity around halogen atoms between AgI crystal and AgBr-Ag<sub>2</sub>O-GeO<sub>2</sub> glass may be one of the reasons for ionic conductivity of the glasses.

The average Ge-O distances were estimated to be 1.76-1.81 Å. The coordination geometry of Ge atom in AgBr-Ag<sub>2</sub>O-GeO<sub>2</sub> glasses were very similar to that in AgI-Ag<sub>2</sub>O-GeO<sub>2</sub> glasses.

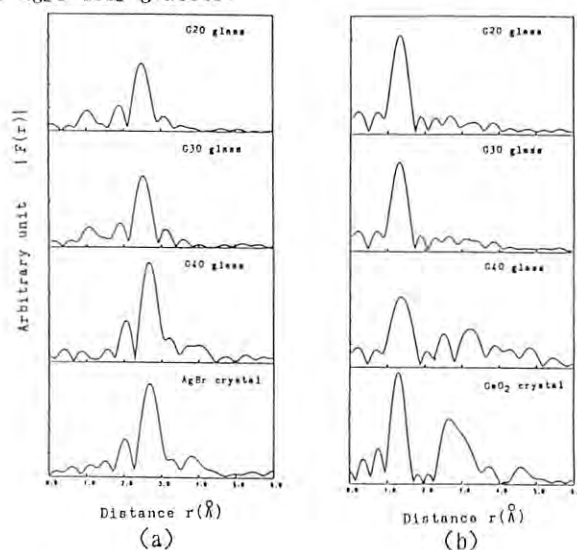


Fig.1 Fourier tranform magnitudes of (a)Br EXAFS data and (b)Ge EXAFS data. No corrections for phase shifts and inner potential energy were applied.

### References

- 1) T. Minami, J. Non-Cryst. Solids, **56**, 15(1983)
- 2) C.D. Yin, T. Osuka, H. Morikawa, F. Marumo and H. Oyanagi, J. Non-Cryst. Solids, **74**, 237(1985)
- 3) H. Morikawa, T. Osuka, C.D. Yin, M. Okuno and F. Marumo, J. Ceram. Soc. Japan, **95**, 551(1987)
- 4) T. Minami and A. Yamane, Chem. Express, **1**, 567(1986)



AN EXAFS STUDY OF Co-Mn and Fe-Mn BIMETALLIC SOLVATED METAL ATOM  
DISPERSED CATALYSTS

Hiroyoshi KANAI, Tsunehiro TANAKA<sup>1)</sup>, Satohiro YOSHIDA,  
Beng Jit TAN<sup>2)</sup>, and Kenneth J. KLABUNDE<sup>2)</sup>  
Department of Hydrocarbon Chemistry, Faculty of Engineering,  
Kyoto University, Sakyo-ku, Kyoto 606

The EXAFS study of highly active Co-Mn/SiO<sub>2</sub> bimetallic SMAD(Solvated Metal Atom Dispersed) catalysts<sup>3)</sup> has revealed that metallic cobalt species are highly dispersed at the expense of manganese fixed to silica.<sup>4)</sup> We will further discuss on the EXAFS of Al<sub>2</sub>O<sub>3</sub> supported Co- and Fe-Mn bimetallic SMAD catalysts to elucidate their characteristic features in relation to the catalysis.

## Experimental

All operations were done under highly purified N<sub>2</sub>. Co- and Fe-Mn/Al<sub>2</sub>O<sub>3</sub> SMAD catalysts prepared according to the method described previously<sup>4)</sup> were mixed with polyethylene powder, followed by pressing into pellets which were sandwiched between two polyethylene pellets. They were sealed in Q-pack pouches. EXAFS measurements were run at the BL-7C station.

## Results and Discussion

**Co- and Co-Mn/Al<sub>2</sub>O<sub>3</sub>(Fig. 1A)** The monometallic Co/SiO<sub>2</sub> contains significant amounts of Co-O bonds with silica.<sup>3)</sup> A low loading monometallic Co/Al<sub>2</sub>O<sub>3</sub> has revealed metallic species with subsidiary amounts of Co-O bonds. Exposure to air changed metallic species into oxides. However, high loading causes agglomeration of Co clusters showing still Co-Co bonds exposure to air. The higher activity of the Co/Al<sub>2</sub>O<sub>3</sub> catalyst in the FT reactions<sup>3)</sup> is ascribed to the more highly dispersed state of metallic Co species than Co/SiO<sub>2</sub>. The addition of Mn causes most of Co species more reactive dispersed metals. The much addition of Mn forces the tendency so that most of Co are reacted into oxides on exposure to air. **Fe- and Fe-Mn/Al<sub>2</sub>O<sub>3</sub>(Fig. 2B)** Complicated FTs can be seen for supported Fe SMAD catalysts. Higher Fe loading than 4% gave rise to agglomeration of Fe metals, some of which were kept metallic on exposure to air. However, some parts of metals were reacted into oxides to result in a lowering of metallic Fe-Fe peaks. All fresh Fe catalysts have Fe-O bonds despite the addition of Mn. The less catalytic activity of Fe SMAD catalysts than that of Co<sup>3)</sup> is due to the less amounts of highly dispersed metallic species.

## References

- 1)Department of Chemistry, Faculty of Science, Hokkaido University, Sapporo 060. 2)Department of Chemistry, Kansas State University, Manhattan, KS 66506, U.S.A. 3)K.J.Klabunde and Y.Imizu, J. Am. Chem. Soc., 106, 2721 (1984); H.Kanai, B.J.Tan and K.J.Klabunde, Langmuir, 2, 760 (1986). 4)H.Kanai, T.Tanaka, S.Yoshida, B.J.Tan and K.J.Klabunde, PF Report, No 4, 181 (1988); B.J.Tan, T.Tanaka, H.Kanai, S.Yoshida and K.J.Klabunde, J. Am. Chem. Soc., 110, 5951 (1988).

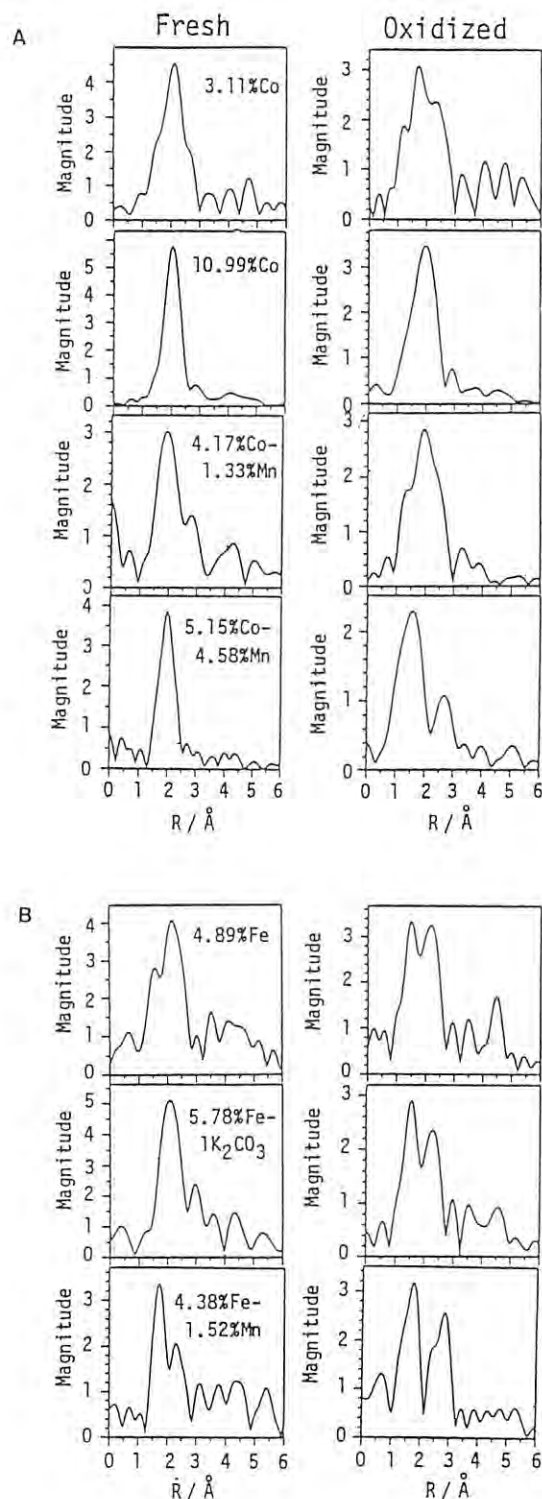


Fig. 1 Fourier transforms of Al<sub>2</sub>O<sub>3</sub> supported Co(A) and Fe(B) SMAD catalysts.

## LOCAL STRUCTURE AROUND Fe ATOM IN Bi-Zn-Fe-O MAGNETIC GLASS

Masaki SAKURAI, Fumitake ITOH, Toshiharu FUKUNAGA, Kenji SUZUKI  
Masaharu NOMURA\*, Tadashi MATSUSHITA\*

Institute for Materials Research, Tohoku University,  
Katahira 2-1-1, Sendai 980

\*Photon Factory, National Laboratory for High Energy Physics  
Oho 1-1, Tsukuba 305

## INTRODUCTION

Ferromagnetic-like glasses have been obtained by melt quenching from a certain mixture of antiferromagnetic  $\text{BiFeO}_3$  and  $\text{ZnFe}_2\text{O}_4$ <sup>1)</sup>. In order to understand why the glass state can be stably formed and why the ferromagnetic-like properties appear only in the glass state, we studied the local structure around Fe atoms by means of EXAFS spectroscopy.

## EXPERIMENTAL

$\text{BiFeO}_3$  glass and  $(\text{BiFeO}_3)_3(\text{ZnFe}_2\text{O}_4)$  glass were prepared by three kinds of method; melt quenching(MQ), Reactive-Ionized-Cluster-Beam(R-ICB) deposition, and solid state amorphization where mechanical alloying(MA) and mechanical grinding(MG) are included. The Fe K-edge EXAFS spectra in these specimen were measured at BL-7C station in both absorption and fluorescence mode. Fused quartz mirror was used to reduce contamination from higher order harmonics. Structure parameters were determined by a curve fitting using empirical phase shift and back scattering amplitude parameter with program EXAFS2<sup>2)</sup>.

## RESULTS AND DISCUSSION

Figure 1 show the Fourier transforms of  $k^3$ -weighted K-edge EXAFS of Fe in  $(\text{BiFeO}_3)_3(\text{ZnFe}_2\text{O}_4)$  glasses without taking account of phase shift. Curve fitting results about the first peak at  $r=1.5\text{\AA}$  which is attributed to Fe-O atomic correlation are tabulated in table-1. It can be seen that coordination number(N) and distance(r) of all glasses under study are decreased from N=6 to 4-5 and from  $r=1.98\text{\AA}$  to  $1.93 - 1.95\text{\AA}$ , respectively, compared to crystalline  $\text{BiFeO}_3$ . These facts mean that almost all Fe atoms are tetrahedrally surrounded by 4 oxygen atoms in glass state, resulting in stability of the glass state. This observation is consistent with the

Table 1 Results of curve fitting analysis for  $(\text{BiFeO}_3)_3(\text{ZnFe}_2\text{O}_4)$  glasses

Method	State	Fe-O	
		N	R / $\text{\AA}$
MA 72hr	Amorphous + crystalline	5.4	1.98
MA 250hr	Amorphous + crystalline	5.3	1.98
ICB	Amorphous, ferrormagnetic	5.1	1.94
ICB	Amorphous, non-ferrormagnetic	5.0	1.93
MQ	Amorphous	3.7	1.93
Standard	$\text{BiFeO}_3$ crystal	( 6.0 )	( 1.98 )

Zachariasen's glass-network formation rule in which the cations surrounded by 4 or less than 4 oxygen atoms form stable glass-network.

A second peak around  $r=2.6\text{\AA}$  in Fig.1 corresponds to Fe-Fe atomic correlation as can be seen from the specimen of MG 0hr. The increase of milling time decreases the height of peak with growth of vitrification. The specimen with milling time of 250hr has still crystalline phase left in the matrix. The shape and position of the 2nd peak in ICB-glass(ferro) and MQ-glass seem different from those in ICB-glass(non-ferro), and also from that in crystalline state. Therefore, ferromagnetic-like behaviors in ICB and MQ glasses may be related to this second peak in F(r).

(1) K. Suzuki, H. Onodera, M. Sakurai, S. Masuda, A. Matsumoto and H. Sadamura, IEEE Trans. Mag. 22(1986)1090.

(2) N. Kosugi, H. Kuroda: PROGRAM EXAFS2/V03, Reserch center for Spectrochemistry, Faculty of Science, Univ. Tokyo (1987).

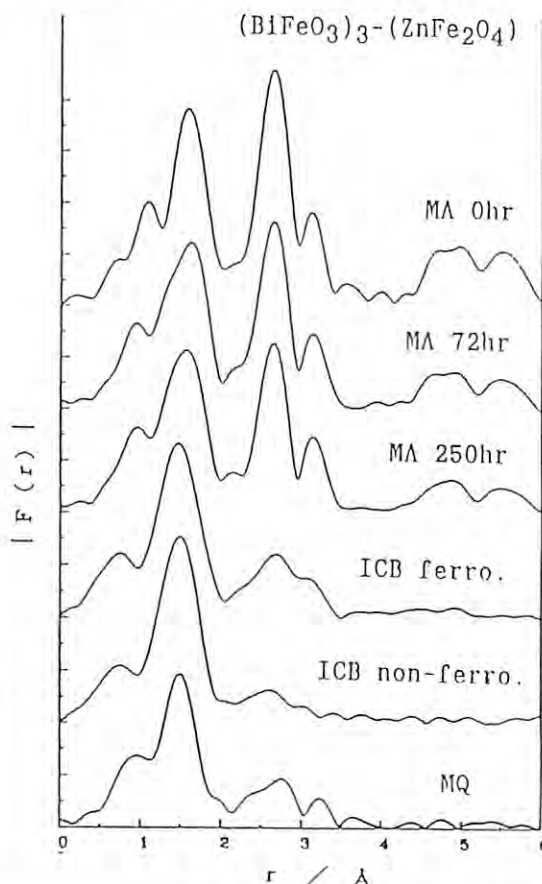


Fig.1 Fourier transform of  $k^3$ -weighted Fe K-edge EXAFS

## EFFECTS OF ALLOYING ELEMENTS IN STEELS ON EXAFS

KOJI SHIBATA, NOBUHIKO KONDOH, KATSURO ODA, KOUZOU FUJITA AND MASAHARU NOMURA\*

Department of Metallurgy and Material Science, Faculty of Engineering,  
The University of Tokyo, Hongo, Bunkyo-ku, Tokyo 113\*Photon Factory, National Laboratory for High Energy Physics  
Oho-machi, Tsukuba-shi, Ibaraki 305Introduction

Carbon and nitrogen atoms strengthen steels remarkably. Shibata et al.<sup>1</sup> suggested the strengthening was due to an existing of short range ordering (I-S complex) between substitutional and interstitial atoms according to their observation of remarkable softening of steels strengthened by carbon and nitrogen through cyclic deformation. Any direct evidence of the existence of such an I-S complex, however, has never been shown. Therefore, the present authors<sup>2,3</sup> examined the effects of C, N and Si and deformation on XANES of various austenitic steels in order to have the direct evidence of the I-S complex. The evidence, however, has never been obtained, although interesting phenomenon was observed concerning the effects of the alloying elements on the depth of the shoulder peak in absorption spectra of Cr K-edge<sup>2,3</sup>. In the present work, the effects of C, N, Si and deformation on EXAFS were examined.

Experimental procedures

The EXAFS observations were performed at room temperature by using the same specimen foils as those used in the previous XANES experiments<sup>3</sup>.

Results

It was found that the height of the first neighbor peak in Fourier transform curve for Cr K-edge changed by the alloying of C, N and Si, and deformation. Fig.1 exhibits the results for the as-solution treated specimen. The peak height is decreased by the alloying of C, N and Si. Fig.2 shows the effect of deformation on the peak height of 32Mn-7Cr steels. Cyclic deformation increases the peak height of the steels with N. The decrease in the peak height by the alloying of C and N is attributable to the wider distribution of atomic distance between Cr atoms and nearest neighbor substitutionals due to the formation of the I-S complex between Cr and interstitial atoms. Silicon may enhance the effects of the interstitial atoms through the increasing their activity. The increase in the peak height by the deformation can be explained by the narrowing of the distribution due to the breakdown of the complex by dislocation movements during the deformations.

Conclusion

The change of the height of the first neighbor peak in Fourier transform curves with the alloying of C, N and Si, and deformations suggested the existence of the I-S complex.

References

- 1) K. Shibata et al.: Fatigue at Low Temperatures, ASTM STP 857(1985), Philadelphia, p.31
- 2) N. Kondoh et al.: Photon Factory Activity Report, KEK, 5(1987), p.173
- 3) K. Shibata et al.: in this activity report (proposal no. 86-082)

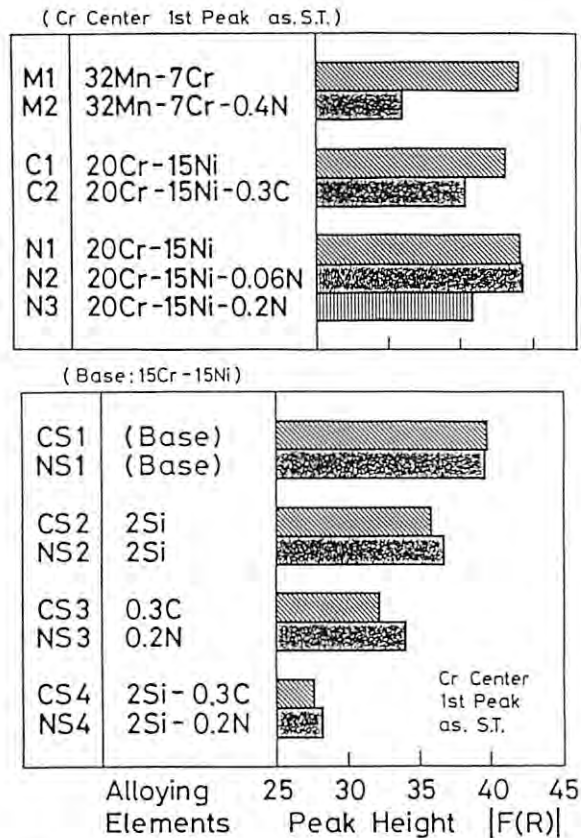


Fig.1 The effect of alloying element on the height of the first neighbor peak in Fourier transform curve for Cr K-edge. Symbols of steels are the same as the previous report.

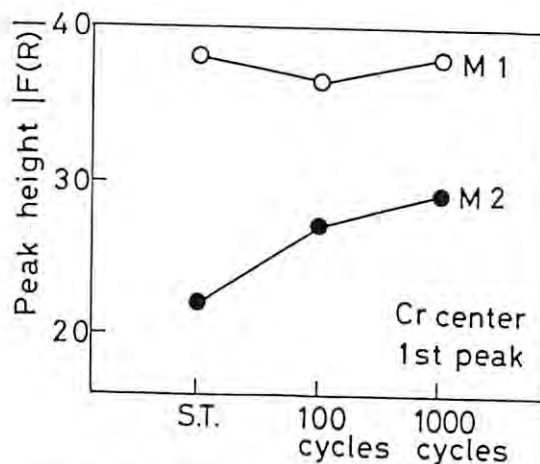


Fig.2 The effect of cyclic deformation on the height of the first neighbor peak in Fourier transform curve for Cr K-edge.

## EXAFS STUDY OF SELENOMETALLOTHIONEIN STRUCTURE

Nobuyoshi ESAKI,<sup>1)</sup> Hironobu MAEDA,<sup>2)</sup> Tadao OIKAWA,<sup>1)</sup> Hiromu SAKURAI,<sup>3)</sup> Yuzuru HIRAGI,<sup>1)</sup> Takatoshi MURATA,<sup>4)</sup> Hidehiko TANAKA,<sup>5)</sup> and Kenji SODA<sup>1)</sup>

<sup>1)</sup>Institute for Chemical Research, Kyoto University, Uji, Kyoto-Fu 611, <sup>2)</sup>Department of Chemistry, Okayama University, Okayama 700, <sup>3)</sup>Department of Pharmaceutical Sciences, Tokushima University, Tokushima 770, <sup>4)</sup>Department of Physics, Kyoto University of Education, Kyoto 612, <sup>5)</sup>Department of Agricultural Chemistry, Okayama University, Okayama 700

### Introduction

Metallothioneins (MTs) are a class of low-molecular weight and cysteine-rich proteins, which bind with high amount of metal ions such as Zn, Cd, and Cu. *Neurospora* Cu-MT consists of only 25 amino acids and binds 6 Cu ions to 7 cysteinyl residues: the smallest MT thus far isolated. Recently, we synthesized selenium analogue of the MT peptide (selenometallothionein (SeMT)), in which all the cysteine residues are replaced by selenium counterparts, to study the structure of the Cu-selenolate cluster in a SeMT-Cu complex. In contrast to the native Cu-MT complex, 3 Cu ions are coordinated in the form of a single Cu(II)-selenolate cluster. To obtain further insight into the structure of the complex, we have attempted an X-ray absorption study.

We here describe the EXAFS spectra of the SeMT-Cu complex to compare with those of the MT-Cu complex.

### Results and Discussion

MT and SeMT were prepared with an Applied Biosystems peptide synthesizer 430A. X-ray spectra were measured by fluorescence mode with a Lytle detector at BL7C. Data were measured on the frozen solution, kept at 18°K, with a thermoelectric cooling module. Two data scans were averaged to give the reported spectra.

The XANES oscillations of the Cu complexes of MT and SeMT revealed a remarkable similarity (Fig. 1). This indicates that the structure of Cu(II)-thiolate cluster in the CuMT is similar to that of Cu(II)-selenolate cluster in the selenium counterpart. CuS was reported to resemble CuSe in the crystal structure: Cu is in a tetrahedral coordination to 3 S<sub>I</sub> (R = 2.09 Å) and 1 S<sub>II</sub> (R = 2.32 Å). We have applied these values to the analysis of the structure of Cu-MT complex. Fig. 2 shows a proposed structure of the Cu(II)-thiolate cluster. Se-MT was analyzed also by Se-EXAFS in order to confirm the proposed structure (Table 1).

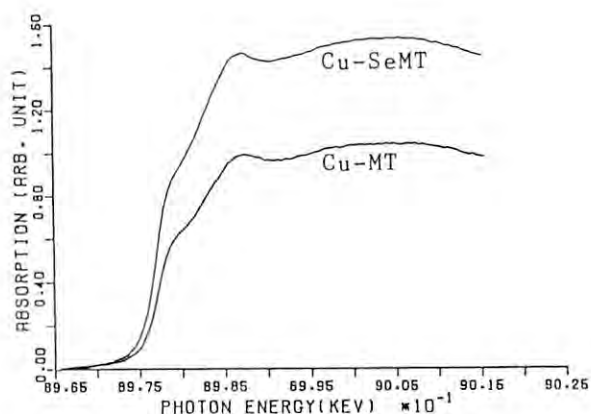


Fig. 1. XANES spectra for Cu-MT and Cu-SeMT

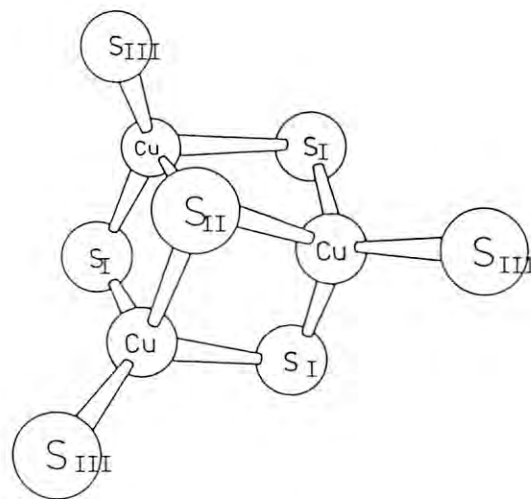


Fig. 2. Proposed arrangement of Cu-thiolate cluster in Cu-MT

Table 1. Interatomic Distances (Å)		
	Cu EXAFS	Se EXAFS
Cu-Se <sub>I</sub>	2.31	2.29
Cu-Se <sub>II</sub>	2.36	2.29
Cu-Se <sub>III</sub>	2.58	2.63
C-Se		1.99
Cu-Cu	3.14	
Se-Se		3.09
Cu-S <sub>I</sub> , Cu-S <sub>II</sub>	2.21	
Cu-S <sub>III</sub>	2.32	



## AN EXAFS STUDY OF THE SILICA SUPPORTED VANADIUM OXIDE CATALYSTS PREPARED BY CVD METHOD

Tadahide SONE, Hiroyoshi KANAI, Yasuo NISHIMURA, Tsunehiro TANAKA\* and Satohiro YOSHIDA  
 Division of Molecular Engineering and Department of Hydrocarbon Chemistry,  
 Kyoto University, Sakyo-ku, Kyoto 606.

### Introduction

Isolated  $\text{VO}_4$  tetrahedra on silica are supposed to be the active species in the photo-oxidation of alcohols.<sup>1)</sup> Previous XANES and EXAFS studies show that isolated  $\text{VO}_4$  species exist on dried catalysts, while  $\text{H}_2\text{O}$  molecules tie adjacent  $\text{VO}_4$  species.<sup>2)</sup> In order to form highly dispersed  $\text{VO}_4$  tetrahedra species on silica, we have applied CVD technique via a direct reaction between silica and vaporized metal oxide precursors.

### Experimental

Three types of silica supported vanadium oxide catalysts ( $\text{V}_2\text{O}_5$ , 6 % by weight) were prepared. Catalysts by CVD method (VSCVD) were prepared as follows;  $\text{VO}(\text{OPr}^i)_3$  was vaporized through bubbling of carrier gas ( $\text{N}_2$ ). It was reacted with silica (JRC-SIO-4 30-48 mesh) in a flow bed reactor. These treatments were carried out at r.t. under the pressure of 6-10 torr, followed by drying in vacuo at 373 K for 1 h. The others were prepared by impregnating silica in an aqueous solution of  $\text{NH}_4\text{VO}_3$  (VSIM), and in an n-hexane solution of  $\text{VO}(\text{OPr}^i)_3$  (VSIV), respectively, followed by drying at r.t. All these catalysts were calcined at 673 K for 3 h in an  $\text{O}_2$  atmosphere.

The catalysts were treated in vacuo at 673 K for 3 h and cooled down to r.t. They were mixed with polyethylene powder, pressed into disks and sealed in polyethylene-nylon-polychlorobinylidene films. X-ray absorption experiments were carried out at the Photon Factory(BL-7C).

### Results and Discussion

Normalized K-edge XANES spectra and magnitudes of Fourier transforms(FT) of the samples together with  $\text{V}_2\text{O}_5$  as a reference compound are shown in Fig. 1. Energy offset is taken to the position of the pre edge peak of  $\text{V}_2\text{O}_5$  (5496.7 eV). Energy resolution is 0.5 eV. The peak (24 eV) appearing in the XANES of  $\text{V}_2\text{O}_5$  is assigned to 1s-4p transition. Shoulders are observed at around 24 eV in the XANES spectra of VSIM and VSIV. The intensities increase in the order VSCVD < VSIV < VSIM, which reflects the formation of microcrystalline  $\text{V}_2\text{O}_5$  on silica supported catalysts.

The FTs of  $k^3$  weighted EXAFS are also shown in Fig. 1. The peaks appearing around 1.5 Å and 2-3 Å are due to V-O bonds and V-V bonds, respectively. The V-V bonds which are seen in VSIM, VSIV and  $\text{V}_2\text{O}_5$  suggest that polymeric vanadates are present in both impregnating catalysts. The heights of the

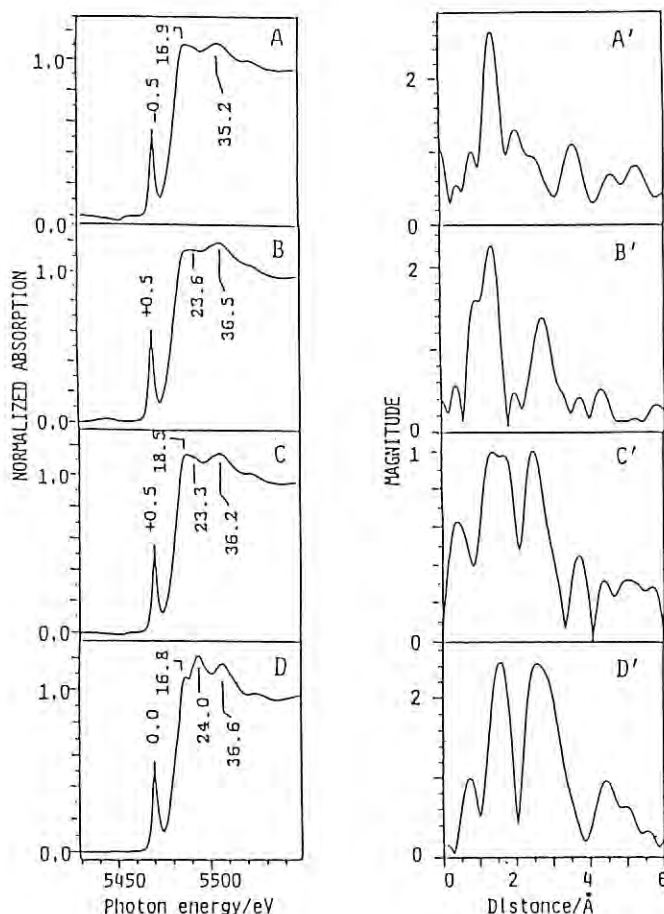


Fig. 1. Vanadium K-edge XANES spectra ( A-D ) and Magnitudes of Fourier transforms ( A'-D' )  
 A: VSCVD B: VSIM C: VSIV D:  $\text{V}_2\text{O}_5$

V-V peaks decrease in the order  $\text{V}_2\text{O}_5$  > VSIM > VSCVD. In particular, there are very low peaks within noise level at longer distance ( $> 2$  Å) in VSCVD. The number of neighbouring vanadium ions in VSIM is smaller than that of  $\text{V}_2\text{O}_5$  crystal, and the vanadium ions in VSCVD are isolated from others. It is concluded that highly dispersed catalyst can be obtained by CVD method.

### References

- (1) S. Yoshida et al., J. Chem. Soc., Faraday Trans. 1, **80**, 119 (1984).
- (2) T. Tanaka et al., Photon Factory Activity Report, #5, 178 (1987).

\* Department of Chemistry, Faculty of Science, Hokkaido University, Sapporo 060.



## STUDY OF Al-Mn QUASI-CRYSTAL BY EXAFS

Hiromitsu INO, Katsuro ODA, Keiichi EDAGAWA, Tatsuo SUGAWARA and Masaharu NOMURA\*

Department of Materials Science, Faculty of Engineering, University of Tokyo,  
7-3-1 Hongou Bunkyo-ku, Tokyo 113\* Photon Factory, National Laboratory for High Energy Physics,  
1-1 Oho Tsukuba-shi, Ibaraki 305

## INTRODUCTION

The Al-Mn quasi-crystalline phase is considered to be constructed by a Penrose aperiodic lattice. Extended X-ray Absorption Fine Structure ( EXAFS ) measurements were performed on the Al-(Mn,Fe) icosahedral alloys containing, in order to obtain the further information on the local configuration of each atoms in this lattice.

## EXPERIMENTAL

We chose  $\text{Al}_{86}\text{Mn}_{14}$  and  $\text{Al}_{73}\text{Si}_{16}\text{Mn}_{11}$  for basic systems. The behavior of Fe was investigated with  $\text{Al}_{86}(\text{Mn}_{1-x}\text{Fe}_x)_{14}$  ( $x = 0, 0.25, 0.50$ ) and  $\text{Al}_{73}\text{Si}_{16}(\text{Mn}_{1-x}\text{Fe}_x)_{21}$  ( $x = 0, 0.25$ ). Samples were made in flake form by melt quenching on a rotating Cu wheel in Ar atmosphere. A crystalline  $\text{Al}_{73}\text{Si}_{16}\text{Mn}_{11}\alpha$ -phase was prepared by annealing the melt quenched alloy for comparison of the EXAFS data. Samples were ground to powder and then rubbed onto Scotch tape. EXAFS measurements were made about the Mn and Fe K- $\alpha$  edges using the beamline BL-7C at the Photon Factory. The EXAFS function,  $k^3\chi(k)$ , were Fourier transformed to real space to obtain the spectra related to the average radial distribution functions of the atoms neighboring the absorbent atoms. The positional order of the atomic sites was evaluated by the sharpness of the first peak of the spectrum. We quantified the sharpness by a parameter  $h/\text{fwhm}$  defined by deviding peak height of the first shell by full width at half maximum.

## RESULTS

Figure 1 shows the spectra of Fourier transformed  $k^3\chi(k)$  of the  $\alpha$ - $\text{Al}_{73}\text{Si}_{16}\text{Mn}_{11}$  crystalline phase and icosahedral  $\text{Al}_{73}\text{Si}_{16}\text{Mn}_{21}$ . The spectrum of the  $\alpha$ -phase is apparently much sharper than those of the icosahedral phases. The parameter  $h/\text{fwhm}$  for the spectra of the Mn and Fe edges of icosahedral  $\text{Al}_{86}(\text{Mn}_{1-x}\text{Fe}_x)_{14}$  and  $\text{Al}_{73}\text{Si}_{16}(\text{Mn}_{1-x}\text{Fe}_x)_{21}$  are shown in Fig. 2. On substitution of Mn by Fe, the sharpness of the peak around Mn increases, while around Fe decreases.

## DISCUSSION

The broadness of the first peak of Fourier transformed EXAFS function in Fig. 1 reflects the ambiguity of the atomic position in icosahedral phase compared with crystalline  $\alpha$ -phase. In icosahedral phase, the atomic sites included in the first shell around the Mn probe atom are much more fluctuating than in the crystalline phase. This would mean that in icosahedral phase, atomic sites can be classified into more groups than in the crystalline phase. From other measurements of  $\text{AlSi}(\text{Mn,Fe})$  icosahedral phase, two kinds of Mn sites, with and without magnetic moment, are proposed, and Fe atoms are considered to occupy the latter sites. Together with the present

result, we propose one simple atomic model. Two kinds of Mn sites are assumed, which differ only in "free volume". Since, Fe atoms are smaller than Mn atoms in size, Fe atoms would first occupy the smallest site when the first Mn atom is substituted. As the substitution rate increases, the distance between the Fe atoms and surrounding atoms will be deviated more from the mean value. At the same time, Mn atoms will gradually be restricted to occupy the larger sites. Therefore, the sharpness of the first peak around Fe atoms decreases and increases around Mn atoms. This further suggests that Mn or Fe atoms in the smaller sites have no magnetic moment.

## REFERENCES

1. A. L. Mackay: Sov. Phys. -Crystallogr., 26 (1987) 517.
2. D. E. Sayers, E. A. Stern and F. W. Lytle: Phys. Rev. Lett. 27(1971) 1204
3. K. Edagawa, H. Ino, S. Nasu, K. Kimura, S. Takeuchi, T. Shinjo, K. Koga, T. Shimizu and H. Yasuoka: J. Phys. Soc. Japan, 56(1987) 2629.

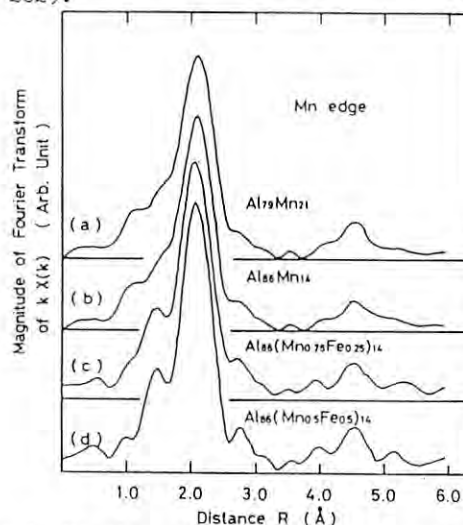


Fig. 1 Spectra of Fourier transformed  $k^3\chi(k)$  of the  $\alpha$ - $\text{Al}_{73}\text{Si}_{16}\text{Mn}_{11}$  crystalline phase and icosahedral  $\text{Al}_{73}\text{Si}_{16}\text{Mn}_{21}$ .

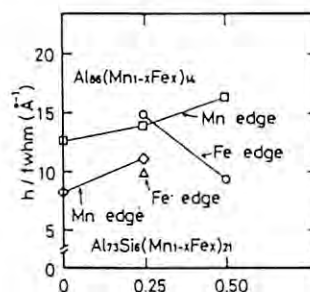


Fig. 2  $h/\text{fwhm}$  for the spectra of the Mn and Fe edges of icosahedral  $\text{Al}_{86}(\text{Mn}_{1-x}\text{Fe}_x)_{14}$  and  $\text{Al}_{73}\text{Si}_{16}(\text{Mn}_{1-x}\text{Fe}_x)_{21}$ .

# XANES MEASUREMENTS FOR Ce VALENCE IN Pd-Ce ORDERING ALLOYS WITH A BASIC STRUCTURE OF FCC LATTICE

Noriyuki KUWANO, Yasutoshi SAITO, Kensuke OKI,  
Seichi YAMASHITA\*, Toshio YAMAGUCHI\* and Hisanobu WAKITA\*

Department of Materials Science and Technology, Graduate School of Engineering Sciences,  
Kyushu University-39, Kasuga, Fukuoka 816

\*Department of Chemistry, Faculty of Science, Fukuoka University,  
Nanakuma, Jonan-ku, Fukuoka 814-01

It is known that Ce has an intermediate valence between 3 and 4. Since anomalies in physical properties of Ce-alloys are attributed to the intermediate valence, the correct values for Ce valence are required in order to understand the origin of the anomalies. In this study, Ce valence in Pd-Ce binary alloys was estimated from the X-ray absorption near edge structure (XANES) as functions of Ce concentration and heat-treatment.

Alloys ingots of Pd-Ce with 12.5, 14.5, 16.7, 17.2 and 24.5 at%Ce were prepared by arc melting in high purity argon. The alloys are known to have ordered structures of an fcc basic lattice.<sup>1-5)</sup> The ingots were annealed for prolonged time at proper temperatures to promote homogenization. Powder specimens made by filing under Ar enriched atmosphere were sealed in evacuated quartz capsules and annealed at various temperatures, followed by quenching. X-ray diffraction patterns were recorded to examine the alloy phases of the powder specimens. XANES spectra were taken, using the facility of BL-7C, at energy intervals of about 0.54 eV with a double crystal monochromator of Si(111).

Figure 1 shows an example of the observed XANES spectra for Pd-16.7 at%Ce annealed at 873 K or 973 K. One can see a doublet of L<sub>III</sub> edge of Ce, corresponding to Ce<sup>3+</sup> and Ce<sup>4+</sup>, respectively. The doublet indicates that the valence of Ce in these alloys has a fractional value between 3 and 4. It should be noted that the ratio of the peak height of Ce<sup>3+</sup> to Ce<sup>4+</sup> for the alloy annealed at 873 K is smaller than the one annealed at 973 K. The variation of peak height implies that the Ce valence decreases with the annealing temperature. We divided the XANES profiles into the components of Ce<sup>3+</sup> and Ce<sup>4+</sup> by the least squares method, preliminarily assuming that each component consists of a single Lorentzian and arctangent curve:

$$P(E) = \sum_{j=3,4} \langle A_j \Gamma_j / \{ (E-E_j)^2 / \Gamma_j + \Gamma_j \} \rangle + B_j \arctan \{ (E-(E_j+\delta_j)) / C_j \} + P_0$$

The line profiles for Ce<sup>3+</sup> and Ce<sup>4+</sup> thus decomposed are also illustrated in Fig. 1. The ratio in area of the components gives the value for Ce valence, yielding  $\nu=3.39$  and  $3.36$  for the alloys annealed at 873 K and 973 K, respectively. The alloys of 16.7 at%Ce has an ordered structure, and then the degree of order can change with temperature. Actually, it was confirmed by electron microscopy<sup>6)</sup> that the degree of order decreases from unity to 0.7 with increasing temperature from 873 to 973 K. The present result is the first evidence for the dependence of Ce valence on the degree of order. We<sup>7)</sup> measured the electrical resistivity of the alloy between 10 K and 300 K, finding that the resistivity shows anomalous variation depending strongly upon the annealing temperature. The anomalies are thought to be due to the "dense

Kondo effect". It is of great interest that the intermediate valence and the dense Kondo effect are both related to the atomic configuration in the alloy.

One can see in Fig. 1 that there is a small disagreement between the observed XANES profile and the calculated one in the tail around 5710 eV. It is due to the assumption that the profile includes a single Lorentzian which is symmetric. Recently, Röhler<sup>8)</sup> proposed a new procedure where such an asymmetrical peak profile is reproduced by a convolution of a sharp Lorentzian and an asymmetric distribution function. Although the simple analysis mentioned above can give the relative change in Ce valence correctly in the present case, it seems necessary to take the asymmetry of profiles into account in order to investigate the dependence of Ce valence on Ce composition and atomic configuration in detail. The XANES for the alloys with other compositions as well as those shown in Fig. 1 are now being analyzed using Röhler's method.

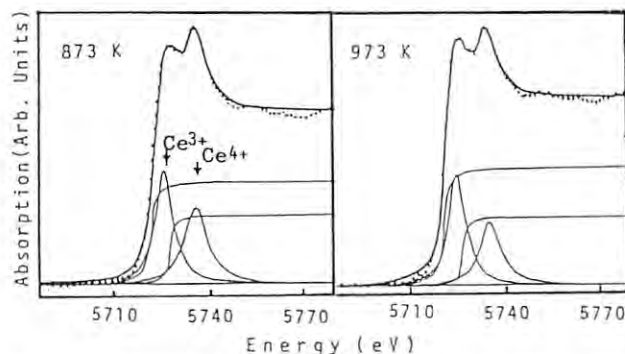


Fig. 1 Observed and calculated XANES spectra for Pd-16.7 at%Ce annealed at 873 K and 973 K

## REFERENCES

- 1) N. Kuwano, T. Shiwaku, Y. Tomokiyo and T. Eguchi: Jpn. J. Appl. Phys., 20, 1603(1981).
- 2) D. A. Smith, I. P. Jones, and T. R. Harris: J. Mater. Sci. Lett., 1, 463(1982).
- 3) N. Kuwano, K. Yamamoto, M. Itakura and K. Oki: Proc. XIth Inter. Cong. Electr. Microsc., Kyoto, (1986), p.1213.
- 4) N. Kuwano, S. Higo, K. Yamamoto, K. Oki and T. Eguchi: Jpn. J. Appl. Phys., 24, L807(1985).
- 5) A. E. Dwight: U. S. At. Ener. Comm., ANL-6330 (1960), p.158.
- 6) M. Itakura, N. Kuwano and K. Oki: (to be submitted to J. Electron Microscopy)
- 7) N. Kuwano et al.: (unpublished work)
- 8) J. Röhler: J. Magn. & Magn. Mater., 47/48, 175(1985).

## STUDIES ON THE LOCAL STRUCTURES OF THE IRON CATALYSTS FOR COAL GASIFICATION

Hiromi YAMASHITA, Yasuo OHTSUKA, Satoshi YOSHIDA<sup>+</sup> and Akira TOMITA

Chemical Research Institute of Non-Aqueous Solutions, Tohoku University, Katahira, Sendai 980, Japan.

<sup>+</sup>Department of Hydrocarbon Chemistry, Faculty of Engineering, Kyoto University, Kyoto 606, Japan.Introduction

Iron compounds are very useful catalysts for the gasification of coal<sup>1</sup>. Many studies have been carried out to know the state of iron catalyst<sup>2</sup>, but the coal with small amount of catalyst loading has not been studied enough. In the present study, the dependence of the structure of iron in the coal on the catalyst loading during the devolatilization or the gasification process has been investigated by EXAFS.

Experimental

Loy Yang brown coal from Victoria, Australia, was used. Several coal samples with different catalyst loading (0.1~20 wt% as metal) were prepared by impregnation method using an aqueous solution of  $\text{Fe}(\text{NO}_3)_3$ . The Fe-loaded coals were devolatilized in  $\text{N}_2$  or gasified in wet- $\text{N}_2$  (steam; 234 Torr) at atmospheric pressure in a small fluidized bed reactor. EXAFS and XANES spectra at Fe K-edge were recorded in a transmission mode on a beam line BL-7C at KEK-PF at room temperature using a Si(111) channel cut monochrometer.

Results and Discussion

Devolatilization of coals were carried out at several temperatures (350~800°C) for 20 min. Figure 1 shows Fourier transforms (F.T.s) of the  $k^3$ -weighted EXAFS spectra. The precursor salt,  $\text{Fe}(\text{NO}_3)_3 \cdot 9\text{H}_2\text{O}$ , in which Fe atom is coordinated octahedrally by six  $\text{H}_2\text{O}$  molecules, exhibited a main peak at near 1.6 Å (phase shift uncorrected). The untreated 10 wt% Fe-loaded coal also exhibited a main peak at 1.6 Å. The smaller peak height indicates that the dehydration occurs and Fe atom is coordinated by oxygen atoms existing on the coal. In the case of char prepared at 550°C, two peaks are observed at near 1.6 and 2.7 Å. The peak at 2.7 Å can be assigned to the neighboring Fe atoms (Fe-Fe) in the oxidized iron compounds. This result suggests that the iron atoms aggregate in the oxidized states. In the case of chars prepared at temperature >600°C, the main peak was observed at near 2.1 Å. This peak can be assigned to the neighboring Fe atoms (Fe-Fe) in the reduced iron compounds. In the case of the char prepared from 0.5 wt% Fe-loaded coal, only a peak due to neighboring O atoms was observed. The aggregation and reduction of iron atoms in the coal with the small amount of catalyst loading are very difficult.

The gasification of coals were carried out at 650°C for 10 min ~ 3 h. Figure 2 shows F.T.s of the  $k^3$ -weighted EXAFS spectra.  $\alpha$ -FeOOH and  $\text{Fe}_3\text{O}_4$  exhibited two main peaks around 1.6 Å (Fe-O) and 2.9 Å (Fe-Fe). The peak at around 2.9 Å (Fe-Fe)

was singlet in the case of  $\alpha$ -FeOOH, but doublet in the case of  $\text{Fe}_3\text{O}_4$ . The predominant features of F.T.s for the 0.5 wt% and 10 wt% sample gasified for 20 min resemble to that of  $\alpha$ -FeOOH. The main peak at around 2.9 Å has a little shoulder in the case of 10 wt% Fe-loaded coal, indicating that some amounts of  $\text{Fe}_3\text{O}_4$ -like crystallites exist in addition to  $\alpha$ -FeOOH. On the other hands, the features of F.T.s of the 10 wt% Fe-loaded coal gasified for 3 h resemble to that of  $\text{Fe}_3\text{O}_4$ . These results indicate that the iron atoms exist as  $\alpha$ -FeOOH crystallites or aggregated  $\text{Fe}_3\text{O}_4$ , and that the proportion of these species much depends on the amount of catalyst loading and on the carbon conversion.

References

- 1) Y.Ohtsuka, Y.Tamai and A.Tomita, *Energy & Fuels*, **1**, 32 (1987).
- 2) Y.Otsuka, Y.Kuroda, Y.Tamai and A.Tomita, *Fuel*, **65**, 1476 (1986).

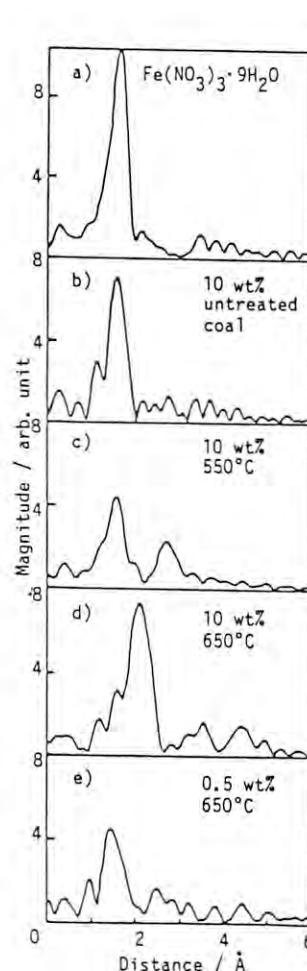


Fig. 1 F.T.s of  $k^3\chi$  after devolatilization (c,d,e)

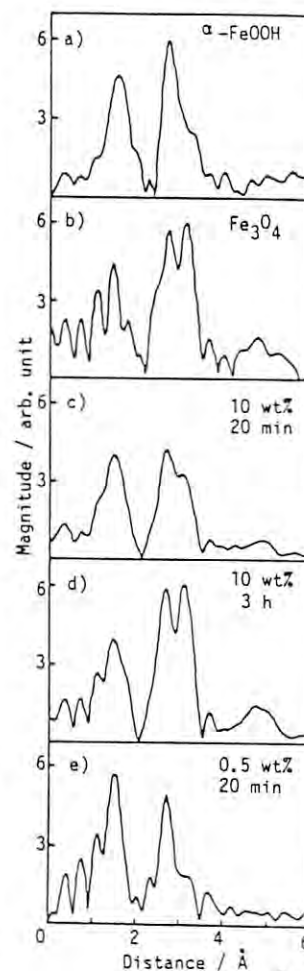


Fig. 2 F.T.s of  $k^3\chi$  after gasification (c,d,e)



STRUCTURE DETERMINATION OF METAL COMPLEXES IN VERY DILUTE  
SOLUTIONS BY FLUORESCENT EXAFS SPECTROSCOPY.  
COPPER(II) CHLORIDE COMPLEXES IN ACETONITRILE

Toshio YAMAGUCHI, Hisanobu WAKITA, and Masaharu NOMURA†

Department of Chemistry, Faculty of Science, Fukuoka University,  
Nanakuma, Jonan-ku, Fukuoka 814-01, Japan

†Photon Factory, National Laboratory for High Energy Physics,  
Oho, Tsukuba 305, Japan

### Introduction

Structural information of metal complexes in solution is essential in understanding details of chemical reactions in solution. X-ray and neutron diffraction methods, which have been used to determine the structure of metal complexes in solution, usually require concentrated solutions to obtain reliable structural parameters, and hence it is very difficult to investigate the structure of intermediate species of very low solubility in solution. In the present study, fluorescent EXAFS spectroscopy is applied to determine metal complexes in very dilute solutions, in which the composition of the metal complexes is known from thermodynamic quantities obtained in the same dilute solutions.

### Experimental

A system investigated was copper(II) chloride in acetonitrile, in which the total copper(II) concentration was kept constant at 10 mM. Figure 1 shows the distribution of each complex calculated from thermodynamic data[1]. Solution samples at compositions B-D were prepared so as to satisfy the compositions used for measurements of thermodynamic data. Sample A was a copper(II) perchlorate acetonitrile solution. X-ray absorption spectra of the CuK-edge were measured in the fluorescent mode at the BL7C of the Photon Factory, KEK.

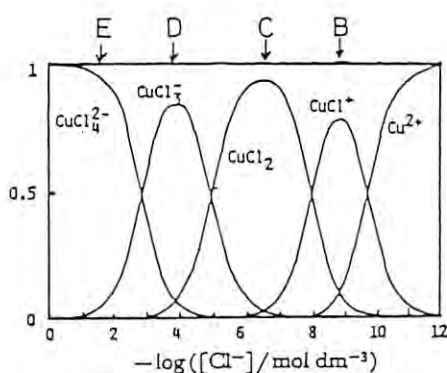


Fig. 1. Distribution of  $[\text{CuCl}_n]^{(2-n)+}$  species in 0.1 M  $(\text{C}_2\text{H}_5)_4\text{NClO}_4$  AN solutions.

### Results and Discussion

Figure 2 shows XANES spectra of sample solutions A-D. A feature of the XANES spectra changes with successive coordination of chloride ions to copper(II). The Fourier transforms of samples A-D are shown in Fig. 3. The first peak is ascribed to interactions between a copper(II) ion and nearest neighbour atoms bound to it. The position of the peak shifts to the longer distance side with formation of copper(II) chloride complexes; the result shows that acetonitrile molecules coordinated to a copper(II) ion are replaced with chloride ions with an increase in chloride ion concentration. At lower chloro complexes the peaks ascribed to non-bonding interactions such as Cu-C and Cu-CH<sub>3</sub> are observed. Structural parameters of each complex were determined by a least-squares fitting procedure applied to Fourier-filtered spectra and summarized in Table 1 with thermodynamic quantities.

### References

- 1) S. Ishiguro, et al. Bull. Chem. Soc. Jpn., 58, 1749 (1985).

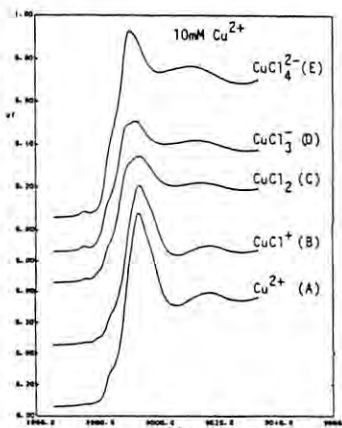


Fig. 2. XANES spectra of solutions A-E.

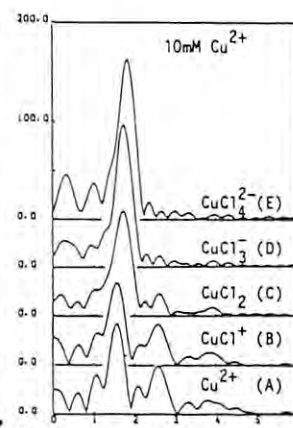


Fig. 3. F.T. of solutions A-E

Table I: Structure and thermodynamic quantities[1]

	Cu - N		Cu - Cl		$\Delta G^a$	$\Delta H^a$	$\Delta S^b$
	$r/\text{\AA}$	$\sigma/\text{\AA}$	$r/\text{\AA}$	$\sigma/\text{\AA}$			
$\text{Cu}(\text{AN})_4^{2+}$	1.98	0.062	—	—	—	—	—
$\text{CuCl}(\text{AN})_3^+$	1.97	0.055	2.18	0.092	-55.3	-11.7	147
$\text{CuCl}_2(\text{AN})_2$	2.01	0.085	2.18	0.075	-45.4	-5.0	135
$\text{CuCl}_3(\text{AN})^-$	2.19	0.19	2.17	0.069	-28.2	-4.4	80
$\text{CuCl}_4^{2-}$	—	—	2.23	0.062	-16.3	-34.3	-61

<sup>a</sup>kJ/mol. <sup>b</sup>J/(K mol).

## EXAFS MEASUREMENTS ON THE COPPER CATALYST PREPARED BY THE NOVEL METHOD.

Hideaki YOSHITAKE, Kiyotaka ASAKURA, Rika KUWABARA\*, and Yasuhiro IWASAWA.

Department of Chemistry, Faculty of Science, the University of Tokyo, Hongo, Tokyo 113.

\*Center for Ceramics Research, Research Laboratory of Engineering Materials, Tokyo Institute of Technology, 4259 Nagatsuta, Midori-ku, Yokohama 227.

### Introduction

The synthesis of a new type of well-defined catalytically active species is one of the intriguing problem in surface science. It is possible that the stepwise double fixation produces bimetallic or dimer clusters with a well-defined structure on the surface.  $\text{Cu}(\text{acac})_2$  is easily reacted with  $\text{CuCl}_2$  to be a dimeric  $\text{Cu}_2$  complex and the precipitate is formed. We first fixed  $\text{Cu}(\text{acac})_2$  complex on the surface of  $\text{SiO}_2$  using the reaction of the silanol and  $\text{Cu}(\text{acac})_2$ . Then  $\text{CuCl}_2$  was reacted with the fixed  $\text{Cu}(\text{acac})_n$  complex to produce the dimer  $\text{Cu}_2$  structure. In this work we measured EXAFS spectra to obtain the information about the surface reaction and the surface transformation.

### Experimental

$\text{SiO}_2$  (ID gel, Fuji Devision) was impregnated with  $\text{CHCl}_3$  solution of  $\text{Cu}(\text{acac})_2$  (Wako Chemical co., Ltd.) under the dry argon atmosphere. After removal of the solvent,  $\text{Cu}(\text{acac})_2/\text{SiO}_2$  (sample ①) was mixed with THF solution of  $\text{CuCl}_2$  and stirred for 3 h at room temperature. Solvent was removed and the catalyst was washed with THF before the drying of the catalyst. The sample (sample ②) was then transferred to the EXAFS measurement cell. EXAFS spectra were taken at BL-7C.

### Results and Discussion

Fig. 1 (a) shows the Fourier transform of  $\text{Cu}(\text{acac})_2$  and  $\text{Cu}(\text{acac})_2/\text{SiO}_2$ , in which the first shell is assigned to be Cu-O bond and the second is to be Cu-C bond for both of the catalysts. This demonstrates  $\text{Cu}(\text{acac})_2$  is supported on  $\text{SiO}_2$  without any transformation of the structure.  $\text{Cu}(\text{acac})_2$  was physically adsorbed on  $\text{SiO}_2$  Fig. 1(b) shows the Fourier transform of the sample catalyst after the addition of  $\text{CuCl}_2$ . The peak was appeared at 0.9 - 1.8 Å which is assigned to be Cu-O bond. No evidence was found for the bond formation of Cu-Cl or Cu-Cu by EXAFS. The comparison between sample ① and ② about C-O bond is illustrated in Table 1. No reaction between surface  $\text{Cu}(\text{acac})_2$  and  $\text{CuCl}_2$  occurred. This must be due to the change of reaction conditions on the surface of  $\text{SiO}_2$ .

Table 1. Results of the Curve-Fitting Analyses of EXAFS Data for the catalysts.

	$\text{CuCl}_2/\text{Cu}(\text{acac})_2$	$\text{Cu}(\text{acac})_2/\text{SiO}_2$	$\text{Cu}(\text{acac})_2$
C.N.	3.8	4.2	4.0
r	1.89	1.91	1.95

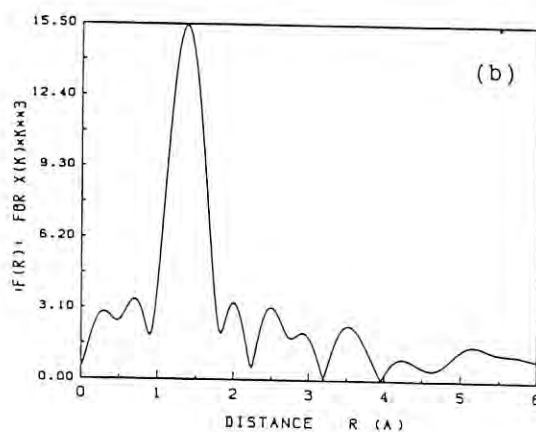
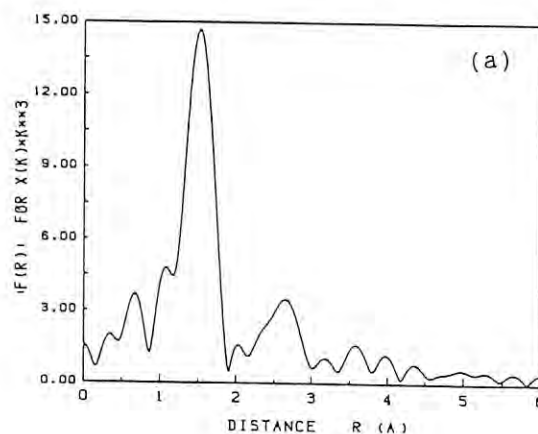


Fig. 1 The Fourier Transform of (a)  $\text{Cu}(\text{acac})_2/\text{SiO}_2$  and (b)  $\text{CuCl}_2/\text{Cu}(\text{acac})_2/\text{SiO}_2$ .

## AN X-RAY (1.7-14keV) BEAM LINE FOR EXAFS STUDIES

Asao Nakano, Osamu Abe<sup>\*3</sup>, Kiyoshi Ogata, Hironaru Yamaguchi and Takao Edamura  
 Production Engineering Research Laboratory, Hitachi, Ltd., 292 Yoshida-cho, Yokohama 244, Japan  
<sup>\*3</sup>Present Address: Hokkaido University of Education, Asahikawa 070, Japan

## Introduction

BL-8B was already utilized for EXAFS measurements of higher energy region than 6keV<sup>1)</sup>. In order to utilize the lower energy region we have improved the double crystal monochromator and accomplished to measure Si-K-EXAFS recently.

## Arrangement of BL-8B

The optical system consists of a double crystal monochromator, a bent cylindrical mirror for focusing and a flat mirror for eliminating the harmonics. The optical system is illustrated schematically in Fig.1. The beryllium X-ray window with the size of 60mm(H) × 8mm(V) and the thickness of 75  $\mu$ m is located between the slits at upstream of the double crystal monochromator. Although the vacuum system is designed to reject the pressure difference between both sides of the beryllium X-ray window even when the BL-8B is broken to the atmosphere, the thickness is determined by a calculation<sup>2)</sup> that the window endures the atmospheric pressure.

Double crystal monochromator is installed in the vacuum chamber evacuated to  $3 \times 10^{-8}$  torr. Two pairs of crystals, InSb(111) and Si(311) are now available and exchangeable automatically without breaking the vacuum. Two rotation angles of the crystals are independently adjusted in 1/8 arc sec step by AC-servo motor controllers. The bent cylindrical and flat mirrors are made of fused SiO<sub>2</sub> and coated by Ni. The bent cylindrical mirror is inclined 6.3mrad to SR beam and the acceptance is 3mrad(H) × 0.15mrad(V).

## Experiments and Results

Some kinds of materials which are applied for electronic devices have been measured. Incident ( $I_0$ ) and transmission ( $I_t$ ) intensities are measured by ionization chambers. On Si-K-EXAFS measurement He and Ar are used for working gases of  $I_0$  and  $I_t$  monitors, respectively. An appropriate

quantity of Ne or Ar is mixed with He gas for the  $I_0$  monitor when the higher energy range is measured. The bent cylindrical mirror reduces the beam size, 25mm(H) × 1mm(V), at 1m upstream of the monochromator, to 1.8mm(H) × 0.5mm(V) (FWHM) at 0.3m downstream of the flat mirror.

Examples of Si-K-EXAFS spectra are shown in Fig.2. The absorption edge energies of Organic Silicon Positive Resist(A), Si<sub>3</sub>N<sub>4</sub>(B) and a-Si(C) are 1845, 1844 and 1840eV, respectively. Each of the spectra indicates a steep peak in XANES region. The energy width of the peak of sample (A) is about 1eV. Each of samples (A), (B) and (C) also exhibits a distinct second peak or a shoulder at 1855eV. The calculated interatomic distances of each sample are 1.63 Å (Si-O,A), 1.97 Å (Si-C,A), 1.71 Å (Si-N,B), 2.36 Å (Si-Si,C), respectively.

## Reference

- 1) Nakano A., Abe O. and Edamura T.: Abstract of IUCr XIVth(1987).
- 2) I. Nagakura : KEK Report, 81-17(1982).

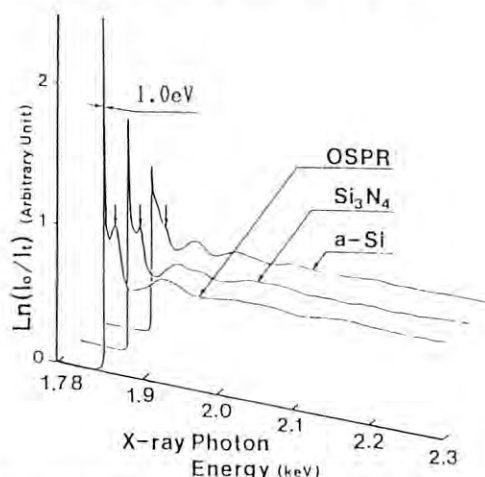


Fig.2 EXAFS spectra of OSPR, Si<sub>3</sub>N<sub>4</sub> and a-Si

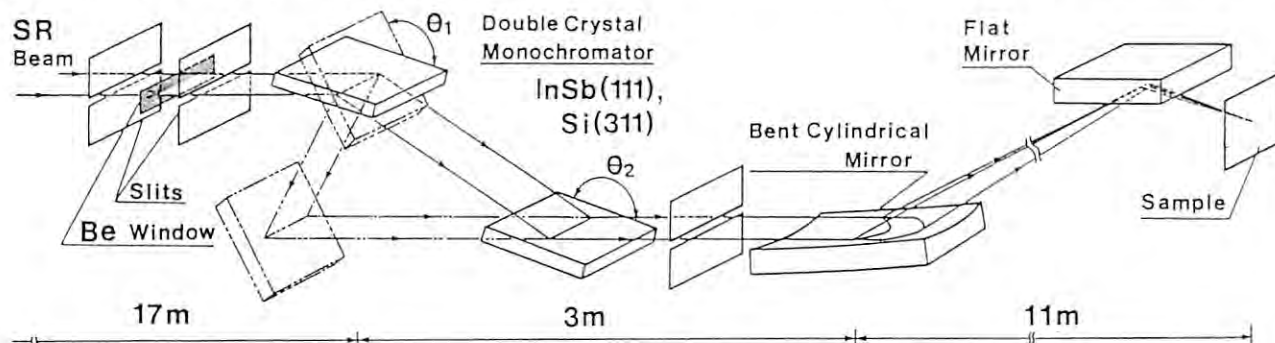


Fig.1 Schematic illustrations of the optical system of BL-8B

## THE LOCAL STRUCTURE OF IRON-TIN COMPOSITE OXIDES STUDIED BY X-RAY ABSORPTION SPECTROSCOPY

Satohiro YOSHIDA, Hiroshi MIZUTANI, Tsunehiro TANAKA, and Takuzo FUNABIKI

Department of Hydrocarbon Chemistry and Division of Molecular Engineering

Kyoto University, Sakyo-ku, Kyoto 606

and Mikio TAKANO

Institute for Chemical Research, Kyoto University, Uji

Introduction

In the previous report,<sup>1)</sup> we discussed the local structural change of iron-tin composite oxides, a gas sensor, with the composition on the basis of K-edge EXAFS of iron and tin. At that time, the quality of EXAFS of tin was unfortunately not so high to carry out a curve fitting analysis. Thus, the K-edge EXAFS of tin was recorded again more precisely in this work. Newly obtained results allow us to discuss the local structures of the composite oxides in detail and the previous tentative conclusion is modified.

Experimental

Samples and experimental procedures for recording EXAFS were the same as that reported previously, but data collection time for K-edge EXAFS of tin was prolonged in comparison with the previous work.

Results and Discussion

From the F.T.s of Fe and Sn K-edge EXAFS, structural parameters were extracted by the curve fitting procedure described elsewhere.<sup>2)</sup> In the analysis backscattering amplitudes and phase shifts are corrected with the theoretical values obtained by Teo and Lee<sup>3)</sup>. The applicability of these values is confirmed for Fe-O, Sn-O, Fe-Fe and Sn-Sn pairs by simulation of EXAFS of reference compounds, but for a Fe-Sn pair, the applicability was not able to be confirmed, because of lack of appropriate compounds. Thus, the obtained structural parameters for the pair, especially for coordination number of Sn atoms to a Fe and vice versa should be regarded as qualitative one. The results are shown in Table 1 and 2.

It is clear from Table 1 that the local structure around a Fe atom is that almost the same that of  $\alpha$ -Fe<sub>2</sub>O<sub>3</sub> (corundum structure) until 15 mol% of SnO<sub>2</sub>. The existence of Fe-Sn pair in-

dicates the formation of a solid solution phase of corundum structure. When the content of SnO<sub>2</sub> exceeds 15 mol%, the structure changed slightly, and almost constant value of coordination number of Sn atoms suggests that the limit of SnO<sub>2</sub> composition in the solid solution is 15 mol%. We could not extract reasonable structural parameters from a oxide of SnO<sub>2</sub> 67 mol% by a curve fitting analysis with 6 shells.

From Table 2, followings can be deduced for the local structure around a Sn atom. 1) The oxides containing SnO<sub>2</sub> up to 33 mol%, Sn-Sn pairs can not be identified and the local structure is the almost the same as that of corundum.

2) The oxide of 50 mol% of SnO<sub>2</sub> contains both SnO<sub>2</sub> (rutile structure) and corundum structure phases. 3) In the oxide of 67 mol% of SnO<sub>2</sub>, only rutile structure phase can be identified.

The item 1) suggests that the composition limit for a solid solution with corundum structure is 33 mol% of SnO<sub>2</sub>. This is apparently discrepant with the results with Fe-edge EXAFS. A possible explanation is that a Fe atom in the corundum structure is replaced by a Sn atom until 33 mol% of SnO<sub>2</sub>, but the regular corundum structure can not be kept for oxides with SnO<sub>2</sub> more than 15 mol% and some disorder is introduced in the structure. This modification in the structure might be related to apparent decrease in coordination numbers of Fe-Fe pairs at R=3.7 Å for oxides of SnO<sub>2</sub> 33 and 50 mol% in Table 1. Apparent constant value of coordination numbers of Sn to a Fe atom above 15 mol% of SnO<sub>2</sub> would result from the structural modification, as structural disorder brings about a decrease of amplitude of EXAFS and eventually the apparent coordination number.

- 1) S. Yoshida, H. Mizutani, T. Tanaka, T. Funabiki, M. Takano, PF Activity Report 1987, p240
- 2) T. Tanaka, H. Yamashita, R. Tsuchitani, T. Funabiki, S. Yoshida, J. Chem. Soc. Faraday Trans. 1, in press.

Table 1. Structural parameters obtained from Fe K-edge EXAFS

Oxide	Fe-O				Fe-Fe						Fe-Sn	
	N	R(Å)	N	R(Å)	N	R(Å)	N	R(Å)	N	R(Å)	N	R(Å)
$\alpha$ -Fe <sub>2</sub> O <sub>3</sub>	3.0	1.95	3.0	2.04	4.1	2.95	3.1	3.37	3.8	3.69		
SnO <sub>2</sub> 5mol%	3.0	1.95	3.1	2.08	3.9	2.96	2.7	3.39	4.1	3.69	0.19	3.36
SnO <sub>2</sub> 15mol%	3.1	1.93	3.0	2.06	4.0	2.95	2.9	3.37	3.6	3.69	0.30	3.32
SnO <sub>2</sub> 33mol%	2.6	1.86	2.7	1.95	4.0	2.95	2.8	3.36	3.1	3.68	0.26	3.31
SnO <sub>2</sub> 50mol%	2.5	1.85	2.5	1.95	4.2	2.95	2.7	3.34	1.8	3.70	0.27	3.13

Table 2. Structural parameters obtained from Sn K-edge EXAFS

Oxide	Sn-O				Sn-Sn		Sn-Fe			
	N	R(Å)	N	R(Å)	N	R(Å)	N	R(Å)	N	R(Å)
SnO <sub>2</sub>	2.0	1.93	4.0	2.05	2.0	3.18				
SnO <sub>2</sub> 5mol%	3.0	1.94	3.0	2.06			4.0	3.08	3.0	3.37
SnO <sub>2</sub> 15mol%	2.9	1.92	3.0	2.05			4.1	3.05	2.9	3.35
SnO <sub>2</sub> 33mol%	3.0	1.96	3.0	2.06			4.1	3.06	3.0	3.37
SnO <sub>2</sub> 50mol%	2.9	1.95	3.0	2.06	2.2	3.23	4.2	3.08	3.0	3.32
SnO <sub>2</sub> 67mol%	2.1	1.96	3.8	2.07	1.9	3.18				



## EXAFS OBSERVATION OF VAPOR QUENCHED Fe-Ag, Fe-Cu AND Fe-Cu-Ag ALLOYS

Yoji NAKAMURA, Kenji SUMIYAMA, Hideyuki YASUDA,  
Koichi TAKEMURA and Yasuhiro HIROSE

Department of Metal Science and Technology, Kyoto University, Kyoto 606, Japan

### Introduction

Fe, Cu and Ag give no equilibrium solid solution at room temperature, whereas Fe and Ag are immiscible in each other even in the equilibrium liquid state at 2300 K. Sputter-deposition is a typical vapor quenching method in which a high energy vapor solution is condensed onto a cold substrate so as to exhibit nonequilibrium alloys<sup>1)</sup>. This report mentions the results of the X-ray diffraction and the extended X-ray absorption fine structure (EXAFS) measurements on vapor quenched Fe-Cu, Fe-Ag and Fe-Cu-Ag alloys.

### Experimental

Alloy specimens with thickness of about 2  $\mu\text{m}$  were prepared by an rf diode sputtering on polyimide film substrates whose temperatures were about 80°C during sputter-deposition. The electron probe microanalysis was made for the determination of chemical compositions of these sputter-deposited alloys. X-ray diffraction patterns at 290 K were observed using Fe-K $\alpha$  radiations and a graphite monochromator. EXAFS spectra were observed at Beam Line 10B and 7C in Photon Factory, National Laboratory for High Energy Physics.

### Results

Figure 1 shows the phase boundary diagram of sputter-deposited Fe-Cu-Ag alloys estimated by X-ray diffraction measurements<sup>2)</sup>. A single bcc phase appears at the Fe-rich corner and single fcc phases at the Cu- and Ag-rich corners, while an amorphous phase at the central concentration range of the ternary phase diagram. Figure 2 shows the Fourier transform of EXAFS oscillation,  $k^3\chi(k)$ , at the Fe-K $\alpha$  edge for fcc Fe-66at%Cu, fcc Fe-67at%Ag and amorphous Fe-28at%Cu-30at%Ag alloys<sup>3)</sup>. A clear peak of the first coordination shell is observed around 2.2 Å for these alloys, where the peak intensity of the ternary alloy is much smaller than those of the binary alloys. Some peaks of higher coordination shells are detectable for the fcc Fe-Cu and Fe-Ag alloys, while they cannot be detected for the amorphous Fe-Cu-Ag alloy, indicating that the atomic stacking is much disordered in the ternary alloy.

### References

- 1) K.Sumiyama: Bull. Japan Inst. Metals 25 (1986) 615.
- 2) K.Sumiyama, Y.Kawawake and Y.Nakamura: Trans. Japan Inst. Metals 29 (1988) 191.
- 3) H.Yasuda, K.Sumiyama, Y.Nakamura, T.Tanaka, H.Mizutani and S.Yoshida: in preparation.

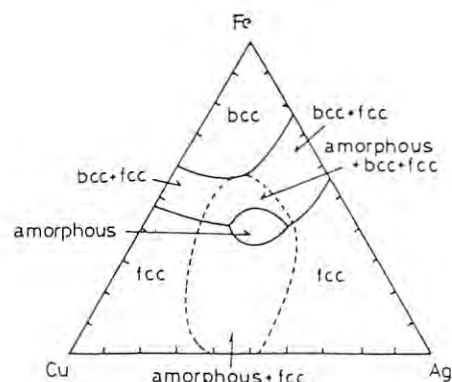


Fig.1

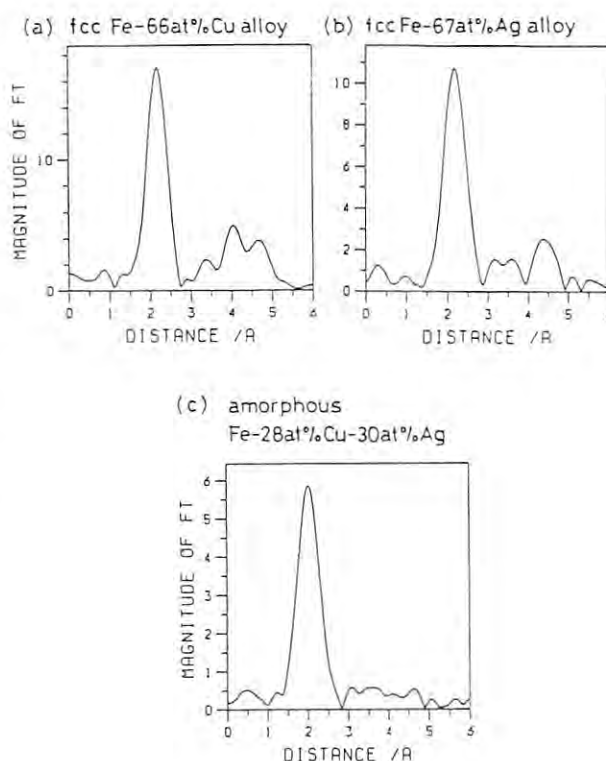


Fig.2



# LOCAL STRUCTURE OF Ni-Al ALLOYS IN CONNECTION WITH PREMARTENSITIC PHENOMENA AND $\omega$ -PHASE CHARACTER

Yukio NODA, Kenichiro OGURA, Moritaka HIDA<sup>+</sup>,  
Kazuya KAMON<sup>++</sup>, Hikaru TERAUCHI<sup>++</sup> and Hironobu Maeda<sup>+++</sup>

Faculty of Engineering Science, Osaka University, Toyonaka Osaka 560  
<sup>+</sup>School of Engineering, Okayama University, Okayama 700  
<sup>++</sup>School of Science, Kwansei Gakuin University, Nishinomiya 662  
<sup>+++</sup>Faculty of Science, Okayama University, Okayama 700

## Introduction

The  $\beta'$ -Ni<sub>x</sub>Al<sub>1-x</sub> alloy has a CsCl type structure for the concentration region 0.45 < x < 0.70. Within this region, the alloy shows complicated behavior in the phase diagram: 1) martensitic phase transformation for x > 0.60 accompanied by premartensitic phenomena, 2)  $\omega$ -phase behavior as a short range ordering, 3) vacancies for x < 0.50. These characteristics of the  $\beta'$ -phase strongly indicate that the local structure is distorted from the regular cubic symmetry while the average structure retains the CsCl structure. Shown in Fig.1 is the lattice constant of the cubic cell as a function of the concentration x. Here, the data are taken by the conventional diffraction technique so that the lattice constant in the figure means the average periodicity of the unit cell. For x > 0.5, the lattice constant decreases with increasing the nickel concentration, which might be consistent with the difference of the atomic size for Ni (r<sub>0</sub> = 1.25 Å) and Al (r<sub>0</sub> = 1.43 Å). On the other hand, the behavior of the lattice constant shows anomalous decreasing for x < 0.5 region where vacancies are introduced in the sample. In this report, we performed the EXAFS experiments in order to investigate the local structure of NiAl alloys especially in connection with premartensitic phenomena and the  $\omega$ -phase character.

## Experimental and Results

Conventional EXAFS experiments around the K-absorption edge of nickel atom were carried out on the 10B beam line mainly at room temperature. Five samples indicated by triangle marks in Fig.1 are currently analyzed. Following the standard procedure, EXAFS signal  $\chi(k)$  and Fourier transformed radial distribution function are obtained.

At the moment, we analyzed the 1st and the 2nd peaks in the radial function by using the

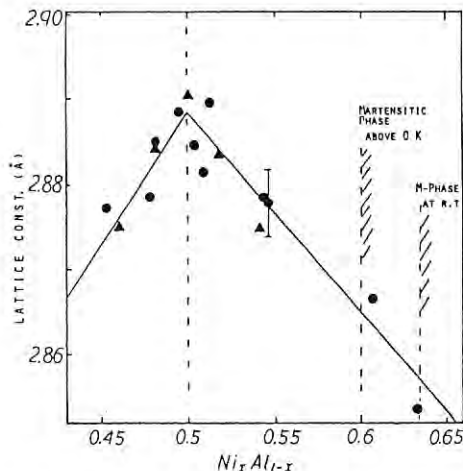


Fig.1 Lattice constant of Ni<sub>x</sub>Al<sub>1-x</sub>

filtering technique. Let us assume a simple two-shell model where coordination numbers ( $N_1, N_2$ ) and distances ( $r_1, r_2$ ) are the fitting parameters. In Fig.2, the obtained and calculated  $k^3\chi(k)$ 's are shown. The essential difference between these five samples is seen in the obtained coordination numbers. In order to move out ambiguities for the coordination number, the ratio of the 1st shell and the 2nd shell coordination numbers is taken and depicted in Fig.3.

## Discussions

Obtained result is interpreted by the density of vacancies introduced into the Al-rich sample. Hence, the coordination number at the 2nd shell decreases to  $6(1-\delta)$  at x < 0.5 and finally  $\delta$  is obtained as 0.057. At x > 0.5 region, nickel atoms will occupy the aluminum site so that the electron density at the 1st shell and the 2nd shell will effectively increase. However, this idea does not give any good agreement with the behavior at x > 0.5 shown in Fig.3. We are now undergoing to analyze the data based on the embryo picture or a local cluster model randomly distributed in a cubic lattice.

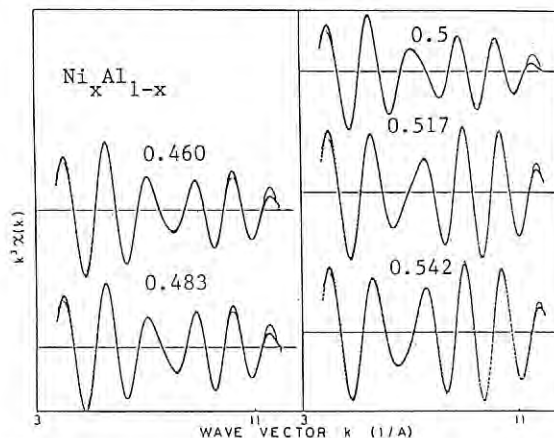


Fig.2 Observed and calculated  $k^3\chi(k)$  of five samples

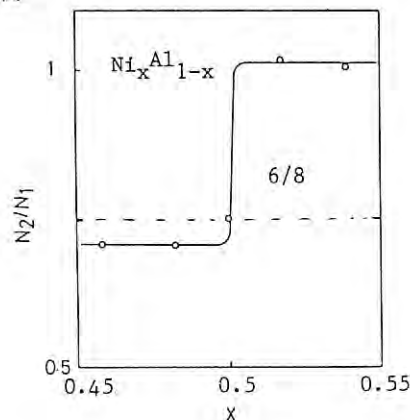


Fig.3

$N_2/N_1$  vs x

LOCAL STRUCTURE OF THE PEROVSKITE-TYPE  $\text{SrCo}_{1-x}\text{Mn}_x\text{O}_3$  SOLID-SOLUTIONAkira YOSHIIASA<sup>1</sup>, Yukari INOUE<sup>2</sup> and Fumikazu KANAMARU<sup>2</sup> and Kichiro KOTO<sup>3</sup>

1) Faculty of Science, Hiroshima University, Hiroshima 730, Japan

2) The Institute of Scientific and Industrial Research, Osaka University, Ibaraki, Osaka 567

3) Faculty of Integrated Arts and Sciences, Tokushima University, Tokushima 770

Introduction

The perovskite-type oxides containing transition metal ions in tetravalent state show interesting electrical and magnetic properties. The system  $\text{SrCo}_{1-x}\text{Mn}_x\text{O}_3$  forms a continuous solid-solution with the perovskite-type structure and the change from ferromagnet to antiferromagnet occurred at about  $x=0.33$  in the solid-solution (1). The change from ferromagnet to antiferromagnet was related to a change of spin state of  $\text{Co}^{4+}$  ions located at the octahedral sites. The spin state of  $\text{Co}^{4+}$  ion changes from low ( $[d\epsilon]^5[d\gamma]^0$ ) to high ( $[d\epsilon]^3[d\gamma]^2$ ) at about  $x=0.33$  in connection with a peculiar variation of the lattice constants. In the  $\text{SrCo}_{1-x}\text{Mn}_x\text{O}_3$  solid-solution, it is expected that the local environments of the  $\text{Co}^{4+}$  ions (e.g. the bond distances to the  $\text{O}^{2-}$  ions) differ from those of the  $\text{Mn}^{4+}$  ions. Positionally averaged information for both ions is obtained by the diffraction methods because the  $\text{Co}^{4+}$  and  $\text{Mn}^{4+}$  ions occupy the crystallographically equivalent positions. EXAFS spectroscopy is a useful probe of the local environment around a particular kind of absorbing atom in the solid-solution.

Experimental

The mixture of  $\text{SrCO}_3$ ,  $\text{MnCO}_3$ , and  $\text{CoCO}_3$  powder in the desired ratio was fired under the appropriate conditions according to the previous study (1). As the compounds obtained in this way were oxygen-deficient, they were annealed under oxygen pressure of 130 MPa at 300 °C for 72 hours. The formation of single phase solid-solution was confirmed by X-ray diffractometry. The lattice constants agree excellently to the published values. The X-ray absorption measurements near the Co K- and Mn K-edges were made with synchrotron radiation by use of the EXAFS facilities installed at the beam line 10B of Photon Factory in KEK. Using a curve fitting analysis of EXAFS, the structure parameters of the solid solution were determined by the least-squares parameter fitting. The amplitude and phase shift parameters are obtained from the reference samples (both end-members).

Results and Discussion

The actual Co-O and Mn-O distances determined by EXAFS in the solid-solutions are plotted in Fig. 1 with the mean (Co,Mn)-O distances by X-ray diffraction (one half of the lattice constant). It is revealed that the Mn-O distance decreases with increase of  $\text{Co}^{4+}$  ion content in the range  $0.33 \leq x \leq 1.0$ , while in the range  $0.0 \leq x < 0.33$  the Mn-O distance has a constant value. On the other hand, the Co-O distance increases with  $\text{Mn}^{4+}$  ion content with a break at  $x=0.33$ . In Fig. 1, it seems that a lever rule is satisfied;  $(1-x) \cdot R[\text{Co-O}] + x \cdot R[\text{Mn-O}] = R[(\text{Co}_{1-x}\text{Mn}_x)\text{-O}]$ , where  $R[\text{Co-O}]$ ,  $R[\text{Mn-O}]$  and  $R[(\text{Co}_{1-x}\text{Mn}_x)\text{-O}]$  are the Co-O, Mn-O and mean (Co,Mn)-O distances, respectively.

These variations in the distances from the  $\text{Co}^{4+}$  or  $\text{Mn}^{4+}$  ion to the first nearest-neighbor can be reasonably interpreted that the  $\text{O}^{2-}$  ion is locally attracted to the  $\text{Mn}^{4+}$  ion by replacing

the  $\text{Mn}^{4+}$  ion with the  $\text{Co}^{4+}$  ion; the  $\text{O}^{2-}$  ion shifts toward the  $\text{Mn}^{4+}$  ion in the Co-O-Mn combination (Fig. 2). In the range  $0.33 \leq x \leq 1.0$ , the decrease in the Mn-O distance is explained by an increase in the number of Co-O-Mn combinations with increase of  $\text{Co}^{4+}$  ion content. In the range  $0.0 \leq x < 0.33$ , a constant Mn-O distance can be also interpreted by forming no Mn-O-Mn combination (i.e., an ordered arrangement of  $\text{Mn}^{4+}$  ions, where only the Co-O-Mn and Co-O-Co combinations exist). The variation of the Co-O distances is explained by increase of Co-O distances due to the formation of Co-O-Mn combinations. The strength of the ligand field for  $\text{Co}^{4+}$  ion becomes weak gradually with increase of  $\text{Mn}^{4+}$  ion content because the  $\text{O}^{2-}$  ions around  $\text{Co}^{4+}$  ions are attracted to  $\text{Mn}^{4+}$  ions. It can be, therefore, understood why  $\text{Co}^{4+}$  ion of larger ionic radius in the high spin state is more stable than in the low spin state in the range  $0.33 \leq x \leq 1.0$  though the solid solutions have smaller unit cell volumes.

We are grateful to Dr. H. Maeda, Okayama University, for the computer programs of EXAFS analysis and to Drs. S. Nomura and A. Koyama, KEK, for their indispensable assistance on EXAFS measurements.

References

- 1) H. Taguchi, M. Shimada, M. Koizumi and F. Kanamaru, J. Solid State Chem., 35, 246 (1980)

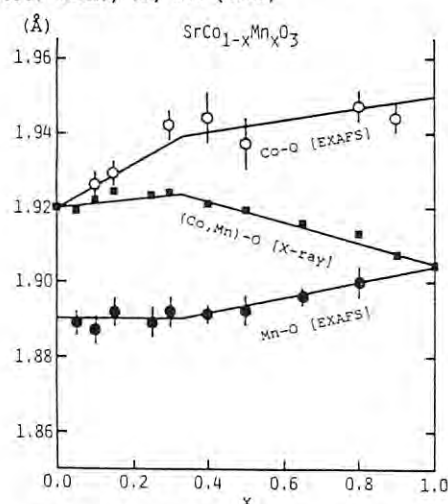


Fig. 1. The Co-O and Mn-O nearest neighbor distances measured by EXAFS and the mean (Co,Mn)-O distances by X-ray diffraction in the perovskite-type  $\text{SrCo}_{1-x}\text{Mn}_x\text{O}_3$  solid-solution.

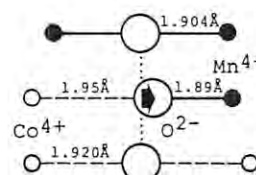


Fig. 2. The Co-O and Mn-O distances in the Co-O-Co, Co-O-Mn and Mn-O-Mn combinations. The  $\text{O}^{2-}$  ion shifts toward the  $\text{Mn}^{4+}$  ion in the Co-O-Mn combination.

## LOCAL CRYSTAL STRUCTURE OF EXCHANGED IONS IN ZEOLITE

Yasushige KURODA, Hironobu MAEDA, Hisaki MORIWAKI, Naruhiko BANBA, Akihisa KOIZUMI and Tetsuo MORIMOTO  
Department of Chemistry, Faculty of Science, Okayama University,  
Okayama 700, Japan

Introduction

Metal species are often substituted onto zeolite to generate a catalytic reactive species or sites. The structure of this site and the adsorbate geometry is of considerable importance for understanding the chemistry of such surfaces. A sufficiently good understanding of the location and adsorbate structure of catalytically active metal species on zeolite may allow optimization and control of the catalytic activity of such systems. EXAFS spectroscopy is a suitable technique to investigate the structural properties of these catalysis. But up to the present, experiment of EXAFS measurement in zeolite system is undertaken under imperfect vacuo and without variation of continuous pretreatment condition, though the effect of contamination such as  $\text{CO}_2$  and  $\text{O}_2$  etc. in air on the properties of zeolites is markedly. So that it is needed to design the simple in-situ cell for EXAFS measurements, by which we can evacuate the sample at elevated temperatures in vacuo, treat the sample quantitatively with the gases such as  $\text{O}_2$  and  $\text{H}_2$  etc. at elevated temperatures, and can be adsorbable the gases on its sample. Here, we design the in-situ cell and describe the results of EXAFS measurements on 215 %  $\text{Cu}^{2+}$  exchanged mordenites which are treated at elevated temperatures in vacuo.

Experimental

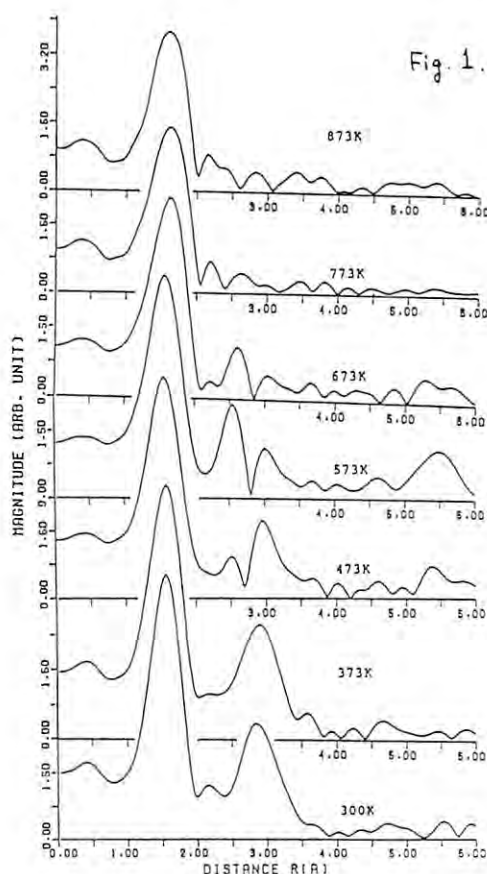
Cu-exchanged mordenites were prepared from Na-mordenite by the usual method.<sup>1)</sup> The extent of ion exchange, determined by chelatometric titration, were found to be 215 for Cu(II) ions (CuM-215). The X-ray absorption measurement was performed by using the synchrotron radiation from the Photon Factory (PF) at the National Laboratory of High Energy Physics (KEK, Tsukuba). The Cu K-edge EXAFS spectra of the CuM samples and the reference samples Cu(II)O and  $\text{Cu}(\text{OH})_2$  were taken with the transmission mode, using a beam line BL-10B with channel-cut silicon (311) crystal monochromator under a ring operating conditions of 2.5 GeV and 200 mA maximal current. The energy resolution is 0.5 eV for near-edge scan and 2.0–3.0 eV for EXAFS scan. The Photon energy,  $E$ , was calibrated with respect to a Cu foil by assigning 8.9788 keV to the pre-edge peak on the absorption edge. Details of the performance for both EXAFS spectrometers and data processing procedure have been described in refs. 2 and 3.

Results and Discussion

The fourier transforms of the EXAFS

function of CuM-215 measured at room temperature as a function of evacuated temperatures are shown in Fig. 1. Using CuO and  $\text{Cu}(\text{OH})_2$  as the reference substances, we attributed the first major peak centered at 1.54 Å (no phase-shift correction) to the backscattering from the nearest neighbor oxygen atoms, and the second major peak centered at 2.85 Å (no phase-shift correction) to the backscattering from the second nearest Cu ions and Si ions. Increasing with pretreatment temperature, the second peak splits into two peaks, and finally these peaks disappear at 773K. These results suggest that the hydroxyl bridged dimer is formed in mordenite at room temperature, the CuO cluster is formed from this hydroxyl bridged dimer at about 473K, and the static disorder is very large in the samples evacuated over 773K.

- 1) J. R. Reearce, W. J. Mortier, J. B. Uytterhoeven, and J. H. Lunsford, *J. Chem. Soc. Faraday 1*, **77**, 937, 1981.
- 2) H. Oyanagi, T. Matsushita, M. Ito and H. Kuroda, KEK Report, 83-30, 1984.
- 3) H. Maeda, *J. Phys. Soc. Jpn.*, **56**, 2777, 1987.





# CHARACTERIZATION OF SUPPORTED RhFe AND PtFe BIMETALLIC CARBONYL CLUSTERS AND THEIR CATALYTIC FUNCTIONS

Masaru ICHIKAWA, Atsushi FUKUOKA, Takuma KIMURA, Nobuhiro KOSUGI\*, and Haruo KURODA\*

Research Institute for Catalysis, Hokkaido University, Kita-11 Nishi-10, Kita-ku, Sapporo 060

\*Department of Chemistry, Faculty of Science, The University of Tokyo, Hongo, Bunkyo-ku, Tokyo 113

## Introduction

In the catalytic CO+H<sub>2</sub> reaction, the conventional Rh-Fe/SiO<sub>2</sub> and Pt-Fe/SiO<sub>2</sub> catalysts exhibit a unique activity for producing C<sub>1</sub>-C<sub>2</sub> alcohols. We have employed RhFe and PtFe bimetallic carbonyl clusters as molecular precursors for preparation of RhFe and bimetallic catalysts.<sup>1),2)</sup> In this study, we have conducted EXAFS evaluations for the RhFe/SiO<sub>2</sub> catalysts to characterize the local structure of RhFe bimetallic clusters fixed on SiO<sub>2</sub>.

## Experimental

The precursor carbonyl clusters were imoregnated on SiO<sub>2</sub> from the adequate organic solution. The catalysts were reduced with H<sub>2</sub> at 673 K. EXAFS measurements were carried out at BL 10B in KEK-PF.

## Results and Discussion

Table 1 summarizes the results of curve-fitting analyses of Fe-K and Rh-K edge EXAFS  $k^3\chi(k)$  for RhFe/SiO<sub>2</sub> catalyst derived from [NMe<sub>3</sub>CH<sub>2</sub>Ph]<sub>2</sub>[Fe<sub>2</sub>Rh<sub>4</sub>(CO)<sub>16</sub>] and RhCl<sub>3</sub>+FeCl<sub>3</sub>.<sup>3)</sup> With the three catalysts, there is a negligible contribution of Fe-Fe bonding. Interestingly, Fe-Rh interatomic length of the Rh<sub>4</sub>Fe<sub>2</sub> cluster catalyst is about 0.1 Å shorter than that of the salt-derived catalysts. These results suggest that bimetallic RhFe particles derived from the Fe<sub>2</sub>Rh<sub>4</sub> carbonyl cluster are highly dispersed on the SiO<sub>2</sub> surface. From <sup>57</sup>Fe Mossbauer study on the Fe<sub>2</sub>Rh<sub>4</sub>/SiO<sub>2</sub> catalyst, it is revealed that the oxidation states of Fe atoms are Fe<sup>0</sup> and Fe<sup>3+</sup>, and that 73 % of Fe atoms are in the state of Fe<sup>3+</sup>.<sup>1)</sup> Neither Fe<sup>+</sup> nor Fe<sup>2+</sup> species were observed.

We propose derive the location model for the cluster derived RhFe/SiO<sub>2</sub> catalyst. Fe atoms which are stable mostly in the state of Fe<sup>3+</sup> are located in the metal-support interface forming chemical bonds with the oxygen atoms of SiO<sub>2</sub>. Since the contribution of Fe-Fe is negligible, Fe atoms should be highly dispersed on the surface. Thus, Fe<sup>3+</sup> has the role to anchor Rh atoms onto the support in forming Rh-Fe<sup>3+</sup>-O(silica support) at the metal-support interface. IR study suggest that the Rh-Fe<sup>3+</sup> bimetallic sites specifically activates the adsorbed CO in forming Rh-CO...Fe<sup>3+</sup>. The Rh-Fe<sup>3+</sup> sites are highly active for migratory CO insertion as judged by the rates of the hydroformylation of olefins which are dramatically enhanced.

## References

- 1) A. Fukuoka, M. Ichikawa, J. A. Hriljac, and D. F. Shriver, *Inorg. Chem.*, **26**, 3643(1987).
- 2) A. Fukuoka, T. Kimura, and M. Ichikawa, *J. Chem. Soc., Chem. Commun.*, 428(1988).
- 3) M. Ichikawa, T. Fukushima, T. Yokoyama, N. Kosugi, and H. Kuroda, *J. Phys. Chem.*, **90**, 1222(1986).
- 4) H. Kuroda, T. Yokoyama, N. Kosugi, M. Ichikawa and T. Fukushima, *J. de Phys.*, **12**, C8-301(1986).

Table 1. Results of the curve-fitting analyses of  $k^3\chi(k)$  of SiO<sub>2</sub>-supported [NMe<sub>3</sub>CH<sub>2</sub>Ph]<sub>2</sub>[Fe<sub>2</sub>Rh<sub>4</sub>(CO)<sub>16</sub>]-derived catalyst.

precursor	metal loading	Fe/Rh ratio	Fe-O(support) C.N.	Fe-O(support) R(Å)	Fe-Rh C.N.	Fe-Rh R(Å)	Rh-Rh C.N.	Rh-Rh R(Å)	Fe <sup>3+</sup> %
[NMe <sub>3</sub> CH <sub>2</sub> Ph] <sub>2</sub> [Fe <sub>2</sub> Rh <sub>4</sub> (CO) <sub>16</sub> ]	4 wt.% Rh	0.5	3.0	1.99	1.8	2.54	7.2	2.65	73
RhCl <sub>3</sub> + FeCl <sub>3</sub>	4 wt.% Rh	0.3	1.5	2.05	4.7	2.63	11.4	2.66	91
	4 wt.% Rh	0.5	0.9	1.99	4.0	2.62	9.5	2.66	86

## EXAFS AND XANES ANALYSIS OF SELENIUM COMPOUNDS (II)

Takuji KAWASHIMA, Ichiro NOMACHI, Tadashi HIRANO, Kazuhiko OZUTSUMI, Izumi NAKAI  
Department of Chemistry, The University of Tsukuba, Tsukuba, Ibaraki 305

## Introduction

The authors have previously elucidated the structures of piaselelenols and the oxidation state of selenium compounds by EXAFS/XANES technique.<sup>1)</sup> The present report describes a further EXAFS/XANES study on the electronic effects of the substituents and various organic solvents on the structures of piaselelenols. The variation of local structure around selenium with time during the reaction of selenious acid with o-phenylenediamine is also reported.

## Experimental

Piaselelenol ( $C_6H_4N_2Se$ ) and its 5-substituted derivatives<sup>2)</sup> were prepared as described previously. Benzene(Bz), nitromethane(NM), dioxane(DO), pyridine(Py), tetrahydrofuran(THF) and hexamethylphosphorotriamide(HMPA) were chosen as organic solvents and their 0.1 mol dm<sup>-3</sup> solutions of piaselelenols were prepared.

A water-ethanol (1:1) solution of 0.5 mol dm<sup>-3</sup> selenious acid and 0.75 mol dm<sup>-3</sup> o-phenylenediamine was prepared. Five cm<sup>3</sup> of each solution were mixed with 15cm<sup>3</sup> of 1.5 mol dm<sup>-3</sup> sodium acetate water-ethanol(1:1) solution to study the reaction process.

Powder samples of piaselelenols were prepared by dusting onto Scotch Tapes and the sample solutions were taken into a specially designed cell for our measurement. Se-K absorption spectra were measured by using a Si(311) channel-cut crystal monochromator on the EXAFS facilities installed at BL-10B at PF.

## Results and Discussion

Fourier transforms for powder samples of piaselelenols are given in Fig. 1. The first intense peak around 1.4 Å in Fig. 1 is due to the Se-N bond distance. The bond distance in piaselelenol determined by the curve fitting analysis in the k-space is 1.83 Å and no significant variation of the Se-N distances is found for all 5-substituted piaselelenols. On the other hand, it is reported that the Hammett's substituent constants well correlate with the position of absorption maxima of piaselelenols in toluene<sup>3)</sup>. The substituents only influence on the electronic state of benzene ring, and, therefore, the electronic state of 5-substituted piaselelenols are varied. As a result, wavelength of maximum absorption is shifted. But the substituent effects are not strong enough to alter the Se-N bond distances, so the Se-N bond distances remain unchanged.

The results of EXAFS analysis for piaselelenols in various organic solvents are summarized in Table 1 in which Δ denotes the difference between the Se-N bond distances in solid state and in solution. As shown in Table 1, the Se-N bond distances of piaselelenols in solution are longer than those in solid state, indicating that the lengthening of the Se-N bond are due to solvation. However, no correlation between the Se-N bond lengths and the properties of these solvents (e.g. donor number, acceptor number, etc.) is observed. Since the solvent molecules may not specifically interact with the selenium or nitrogen atoms of piaselelenols, there is no correlation between the properties of solvents and the Se-N bond length.

XANES spectra were measured to study the reaction process of selenious acid with o-phenylenediamine from a view point of the local structures of selenium. Figure 2 shows the Se K-edge XANES spectra measured at regular time

intervals during the reaction. The position of the Se K-edge shifts toward lower energy side with time. From a comparison of these XANES spectra with those of the standard samples of  $(C_6H_5)_2Se_2$ ,  $Na_2SeO_3$  and  $Na_2SeO_4$ , the shift is attributed to a decrease in the oxidation number of selenium from quadrivalent to divalent. The process of the reaction can thus be observed directly as the variation of the oxidation state of selenium, i.e. the reaction of selenious acid with o-phenylenediamine begins with the reduction of selenium, is followed by the formation reaction of piaselelenol. So it is expected that this reaction mechanism can be clarified structurally by using the energy dispersive EXAFS technique.

## References

- 1) T. Kawashima, I. Nomachi, T. Hirano, I. Nakai, PF Activity Report, #5, 223 (1987)
- 2) M. Tanaka, T. Kawashima, Talanta, 12, 211 (1964)
- 3) M. Goto, K. Toei, Talanta, 12, 124 (1965)

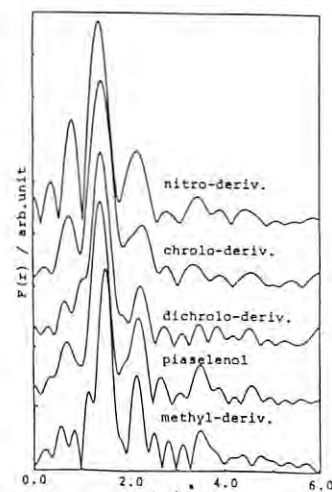


Fig. 1 Fourier transforms of EXAFS for piaselelenol and its derivatives

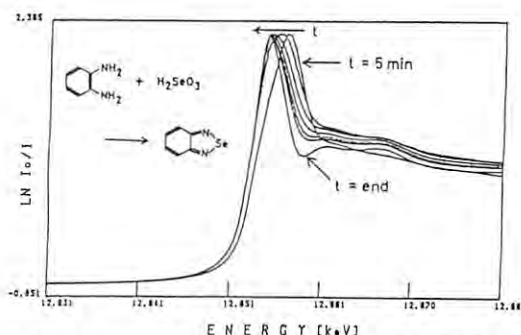


Fig. 2 Variation of the Se-K XANES spectra of piaselelenol in the course of its formation reaction

Table 1 Solvent effects on the Se-N bond distance of piaselelenol and its derivatives

Solvent	Donor Number	Acceptor Number	piaselelenol		methyl derivatives		nitro derivatives	
			Se-N (Å)	Δ (Å)	Se-N (Å)	Δ (Å)	Se-N (Å)	Δ (Å)
Bz	0.1	8.2	1.85	0.03	1.84	0.01		
NM	2.7	20.6	1.84	0.01	1.85	0.02		
DO	14.8	10.8	1.85	0.02	1.86	0.03	1.87	0.04
THF	20.0	8.6	1.85	0.02	1.86	0.03	1.84	0.01
Py	30.1	14.2	1.84	0.01	1.84	0.01	1.83	0.00
HMPA	38.8	10.8	1.84	0.01	1.83	0.00	1.84	0.01



CHARACTERISTICS AND STRUCTURE OF NbC FILMS FABRICATED BY ION BEAM SPUTTERING

Osamu Tunekki, Ryuji Hayahara, Mituru Taguchi, Yasushi Kobayashi, Yoshinori Kuwasawa, Shigeru Nakano, Atsushi Koyama\* and Tadashi Matsushita\*

Department of Physics, Faculty of Science, Chiba University,  
Yayoicho 1-33, Chiba, Chiba 260

\*Photon Factory, National Laboratory for High Energy Physics,  
Oho-machi, Tsukuba, Ibaragi 305

1. Sample Preparation

The films used in this study were fabricated by ion beam sputtering. The Nb target (99.95%) were bombarded by 8keV Ar ion beam and Nb was evaporated on the single crystal sapphire substrates at a pressure  $2-6 \times 10^{-5}$  Torr. The composition of residual gas is given in Table 1. It is supposed NbC or Nb-oxides were formed in the sputtering processes, considering the very slow deposition rate (about 10-50 Å/h) and the highly contaminated residual gas.

2. Experimental and Discussions

The measured electrical resistance of the films are given in Fig. 2. From the figure, samples are divided into three categories.

- A: The temperature coefficient of resistance  $\beta = \frac{1}{\rho} \frac{d\rho}{dT}$  of the films is positive and the films become superconducting at low temperature (metallic behavior).
- B:  $\beta$  is negative and films become superconducting.
- C:  $\beta$  is negative but films are not superconducting in the temperature range of measurement (non-metallic).

From the analysis of X-ray diffraction and of XPS measurements, films are NaCl structure and are NbC (cf. NbC C<sub>1s</sub> peak in Fig. 2 upper, C peak is that of surface contamination and disappears by etching). Fig. 3 shows the results of analysis of fluorescence EXAFS for A<sub>1</sub> and C<sub>1</sub>. The narrow slit was placed before the detector to avoid the Bragg reflections from the sapphire substrate but it was difficult to remove them over the

whole measured energy range. As a results of computer simulation method used for such reflections, three Nb-Nb peaks were separated for C<sub>1</sub> as shown in Fig. 3. This difference between A<sub>1</sub> and C<sub>1</sub> may predict the characteristics of the films above mentioned.

The Table 2 shows the characteristics of the films. The chemical shift of Nb3d5/2 suggests that A<sub>1</sub> is NbC and C<sub>1</sub> has vacancies at C-sites. The same tendencies are also seen in EXAFS data, but further analysis are needed. The detailed discussions will be reported later.

Ar	CO	CO <sub>2</sub>	O <sub>2</sub>	C <sub>2</sub> H <sub>4</sub> O	Ne	H <sub>2</sub> O
	N <sub>2</sub>					
70.3	14.1	1.0	2.6	1.3	8.6	2.0

Table 1. Ratio of partial pressure of component residual gases to total pressure(%).

Sample	d (Å)	3d 5/2 shift (ev)	a (Å)	Nb-O	Nb-C	Nb-Nb
NbC	bulk	1.7	4.47	----	2.24	3.16
A <sub>1</sub>	1134	1.6	4.46	----	2.21	3.20
B	875	1.3	4.42			
C <sub>1</sub>	3985	1.0	4.33	1.77	2.20	2.64
						3.19
						3.72

Table 2. Characteristics of the Films.  
a: lattice const., d: thickness.

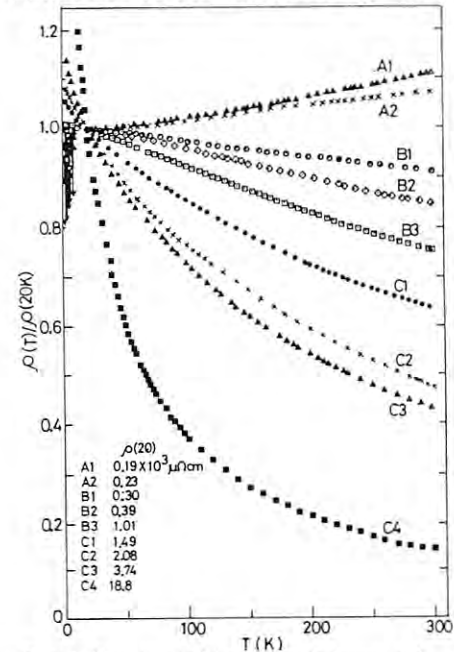


Fig. 1 The normalized resistance of the films versus temperature. The resistance are normalized at 20K.

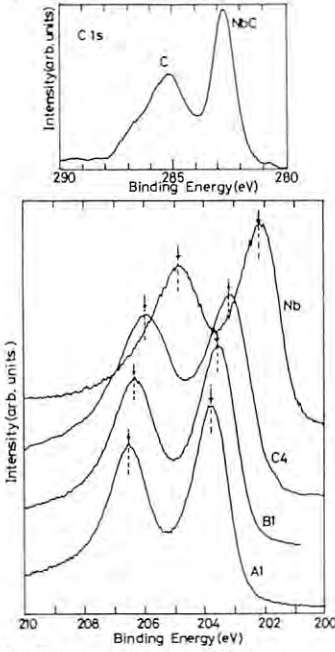


Fig. 2 The results of XPS measurements. The chemical shifts of Nb 3d peaks corresponding A, B, and C are different.

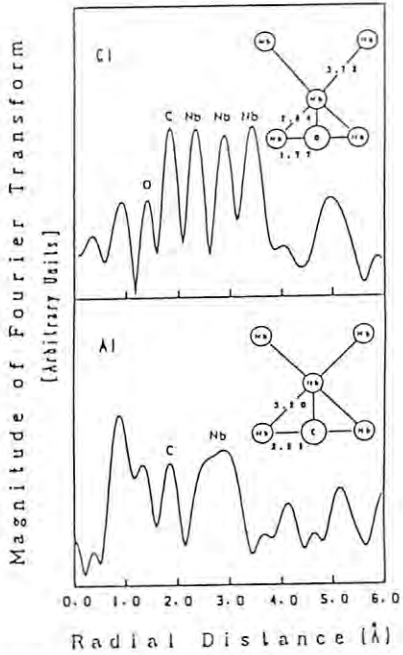


Fig. 3 The results of fluorescence EXAFS. For C<sub>1</sub>, three peaks corresponding Nb-Nb are separated.

## CHANGES IN LOCAL STRUCTURE OF ULTRA-FINE RHODIUM PARTICLES BY CHEMISORPTION

Takakazu FUKUSHIMA, Sadao OGASAWARA, Toshihiko YOKOYAMA<sup>+</sup> and Haruo KURODA<sup>+</sup>Department of Materials Science and Chemical Engineering, Faculty of Engineering,  
Yokohama National University, 156 Tokiwadai, Hodogaya-ku, Yokohama 240<sup>+</sup>Department of Chemistry, Faculty of Science, University of Tokyo, Hongo, Bunkyo-ku, Tokyo 113

## Introduction

Recently Van't Blik et al.<sup>1)</sup> showed that ultra-fine particles of Rh are disrupted by the addition of CO by using EXAFS technique. They also studied the surface species on Rh by IR and found only the gem-dicarbonyl species. We have been studying the surface species on Rh/Al<sub>2</sub>O<sub>3</sub> but have not been able to get such a sample that shows only gem-species by the addition of CO. It has been observed that linear type species are always accompanied with gem-species and this is a common feature on IR spectra for Rh/Al<sub>2</sub>O<sub>3</sub> systems studied in many papers. So, we used EXAFS technique to study our Rh/Al<sub>2</sub>O<sub>3</sub> samples<sup>2)</sup>, which are well characterized by IR technique<sup>3)</sup>.

## Experimental

The catalysts were prepared and reduced by the method described elsewhere<sup>3)</sup>. The sample powder was pressed into wafer and mounted in a glass cell. The EXAFS measurements were carried out in appropriate gas atmospheres at r.t. by use of the EXAFS spectrometer at the Beam Line 10B.

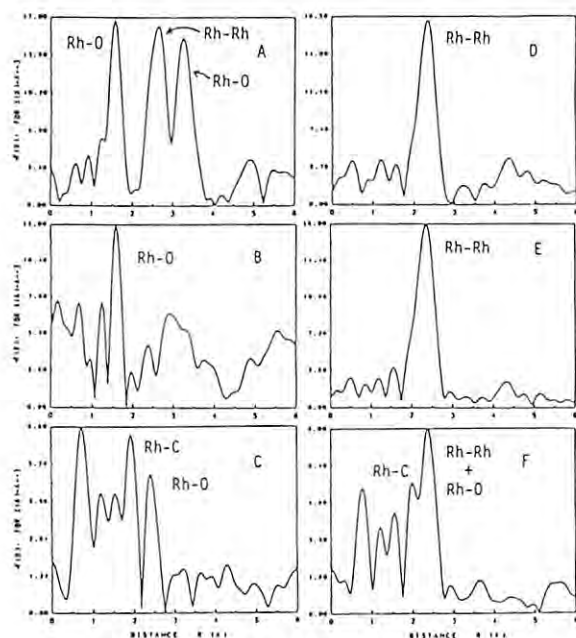


Fig. 1. Fourier transforms of the Rh K-edge EXAFS of 0.5wt%Rh/Al<sub>2</sub>O<sub>3</sub> catalysts.

- A: Rh<sub>2</sub>O<sub>3</sub>; B: Passivation only after H<sub>2</sub> reduction at 400°C for 16 hr.  
C: CO adsorption for 30 hr after passivation.  
D: H<sub>2</sub> re-reduction at 400°C for 1 hr.  
E: H<sub>2</sub>(1atm) treatment at r.t. for 45 hr.  
F: CO(30torr) adsorption for 4 hr after E.

## Results and Discussion

Fourier transforms of the Rh K-edge EXAFS of 0.5 wt% Rh/Al<sub>2</sub>O<sub>3</sub> catalysts are shown in Fig. 1 and EXAFS parameters obtained by curvefitting analyses are tabulated in Table 1. The Fourier transform of the passivated sample shows only Rh-O peak and no Rh-Rh bonding in metal Rh(1-B). This indicates that the Rh oxide exists atomically on the surface of support after passivation and storage in air. Metal-metal bonding is restored after re-reduction at 400°C(1-D). It is interesting to know that this restoration of bonding occurs even at r.t.(1-E). The coordination number(N) of 6.3 is obtained for Rh re-reduced at 400°C and this corresponds to 12A semispherical particle with 35 atoms assuming FCC structure. These results again indicate that small particles of Rh are undergone oxidative disruption by the oxygen chemisorption and that thus dispersed oxide particles agglomerate reductively and restore the Rh-Rh bonding even at r.t. by H<sub>2</sub>. CO is adsorbed on the passivated and evacuated sample and it can be seen two peaks derived from carbonyl CO(1-C). Because of the noise it is not clear at which extent exists the Rh-O bonding in Rh oxide, but Rh carbonyls are dispersed atomically on the support in any case. Fig. 1-F shows the result of CO adsorption on Rh surface pre-treated by H<sub>2</sub> at r.t. after passivation. Compared with 1-E, one can notice the decrease in magnitude of Rh-Rh peak and the coordination number obtained is about 1.2. This suggests the extent of oxidative disruption by CO is less than by O<sub>2</sub>. Our purpose of this study is to get informations of morphology change in Rh particles by CO chemisorption. It becomes clear that on our sample, the small Rh clusters remain even after CO adsorption together with atomically dispersed carbonyls on the support surface. This explains why linearly adsorbed species exist when CO is introduced on Rh/Al<sub>2</sub>O<sub>3</sub> in IR measurements. Thus it is concluded that the appearance of both linear and gem-dicarbonyl peaks is the proof of existence of both small cluster and atomically dispersed phases.

## References

- 1) H.F.J. Van't Blik et al., J.Am.Chem.Soc., **107**, 3139(1985).
- 2) T.Fukushima et al., 61th CATSJ Meeting Abstract No.81(1988)
- 3) T.Fukushima et al., Photon Factory Activity Report 233(1987).

Table 1. Curvefitting results for 0.5wt% Rh/Al<sub>2</sub>O<sub>3</sub>

Fig.	Sample	Coordinated Atom	Coordination Number (N)	Distance (Å)
A	Rh <sub>2</sub> O <sub>3</sub>	Rh-O	6	2.05
B	Rh(Cl)/Al <sub>2</sub> O <sub>3</sub>	Rh-O	3.4	2.05
C	Rh(Cl)/Al <sub>2</sub> O <sub>3</sub>	Rh-C	-	-
	Fo11	Rh-Rh	12	2.69
D	Rh(Cl)/Al <sub>2</sub> O <sub>3</sub>	Rh-Rh	6.3	2.68
E	Rh(Cl)/Al <sub>2</sub> O <sub>3</sub>	Rh-Rh	6.1	2.69
F	Rh(Cl)/Al <sub>2</sub> O <sub>3</sub>	Rh-Rh	1.2	-
		Rh-C	-	-

IN-SITU EXAFS STUDIES ON THE STRUCTURE CHANGE OF Rh<sub>2</sub> ATTACHED ON SiO<sub>2</sub> DURING THE CO INSERTION REACTION

Kiyotaka Asakura, Kyoko Bando, Masayuki Shirai, and Yasuhiro Iwasawa

Department of Chemistry, Faculty of Science,  
the University of Tokyo, Hongo, Bunkyo-ku, Tokyo 113, Japan

## 1. Introduction

In order to understand the catalysis of the surface on a molecular level, it is important to accumulate the knowledge about the dynamic structure of surface in a working state. EXAFS offers potential for probing the surface structure of the catalysts in the working conditions. The Rh<sub>2</sub> attached on SiO<sub>2</sub> using the reaction between the Rh<sub>2</sub>(CH<sub>3</sub>)<sub>2</sub>(μ-CH<sub>2</sub>)<sub>2</sub>cp\*<sub>2</sub> (cp\* = C<sub>5</sub>Mes) and OH group of SiO<sub>2</sub> showed an interesting behavior in the interaction of CO. The attached Rh<sub>2</sub> had the surface structure as shown in Fig.1a, which possessed the Rh-Rh, Rh-CH<sub>3</sub> and Rh-CH<sub>2</sub> bondings. The IR spectra showed that the twin CO was adsorbed on the attached Rh<sub>2</sub> after the exposure to CO. The subsequent evacuation of the sample at 473 K, the CO was inserted into the Rh-CH<sub>3</sub> bonding and acetyl group was produced. When CO was introduced again, the acetyl was broken and twin carbonyl species with CH<sub>3</sub> ligand was regenerated. The phenomenon was completely reversible. However, it was against the general knowledge about the CO insertion reaction more easily proceeds under high pressure of CO. In this work we studied the structure of Rh<sub>2</sub> during the reversible CO insertion and COCH<sub>3</sub> decomposition on the attached Rh<sub>2</sub> by means of in-situ EXAFS technique.

## 2. Experimental

The preparation of catalysts was carried out described elsewhere.[1] EXAFS spectra were taken at BL-10B of Photon Factory in National Laboratory for High Energy Physics.

## 3. Results and discussion

Figs.2 and 3 show the k-weighted EXAFS oscillations and the Fourier transforms of Rh<sub>2</sub> attached on SiO<sub>2</sub>. The first peak was composed of Rh-C(cp\*, CH<sub>3</sub>, CH<sub>2</sub>) and the second one was corresponding to Rh-Rh interaction. The curve fitting analysis showed that the Rh-Rh bonding was found at 0.262 nm in the incipient sample. The Rh-Rh distance was almost equal to that of the original Rh<sub>2</sub>(CH<sub>3</sub>)<sub>2</sub>(CH<sub>2</sub>)<sub>2</sub>(Cp\*)<sub>2</sub>. Fig.3b shows the Fourier transform of the Rh<sub>2</sub> after the exposure to CO which was similar to that of incipient Rh<sub>2</sub>/SiO<sub>2</sub> as shown in Fig.3a. However, the k-weighted EXAFS oscillation of the Rh<sub>2</sub> exposed to CO drastically changed as shown in Fig.2b. The EXAFS oscillation in a high k region disappeared indicating the cleavage of Rh-Rh bonding. As a result of the curve fitting analysis, the peak was attributed to the oxygen atom of the carbonyl and no contribution of the Rh-Rh bonding was found. Fig. 2c showed k-weighted EXAFS

oscillation of the 473 K evacuation of the sample. The EXAFS oscillation corresponding to the Rh-Rh appeared in the high k-region. The curve fitting showed that the distance of Rh-Rh is 0.270 nm, a little longer than that of the incipient Rh<sub>2</sub>/SiO<sub>2</sub>. The reintroduction of CO on this sample caused the cleavage of the Rh-Rh bonding. Thus in-situ EXAFS studies clearly showed that the reversible cleavage and formation of Rh-Rh bonding occurred during the inter of the CO insertion and COCH<sub>3</sub> decomposition reaction as shown in Fig.1.

## Acknowledgement

We thank Prof. K.Isobe (Institute for Molecular Science) and Dr.Y.Arakawa(National Chemical Laboratory for Industry)

(1)K.Bando, K.Asakura, Y.Iwasawa, Y.Arakawa, and K.Isobe, in preparation

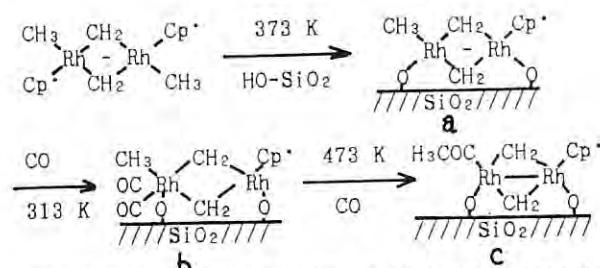


Fig.1 The scheme for the attachment reaction and surface reaction.

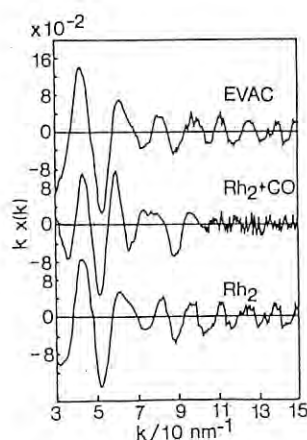


Fig.2 EXAFS oscillations  
(a) Rh<sub>2</sub>, (b) Rh<sub>2</sub>+CO,  
(c) evacuation

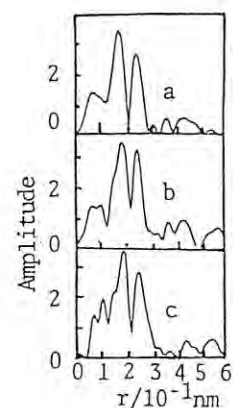


Fig.3 Fourier transforms  
(a) Rh<sub>2</sub>, (b) Rh<sub>2</sub>+CO,  
(c) evacuation



EXAFS STUDIES ON THE STRUCTURES OF THE Se-Rh/SiO<sub>2</sub> AND ITS HIGH CO INSERTION ACTIVITY

Kiyotaka Asakura, Yasuo Izumi, Masayuki Shirai and Yasuhiro Iwasawa

Department of Chemistry, Faculty of Science, the University of Tokyo, Hongo, Tokyo 113.

Introduction

Se has been widely accepted as a poison to catalyst similarly to S and Cl. However, we have revealed that Se has a promotion effect for the CO insertion reaction when a very small amount of Se is deposited on Rh/ZrO<sub>2</sub>. The C<sub>2</sub>H<sub>5</sub>CHO was 2-4 times more selectively produced from C<sub>2</sub>H<sub>4</sub>, H<sub>2</sub> and CO on the Rh modified with a quite small amount of Se than on the unmodified Rh catalyst. In this work we examined the local structure of Se to understand the function of Se in the hydroformylation reaction.

Although the Se-modified Rh/ZrO<sub>2</sub> is the most effective catalyst where the absolute activity toward CO hydroformylation increases with the Se content, yet EXAFS measurements on the Se/Rh/ZrO<sub>2</sub> are difficult because of the large absorbance of ZrO<sub>2</sub> and low concentration of Se. In this work we used SiO<sub>2</sub>-supported Rh system. We found the existence of the direct bonding of Se-Rh.

Experimental

To increase the dispersion of the Rh particle, the supported Rh was derived from Rh<sub>6</sub>(CO)<sub>16</sub>. Rh<sub>6</sub>(CO)<sub>16</sub> was deposited on SiO<sub>2</sub> from the hexane solution. The amount of Rh loading was 5 wt%. Se was introduced on the Rh surface using Se(CH<sub>3</sub>)<sub>2</sub> which was reacted with Rh<sub>6</sub>(CO)<sub>16</sub> at 400 K. The preliminary studies on the activity showed that the Se-modified system showed the maximum activity for hydroformylation at Se/Rh=1/6. In this work we studied two different concentration of Se (Se/Rh=1/6 and 3/6). EXAFS spectra were measured at BL-10B.

Results and Discussion

Fig.1 shows the Se K-edge EXAFS oscillations of Se/Rh/SiO<sub>2</sub> (Se/Rh=1/6 and 3/6). The EXAFS oscillations appearing at high k region mean the existence of Se-Rh bonding. Fig.2 showed Fourier transforms of the corresponding K-edge EXAFS. Only one dominant peak appeared. The good fitting results of the observed and calculated EXAFS oscillation based on the assumption of Se-Rh bonding also demonstrated that the Se was dispersed on Rh particle as shown in Fig.3. The coordination number of Rh around Se in the sample of Se/Rh/SiO<sub>2</sub> (Se/Rh=1/6) was nearly 3 and Se-Rh bond length

was 0.231 nm, indicating that the Se exists in the three fold hollow site. We have proposed the model structure for Se/Rh system as shown in Fig.4. No difference in the structures of Se/Rh/SiO<sub>2</sub> (1:6 and 3:6) was found. The curve fitting result for Se/Rh/SiO<sub>2</sub> (Se:Rh=3/6) showed that the coordination number was 3 and Se-Rh bond length was 0.233 nm. Thus the activation mechanism for CO insertion reaction is related to the electronic effect of Se. The excess addition of Se might block the active Rh site and cause the decrease of the hydroformylation activity.

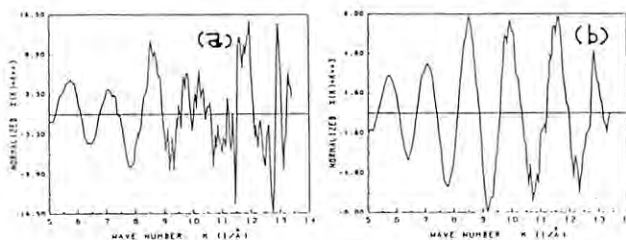


Fig.1 EXAFS (a) Se/Rh=1/6, (b) Se/Rh=3/6

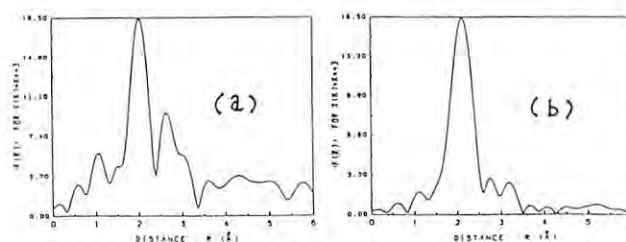


Fig.2 FT of (a) Se/Rh=1/6, (b) Se/Rh=3/6

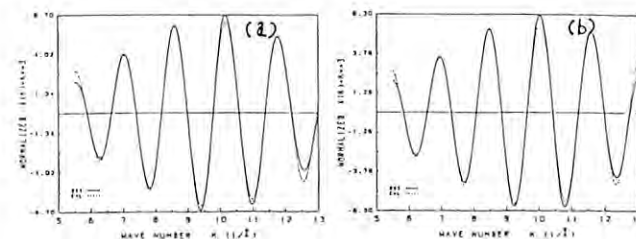
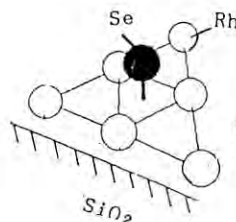


Fig.3 CF of (a) Se/Rh=1/6, (b) Se/Rh=3/6

Fig.4 The model for Se/Rh/SiO<sub>2</sub>

## STUDIES ON THE STRUCTURE OF BIMETALLIC COLLOIDAL CATALYSTS

Naoki Toshima, Hiroyuki Asanuma, Michitaka Ohtaki, Masafumi Harada,  
Tetsu Yonezawa, Kiyotaka Asakura, and Yasuhiro Iwasawa

Department of Industrial Chemistry, Faculty of Engineering, and  
Department of Chemistry, Faculty of Science,  
The University of Tokyo, Hongo Bunkyo-ku, Tokyo 113

Introduction

Bimetallic colloidal catalysts are highly dispersed metallic particles composed of atoms of two different metals. The colloidal catalysts protected by water-soluble polymers are prepared by reducing noble metal salts in the presence of polymers and have been shown to represent a high activity and selectivity for hydrogenation of olefins.

Recently it has been found that palladium-platinum bimetallic colloids are produced by refluxing the mixed solution of palladium chloride and hexachloroplatinic acid in alcohol in the presence of poly(N-vinyl-2-pyrrolidone) (PVP).<sup>1)</sup> When these colloids were used for the catalyst for selective partial hydrogenation of 1,3-cyclooctadiene,<sup>2)</sup> they represented higher activity than colloidal palladium, colloidal platinum or the mixture of them. The formation of the bimetallic colloid has been suggested by UV and TEM observations.<sup>1)</sup> The determination of the structure of bimetallic colloids was made of the extended x-ray absorption fine structure (EXAFS) associated with the K edge of palladium and the L<sub>3</sub> edge of platinum. The results of the measurement using a BL-10B PF-EXAFS station are suggesting a special structure for the most active bimetallic catalyst.

Experimental and Results

The bimetallic colloids at the various ratios of platinum and palladium were prepared by refluxing in the water-ethanol mixed solution under nitrogen atmosphere. These bimetallic colloids were concentrated by evaporation of the solvent under reduced pressure, and the concentrated solutions were sealed in the 50 mm (for palladium) and 10 mm (for platinum) cells under nitrogen atmosphere. The EXAFS data of this measurement were analyzed by a program EXAFS4 (Research Center for Spectrochemistry, the University of Tokyo).<sup>3,4)</sup>

Table 1. Coordination number of the Pd/Pt (4/1) bimetallic particles

Particle	Diameter /nm	Coordination No. around Pd	
		Pd	Pt
Observed	1.5	3.7	2.9
Pt Core Model(55atoms)	1.4	3.86	2.00
Random Model(55atoms)	1.4	5.58	1.73

Colloidal palladium is an active catalyst for hydrogenation of 1,3-cyclooctadiene, while colloidal platinum is little active for the hydrogenation. When palladium-platinum bimetallic colloids at different molar ratio were examined as the hydrogenation catalysts, it has been found that the activity varies with the ratio and the catalyst at palladium/platinum=4 has the highest activity.<sup>5)</sup> The EXAFS data of this sample provide information on the structure of the palladium-platinum bimetallic colloids. This EXAFS data has indicated that the palladium atoms coordinate predominantly to other palladium atoms and only to a minor extent to platinum atom (Table 1).<sup>5)</sup> This fact suggests the model structure shown in Fig.1, in which the palladium atoms surround the platinum atoms at the core. The coordination number around palladium in this model well corresponds to the observed one.<sup>5)</sup> The change in the structure with the variation in palladium/platinum ratio is under investigation. The present results are expected to provide a new concept on the activity of a bimetallic catalyst.

Reference

- 1) N. Toshima, K. Kushihashi and H. Hirai, Preprints of 54th Spring Meeting of the Chemical Society of Japan, p.720 (1987).
- 2) H. Hirai, H. Chawanya and N. Toshima, Reactive Polymers, 3, 127 (1985).
- 3) K. Asakura and Y. Iwasawa, Petrotech, 8(12), 41 (1985).
- 4) K. Asakura, N. Kosugi, H. Kuroda and Y. Iwasawa, Shokubai(catalyst), 26(5), 390 (1984).
- 5) N. Toshima, K. Kushihashi, T. Yonezawa, K. Asakura and Y. Iwasawa, Preprints of 56th Spring Meeting of the Chemical Society of Japan, 2ID47 (1988) : N. Toshima, B. Zhao and T. Yonezawa, Polymer Preprints, Japan, 37(3), p.550 (1988).

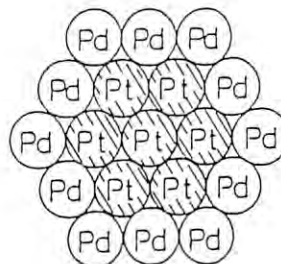


Fig. 1. A Pt core model of the Pd/Pt(4/1) bimetallic particle composed of 55 atoms



AN EXAFS STUDY OF  $\text{Ag}_3\text{SbS}_3$ - $\text{Ag}_3\text{AsS}_3$  SOLID SOLUTION

Hideyuki SUGAYA, Masayuki OKUNO, Takeo MATSUMOTO, Hiroto ANDO

Tsuyoshi MOTOYAMA, Hiroki OKUDERA

Department of Earth Sciences, Faculty of Science, Kanazawa University, Marunouchi 1-1, Kanazawa, Ishikawa 920

Introduction

$\text{Ag}_3\text{SbS}_3$  and  $\text{Ag}_3\text{AsS}_3$  are isostructural and form a complete solid solution<sup>1)</sup>. In these structures,  $\text{SbS}_3$  and  $\text{AsS}_3$  groups form trigonal pyramids and Ag atom bridges two trigonal pyramids<sup>2)</sup>. For intermediate composition of these solid solutions, there is no data of X-ray single crystal study and it is difficult to synthesize the single crystal. We applied EXAFS analysis to estimate the local structures of these solid solutions and to reveal the changes of forms for  $\text{AsS}_3$  and  $\text{SbS}_3$  groups as a function of the composition.

Experimental

Seven crystalline specimens whose compositions were given in Table 1 were prepared by silica-glass quenching method. Powdered specimens coated on adhesive tapes were used for EXAFS measurements. X-ray absorption spectra were collected in the energy ranges of 11.36-13.06 keV and 29.98-31.68 keV for As K and Sb K absorption edge, respectively, by a transmission mode at Beam Line 10B at 300K.

Results and Discussion

Figs. 1 and 2 show the magnitudes of the Fourier transform  $|F(r)|$ 's of  $k^3\chi(k)$  for As K and Sb K EXAFS spectra, respectively. Since the small contents of Sb, the EXAFS spectra of Sb K edge for Sb 30mol% and 10mol% specimens could not be mea-

sured. By comparing the peak positions and the crystal structures of  $\text{Ag}_3\text{SbS}_3$  and  $\text{Ag}_3\text{AsS}_3$  analyzed by Engel & Nowacki, it is clear that the prominent peaks at about  $r = 1.90\text{\AA}$  in Fig. 1 and  $1.95\text{\AA}$  in Fig.2 correspond to the As-S atomic pairs within  $\text{AsS}_3$  groups and the Sb-S atomic pairs within  $\text{SbS}_3$  groups, respectively. Because of the abscissa scales are not corrected for phase shifts, the position of each prominent peak indicates smaller value than their real atomic distances, As-S= $2.254\text{\AA}$ , Sb-S= $2.463\text{\AA}$ , by about  $0.35\text{\AA}$  for As-S and about  $0.5\text{\AA}$  for Sb-S. In Figs. 1 and 2, all the prominent peaks have similar peak positions. These facts suggest that in the  $\text{Ag}_3\text{SbS}_3$ - $\text{Ag}_3\text{AsS}_3$  solid solution,  $\text{AsS}_3$  and  $\text{SbS}_3$  groups have similar As-S and Sb-S distances, respectively. This proves that  $\text{AsS}_3$  and  $\text{SbS}_3$  groups are rigid in the crystal structures of  $\text{Ag}_3\text{SbS}_3$ - $\text{Ag}_3\text{AsS}_3$  solid solution series.

References

- 1) P.Toulmin, Am. Min., 48, pp.725-736 (1963)
- 2) P.Engel and W.Nowacki, Neues Jahrb. Miner. Monatsh., pp.181-184 (1966)

$\text{Ag}_3\text{SbS}_3$
$\text{Ag}_3(\text{Sb}_{0.9}, \text{As}_{0.1})\text{S}_3$
$\text{Ag}_3(\text{Sb}_{0.7}, \text{As}_{0.3})\text{S}_3$
$\text{Ag}_3(\text{Sb}_{0.5}, \text{As}_{0.5})\text{S}_3$
$\text{Ag}_3(\text{Sb}_{0.3}, \text{As}_{0.7})\text{S}_3$
$\text{Ag}_3(\text{Sb}_{0.1}, \text{As}_{0.9})\text{S}_3$
$\text{Ag}_3\text{AsS}_3$

Table 1. Chemical compositions of specimens.

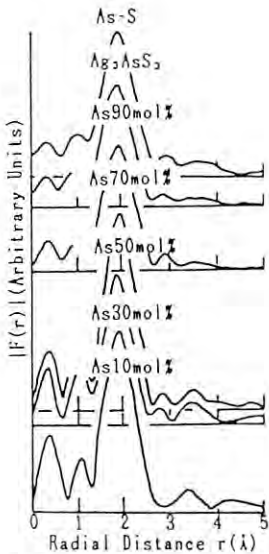


Fig.1. The  $|F(r)|$ 's for As-Kedges.

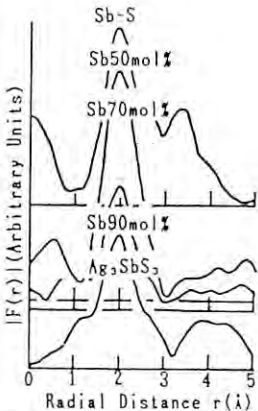


Fig.2. The  $|F(r)|$ 's for Sb-Kedges.

AN EXAFS STUDY OF  $\text{Ag}_3\text{AsS}_3$  GLASS

Masayuki OKUNO, Hideyuki SUGAYA, Takeo MATSUMOTO, Tsuyoshi MOTOYAMA,  
Hideki OKUDERA and Hiroto ANDO

Department of Earth Sciences, Faculty of Science, Kanazawa University, Kanazawa 920, Japan.

### Introduction

$\text{Ag}_3\text{AsS}_3$  crystal is an important ore of silver. The crystal structure consists of  $\text{AsS}_3$  trigonal pyramid groups and Ag atoms link the groups. The glass phase of this crystal arouses interested in their electrical properties as containing Ag atoms. We measured EXAFS spectra for Ag and As and analysed the local structures around Ag and As atoms of the glass.

### Experimental

$\text{Ag}_3\text{AsS}_3$  glass was prepared from Ag, As and S by the melt quenching method in the evacuated silica tube. EXAFS measurements were carried out over the ranges of 11.36 - 13.06 keV (As K absorption edges = 11.865 keV) at 300K, and 25.03 - 26.70 keV (Ag K absorption edge = 25.508 keV) at 80 and 300K by a transmission mode with a channel-cut Si(311) monochromator.  $\text{Ag}_3\text{AsS}_3$  crystals (proustite) were used for a reference sample.

### Results and Discussion

The EXAFS  $\chi(k)$  spectra of  $\text{Ag}_3\text{AsS}_3$  glass were shown in Fig.1 with the spectra of  $\text{Ag}_3\text{AsS}_3$  crystals. Fig.2 presents the  $|F(r)|$  curves for As and Ag atoms of  $\text{Ag}_3\text{AsS}_3$  glass and the crystal. In the  $|F(r)|$  curves of As and Ag, prominent peaks at  $r \approx 2$  Å are observed. By comparing the peak positions and the crystal structure of  $\text{Ag}_3\text{AsS}_3$  (Engel and Nowacki, 1966)<sup>1)</sup>, it is clear these peaks correspond to the As-S atomic pairs within  $\text{AsS}_3$  groups and the Ag-S atomic pairs. Because these  $|F(r)|$  curves were not corrected for the phase shifts, the position of each peak should be shifted by about 0.35 Å for As and 0.45 Å for Ag.

All the As-S peaks have similar peak heights and shapes. This fact suggests that even in the glass structure the As atom forms a  $\text{AsS}_3$  group and the form of the group is very similar to that in the crystal. The Ag-S atomic distances are nearly equal in the glass and the crystal. However, the peak height of the glass is about only 40% of that of the crystal. Therefore, it is supported that the glass has rather random distribution of Ag atoms around  $\text{AsS}_3$  groups.

### Reference

- 1) P.Engel and W.Nowacki, Neues Jahrb. Miner. Monatsh., 181-184(1966)

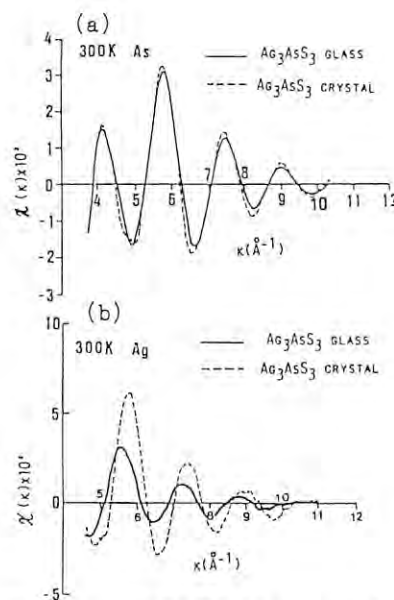


Fig. 1. EXAFS  $\chi(k)$ 's for (a) As and (b) Ag edges in the  $\text{Ag}_3\text{AsS}_3$  glass and the crystal at 300 K.

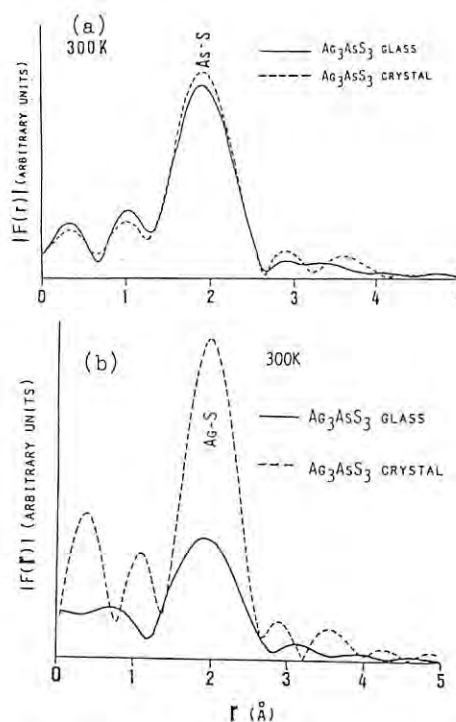


Fig. 2. The  $|F(r)|$ 's for (a) As and (b) Ag atoms in the  $\text{Ag}_3\text{AsS}_3$  glass and the crystal at 300 K.

STRUCTURE OF ZINC(II) IODIDE COMPLEXES IN AQUEOUS LIQUID AND GLASSY SOLUTIONS

Toshio YAMAGUCHI, Keitaro KAMIHATA, Hisanobu WAKITA, and Masaharu NOMURA†

Department of Chemistry, Faculty of Science, Fukuoka University,  
Nanakuma, Jonan-ku, Fukuoka 814-01, Japan

†Photon Factory, National Laboratory for High Energy Physics,  
Oho, Tsukuba 305, Japan

Introduction

Chemical equilibria of metal complexes in aqueous glassy solutions, often used in Mössbauer and ESR spectroscopies, are neither the ones simply expected from temperature dependence of equilibrium constants of metal complexes, nor those in the liquid state at room temperature[1]. In the present study we have performed XANES and EXAFS measurements of aqueous zinc(II) iodide solutions in liquid and glassy states and revealed structural difference in the liquid and glassy state.

Experimental

Sample solutions were prepared by dissolving zinc(II) iodide of reagent grade into distilled water. The samples measured were  $\text{ZnI}_2 \cdot R\text{H}_2\text{O}$  ( $R=4.7, 10, 20$ ), and crystalline powder  $\text{ZnI}_2$  and  $\text{ZnSO}_4 \cdot 7\text{H}_2\text{O}$  as a structure standard. Liquid samples were measured at room temperature, while glassy samples, prepared as previously described [1], were measured at liquid nitrogen temperature. X-ray absorption spectra of samples were measured around the Zn K-edge at the BL10B of the Photon Factory, KEK.

Results and Discussion

Figure 1 shows XANES spectra of sample solutions in the liquid and glassy states. In the liquid state the peak at 9670 eV, characteristic for aqua zinc(II) complex, decreases, whereas the peak at 9663 eV, probably due to  $[\text{ZnI}_4]^{2-}$ , increases with increasing solute concentration. These changes in the peaks suggest stepwise formation of zinc(II) iodide complexes accompanied with a decrease in water content. The XANES spectra in the glassy state show a peculiar trend; at  $R=10$  the XANES spectra in both glassy and liquid states are very similar, but the equilibrium seems to shift to form the lower complexes at  $R=4.7$ , but to form the higher complexes at  $R=20$  in the glassy solutions. Figure 2 shows the Fourier transforms (not corrected for the phase shifts) of samples investigated. In the liquid solutions, the sharp peak at 1.72 Å, ascribed to Zn-OH<sub>2</sub> bonds within hexaaqua zinc(II) ions, decreases with increasing solute concentration, while the peak due to Zn-I interactions increases at 2.50 Å. On the contrary, in the glassy state the Fourier transforms of the three solutions are very similar, suggesting the presence of similar species formed in the solutions. Least-squares fits, applied to Fourier-filtered spectra, were then performed and the final results are given in Table 1.

References

1) T. Yamaguchi, O. Yata, H. Wakita, and M. Nomura, Activity Report, p. 230 (1987).

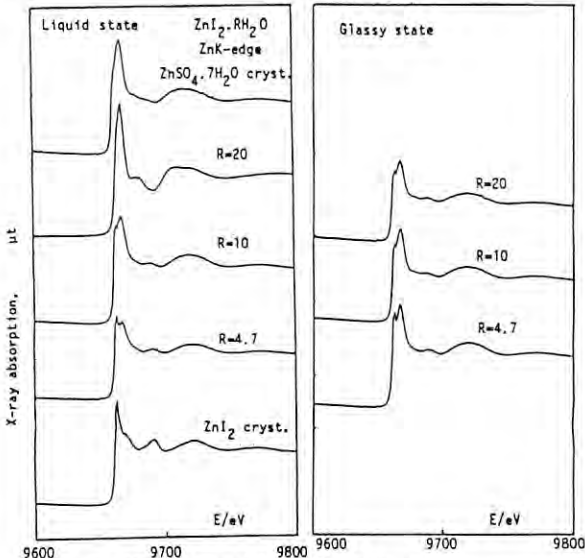


Fig. 1. XANES spectra of  $\text{ZnI}_2 \cdot R\text{H}_2\text{O}$  solutions

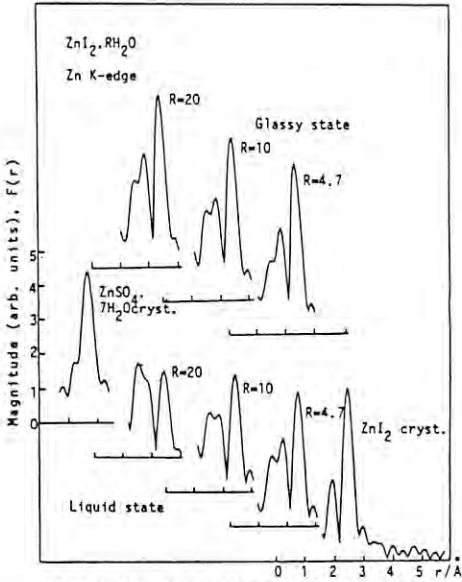


Fig. 2. Fourier transforms of  $\text{ZnI}_2 \cdot R\text{H}_2\text{O}$  solutions

Table 1. Structural parameters of  $\text{ZnI}_2 \cdot R\text{H}_2\text{O}$

Zn K-edge	Liquid				Glass			
	Zn-I r/Å	N	Zn-O r/Å	N	Zn-I r/Å	N	Zn-O r/Å	N
$\text{ZnI}_2 \cdot 4.7\text{H}_2\text{O}$	2.56	2.2	1.99	3.2	2.57	2.7	2.04	3.4
$\text{ZnI}_2 \cdot 10\text{H}_2\text{O}$	2.57	2.2	2.03	2.8	2.58	2.6	2.03	3.0
$\text{ZnI}_2 \cdot 20\text{H}_2\text{O}$	2.57	1.8	2.03	3.1	2.57	2.5	2.02	3.9
$\text{ZnI}_2$ cryst.	2.58	4*						
$\text{ZnSO}_4 \cdot 7\text{H}_2\text{O}$ cryst.			2.08	6*				

\* Fixed

## STRUCTURE OF ZINC(II) CHLORIDE COMPLEXES IN AQUEOUS LIQUID AND GLASSY SOLUTIONS

Toshio YAMAGUCHI, Osamu YATA, Hisanobu WAKITA, and Masaharu NOMURA†

Department of Chemistry, Faculty of Science, Fukuoka University,  
Nanakuma, Jonan-ku, Fukuoka 814-01, Japan†Photon Factory, National Laboratory for High Energy Physics,  
Oho, Tsukuba 305, Japan

## Introduction

Structure of metal complexes in glassy aqueous solutions has attracted the attention of people in the fields of solution chemistry and biochemistry. We have developed an EXAFS system for glassy solutions[1]. In the present study we have performed EXAFS measurements on aqueous zinc(II) chloride solutions in liquid and glassy states.

## Experimental

Sample solutions were prepared by dissolving zinc(II) chloride of reagent grade into distilled water. The samples measured were solutions of compositions of  $\text{ZnCl}_2 \cdot R\text{H}_2\text{O}$  ( $R=3.5, 4.5, 10$ ) and  $\text{ZnCl}_2 \cdot 3\text{LiCl} \cdot 20\text{H}_2\text{O}$ , and crystalline  $\text{ZnSO}_4 \cdot 7\text{H}_2\text{O}$  as a structure standard. Liquid samples were measured at room temperature, while glassy samples, prepared in a previous manner [1], were measured at liquid nitrogen temperature. X-ray absorption spectra of samples were measured around the Zn K-edge at the BL10B of the Photon Factory, KEK.

## Results and Discussion

Figure 1 shows the Fourier transforms of the samples. The predominant peak for  $\text{ZnSO}_4 \cdot 7\text{H}_2\text{O}$  is ascribable to Zn-O bonds within hexaqua zinc(II) ions. The sharp peak seen for  $\text{ZnCl}_2 \cdot 3\text{LiCl} \cdot 20\text{H}_2\text{O}$  arises from Zn-Cl interactions within tetrahedral tetrachloro zinc(II) ions. The dominant peak for other solution samples will consist of both Zn-O and Zn-Cl interactions of zinc(II) chloride complexes formed in the solutions. The peak in the Fourier transforms in the glassy state is more enhanced than that in the liquid state. Structure parameters of zinc(II) chloride complexes in both glassy and liquid solutions were obtained by a least-squares fit for Fourier filtered spectra and summarized in Table 1. The Zn-Cl distance within tetrachloro complex was determined to be 2.26 Å in both states. The Zn-Cl distance does not change significantly for solutions of  $R=3.5, 4.5$ , and 10. On the contrary, the distance and coordination number of Zn-O interactions differ in both liquid and glassy states; the coordination number increases from 3.3 to 4.5 while the Zn-O distance increases from 2.04 to 2.08 Å in vitrification. This result indicates that hexaqua and tetrachloro complexes coexist in the glassy solutions, while di- and trichloro complexes are predominantly formed in the liquid state.

## References

- 1) T. Yamaguchi, M. Nomura, H. Ohtaki, PF-Activity Report, p. 194 (1987); J. Chem. Phys. (1988), in press.

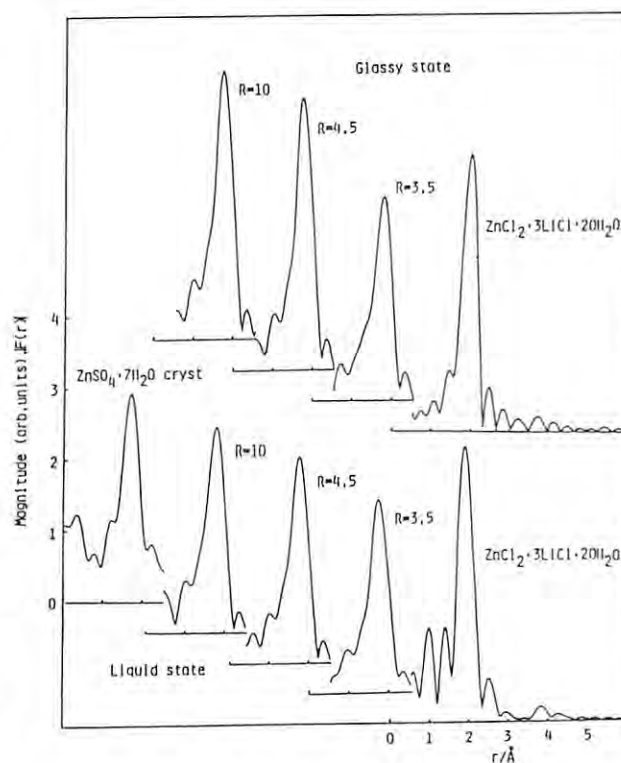


Fig. 1 Fourier transforms of the samples

Table 1. Structure parameters of  $\text{ZnCl}_2$  solutions

	Liquid(298K)				Glass(80K)			
	Zn-Cl		Zn-O		Zn-Cl		Zn-O	
	r/Å	N	r/Å	N	r/Å	N	r/Å	N
$\text{ZnCl}_2 \cdot 3.5\text{H}_2\text{O}$	2.24	1.5	2.04	3.1	2.29	1.1	2.09	4.5
$\text{ZnCl}_2 \cdot 4.5\text{H}_2\text{O}$	2.25	1.6	2.04	3.3	2.25	1.7	2.08	4.1
$\text{ZnCl}_2 \cdot 10\text{H}_2\text{O}$	2.25	1.5	2.04	3.5	2.25	1.4	2.08	4.7
$\text{ZnCl}_2 \cdot 3\text{LiCl} \cdot 20\text{H}_2\text{O}$	2.26	4*	—	—	2.26	4*	—	—
$\text{ZnSO}_4 \cdot 7\text{H}_2\text{O}$ cryst.	—	—	—	—	—	—	2.07	6*

\*Fixed r: distance in Å, N: Coordination number



# STRUCTURE OF GALLIUM(III) CHLORIDE AND BROMIDE COMPLEXES IN AQUEOUS LIQUID AND GLASSY SOLUTIONS

Toshio YAMAGUCHI, Osamu YATA, Hisanobu WAKITA, and Masaharu NOMURA†

Department of Chemistry, Faculty of Science, Fukuoka University,  
Nanakuma, Jonan-ku, Fukuoka 814-01, Japan

†Photon Factory, National Laboratory for High Energy Physics,  
Oho, Tsukuba 305, Japan

## Introduction

Glassy solutions formed by quick vitrification of liquid solutions are of interest in solution chemistry since the motions of ions and solvent molecules are suppressed in the glassy state. In the present study we have performed EXAFS measurements of aqueous gallium(III) chloride and bromide solutions in liquid and glassy states to investigate the structure of gallium halide complexes in both states.

## Experimental

Gallium(III) chloride solutions were prepared by dissolving anhydrous gallium(III) chloride into distilled water. Gallium(III) bromide aqueous solutions were prepared by reaction of gallium oxide with hydrobromic acid. Solutions of  $\text{GaX}_3 \cdot 3\text{LiX} \cdot 20\text{H}_2\text{O}$  ( $\text{X}=\text{Cl}, \text{Br}$ ) were prepared by addition of  $\text{LiX}$  to the above gallium(III) halide solutions. An aqueous gallium(III) perchlorate solution was also measured as a structure standard. Liquid samples were measured at room temperature, while glassy samples, prepared as described elsewhere[1b]0, were measured at liquid nitrogen temperature. X-ray absorption spectra of samples were measured around the GaK-edge at the BL10B of the Photon Factory, KEK.

## Results and Discussion

Figures 1 and 2 show the Fourier transforms of gallium(III) chloride and bromide solutions, respectively. The predominant peak for a gallium(III) perchlorate solution is ascribable to Ga-O bonds within hexaqua gallium(III) ions. The sharp peak seen for  $\text{GaX}_3 \cdot 3\text{LiX} \cdot 20\text{H}_2\text{O}$  ( $\text{X}=\text{Cl}, \text{Br}$ ) arises from Ga-X interactions within tetrahedral tetrahalogallium(III) ions. The dominant peak for other solution samples will consist of both Ga-O and Ga-X interactions of gallium(III) complexes formed in the solutions. In both chloride and bromide solutions of  $R=20$  the peak position shifts to the lower distance side in the glassy state, indicating the equilibrium shifts to form lower halogeno complexes in the glassy solutions. Quantitative analysis was made by a least-squares fit for Fourier-filtered spectra and the final results are given in Table 1. In the chloride system the coordination number of the Ga-Cl interactions decreased from 1.2 to 0.6, while that of the Ga-O interactions increased from 4.0 to 5.7 in the glassy state; this result shows hexaqua gallium(III) ions predominantly form in the glassy solutions. A similar trend has also been found in the bromide system. The number of Ga-X

interactions at the same composition is significantly larger in the chloride solution than in the bromide solution, showing that a hard gallium(III) ion prefers chloride to bromide ions as expected from the HSAB principle.

## References

- 1) T. Yamaguchi, M. Nomura, H. Ohtaki, PF-Activity Report, p. 194 (1987); J. Chem. Phys. (1988), in press.

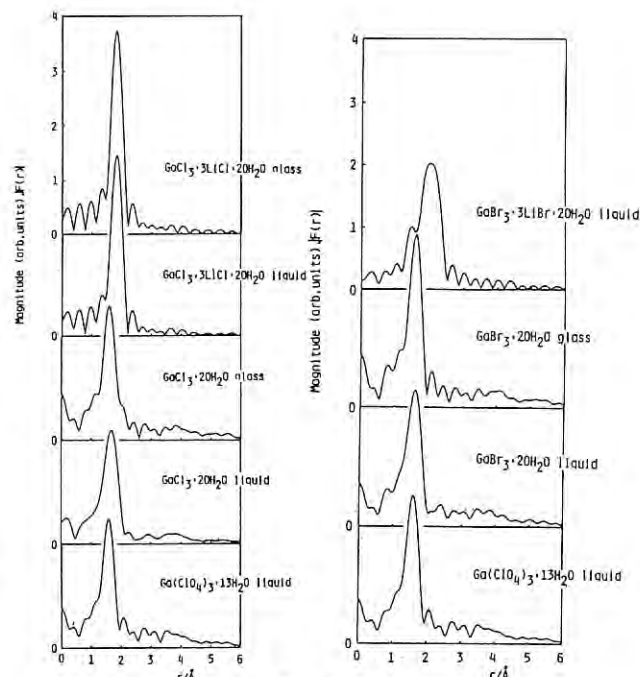


Fig 1. Fourier transforms of the samples. Fig 2 Fourier transforms of the samples

Table 1. Structure parameters of  $\text{GaCl}_3$  and  $\text{GaBr}_3$  solutions

	Liquid(298K)				Glass(80K)			
	Ga-X		Ga-O		Ga-X		Ga-O	
	r/Å	N	r/Å	N	r/Å	N	r/Å	N
$\text{GaCl}_3 \cdot 20\text{H}_2\text{O}$	2.18	1.2	1.93	4.0	2.21	0.6	1.94	5.7
$\text{GaCl}_3 \cdot 3\text{LiCl} \cdot 20\text{H}_2\text{O}$	2.17	4*	—	—	2.17	4*	—	—
$\text{Ga}(\text{ClO}_4)_3 \cdot 13\text{H}_2\text{O}$	—	—	1.93	6*	—	—	—	—
$\text{GaBr}_3 \cdot 20\text{H}_2\text{O}$	2.30	0.6	1.93	5.5	—	—	1.93	6.6
$\text{GaBr}_3 \cdot 3\text{LiBr} \cdot 20\text{H}_2\text{O}$	2.30	4*	—	—	—	—	—	—

\*Fixed r: distance in Å, N: Coordination number



EXAFS STUDY ON ACTIVE SITES FOR HYDROCRACKING AND HYDROGENATION  
ACTIVITIES OF Mo SUPPORTED CATALYSTS II. EFFECT OF Mo LOADINGNobuyuki MATSUBAYASHI, Hiromichi SHIMADA, Nobuhiro KOSUGI\*, Haruo KURODA\*  
Yuji YOSHIMURA, Toshio SATO, and Akio NISHIJIMA

National Chemical Laboratory for Industry, Tsukuba, Ibaraki 305

\*Department of Chemistry, Faculty of Science, The University of Tokyo,  
Hongo, Bunkyo, Tokyo 113Introduction

Supported molybdenum sulfide catalysts have been widely used for hydrotreating of heavy oil. The previous report<sup>1)</sup> showed that the local structure around Mo in the catalysts was different when the presulfiding condition was different. In the present report, EXAFS method was applied to the investigation of the local environment around Mo using various catalysts with different Mo loading.

Experimental

Eight kinds of catalysts were prepared by impregnating alumina supports with solutions of ammonium paramolybdate. MoO<sub>3</sub> loading was varied from 2.5 wt% to 30 wt%. Before measurements, the catalysts were presulfided in a stream of 5 vol% of H<sub>2</sub>S/H<sub>2</sub> at 400 °C for 4h. Mo K-absorption EXAFS spectra were then measured at the BL-10B of the Photon Factory.

Results and Discussion

Figure 1 shows the Fourier transforms of the EXAFS for the 2.5 and 10 wt% MoO<sub>3</sub>/Al<sub>2</sub>O<sub>3</sub> catalysts. Peaks at 1.8 Å in the Fourier transforms are corresponding to Mo-O bonds. In the case of low MoO<sub>3</sub> loading, the Mo-O peak still remained after presulfiding. This Mo-O peak intensity decreased with increase of the MoO<sub>3</sub> loading. Peaks at 2.4 and 3.2 Å in the Fourier transforms are corresponding to Mo-S and Mo-Mo bonds in MoS<sub>2</sub> crystal, respectively. The intensities of the Mo-S and Mo-Mo peaks for the catalyst with 10 wt% of MoO<sub>3</sub> loading were larger than those for 2.5 wt% MoO<sub>3</sub>/Al<sub>2</sub>O<sub>3</sub> catalyst.

The average numbers of coordinating S atoms (N(S)) and the nearest Mo atoms (N(Mo)) around Mo were calculated from the intensities of the Mo-S and Mo-Mo peaks. In this calculation, MoS<sub>2</sub> crystal was used as standard. Figure 2 shows the changes in N(S) and N(Mo) for the catalysts. At Mo loading below 20 wt% both N(S) and N(Mo) increased with the increase of Mo loading. N(Mo)/N(S), which indicates a degree of the growth of MoS<sub>2</sub> crystal-like structure<sup>1)</sup>, also became larger as Mo loading increased in this region. These results clearly show the growth of MoS<sub>2</sub> crystal-like structure at high MoO<sub>3</sub> loading.<sup>2)</sup> However, when the MoO<sub>3</sub> loading increased beyond 20 wt%, these values did not increase further. This result seems to show that disordered structures increase at the higher MoO<sub>3</sub> loading.

References

- 1) N.Matsubayashi, H.Shimada, N.Kosugi, H.Kuroda, Y.Yoshimura, T.Sato, and A.Nishijima, PF Acti. Rep. 1987,
- 2) A.Nishijima et al., Sekiyu Gakkaishi, in press.

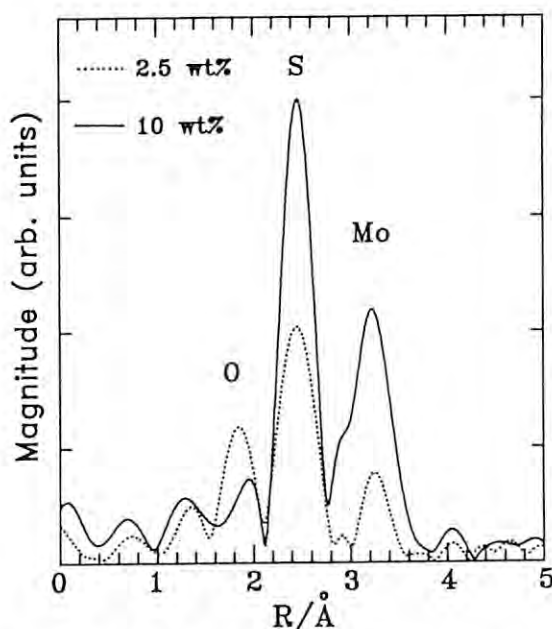


Fig.1 Fourier transforms of the Mo K-edge EXAFS for Mo/Al<sub>2</sub>O<sub>3</sub> catalysts.

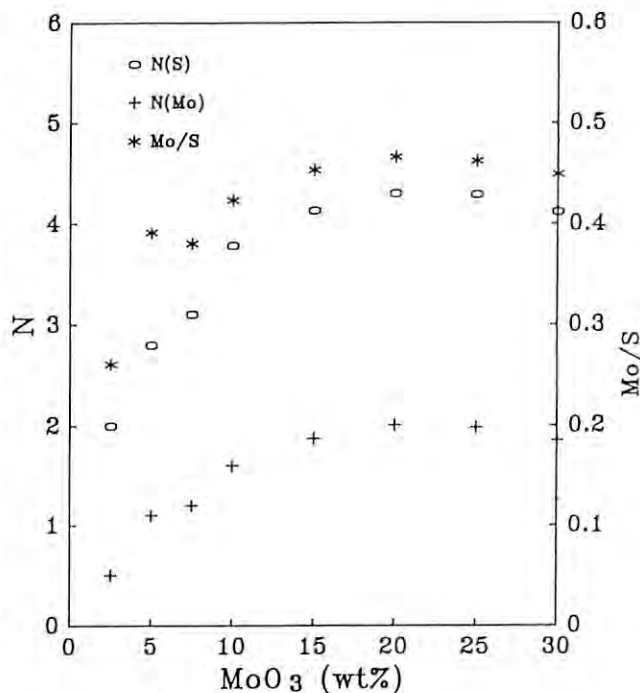


Fig.2 EXAFS results for Mo/Al<sub>2</sub>O<sub>3</sub> catalysts with varied amounts of loading of MoO<sub>3</sub>.

**XANES and EXAFS of Nickel Thiolate Complexes**  
**---in Terms of Nickel Containing Hydrogenases---**

Takeshi Yamamura,<sup>a</sup> Nobuhumi Nakamura,<sup>a</sup>  
 Kiyotaka Asakura,<sup>b</sup> Yasuhiro Iwasawa<sup>b</sup>

<sup>a</sup>Department of Chemistry, Faculty of  
 Science, Science University of Tokyo,  
 Shinjuku-ku, Tokyo 162

<sup>b</sup>Department of Chemistry, Faculty of  
 Science, The University of Tokyo,  
 Bunkyo-ku, Tokyo 113

The hydrogen uptake site of hydrogenases of arcaic bacteria is known to be a low spin  $Ni^{3+}$ ,<sup>1)</sup> which interacts with  $Fe_4S_4$  cluster core. EXAFS studies revealed that this  $Ni^{3+}$  has 3 or 4 sulfur atoms<sup>2,3)</sup> as the backscatterers depending on the species studied. However there is a possibility of the migration of another atoms such as nitrogen or oxygen in the Ni-S peak of the Fourier transform, considering the discrepancy in scattering amplitude between sulfur and nitrogen or oxygen. The Fourier transform of D. gigas hydrogenase could be the example of such migration showing the existence of a shoulder in its Ni-S peak, although the authors did not argue about it.<sup>3)</sup>

We have prepared several kind of thiolatonickel compounds in terms of this site;  $NiS_4$ ,  $NiNS_3$ ,  $NiN_2S_2$  and Ni-Ni interacting cases, and revealed the structures for several of these.<sup>4-6)</sup> The purpose of this experiment was settled to accumulate the knowledges for the EXAFS and XANES pattern of thiolato nickel complexes by using the complexes with known structures, and thereby to understand the EXAFS of hydrogenases. We examined EXAFS and XANES measurement also for structurally unknown thiolato-nickel compounds.

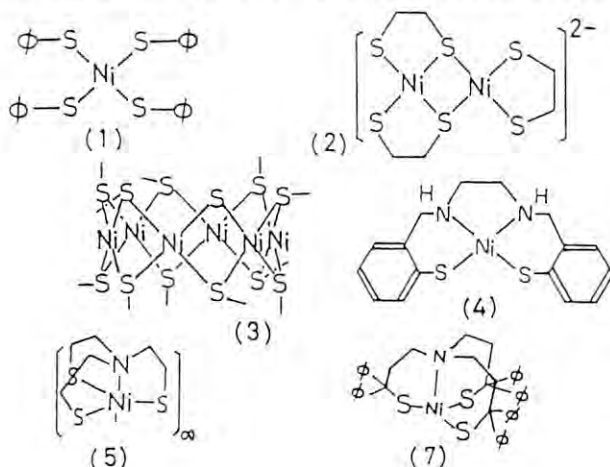
**Experiment** Materials used are (1)  $[Ni(SPh)_4]^{2-}$ , (2)  $[Ni_2(SCH_2CH_2S)_3]^{2-}$ , (3)  $Ni_6(SET)_{12}$ , (4)  $Ni(bmbzylen)$ , (5)  $[Ni(tmea)]_{ox}$ , (6)  $[Ni(tmea)]_{red}$ , (7)  $[Ni(tdpmpa)]_{ox}$ , (8)  $[Ni(Boc-Cys-Pro-Leu-Cys-OMe)_2]$ , within which (1) - (4) are structurally known, and (5) - (8) are not known (Fig. 1). The measurement was

performed by using the beam lines BL-10B and BL-7C at standard conditions. The result was analyzed by EXAFS 1 (by N. Kosugi and H. Kuroda, Research Center for Spectrochemistry, The University of Tokyo).

**Result** The Fourier transform of the EXAFS of compound (1) apperared an well resolved Ni-S peak. This was used as the general base for Ni-S analyses of other compounds. The Fourier transform of (2) and (3) showed small peaks neighboring the large Ni-S peaks. Although these were assigned for the backscatterings from the nickel which interact with the absorber nickel, the number calculated from the theoretical scattering amplitude and phase shift were only 0.5 and 1.2, respectively. These are not enough comparing the number, 1 and 2, of nickel atoms for the complex (2) and (3), respectively. The result suggests the necessity of long time measurement at low temperature, or the practical decision of the parameters for Ni-Ni case. In the Fourier transform of the EXAFS of the complex (4), the radial distributions of Ni-S and Ni-N were not separated. Nevertheless the analysis for this complex afforded reasonable result both in distances and coordination numbers for Ni-S and Ni-N. It should be noticed that the scattering by N appeared as a shoulder in the Ni-S peak for this compound. This is suggestive of a possibility that the shoulder which is observed in the Ni-S radial distribution of the Fourier transform of the nickel EXAFS for D. gigas<sup>3)</sup> originates also from the back-scattering by nitrogen. The same migration of Ni-N into Ni-S was observed also in all the compound, (5) - (8). We decided the Ni-S and Ni-N distances and the coordination numbers for all of these compounds.

## References

- 1) J. R. Lancaster Jr., FEBS LETTERS, 115, 285 (1980).
- 2) P. A. Lindahl, N. Kojima, R. P. Hausinger, J. A. Fox, B. K. Teo, C. T. Walsh, and W. H. Orme-Johnson, J. Am. Chem. Soc., 106, 3062 (1984).
- 3) R.A. Scott, S. A. Wallin, M. Czecowski, D. V. DerVartanian, J. LeGall, H. D. Peck, Jr., and I. Moura, J. Am. Chem. Soc., 106, 6864 (1984).
- 4) T. Yamamura, H. Miyamae, Y. Katayama, and Y. Sasaki, Chem. Lett., 1985, 269.
- 5) H. Miyamae and T. Yamamura, Acta Cryst., C44, 606 (1988).
- 6) Ch. Rao, J. R. Dorfman, and R. H. Holm, Inorg. Chem., 25, 428 (1986).



THE STRUCTURE OF INTERCALATED METAL PARTICLES IN LAYERED  $K_4Nb_6O_{17}$ 

Joji YOSHIMURA, Satoko HOSHI, Tokihisa HIKITA, Akihiko KUDO, Kiyotaka ASAKURA\*, Kazunari DOMEN and Takaharu ONISHI

Research Laboratory of Resources Utilization, Tokyo Institute of Technology,  
4259 Nagatsuta, Midori-ku, Yokohama 227

\*Faculty of Science, The University of Tokyo, Hongo, Bunkyo-ku, Tokyo 113

### Introduction

We have studied on the photocatalytic activity of  $K_4Nb_6O_{17}$ . It has mica like layered structure, and  $K^+$  ions which locate at the interlayer of niobate sheets are ion exchangeable. If metal particles are able to intercalate into the interlayers of  $K_4Nb_6O_{17}$ , this catalyst will be useful not only for photocatalytic but also for other thermal catalytic reactions. Therefore,  $Ag^+$ -exchanged  $K_4Nb_6O_{17}$  was prepared and was investigated the structure by means of EXAFS and XANES spectroscopy after various treatments.

### Experimental

The catalyst were prepared by the method discribed elsewhere. Six samples were measured, (1)  $Ag^+/K_4Nb_6O_{17}$ : untreated, (2)  $Ag^+/K_4Nb_6O_{17}$ : after reaction of photodecomposition of water, (3)  $Ag^+/K_4Nb_6O_{17}$ : after reaction of  $H_2$  photoevolution from  $MeOH$ , (4)  $Ag^+/K_4Nb_6O_{17}$ : reduction by  $H_2$  at  $200^\circ C$ , (5)  $Ag$  foil. Sample (5) was used as reference. Sample (2) and (3) were measured at the steady state reaction condition.

### Results and Discussion

Figure 1 shows the XANES-spectra of  $Ag$  K-edge. Spectra (4) is actually identical with  $Ag$  metal. Spectrum (2) and (3) are also similar to spectrum (5). But their amplitude are smaller than that of (5), and rather similar to (1) because of amplitude of the first peak is larger than the others.

Figure 2 shows the Fourier transform of  $K^3X$  (K) of  $Ag$  K-edge EXAFS data. In there spectra, the peak at  $R=2.89$  corresponds to  $Ag-Ag$  of  $Ag$  metal and the peak at  $R=1.68$  is attributed to  $Ag-O$  of untreated  $Ag^+/K_4Nb_6O_{17}$  sample. In  $H_2$  reduced sample, only  $Ag$  metal is observed and its coordination number is 9. On the other hand, in samples after photocatalytic reaction, the  $Ag$  metal also exists but their coordination number are 3 and 4 for (2) and (3) respectively and  $Ag-O$  peak still remains.

Taking these results into consideration, it is concluded that some part of exchange  $Ag^+$  ions are photo-reducible and the produced  $Ag$  metals are highly dispersed ultra fine particles.

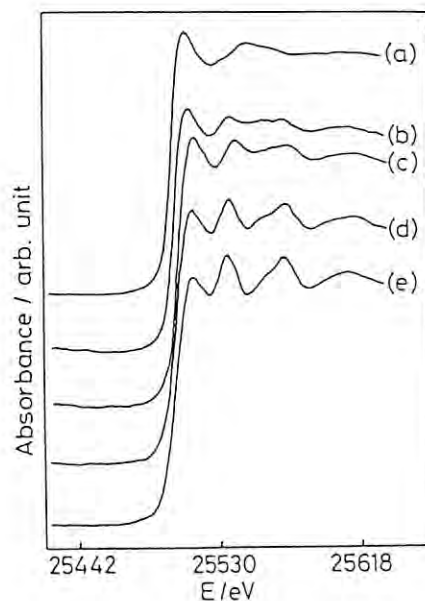


Fig. 1 The XANES-spectra of  $Ag$  K-edge.

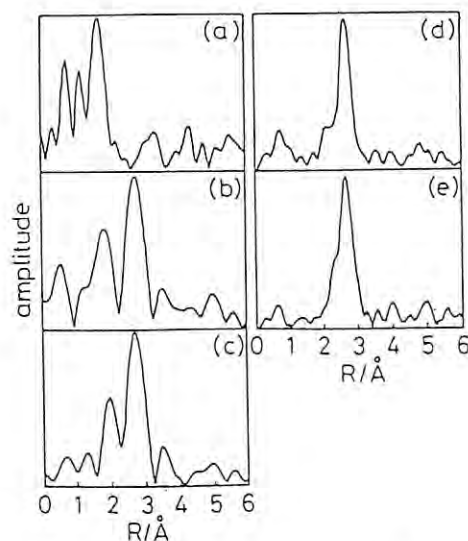


Fig. 2 Fourier transform of  $Ag$  K-edge EXAFS data.

# A STUDY ON THE CORRELATION BETWEEN THE LOCAL STRUCTURE AND PHOTO-CATALYTIC ACTIVITY BY SUPPORTED NIOBIUM OXIDES CATALYSTS

Yasuo NISHIMURA, Tanehiro TANAKA, Hiroshi MIZUTANI,  
Takamaro KAKEHI, Takahiro INOUE, Takuzo FUNABIKI and Satoshi YOSHIDA

Division of Molecular Engineering and Department of Hydrocarbon Chemistry,  
Kyoto University, Sakyo-ku, Kyoto 606.

## Introduction

Niobium oxide supported on silica exhibits the catalytic activity for photo-assisted partial oxidation of propene. Generally, the activity of supported metal oxide catalysts are related to the local structure of the oxide. To clarify this correlation in  $\text{Nb}_2\text{O}_5/\text{SiO}_2$ , we carried out EXAFS and XANES experiments.

## Experimental

The catalysts were prepared by impregnation method with ethanol solutions of  $\text{Nb}(\text{OEt})_5$  in the different concentration. Some of the catalysts were pretreated with oxygen, and spectra were recorded *in situ* ( $\text{Nb x}$ ). The other samples were exposed to air ( $\text{Nb x}'$ ). X-ray absorption spectra were recorded with the facilities at BL10B of KEK-PF.

## Results and Discussion

Fig. 1 shows XANES spectra of the catalysts and reference compounds. The characteristic pre-edge peak is attributed to the so-called Nb 1s - 4d transition caused by mixing O 2p orbitals with Nb 4d. The shape of this peak depends on the coordination symmetry around the central Nb atoms. The pre-edge peak becomes more intense when a niobium atom is in tetrahedral coordination, as in  $\text{YbNbO}_4$ . The peak height increases with a decrease in  $\text{Nb}_2\text{O}_5$  loading. The catalyst without pretreatment ( $\text{Nb x}'$ ) exhibits a smaller peak than that with pretreatment ( $\text{Nb x}$ ) does. The decrease of this peak is due to the formation of coordinatively saturated niobates with  $\text{H}_2\text{O}$  in highly dispersed catalysts.

Fig. 2 shows the fourier transforms of  $k^3$ -weighed EXAFS spectra. Peaks appeared in 1-2 Å are due to Nb-O bonds. These peaks change with an increase in  $\text{Nb}_2\text{O}_5$  loading. The peaks in 2-3 Å are due to the scattering from neighboring Nb atoms. These peaks become high when the samples are exposed to air, and this effect is more remarkable with the lower content of  $\text{Nb}_2\text{O}_5$ . This increase in the peak height is due to linkage of two coordinatively unsaturated niobates with  $\text{H}_2\text{O}$  as in the case of vanadates.<sup>1)</sup> These results are explained by that niobates on silica is tetrahedral when they are in a low-loaded and a dehydrated state, but octahedral when in a high-loaded or a hydrated state.

## Reference

- 1) S. Yoshida, T. Tanaka, Y. Nishimura, H. Mizutani and T. Funabiki, Proceedings 9th International Congress on Catalysis, 1473(1988).

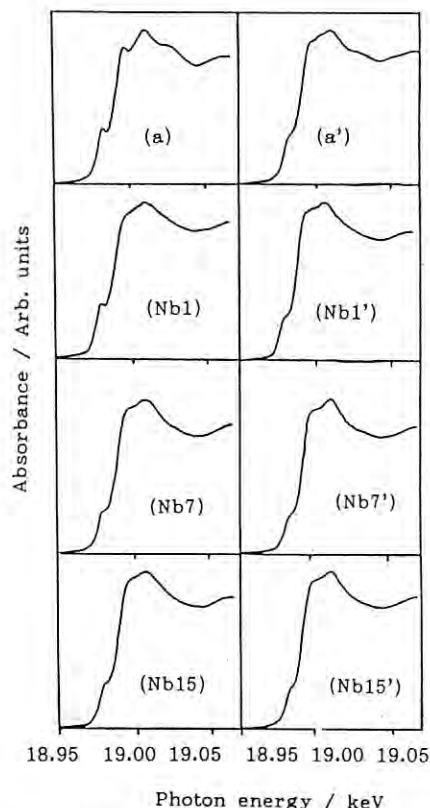


Fig. 1 XANES of  $\text{YbNbO}_4$ (a),  $\text{Nb}_2\text{O}_5$ (a') and x wt%  $\text{Nb}_2\text{O}_5/\text{SiO}_2$ (Nb<sub>x</sub>,Nb<sub>x</sub>'). (Nb<sub>x</sub>)s were recorded *in situ*, (Nb<sub>x</sub>')s were *ex situ*.

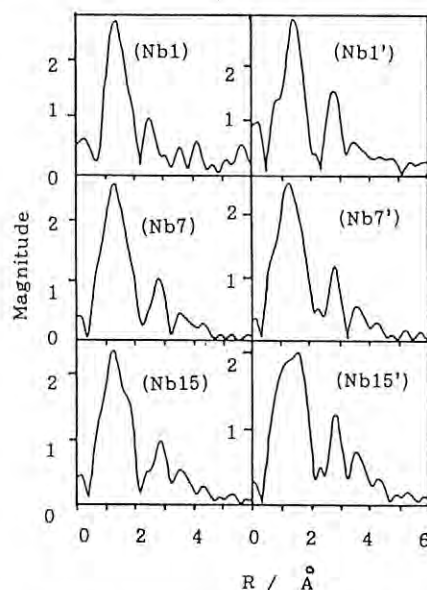


Fig. 2 Fourier transforms of EXAFS of (Nb<sub>x</sub>)s and (Nb<sub>x</sub>')s.



XAFS STUDIES ON LOCAL STRUCTURE OF HIGH  $T_c$  SUPERCONDUCTORS.

Hitoshi YAMAZAKI, Hironobu MAEDA\*, Hiroshi MARUYAMA, Akihisa KOIZUMI, Naruhiko BAMBA, Hiroyuki AOKI, Jun SHI, Kazuaki SHIMIZU, Michinobu MINO, Yasuharu IWAMOTO and Yasushi OKA.

Department of Physics, Faculty of Science, Okayama University,  
\* Department of Chemistry, Faculty of Science, Okayama University,  
3-1-1 Tsushima-Naka, Okayama 700.

Introduction

Since the discovery of oxides which have a stable and reproducible superconductivity transition, intensive studies on the superconducting properties and the crystal structure have been reported. The following materials have been presently established as the high- $T_c$  superconductor, i.e., the La-(Sr-Ba)-Cu-O, R-Ba-Cu-O and Bi-Sr-Ca-Cu-O systems. In order to clarify the relation between the crystal structure and superconductivity, it is desirable to elucidate the local environment on valence and coordination state of metal ions, temperature variation of interatomic distance and thermal vibration between metal and oxygen atoms, and so on. For this purpose, the X-ray Absorption Fine Structure (XAFS) measurement is one of most useful techniques.

Experimental

The following oxides were prepared by the usual method for the present experiments; the  $YBa_2Cu_3O_{7-y}$ ,  $YBa_2(Cu_{1-x}Fe_x)_3O_{7-y}$  ( $x=0.05, 0.1-0.5$ ),  $Y_{1.2}Ba_{1.8}Cu_3O_{7-y}$  and  $Bi_2(Sr,Ca)_{3-x}Cu_2O_{9-y}$  compounds. The synthesized compounds were characterized by the transition temperature  $T_c$  estimated from the resistivity measurements by a conventional four-terminal method, and by the lattice parameters determined from the X-ray diffraction measurements on the powdered samples. X-ray absorption measurements were performed using the facilities of BL-10B and BL-7C. The energy resolution was about 0.5eV for near-edge scans and 2.0-3.0eV for EXAFS scans. The photon energy was calibrated with respect to the pre-edge peak of the Cu-K absorption. The following oxides were used for reference materials;  $Cu_2O$  and  $CuO$  for Cu-K edge,  $Bi_2O_3$  for Bi-L<sub>3</sub> edge,  $Y_2O_3$  for Y-K edge and  $Fe_2O_3$  for Fe-K edge.

Results and Discussion

- (1) Temperature dependence of mean-square relative displacement (MSRD) in the  $YBa_2Cu_3O_y$  oxides.<sup>(1,2)</sup>

The temperature variation of XAFS spectrum of the Cu-K edge was taken in the temperature range 20-300K on the orthorhombic-I, orthorhombic-II and tetragonal phases in the  $YBa_2Cu_3O_y$  oxides system. From the analysis of EXAFS spectrum, an anomalous reduction in the peak height of Fourier transform with decreasing temperature is found on the nearest neighbor pairs (Cu-O) in the ortho-I and ortho-II superconducting phases below a temperature corresponding to  $T_c$ . It can be thought to result from the Debye-Waller type broadening of the relevant atom pair. Therefore, in order to determine the Debye-Waller factors of two nonequivalent oxygens around each of two kinds of Cu ions, four-shell model was

employed in the curve fitting analysis. In the temperature dependence of the Debye-Waller factors thus determined, anomalous jump is observed in the factor with respect to the axial Cu-O bond in the vicinity of  $T_c$  for the ortho-I and ortho-II phases; however, no anomaly is found in the relevant factor for the non-superconducting tetragonal phase. The Debye-Waller factor of the equatorial Cu-O bonds, on the other hand, shows the normal temperature dependence, which decreases monotonically with decreasing temperature. These features would suggest that the lattice vibration is strongly correlated with the superconducting transition.

- (2) Local structure of the Bi-Sr-Ca-Cu-O superconductor.<sup>(3)</sup>

X-ray absorption spectroscopy has been used to study the local structure of a new superconducting phase in the Bi-Sr-Ca-Cu-O system. From EXAFS analysis on the Cu-K edge, Cu ions are pyramidally coordinated with five oxygen atoms without stretching in the axial direction. The Cu-O and Bi-O distances are determined to be 1.91 and 2.10 Å, respectively.

- (3) Substitution effect in Fe doped  $YBa_2Cu_3O_y$  superconductors.<sup>(4)</sup>

It is well known that substitution of 3d transition metal atoms for Cu results in a reduction of  $T_c$ . In order to study which site the Fe atoms are substituted for and how the local environment changes, therefore, we have carried out the XAFS measurements on  $YBa_2(Cu_{1-x}Fe_x)_3O_y$  as Fe concentration is increased. The following conclusions are derived from EXAFS analysis: The Fe ions substituted for the Cu(I) site are octahedrally coordinated with six oxygen atoms without stretching in the axial direction; the axial Cu-O distance has a tendency to decrease with increasing Fe content; the local environment around Y ions is hardly affected by substitution.

References

- (1) H. Maeda, N. Bamba, A. Koizumi, Y. Yoshikawa, T. Ishii, H. Maruyama, M. Hida, Y. Kuroda, H. Yamazaki and T. Morimoto: J. Phys. Soc. Jpn. 56 (1987) 3414-3416.
- (2) N. Bamba, H. Maeda, A. Koizumi, H. Maruyama, J. Shi, K. Shimizu, M. Mino and H. Yamazaki: (in preparation).
- (3) H. Maeda, A. Koizumi, N. Bamba, E. Takayama-Muromachi, F. Izumi, M. Onoda, Y. Kuroda, H. Maruyama, Y. Yoshikawa, T. Ishii, M. Hida and H. Yamazaki: Jpn. J. Appl. Phys. 27 (1988) L807-L810.
- (4) A. Koizumi, H. Maeda, N. Bamba, H. Maruyama, E. Takayama-Muromachi, J. Shi, K. Shimizu, M. Mino and H. Yamazaki: (in preparation).



## CHEMICAL SHORT RANGE ORDER IN LIQUID Rb-Se ALLOYS

Hirohisa ENDO, Makoto YAO, Masanori INUI, Yoshinori KATAYAMA and Kenji MARUYAMA

Department of Physics, Faculty of Science, Kyoto University, Kyoto 606

Kozaburo TAMURA and Shinya HOSOKAWA

Faculty of Integrated Arts and Sciences, Hiroshima University, Hiroshima 730

Hideoki HOSHINO

Faculty of Education, Hirosaki University, Hirosaki 036

Hiroyuki OYANAGI

Electrotechnical Laboratory, Tsukuba 305

Masaharu NOMURA

National Laboratory for High Energy Physics, Tsukuba 305

Introduction

Liquid selenium (l-Se) is composed of chain molecules and exhibits semiconducting behavior. Recently it has been found that an addition of alkali metal impurities to l-Se remarkably increases the electrical conductivity and changes the sign of the thermopower.<sup>1)</sup> It is interesting to study how the chain structure of l-Se is modified by adding alkali metal. In this paper we report the EXAFS results on both Se and Rb K-edges for liquid Se-Rb mixtures.

Experimental

RbSe<sub>3</sub> and RbSe<sub>2</sub> alloys were prepared by exposing liquid Se to Rb vapor at 400°C in a pyrex tube. Rb metal was carefully handled under dry argon. For EXAFS measurements of liquid samples, we have made special polycrystalline sapphire cells with X-ray windows 250 μm thick. We could keep the sample stably in the space with 30 μm thickness up to 650°C. X-ray absorption measurements near Se and Rb K-edges were made using the EXAFS facilities installed at BL-10B.

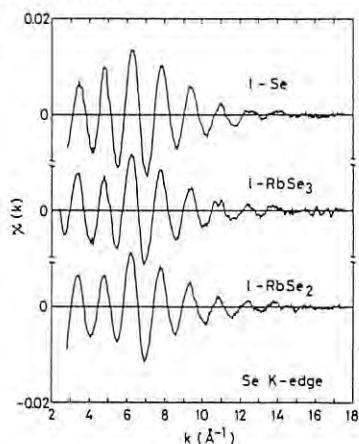


Fig.1. The Se K-edge EXAFS oscillation  $\chi(k)$  of l-Se at 400°C, l-RbSe<sub>3</sub> at 350°C and l-RbSe<sub>2</sub> at 350°C.

Results and Discussion

Figure 1 shows EXAFS oscillation  $\chi(k)$  near Se K-edge of l-Se at 400°C, l-RbSe<sub>3</sub> at 350°C and l-RbSe<sub>2</sub> at 350°C. The amplitude of the Rb-Se mixtures is as large as that of l-Se. This evidence indicates that the chain structure is also preserved in the mixtures.

Figure 2 shows the magnitude of Fourier transform  $|F(r)|$  of  $k\chi(k)$  near Se K-edge for l-Se at 400°C, l-RbSe<sub>3</sub> at 350°C and l-RbSe<sub>2</sub> at 350°C. The first peak is clearly seen in the  $|F(r)|$  of the Rb-Se mixtures. The width becomes large and the position is shifted toward larger distance with increasing Rb content. These results suggest that disorder of the Se chain structure increases and the bond length elongates with addition of Rb. The EXAFS oscillation near Rb K-edge of the liquid Rb-Se mixtures is damped and nearly disappears, suggesting that there is no strong Rb-Rb and Rb-Se bonds. Detailed analysis is now in progress.

1) S. Hosokawa, M. Yao, T. Yoshimura and H. Endo, J. Phys. Soc. Jpn., **54** (1985) 4717.

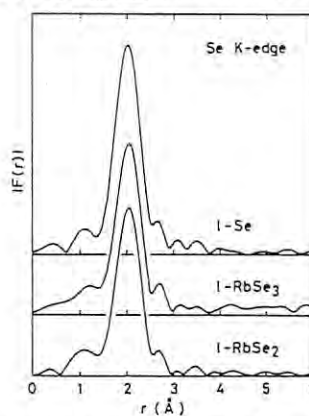


Fig.2. The magnitude of Fourier transform  $|F(r)|$  of  $k\chi(k)$  near Se K-edge for l-Se at 400°C, l-RbSe<sub>3</sub> at 350°C and l-RbSe<sub>2</sub> at 350°C.

AsO<sub>4</sub> MOLECULE DISTORTION IN KDA

Yukio NODA, Kenichiro OGURA,  
Kazuya KAMON<sup>†</sup>, Hikaru TERAUCHI<sup>†</sup> and Hironobu Maeda<sup>††</sup>

Faculty of Engineering Science, Osaka University, Toyonaka Osaka 560

<sup>†</sup>School of Science, Kansai Gakuin University, Nishinomiya 662

<sup>††</sup>Faculty of Science, Okayama University, Okayama 700

## Introduction

Such KDP(KH<sub>2</sub>PO<sub>4</sub>) type materials as KDP, KDA, ADP, RDP etc. show phase transitions, at some critical temperature T<sub>c</sub>, in which hydrogen ordering or softening of hydrogen tunneling mode plays an important role. However, recent works cast some doubts on the above tunneling model. There are several key points to consider the recent discussions between 'tunneling group' and 'order-disorder group'.

(1) Does a tunneling mode exist or not? If there is, what is the direct contribution to T<sub>c</sub>.

(2) Does a PO<sub>4</sub> molecule distort or not? If it distorts, what is the contribution of the dipole-dipole interaction to T<sub>c</sub>.

Question (1) relates to the recent model so called 'geometrical isotope effect' and involves quite complicated problem. On the other hand, question (2) seems to be much simpler than the tunneling problem to be revealed by experiments.

We report the AsO<sub>4</sub> molecule distortion observed by EXAFS experiments around As atoms, in the low temperature phase and the high temperature phase.

## Experimental and Results

Conventional EXAFS experiments around the K-absorption edge of an arsenic atom were carried out at the 10B beam line from 10K to 300K. The phase transition temperature of KDA(KH<sub>2</sub>AsO<sub>4</sub>) is about 90K. Following the standard procedure, EXAFS signal  $\chi(k)$  and Fourier transformed radial distribution function are obtained. In Fig.1, EXAFS signals  $k^3\chi(k)$  obtained at 300K and 30K are shown. Well defined signals were obtained up to 18 Å<sup>-1</sup> (with 2 $\pi$  unit). As is shown,  $k^3\chi(k)$  at 300K is very simple, while  $k^3\chi(k)$  at 30K is very complicated and contains higher order frequencies. The transformed distribution function of  $k^3\chi(k)$  (right hand side figure) shows many peaks at 30K and single peak at 300K, corresponding to the structure of  $k^3\chi(k)$ . The first peak(I<sub>1</sub>) reflects the oxygen atoms around the probed arsenic atom. Other peaks(I<sub>2</sub>, I<sub>3</sub>) gradually decreased at raising temperature, and nothing happened at T<sub>c</sub>.

The first peak(I<sub>1</sub>) was analyzed to investigate the local structure of the AsO<sub>4</sub> molecule. There are two alternative models; two-shell model in which the AsO<sub>4</sub> molecule distorts, and one-shell model in which the AsO<sub>4</sub> molecule forms a regular tetrahedron. Inverse Fourier transformed  $k^3\chi(k)$  around the first peak was fitted by the calculated one with parameters; distance  $r_1$  and  $r_2$ , Debye-Waller factor  $\sigma$ , mean free path of photo electron  $\tau$ , the energy of the absorption edge  $E_0$ , and the scale factor. The Debye-Waller factor at the different site of oxygen atoms was assumed to be the same, for the sake of simplicity. The coordination numbers were fixed to be  $N_1=N_2=2$  for the two-shell model and  $N=4$  for the one-shell model. Thus, the number of fitting parameters were 5 for the one-shell model and 6

for the two-shell model. Examples of calculated and observed  $k^3\chi(k)$  at 300K and 30K are shown in Fig.2, for two different models. The ratio of the R-factors of the two-shell model(R<sub>2</sub>) and the one-shell model(R<sub>1</sub>) was  $R_2/R_1=0.8$ . Obtained bond lengths of As-O are  $r_1=1.685$  Å and  $r_2=1.764$  Å for two-shell model, and  $r_0=1.716$  Å for the one-shell model. It is obvious to consider that the AsO<sub>4</sub> molecule distorts at the low temperature phase, and the observed result is consistent with the predicted structure of the low temperature phase.

When the temperature was raised up to 300K, the feature of  $k^3\chi(k)$  was almost the same through all temperature region, and the ratio  $R_2/R_1$  was around 0.8. Parameters at 300K were  $r_1=1.671$  Å,  $r_2=1.754$  Å and  $r_0=1.712$  Å.

## Conclusion

We summarize the experimental results:

(1) The AsO<sub>4</sub> molecule already distorts at the high temperature phase. This means that the phase transition includes the configurational ordering of the distorted molecule. (2) We found extraordinary temperature dependence of the higher frequencies in  $k^3\chi(k)$ . At the moment, we have no idea to explain these phenomena, but we speculate that these intensities come from the multiple scattering process of EXAFS.

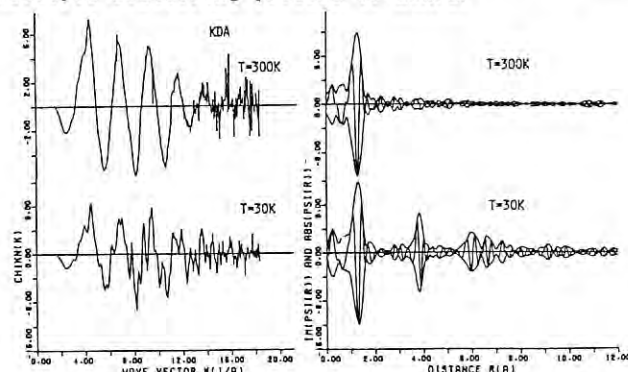


Fig.1 Observed  $k^3\chi(k)$  and Fourier transformed distribution function

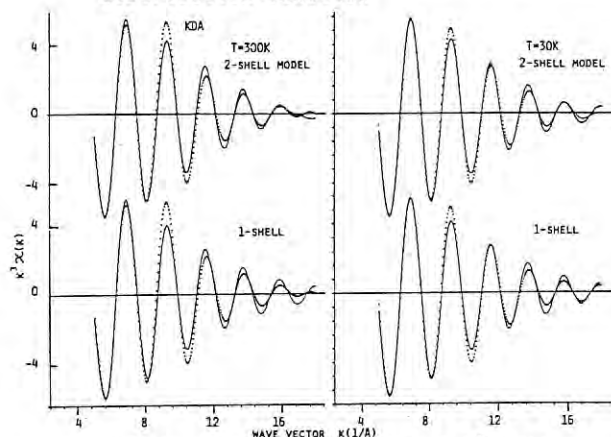


Fig.2 Observed and calculated  $k^3\chi(k)$

A STUDY ON THE  $\text{Ni}^{2+}$  IONS IN SODIUM BORATE GLASSES BY EXAFS

Qiang XU, Takashi MAEKAWA and Toshio YOKOKAWA

Department of Chemistry, Faculty of Science,  
Hokkaido University, Sapporo 060Introduction

It is well-known that in the binary sodium borate glasses containing  $\text{Ni}^{2+}$  ions their colour changes from greenish yellow to deep brown with increasing  $\text{Na}_2\text{O}$  content. By comparing with some crystal structures, Paul and Douglas<sup>(1)</sup> showed that three coordination states of  $\text{Ni}^{2+}$  ions may exist in the glasses, i.e. octahedral, square planar and tetrahedral species. Beyond 19±1 mol% alkali content, the conversion of the octahedral to 4-fold coordinated  $\text{Ni}^{2+}$  species occurs. In this paper we report the results of study on the change of coordination number around  $\text{Ni}^{2+}$  ions in sodium borate glasses by XANES and EXAFS.

Experimental

$x\text{Na}_2\text{O} \cdot (1-x)\text{B}_2\text{O}_3$  oxide glasses containing 1 mol%  $\text{NiO}$ , where  $x$  are 0.1, 0.15, 0.2, 0.25, 0.3, 0.35, 0.4, were prepared from reagent grade  $\text{Na}_2\text{CO}_3$ ,  $\text{H}_3\text{BO}_3$  and  $\text{NiO}$ . Powder samples placed on Scotch tape were used for the measurements. The X-ray absorption measurements were carried out at the BL-10B line of the Photon Factory in the National Laboratory for High Energy Physics (KEK-PF).

Results and Discussion

It is found that the shapes of the XANES spectra of the glasses below 20mol%  $\text{Na}_2\text{O}$  are rather similar to that of  $\text{NiO}$ . On the other hand, the several peaks of the XANES spectra of the glasses disappear gradually with an increase of  $\text{Na}_2\text{O}$  content. It seems that there is a meaningful change of the local structure around  $\text{Ni}^{2+}$  ions.

Figure 1 shows the results of Fourier transforms of the EXAFS for the  $\text{NiO}$  crystal and the glasses. The main peaks in the spectra of the glasses within the region of 1.2~2.0 Å are attributable to Ni-O bonds. The next peaks around 2.5~3.0 Å are considered to be due to Ni-B interactions. The peaks below 1.0 Å are merely ghosts.

It is found from Fig.1 that the

intensities of the main peaks in the spectra of the glasses decrease with an increase of  $\text{Na}_2\text{O}$  content. This decrease corresponds to the decrease of the  $\text{Ni}^{2+}$  coordination.

The curve-fitting analyses for sodium borate glasses containing 1 mol%  $\text{NiO}$  were performed. As the result, the nearest Ni-O bond length remains almost constant below 15 mol%  $\text{Na}_2\text{O}$ . However, when the  $\text{Na}_2\text{O}$  content is above that composition, the length decreases remarkably. It appears that the structural change occurs gradually in the region of 15~30 mol%  $\text{Na}_2\text{O}$ .

The composition dependence of the coordination number of  $\text{Ni}^{2+}$  ions obtained by a curve-fitting method, is similar to that of the nearest Ni-O bond length. It is indicated that the coordination number of  $\text{Ni}^{2+}$  ions decreases largely in the region of 15~30 mol%  $\text{Na}_2\text{O}$ . However, the coordination number remains constant both above and below 15~30 mol%  $\text{Na}_2\text{O}$ . This corresponds to the conversion of the  $\text{Ni}^{2+}$  octahedral species to a 4-fold coordinated one.

Reference

- (1) A. Paul and R. W. Douglas, Phys. Chem. Glasses 8(1967)233.

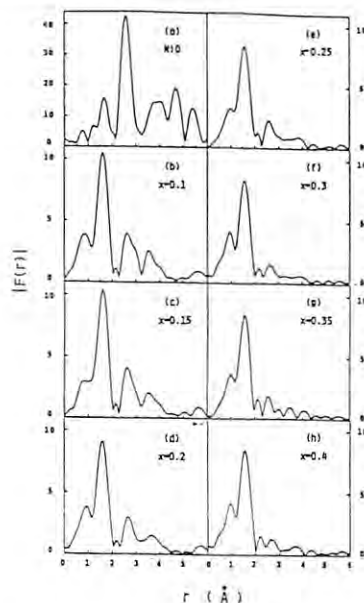


Fig.1.  $k^3$  Fourier transform of the EXAFS spectra.



## CHARACTERIZATION OF ZEOLITE-ENCAPSULATED METAL PHTHALOCYANIN CATALYSTS

Masaru ICHIKAWA, Atsushi FUKUOKA, Takuma KIMURA, Toshiyuki FUJIMOTO,  
Nobuhiro KOSUGI\*, and Haruo KURODA\*

Research Institute for Catalysis, Hokkaido University, Sapporo 060

\*Department of Chemistry, Faculty of Science, The University of Tokyo, Hongo, Bunkyo-ku, Tokyo 113

### Introduction

Metal phthalocyanin complexes encapsulated inside zeolite framework are one of the models of natural monooxygenase enzymes such as cytochrome P 450, which exhibits a high selectivity in the partial oxidation of inactive alkanes.<sup>1)</sup> We synthesized NaY zeolite-encapsulated iron phthalocyanin (FePc) from  $[\text{HFe}(\text{CO})_5]^-/\text{NaY}$  and phthalonitrile. The structural properties of FePc inside the supercage were studied by Fe K-edge XANES and EXAFS,  $^{57}\text{Fe}$  Mossbauer, FTIR, and UV-VIS. We report here that FePc highly dispersed within the NaY supercage is distorted from its original plane structure.

### Experimental

Iron phthalocyanin in NaY supercage (FePc/NaY) was synthesized from  $[\text{HFe}(\text{CO})_5]^-/\text{NaY}$  and 1,2- $\text{C}_6\text{H}_4(\text{CN})_2$ .<sup>2)</sup> FePc on the NaY surface (FePc+NaY) was prepared by impregnation of NaY with pyridine solution of FePc. Fe K-edge XANES and EXAFS measurements were carried out at room temperature at BL 10B in KEK-PF.

### Results and Discussion

Figure 1 shows the Fe K-edge XANES spectra for FePc/NaY, FePc+NaY, FePc crystalline, and FePc(pyridine)<sub>2</sub> complex. FePc/NaY, FePc+NaY, and FePc have the sharp peak at about 7110 eV, arising from  $1s \rightarrow 4p\pi^*$  transition of Fe core electron. On the other hand, FePc(Py)<sub>2</sub> gave no absorption at 7110 eV, because two pyridine molecules coordinate to Fe perpendicularly ( $\pi$ ) with respect to FePc plane of FePc(Py)<sub>2</sub>. XANES spectra suggest that Fe of FePc within NaY supercage is in the similar states to that of FePc crystalline. From  $^{57}\text{Fe}$  Mossbauer study, it is certificated that the valence states of Fe in FePc/NaY is almost the same as those in FePc. Mossbauer data for FePc/NaY revealed also that FePc is highly dispersed in the NaY supercage network.

Figure 2 shows the Fourier transform of  $k^3\chi(k)$  of Fe K-edge EXAFS for FePc/NaY. The strong peak at 1.8 Å can be attributed to first neighbor Fe-N. Table 1 summarizes the results of curve-fitting analyses. By comparison, FePc/NaY gave less coordination number (C.N.) and longer interatomic distance (R) than FePc crystalline and FePc on the NaY surface did, although the shifts of C.N. and R are not so large. These results suggest that Fe is slightly out of the phthalocyanin plane. The difference of the Debye-Waller like factor ( $\Delta\sigma^2$ ) for FePc/NaY was larger than that for FePc+NaY, presumably due to the encapsulation of FePc within NaY supercage.

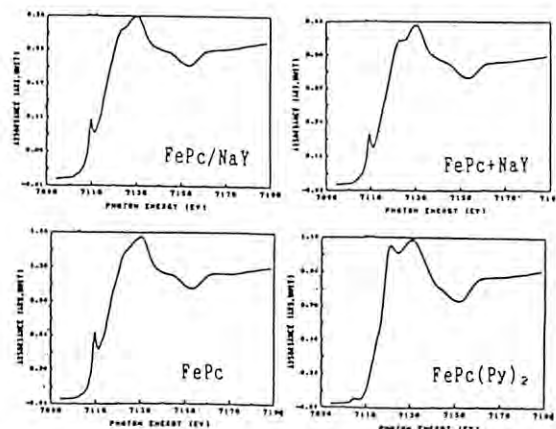


Fig. 1. XANES spectra for FePc/NaY, FePc+NaY, FePc, and FePc(Py)<sub>2</sub>.

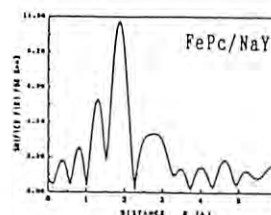


Fig. 2. Fourier transform of  $k^3\chi(k)$  of Fe K-edge EXAFS for FePc/NaY.

Tab. 1. Results of curve-fitting analyses for FePc/NaY, FePc+NaY, and FePc.

Sample	C.N.	R(Å)	$\Delta\sigma^2$
FePc/NaY	3.6	1.84	$-1.20 \times 10^{-3}$
FePc+NaY	4.0	1.83	$-0.47 \times 10^{-3}$
FePc	4.0	1.83	0.00

FTIR and UV-VIS studies showed that the electronic states of phthalocyanin of FePc/NaY are shifted compared with FePc and FePc+NaY.

From these spectroscopic data, it is suggested that FePc in the NaY supercage is comparatively distorted from its original plane structure. EDA complex  $[\text{Na}^+]_n[\text{FePc}^{n-}]/\text{NaY}$  ( $n=1-4$ ) derived from FePc/NaY gave trans-2-butene selectively in the catalytic butadiene hydrogenation.

### References

- 1) N. Herron, G. D. Stucky, and C. A. Tolman, J. Chem. Soc., Chem. Commun., 1521(1986).
- 2) T. Kimura, A. Fukuoka, and M. Ichikawa, Shokubai(Catalyst), 30, 444(1988).



# TEMPERATURE DEPENDENCE OF THE EXAFS SPECTRA FOR SILVER AND PALLADIUM SMALL METAL CLUSTERS: DISSIMILARITIES OF THE THERMAL VIBRATION AND THERMAL EXPANSION IN COMPARISON WITH BULK METALS

Toshihiko YOKOYAMA, Sanae KIMOTO, and Toshiaki OHTA

Dept. Materials Science, Fac. Science, Hiroshima Univ., Hiroshima 730, JAPAN

## Introduction

Recently EXAFS study of the temperature-dependence has become a useful tool for investigating the thermal vibration and also the thermal expansion by using an appropriate analysis including anharmonicity. It is an interesting subject to investigate thermal properties of small metal clusters in comparison with those of bulk metals. The purpose of the present study is (1) to confirm that temperature dependent EXAFS analysis can predict thermal vibration and thermal expansion quantitatively for bulk fcc metals and (2) to apply this method to small metal clusters of Ag and Pd, and to discuss similarities and dissimilarities of thermal and/or structural properties between small metal clusters and their corresponding bulk metals.

## Experimental

Silica-supported Pd and Ag clusters were prepared according to the ion-exchange method. Precursor materials were reduced with hydrogen at 400 C for Pd and 200 C for Ag, and then evacuated to result in hydrogen-free metal clusters. The present EXAFS analysis indicates that each cluster has <20 Å diameter. Pd K-edge and Ag K-edge EXAFS spectra of supported small metal clusters were recorded under inert atmosphere at several temperatures at Beam Line 10B of the Photon Factory in the National Laboratory for High Energy Physics[1]. The EXAFS spectra for bulk metal foils (25µm thick) were also taken in a similar manner.

EXAFS data were analyzed by means of the fourth-order cumulant-expansion technique[2] in order to account for anharmonicity. Debye temperature was evaluated according to the well-known formula[3].

## Results and Discussion

Table 1 shows the results for the bulk metals, together with the thermodynamical data. Table 2 gives the results for the small metal particles. The results of bulk metals (Table 1) show excellent agreement with the thermodynamical data, indicating that EXAFS could be a suitable method to estimate such thermal properties if the higher-order cumulant moments are explicitly taken into account. The Debye temperatures of the metal clusters (Table 2) are noticeably lowered compared with those of bulk metals (Table 1), as mentioned by Balerna et al[4]. This implies that the surface atoms are likely to move much more freely, and that the effective potential depth of clusters should be shallower. The degree of thermal expansion of the clusters is

significantly larger and hence their thermal vibrations are of strong anharmonicity, again indicating the shallower potential of clusters. It should be noticed that the interatomic distance of each cluster is shorter than that of the corresponding bulk metal. Although such behavior appears to be contradictory to the above description, it is caused by the decrease of the coordination number in the small metal clusters. These observations such as the shallower potential and the shorter equilibrium distance have been actually predicted by the MO calculations of Cu clusters[5].

## References

- [1] H.Oyanagi et al. KEK-report 83/30 (1984).
- [2] G.Banker NIM 207 437 (1983).
- [3] G.Beni et al. PR B14 1514 (1976).
- [4] A.Balerna et al. PR B31 5058 (1985).
- [5] B.Delly et al. PR B27 2132 (1983).

Table 1. Temperature dependence of interatomic distances and Debye temperature for bulk metals

metal	temp.(K)	interatomic distance (Å)		Debye temp. (K)	
		EXAFS	thermal <sup>+</sup>	EXAFS	thermal <sup>+</sup>
Pd	100	(2.745)*	2.745	282	275
	200	2.747	2.748		
	295	2.747	2.751		
	360	2.753	2.753		
Ag	30	(2.877)*	2.877	228	228
	184	2.884	2.883		
	295	2.891	2.889		
	362	2.896	2.893		

<sup>+</sup>referred to the thermodynamical data.

\*Values in parentheses are assumed in the present analysis.

Table 2. Temperature dependence of interatomic distances and Debye temperature for small metal clusters

metal	temp.(K)	distance(Å)	Debye temp.(K)
Pd	196	2.695	236
	295	2.712	
Ag	208	2.875	160
	295	2.901	

# STRUCTURE OF GERMANIUM CVD ZEOLITE BY EXAFS AND XPS

Takashi HIBINO<sup>1</sup>, Mitsuru SANO<sup>2</sup>, Miki NIWA<sup>1</sup>, Yuichi MURAKAMI<sup>1</sup>

<sup>1</sup>Department of Synthetic Chemistry, Faculty of Engineering,  
Nagoya University, Furo-cho, Chikusa-ku, Nagoya 464 Japan, and

<sup>2</sup>Department of Chemistry, College of General Education, Nagoya  
University, Furo-cho, Chikusa-ku, Nagoya 464 Japan.

## Introduction

We have proposed the chemical vapor deposition (CVD) of  $\text{Si}(\text{CH}_3)_4$  to control the pore-opening side of zeolites. This method has been applied to mordenite<sup>1</sup> and ZSM-5<sup>2</sup>, and the shape-selectivity in the cracking of octane isomers or in the methanol conversion has been finely improved. A direct observation of the deposited silica, however, is entirely difficult because of its similarity with bulk zeolite as well as extremely small contents. As one of the countermeasures, we will use  $\text{Ge}(\text{OCH}_3)_4$ <sup>3</sup>, and estimate the structure of the deposited  $\text{GeO}_2$  as a model for the deposited silica by the EXAFS and XPS measurements.

## Experimental and Results

The CVD mordenite in a glasscell with capton windows was calcined in vacuo at 773 K at 1 h. The Ge-edge spectrum was measured at room temperature with the EXAFS facilities of Photon Factory at the National Laboratory for High Energy Physics (KEK-PF). The incident and transmitted beam intensities were evaluated with ionization chambers filled with  $\text{Ar}(15\%)\text{-N}_2$  and with  $\text{Ar}(100\%)$ , respectively. The other instrumental details are given in reference<sup>4</sup>.

The Fourier transform of the EXAFS spectrum in  $\alpha$ -quartz type  $\text{GeO}_2$  exhibited two peaks at about 0.14 nm and 0.27 nm (before phase-shift correction), which were corresponding to the Ge-O and Ge-Ge distances, respectively. Similarly, the GeHM10 gave two peaks at about 0.14 nm and 0.27 nm (before phase-shift correction). However, the intensities of Ge-Ge on these samples were lower than that in  $\alpha$ -quartz type  $\text{GeO}_2$ .

An information about the structure was gained by the EXAFS measurement. Initially, the first-nearest neighbors of the deposited Ge atom were four oxygens with tetrahedral coordination on these CVD mordenites, because of its consistency with the first peak of  $\alpha$ -quartz type  $\text{GeO}_2$ . However, the intensities of the second peak on these CVD mordenites were lower than that in  $\alpha$ -quartz type  $\text{GeO}_2$ . This was caused by a decrease in number of coordinated Ge atoms. Further, the coordination number did not increase with increasing the amount of deposited  $\text{GeO}_2$ . From these findings, the structure of the deposited  $\text{GeO}_2$  was considered as below. The deposited  $\text{GeO}_2$  does not have a long range order of tetrahedral  $\text{GeO}_4$  unit because of its little coordinated Ge atoms. Therefore, the deposited  $\text{GeO}_2$  is distinguished from  $\alpha$ -quartz type  $\text{GeO}_2$  with a long range order of tetrahedral  $\text{GeO}_4$  unit, and this may be rather similar to either a bulky amorphous type  $\text{GeO}_2$  or a thin layer of  $\text{GeO}_2$ . The amorphous type  $\text{GeO}_2$  is commonly known to have a short range order of tetrahedral  $\text{GeO}_4$  unit. Similarly, the thin

layer of  $\text{GeO}_2$  also have such a short range order, because the thin layer grows epitaxially, depending on the external surface structure of mordenite and it, thus, can not keep a usual crystal structure of germanium dioxide. On the other hand, it is hardly expected that the bulky amorphous  $\text{GeO}_2$  caused the fine-control of pore-opening size. The uniform deposition on the external surface is required for achieving such a function. Therefore, the  $\text{GeO}_2$  may be considered to deposit as the thin layer. This is also supported by the fact that the thickness of the deposited  $\text{GeO}_2$  increased linearly with increasing the deposition extent. Although this had been already concluded to some extent<sup>5</sup>, this became more apparent in the present study.

## Reference

- (1) M.Niwa, S.Kato, T.Hattori, and Y.Murakami, J. Chem. Soc., Faraday Trans. 1 1984, **80**, 3135.
- (2) M.Niwa, M.Kato, T.Hattori, and Y.Murakami, J. Phys. Chem., 1986, **90**, 6233.
- (3) M.Niwa, C.V.Hidalgo, T.Hattori, and Y.Murakami, Proc. 7th International Zeolite Conf., 1986, p297.
- (4) H.Oyanagi, T.Mathusita, M.Ito, and H.Kuroda, KEK report, 1983, 83-10.
- (5) M.Niwa, Y.Murakami, Materials Chemistry and Physics, 1987, **17**, 73.

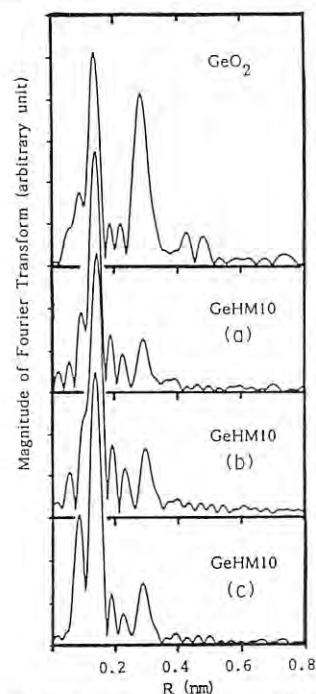


Fig.1. Fourier transforms of EXAFS spectra of (a) the GeHM10 (10.0 Ge nm<sup>-2</sup>), (b) GeHM10 (16.0 Ge nm<sup>-2</sup>), (c) GeHM10 (30.2 Ge nm<sup>-2</sup>) with  $\alpha$ -quartz type  $\text{GeO}_2$ .

XAFS STUDY OF  $(\text{Bi}_2\text{O}_3)_{1-x}(\text{Y}_2\text{O}_3)_x$  SYSTEM AT HIGH TEMPERATURES

Nagao KAMIJO, Hiroyuki KAGEYAMA and Hironobu MAEDA\*

Government Industrial Research Institute, Osaka. Midorigaoka 1-8-31 Ikeda Osaka 563

\* Department of Chemistry, Faculty of Science, Okayama University Tsushima-Naka Okayama 700

Introduction

$\text{Bi}_2\text{O}_3$  crystal has high ionic conductivity and has fluorite type structure above 1003 K which undergoes a phase transition to a monoclinic structure at the lower temperatures. Several lanthanum series oxides are effective in stabilizing defect-fluorite at the lower temperatures.  
 $(\text{Bi}_2\text{O}_3)_{1-x}(\text{Y}_2\text{O}_3)_x$  ( $x=0.1\sim 0.4$ ) contains large concentration of oxygen vacancies and has high ionic conductivity as compared with stabilized zirconia at elevated temperatures.

Experimental and Results

Here, we report XAFS (X-ray Absorption Fine Structure) study of  $(\text{Bi}_2\text{O}_3)_{1-x}(\text{Y}_2\text{O}_3)_x$  ( $x=0.25, 0.4$ ) at 910 K and 1080 K which are below and above the transition temperatures of  $\text{Bi}_2\text{O}_3$  crystal to elucidate the origin of ion conductivity and stabilized mechanism of the system.  
The sample used in the XAFS measurements were prepared by conventional method as described in the previous paper<sup>1)</sup>. XAFS measurements were made by use of the EXAFS facilities installed at the beam line 10B.

Fig. 1 shows the XANES spectra of Bi  $L_{2,3}$ -edge and Y K-edge in  $(\text{Bi}_2\text{O}_3)_{1-x}(\text{Y}_2\text{O}_3)_x$  ( $x=0.25, 0.4$ ) at 910 K and 1080 K respectively. It is noted that XANES spectra of Bi  $L_{2,3}$ -edges of the system are different between above and below the transition temperature of  $\text{Bi}_2\text{O}_3$  (1003 K): above the transition temperature, 1080 K, appreciable XAFS signals can scarcely be found for Bi  $L_{2,3}$ -edge. However, such remarkable decrease of XAFS signals can not be observed at 1080 K for Y K-edge of the system.

We also have obtained the Fourier transform of EXAFS spectra in Bi  $L_{2,3}$ - and Y K-edge of the system at 910 K and 1080 K respectively. For near neighbor oxygen peaks around Y and Bi ions curve-fitting technique is applied using the theoretical amplitude and phase shift values given by Lee and Teo. The structure parameters thus obtained are shown in Table 1. The coordination number of oxygen ion around Bi in the system is extremely small at 1080 K as compared with that of 910 K. The oxygen ions around Bi seem to go out from the system above the transition temperature. They are shown to be partially returned at 300 K after heating at 1080 K, whereas XANES spectra exhibit the similar structure with that of  $\text{Bi}_2\text{O}_3$  at 300 K.

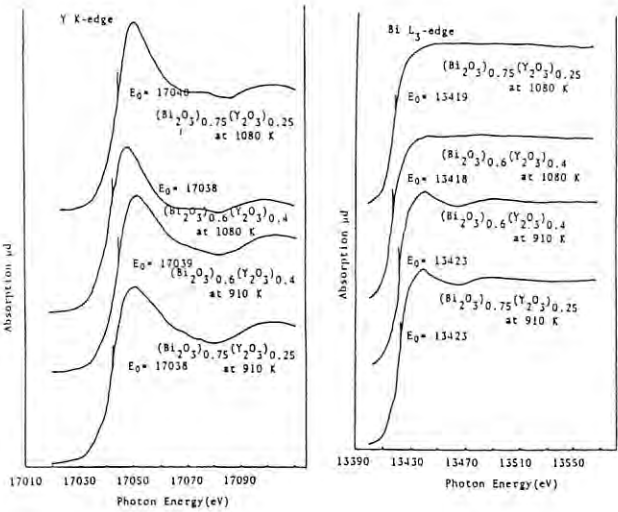


Fig. 1 XANES spectra of  $(\text{Bi}_2\text{O}_3)_{1-x}(\text{Y}_2\text{O}_3)_x$  ( $x=0.25, 0.4$ ) at 910 K and 1080 K respectively.  
 $E_0$  represents the inflection point of absorption edge.

Table 1 Structure parameters obtained by EXAFS with those of standard samples  $\text{Y}_2\text{O}_3$  and  $\text{Bi}_2\text{O}_3$

sample	Y - O (Double shell)		Bi - O (single shell)	
	N	r(Å)	N	r(Å)
(B-Y75)* 980K	2	2.19	4	2.35
	4	2.35		
(B-Y75) 1080K	1	2.17	N<0.5	2.20
	4	2.33		
(B-Y60)** 980K	4	2.20	4	2.39
	3	2.37		
(B-Y60) 1080K	4	2.21	N<0.5	2.35
	2	2.39		
$\text{Bi}_2\text{O}_3$ 300K	—	—	3	2.19 (x-ray diff.)
$\text{Bi}_2\text{O}_3$ 1080K	—	—	N<0.8	2.15 (EXAFS)
$\text{Y}_2\text{O}_3$ 300K	4	2.269	—	
	2	2.354 (x-ray diff.)		

\* (B-Y75)----- $(\text{Bi}_2\text{O}_3)_{0.75}(\text{Y}_2\text{O}_3)_{0.25}$  N -----Coordination number  
\*\* (B-Y60)----- $(\text{Bi}_2\text{O}_3)_{0.6}(\text{Y}_2\text{O}_3)_{0.4}$  r(Å)-----Bond distance

Reference

1) N. Kamijo, H. Kageyama, K. Koto, H. Maeda, M. Hida, T. Ishida and H. Terauchi, J. Phys. Soc. Jpn. 55, 2217(1986)



## STRUCTURAL STUDIES ON PRECIPITATION REACTIONS IN QUALITATIVE ANALYSIS BY EXAFS AND XANES TECHNIQUE (I)

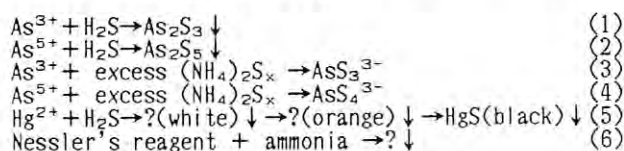
Izumi NAKAI, Ichiro NOMACHI, Tadashi HIRANO, Kazuhiko OZUTSUMI, Takuji KAWASHIMA  
Department of Chemistry, The University of Tsukuba, Tsukuba, Ibaraki 305

## Introduction

Qualitative analysis is the oldest and nevertheless, still an important methodology of analytical chemistry. However, products of the precipitation reactions in qualitative analysis are not fully understood, because the precipitates are often amorphous.

The EXAFS/XANES technique is suitable for structural study of these precipitates because this technique is independent of the sample condition. The purpose of this study is to clarify structures of reaction products in solution, as-grown precipitates (with mother liquid), and crystallized products by the EXAFS/XANES technique in combination with the X-ray diffraction method and the SEM-EDX technique.

The precipitation reactions studied in the present study is shown below.



## Experimental

Samples containing As or Hg were prepared by conventional method in qualitative analysis. As K-edge and Hg L<sub>III</sub>-edge absorption spectra were measured by using a Si(311) channel-cut crystal monochromator on the EXAFS facilities installed at BL-10B at PF.

## Results and Discussion

As K-edge XANES spectra and Fourier transforms(FT) of EXAFS are given in Figs. 1, 2 and 3. The As-S bond distance of the As<sub>2</sub>S<sub>3</sub> precipitates (reaction 1) is shorter than that of orpiment(crystalline As<sub>2</sub>S<sub>3</sub>), and is almost equal to that of As<sub>2</sub>S<sub>3</sub> glass. Moreover, the second peak of FT appearing around 3 Å for the As<sub>2</sub>S<sub>3</sub> crystal is not observed for both As<sub>2</sub>S<sub>3</sub> precipitate and glass. Therefore, the structure of As<sub>2</sub>S<sub>3</sub> precipitate is similar to that of As<sub>2</sub>S<sub>3</sub> glass. The As-S bond distance of the product of reaction (2), which is considered as As<sub>2</sub>S<sub>5</sub>, is the same as that of the As<sub>2</sub>S<sub>3</sub> precipitate. The energy of As K-edge for the As<sub>2</sub>S<sub>5</sub> precipitate agrees with that for the As<sub>2</sub>S<sub>3</sub>. Moreover, the existence of crystalline sulfur in the As<sub>2</sub>S<sub>5</sub> precipitate was confirmed by the X-ray diffraction technique. This observation indicates that the oxidation number of the arsenic ion is reduced from V to III by addition of sulfide ion, which is instantly oxidized to elemental sulfur. Therefore, it can be concluded that the precipitate containing arsenic (V) does not exist, and the product of reaction (2) is a mixture of As<sub>2</sub>S<sub>3</sub> and S.

The As-S bond distance in solution containing AsS<sub>3</sub><sup>3-</sup>, which is prepared by dissolving the As<sub>2</sub>S<sub>3</sub> precipitate in (NH<sub>4</sub>)<sub>2</sub>S<sub>x</sub> (reaction 3) is found to be shorter than that of the As<sub>2</sub>S<sub>3</sub> precipitate. Unexpectedly, the formation of As-O bond was observed when a mixture of As<sub>2</sub>S<sub>3</sub> and S was dissolved in (NH<sub>4</sub>)<sub>2</sub>S<sub>x</sub> (reaction 4)(Fig. 3). This means that AsS<sub>3</sub><sup>3-</sup> like species is not present but oxygen-containing compound is formed in the sulfide solution. A further study will be necessary to clarify this reaction.

FT of Hg L<sub>III</sub>-edge spectra is given in Fig. 4. When Na<sub>2</sub>S was added to HgCl<sub>2</sub> solution, the precipitates changed their color(cream → gray → black) with increasing amount of Na<sub>2</sub>S. It is observed that the Hg-S bond distance of HgS

crystal is longer than Hg-Cl distance of HgCl<sub>2</sub> crystal. The Hg-S distance of HgS precipitate (black) (reaction 5) agrees well with that of HgS crystal. Moreover, no significant relationship was observed between the positions of Fourier peaks and the amount of Na<sub>2</sub>S added. Therefore, it is thought that this color change is not caused by changing the HgS/HgCl<sub>2</sub> ratio in the precipitate. Besides, X-ray powder diffraction data suggested that Hg<sub>3</sub>S<sub>2</sub>Cl<sub>2</sub> formed first and turned into HgS (cinnabar) by the addition of Na<sub>2</sub>S. This evidence was also supported from the results of the SEM-EDX analysis. X-ray diffraction technique revealed that the product of reaction (6) is NHg<sub>2</sub>I.

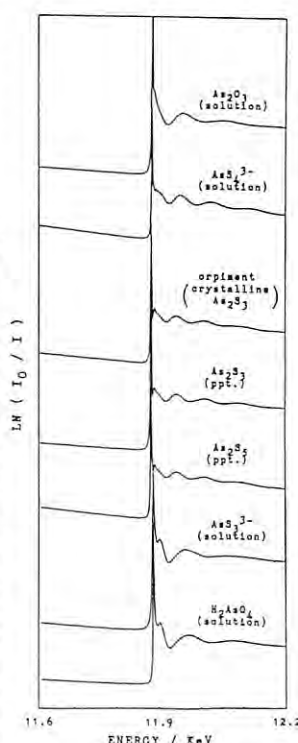


Fig. 1 As K-edge spectra of arsenic compounds

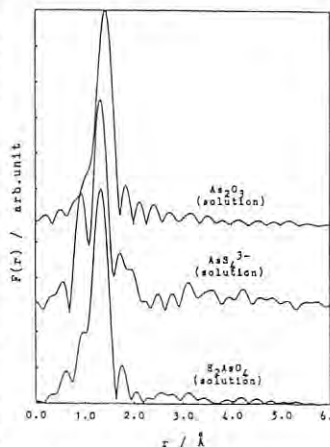


Fig. 3 Fourier transforms for arsenic oxides

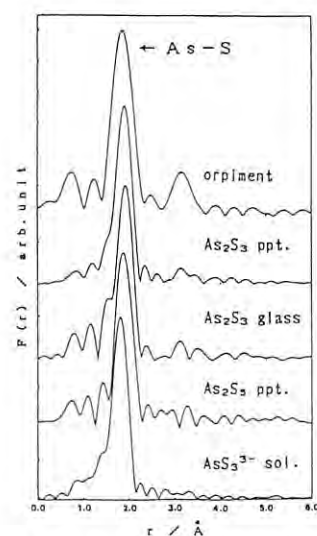


Fig. 2 Fourier transforms for arsenic sulfides

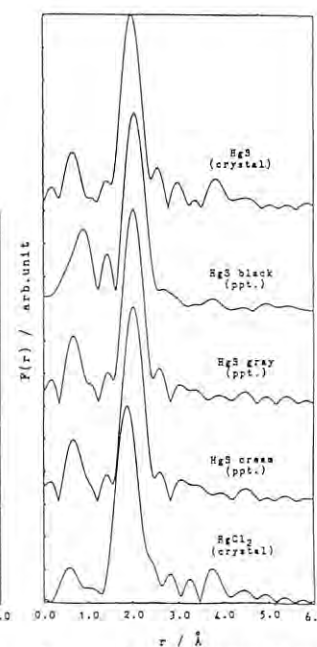


Fig. 4 Fourier transforms for mercury compounds



## A XANES STUDY ON Ni Zr AMORPHOUS ALLOYS PREPARED BY MECHANICAL ALLOYING METHOD

Masaki SAKURAI, Tetsuro SEKIUCHI\*, Fumitake ITOH, Toshiharu FUKUNAGA, Kenji SUZUKI

Institute for Materials Research, Tohoku University,  
Katahira 2-1-1, Sendai, Japan 980

## INTRODUCTION

Recently, much attention has been paid to the mechanical alloying technique as new method for preparing amorphous alloys. In previous paper<sup>1)</sup>, we have reported the amorphization process of NiZr alloy by the mechanical alloying by means of X-ray diffraction and EXAFS. This paper reports of XANES spectra in NiZr amorphous alloys prepared by a ball milling.

## EXPERIMENTAL

NiZr amorphous powders were prepared in a laboratory ball mill using stainless vials and hardened balls. The milling was carried out at ambient temperature for 400 hours at the rate of 110 rpm. Amorphous alloy thus obtained is called the mechanical alloying(MA) when a mixture of Ni and Zr powders is used as a starting material while the mechanical grinding(MG) is named when the milling starts from crystalline powders of NiZr intermetallic compounds.

XANES measurements were carried out with a Si(311) channel-cut monochromator at BL-10B for K-absorption edges of both Ni and Zr atoms in NiZr amorphous alloys.

## RESULTS AND DISCUSSION

Figures 1 and 2 show XANES spectra of Ni and Zr K-edge, respectively, in NiZr amorphous alloys prepared by MA and MG method mentioned above. XANES spectra in (a) pure Ni or Zr element, (b) crystalline NiZr compound (c-NiZr) and (c) melt quenched amorphous alloy(MQ a-NiZr) are shown together for comparison.

In XANES of Ni K-edge(Fig.1), a prepeak around 8,330 eV which is responsible for 1s→3d transition<sup>2)</sup> and a main peak around 8,352 eV characteristic of NiZr alloys can be seen irrespective of its state. It is interesting to see that the shapes of both the prepeak and the main peak in MQ a-NiZr are more blurred compared to those in its crystalline counterpart but are more sharpened compared to MA and MG a-NiZr alloys. The situation is similar to XANES of Zr K-edge in NiZr alloys in which a shoulder around 17,990 eV and a characteristic peak around 18,015 eV are weakened in both MA and MG a-NiZr.

These facts imply that the chemical state of Ni and Zr atoms in both MA and MG a-NiZr are slightly different from that not only in c-NiZr but also in MQ a-NiZr in association with slight modification of atomic arrangement.

(1) F. Itoh, T. Sekiuchi, M. Sakurai, T. Fukunaga and K. Suzuki, 'Non-equilibrium Solid Phases of Metals and Alloys', Suppl. Trans. JIM 29(1988)127.

(2) M. Lenglet, R. Guillet, A. D'huysser, J. Durr and C. K. Jørgensen, J. de Phys. Colloque C8(1986)765.

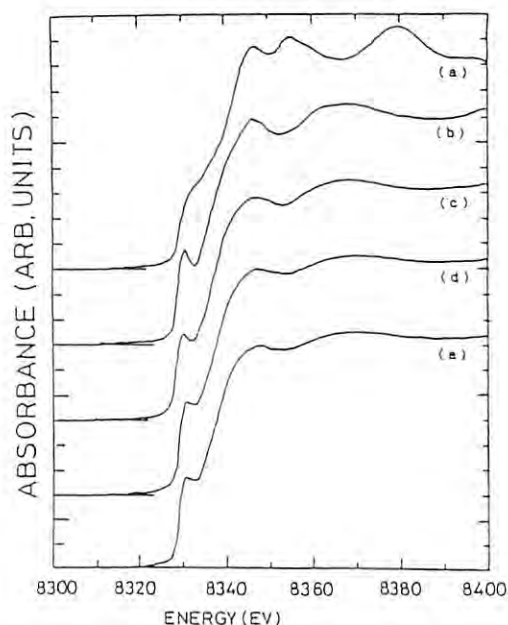


Fig.1 Ni K-edge X-ray absorption spectra. (a) pure Ni, (b) crystalline NiZr(c-NiZr), (c) MQ a-NiZr, (d) MA a-NiZr and (e) MG a-NiZr.

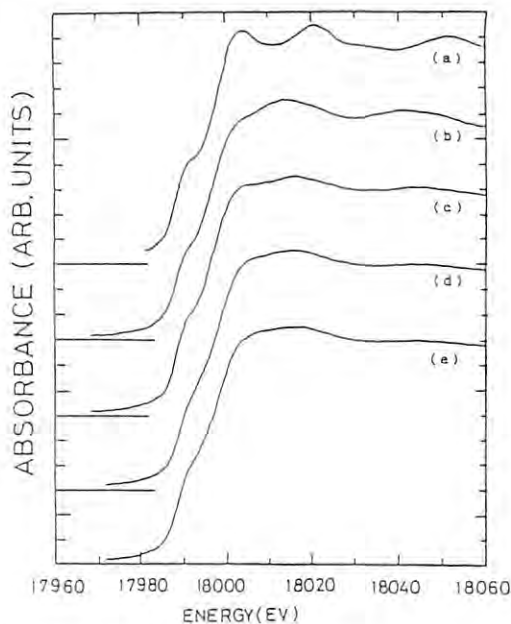


Fig.2 Zr K-edge X-ray absorption spectra. (a) pure Zr, (b) crystalline NiZr(c-NiZr), (c) MQ a-NiZr, (d) MA a-NiZr and (e) MG a-NiZr.

\*Present address : Muroran Works, Nippon Steel Corporation, Muroran, Hokkaido, Japan 050

EXAFS Study on Fluoride Ion-conductive ZrF<sub>4</sub>-BaF<sub>2</sub>-CsF Glasses

Yoji KAWAMOTO, Yukihiro UMETANI, Kazuyuki TOHJI\* and Hideki MORIKAWA\*\*.

Faculty of Science, Kobe University, Rokkodai, Nada, Kobe 657

\*Institute for Molecular Science, Myodaiji, Okazaki, Aichi 444

\*\*Research Laboratory of Engineering Materials, Tokyo Institute of Technology, Nagatsuta, Yokohama 227

Introduction

Recently ZrF<sub>4</sub>-based glasses have become of interest as a vitreous solid electrolyte of F<sup>-</sup> ion. The ionic conductivities, however, are the order of 10<sup>-6</sup>Scm<sup>-1</sup> at 200°C. Thus the enhancement of conductivity is necessiated for practical use of these glasses. For the improvement of conductivity, the elucidation of F<sup>-</sup> conduction-governing factors is inquired. The compositional dependence of the conductivities of ZrF<sub>4</sub>-BaF<sub>2</sub>-CsF glasses suggested that the activation energy for conduction is largely influenced by the average Zr-F bond length and/or by the average F coordination number of Zr.<sup>1)</sup> The present EXAFS study is undertaken in order to confirm the validity of this suggestion.

Experimental and Results

The compositions of ZrF<sub>4</sub>-BaF<sub>2</sub>-CsF glasses chosen for EXAFS measurements are 55ZrF<sub>4</sub>·45BaF<sub>2</sub>, 55ZrF<sub>4</sub>·25BaF<sub>2</sub>·20CsF, and 55ZrF<sub>4</sub>·5BaF<sub>2</sub>·40CsF. On the other hand, polycrystalline Li<sub>2</sub>ZrF<sub>6</sub>, β-Cs<sub>2</sub>ZrF<sub>6</sub>, and β-ZrF<sub>4</sub> were synthesized and utilized as the references of EXAFS analysis of ZrF<sub>4</sub>-BaF<sub>2</sub>-CsF glasses.<sup>2),3),4)</sup> For the EXAFS measurements, these specimens were finely powdered and pressed into discs with polyethylene powder. The measurements of Zr-K EXAFS spectra were carried out using the EXAFS facilities at BL-10B.

Fig. 1 shows the X-ray absorption spectra obtained for glass samples. Fig. 2 shows the Fourier transformation of k<sup>3</sup>χ(k) by using data from 3.5 to 13.5Å<sup>-1</sup> in k. As can be seen from Fig. 1, the first peaks at around 1.5Å which correspond to the Zr-F distances shift toward smaller distances with increasing CsF content. Next, the inverse Fourier transformation and curve fitting were performed for these peaks. The amplitude and the phase shift in the calculation were obtained by employing Li<sub>2</sub>ZrF<sub>6</sub> as reference. The structure parameters (interatomic distance, coordination number and Debye-Waller factor), except those of the 55ZrF<sub>4</sub>·5BaF<sub>2</sub>·40CsF glass, are listed in Table 1. The present EXAFS study seems to support the hypothesis mentioned in Introduction.

As seen from Fig. 2, the first peak of the 55ZrF<sub>4</sub>·5BaF<sub>2</sub>·40CsF glass exhibited an obvious shoulder at the right-hand side of the peak. Thus, the Fourier filtering was practically difficult for this glass. On this glass, therefore, we are planning the analysis using "two shell model".

References

1) Y. Kawamoto and I. Nohara, Solid State Ionics, 22, 207-12 (1987).  
2) G. Brunton, Acta Cryst., B29, 2294-96 (1973).  
3) H. Bode and G. Teufer, Z. Anorg. Allg. Chem., 283, 18-25 (1956).

4) R. D. Burbank and F. N. Benzey, U. S. Atomic Energy Comm. Report, No. K1280, 14-17 (1956).

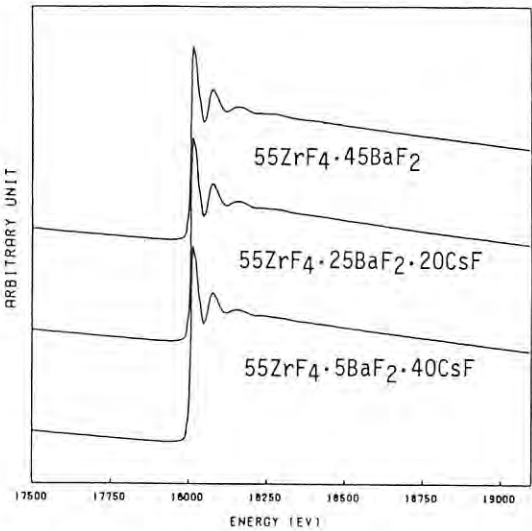


Fig. 1

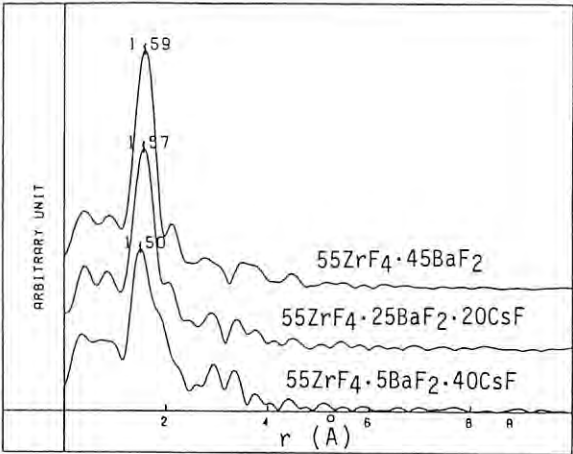


Fig. 2

Table 1

Sample	r/Å	N	σ
Li <sub>2</sub> ZrF <sub>6</sub>	2.016	6.0	0.070
β-ZrF <sub>4</sub>	2.09	7.3	0.086
	(2.116)	(8.0)	
β-Cs <sub>2</sub> ZrF <sub>6</sub>	2.01	5.6	0.072
	(2.04)	(6.0)	
55ZrF <sub>4</sub> ·45BaF <sub>2</sub>	2.04	6.3	0.098
55ZrF <sub>4</sub> ·25BaF <sub>2</sub> ·20CsF	2.03	6.4	0.109

Numerals in brackets are values determined by X-ray structural analysis.<sup>2),3),4)</sup>

EXAFS STUDY ON ACTIVE INTERMEDIATES  
OF CYTOCHROME P-450 MODELS

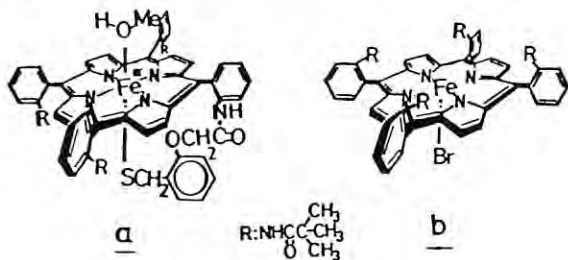
Masaaki HIROBE, Tsunehiko HIGUCHI, Shinobu UZU, Isao KOJIMA,\* and Kazumasa HONDA\*  
Faculty of Pharmaceutical Sciences, University of Tokyo,  
Hongo, Bunkyo-ku, Tokyo 113.  
\*National Chemical Laboratory for Industry, Tsukuba-City,  
Ibaraki 305.

Introduction

The reaction mechanism and active intermediates of cytochrome P-450 have been the targets of extensive investigation. The importance of synthetic porphyrin models for P-450 in understanding the properties of the protein-free metal center has been emphasized recently. It is necessary to obtain structural information of a wide variety of metallo porphyrin derivatives in order to reveal the local structure of the reactive intermediate of cytochrome P-450. Therefore a preliminary EXAFS measurements was done with several P-450 model compounds of which each works characteristically as catalysts for oxidation.

Experimental

Powder samples of metal (Ru, Mo, Fe) -porphyrin (tetramesitylporphyrin:TMP, tetraphenylporphyrin:TPP, 'picket-fence' porphyrin:TpivPP) were sealed in polyethylene bags. X-ray absorption spectra near metal K-edge were measured in transmission mode by using the EXAFS facilities at BL-10B. A cryocooler apparatus was used for the low temperature measurements (170 -250 K).

Results and Discussion

It is postulated that a thiolate anion (S<sup>-</sup>) of the axial ligand of iron porphyrin in the active center of cytochrome P-450 plays a great part in the activation of dioxygen molecule ligated at the another axial site. It is therefore essential to reveal the local structure around the axial ligands for the analysis of the reaction mechanism for P-450 systems. Very recently we succeeded in the synthesis of a new porphyrinatoiron coordinated by thiolate anion intramolecularly (a)<sup>1)</sup>. The complex (a) is adequately stable during

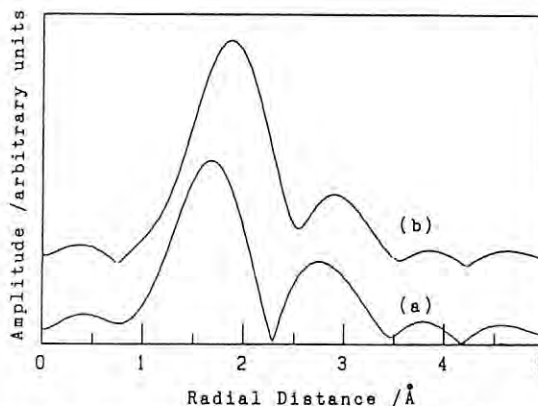


Fig. 1. Fourier transform of the  $k^3$ -multiplied EXAFS data of FeTpivPPS<sup>-</sup>(a) and FeTpivPPBr<sup>-</sup>(b).

oxidations and has much higher catalytic activity than iron porphyrin not ligated with thiolate anion. We therefore chose (a) as a sample for EXAFS since it is a preferable model for cytochrome P-450. Besides the result about EXAFS data of the complex (b) was mentioned in this report.

The Fourier transform of the  $k^3$ -multiplied EXAFS function of a P-450 model, FeTpivPPS(a), is shown in Fig. 1. This indicates that the Fe-N<sub>p</sub> and Fe-axial(S) ligands contributions combine to form a single broad peak of 0.95-2.2 Å and a curve-fitting analysis is required for the determination of the ligand structure. A least-squares curve fitting analysis based on the single scattering model was performed using theoretical phases and amplitudes.<sup>2)</sup> The average Fe-N<sub>p</sub>, Fe-axial(S) and Fe-axial(O) distances were calculated to be 1.99, 2.20 and 2.21 Å respectively, which are consistent with the values in other P-450 systems reported before.

Next the fourier transfer and its curve fitting analysis of the  $k^3$ -multiplied EXAFS function of compound (b) was performed as same as above. The average Fe-N<sub>p</sub> and Fe-Br distances were calculated to be 2.03 and 2.35 Å, respectively.

The authors thank Dr. Nobuhiro Kosugi of University of Tokyo for offering us the computer program of curve fitting analysis.

1) T. Higuchi, S. Uzu, and M. Hirobe, in preparation.

2) N. Kosugi, H. Kuroda, Program EXAFS1/V04 Research Center for Spectrochemistry, Faculty of Science, University of Tokyo (1987).

EXAFS STUDY ON THIN FILM OF  $\text{ZrO}_2$  ON  $\text{TiO}_2$ .Tsunehiro TANAKA, Tarek M. SALAMA, Masaki TANNO, Tsutomu YAMAGUCHI  
And Kozo TANABEDepartment of Chemistry, Faculty of Science, Hokkaido University,  
Sapporo 060, Japan

The sol-gel method using metal alkoxide is one of the promising methods to prepare homogeneously combined mixed metal oxide. Recently this method has been applied to preparation of thin film oxides on surface of the pertinent carrier material including glass. The first step of the preparation is a reaction between alkoxide and surface OH groups, which is the same as that utilized in the preparation of supported catalyst. In the present study, we have prepared the new supported catalyst of zirconium oxide on several carriers using alkoxide and have investigated the structure of zirconium oxide species on the surface by means of EXAFS.

Experimental

The catalyst samples were prepared by the impregnation of an inorganic carrier, titania ( $78 \text{ m}^2 \text{g}^{-1}$ ), in the toluene solution of zirconium tetraisopropoxide, followed by calcination at 773 K. The deposition of zirconium cations on the carrier in this way was repeated several times to obtain a desired amount of zirconium. The samples were mixed with polyethylene powder and pressed into discs. X-Ray absorption spectra were collected on EXAFS facility installed at BL10B in KEK-PF using a channel cut Si(311) monochromator.

Results and Discussion

In the present study four kinds of  $\text{ZrO}_x/\text{TiO}_2$  were prepared by depositing Zr one to four times (ZT1 to ZT4). Figure 1 shows the Fourier transforms (FTs) of the Zr K edge EXAFS of ZT2, ZT3, and ZT4. Evidently, the FTs of ZT2 and ZT3 are very similar to each other while the FT of ZT1 is different. The peaks appearing at around 2 Å due to the scattering by oxygen atoms seems the same for all samples. However, a Zr-Zr peak found in the vicinity of 3 Å is high in case of ZT4. This suggests that bulk zirconium oxide is grown on  $\text{TiO}_2$  surface while not on either ZT2 or ZT3. Actually, the FT of ZT4 EXAFS is almost identical with that of monoclinic  $\text{ZrO}_2$  shown together in Fig. 1. However, it should be noted that the relative peak height of Zr-Zr to that of Zr-O in ZT4 is a little smaller than that of  $\text{ZrO}_2$  bulk oxide, indicating that crystal growth to a monoclinic phase is not completed in case of ZT4, which is consistent with the X-ray diffraction results of these samples.

In order to examine the environment of a zirconium cation more in detail, the curve-fitting of EXAFS considering the exclusive contribution of the oxygen ligands was carried out using theoretical parameters calculated by Teo and Lee. The versatility of this method was verified by comparing the results of EXAFS data of known samples to the data with the crystallographic parameters, given in Table 1. Coordination number(s) are not reliable in this case while the bond distance(s) can be estimated

in the 0.02 Å accuracy. As suggested in Fig. 1, the parameters for Zr-O moiety of ZT4 is very close to that of monoclinic  $\text{ZrO}_2$ , while zirconium oxide species in ZT3 consists of at least two kinds of  $\text{ZrO}_x$  species, one of which, the predominant species, has shorter bonds with length at around 2.08 Å. In the case of ZT2, such species is dominant. Since Zr-O bond length is generally fairly long, ca. 2.2 Å,  $\text{ZrO}_x$  species with short Zr-O bonds found in cases of ZT3 and ZT2 are presumably the species affected by  $\text{TiO}_2$  carrier.

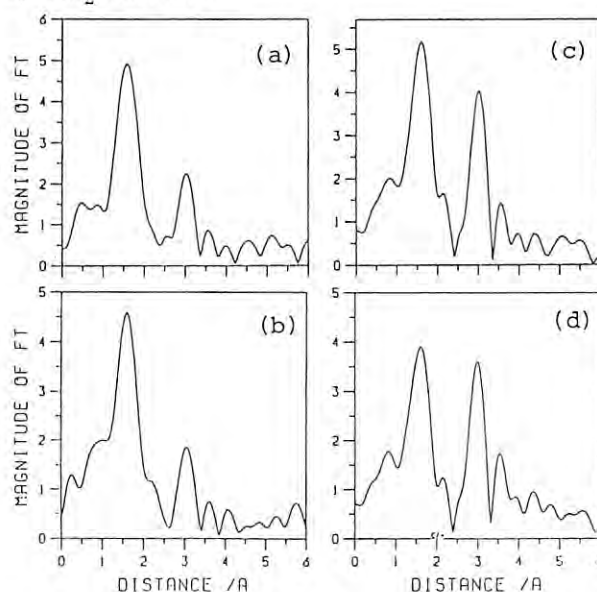


Figure 1 Fourier transforms of Zr K-edge EXAFS of ZT2 (a), ZT3 (b), ZT4(c), and monoclinic  $\text{ZrO}_2$

TABLE I Structural parameters for Zr-O shells

sample	CN <sup>a)</sup>	R <sup>b)</sup> /Å	$\sigma^2/\text{\AA}^2$
$\text{ZrO}_2$ <sup>c)</sup>	3.3 (3)	2.09 (2.10)	0.0072
	2.2 (4)	2.22 (2.22)	0.0074
$\text{Zr}(\text{acac})_2$	8.0 (8)	2.19 (2.20)	0.0055
ZT2	5.9	2.11	0.0086
ZT3	3.9	2.08	0.0076
	1.4	2.20	0.0027
ZT4	2.8	2.07	0.0017
	2.8	2.22	0.0020

a) Coordination number. The values in parentheses are those obtained with XRD. b) Bond distance. The values in parentheses are those obtained with XRD. c) Monoclinic crystal.



## RHODIUM-NIOBIA INTERACTION ON SILICA FORMED BY AIR CALCINATION AT HIGH TEMPERATURE

Kimio KUNIMORI, Zhicheng HU, Toshio UCHIJIMA, Kiyotaka ASAKURA,\* and Yasuhiro IWASAWA\*

Institute of Materials Science, University of Tsukuba, Tsukuba, Ibaraki 305

\*Department of Chemistry, Faculty of Science, University of Tokyo, Hongo, Tokyo 113

Introduction

In the course of investigating  $\text{Nb}_2\text{O}_5$ -promoted  $\text{Rh}/\text{SiO}_2$  catalysts (atomic ratio;  $\text{Nb}/\text{Rh} = 1 - 9$ ), which exhibited strong metal-support interaction (SMSI) behavior in ethane hydrogenolysis studies [1], we have found that the extent of  $\text{Rh}-\text{Nb}_2\text{O}_5$  interaction was increased significantly by calcining the niobia-promoted  $\text{Rh}$  catalysts in air at high temperature (973 K - 1173 K). In this work, structural transformation in the  $\text{Nb}_2\text{O}_5/\text{Rh}/\text{SiO}_2$  system during the calcination and reduction treatments has been studied by means of EXAFS spectroscopy.

Experimental

Niobia-promoted  $\text{Rh}$  catalysts ( $\text{Nb}/\text{Rh} = 1$  or  $3$ ) were prepared by impregnating 4wt%  $\text{Rh}/\text{SiO}_2$  catalyst with an aqueous solution of  $(\text{NH}_4)_3[\text{NbO}(\text{C}_2\text{O}_4)_3]$ , followed by calcination in air at high temperature (773 K - 1173 K) for 3h. The EXAFS spectra were measured at BL-10B of Photon Factory.

Results and Discussion

The  $\text{Rh}$  K-edge EXAFS spectrum of the niobia-promoted  $\text{Rh}/\text{SiO}_2$  catalyst ( $\text{Nb}/\text{Rh} = 3$ ) calcined at 1173 K appeared to be quite different from that of  $\text{Rh}_2\text{O}_3$ . Figure 1 shows the Fourier transform of the  $\text{Rh}$  spectrum, and tentative assignments are also shown in the figure. An X-ray diffraction (XRD) study suggested the formation of a mixed oxide ( $\text{RhNbO}_4$ ), having the rutile structure (the unit cell parameters;  $a = 4.708 \text{ \AA}$ ,  $c = 3.017 \text{ \AA}$ ). These results show that  $\text{RhNbO}_4$  compound was formed almost exclusively on the  $\text{SiO}_2$  surface by the calcination treatment.

As shown in Figs. 2 and 3, the Fourier transform of  $\text{Nb}$  K-edge EXAFS of the catalyst after the reduction in  $\text{H}_2$  at 773 K was a little different from that after the calcination at 1173 K. The XRD study suggested that the  $\text{RhNbO}_4$

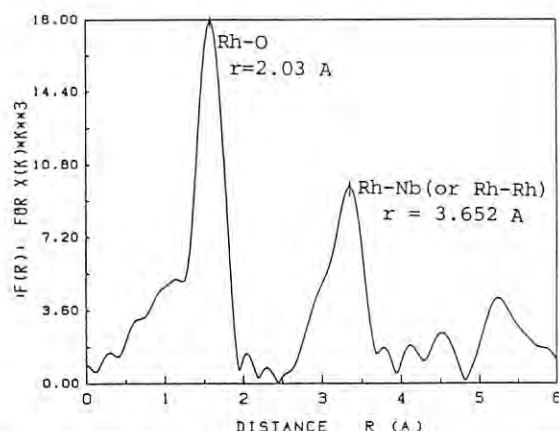


Fig. 1 Fourier transform of  $\text{Rh}$  K-edge EXAFS of the  $\text{Nb}_2\text{O}_5/\text{Rh}/\text{SiO}_2$  catalyst calcined at 1173 K.

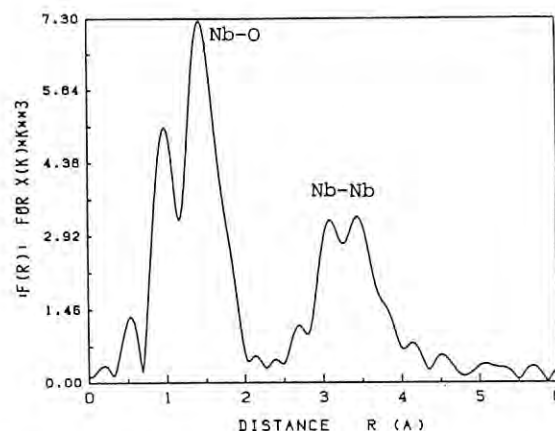


Fig. 2 Fourier transform of  $\text{Nb}$  K-edge EXAFS of the  $\text{Nb}_2\text{O}_5/\text{Rh}/\text{SiO}_2$  catalyst calcined at 1173 K.

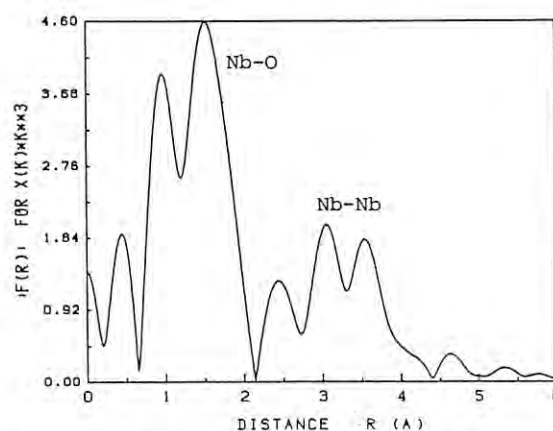


Fig. 3 Fourier transform of  $\text{Nb}$  K-edge EXAFS of the  $\text{Nb}_2\text{O}_5/\text{Rh}/\text{SiO}_2$  catalyst reduced in  $\text{H}_2$  at 773 K.

compound was reduced to  $\text{Rh}$  metal and  $\text{NbO}_2$  by the high-temperature  $\text{H}_2$  treatment. However, it should be noted that this catalyst ( $\text{Nb}/\text{Rh} = 3$ ) contains an excess amount of niobia promoter, a large part of which would not interact strongly with  $\text{Rh}$ . Therefore, we have prepared the  $\text{RhNbO}_4/\text{SiO}_2$  catalyst ( $\text{Nb}/\text{Rh} = 1$ ) as a starting material to study chemical behaviors taking place on the  $\text{SiO}_2$  surface after the calcination and reduction treatments [2]. The EXAFS spectra of these catalysts have also been measured, and further analyses are now in progress.

References

- [1] Z. Hu, H. Nakamura, K. Kunimori, H. Asano, and T. Uchijima, *J. Catal.*, **112**, 478 (1988).
- [2] Z. Hu, H. Nakamura, K. Kunimori, and T. Uchijima, *Catalysis Letters*, in press (1988).

EXAFS STUDY ON THE LOCAL STRUCTURE OF AMORPHOUS  $\text{Te}_x\text{C}_{1-x}$  ALLOYS

Keiji TSUNETOMO, Tatsumi SUGISHIMA, Takeshi IMURA and Yukio OSAKA

Department of Electrical Engineering, Faculty of Engineering,  
Hiroshima University, Higashi Hiroshima 724

Introduction

Amorphous Te compounds have been much interested for optical recording medium. In amorphous  $\text{Te}_x\text{C}_{1-x}$  films prepared by sputtering technique, Te atoms make amorphous clusters in graphite-like carbon matrix.  $^{129}\text{Te}$  Mossbauer effect and other measurements suggest that the randomness around Te atoms increases with C content increasing.

We report the local structure around Te atoms in  $\text{Te}_x\text{C}_{1-x}$  by means of Te-K EXAFS.

Experimental and Results

All samples were prepared onto 8  $\mu\text{m}$  thick Kapton substrates by sputtering a carbon target upon which Te chips were placed. Sputtering conditions, RF power, substrate temperature and Ne gas pressure, are 20-30 W, 20  $^\circ\text{C}$  and 0.67 Pa, respectively. About 32 layers of the film were stacked to attain a best fit.

EXAFS above Te-K edge ( $\sim 31.8$  keV) were measured at 77 K on the Beam Line 10-B of the Photon Factory.

Figure 1 shows the magnitude of Fourier transform  $|F(r)|$  of  $k^2$  times  $\chi(k)$  for t-Te (trigonal Te) and amorphous  $\text{Te}_x\text{C}_{1-x}$  ( $x=0.08, 0.56, 0.72$ ). We can observe three main peaks for t-Te. These peaks are related to the short range order around Te atoms in t-Te crystal.

In the  $\text{Te}_x\text{C}_{1-x}$  films, only one main peak and small second peak are observed. Peak area of first peak decreases about 15% compared to t-Te. Furthermore, peak position of first nearneighbor shift to left side with increasing carbon content. This shortening has been investigated in several amorphous chalcogenide<sup>1),2)</sup>, and explained by the reduction of interaction between the chalcogen on the next chain. Thus, in amorphous  $\text{Te}_x\text{C}_{1-x}$ , the interaction between the Te chains is decreases with increasing carbon content. This results is also suggested by decrease of second peak area.

In table 1, the structure parameters derived by fitting the theoretical curve for Fourier filtered data are listed.

The authors are grateful to Drs. S. Nomura and A. Koyama, KEK, for their help and useful advice in the experiments.

References

- 1) M. Inui, M. Yao and H. Endo, J. Phys. Soc. Jpn. **57** (1988) 553.
- 2) P. Boolchand, T. Henneberger and J. Oberschmidt, Phys. Rev. Lett., **30** (1973) 1292.

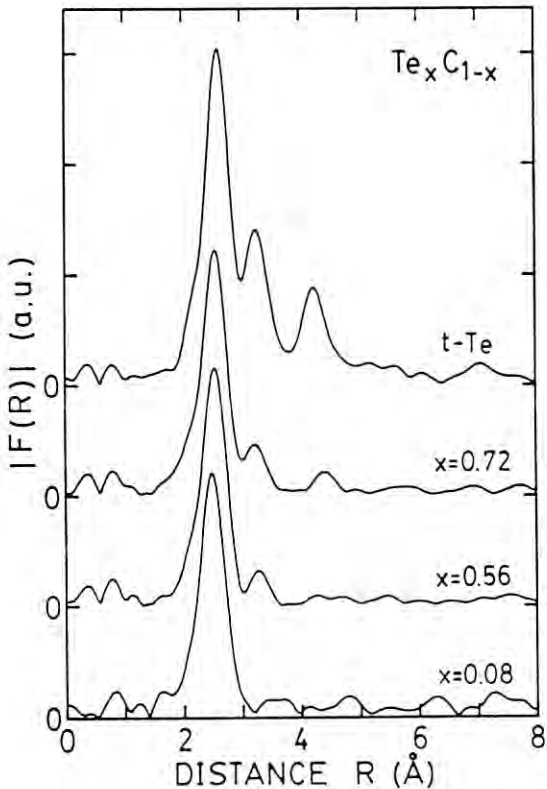


Fig. 1. Magnitude of Fourier transform of  $k^2$  times  $\chi(k)$  for t-Te and amorphous  $\text{Te}_x\text{C}_{1-x}$ .

Table 1. Structure parameters derived by curve fitting.

Sample	x	$r_1$	$S_0^2 N$	$\sigma$
$\text{Te}_x\text{C}_{1-x}$	0.72	2.821	0.53	0.03
	0.56	2.809	0.55	0.03
	0.08	2.765	0.54	0.03
t - Te		2.859	0.71	0.03

Te-K EXAFS STUDY ON THE STRUCTURE OF AMORPHOUS  $\text{Si}_x\text{Te}_{1-x}$  ALLOYS

Keiji TSUNETOMO, Tatsumi SUGISHIMA, Takeshi IMURA and Yukio OSAKA

Department of Electrical Engineering, Faculty of Engineering,  
Hiroshima University, Higashi Hiroshima 724Introduction

Amorphous  $\text{Si}_x\text{Te}_{1-x}$  alloys with a content of 13~27 % Si can be obtained by the melt-quenching or the splat-cooling technique.<sup>1)2)</sup> The radial distribution function obtained from X-ray diffraction were interpreted by a model of configuration of tetrahedrons with Si having 4 and Te having 2 neighboring atoms.<sup>2)</sup>

Using the sputtering technique, the Si content in which  $\text{Si}_x\text{Te}_{1-x}$  become amorphous was extended to 10-90 at % Si. In this report, the short range order of the Te atoms in amorphous  $\text{Si}_x\text{Te}_{1-x}$  has been studied using Te-K EXAFS measurement.

Experimental and Results

All samples were prepared onto 8  $\mu\text{m}$  thick Kapton substrates by sputtering a Si target upon which Te chips were placed. The film thicknesses of the samples were about 2~3  $\mu\text{m}$ . About 16 layers of the film were stacked to attain a best wt. The composition of the samples were determined by X-ray photo electron spectroscopy.

Extended X-ray absorption fine structure (EXAFS) above Te-K edge ( $\sim 31.8$  keV) were measured for amorphous  $\text{Si}_x\text{Te}_{1-x}$  alloys (12, 31, 57, 76 and 87 at % content Si) on the Beam Line 10-B of the Photon Factory. The samples were cooled down at 77K throughout measurement. Ar and Kr gas were used for the front and the rear ion chamber.

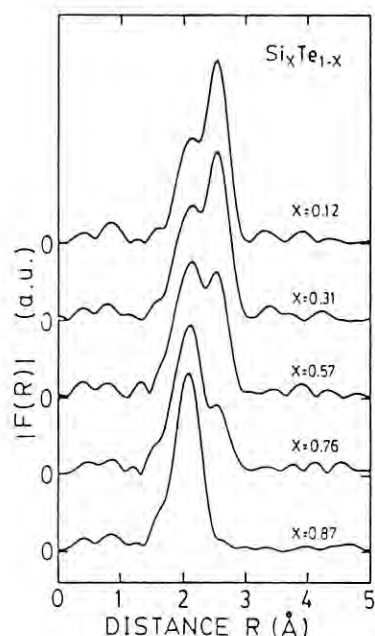


Fig. 1. Fourier transform of  $k$  times  $\chi(k)$  for  $\text{Si}_x\text{Te}_{1-x}$  alloys.

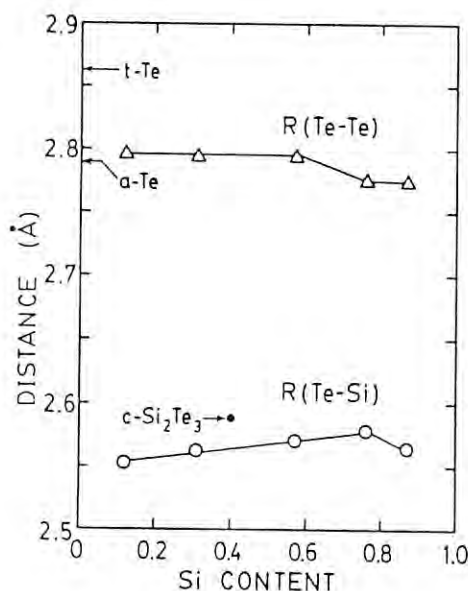


Fig. 2. Radial distances obtained by curve fitting.

Figure 1 shows the magnitude of Fourier transform  $|F(r)|$  of  $k$  times  $\chi(k)$  for several amorphous  $\text{Si}_x\text{Te}_{1-x}$  alloys. Two main peaks are observed and the amplitudes change systematically. The first and second peaks are related to Te-Si and Te-Te bonding, respectively.

The structure parameters, coordination number  $N$  and inter atomic distance  $R$ , derived by curve fitting<sup>3)</sup> are shown in Figs. 2 and 3.

The Te-Te distance decreases from 2.79 Å (very close to that of  $\text{a-Te}^2$ ) to 2.77 Å, and Te-Si separation slightly increases with increasing Si content.

In Fig. 3, the number of Te(Si) atoms connected to a Te atom,  $N_{\text{Te-Te}}$  ( $N_{\text{Te-Si}}$ ) are plotted. The solid lines are calculated from tetrahedron model described in ref. 2, and the dashed lines are calculated from covalent random network (CRN) model. In Si poor region, CRN model doesn't fit to our data. But, in Si rich region, CRN model fit to our data very well. So, we conclude that the CRN model seems to be exactly in Si rich region, and the tetrahedron model or another model is necessary to explain the amorphous structure in Si poor region.

References

- 1) K. Ploog, W. Stetter, A. Nowitzki and E. Schonherr, Mat. Res. Bull., **11** (1976) 1147.
- 2) G.E.A. Bartsch, H. Bromme and T. Just, J. Non-Cryst. Solids, **18** (1975) 65.
- 3) M. Inui, M. Yao and H. Endo, J. Phys. Soc. Jpn. **57** (1988) 553.

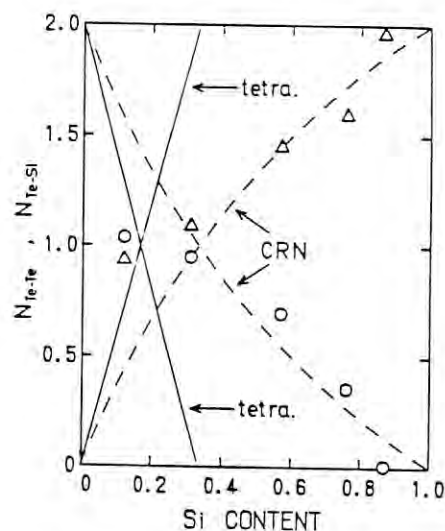


Fig. 3. Number of Te(Si) atoms connected to a Te atom,  $N_{\text{Te-Te}}$  ( $\circ$ ),  $N_{\text{Si-Si}}$  ( $\Delta$ ). Solid and dashed lines are calculated for structural models.

## XAFS STUDIES ON PHASE TRANSITION IN IRON AND IRON BASE ALLOYS.

Hitoshi YAMAZAKI, Hironobu MAEDA\*, Hiroshi MARUYAMA, Hiroyuki AOKI, Jun SHI,  
Kazuaki SHIMIZU, Michinobu MINO, Akihisa KOIZUMI and Naruhiko BAMBA.

Department of Physics, Faculty of Science, Okayama University,  
\* Department of Chemistry, Faculty of Science, Okayama University,  
3-1-1 Tsushima-Naka, Okayama 700.

## Introduction

It has long been known that iron exhibits complex phase transitions: Ferromagnetic BCC iron ( $\alpha$ ) is transformed into paramagnetic BCC iron ( $\beta$ ) at 1041K; when the temperature is further increased, structural phase transition from BCC to FCC occurs at 1183K; furthermore, anti-ferromagnetic FCC iron ( $\gamma$ ) is transformed again into paramagnetic BCC iron ( $\delta$ ) at 1673K. The unique physical properties of iron has been widely utilized in steel technology. However, microscopic explanation of the phase transitions of iron has remained controversial.

Recently, Hasegawa et al.<sup>(1)</sup> have argued theoretically that the structural phase transition arises from a magnetic contribution to phonon softening via the band Jahn-Teller effect. They have succeeded in interpreting qualitatively the phase diagram and several precursory phenomena of the phase transitions.

In order to investigate electronic state and local structure changes accompanied with the phase transitions, X-ray Absorption Fine Structure (XAFS) study is a powerful technique.

## Experimental

The disordered 25.0at%Pt-Fe and 26.4at%Ni-Fe alloys were prepared by induction melting. After grinding the ingots, the powdered samples were annealed for 2 hours at 800°C under vacuum and subsequently given a suitable thermal treatment. These samples undergo the martensitic transformation from the high-temperature FCC phase to the low-temperature BCC phase at about  $M_s=260$  K with decreasing temperature, which was determined previously by X-ray diffraction. Temperature dependence of XAFS on the Fe-K, Ni-K and Pt-L<sub>3</sub> edges for these alloys was taken in the vicinity of the  $M_s$ -temperature.

Single crystal sheet of pure iron was grown by strain annealing technique. The [110] direction was almost normal to the surface. The sample was formed into a foil with about 10  $\mu$ m in thickness. XANES spectrum of the Fe-K edge was taken at R.T. as the angle between the direction of linearly polarized X-ray and the [100] axis in (110) plane was changed. Temperature dependence of EXAFS on the Fe-K edge was taken in the temperature range of 25-1000 °C

## Results

XANES spectrum provides informations on unfilled density of state above Fermi level and about coordination symmetry of absorbing atoms. Then, we have taken XANES spectrum above and below the  $M_s$ -temperature to study the electronic state. Figures 1(a) and (b) show XANES spectrum of the Fe-K edge of the disordered 25.0at%Pt-Fe alloy at 295 and 20K, respectively. Several fine-structure peaks of varying intensities are

discerned and labeled B<sub>1</sub>-E<sup>(2,3)</sup> in each of the spectra. By the martensitic transformation, the XANES spectrum changes clearly from double peak in FCC phase at 295K into single peak in BCC phase at low temperatures: no change is recognized in the peaks B<sub>1</sub> and C; on the other hand, in BCC phase the peak B<sub>2</sub> collapses drastically, peak D appears distinctly and peak E is broadened out; consequently, the XANES spectrum is identical with that of pure Fe. The similar change in XANES spectrum was observed also for the Ni-K edge of the disordered Fe-Ni alloys. However, no change has been recognized in the XANES of Pt-L<sub>3</sub> edge. Radial structure function obtained by the Fourier transform of EXAFS spectrum indicates clearly a change from the pattern reflecting FCC structure to that resulting from BCC phase. These features insist that the structural phase transition affects significantly the electronic state of Fe atoms.

## References

- (1) H. Hasegawa, M.W. Finnis and D.G. Pettifor: J. Phys. F: Met. Phys. 17 (1987) 2049.
- (2) L.A. Grunes: Phys. Rev. B27 (1983) 2111.
- (3) M. Kitamura, S. Muramatsu and C. Sugiyara: Phys. Rev. B33 (1986) 5294.

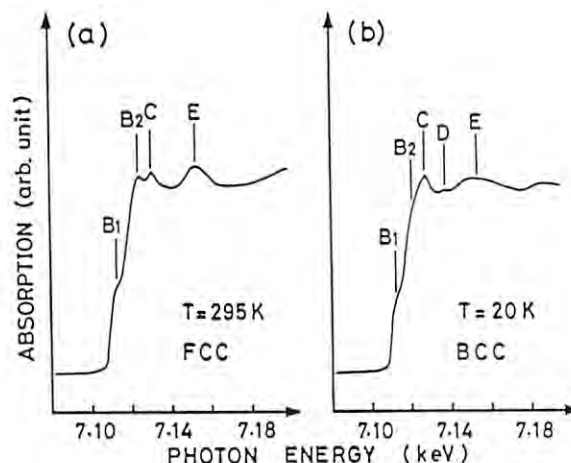


Fig. 1. XANES spectrum of the Fe-K edge of the disordered 25.0at%Pt-Fe alloy; (a) at 295K, (b) at 20K.



EXAFS STUDIES ON THE  $\text{SiO}_2$  - ATTACHED Nb DIMER CATALYST

Rika KUWABARA\*, Masayuki SHIRAI, Kiyotaka ASAKURA and Yasuhiro IWASAWA.

Department of Chemistry, Faculty of Science, the University of Tokyo, 7-3-1 Hongo, 113.

\* Present address: Center for Ceramics Research, The Research Laboratory of Engineering Materials, Tokyo Institute of Technology, 4259 Nagatsuta, Midori-Ku Yokohama 227.

## Introduction

The attached inorganic-oxide metal catalysts obtained by reactions between metal complexes and surface OH groups of inorganic oxides have well-defined structures and novel catalytic activities different from conventional supported catalysts. We have already investigated the structures and the reactivities of the attached Nb monomer catalysts and the one atomic layer Nb catalysts and found that each catalyst shows distinct catalytic activity. Therefore, we synthesized a new  $\text{SiO}_2$ -attached Nb dimer catalyst to clarify the cause of difference of the two types of attached catalysts.

## Experimental

The  $\text{SiO}_2$ -attached Nb dimer catalyst was prepared using a dinuclear Nb complex  $[(\text{C}_5\text{H}_5)(\text{C}_5\text{H}_4)\text{NbH}]_2$  (0) which was synthesized by the reaction between  $\text{Nb}(\text{C}_5\text{H}_5)_2\text{Cl}_2$  and NaH in THF[1] solution. The Nb dimer structure is stabilized in the existence of the bridging  $\text{C}_5\text{H}_4$  ligands. The room temperature EXAFS measurement was carried out at BL-10B of Photon Factory for THF solution of the original dimer complex (1), the attached catalyst without pretreatment (2), the catalyst preheated with  $\text{H}_2$  (100 Torr) to 623 K (3) and the catalyst pretreated with  $\text{O}_2$  (100 Torr) at 793 K for 1 hour (4).

## Results and Discussions

Figure 1 shows Fourier transform of the samples from 1 to 4. 1 and 2 have two main peaks near 0.2 nm and 0.3 nm, but on the other hand 3 and 4 have only one main peaks about 0.15 nm. The former peaks common with all the samples are attributed to the bonding between Nb-C or/and Nb-O. The latter peaks observed only in 1 and 2, of which theoretical fit of the inversely Fourier transform are shown in Fig. 2, are arisen from the bonding between Nb-Nb. The bond distances obtained by the curve-fitting analysis are indicated in Table I, with the bond parameters of the crystal of original Nb dimer complex 0. The bond length of Nb-Nb for 1 are rather longer than that for 0. This fact suggests that the complex in THF

solution is deformed from the crystal by the effect of the solvent. The comparison of the bonding distances Nb-Nb between 1 and 2 indicates that the dimer structure of the complex is held after the reaction with the OH and complex 0. For the samples 3 and 4, the Nb-Nb bonding is not observed. This is explained as follows. The bridging ligands ( $\text{C}_5\text{H}_4$ ) in the initial  $\text{Nb}_2$  complex desorb after the thermal treatment and hence the thermal vibration of this bonding is too large at room temperature. The observation of Nb-Nb is possible if the measurement is carried out at low temperature. The Nb-O distances for 2-4 are determined to be 0.194-0.199 nm, which are comparable with 0.193 nm for the  $\text{SiO}_2$ -attached Nb monomer catalyst.[3]

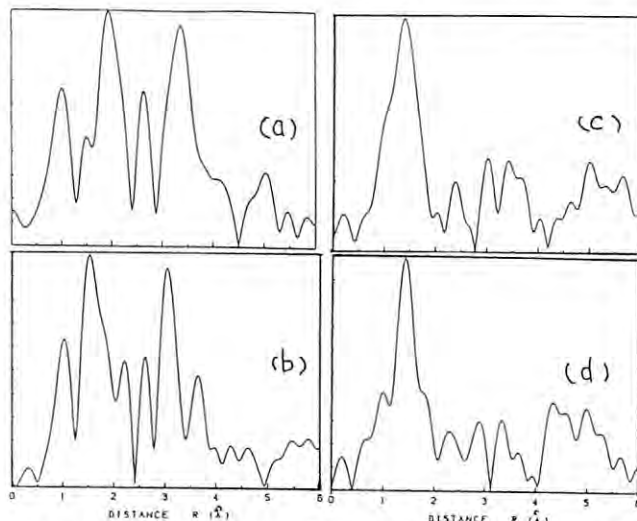


Fig. 1. Fourier transform of the samples 1(a), 2(b), 3(c) and 4(d).

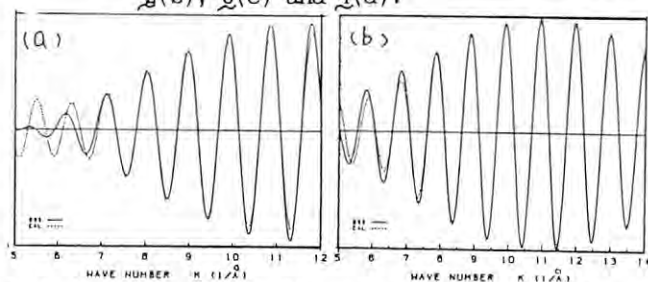


Fig. 2. Theoretical fit of the data inversely Fourier filtered over 0.28 and 0.35 nm for the samples 1(a) and 2(b).

TABLE I. Bond Distances for Nb Dimer Complex and Attached Catalyst from Curve-Fitting Analysis of EXAFS Data.

Sample	Bond Distances / nm		
	Nb-C	Nb-O	Nb-Nb
0	0.22-0.24*	--	0.311*
1	0.223	--	0.348
2	0.203	0.194	0.335
3	0.219	0.199	--
4	--	0.196	--

\* Distances determined by X-ray diffraction.[2]

- [1] D.A.Lemenovskii, I.F.Urazowski, I.E.Nifant'ev and E.G.Perevalova, J. Organomet. Chem., 217, 292(1985).
- [2] L.J.Guggenberger, Inorg.Chem. 294, 12(1973)
- [3] M.Nishimura, K.Asakura and Y.Iwasawa, J.Chem. Soc., Chem.Comm., 1660(1986).

## THE STRUCTURE OF THE ONE-ATOMIC LAYER Rh CATALYST IN THE CO OXIDATION REACTION

Kiyotaka Asakura, Masayuki Shirai, and Yasuhiro Iwasawa

Department of Chemistry, Faculty of Science, the University of Tokyo, Hongo, Tokyo 113.

Introduction

The reaction between  $\text{Rh}(\eta^3\text{-C}_3\text{H}_5)_3$  and OH groups on  $\text{SiO}_2$  followed by  $\text{H}_2$  treatment at room temperature and subsequently at 473 K produces one-atomic layer Rh cluster on  $\text{SiO}_2$  surface. Since all the Rh atoms are located at surface, the one-atomic Rh cluster is suitable for the investigation of the behavior of the Rh atom in the interaction of the adsorbed gas species on the standpoint of the catalysis of the small cluster. In this work we studied the structure change of the Rh one-atomic layer cluster on  $\text{SiO}_2$  during CO oxidation reaction by means of EXAFS.

Experimental

$\text{Rh}(\eta^3\text{-C}_3\text{H}_5)_3$  was prepared in the previously reported way.[1] The  $\text{Rh}(\eta^3\text{-C}_3\text{H}_5)_3$  was reacted with OH group of  $\text{SiO}_2$  at 293 K. The attached  $\text{Rh}(\eta^3\text{-C}_3\text{H}_5)(\text{OSi})_2$  was reduced with  $\text{H}_2$  at room temperature and then at 473 K. The sample thus obtained was denoted as A-Rh/ $\text{SiO}_2$ . The Transmission electron microscopy showed that the Rh cluster exists in a small cluster with 1.3 nm in diameter. The  $\text{H}_2$  was adsorbed on the Rh cluster with a H/Rh ratio = 1. EXAFS measurements were carried out at BL-10B, using the EXAFS reaction chamber.

Results and Discussion

The curve fitting analysis of EXAFS of the A-Rh/ $\text{SiO}_2$  showed that the coordination number is 5 and bond distance is 0.265 nm. Considering from the coordination number to be 5.0 and the particle size 1.3 nm. We proposed one-atomic layer Rh cluster structure.

The one-atomic layer Rh cluster has a high activity toward CO oxidation reaction at room temperature. We examined the structure of Rh cluster by means of EXAFS in the atmosphere of  $\text{O}_2$  and CO. The reactivity of oxygen on Rh cluster preadsorbed at 293 K is much higher than that preadsorbed at 373 K. After the exposure to  $\text{O}_2$ , Rh-Rh bond maintained with the appearance of a new peak corresponding to Rh-O as shown in Fig.1a. On the other hand the structure of Rh cluster changed by the exposure to  $\text{O}_2$  at 373 K in Fig.1c. The first and second peaks in the Fourier transform can be attributed to the Rh-O and Rh-Rh and the second peak is composed of two type of the Rh-Rh bonding of Rh metal cluster and  $\text{Rh}_2\text{O}_3$ -like cluster. After the CO introduction, the oxygen atoms adsorbed on Rh cluster at room temperature easily reacted with the CO as shown in Fig.1b. On the other hand the oxygen adsorbed at 373 K was slowly reacted with CO in Fig.1d. Thus the high activity of adsorbed

oxygens toward CO oxidation reaction requires metallic structure.

[1] K.Asakura and Y.Iwasawa J.Chem.Soc., Faraday Trans.I, 84,1329(1988).

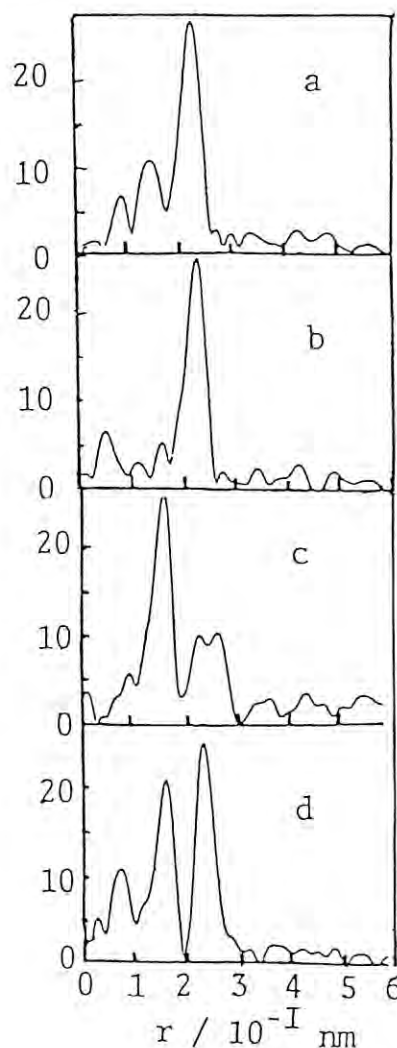


Fig.1 Fourier transforms of Rh K-edge EXAFS oscillations  
(a) Rh/ $\text{SiO}_2$  preadsorbed with  $\text{O}_2$  at 293 K  
(b) Rh/ $\text{SiO}_2$  obtained from (a) by exposure to CO  
(c) Rh/ $\text{SiO}_2$  preadsorbed with  $\text{O}_2$  at 373 K  
(d) Rh/ $\text{SiO}_2$  obtained from (a) by exposure to CO

# THE STRUCTURE STUDIES ON THE REVERSIBLE ACTIVITY CHANGE OF THE NOBLE METAL CATALYSTS

Kiyotaka ASAKURA, Junji Inukai, Yasuo Izumi and Yasuhiro Iwasawa

Department of Chemistry, Faculty of Science, the University of Tokyo, Hongo, Tokyo 113.

## Introduction

The noble metals (Pd, Pt, Rh) deposited on SiO<sub>2</sub> efficiently catalyzed C<sub>2</sub>H<sub>4</sub> hydrogenation reaction. Recently, we found that the activity of Pt, Pd, Rh/SiO<sub>2</sub> for C<sub>2</sub>H<sub>4</sub> hydrogenation increases by one order or two when they are pretreated above a certain transition temperature and decreases reversibly when pretreated below that temperature. Such phenomenon can be only seen in the supported metal particles with an appropriate particle size characteristic to the metal. (1-10 nm for Pt/SiO<sub>2</sub> for example) The large particle as well as the small one showed no such reversible change of the activity. It is considered to be relevant to some kind of structure transition of the small metal particle in the range of an appropriate particle size. We measured in-situ EXAFS spectroscopy to find out the transition of structure and investigate the relationship between the structure change and the reversible activity change of catalysis.

## Experimental

The supported Pt, Rh, Pd catalysts were prepared from the Pt(NO<sub>3</sub>)<sub>2</sub>, Rh(NO<sub>3</sub>)<sub>3</sub>, and Pd(NO<sub>3</sub>)<sub>2</sub> aqueous solutions. The loadings of the metal were 2 wt%. They were calcined at 673 K and reduced at 773 K in the EXAFS reaction chamber. The chamber was set in the X-ray light. The sample was raised to a certain temperature and then EXAFS spectrum was measured at the temperature. The sample was heated from RT and up to 773 K.

EXAFS was analyzed by decomposing the EXAFS signal into amplitude and phase parts. Coordination number and Debye Waller factor were extracted by means of ratio method using the Pt, Pd, and Rh foil as reference compounds.

## Results and discussion

Fig.1 showed EXAFS spectrum of Rh K-edge measured at 293 K and 773 K above and below the transition temperature of activity, respectively. The amplitude of EXAFS oscillation damps more quickly in the spectrum of 773 K owing to the Debye-Waller factor. The curve fitting analyses showed that no change in the coordination number was found in the Rh/SiO<sub>2</sub>. Fig.2 showed Debye-Waller factors of Rh-Rh bonding in the first coordination shell of Rh metal and Rh/SiO<sub>2</sub>. The Debye-Waller factor of Rh metal factor monotonically increased with the increase

of the temperature. However, the curve of Debye-Waller factor of Rh/SiO<sub>2</sub> inflected at the transition temperature. The slope of the curve corresponds to the strength of the Rh-Rh bonding. This change means that the Rh-Rh bonding becomes weaker at this temperature. We have not reached the full understanding of the change of the Debye-Waller factor and the relevance between the behavior of Debye-Waller factor and the increase of the activity. However, some structure transition should occur at that transition temperature which must be related to the change of thermal disorder of the Rh-Rh bonding.

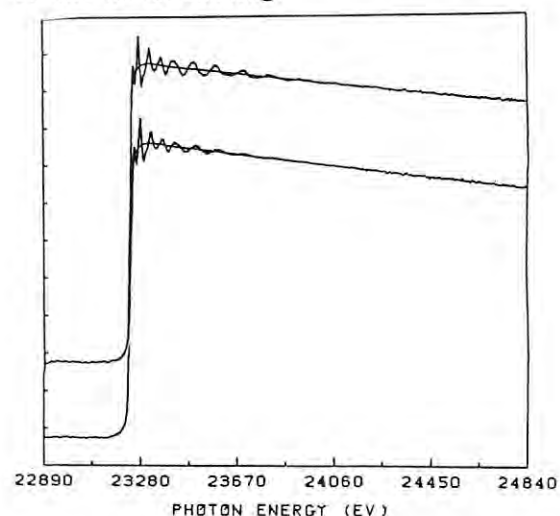


Fig.1 EXAFS spectra of Rh/SiO<sub>2</sub> (a) 293 K, (b) 773 K

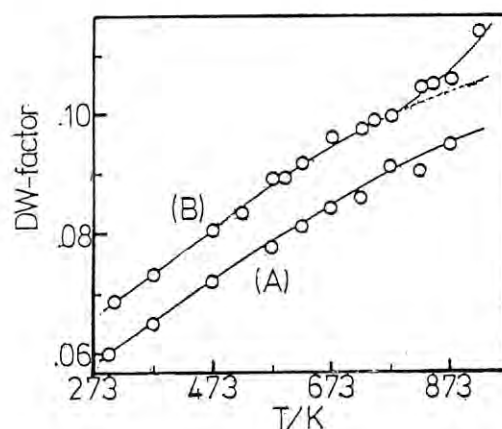


Fig.2 Temperature dependency of Debye-Waller Factor (a) Rh metal, (b) Rh/SiO<sub>2</sub>

# Elucidation of Structure of Catecholdioxygenase-model Complexes and Mechanism of Oxygenation of Aromatic Ring

Takuzo FUNABIKI, Takahiro INOUE, Tanehiro TANAKA,  
Yasuo NISHIMURA, Hiroshi MIZUTANI and Satohiro YOSHIDA

Division of Molecular Engineering and Department of Hydrocarbon Chemistry,  
Kyoto University, Sakyo-ku, Kyoto 606.

## Introduction

As a model for oxygenation of catechol by enzyme, 3,5-di-*t*-butyl-catechol(I) is oxygenated by pyridineiron(III) in tetrahydrofuran to give intra- and extra- oxygenation products in addition to quinone<sup>1</sup>). The yield of oxygenation are affected by the pyridine concentration. It is important to clarify the structure of active species in order to know the oxygenation mechanism. In the present study, the variations of oxidation states and structures of complexes formed in the presence of different pyridine, are investigated by XANES and EXAFS.

## Experiment

1 and FeCl<sub>3</sub> were dissolved in THF-pyridine solvents in argon atmosphere. The solutions were packed into polyethylene-nylon-polychlorobinylidene films under argon bubbling. X-ray absorption spectra were recorded with the facilities at BL10B of KEK-PF.

## Results and Discussion

Figure 1 shows the Fe K-edge XANES spectra of the solutions of iron-catechol complexes formed in THF-pyridine solvents and the diethylether solution of FeCl<sub>3</sub>. All spectra show a pre-edge peak which is attributed to the 1s-3d transition. Its intensity decreases with increasing pyridine concentration. The spectrum of the complex formed with the very low pyridine concentration is similar to that of tetrahedral complex [FeCl<sub>3</sub>(OEt<sub>2</sub>)] which is formed with FeCl<sub>3</sub> in diethylether (Fig.1 (a)). This result indicates that tetrahedral coordinated by chloro and catechol ligands is dominant in the case of the low pyridine concentration, and the complex is converted to an octahedral complex by increasing the pyridine concentration. By Mossbauer spectroscopy we have detected high-spin Fe(II) species which we considered Fe(II)-semiquinone complexes, and they increased when pyridine concentration became higher<sup>2</sup>). We expected that the energy shift of K-edge caused by variation of pyridine concentration, but it was hardly observed. So clear supports for formation of Fe(II)-semiquinone species have not been obtained by X-ray absorption spectroscopy.

Figure 2 shows the fourier transforms of k<sup>3</sup>-weighted EXAFS spectra. No peak corresponding to Fe-Fe can be found in Fig. 2. Thus, the solution includes only monomer complexes and no dimer complex in which two irons are bridged by catecol.

## References

- 1) T. Funabiki, A. Mizoguchi, T. Sugimoto, S. Tada, M. Tuji, H. Sakamoto, and S. Yoshida, *J. Am. Chem. Soc.*, 1986, 108, 2921.
- 2) T. Funabiki, S. Tada, T. Yoshioka, M. Takano, and S. Yoshida, *J. Chem. Soc., Chem. Commun.*, 1986, 1699

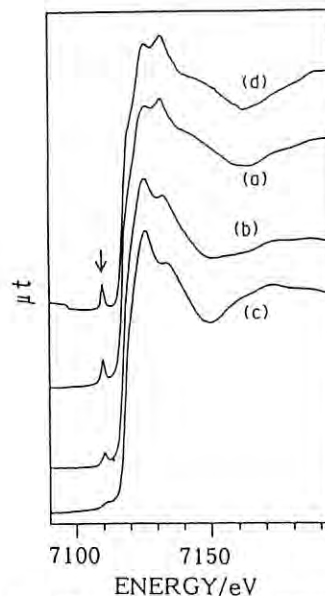


Figure 1. XANES spectra of Fe-DTBC complex and [FeCl<sub>3</sub>(OEt<sub>2</sub>)]

(a)-(c): Fe-DTBC complex in THF-pyridine solvent  
(a) [pyridine]/[Fe]=4, (b) [pyridine]/[Fe]=100  
(c) in pyridine  
(d) FeCl<sub>3</sub> in Et<sub>2</sub>O ([FeCl<sub>3</sub>(OEt<sub>2</sub>)])

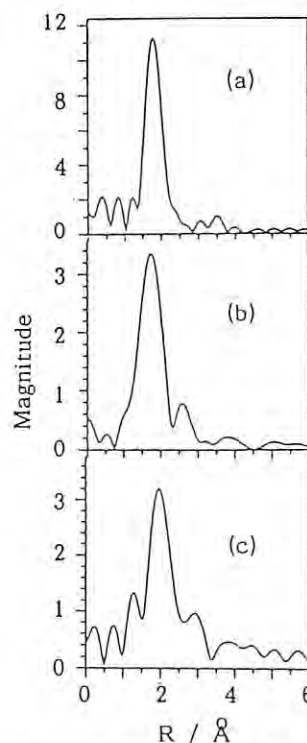


Figure 2. Fourier transforms of Fe-DTBC complex in THF-pyridine solvent

(a) [pyridine]/[Fe]=4, (b) [pyridine]/[Fe]=100  
(c) in pyridine



EXAFS AND XANES STUDIES ON DYNAMIC BEHAVIOR OF TWO-SITE PROMOTION  
OF CO CATALYZED BY BIMETAL CLUSTERSMasaru ICHIKAWA, Atsushi FUKUOKA, Takuma KIMURA, Toshiyuki FUJIMOTO,  
Nobuhiro KOSUGI,\* AND Haruo KURODA\*

Research Institute for Catalysis, Hokkaido University, Kita-11, Nishi-10, Kita-ku, Sapporo 060

\*Department of Chemistry, Faculty of Science, The University of Tokyo, Hongo, Bunkyo-ku, Tokyo 113

Introduction

The use of bimetallic cluster compounds as the catalyst precursors is an important aspect of homogeneous and heterogeneous bimetallic catalysis.<sup>1)</sup> The bimetallic clusters offer prospects of synergistic effect for the two metal compounds in many useful catalytic reactions. Particularly, bimetallic clusters grafted on solid surface have attracted much attention, because they may provide the advantage obtaining highly dispersed bimetallic species. This can pave the way for catalyst design in a molecular-level.<sup>2-5)</sup>

In a CO+H<sub>2</sub> reaction, SiO<sub>2</sub>-supported Rh-Fe and Pd-Fe catalysts derived from metal salts showed a unique activity for producing C<sub>1</sub>+C<sub>2</sub> alcohols.

Accordingly, as a tailored model for the Fe-promoted Rh and Pd catalysts, we have prepared RhFe/SiO<sub>2</sub> and PdFe/SiO<sub>2</sub> catalysts by using RhFe and PdFe bimetallic carbonyl clusters as molecular precursors. The bimetallic clusters grafted on SiO<sub>2</sub> were structurally characterized by Fe K-, Rh K-, and Pd K-edge EXAFS.

Experimental

FeRh<sub>4</sub>, Fe<sub>2</sub>Rh<sub>4</sub>, Fe<sub>6</sub>Pd<sub>6</sub>, and Fe<sub>4</sub>Pd carbonyl clusters were used as the precursors. The carbonyl clusters were supported on SiO<sub>2</sub> from adequate organic solutions. After drying in vacuo and mild oxidation by air, the catalysts were reduced with H<sub>2</sub> at 673 K for 2 h. EXAFS measurements were performed at room temperature at BL 10B in KEK-PF.

Results and Discussion

Figure 1 shows the Fourier transforms of  $k^3\chi(k)$  of Fe K-edge EXAFS for [NMe<sub>4</sub>CH<sub>2</sub>Ph]<sub>2</sub>[Fe<sub>4</sub>Pd(CO)<sub>10</sub>], Fe<sub>6</sub>Pd<sub>6</sub>/SiO<sub>2</sub>, and Fe<sub>4</sub>Pd/SiO<sub>2</sub>. In the Fourier transform of [NMe<sub>4</sub>CH<sub>2</sub>Ph]<sub>2</sub>[Fe<sub>4</sub>Pd(CO)<sub>10</sub>], the peak at about 2.5 Å is attributable to Fe-Pd bonding. Fe<sub>6</sub>Pd<sub>6</sub>/SiO<sub>2</sub> has the strong peak at the similar position, possibly due to the Fe-Rh bonding. On the other hand, Fe<sub>4</sub>Pd/SiO<sub>2</sub> has no strong peak at about 2.5 Å, suggesting the absence of Fe-Pd bonding. The strong peak at 2.2 Å may arise from Fe-Fe bonding.

The different contribution of Fe-Pd bonding between Fe<sub>6</sub>Pd<sub>6</sub>/SiO<sub>2</sub> and Fe<sub>4</sub>Pd/SiO<sub>2</sub> well reflects the activity difference for MeOH production in catalytic CO+H<sub>2</sub> reaction; i.e., Fe<sub>6</sub>Pd<sub>6</sub>/SiO<sub>2</sub> was a highly selective catalyst toward MeOH, while Fe<sub>4</sub>Pd/SiO<sub>2</sub> gave lower activity for MeOH production.

Combining with <sup>57</sup>Fe Mossbauer study, we revealed that bimetallic Pd-Fe<sup>3+</sup> species derived from the Fe<sub>6</sub>Pd<sub>6</sub> carbonyl cluster promote the MeOH production due to the enhancement of CO

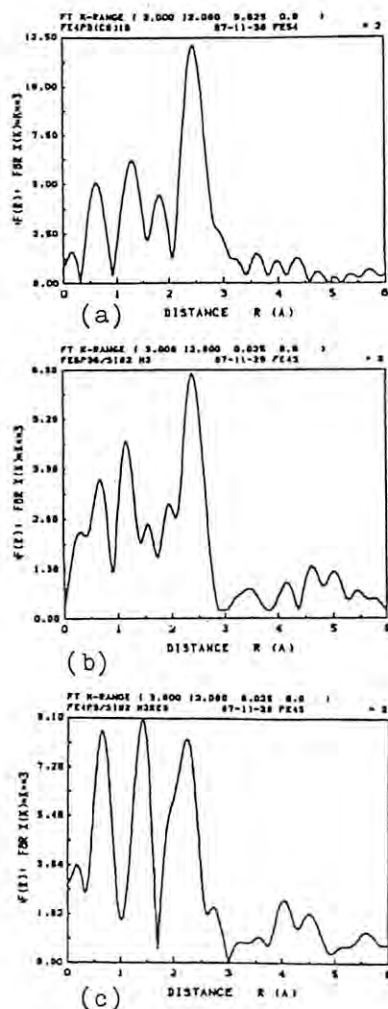


Figure 1. Fourier transforms of  $k^3\chi(k)$  of Fe K-edge EXAFS for [NMe<sub>4</sub>CH<sub>2</sub>Ph]<sub>2</sub>[Fe<sub>4</sub>Pd(CO)<sub>10</sub>] (a), Fe<sub>6</sub>Pd<sub>6</sub>/SiO<sub>2</sub> (b), and Fe<sub>4</sub>Pd/SiO<sub>2</sub> (c).

insertion. It is also shown that the Pd-Fe<sup>3+</sup> sites were not formed effectively from the Fe-rich Fe<sub>4</sub>Pd carbonyl cluster imoregnated on SiO<sub>2</sub>.

References

- 1) B. C. Gates et al. ed., "Metal Clusters in Catalysis", Elsevier(1986).
- 2) A. Fukuoka, H. Matsuzaka, M. Hidai, and M. Ichikawa, Chem. Lett., 941(1987).
- 3) A. Fukuoka, M. Ichikawa, J. A. Hriljac, and D. F. Shriver, Inorg. Chem., 26, 3643(1987).
- 4) A. Fukuoka, T. Kimura, and M. Ichikawa, J. Chem. Soc., Chem. Commun., 428(1988).
- 5) M. Ichikawa, A. Fukuoka, and T. Kimura, Proc. 9th Intl. Congr. Catal.(Calgary), vol. 1, 569(1988).

# COMPACT FLUORESCENCE X-RAY DETECTOR FOR SURFACE EXAFS AND X-RAY STANDING-WAVE MEASUREMENTS

M.Funabashi[1], T.Ohta[2], T.Yokoyama[2], Y.Kitajima[3] and H.Kuroda[1,4]

[1]J.R.D.C., Tokodai, Tsukuba, Ibaraki 300-26, Japan

[2]Dept.Materials Science, Hiroshima Univ., Hiroshima 730, Japan

[3]KEK-PF, Oho, Tsukuba, Ibaraki 305, Japan

[4]Dept.Chemistry, Univ.of Tokyo, Tokyo 113, Japan

## 1.Introduction

Surface EXAFS spectroscopy and X-ray standing-wave (XSW) method are powerful techniques to investigate the surface structures. In the surface EXAFS measurement electron-yield modes are often employed because of their good surface-sensitivity. X-ray fluorescence-yield mode, however, seems to be more promising for the XSW measurements and for the systems with very low concentration of X-ray absorbing atoms.<sup>1,2)</sup> We have developed a compact fluorescence detector for these purposes.

## 2.Design

The X-ray detector is a type of gas-flow proportional counter (FPC) as shown in Fig.1. It can be mounted to a UHV chamber with an ICF-70 flange, and is linearly movable through a bellows for optimizing its position. A pinhole-free Be film with 25  $\mu\text{m}$ -thick is used for vacuum seal and for X-ray window. In or Au gasket allows to keep ultra high vacuum ( $<1 \times 10^{-10}$  mbar). In order to detect low-energy X-ray photons a center wire supported on the inner tube (see Fig.1) can move to an appropriate position where the detection gas is sufficiently ionized.

## 3.Experiments

The detector is tested at BL11B. The typical operating HV on center wire is 1800V and the counting gas (P-10) flow-rate is about 50 cc/min. Fig.2 shows the pulse height distribution curve for Cl adsorbed on Ni. The energy resolution is about 20-30%.

For the EXAFS and XSW measurements of 1/4 monolayer sulfur adsorbed on a Ni(111) single crystal, the S/B ratio is 12 times higher than that of Auger-electron-yield(AEY) mode. The intensity of signal is about  $10^4$  cps (see Fig.3).

It was impossible to extract a pure XSW profile from adsorbates with AEY mode due to dominant background electrons from substrates. On the contrary, the XSW profiles monitored by X-ray fluorescence yields (XFY) show clear difference from each other.<sup>3)</sup> The results indicates that the XFY-monitored SW

profile can be used for the surface-structure analysis with high accuracy.

## Reference

- 1)J.Stohr et al., Phys.Rev.Lett. 55, 1468(1985)
- 2)D.A.Fischer et al., Nucl.Instr.Methods A246, 561(1986)
- 3)T.Yokoyama et al., in this issue

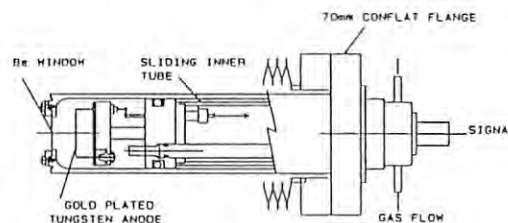


Fig.1 Schematic of X-ray Proportional Counter

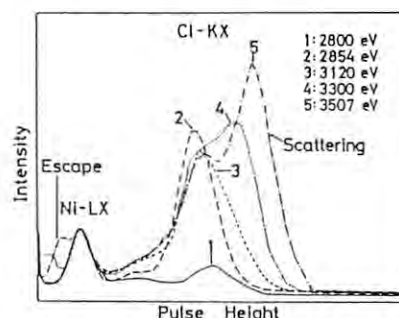


Fig.2 Pulse-height distribution curve

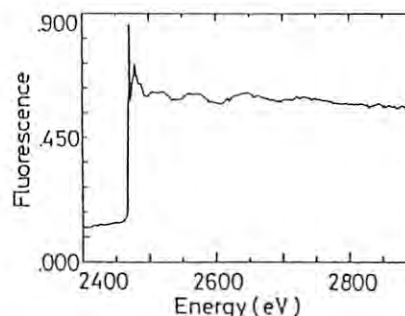


Fig.3 X-ray Fluorescence yield SEXAFS spectrum of S/Ni(111)

## La K-EDGE EXAFS STUDIES ON THE STRUCTURES OF La OXIDE THIN LAYER CATALYSTS

Kiyotaka Asakura, Yoshinori Satow\*, and Yasuhiro Iwasawa

Department of Chemistry, Faculty of Science, the University of Tokyo,  
Hongo, Bunkyo-ku, Tokyo 113.\*Photon Factory, National Laboratory for High Energy Physics, Oho-cho,  
Tsukuba, Ibaraki 305.

ZSM-5 attached 3-atomic layer  $\text{La}_2\text{O}_3$  showed a unique nature as a support(1). When Pd was deposited on it, the  $\text{CO}+\text{H}_2$  was selectively converted into  $\text{C}_3\text{H}_6$ . We have tried to elucidate the structure of La oxide by means of EXAFS. However, it is quite difficult to apply the conventional transmission technique on the L<sub>3</sub>-edge of La, because of the large absorption of ZSM-5 substrate. Thus we examined K-edge EXAFS using the high energy X-ray emitted from the superconducting wiggler beam line. In this work we will report the preliminary EXAFS results of the 3-atomic layer  $\text{La}_2\text{O}_3$  deposited on ZSM-5.

Experimental

The ZSM-5 attached 3-atomic layer  $\text{La}_2\text{O}_3$  was prepared in a previously described way(1). The EXAFS spectra were measured at BL14A beam line using the Si(553) double crystal monochromator. The ionization chamber was filled with Kr.

Results and Discussion.

Figs.1 and 2 showed  $k^3$ -weighted EXAFS oscillation and the Fourier transform of  $\text{La}_2\text{O}_3$  powder. One can measure the EXAFS oscillation at high  $k$ -region. Comparing to the  $\text{CeO}_2$  EXAFS oscillation previously reported, the EXAFS oscillation of  $\text{La}_2\text{O}_3$  damps quickly, indicating the contribution of La-La EXAFS oscillation to the total EXAFS oscillation. The first and second peaks were immediately attributed to La-O and La-La. Figs.3 and 4 showed the Fourier transform of ZSM-5 attached 3-atomic layer  $\text{La}_2\text{O}_3$ . The EXAFS oscillation smears at  $k=90 \text{ nm}^{-1}$ , indicating the little interaction of La-La. Only one prominent peak corresponding to the La-O can be found in the Fourier transform. The peak corresponding to La-La was not found. This observation suggested that the La exists in the amorphous state. The previous studies on the one-atomic  $\text{Nb}_2\text{O}_5$  and  $\text{ZrO}_2$  produced in a similar way showed that the one-atomic oxides took an amorphous structure though the deposition amount exceeds the amount equivalent to the 2-atomic layer the corresponding oxide crystallines were observed both in the EXAFS analyses and X-ray diffraction studies. The amorphous structure in the one-atomic layer oxide was caused by the mismatch of the oxide lattice and substrate one. In the case of ZSM-5 supported  $\text{La}_2\text{O}_3$  the situation is quite different. No crystalline of  $\text{La}_2\text{O}_3$  was observed either in EXAFS and in the X-ray diffraction. Thus the effect of mismatch between the  $\text{La}_2\text{O}_3$  and ZSM-5 lattice prevails through the 3-atomic layer.

1) A.Kase, K.Asakura, C.Egawa, and Y.Iwasawa, Chem.Lett., 855(1986)

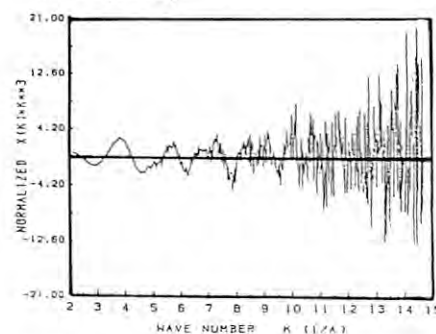
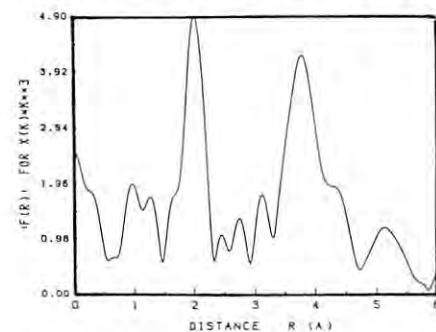
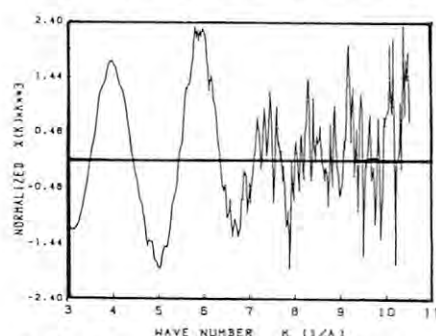
Fig.1 La K-edge EXAFS of  $\text{La}_2\text{O}_3$ Fig.2 Fourier transform of  $\text{La}_2\text{O}_3$ 

Fig.3 La K-edge EXAFS of La/ZSM-5

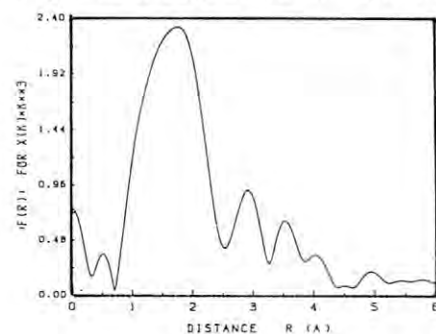


Fig.4 Fourier transform of La/ZSM-5

# MEASUREMENT OF SPECTRA OF SYNCHROTRON RADIATION IN SOFT X-RAY REGION BY MEANS OF HELIUM GAS SCATTERING

Syunji GOTOH, Takao TAGUCHI, Shigeru OKAMURA, and Tokushige HISATSUGU  
FUJITSU LABORATORIES LTD., 10-1 Morinosato-Wakamiya, Atsugi 243-01, Japan

## INTRODUCTION

We designed the spectrometer using gas scattering method and a Si(Li)-detector to investigate the spectra of synchrotron radiation of soft X-ray region.

We chose helium gas because it transmits soft X-rays sufficiently, and its scattering theory is very simple and we can adequately reduce the high SR intensity by helium gas scattering<sup>2</sup>.

## EXPERIMENT

Our measuring system is shown in Fig. 1. The He gas chamber was evacuated and filled with pure He gas. The pressure of the chamber was held at 1 atm. We defined the detectable scattering region by slits and the sensitive area of a Si(Li)-detector. We determined the dimensions of the spectrometer by estimating adequate reduction rate for Si(Li)-detector using the scattering theory of helium gas.

We placed the measuring system at 31 m from the source of the beam line, BL-17C. SR X-rays can be taken into the air through a 200- $\mu$ m-thick Be window, 2.0-cm thick He gas and a 25- $\mu$ m-thick Kapton window.

We measured the spectra of the direct beam and reflected beam from two plane fused quartz mirrors which were set in parallel.

## RESULTS

We compared the measured spectrum of the SR emitted in the orbital plane with the calculated one (Fig. 2). The measured intensity was about 30% less than that of calculated.

We believe this difference is mainly caused by the geometrical errors of energy-independent factors, (scattering volume and solid angle).

Next, we estimated the spectra of the reflected beam from fused quartz mirrors by fitting the measured and calculated intensities of direct beam.

The measured and calculated spectra of reflected beam from fused quartz mirrors with glancing angles of 8, 10, and 12 mrad are shown in Fig. 3. The profile of measured spectra agreed with the calculated, but the measured intensities were about 30% - 50% less than calculated.

We believe this result was caused by the roughness and imperfect flatness in the mirror surfaces.

We confirmed, we can measure the absolute intensity spectra within accuracy of 30% using a Si(Li)-detector and He gas scattering, and we also apply this system to evaluate the spectral characteristics of X-ray lithography beam line.

## REFERENCES

- 1) T. Mitsuhashi, T. Shioya, M. Ando, and T. Yamakawa, Nucl. Instrum. Methods **A246**, 54 (1986).
- 2) S. Gotoh, T. Taguchi, S. Okamura, and T. Hisatsugu, submitted to Rev. Sci. Instrum.

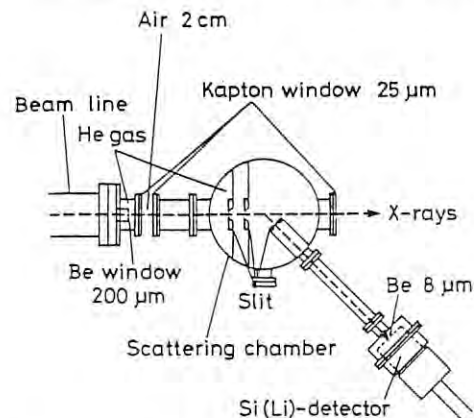


Fig. 1 Measuring system (top view).

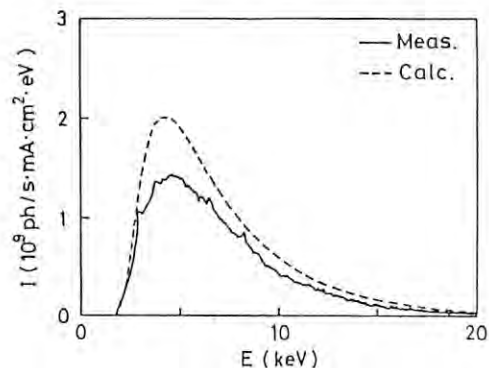


Fig. 2 Spectra of direct beam

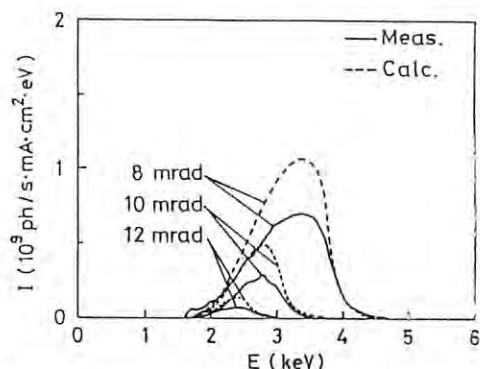


Fig. 3 Spectra of reflected beam from fused quartz mirrors.



## STUDY OF QUARTER-MICRON PATTERN REPLICATION BY X-RAY LITHOGRAPHY

Hidetoshi ISHIWARI, Yoshimi YAMASHITA, Syunji GOTOH, Takao TAGUCHI,  
Shigeru OKAMURA, and Tokushige HISATSUGU

FUJITSU LABORATORIES LTD., 10 - 1 Morinosato - Wakamiya, Atsugi 243 - 01

### Introduction

X-ray lithography using synchrotron radiation is promising for mass production of quarter-micron VLSIs.

Synchrotron radiation spectra in the beam line BL-17C can be changed by adjusting the glancing angle of the two plane-fused quartz mirrors (1).

We investigated the relation between the glancing angle of the mirrors and the exposure characteristics of resist.

### Experiment and Results

Synchrotron radiation emitted from an electron storage ring was introduced into an exposure chamber through a 200- $\mu\text{m}$ -thick Be window. An X-ray mask and a 1- $\mu\text{m}$ -thick PMMA resist on a Si wafer were mounted on the stage in the chamber. The gap between the mask and wafer was kept to about 25  $\mu\text{m}$ . The X-ray mask was made of 0.65- $\mu\text{m}$ -thick Ta absorber patterns (2) and a 2- $\mu\text{m}$ -thick SiN membrane fabricated on the Si substrate. The resist was

developed by dipping the wafer into methyl iso-butyl ketone (MIBK) for 120 s.

Figure 1 shows the dose of PMMA resist for two glancing angles. The horizontal axis is the product of the current in the electron storage ring and exposure time. The dose of PMMA resist for a glancing angle of 10 mrad must be larger than that for 8 mrad. This is due to the decrease the intensity of the synchrotron radiation on resist. However, the X-ray mask contrast for 8 mrad is smaller than that of 10 mrad, because the peak wave length of synchrotron radiation is shorter. The X-ray mask contrast is about 4 for 8 mrad and 10 for 10 mrad. Therefore, fine resist patterns are difficult to make with an 8 mrad glancing angle.

Figure 2 is SEM micrograph of the 0.2- $\mu\text{m}$  line and 0.3- $\mu\text{m}$  space fine patterns replicated in PMMA at glancing angle of 10 mrad.

### References

- (1) S. Okamura *et al.*: Photon Factory Activity Report, No. 5, 81 (1987).
- (2) M. Sekimoto *et al.*: Extended Abstract of the 16th Conf. on SSDM, Kobe, 23 (1984).

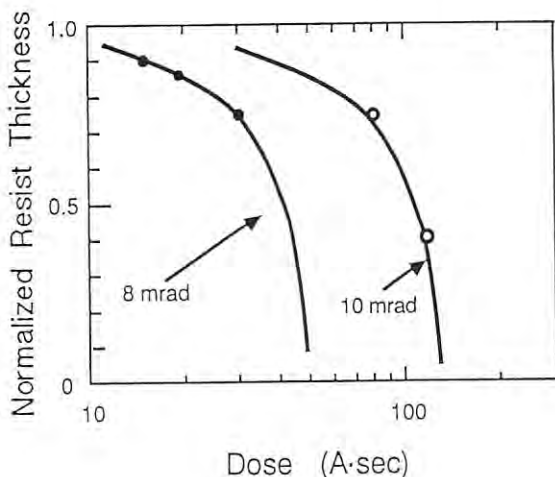


Figure 1. Dose of PMMA resist for two glancing angle of the mirrors.

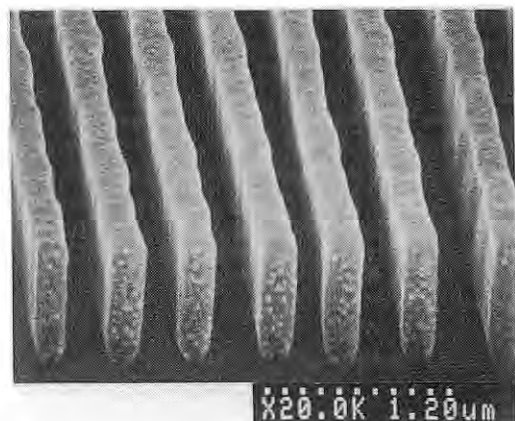


Figure 2. SEM micrograph of the patterns replicated in PMMA.

## RADIATION DURABILITY OF a-BNC:H FOR X-RAY MASK MEMBRANES

Masao YAMADA, Masafumi NAKAISHI

Advanced Technology Division, FUJITSU LIMITED  
1015 Kamikodanaka, Nakahara-ku, Kawasaki, 211 JAPAN

### 1. Introduction

Because of rapid progress of synchrotron radiation (SR) lithography, the radiation durability of X-ray mask materials has become very important. We investigated radiation durability of boron compound materials, a-BNC:H and a-BN:H, observing changes of the optical transparency and stress under X-ray irradiation.

### 2. Experimental

Amorphous BN:H films of 4 $\mu$ m thick were prepared by a low pressure CVD at 400°C. Amorphous BNC:H films of 2 $\mu$ m thick were prepared by a plasma enhanced CVD at 500°C. These samples were uniformly exposed by a white beam in the air. The stress during X-ray irradiation was monitored by the bulge method, and the optical transparency was monitored for a He-Ne laser.

### 3. Results and Discussions

Figure 1 shows stress change due to X-ray irradiation as a function of absorbed energy per

unit volume. The internal stress of a-BN:H started to change after absorbing 30 kJ/cm<sup>3</sup>, and became compressive after absorbing 100 kJ/cm<sup>3</sup>. This results agreed with the work of Johnson et. al.(1). The internal stress characteristics of a-BNC:H were similar to those of a-BN:H. However, the absorbed energy at which the stress began to degrade was about one order of magnitude larger than that of a-BN:H. The stress of a-BNC:H withstood tension up to 6 MJ/cm<sup>3</sup>.

The optical transparency of a-BN:H monotonically decreased with increasing absorbed energy. However, there was no change of optical gap for a-BNC:H.

We found that the a-BNC:H had a higher radiation durability than conventional a-BN:H. The a-BNC:H can be used without mask distortion up to an absorbed energy of 1 MJ/cm<sup>3</sup>.

### Reference

- 1) W.Johnson, R.Levy, D.Resnick, T.Saunders, A.Yanof, H.Bets, H.Huber and H.Oertel, J.Vac.Sci.Technol.,B5(1), 257 (1987).

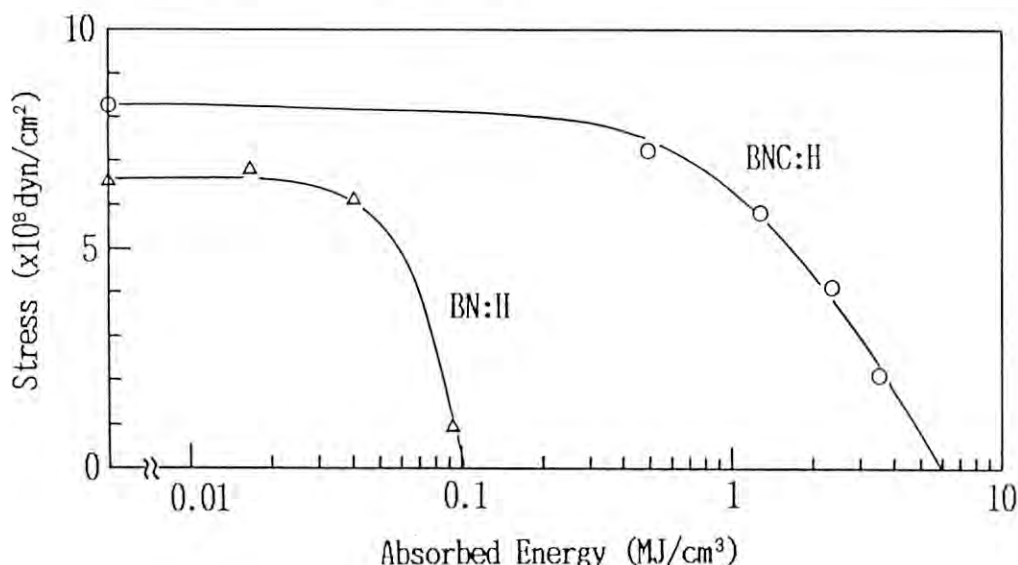


Figure 1. Stress change of a-BNC:H and a-BN:H due to X-ray irradiation as a function of absorbed energy per unit volume.

## LOCAL STRUCTURE AROUND Zn ATOMS DIFFUSED INTO GaAs CRYSTAL

Tomohisa KITANO, Yoshishige MATSUMOTO, Hisao WATANABE and Junji MATSUI

Fundamental Research Laboratories, NEC Corporation, 4-1-1 Miyazaki  
Miyamae-ku Kawasaki Kanagawa, 213Introduction

On the study of Zn diffusion into GaAs, a number of experiments which have plotted diffusion profiles of Zn concentration versus diffusion depth have shown anomalous diffusion. We also note that the introduction of Zn atoms into GaAs/AlAs or GaAs/GaAlAs multilayers enhances the intermixing of host atoms, which may create a problem. Defect reactions in this way play an important role in impurity diffusion. None of these phenomena can be understood without a knowledge of the local structure around Zn atoms. In this study, local structures around Zn atoms doped in LEC-grown GaAs (grown-in) and diffused into GaAs (diffused-in) were investigated using EXAFS method.

Experimental

Zn diffusion was made at 616°C for 3h. in an evacuated sealed quartz ampoule using ZnAs<sub>2</sub> source. The diffusion depth was determined to be 3  $\mu\text{m}$  and the surface Zn concentration about  $1 \times 10^{20} \text{cm}^{-3}$ . X-ray from SR was monochromatized by Si(111) double crystals and Zn K $\alpha$  fluorescence yield was detected using a pure Ge SSD.

Results and Discussion

Figure 1 shows diffused-in and grown-in Zn K-EXAFS oscillations. Ga K-EXAFS of undoped

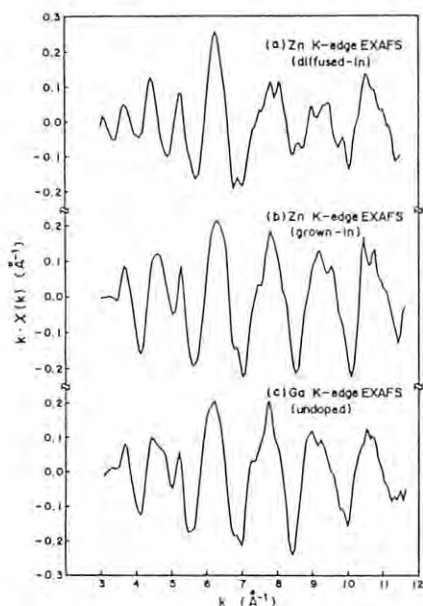


Fig. 1 EXAFS oscillations of each materials.

GaAs is also given for comparison.  $|F(r)|$  of grown-in Zn K-EXAFS is shown together with that of Ga K-EXAFS in Fig.2. The first and the second peak positions, magnitudes and FWHM values of the two lines profiles are in good agreement with each other. It is said that grown-in Zn atoms have the four As atoms as the first NN and twelve Ga atoms as the second NN, and the bond lengths of Zn-As and Zn-Ga are nearly the same as those of Ga-As and Ga-Ga in undoped GaAs, respectively.

Figure 3 shows  $|F(r)|$  of diffused-in Zn K-EXAFS. The first peak positions are in agreement with each other but the magnitude is remarkably different. In order to determine the coordination number (CN) and Debye-Waller factor, each of the first peaks is back Fourier transformed to  $k$  space. By plotting the logarithm ratio versus  $k^2$ , CN is determined to be 2.5 and the difference  $\sigma^2$  is less than 0.001. Extra peak as the second nearest neighbor (NN) is observed at distance of 3.35 Å between the first and the second NN distances of undoped GaAs. As for the third peak, since the position and magnitude are in agreement with the second peak position and magnitude of undoped GaAs, respectively, it is said that Zn atoms have 12 atoms near distance of 4.00 Å. From the above results, almost all diffused-in Zn atoms occupy the substitutional site. However, the local structure around Zn atoms is different from that of regular zinc-blende structure and Zn atoms are associated with vacancies.

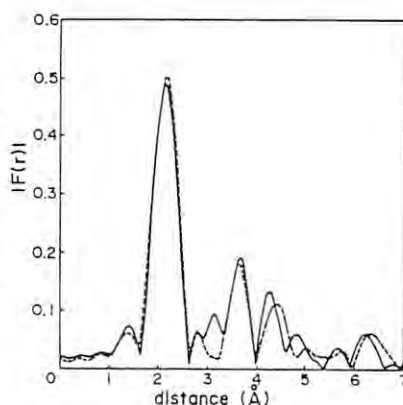


Fig. 2

$|F(r)|$  for grown-in Zn doped GaAs (solid line) and undoped GaAs (dashed line).

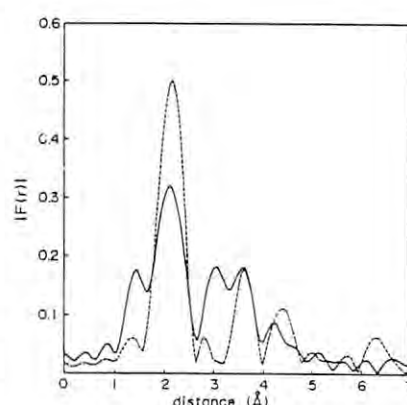


Fig. 3

$|F(r)|$  for diffused-in Zn doped GaAs (solid line) and undoped GaAs (dashed line).

EXAFS study of Rh/Al<sub>2</sub>O<sub>3</sub> catalysts

Yasuyuki Murofushi and Kouiti Kuno  
Material Research Laboratory  
Central Engineering Laboratories  
Nissan Motor Co., Ltd.

Rhodium is a common constituent of catalysts for the purification of automobile exhaust gas. However, the atomic structure of the supported rhodium has not been characterized satisfactorily. The Rh/Al<sub>2</sub>O<sub>3</sub> catalysts were studied with the EXAFS of the rhodium and some complementary techniques.

**EXPERIMENT.** Rh/Al<sub>2</sub>O<sub>3</sub> catalysts were prepared by the incipient wetting technique. A known amount of  $\gamma$ -Al<sub>2</sub>O<sub>3</sub> (BET area 170m<sup>2</sup>/g) was wetted with an aqueous solution of RhCl<sub>3</sub>. After impregnation, catalysts were dried in air (120°C, 1hr), reduced with flowing H<sub>2</sub> (400°C, 2hrs), cooled down to room temperature. They were then stored in air until needed. The rhodium loadings of the catalysts were 0.05, 0.1, 0.3 and 0.6wt%, respectively. The catalysts were pressed into thin self-supporting wafers.

**RESULTS.** Figure 1 shows the Fourier transforms of the catalysts and the reference materials. In table 1 are listed best fit values of structural parameters of them, also listed the results of XPS and CO chemisorption measurements.

Rh-O and Rh-Rh bonds were obtained from EXAFS measurements on 0.6wt% Rh/Al<sub>2</sub>O<sub>3</sub> catalyst. This Rh-Rh bond has a coordination distance of 2.67 Å which is nearly equal to the distance found in rhodium metal lump. So in this catalyst, rhodium metal clusters are formed.

While, below 0.3wt% of the rhodium loading, the Rh-Rh bond disappears and the measured coordination number of the Rh-O bond increases. This Rh-O bond is assigned to a coordination of the interfacial rhodium ions with support oxygen ions. These spectrums of 0.05, 0.1 and 0.3wt% Rh loading catalysts are different from the spectrums of rhodium metal and Rh<sub>2</sub>O<sub>3</sub> powder. This results suggest that the rhodium in the low rhodium loading catalysts form isolated ions on support oxygen ions.

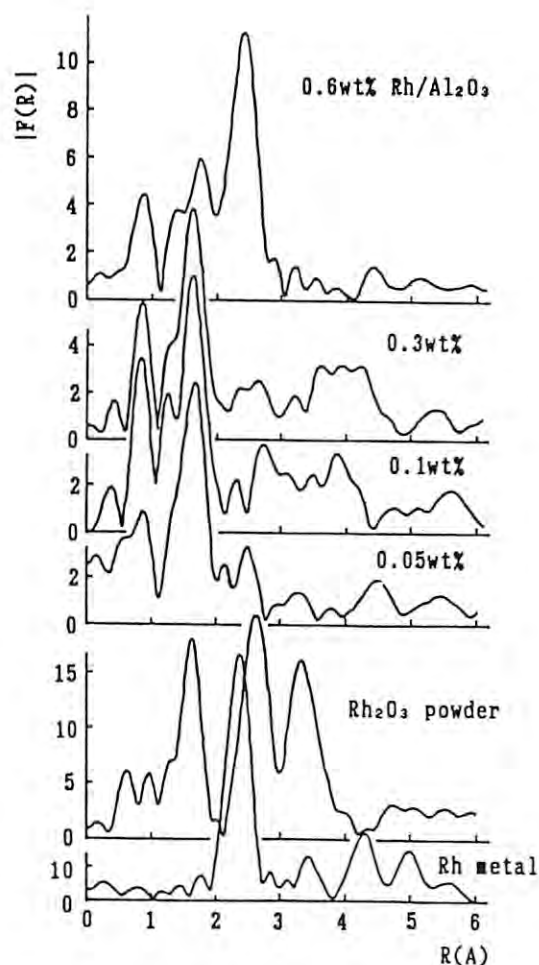


Figure 1. The  $|F(R)|$  of Rh EXAFS

Table 1. Results of EXAFS, XPS and CO Chemisorption Measurements

Rh loading (wt%)	EXAFS parameter values				CO chemisorption (CO/Rh)	Rh3d <sub>5/2</sub> electron binding energy (eV)
	Rh-O		Rh-Rh			
	N	R(A)	N	R(A)		
0.6	2.8	2.09	3.6	2.67	0.66	307.6
0.3	3.5	2.04	0.4	2.60	0.79	308.4
0.1	4.2	2.04	0.3	2.59	0.92	309.2
0.05	3.7	2.06	0.3	2.49	0.75	309.1
Rh metal lump	—		(12)	2.69	—	307.4
			(6)	3.79		
Rh <sub>2</sub> O <sub>3</sub> powder	5.0	2.04	3.1	2.83	—	308.4



STRUCTURE OF LIQUID STATE OF  $\text{Bi}_2\text{O}_3$  BY EXAFS

Kichiro KOTO, Shuichi EMURA# and Akira YOSHIASA##

Dept. of Materials Science, Faculty of Integrated Arts and Sciences, Tokushima Univ., Minami-Josanjima, Tokushima 770, Japan

#Institute of Scientific and Industrial Research, Osaka Univ., Ibaraki, Osaka

##Faculty of Science, Hiroshima Univ., Naka-ku, Hiroshima 730

Introduction

A high temperature form of  $\text{Bi}_2\text{O}_3$ ,  $\delta$ -form, is the best known oxide ion conductor. It has an oxygen deficient structure with the fluorite-type in which one-fourth of oxide ions are missing. The  $\gamma$ -form is supercooled and the metastable forms are influenced not only by the temperature before cooling and the cooling rate but also the duration of melting [1]. To elucidate the phase transition mechanism, local structures of  $\delta$ -form and liquid state of  $\text{Bi}_2\text{O}_3$  were investigated by EXAFS.

Experimental and Results

A sample of commercial  $\text{Bi}_2\text{O}_3$  (99.9%, Nakarai) was used in this experiment.  $\text{Bi}_2\text{O}_3$  (30mg) and c-BN (50mg) in powder form were well blended in agate mortar and then pressed to make a disk with 13mm in diameter and 0.7mm in thickness. The EXAFS measurements were carried out at from room temperature to above the melting point with a stability of a few kelvins. X-ray thickness is about 2.0.  $\text{Bi}_2\text{O}_3$  in liquid state exists on the surface of BN grains.

The X-ray absorption measurements near the Bi L3 edge were made in transmission on the Beam Line 10B at Photon Factory. The data analysis was made using the program written by Dr. H. Maeda, Okayama Univ..

No appreciable changes in XANES spectra except the second sharply raised area of liquid state at 826°C (Table 1).

The Fourier transform of liquid state is similar to those of the  $\delta$ -form (up to 810°C) but only different in magnitude, about one-half of the  $\delta$ -form. (Fig. 1).

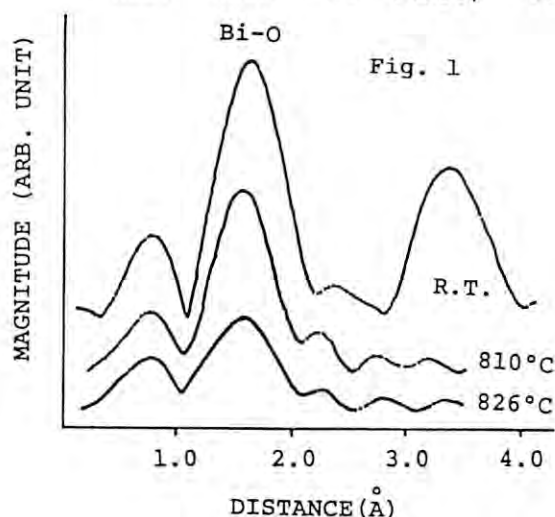
Table 1. Absorption edges of  $\text{Bi}_2\text{O}_3$  versus temperature.

Temperature(°C)	Absorption edge(eV)		
	a	b	c
room temp.	13415	13423	13441
700	13417	13424	13442
732	13417	13424	13442
751	13416	13424	13442
776	13416	13424	13443
800	13416	13424	13443
810	13416	13424	13443
826	-	13423	13443

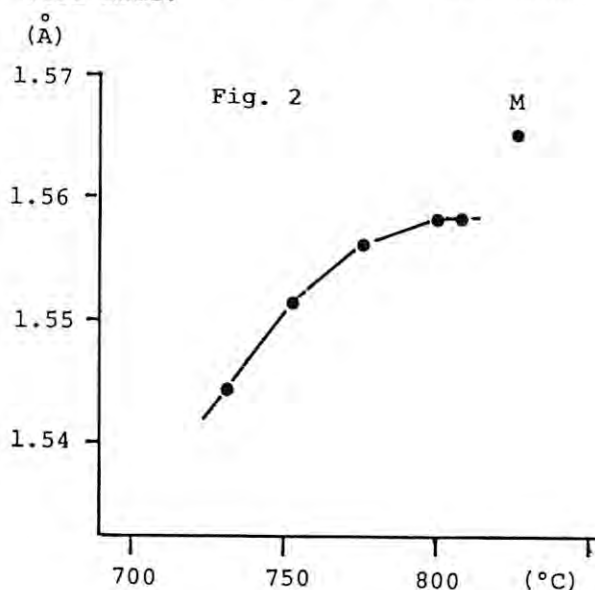
a: the second most sharply raised point  
b: the most sharply raised point  
c: the first absorption peak

Increase of the Bi-O distance is small near the melting point but large increase when melt (Fig. 2).

The authors thank to Drs. S. Nomura and A. Koyama, KEK, for useful advices and also to Mr. F. Kihara and H. Ito, Osaka Univ., for help in the experiments. Ref. 1) M. Tsubaki and K. Koto: Mat. Res. Bull. 19 (1984) 1613.



The Fourier transforms for Bi L3 edge of  $\text{Bi}_2\text{O}_3$ . No phase shift corrections were made.



Bi-O distances of  $\delta$ - $\text{Bi}_2\text{O}_3$  from EXAFS versus temperature. No phase shift corrections were made. M stands for melt.

EXAFS STUDIES OF HIGH  $T_c$  SUPERCONDUCTOR  $\text{Ca}_x\text{Y}_{1-x}\text{Ba}_2\text{Cu}_3\text{O}_{7-y}$ 

Toshio AKAI, Jun TSUCHIYA, Takashi USHIKUBO, Yasuo KOIKE, and Konoe MIURA

Research Center, Mitsubishi Kasei Corporation,  
1000 Kamoshida-chou, Midori-ku, Yokohama 227Introduction

It is known that the electronic state around Cu atoms in the high  $T_c$  superconductor  $\text{YBa}_2\text{Cu}_3\text{O}_{7-y}$  plays an important part in the superconductivity.<sup>1)</sup>

Recently, we have synthesized a new series of superconductors with the nominal composition of  $\text{Ca}_x\text{Y}_{1-x}\text{Ba}_2\text{Cu}_3\text{O}_{7-y}$  ( $x=0.1, 0.3, 0.5, 0.6$ ), for the purpose of increasing the valence of Cu. Although Ca atoms did not show the full substitution of Y sites, the specimens with nominal composition of  $\text{Ca}_x\text{Y}_{1-x}\text{Ba}_2\text{Cu}_3\text{O}_{7-y}$  ( $x=0.5, 0.6$ ) showed the superconductivity even if they were quenched into liquid nitrogen.

In order to clarify the phenomena, we attempted to reveal the local structure and the electronic environment around Cu atoms by using EXAFS (XANES).

Experimental and Results

The Cu K-edge and Y K-edge EXAFS spectra of these superconductors have been measured by using EXAFS apparatus at Beam Line 10B. All specimens were prepared by using solid state reaction.

Table 1 shows the  $T_c$  of these specimens prepared by cooling slowly in air, and by quenching into liquid N<sub>2</sub>, respectively.

Figures 1, and 2 show the Cu K-edge XANES for  $\text{Ca}_x\text{Y}_{1-x}\text{Ba}_2\text{Cu}_3\text{O}_{7-y}$  by cooling slowly in air, and by quenching into liquid N<sub>2</sub>, respectively. In the species obtained by quenching into liquid N<sub>2</sub> (Fig. 2), Cu  $1s \rightarrow 4p\pi$  transitions are observed, and the intensity of the transition is increasing as  $x$  value decreased from  $x=0.6$  to  $x=0.1$ . On the other hand, there is no absorption of the transition in the species obtained by cooling slowly in air.

The energy position of the  $1s \rightarrow 4p\pi$  transition is dependent on the coordination number, the coordination bond length and bonding character.<sup>2)</sup> The energy position of the  $1s \rightarrow 4p\pi$  transition of these specimens is the same with  $\text{Cu}_2\text{O}$ , which has Cu ions coordinated by two oxygen atoms. Therefore, these observations indicate that the Ca rich species ( $x=0.5, 0.6$ ) have less Cu ions coordinated by two oxygens than the Ca free specimens. This may imply the less amount of oxygen vacancy.

Figure 3 shows the results of Fourier transform of the EXAFS data. A new peak A appears in the species with  $x=0.3, 0.5, 0.6$ . Although the peak is related to Ca atoms in the superconductive phase, it is difficult to explain the detail of the structure.

The analyses of Y K-edge EXAFS spectra and curve fitting are in progress.

References

- 1) H. Oyanagi et al., Jpn. J. Appl. Phys. **26**, L1233 (1987)
- 2) H. Kuroda, N. Kosugi, and H. Tajima, KEK-PF ACTIVITY REPORT, 219 (1987)

Table 1  $T_c$  for specimens

$x$ in $\text{Ca}_x\text{Y}_{1-x}\text{Ba}_2\text{Cu}_3\text{O}_{7-y}$	$T_c(\text{onset})/T_c(\text{end})$ (K)	
	slowly cooled	liq. N <sub>2</sub> quenched
0.0	93/90	—
0.1	90/85	not super
0.3	85/81	not super
0.5	84/79	52/33
0.6	85/80	70/34

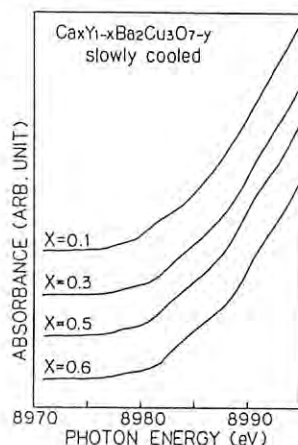


Fig. 1 XANES spectra

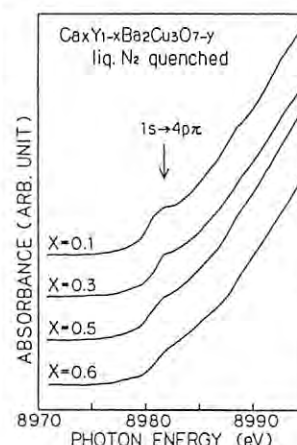
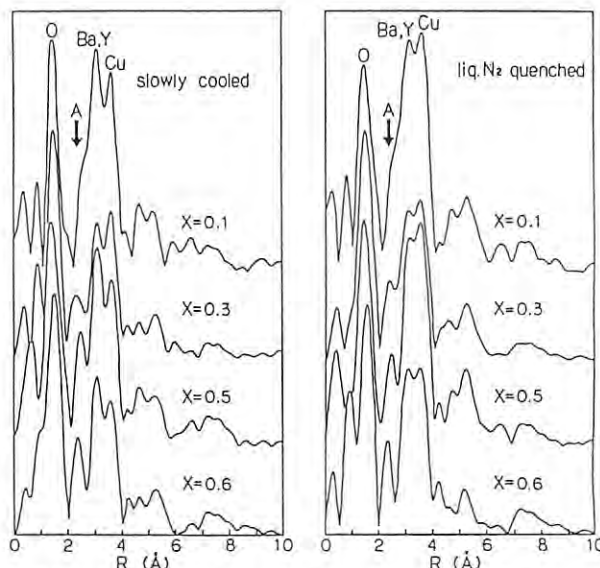


Fig. 2 XANES spectra

Fig. 3 Fourier transform of Cu K-edge EXAFS of  $\text{Ca}_x\text{Y}_{1-x}\text{Ba}_2\text{Cu}_3\text{O}_{7-y}$

# EXAFS STUDIES ON Ca-Ni-Mo/Al<sub>2</sub>O<sub>3</sub> CATALYST FOR HYDROGENATION OF COAL LIQUID BOTTOMS

Takashi USHIKUBO, Takao KANEKO, Takao KIMURA, Toshio AKAI,  
Yasuo KOIKE, Yoichi KAGEYAMA, Keisuke WADA, and Satoshi KAWAI\*

Research Center, Mitsubishi Kasei Corporation, 1000 Kamoshida-  
chou, Midori-ku, Yokohama 227

\*Nippon Brown Coal Liquefaction Company L.t.d., 5-20, 1-choume,  
Yaesu, Chuou-ku, Tokyo 103

## Introduction

BCL Process, which is a two stage coal liquefaction process, is now under development for Australian (Victorian) brown coal. This process includes a fixed-bed hydrogenation of Coal Liquid Bottoms (CLB) at second stage. It was found that the deactivation of the hydrogenation catalyst might be due to coke formation derived from preasphaltenes which adsorbed on the active sites. A new catalyst, Ca-Ni-Mo/Al<sub>2</sub>O<sub>3</sub>, having less coke formation, has been developed. (1,2) In the present report, EXAFS method was applied to the investigation of the effect of Ca on the less coke formation and the longer life.

## Experimental

The catalysts studied in this report were (a) Ni-Mo/Al<sub>2</sub>O<sub>3</sub> (fresh) (8 wt% NiO-8 wt% MoO<sub>3</sub>), (b) (a) presulfided and used for hydrotreating CLB<sub>2</sub> (reaction conditions : 400 °C, 150 Kg/cm<sup>2</sup> G, 100 h), (c) Ca-Ni-Mo/Al<sub>2</sub>O<sub>3</sub> (fresh) (3 wt% Ca-8 wt% NiO- 8 wt% MoO<sub>3</sub>), and (d) (c) presulfided and used for hydrotreating CLB (reaction conditions : the same as (b)). Furthermore, MoS<sub>2</sub> and CaMoO<sub>4</sub> were analyzed as standard samples. Before EXAFS measurements, the used catalysts were washed with tetrahydrofuran to remove coal-derived liquids from the catalysts, dried, and pressed into pellets. The Mo K-edge EXAFS data of these catalysts were obtained at EXAFS apparatus (BL-10B).

## Results and Discussion

Figure 1 shows the results of Fourier transformations of the EXAFS data for the catalysts, MoS<sub>2</sub>, and CaMoO<sub>4</sub>. In the oxidation state, before sulfided, the atomic distance and coordination number of Mo-O of Ca-Ni-Mo/Al<sub>2</sub>O<sub>3</sub> were the same as those of CaMoO<sub>4</sub>. The results of curve-fitting analyses for the used catalysts are shown in Table 1. For Ni-Mo/Al<sub>2</sub>O<sub>3</sub> and Ca-Ni-Mo/Al<sub>2</sub>O<sub>3</sub>, the MoS<sub>2</sub> like crystal structure appeared. However, in the Ni-Mo/Al<sub>2</sub>O<sub>3</sub> catalyst, the coordination numbers of Mo-S and Mo-Mo were smaller than those in the Ca-Ni-Mo/Al<sub>2</sub>O<sub>3</sub> catalyst. It seems that this result implies that sulfurization treatment was incomplete for the Ni-Mo/Al<sub>2</sub>O<sub>3</sub>

catalyst, or the elimination of S from the catalyst occurred through the hydrotreating CLB in the Ni-Mo/Al<sub>2</sub>O<sub>3</sub> catalyst. More detailed studies on the structure of the catalyst are now progressing.

The research and development of the BCL process is supported by the New Energy Development Organization (NEDO). We wish to thank NEDO for his permission to present this report.

## References

- (1) Y. Kageyama and T. Masuyama, 1985 Intern. Conf. on Coal Sci., Sydney, 157 (1985).
- (2) Y. Kageyama, K. Saito, and Y. Nakako, Australian Coal Sci. Conf. 1988, Adelaide, B1:7.1 (1988).

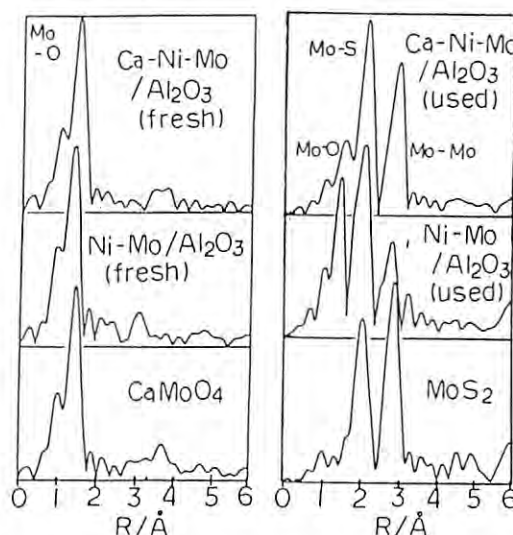


Fig. 1. Fourier transforms of the Mo K-edge EXAFS of Ni-Mo/Al<sub>2</sub>O<sub>3</sub> and Ca-Ni-Mo/Al<sub>2</sub>O<sub>3</sub> catalysts.

Table 1. Results of curve-fitting analyses of EXAFS for used catalysts.

Sample	Mo-S		Mo-Mo	
	R / Å	N	R / Å	N
MoS <sub>2</sub>	2.40	6	3.15	6
Ni-Mo/Al <sub>2</sub> O <sub>3</sub>	2.39	1.80	3.11	0.56
Ca-Ni-Mo/Al <sub>2</sub> O <sub>3</sub>	2.39	3.02	3.15	2.43

## ANALYSIS OF MODIFIED HOPEITE FILMS BY MEANS OF EXAFS

Noboru SATO

HONDA MOTOR Co., Ltd. Suzuka Factory, Hirata-cho, Suzuka 513 Japan

## 1. Introduction

By using ESR, it was found that Hopeite films are modified by manganese or nickel components<sup>1),2)</sup>. To elucidate the characterization of modified Hopeite films in detail, the analysis by means of EXAFS was done.

## 2. Experiment

Two kinds of Hopeite films were prepared as powdered samples. The metal compositions of these films determined by atomic absorption were as follows.

Hopeite (A) ..... Zn : 42.6 wt. %

Hopeite (B) ..... Zn : 38.0 wt. %, Mn : 4.8 wt. %

Analysis was done by observing XANES spectra and Fourier transformation of EXAFS.

## 3. Results and discussion

XANES spectra of Zn-K absorption edge for Hopeite (A) and (B) were shown in Fig.1.

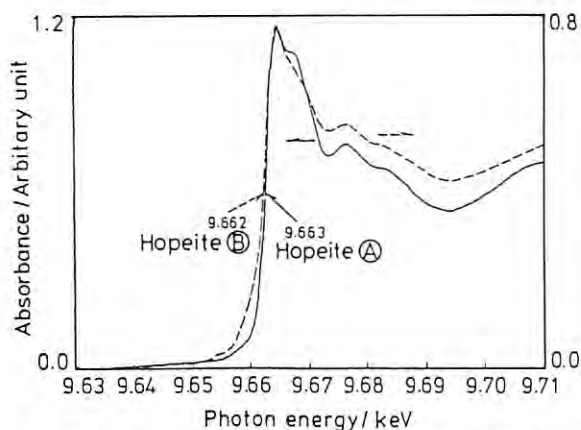


Fig.1 XANES spectra for Zn-K absorption edge

Both spectra showed almost same values of the absorption edge, but the amplitude of spectra for the latter was smaller than that for the former. These facts are interpreted that the manganese component generated a crystalline strain and the local structure of the crystal

was disordered.

Fourier transformation of Mn-K absorption edge for Hopeite (B) and MnO were shown in Fig.2.

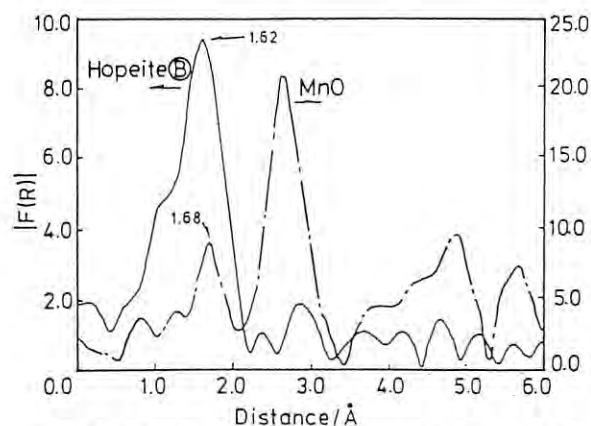


Fig.2 Fourier transformation for Mn-K absorption edge

The peak position of EXAFS relating to first neighboring atom showed the same difference. The facts suggest that manganese exists as Mn(II) in the modified Hopeite (B) films. However, the patterns of Fourier transformation were different between the modified Hopeite films and MnO.

XANES spectra and Fourier transformation of EXAFS provided a conclusion that the modified Hopeite films have a structure of  $\text{Zn}_{3-x}\text{Mn}_x(\text{PO}_4)_2 \cdot 4\text{H}_2\text{O}$  instead of a conventional one of  $\text{Zn}_3(\text{PO}_4)_2 \cdot 4\text{H}_2\text{O}$ . Analysis by means of EXAFS was thought to be useful to clear the characterization of Hopeite films.

## References

- 1) N. Sato and T. Minami, *Kinzoku Hyomen Gijutsu*, **38**, 30 (1987)
- 2) N. Sato and T. Minami, *Nippon Kagaku Kaishi*, **1987**, 1741 (1987)



XANES of Tb-L<sub>III</sub> in ZrO<sub>2</sub>-Tb<sub>2</sub>O<sub>3</sub> Mixed Conductors

Haruo ARASHI, Shigi SHIN, Hisashi MIURA, Anri NAKASHIMA  
Mareo ISHIGAME and Osamu SHIMOMURA\*

Research Institute for Scientific Measurements, Tohoku Univ. Sendai, Japan

\*National Institute for Research in Inorganic Materials, Tekuba, Japan

Mixed electronic-ionic conductors have the wide fields of applications such as electrode and gas separation. Fundamental researches of the physical and chemical properties of these conductors are required before its application. ZrO<sub>2</sub>-Tb<sub>2</sub>O<sub>3</sub> systems show a mixed conduction. The reason for electronic conduction is considered as a result of valence change of Tb ions from trivalent state to tetravalent state. The electronic conductivity in these terbium compounds is supposed to arise from hopping of localized charges and can be described by the small polaron model. Following the paper by Van Dijk et al.,<sup>1)</sup> the mobility depends on the fraction of Tb in the tetravalent state. To clarify the relationship between Tb<sup>4+</sup>/Tb<sup>3+</sup> ratio and electronic conduction, the temperature dependence of Tb<sup>4+</sup>/Tb<sup>3+</sup> ratio in ZrO<sub>2</sub>-Tb<sub>2</sub>O<sub>3</sub> systems were investigated by XANES measured at various temperatures.

The solid solutions were prepared by means of a solid-state reaction between ZrO<sub>2</sub> and Tb<sub>2</sub>O<sub>3</sub> with a level of purity 99.9%. Appropriate proportions of ZrO<sub>2</sub> and Tb<sub>2</sub>O<sub>3</sub> powder were mixed and ball-milled in distilled water for 24 h with alumina ball. After being dried at 150°C for 24 h, the mixed powder was then isostatically pressed into rods under 2 ton/cm<sup>2</sup> and sintered for 5 h at 1750 °C in air.

For XANES measurements, the sintered materials were crushed and milled. The fine powder of ZrO<sub>2</sub>-Tb<sub>2</sub>O<sub>3</sub> solid-solution was mixed with BN powder and pressed into a disc 25 mm in diameter and 1 mm in thickness. XANES spectra were measured using BL-10B beam line.

The temperature dependence of XANES spectra in 0.5ZrO<sub>2</sub>-0.5Tb<sub>2</sub>O<sub>3</sub> and 0.6ZrO<sub>2</sub>-0.4Tb<sub>2</sub>O<sub>3</sub> was measured in the temperature range from room temperature to 1000 °C and results are shown in Fig. 1. The large peak is ascribed to Tb<sup>3+</sup> ion absorption and the shoulder observed on the higher energy side is ascribed to Tb<sup>4+</sup> ion absorption. The co-existence of trivalent and tetravalent state of Tb ions was confirmed in ZrO<sub>2</sub>-Tb<sub>2</sub>O<sub>3</sub> solid-solution from these XANES measurements. The line width and peak position of absorption caused from Tb<sup>3+</sup> ions do not show any change with increasing temperature. The intensity of the shoulder which corresponds to the amount of Tb<sup>4+</sup> ions decreases with increasing the temperature.

Least squares fitting method was used to decompose the observed XANES spectra into the contributions from Tb<sup>3+</sup> and Tb<sup>4+</sup> ions. We have used a Lorentzian combined with arctan function as a model function

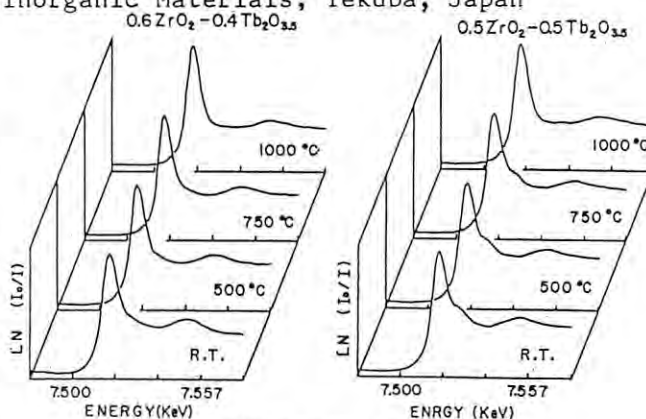


Fig. 1 XANES spectra measured at various temperature.

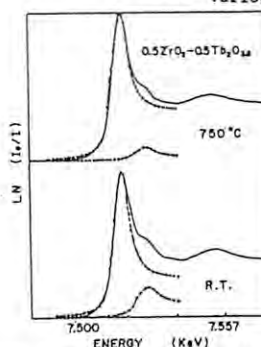


Fig. 2 Decomposition of XANES spectra into Tb<sup>3+</sup> and Tb<sup>4+</sup> contributions.

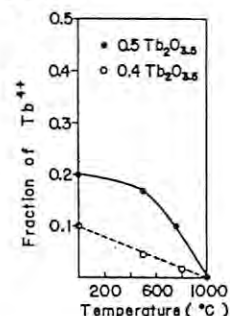


Fig. 3 Temperature dependence of Tb<sup>4+</sup>/Tb<sup>3+</sup> ratio.

for least squares fitting. The results of decomposition of XANES spectra for 0.5ZrO<sub>2</sub>-0.5Tb<sub>2</sub>O<sub>3</sub> measured at room temperature and 750 °C are shown in Fig. 2. The Tb<sup>4+</sup>/Tb<sup>3+</sup> ratio was determined from the ratio of the height parameter of Lorentzian for Tb<sup>4+</sup> ion absorption peak to that of Tb<sup>3+</sup> ion absorption peak. The temperature dependence of the ratio of Tb<sup>4+</sup>/Tb<sup>3+</sup> is shown in Fig. 3 for two Tb<sub>2</sub>O<sub>3</sub> concentrations. It clearly shows that the fraction of Tb<sup>4+</sup> increases with increasing Tb<sub>2</sub>O<sub>3</sub> contents and decreases with increasing temperature. Iwahara et al.<sup>2)</sup> have been reported that an electronic transport number increased for increase in Tb<sub>2</sub>O<sub>3</sub> contents and decreased for increase in temperature in ZrO<sub>2</sub>-Tb<sub>2</sub>O<sub>3</sub> system. Comparing our experimental results with those reported by Iwahara, it is concluded that the fraction of Tb<sup>4+</sup> ions controls the electronic conduction in ZrO<sub>2</sub>-Tb<sub>2</sub>O<sub>3</sub> system. Using the ratio of Tb<sup>4+</sup>/Tb<sup>3+</sup> determined by XANES measurements, investigations for hopping conduction mechanism in ZrO<sub>2</sub>-Tb<sub>2</sub>O<sub>3</sub> system are now in progress.

## References

- 1) M. P. Van Dijk, K. J. De Vries and A. J. Burggra, Solid State Ionics 16, 211 (1985).
- 2) H. Iwahara, T. Esaka and K. Takeda, Advances in Ceramics, vol. 24, in press.

## EXAFS STUDIES OF WSiN FILMS

Satoshi MAEYAMA, Hirohiko SUGAHARA\*, Masaharu OSHIMA and Yoshinori SATOW\*\*

NTT Applied Electronics Laboratories, Musashino-shi, Tokyo 180

\*NTT LSI Laboratories, Atsugi-shi, Kanagawa 243-01

\*\*Photon Factory, National Laboratory for High Energy Physics,  
Oho, Tsukuba-shi, Ibaraki 305Introduction

WSiN metal is a new refractory material for fabricating GaAs FFT devices. The WSiN layer suppresses an As-outdiffusion from GaAs substrates during high temperature annealing<sup>1)</sup>, thus GaAs FFT with WSiN gate have a superior performance. No information about the structure of the WSiN has been obtained by X-ray diffraction analysis because it is amorphous. We analyzed the location of nitrogen atoms in WSiN by measuring W L-edge EXAFS.

Experimental

The three samples used for the measurements were prepared by depositing  $W_2Si$  films on Si substrates by sputtering under three different atmosphere conditions; gas flow rates ( $N_2/Ar+N_2$ ) were 0, 0.1 and 0.2. GaAs substrates were not used for the samples because the Ga K-edge is near the W L-edge. Sample(a) is a  $W_2Si$  film and samples(b) and (c) are  $W_2SiN$  films with low and high nitrogen contents, respectively. These samples were annealed at 800°C in an Ar atmosphere; however, X-ray diffraction measurements confirmed that all the samples were amorphous. W L3-edge EXAFS were measured at room temperature in the fluorescence mode at beam line 14A of the Photon Factory.

Results

EXAFS fluorescence spectra for the samples(a), (b), and (c) at the W L3-edge are shown in Fig.1. The amplitude of EXAFS oscillations increases as the nitrogen content increases. Figures 2(A) and 2(B) compare the Fourier transforms of the W L3-edge EXAFS oscillations for the samples (a), (b), and (c). The peaks positioned at 1.5 - 2Å are not seen in the Fourier transform for the  $W_2Si$  and peak height increases with nitrogen content in the  $W_2SiN$ . Thus the peaks can be assigned to the nitrogen atoms in the  $W_2SiN$ . Figure 2 indicates that the nitrogen atoms are located in interstitial sites between the tungsten atoms and nearest silicon atoms; consequently the higher nitrogen content increases the radial distance from a tungsten atom to its nearest silicon. These results suggest that  $W_2SiN$  has higher atomic packing density than  $W_2Si$ . This physical property of the  $W_2SiN$  is primarily responsible for suppressing the As-outdiffusion during the annealing.

References

- 1) K. Asai, H. Sugahara, Y. Matsuoka and M. Tokumitsu, to be published in J. Vac. Sci. Technol.

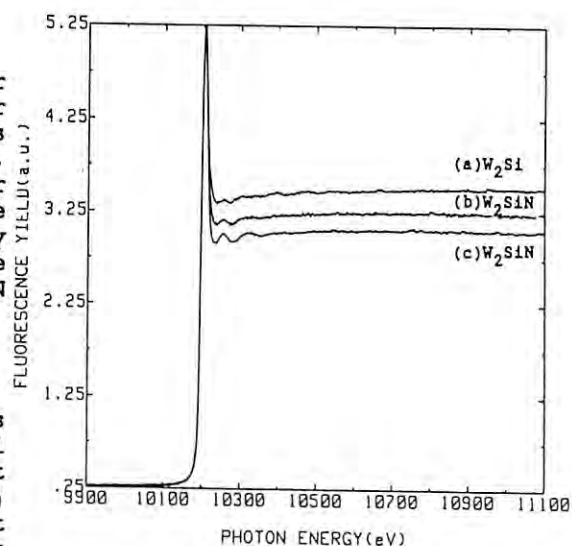


Fig.1. EXAFS spectra at W L3-edge for (a)  $W_2Si$  and (b), (c)  $W_2SiN$ .

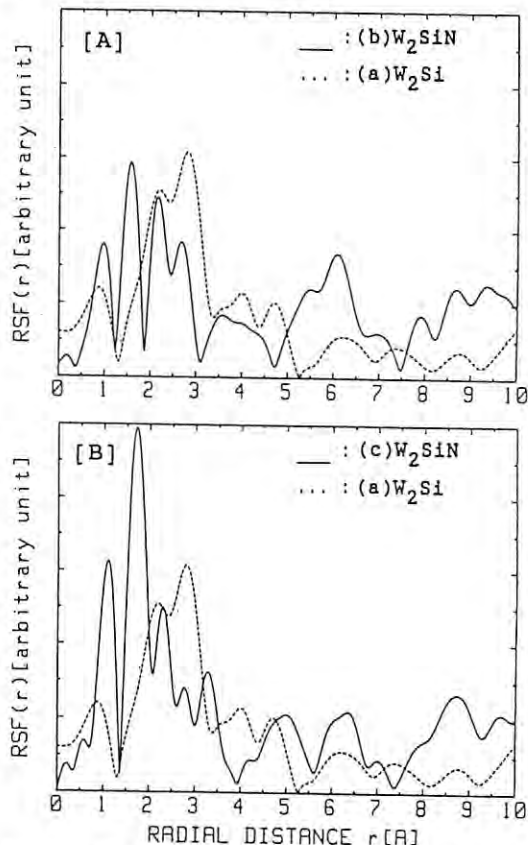


Fig.2. Comparison of Fourier transforms of W L3-edge EXAFS oscillations: [A] (a)  $W_2Si$  vs. (b)  $W_2SiN$  with low nitrogen content and [B] (a)  $W_2Si$  vs. (c)  $W_2SiN$  with high nitrogen content.

# COPPER K-EDGE POLARIZED EXAFS OF HIGH-Tc SUPERCONDUCTING SINGLE-CRYSTAL $\text{YBa}_2\text{Cu}_3\text{O}_y$

Satoshi MAEYAMA, Yoshinori SATOW\*, Masaharu OSHIMA and Akinori KATSUI\*\*

NTT Applied Electronics Laboratories, Musashino-shi, Tokyo 180

\*Photon Factory, National Laboratory for High Energy Physics,  
Oho, Tsukuba-shi, Ibaraki 305

\*\*NTT Opto-Electronics Laboratories, Tokai, Ibaraki 319-11

## Introduction

A local structure analysis by means of EXAFS does not provide sufficient structure information for the complicated crystal structure of  $\text{YBa}_2\text{Cu}_3\text{O}_y$  (YBCO), because the results are generally averaged over all the crystal orientation. However, it is possible to determine the local structure along the crystal axis by analyzing polarized EXAFS. Thus Cu K-edge polarized EXAFS of YBCO have been measured by using a single-crystal sample.

## Experimental

A small orthorhombic single-crystal sample of YBCO<sup>1)</sup> was used for the measurement. The measurements were carried out at room temperature using a Si(111) double-crystal monochromator with a four-circle diffractometer installed at beam line 14A of the Photon Factory. The Cu K-edge EXAFS spectrum under the condition of the X-ray polarization vector  $E$  parallel to the  $ab$  axes ( $E//ab$ ) in the transmission mode. The spectrum under the  $E//c$  condition was measured in the fluorescence mode.

## Results

EXAFS absorption spectrum for  $E//ab$  and fluorescence spectrum for  $E//c$  at the Cu K edge are shown in Fig.1. EXAFS oscillations obtained from the EXAFS spectra are shown in Fig.2. Figure 3 shows the magnitude of the Fourier transform of the Cu K-edge EXAFS oscillations for  $E//ab$  and  $E//c$ . There are two types of Cu in the orthorhombic crystal structure of YBCO<sup>2)</sup>, so called Cu(1) and Cu(2). The Cu(1) is in a  $\text{CuO}_4$  plane due to the oxygen vacancies. The Cu K-edge EXAFS cannot be measured for the Cu(1) and the Cu(2) separately. The first peaks positioned at 1-2 Å in Fig.3 are assigned to the O neighbors located around the Cu(1) and Cu(2) atoms, but not the same O neighbors because of the polarization effect. The first peak in the Fourier transform for  $E//c$  is mainly due to the O neighbors of the Cu(1). The overlapping peaks at 2-4 Å in the Fourier transforms for  $E//ab$  and  $E//c$  are assigned to heavy atom neighbors located in the  $ab$  plane and along the  $c$  axis direction from the Cu(1) and the Cu(2), respectively. The relative position and height of the peaks in Fig.3 are considered to correspond to the radial structure expected from the structure model presented by neutron diffraction analysis<sup>2)</sup>.

## References

- 1) Y. Hidaka et al., Jpn. J. Appl. Phys., **26**, L726 (1987)
- 2) F. Izumi et al., Jpn. J. Appl. Phys., **26**, L1193 (1987)

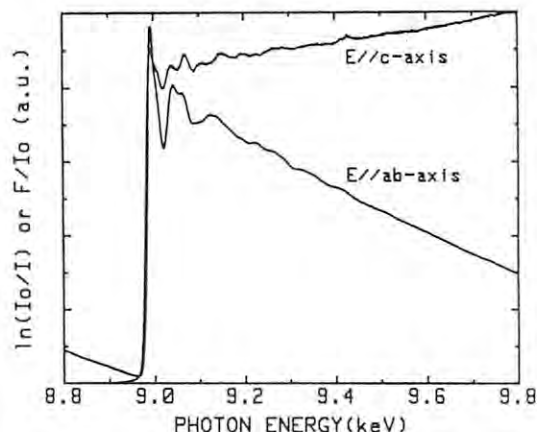


Fig.1. Cu K-edge EXAFS spectra of single-crystal  $\text{YBa}_2\text{Cu}_3\text{O}_y$  with the condition  $E//ab$  and  $E//c$ .

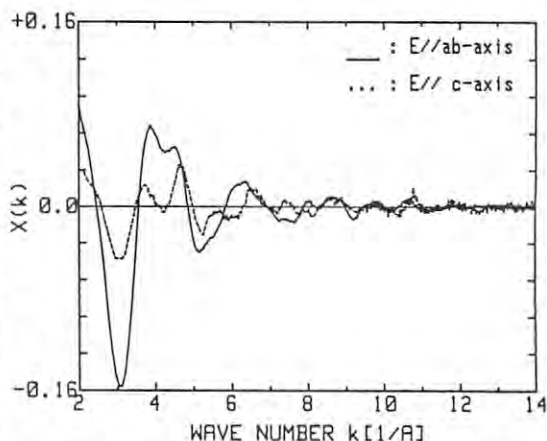


Fig.2. EXAFS oscillations obtained from Cu K-edge EXAFS spectra of single-crystal  $\text{YBa}_2\text{Cu}_3\text{O}_y$ .

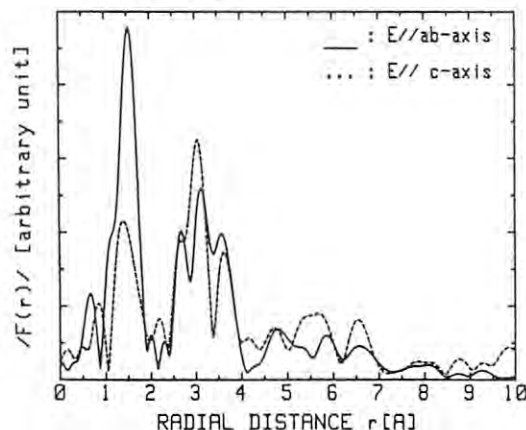


Fig.3. Fourier transforms of Cu K-edge EXAFS oscillations for  $E//ab$  and  $E//c$  in single-crystal  $\text{YBa}_2\text{Cu}_3\text{O}_y$ .



# YTTRIUM K-EDGE POLARIZED EXAFS OF HIGH-Tc SUPERCONDUCTING SINGLE-CRYSTAL $\text{YBa}_2\text{Cu}_3\text{O}_y$

Satoshi MAEYAMA, Yoshinori SATOW\*, Masaharu OSHIMA and Akinori KATSUI\*\*

NTT Applied Electronics Laboratories, Musashino-shi, Tokyo 180

\*Photon Factory, National Laboratory for High Energy Physics,  
Oho, Tokuba-shi, Ibaraki 305

\*\*NTT Opto-Electronics Laboratories, Tokai, Ibaraki 319-11

## Introduction

$\text{YBa}_2\text{Cu}_3\text{O}_y$  (YBCO) is a representative superconductor with  $T_c$  above liquid nitrogen temperature. There have been many reports of Cu K-edge EXAFS studies on high- $T_c$  superconductors, but a few reports about Y K-edge EXAFS of YBCO. The authors measured the Y K-edge polarized EXAFS of a single-crystal YBCO as well as polarized EXAFS at Cu K-edge. This report described the results of the Y K-edge polarized EXAFS.

## Experimental

The Y K-edge polarized EXAFS were measured at room temperature for the same single-crystal sample as used for Cu K-edge measurements at the beam line 14A of the Photon Factory. This sample was prepared by oxygen annealing as as-grown crystal from Y-Ba-Cu-O solution<sup>1)</sup>. The transmission and the fluorescence modes were employed for the measurements under the  $E//ab$  and the  $E//c$  conditions, respectively. The experimental procedure is almost same as the measurements at the Cu K-edge.

## Results

Figure 1 shows EXAFS absorption spectrum for  $E//ab$  and EXAFS fluorescence spectrum for  $E//c$  at the Y K-edge. Figure 2 shows EXAFS oscillations obtained from the EXAFS spectra. These were normalized by the smoothed background function and plotted as a function of photoelectron wave number  $k$ . Figure 3 shows the Fourier transforms of the Y K-edge EXAFS oscillations for  $E//ab$  and  $E//c$ . These oscillations multiplied by  $k^3$  were Fourier transformed into a real space without correction for phase shift. The first peaks positioned at 1.5 - 2Å in Fig.3 are assigned to the nearest O neighbors located in the  $ab$  plane based on the radial structure calculated from the reported structure model<sup>2)</sup>. The second peaks at 2.5 - 3Å are assigned to the Cu(2) neighbors located in  $\text{CuO}_5$  pyramids. The third peaks at about 2.5Å can be assigned to the different neighbors because of the polarization effect. The third peaks for  $E//ab$  and  $E//c$  are due to the Y neighbors located in a horizontal direction and Ba neighbors located in a vertical direction from the Y atoms, respectively.

## References

- 1) Y. Hidaka, Y. Enomoto, M. Suzuki, M. Oda, A. Katsui and T. Murakami, Jpn. J. Appl. Phys., **26**, L726 (1987)
- 2) F. Izumi, H. Asano, T. Ishigaki, E. Takeyama-Muromachi, Y. Uchida and N. Watansabe Jpn. J. Appl. Phys., **26**, L1193 (1987)

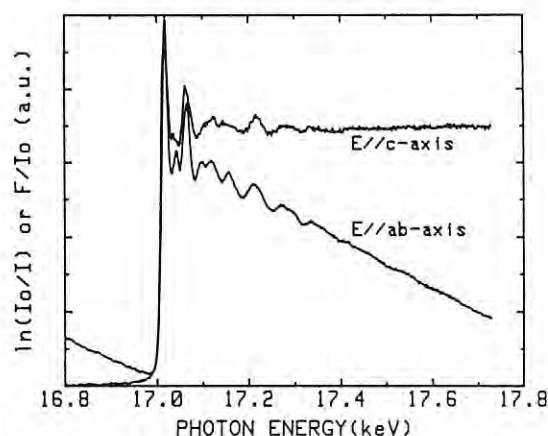


Fig.1. Y K-edge EXAFS spectra of single-crystal  $\text{YBa}_2\text{Cu}_3\text{O}_y$  with the condition  $E//ab$  and  $E//c$ .

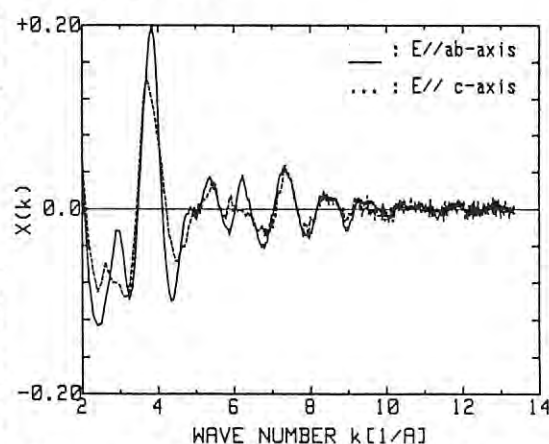


Fig.2. EXAFS oscillations obtained from Y K-edge EXAFS spectra of single-crystal  $\text{YBa}_2\text{Cu}_3\text{O}_y$ .

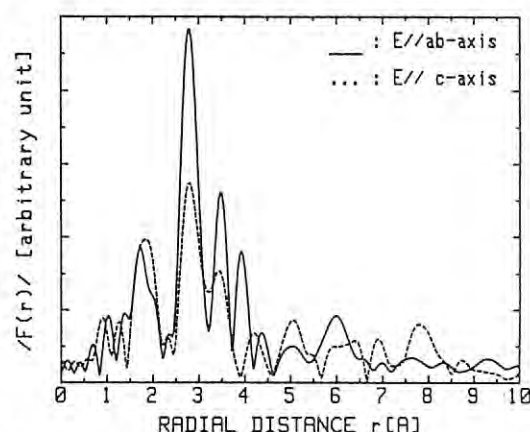


Fig.3. Fourier transforms of Y K-edge EXAFS oscillations for  $E//ab$  and  $E//c$  in single-crystal  $\text{YBa}_2\text{Cu}_3\text{O}_y$ .



# BARIUM K-EDGE POLARIZED EXAFS OF HIGH-Tc SUPERCONDUCTING SINGLE-CRYSTAL $\text{YBa}_2\text{Cu}_3\text{O}_y$

Satoshi MAEYAMA, Yoshinori SATOW\*, Masaharu OSHIMA and Akinori KATSUI\*\*

NTT Applied Electronics Laboratories, Musashino-shi, Tokyo 180

\*Photon Factory, National Laboratory for High Energy Physics,  
Oho, Tsukuba-shi, Ibaraki 305

\*\*NTT Opto-Electronics Laboratories, Tokai, Ibaraki 319-11

## Introduction

EXAFS at Ba K-edge has not been measured because it is in high energy region (37.5 keV). Synchrotron radiation emitted from a superconducting vertical wiggler is available at beam line 14 of the Photon Factory, thus it is possible to measure the Ba K-edge EXAFS at this beam line. The authors tried to measure the Ba K-edge polarized EXAFS of a single-crystal  $\text{YBa}_2\text{Cu}_3\text{O}_y$  (YBCO) in order to obtain EXAFS of YBCO at all three metal elements K-edge.

## Experimental

Two pieces of orthorhombic single-crystal thin plate were used to get the adequate sample thickness for X-ray absorption at the Ba K-edge. Ba K-edge EXAFS measurements were made at room temperature using a Si(553) double-crystal monochromator with a four-circle diffractometer at the beam line 14A of the Photon Factory. The EXAFS spectra under the  $E//ab$  and  $E//c$  conditions were measured in transmission mode, and the Ba K fluorescence yields were also recorded as reference data.

## Results

EXAFS absorption spectra for  $E//ab$  and  $E//c$  at the Ba K-edge are shown in Fig.1. Reference fluorescence spectra confirmed EXAFS observed in the EXAFS absorption spectra. Figure 2 shows a comparison of the normalized EXAFS oscillations for  $E//ab$  and  $E//c$ . These oscillations were obtained from the absorption spectra after removing the pre-edge and smoothed backgrounds. The polarization dependence of EXAFS is clearly observed in Fig.2. Figure 3 shows the Fourier transforms of the Ba K-edge EXAFS oscillations multiplied by  $k^3$  for  $E//ab$  and  $E//c$ . Owing to the polarization effect, the first peaks positioned at about 2 Å in Fig.3 can be assigned to the different O neighbors; the O atoms located on the  $c$  axis and in the  $ab$  plane, respectively. However, these first peaks are positioned at the almost same distance. This result is not consistent with the structure model presented by a neutron diffraction analysis<sup>2</sup>, because the radial structure calculated from the reported model indicates that the radial distance from the Ba atom to the O atom located in the  $ab$  plane is 0.2 Å longer than that to the O atom on the  $c$  axis.

## References

- 1) Y. Hidaka et al., Jpn. J. Appl. Phys., **26**, L726 (1987)
- 2) F. Izumi et al., Jpn. J. Appl. Phys., **26**, L1193 (1987)

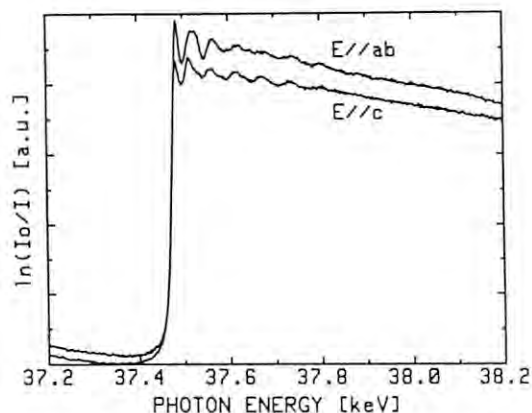


Fig.1. Ba K-edge EXAFS spectra of single-crystal  $\text{YBa}_2\text{Cu}_3\text{O}_y$  with the condition  $E//ab$  and  $E//c$ .

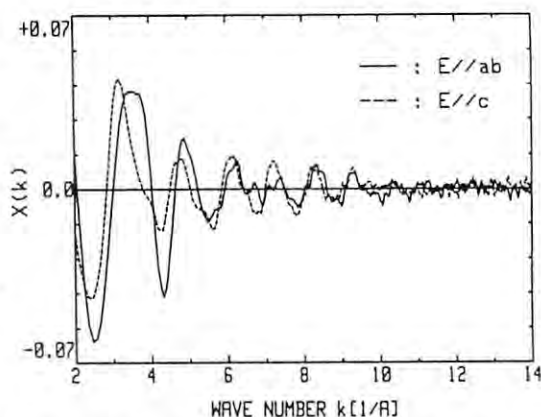


Fig.2. EXAFS oscillations obtained from Ba K-edge EXAFS spectra of single-crystal  $\text{YBa}_2\text{Cu}_3\text{O}_y$ .

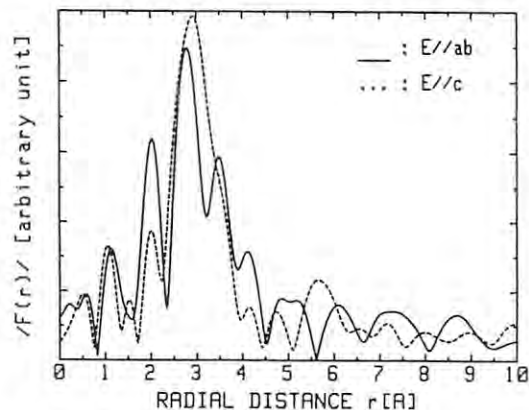


Fig.3. Fourier transforms of Ba K-edge EXAFS oscillations for  $E//ab$  and  $E//c$  in single-crystal  $\text{YBa}_2\text{Cu}_3\text{O}_y$ .

# KILLING ON *E. COLI* AND *DEINOCOCCUS RADIODURANS* BY MONOCHROMATIC X-RAYS AT RESONANCE ENERGY OF PHOSPHORUS K-ABSORPTION EDGE.

Hiroshi MAEZAWA, Yoshiya FURUSAWA<sup>#</sup>, Kotaro HIEDA<sup>S</sup>, Katsumi KOBAYASHI<sup>&</sup>, Tomoyuki MORI, Kenshi SUZUKI<sup>#</sup> and Takashi ITO\*.

Dept. Radiation Oncology, School of Medicine, Tokai Univ., Kanagawa 259-11, <sup>#</sup>Dept. Molecular Biology, School of Medicine, Tokai Univ., Kanagawa 259-11, <sup>S</sup>Biophys. Lab., Dpt. Phys., Rikkyo Univ., Tokyo 171, <sup>&</sup>National Lab., High Energy Phys., Ibaraki 305, \*Inst. Phys., College of Arts and Sciences, University of Tokyo, Tokyo 153.

## Introduction

In our previous experiments<sup>1,2)</sup> the killing enhancement has been observed on *E. coli*, *Deinococcus radiodurans* and dry bacteriophages at the resonance energy of phosphorus K-absorption edge. It has been suggested that the observed enhancement was caused by the direct absorption of photon in phosphorus of organisms. The reparability of cells for damages by K-shell photoionization in phosphorus atoms is an important object of radiation biological research. In this short note, the experimental results are reported on radiation sensitive strain of *E. coli* and *D. radiodurans*.

## Materials and Methods

*E. coli* H/r30 (wild type), and *B<sub>s-1</sub>* (*uvr<sup>-</sup>*, *lex<sup>-</sup>*) strains and radiosensitive *S<sub>s-1</sub>* strain of *D. radiodurans* were used through the experiments. Exponentially growing cells of bacteria out of culture were washed and suspended in saline (0.15M NaCl). The cells were loaded on a millipore membrane filter. The filter, which was placed on a wet paper soaked in saline, was mounted on a plastic dish. The plastic dish was moved up and down on a sample scanning stage. After irradiation, cells were resuspended in saline, diluted appropriately and placed on the agar medium for colony formation. Beam lines used were 1B and 11B. Irradiation energies of monochromatic X-rays were 2.153 keV (the resonance energy of K-shell absorption of phosphorus), and above (2.160 keV) and below (2.146 keV) of the resonance energy. Exposure rate was measured by an ionization chamber.

## Results

Exposure-survival curves of *E. coli* H/r30 and *B<sub>s-1</sub>* strains were shown in figure 1. Killing sensitivity at 2.146 keV was similar to that at 2.160 keV, in each strain. Killing at 2.153 keV was enhanced as compared with other two X-rays. In radiation sensitive strain of *D. radiodurans*, killing at 2.153 keV was most sensitive as compared with that at 2.146 keV and 2.160 keV, as well as *E. coli* cells. The killing sensitivity per unit exposure at 2.153 keV for *E. coli* and *D. radiodurans* was 1.3 times and 1.4 times higher than that at 2.146 keV, respectively. This value are comparable to the previous results in H/r30 *recA<sup>-</sup>* strain. The calculated energy absorption per unit exposure per cell (*f*-factor) was  $9.35 \times 10^{-3}$  Gy/R at 2.146 keV and  $1.085 \times 10^{-2}$  Gy/R at 2.153 keV. The calculated ratio was 1.16 ( $=1.085/0.935$ ) at 2.153 keV as compared at 2.146 keV. The experimental value is larger than the calculated value. It is suggested that the energy

deposition by K-shell ionization followed by Auger cascade produces the lethal damages effectively as compared with that by normal photoionization in materials. Further analysis proceeds concerning of the identification of the species and the reparability in cell system for damage produced by K-shell ionization in phosphorus atoms.

## References

- 1) H. Maezawa, et al., Photon Factory Activity Report, 4, 235 (1986)
- 2) H. Maezawa, et al., Photon Factory Activity Report, 5, 285 (1987)

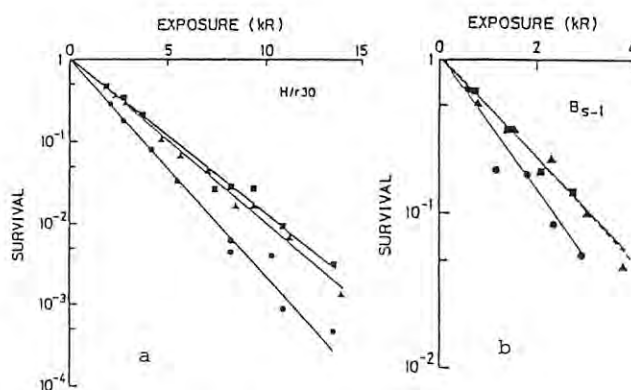


Fig. 1. Survival of *E. coli* H/r30 (a) and *B<sub>s-1</sub>* (b) cells irradiated with X-rays *S<sub>s-1</sub>* at 2.146 keV, 2.153 keV and 2.160 keV.

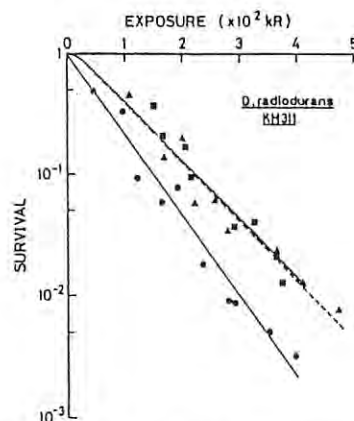


Fig. 2 Survival of radiation-sensitive mutant of *D. radiodurans* irradiated with X-rays at 2.146 keV, 2.153 keV and 2.160 keV.

# ENHANCED KILLING ON CULTURED MAMMALIAN CELLS BY SOFT-X-RAYS WITH RESONANCE ENERGY OF PHOSPHORUS K-ABSORPTION EDGE.

Hiroshi MAEZAWA, Yoshiya FURUSAWA<sup>#</sup>, Kotaro HIEDA<sup>&</sup>, Katsumi KOBAYASHI<sup>\*</sup>, Takashi ITO<sup>§</sup> and Tomoyuki MORI.

Dept. Radiation Oncology, School of Medicine, Tokai Univ., Kanagawa 25911, <sup>#</sup>Dept. Molecular Biology, School of Medicine, Tokai Univ., Kanagawa 25911, <sup>&</sup>Biophys. Lab., Dept. Phys., Rikkyo Univ., Tokyo 171, <sup>§</sup>KEK, National Lab. High Energy Phys., Ibaraki 305, <sup>\*</sup>Inst. Phys., College of Arts and Sci., Univ. Tokyo, Tokyo 153.

## Introduction

Biological effects of X-ray induced inner-shell ionization of an atom in several organisms<sup>1,2)</sup> and DNA molecules<sup>3)</sup> have been investigated. Phosphorus atoms links the sugar of each nucleotide in DNA. The inner-shell photoionization of phosphorus is followed by Auger cascade, and it is expected that the released energy was deposited in the vicinity (within 10 nm diameter) of phosphorus atoms.

In this note, the enhanced killing on mammalian cells irradiated with monochromatic X-rays at the energy of K-shell resonance absorption of phosphorus atoms was discussed.

## Materials and Methods

FM3A (C3H mouse mammary carcinoma) cells were grown in ES medium (Nissui) supplemented with 5% calf serum (GIBCO). Exponentially growing cells were used through the experiments. Cells ( $1 \times 10^5$ ) were loaded with monolayer on a membrane filter (pore size of  $0.45 \mu\text{m}$ ) which was placed on the 1% agar medium in a plastic dish. The plastic dish was mounted on a sample scanning stage for moving vertically during irradiation. Irradiation was carried out with the monochromatic X-rays at beam line 11B. X-ray energies were 2.153 keV, corresponding to the resonance absorption peak of phosphorus, 2.146 keV and 2.160 keV. Exposure rate was measured by an ionization chamber. Irradiated cells were resuspended in ES medium, appropriately diluted and plated in 0.33% soft agar medium (supplemented with 10% fetal bovine serum) for the measurement of colony forming ability.

## Results

Survival curves of cells were shown in figure 1 with three energies of monochromatic X-rays. On the basis of exposure (Röntgen unit), X-rays at 2.153 keV was most effective for lethality. No difference of lethality between the X-rays below (2.146 keV) and above (2.160 keV) the resonance peak was observed. Killing sensitivity at 2.153 keV was 1.3 times higher than that at 2.146 keV, using the exposure required to decrease survival of 37%.

Above situation was examined in terms of the absorbed energy in cells for 2.153 keV and 2.146 keV radiation. Calculations of the absorbed energy were performed with the bulk of cells. The absorbed energy in cells for the two X-ray energies may be compared by calculating a f-factor (Röntgen-Gray conversion factor). The ratio of f-factor at 2.153 keV to that at 2.146

keV was about 1.1 (calculated enhancement ratio). The experimental enhancement ratio (1.3) is significantly large as compared with the calculated enhancement ratio.

This means that the energy deposition from K-shell photoionization of P atoms followed by Auger cascade is more lethal as compared with that from normal fashion of X-ray photoionization.

## References

- 1) H. Maezawa, Y. Furusawa, K. Hieda, K. Kobayashi, T. Mori, K. Suzuki and T. Ito, Photon Factory Activity Report, 5, 285 (1987).
- 2) K. Kobayashi, N. Usami, A. Yokoya, K. Hieda, H. Maezawa, Y. Furusawa and T. Ito, Photon Factory Activity Report, 5, 287 (1987).
- 3) K. Hieda, A. Azami, M. Suzuki, H. Maezawa, Y. Furusawa and K. Kobayashi, Photon Factory Activity Report, 5, 286 (1987).

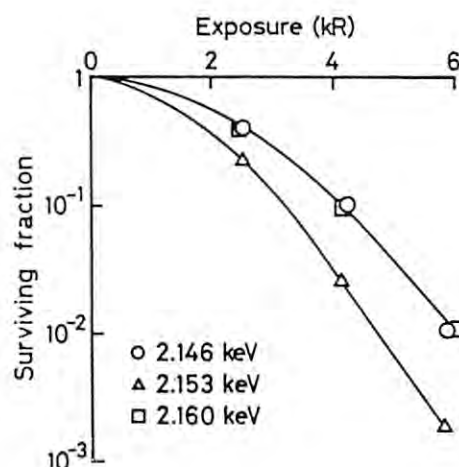


Figure 1.

Exposure-survival curves of FM3A cells irradiated with monochromatic X-rays at 2.146, 2.153 and 2.160 keV.



## X-RAY CONTACT MICROSCOPY OF HYDRATED HUMAN NUCLEI

Kunio SHINOHARA, Atushi ITO, Makoto WATANABE\*, Yasuhito KINJO\*,  
Sachiko KIKUCHI\*\*, Katsumi KOBAYASHI\*\*\*, and Hideki MAEZAWA\*\*\*

Tokyo Metropolitan Institute of Medical Science, Bunkyo-ku, Tokyo 113

\*Tokyo Metropolitan Isotope Research Institute, Setagaya-ku, Tokyo 158

\*\*Toshiba VSLI Research Center, Saiwai-ku, Kawasaki-shi, Kanagawa 210

\*\*\*Photon Factory, National Laboratory for High Energy Physics, Ibaraki 305

### Introduction

Observation of intact biological specimens with X-ray contact microscopy using PMMA resist has been developed extensively. In a line of this progress, we have observed unstained human chromosomes dried with no fixative by X-ray contact microscopy using undulator radiation in vacuum (1). The next step is to observe an intact material in a hydrated condition. In the present experiment, we observed hydrated intact human nuclei in a moist chamber.

### Materials and Methods

Nuclei were isolated from human lymphocytes (RPMI 1788) by syringing cells in a nucleus isolation buffer (2). A droplet of nuclei suspension was placed on a window of a silicon nitride film (1.0  $\mu\text{m}$  thick) supported by a silicon plate and covered with PMMA resist on a silicon plate. The thickness of the water layer was adjusted to be as thin as possible (less than 14  $\mu\text{m}$  thick) by controlling the volume of the droplet and absorbing the excess water with a piece of filter paper. The sample was mounted in a moist chamber tightly sealed with O-ring (Fig.1).

The moist chamber was set on a sample holder and exposed to the 2.65 nm monochromatic undulator radiation from BL-2B at the Photon Factory in a vacuum ( $2 \times 10^{-6}$  Torr). A zone plate monochromator (stopping material, gold; thickness, 3  $\mu\text{m}$ ; inner-most diameter, 59.8  $\mu\text{m}$ ; outermost diameter, 946  $\mu\text{m}$ ) was installed. Exposure time was 120 min.

Nuclei were removed with sodium hypochlorite from the PMMA resist and the resist was developed with a mixture of methylisobutylketone and isopropanol.

### Results and Discussion

The developed X-ray images of hydrated nuclei as well as dried nuclei were observed under differential interference microscope (Fig.2 and 3).

Intact hydrated nucleus was observable with X-ray contact microscopy in the moist chamber. Further analysis is now on the way using transmission electron microscope together with the plasma polymerization replica method.

The present results suggest the strong possibility to observe the *in situ* organization of chromatin and chromosomes in the physiological hydrated condition.

### References

- 1) K.Shinohara et al., Photon Factory Activity Report 1987, #5,124 (1987).
- 2) W.Wray and E.Stubblefield, Experimental Cell Res., 59, 469 (1970).

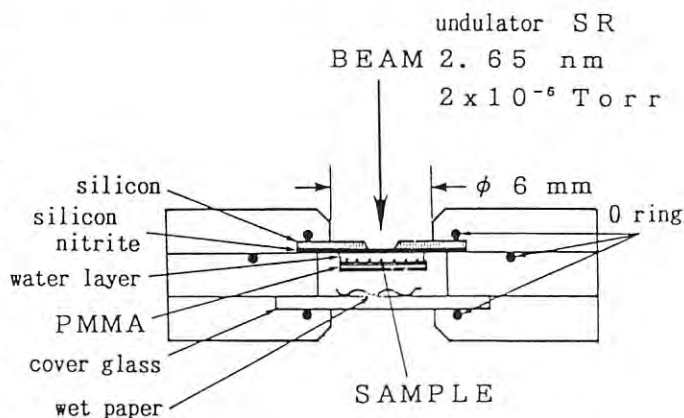


Fig.1 A moist chamber for exposure.

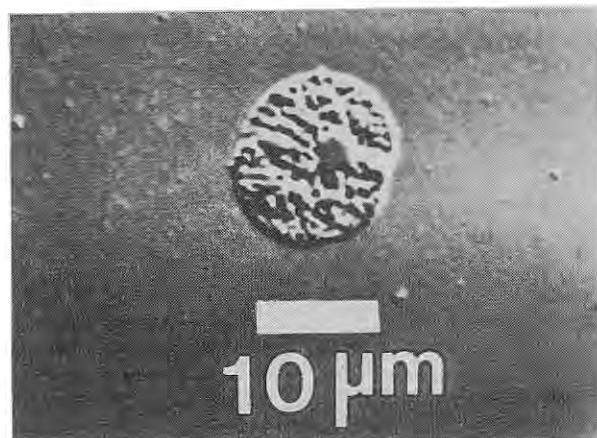


Fig.2 X-ray image of a dry nucleus.



Fig.3 X-ray image of a hydrated nucleus.



# NMR STUDY OF THE IRRADIATION EFFECT BY SR MONOCHROMATIC X-RAYS ON BR-DEOXYURIDINE-MONOPHOSPHATE

Kaoru TAKAKURA, Kotaro HIEDA<sup>†</sup>, Hiroshi MAEZAWA<sup>††</sup> and Katsumi KOBAYASHI<sup>†††</sup>

Department of Physics, College of Liberal Arts, International Christian University, Osawa, Mitaka-shi, Tokyo 181

<sup>†</sup>Department of Physics, Faculty of Science, Rikkyo(St.Paul's) University Nishiikebukuro, Toshima-ku, Tokyo 171

<sup>††</sup>Department of Radiation Oncology, School of Medicine, Tokai University, Bouseidai, Isehara-shi, Kanagawa 259-11

<sup>†††</sup>Photon Factory, National Laboratory for High Energy Physics, Oho-machi, Tsukuba-gun, Ibaraki 305

## Introduction

Previously we have studied the Auger enhancement of the yield of radiation products from Br-dUMP irradiated with X-rays, using high performance liquid chromatography.<sup>1)</sup> From the result it was observed that Auger electrons from K-shell of bromine atoms might play the main role for energy dependent enhancement at induction of radiation products from irradiated Br-dUMP. Here we report the Nuclear Magnetic Resonance (NMR) study of the Auger enhancement of Br-dUMP irradiated with monochromatic X-rays at 13.49 keV and 13.43 keV, just above and below the K-absorption edge of bromine.

## Materials and Methods

5-Bromo-2'-Deoxyuridine-5'-Monophosphate (Br-dUMP) and 2'-Deoxyuridine-5'-Monophosphate (dUMP) purchased from Sigma Co. Ltd. were dissolved in D<sub>2</sub>O at concentration of 25 mg/ml. 50  $\mu$ l of solution was irradiated in a specially designed cell. Mono-energetic synchrotron radiation at Photon Factory was used as a radiation source. Two wavelengths, 0.919 Å (13.49 keV) and 0.923 Å (13.43 keV) were selected for irradiation. FT-proton NMR and FT-phosphorous NMR spectra were recorded at 21°C on a Varian XL-300 spectrometer.

## Results and Discussion

Proton NMR spectra of Br-dUMP irradiated in D<sub>2</sub>O solution with soft X-rays of 13.43 keV and 13.49 keV at 300 kR were shown in Fig.1. Some new signals were observed (peak A1, A2, B1 and B2 in Fig.1) in the spectra of irradiated Br-dUMP solution. The peak A1 and A2 might correspond to the proton signals of dUMP, therefore the areas of the peaks might represent the amount of dUMP as a radiation product from irradiated Br-dUMP. The amount was larger at 13.49 keV X-rays irradiation than at 13.43 keV, suggesting Auger enhancement caused of the absorption of K-edge of bromine. However, Peaks of B1 and B2 were not clearly defined. These peaks were also observed in spectrum of irradiated dUMP solution. (Figure is not shown)

Phosphorous NMR spectra of Br-dUMP irradiated in D<sub>2</sub>O solution with soft X-rays of 13.43 keV and 13.49 keV at 300 kR were shown in Fig.2. Only one signal for phosphorous in Br-dUMP became to be doublet after the irradiation of 13.43 keV and 13.49 keV X-rays. The reason of duplication is not clear, but the duplication might reflect the change of backbone structure of Br-dUMP caused by X-ray irradiation.

1) Report on annual meeting of Japan Radiation Research, 1988.

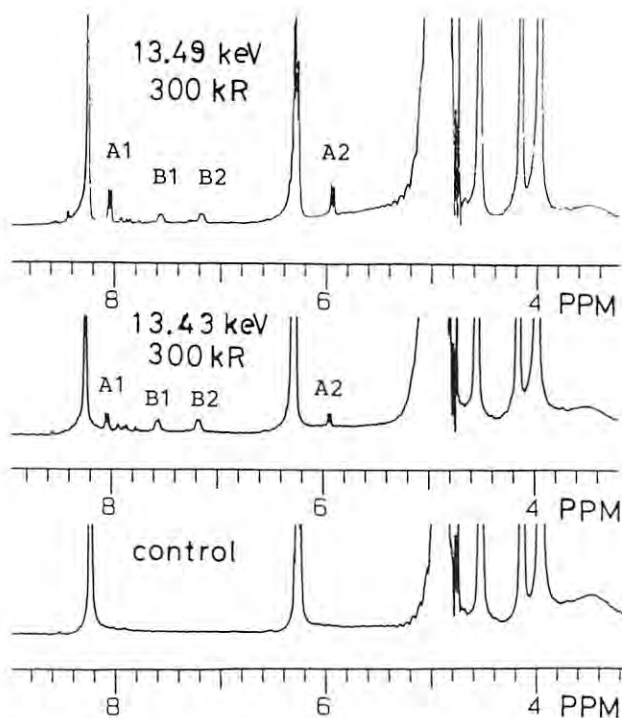


Fig.1 Proton NMR spectra of Br-dUMP irradiated in D<sub>2</sub>O solution with X-rays of 13.43 keV and 13.49 keV at 300 kR, and control.

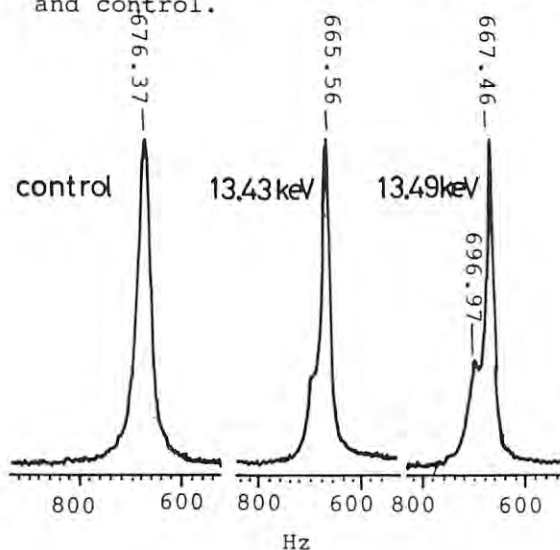


Fig.2 Phosphorous NMR spectra of Br-dUMP irradiated in D<sub>2</sub>O solution with X-rays of 13.43 keV and 13.49 keV, and control.

## NONDESTRUCTIVE X-RAY FLUORESCENCE SPECTROSCOPIC IMAGING OF TRACE ELEMENTS IN ANIMAL TISSUES

Izumi NAKAI, Nobuhiro SHIMOJOU\*, Shino HONMA\*, Takuji KAWASHIMA, Atsuo IIDA\*\*

Department of Chemistry, The University of Tsukuba, Ibaraki 305

\*Institute of Community Medicine, The University of Tsukuba, Ibaraki 305

\*\*Photon Factory, National Laboratory for High Energy Physics, Tsukuba, Ibaraki 305

Introduction

Ingestion of toxic metallic elements causes intoxication after accumulation at various biological organs and tissues such as brain, liver, kidney. For example, toxicology of alkyl mercury is well known as Minamata disease. In order to study metal intoxication, it is very important to clarify distribution of metallic elements in each biological tissues. It is expected that the chemical imaging by SR-XRF is an ideal analytical technique for these samples, because it allows nondestructive two-dimensional multielemental analysis of trace elements. Thus, we have applied the technique to study behavior of toxic elements at ppm levels in biological tissues. This paper reports results of two-dimensional analysis of brains of rats and guinea pigs, which are dosed with Hg and Se. The latter element is known as antagonist in mercury intoxication.

Experimental

The experimental animals consist of rats and guinea pigs that received daily subcutaneous injection of solution of methyl mercury chloride and/or sodium selenious acid with ratio of 1:0, 1:0.5 and 0:0.5 under the rate of 3mgHg/kg of body weight. After the 7 days successive subcutaneous injection, the animals were killed by withdrawing an excess volume of blood from the heart. The brains were quickly excised after perfusion with cold saline, then fixed in 10% formalin and were paraffined. The brains were cut into slices of 5mm width from center of the brains and subjected to the analysis.

The measurements were carried out at BL-4A using the XRF-analysis facilities. Samples were excited by monochromated X-ray at 16 keV using Si(111) double crystal monochromator. The analysis was made by energy dispersive mode using a Si(Li) detector. Microbeam was obtained by a set of vertical and horizontal slits. During the two dimensional analysis the sample was placed on a remote controlled X-Z stage with pulse motors (ca. 2.5 u/pulse) and the analyzed point was monitored with a TV camera. The intensity data were stored in a PC9801 personal computer.

Results and Discussion

Figure 1 shows a photograph of a brain of guinea pig dosed with Hg and Se. The fluorescence intensity data were processed with the personal computer into two dimensional image on a color display. Figure 2 shows the chemical imaging of the sample of Fig. 1. The intensity was scaled with 8 densities. Figures 2 (a), (b), (c), and (d) indicate Hg, Zn, Cu and Se distribution in the brain. It is found that the distribution of Hg corresponds to that of Zn and Cu to Se. The rats and guinea pigs dosed with Se only, Hg only and Hg + Se, and control samples were analyzed. The results are summarized as follows:

(1) The accumulation of both Hg and Se increased

with their simultaneous dose compared with single dose of each element.

(2) There exists a correlation in concentration between Hg and Zn, and between Cu and Se, respectively.

(3) Concentrations of Hg in cerebellum and medulla are lower than that in cerebral cortex.

(4) The present technique does not require such pre-treatment of sample as separation of each tissues or dissolution before the analysis.

(5) The present technique enables us to carry out multielemental analysis of ppm levels without destroying the form of tissues. Consequently, we can make one to one correspondence between morphological information and chemical information in biological tissues.

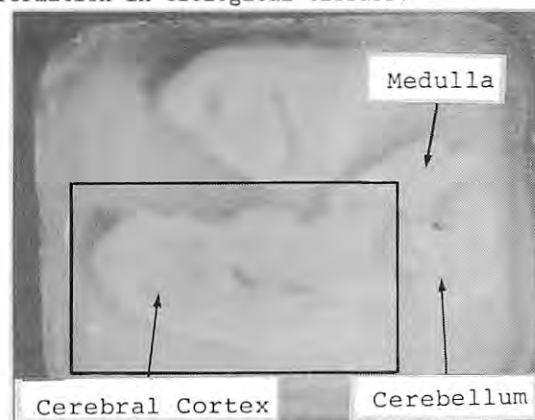


Fig. 1. Sliced brain of guinea pig dosed with Hg and Se.

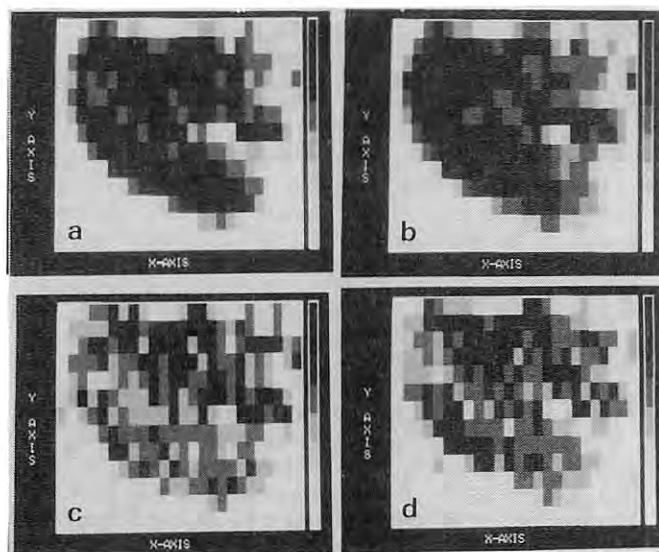


Fig. 2. Results of the chemical imaging of the sample shown in Fig. 1.  
(a) Hg distribution (b) Zn distribution  
(c) Cu distribution (d) Se distribution

# INDUCTION OF MUTATION AND CHROMOSOME ABERRATIONS IN CULTURED MAMMALIAN CELLS BY SYNCHROTRON-PRODUCED MONOCHROMATIC X-RAYS

Yosuke EJIMA<sup>1</sup>, Masao S. SASAKI<sup>1</sup>, Shin SAIGUSA<sup>1</sup>, Katsumi KOBAYASHI<sup>2</sup>, Kotaro HIEDA<sup>3</sup>,  
Hiroshi MAEZAWA<sup>4</sup>, Takeshi YAMADA<sup>5</sup> and Takashi ITO<sup>6</sup>

<sup>1</sup>Radiation Biology Center, Kyoto University, Sakyo-ku, Kyoto

<sup>2</sup>Photon Factory, National Laboratory for High Energy Physics, Tsukuba-shi, Ibaraki

<sup>3</sup>Faculty of Science, Rikkyo University, Toshima-ku, Tokyo

<sup>4</sup>Tokai University Medical School, Isehara-shi, Kanagawa

<sup>5</sup>National Institute of Radiological Sciences, Chiba-shi, Chiba

<sup>6</sup>College of General Education, University of Tokyo, Meguro-ku, Tokyo

## Introduction

Monochromatic soft X-rays provide a useful tool for probing the mechanisms of radiation action because of their well defined initial energies and ranges. Radiation-induced mutation has been supposed to be closely related to chromosome structural aberrations. In the present study, induction of mutation and chromosome aberrations were compared among X-rays with different wavelengths in cultured mammalian cells to examine the relationships between the two biological endpoints.

## Experimental and Results

A near diploid cell line established from mouse embryos (m5S/1M) was used<sup>1</sup>. Density-inhibited cells were dispersed by trypsin and cell suspensions were irradiated with monochromatic X-rays ranging 0.85A-2.6A. After 15-day expression, cells were replated onto selective media containing 6-thioguanine (6TG) and cultured for further 21 days to determine the mutation frequency. Small aliquots were fixed 40 hours after irradiation and C-banded for the analysis of chromosome aberrations (dicentrics).

The results of a typical experiment were shown in Table 1. X-rays of either wavelengths induced mutations in a dose-dependent manner. The effectiveness was higher in 1.8A than in other wavelengths. 1.8A X-rays were the most effective even when mutation frequencies were plotted against dicentric yields (Fig. 1).

The results suggest that quantitative relationships between mutation induction and

chromosome aberration formation are not uniform among X-rays of different wavelengths. Relatively higher mutagenicity of 1.8A X-rays may be relevant to the transient RBE peak around this LET region<sup>2</sup>.

## References

- 1) M.S. Sasaki and S. Kodama: J. Cell.Physiol., 131,114 (1987).
- 2) M.S. Sasaki, Y. Ejima, K.Kobayashi, K.Hieda, H. Maezawa, T. Yamada and T. Ito: Photon Factory Activity Report, 5, 129 (1987).

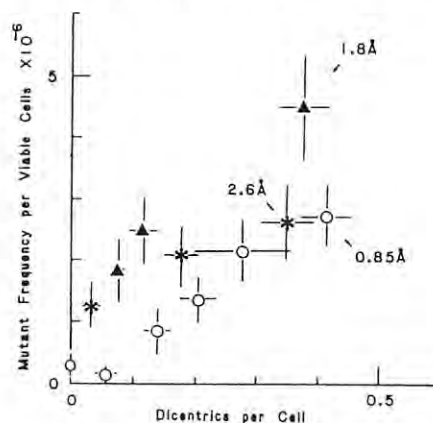


Fig. 1. Mutation frequencies plotted against dicentric yields in m5S cells irradiated with monochromatic X-rays with wavelengths of 0.85A(O), 1.8A(Δ) and 2.6A(●).

Table 1. Induction of 6TG<sup>R</sup> Mutation and Chromosome Aberrations in Mouse m5S/1M Cells by Synchrotron-Produced Monochromatic X-Rays

Wave length (A)	Dose* (R)	Mutation				Chromosome aberrations	
		# cells assayed	P.E. (%)	# 6TG <sup>R</sup> mutants	Mutants/ 10 <sup>6</sup> viable cells	# cells analyzed	Dicentrics per cell
0.85	520	9X10 <sup>4</sup>	82.0	20	2.71	200	0.415
0.85	416	9X10 <sup>4</sup>	87.5	17	2.16	36	0.278
0.85	312	10 <sup>7</sup>	88.6	12	1.35	200	0.205
0.85	208	9.5X10 <sup>4</sup>	75.8	6	0.83	200	0.140
0.85	104	10 <sup>7</sup>	85.1	1	0.12	200	0.060
1.8	490	10 <sup>7</sup>	79.3	103	12.99	200	0.405
1.8	392	10 <sup>7</sup>	78.3	35	4.47	200	0.380
1.8	196	9.5X10 <sup>4</sup>	81.3	19	2.46	200	0.120
1.8	98	10 <sup>7</sup>	78.6	14	1.84	200	0.080
2.6	485	10 <sup>7</sup>	76.7	12	1.56	200	0.585
2.6	291	10 <sup>7</sup>	83.7	22	2.63	200	0.350
2.6	194	9.5X10 <sup>4</sup>	85.9	17	2.08	200	0.180
2.6	97	10 <sup>7</sup>	87.7	12	1.37	200	0.060

\* Doses at the sample surfaces



## DETECTION OF DAMAGED DNA IRRADIATED WITH MONO-X-RAY IN THE PRESENCE OF BrdU

Norio MIYOSHI<sup>1</sup>, Masaru FUKUDA<sup>1</sup>, Sakon NORIKI<sup>1</sup>, Yoshiaki IMAMURA<sup>1</sup>, Nobuo MATSUMOTO<sup>1</sup>,  
Katsumi KOBAYASHI<sup>2</sup>, Hiroshi MAEZAWA<sup>3</sup>, Yoshiya FURUSAWA<sup>3</sup>, Kotaro HIEDA<sup>4</sup>, Takashi ITO<sup>5</sup>.

<sup>1</sup>Dept. Pathol., Fukui Med. Sch.; <sup>2</sup>Photon Fact., Natl. Lab. High Energy Phys.; <sup>3</sup>Dept. Molecular Biol., Sch. Med., Tokai Univ.; <sup>4</sup>Biophys. Lab., Dept. Phys., Rikkyo Univ.;

<sup>5</sup> Inst. Phys., College of Arts and Sci., Univ. Tokyo.

## INTRODUCTION

In previous works, there was a density gradient by ultracentrifuging of sucrose solution for quantitative detection of the single stranded DNA. Recently, we have been studying the detection of instability of nuclear DNA at acid hydrolysis by fluorescent staining with acridine orange (AO) (1,2). Then, we examined quantitative detection of nuclear DNA damaged by mono-X-ray irradiation in the presence of BrdU using acid hydrolysis and AO fluorescent staining.

## EXPERIMENTS

Healthy human lymphocytes (LYM) and chronic myelocytic leukemia (CML) were treated with 100 µg/ml BrdU 6hr before harvesting. The cells were irradiated 0.5, 5, 10 and 20 krad by mono-X-ray at 0.919 and 0.923 Å, respectively.

Almost immediately after the irradiation, these cells were smeared on non-fluorescent glass slide and were fixed with 70 % EtOH aqueous solution for 16 hr at 4 °C. The fixed cells were washed with McIlvaine buffer solutions (pH=6.8) and were treated with RNase (type I, Sigma) for 1 hr at 37 °C. These treated cells were hydrolysed with 2N-HCl at 30 °C for 10, 20, 30, 60 and 120 min, respectively. The hydrolysed cells were stained with 30 µg/ml acridine orange (AO) for 20 min at room temperature.

Fluorescence microphotograph and fluorescence emission spectra of CML cells stained with AO were obtained using a fluorescence microphotometer (model IMT2-SRF, Olympus).

Fluorescence intensities of AO green and red fluorescence were measured by fluorescence cytophotometry (model QH-2, Olympus). The hydrolysis curves were determined by the fluorescence cytophotometry and were computer fitted to the Bateman function  $y(t) = y_0 k_1 / (k_2 - k_1) \cdot \exp(-k_2 t) - \exp(-k_1 t)$  (1) to determine the kinetic parameters, the initial yield of apurinic acid or single-stranded DNA ( $y_0$ ), and the rate constant of depolymerization ( $k_2$ ). The values for  $k_2$  (which reflects the degree of DNA instability) and  $y_0$  (which may indicate the degree of DNA denaturation) was plotted against X-ray doses.

## RESULTS AND DISCUSSION

Figure 1 shows AO fluorescence microphotograph of AML cells treated with BrdU for 6 hr before harvesting. Bright white cells (marked as ○) in this figure emitted green and yellow. Dark cells (marked as \*) emitted red colour. The marked cells were estimated as G1 (○) and S (\*) phases from DNA histogram measuring, respectively.

The fluorescence emission spectra of these labeling cells (○ and \*) were measured throughout a pinhole that size was same as those of the cells as showed in Fig. 2. The peak of spectrum of G1 appeared at 530 nm (green colour). That of spectrum of S was 630 nm (red colour) besides a shoulder at 530nm. It was said that the green fluorescence was estimated as intercalated binding of AO molecule into the base pairs, and

that the red one was as aggregate of AO molecules bound the single stranded DNA. Accordingly, S phase cells incorporated BrdU in the late replicate stage to be damaged selectively by mono-X-ray (0.919 Å, 0.5 krad) irradiation.

Figure 3 shows the double dimension plotting of the red (horizontal axis) and green (vertical axis) fluorescence intensities of AO bound to nucleas DNA irradiated by mono-X-ray at 0.919 Å (0.5 krad). The CML cells were hydrolysed with 2N-HCl for 10 min at 30 °C, and they were stained with AO. The slope of the double dimension plotting in the absence of X-ray irradiation was larger than that in the presence of one. When the cells were irradiated 0.5 krad, the green fluorescent DNA histogram shifted to weak intensity and the red one to large intensity. Accordingly, the fluorescence intensity of the irradiated cells increased, especially, that of S phase increased largely. It was considered that the DNA damage increased by X-ray irradiation.

Figure 4 shows the double dimension plotting of the red (horizontal axis) and green (vertical axis) fluorescence intensities. When in the presence of BrdU, the DNA damage increased comparing with that in the absence of one. It was suggested that BrdU enhanced the DNA damage irradiated by mono-X-ray at 0.919 Å.

Furthermore, the red fluorescence intensity at G1 phase peak were plotted against the different hydrolysis times as shown in Fig. 5. These values were fitted by computer to Bateman function (1). The peak of curve BrdU(+) appeared at short hydrolysis time, and the fluorescence intensity of the peak was larger than that of curve BrdU(-).

By computer analysis, the parameters  $y_0$  (initial yield of apurinic acid or single stranded DNA) and  $k_2$  (rate constant of depolymerization) were obtained as shown in Table 1. These values of  $y_0$  and  $k_2$  increased in the presence of BrdU and X-ray irradiation (0.919 Å). And these values of CML cells were larger than those of LYM cells. Accordingly, BrdU molecules enhanced the nuclear DNA damage for the mono-X-ray irradiation at 0.919 Å.

Furthermore, the values of  $y_0$  and  $k_2$  increased linearly against the different X-ray doses as shown in Fig. 6. The slopes of these relationship were listed as shown in Table 2. The slope of the malignant CML cells was larger than that of the normal LYM cells. In conclusion, the malignant cells were sensitive for X-ray irradiation at 0.919 Å in the presence of BrdU.

## REFERENCES

- 1) M.Fukuda, N.Miyoshi, et al., *Histochem.*, **84**, 556-560 (1986).
- 2) N.Miyoshi, M.Fukuda, *Histochem.*, **84**, 561-565 (1986).



Fig.1



Fig.5

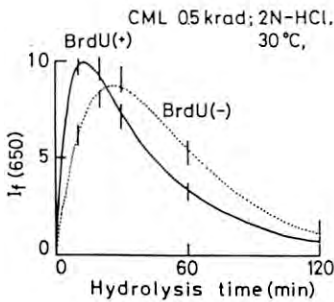


Fig.2

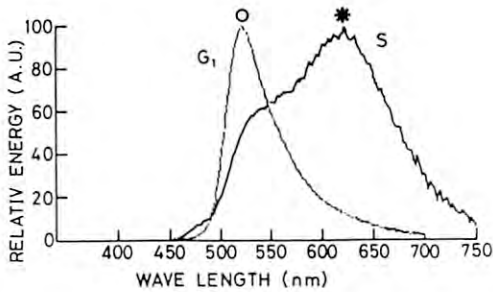


Table 1

X-ray dose		LYM	CML
BrdU- 0 kR	$y_0$	1.1	1.9
	$k_2$	$1.3 \times 10^{-3}$	$8.0 \times 10^{-3}$
0.919 Å	$y_0$	1.8	2.8
	$k_2$	$2.0 \times 10^{-3}$	$1.5 \times 10^{-2}$
0.919 Å 5.0 kR	$y_0$		3.5
	$k_2$		$1.8 \times 10^{-2}$
BrdU + 0 kR	$y_0$	1.9	4.9
	$k_2$	$2.1 \times 10^{-3}$	$5.1 \times 10^{-2}$
0.919 Å	$y_0$	2.1	5.5
	$k_2$	$3.8 \times 10^{-3}$	$5.3 \times 10^{-2}$
0.919 Å 5.0 kR	$y_0$		6.9
	$k_2$		$5.9 \times 10^{-2}$

Fig.3

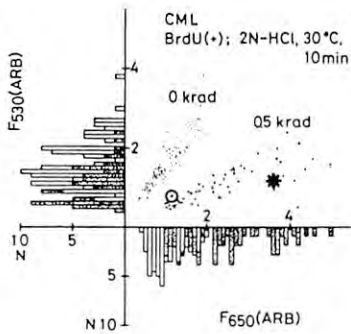


Fig.6

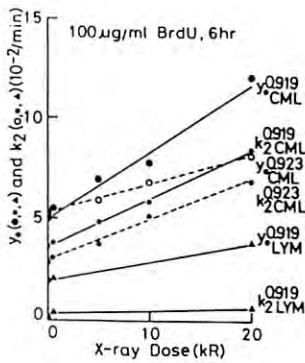


Fig.4

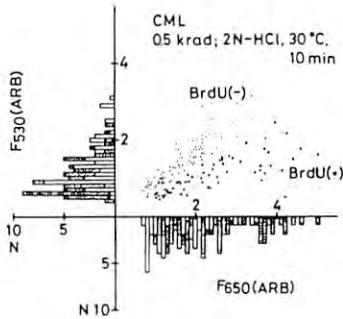


Table 2

X-ray		LYM	CML
BrdU+ 0.919 Å	$y_0$	$(9.5 \pm 0.2) \times 10^{-2}$	$(3.3 \pm 0.1) \times 10^{-1}$
	$k_2$	$(1.8 \pm 0.1) \times 10^{-4}$	$(2.4 \pm 0.1) \times 10^{-3}$
BrdU+ 0.923 Å	$y_0$		$(1.4 \pm 0.1) \times 10^{-1}$
	$k_2$		$(2.1 \pm 0.1) \times 10^{-3}$

$y_0$ /kR,  $k_2$ /min·kR

## DETECTION OF THE DAMAGED AND FRAGILE SITES IRRADIATED WITH MONO-X-RAY ON CHROMOSOME

Norio MIYOSHI<sup>1</sup>, Masaru FUKUDA<sup>1</sup>, Sakon NORIKI<sup>1</sup>, Yoshiaki IMAMURA<sup>1</sup>, Nobuo MATSUMOTO<sup>1</sup>,  
Katsumi KOBAYASHI<sup>2</sup>, Hiroshi MAEZAWA<sup>3</sup>, Yoshiya FURUSAWA<sup>3</sup>, Kotaro HIEDA<sup>4</sup>, Takashi ITO<sup>5</sup>.

<sup>1</sup>Dept. Pathol., Fukui Med. Sch.; <sup>2</sup>Photon Fact., Natl. Lab. High Energy Phys.; <sup>3</sup>Dept. Molecular Biol., Sch. Med., Tokai Univ.; <sup>4</sup>Biophys. Lab., Dept. Phys., Rikkyo Univ.;  
<sup>5</sup>Inst. Phys., College of Arts and Sci., Univ. Tokyo.

## INTRODUCTION

In a previous work, risk of chromosomal disease due to radiation had been estimated tentatively from the study of radiation-induced traslocations in human fibroblasts. On the other hand, we has been studied the mechanism of fluorescence banding on chromosomes using fuluorescence dyes and polynucleotides. Then, we examined the detection of the damaged and fragile sites irradiated with mono-X-ray on chromosome.

## EXPERIMENTS

Healthy human lymphocytes were exposed with 100ug/ml BrdU 6hr before colucemide treatment. The cells treated with 10ug/ml colucemide were harvested and were irradiated 5krad by mono-X-ray at 0.919Å. Almost immediately after the irradiation, mitoses were harvested and were stained with 30ug/ml acridine orange (AO) for 30 min.

## RESULTS AND DISCUSSION

Figure 1 shows a fluorescence microphotograph of human lymphocytes chromosomes (1 and Y) which were irradiated and stained with AO. The RBA bands of 1p36 and Yq12 were green and red, respectively.

Figure 2 shows fluorescence spectra on the red (Yq12) and green (1p36) bands measured with a fluorescence microphotometer (model IMT2-SRF, Olympus). The emission peak of Curve 1 was presented at 530 nm. This peak was estimated that AO molecule was intercalated into the DNA base pairs. The shoulder of Curve Y at 630nm was considered that AO aggregate was bound to the single stranded DNA irradiated by mono-X-ray with metachromatic-shift. These estimation was identified by following Fig. 3.

Figure 3 shows ratio ( $F/F_0$ ) of the green fluorescence intensities in the presence ( $F$ ) and absence ( $F_0$ ) of polynucleotides against the different concentration of polynucleotides measured by a fluorescence photometer (model 850, Hitachi). Curves 1 and 1' are homo double A-T and G-C, respectively. Curves 2 and 2' are hetero double A-T and G-C, respectively. Curves 3 and 3' are hetero single A,T and G,C bases, respectively. The fluorescence intensity of AO was enhanced by double polynucleotides, especially, by A-T base pairs. But, when single A,T, the ratio value was decreased to be 20 % of double A-T. Accordingly, it was considered that green band (1p36) was rich with double G-C and red band (Yq12) was rich with single A,T bases.

Table 1 shows rate of photofading of AO green fluorescence in various polynucleotide solutions in the presence and absence of BrdU. The rate values in the single A,T bases slutions was larger than that in the double or single G,C bases in the presence of BrdU. It was considered that contrast of AO band was enhanced on the chromosomes throughout a fluorescence micrometer.

Fig.1

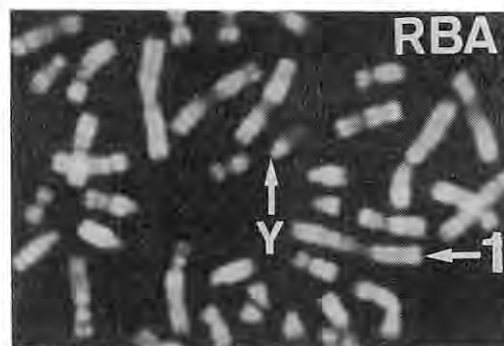


Fig.2

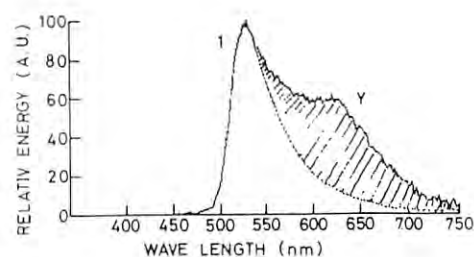


Fig.3

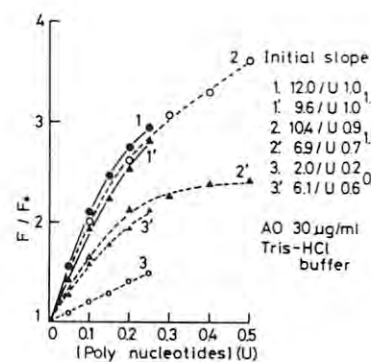


Table 1

Rate of photofading of AO fluorescence

[polynucleotide]=0.4 U  
[AO]= $4 \times 10^{-6}$  M  $\lambda_{ex}=500$  nm,  $\lambda_{em}=530$  nm

Solutions	BrdU(-)	BrdU(+)	(+/-)
PBS	38.4%/h(100)	40.3%/h(100)	1.08
poly(dA-dT) x 2	42.9%/h(112)	84.0%/h(208)	1.96
poly(dA,dT)	39.9%/h(104)	120.0%/h(298)	3.01
poly(dG-dC) x 2	24.9%/h(66.5)	21.3%/h(53)	0.84
poly(dG,dC)	27.0%/h(70)	18.9%/h(47)	0.67

STUDIES ON AUGER ENHANCEMENT IN CULTURED MAMMALIAN CELLS WITH THE USE OF RADICAL SCAVENGERS

Kunio SHINOHARA\*, Atsushi ITO\*, and Katsumi KOBAYASHI\*\*

\*Dept. Radiat. Res. Tokyo Metropolitan Inst. Med. Sci., Tokyo 113;  
\*\*Photon Factory, Nat'l. Lab. High Energy Phys., Ibaraki 305.

Introduction

In the previous experiments (1), we have found the increased lethality in the cells labeled with 5-bromodeoxyuridine (BUdR) irradiated with x-rays at 0.9 A, just below the K-absorption edge of bromine (0.92 A), compared with those irradiated at 1.00 A. Although the difference was small, the results suggested the killing enhancement in mammalian cells due to the induction of Auger effect. To elucidate the mechanisms underlying the biological effects of low energy x-rays through K-absorption followed by Auger cascade, it is useful to study the effects of radioprotectors. For this purpose, the previous method (1) where cells were grown on a membrane filter disc is not suitable for radioprotector experiments. In the present study, we have developed the method for these experiments with the use of small tissue culture flask.

Materials and Methods

HeLa cells were allowed to attach themselves to the surface of the plastic culture flask (Costar, #3393), and grown in Eagle's minimum essential medium supplemented with 10% fetal bovine serum in the presence or absence of BUdR. The culture medium was discarded and the fresh medium containing cysteamine was poured into the flask. The irradiation was performed at the wavelength of 0.9 A and 1.0 A on the sample scanning stage installed at the BL-4A. The irradiated cells were collected by trypsinization, plated into 60 mm plastic Petri dishes, and incubated for 10-12 days to develop colonies.

Results and Discussion

Figure 1 shows the dose survival curves of HeLa cells irradiated at 0.9 A and 1.0 A in the absence of radioprotector. These results totally confirmed the previous results obtained with the different irradiation system: The small enhancement of the killing at 0.9 A was observed compared with the killing at 1.0 A. The preliminary results of the radioprotection experiments are presented in Table 1. 10 mM cysteamine showed the large protection against the cell killing at 0.9 A in the presence or absence of BUdR.

These results demonstrate that our new irradiation system is extremely useful in the experiments with radioprotectors. Quantitative study is in progress.

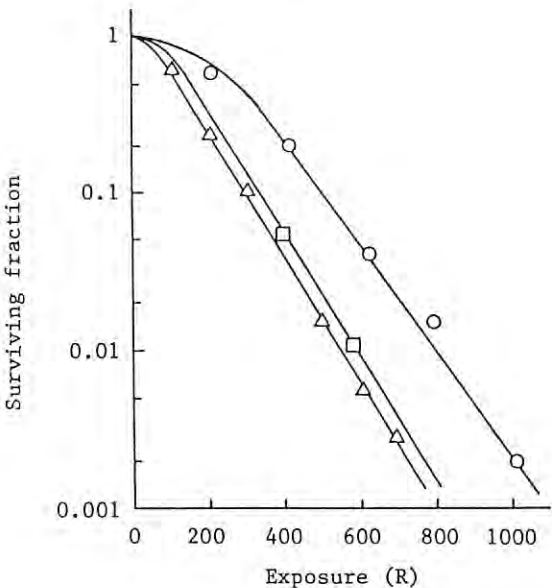


Fig. 1. Survival curves of HeLa cells irradiated with monochromatic synchrotron radiation. (O): 0.9 A, -BUdR. (Δ): 0.9 A, +BUdR. (□): 1.0 A, +BUdR.

Table 1. Protective effects of cysteamine on BUdR-labeled HeLa cells irradiated with 0.9 A monochromatic synchrotron radiation.

Exposure (R)	BUdR	Cysteamine (10 mM)	Surviving fraction
845	-	-	0.0032
	-	+	0.305
515	+	-	0.0066
	+	+	0.272

Wavelength: 0.9 A

Reference

1) K. Shinohara, et al., J. Radiat. Res., 26, 334 (1985).

## CRYSTALLOGRAPHIC STUDIES ON INTACT RIBOSOMAL PARTICLES

K. von Bohlen(1), H.G. Wittmann (2) and A. Yonath (1),(3)

(1) Max Planck Research Unit for Structural Molecular Biology, Hamburg, FRG

(2) Max Planck Institute for Molecular Genetics, Berlin (West).

(3) Department of Structural Chemistry, Weizmann Institute, Rehovot, Israel.

One of the major questions in biochemistry still awaiting clarification relates to the detailed molecular mechanism of the expression of genetic information in the construction of proteins. Ribosomes are the cell organelles where this process takes place in every living cell.

The ribosomes themselves are complex assemblies composed of several strands of RNA and a large number of different proteins arranged into two subunits of unequal size which associate upon initiation of protein synthesis. A typical bacterial ribosome contains 32 different proteins and two RNA chains in the large and 21 proteins and one RNA chain in the small subunit. The molecular weights of bacterial ribosomes are  $2.3 \times 10^6$  for the assembled particles,  $1.45 \times 10^6$  for the large subunit, and  $8.5 \times 10^5$  for the small subunit. There is no internal symmetry that could be utilized in structure determination.

In a program aimed at the unraveling of their three-dimensional structure we have initiated crystallographic studies of ribosomal particles. Despite their enormous size, inherent flexibility, and tendency to disintegrate, it has been possible to grow several types of crystals of intact ribosomes, their small and large subunits, as well as of complexes of the latter with other components involved in biosynthesis of proteins (e.g. tRNA).

Some of these crystals are suitable for crystallographic studies at reasonable resolution. The best are the crystals of large ribosomal subunits from *Halobacteria marismortui* which diffract to  $4.5 \text{ \AA}$ .

All types of crystals grown by us have been obtained from functionally active particles, and, despite the natural tendency of isolated ribosomes to disintegrate, the crystalline material has retained its integrity and biological activity for long periods. Those crystals which were found useful for diffraction studies were grown under conditions not very different from natural ones.

The crystals are extremely fragile, and have required development of special techniques for initial manipulation, mounting in different orientations for x-ray studies, and soaking in heavy-atom solutions.

The diffracting power of crystalline ribosome particles is so low that virtually all diffraction studies have been carried out with synchrotron radiation. At ambient temperature the useful life-time of these crystals under synchrotron irradiation is limited to a few minutes. <thus, in an attempt to obtain a complete data set, over 260 individual crystals had to be exposed on an oscillation camera. In order to conserve precious higher resolution reflections, no alignment photos were taken. In spite of this, only one data exposure could be obtained from each crystal. However, upon cooling to cryo temperature (around 85 K) there was virtually no radiation damage observed even after hours in the synchrotron X-ray beam. In favorable cases a complete dataset could be collected from one crystal.

Additional difficulties arise from the generally wide mosaic spread (up to  $3^\circ$ ) of these crystals. With the long axis ( $581 \text{ \AA}$ ) oriented nearly parallel to the x-ray beam, the oscillation ranges must be kept small in order to avoid overlap of reflections, and for many exposures not a single reflection could be recorded in full, rendering proper integration of intensities virtually impossible. The problems described here constitute nearly insurmountable difficulties in data collection, and significant sophistication is essential for future progress of our studies.

Although the cryogenic treatment does not appear to offer any improvement in resolution or in mosaic spread, for crystals of ribosomal particles it provides the only practical route to data collection found so far. Considering the wide variety in intensity distribution from crystal to crystal, the ability to collect a complete data set from one crystal becomes the major advantage of this method.



There are 40000 reflections in a set of data to 6Å resolution which is collected from the crystals of the large ribosomal subunits from *Halobacterium marismortui*. Considering the need for a few sets of data to be collected from native as well as from heavy-atom derivatized crystals, and the expected problem concerning the evaluation of these data, it is not desired to use conventional films. Since the spatial resolution of most diffractometers and commercially available area detectors is not sufficient to resolve the reflections (unit cell dimensions reach 720 Å), diffraction data cannot be collected on conventional area detectors. Thus, recording the data on imaging plates seems to be most suitable.

Dr. N. Sakabe from KEK has developed and constructed a camera (based on the "Weissenberg" geometry) which enables recording of thousands of reflections simultaneously. The geometry of this camera permits rotation angles which are larger than the mosaic spread of our crystals. Hence a large part of the diffraction data collected using this camera is expected to contain fully recorded reflections. Furthermore, Dr. Sakabe

has constructed a special cassette of a size suitable for the large unit cell dimensions of our crystals. We felt that the using this cassette with imaging plates will greatly advanced our research, and may contribute significantly to the improvement of the quality of the diffraction data.

During our work at KEK we were able to test the newly built cassette of Dr. Sakabe. We showed that the recorded reflections could be indexed and measured. We also could, for the first time, observe and resolve some high resolution terms (up to 4.5Å).

Unfortunately, the original cassette was designed and built before the method of cryo-crystallography of biological macromolecules has been developed. Therefore the original cassette which was built for us did not allow mounting crystals under a constant flow of liquid nitrogen. Consequently we have used part of our beam time as a test period and designed a suitable cooling equipment. In parallel, Dr. Sakabe has modified his cassette to accommodate this equipment. We hope to be able to use this facility in the near future.

# STRUCTURAL STUDIES OF LIPOAMIDE DEHYDROGENASE AND 3-ISOPROPYLMALATE DEHYDROGENASE BY RAPID MEASUREMENT OF HIGH RESOLUTION X-RAY DIFFRACTION DATA

BY AKIO TAKENAKA

Faculty of Science, Tokyo Institute of Technology

Nagatsuta, Midori-ku, Yokohama 227

Lipoamide dehydrogenase (E3) is a component enzyme of pyruvate dehydrogenase complex and  $\alpha$ -ketoglutarate dehydrogenase complex, which catalyze the oxidative decarboxylation of pyruvate and  $\alpha$ -ketoglutarate to form acetyl-CoA and succinyl-CoA, respectively. The amino acid sequence of the active site of E3 from baker's yeast is highly homologous with those from the *E. coli* pyruvate and  $\alpha$ -ketoglutarate dehydrogenase complexes. Recently, from a comparison of the primary structure of *E. coli* E3 with that for human erythrocyte glutathione reductase (GR), it has been proposed that the three-dimensional structure of E3 should be very similar to the structure of GR, which has been already been determined by the X-ray method.

E3 from baker's yeast was crystallized by desalting. Precession photographs indicated an orthorhombic space group  $P2_12_12_1$  with unit-cell dimensions of  $a=98.6(2)$ ,  $b=162.0(2)$ , and  $c=69.4(2)$  Å. The enzyme is a dimeric protein of identical subunits with a molecular weight of 56000. The assumption that there is one dimer per asymmetric unit gave a reasonable  $V_m$  of  $2.62 \text{ Å}^3/\text{dalton}$ . Assuming a partial specific volume of  $0.74 \text{ cm}^3/\text{g}$ , the solvent content of the crystals is calculated to be 53 % in volume.

A crystal with typical dimensions of  $0.2 \times 0.1 \times 0.4$  mm was chosen for data collection. Diffractions of SR ( $\lambda=1.38059 \text{ Å}$ ) were recorded on imaging plates packed in the Sakabe's screen-less Weissenberg camera at BL-6A2 of the Photon Factory. The range of rotation angle of  $\phi$  was  $11.4^\circ$  for each plate around the  $c$  axis and the overlapping between the two ranges was  $0.4^\circ$ . Each Weissenberg pattern was digitized by BA-100 reader, and processed by the computer program "WEIS" to assign the reflexion indices and to integrate the intensities within a certain range around the Bragg peak. The intensity data thus obtained were then combined into the same file and put on a common scale by the program "COMBINE" and "SCALE". A total of 53633 reflexions was observed, the unique reflexions of which were numbered 23846 ( $h=0-39$ ,  $k=0-59$ ,  $l=0-24$ ). The maximum resolution of the data was  $2.49 \text{ Å}$  in which 64.4 % reflexions were obtained. The consistency index  $R(\text{sym})$  for each imaging plate was 5.0-6.2 % and  $R(\text{merge})$  for all the observed reflexions was 6.4 %.

Atomic coordinates of the GR molecule were obtained from the Protein Data Bank. The reference molecule was constructed as a dimer of polyanilines and put at the origin of an orthogonal  $P2_1$  cell with dimensions of  $115 \times 100 \times 103 \text{ Å}$ . The structure factors were calculated for the 5503 independent reflexions

within the  $4.5 \text{ Å}$  resolution sphere. A cross-rotation function between the E3 and the reference crystals showed the maximum peak at  $\alpha=155.0^\circ$ ,  $\beta=42.5^\circ$ , and  $\gamma=135.0^\circ$ , corresponding to the peak found in the self-rotation function. An R-factor map procedure was applied to position the reference molecule oriented correctly in the E3 unit cell. The R factors calculated using data within  $7 \text{ Å}$  resolution in the range of  $0-\frac{1}{2}$  lattice along the three crystallographic axes indicated the lowest value at  $x=0.0823$ ,  $y=0.1524$ , and  $z=0.0238$ .

Phases calculated from the structure thus obtained were refined with a procedure proposed by Bricogne. The electron densities in the protein region were averaged by employing the local 2-fold symmetry, while those in the solvent region were fixed at their averaged values. The improved electron density map was Fourier-transformed to give new amplitudes and phases. These new Fcs and phases were combined with the initial or older ones by using Sim's weighting, and again the Fourier series thus resulted were applied to the calculation of the electron density map for the next refinement. This process was repeated until the mean phase change was less than  $10^\circ$ .  $2F_o - F_c$  maps were used to accelerate the convergence. The phase determination was then extended in steps from  $7 \text{ Å}$  to  $6 \text{ Å}$ , to  $5.5 \text{ Å}$ , and finally to  $4.5 \text{ Å}$  by alternating cycles of phase extension and refinement to convergence. Phase extension consisted simply of appending molecular replacement phases at high resolution to previously refined phases at lower resolution.

At the present, the phase extension from  $4.5 \text{ Å}$  to the higher resolution is in progress.

A leucine biosynthetic enzyme, 3-isopropylmalate dehydrogenase from a mesophile, *Bacillus coagulans*, the gene of which has been cloned and expressed in *E. coli*, was crystallized by the hanging-drop vapor diffusion method in a phosphate buffer solution (pH 6.5). Precession photographs revealed the space group to be  $P2_12_12_1$  with unit-cell dimensions of  $a=134.6$ ,  $b=240.8$ , and  $c=121.6 \text{ Å}$ . The enzyme is composed of two identical subunits, each with a molecular weight of 39808 (366 amino acid residues). Assuming that there is one dimeric molecule per asymmetric unit,  $V_m$  was estimated to be  $3.07 \text{ Å}^3/\text{dalton}$ , which is reasonably within the range of  $1.6$  to  $3.6 \text{ Å}^3/\text{dalton}$ . The volume occupied by the solvent was calculated to be 60 % of the unit cell. In order to obtain the different crystal forms, we are now examining the crystallizing conditions.

# HIGH RESOLUTION DATA COLLECTION FOR THE COMPLEX OF SUBTILISIN BPN' WITH *STREPTOMYCES* SUBTILISIN INHIBITOR

Yasuo TAKEUCHI, Hiroyuki KURIHARA, Kazuo NAKAMURA, Yukio MITSUI

Faculty of Pharmaceutical Sciences, University of Tokyo, Hongo, Tokyo 113

## Introduction

The crystal structure of the complex of a bacterial alkaline serine protease, subtilisin BPN', with its proteinaceous inhibitor SSI (*Streptomyces* subtilisin inhibitor) was solved at 2.6Å resolution<sup>1)</sup>. Compared with other similar complexes involving serine proteinases of the trypsin family, the present structure is unique in several respects. The inhibition of subtilisin by SSI occurs when one subunit (I) of SSI inhibits one molecule (E) of subtilisin forming an E<sub>2</sub>I<sub>2</sub> complex. To obtain the data set at a higher resolution, the data collection for the native crystal (space group I222, a=77.2Å, b=185.9Å, c=69.5Å) was undertaken using the SR sources and the macromolecule-oriented Weissenberg camera devised by Sakabe<sup>2)</sup>.

## Experimental

The experiments were carried out using the Sakabe's Weissenberg camera associated with BL6A. The wavelength was set to 1.04Å. The sample was cooled at about 15°C. Two separate crystals were mounted, one with its b\*-axis and the other with its c\*-axis, coinciding with the rotation axis of the camera. Experimental conditions of data collection are shown in Table 1. The diffraction image was recorded on 26 Imaging Plates and the intensities were collected up to 1.8Å resolution. The reflections were processed using program WEIS<sup>3)</sup>.

## Results

The scaling between Imaging Plates was carried out using program SCALE. Rsym was 4.72% and 4.75% for the data sets taken around the b\*- and c\*-axes respectively. The merging R factor between the two data sets was 5.56% for 28118 independent reflections. The Rsym values are shown in Table 2. The refinement is now being carried out using this data set.

On the other hand the relative difference (RF) between the 1.8Å synchrotron and the 2.6Å Rigaku AFC-4 (45kV, 24mA) data sets were 6.09% for the b\*-axis data set and 7.11% for the c\*-axis data set and 6.02% for the two-axes-merged data set (Fig.1).

## Acknowledgment

We thank Prof. N. Sakabe for cooperating in the experiment using the Sakabe's Weissenberg camera.

## References

- 1) S. Hirano, H. Akagawa, Y. Mitsui and Y. Iitaka, *J. Mol. Biol.*, **178**, 389 (1984)
- 2) N. Sakabe, *J. Appl. Cryst.*, **16**, 542 (1983)
- 3) T. Higashi, *J. Crystallogr. Soc. Japan*, **28**, 356 (1986) (in Japanese)

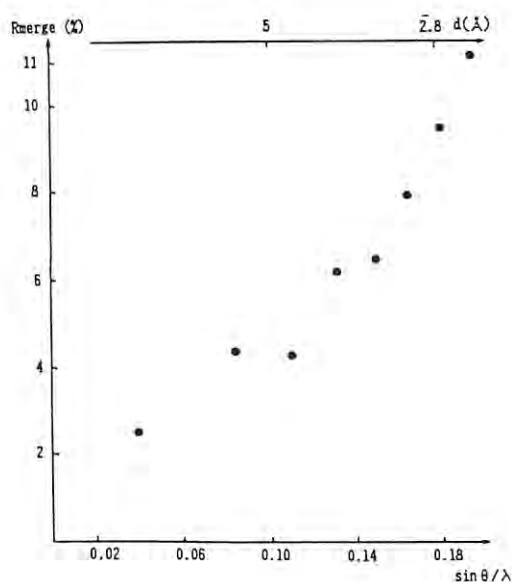
Table 1. Experimental conditions of data collection  
(film below is actually Imaging Plate)

Crystal	1	2
Size of crystal (mm)	0.35(a) × 0.65(b) × 0.1(c)	0.4(a) × 0.75(b) × 0.12(c)
Rotation axis	b *	c *
Beam current (mA)	172-167	265-249
Collimator aperture	0.3mm × 0.3mm	
Crystal-to-film distance	430 mm	
Oscillation angle ω (deg) / film	8.0	9.0
ω-Rotation/film movement (deg/mm)	4.0	1.5
Number of oscillations / film	5	3
ω-scan speed (deg/sec)	2.0	2.0
Number of films	13	13
Total exposure time (sec)	520	351

Table 2. The Rsym values of processed data sets

Resolution range(Å)	15.0	7.5	5.0	3.8	3.0	
The b*-axis data set	2.6%	3.0	3.9	3.8	5.6	10.5
The c*-axis data set	2.7	2.9	3.8	4.1	5.1	8.7
The two-axes-merged data set	3.2	3.4	4.8	4.9	6.1	10.1

Fig. 1. Plot of the relative difference (RF) between the 1.8 Å synchrotron and the 2.6 Å AFC-4 data sets vs. resolution range.



## CRYSTAL STRUCTURAL STUDIES OF BIOLOGICAL MACROMOLECULAR ASSEMBLY

Tomitake TSUKIHARA, Yukio YOKOTA, Kazuhiko TAKAHASHI, Masami OHTA, Toshio ABE, Keiichi FUKUYAMA\*, Shinya YOSHIKAWA\*\* and Atsushi NAKAGAWA\*\*\*

Faculty of Engineering, Tottori University, Tottori 680, \*Faculty of Science, Osaka University, Toyonaka 560, \*\*Himeji Institute of Technology, Shosha, Himeji 671-22, and \*\*\*KEK, National Laboratory for High Energy Physics, Oho-machi, Tsukuba, Ibaraki 305

Introduction

A spherical plant virus, tobacco necrosis virus (TNV), consists of a single-stranded RNA of molecular weight about  $1.3 \times 10^6$  and 180 copies protein subunits, which are arranged in a T=3 icosahedral surface lattice (1). High-resolution X-ray analyses of spherical viruses have shown not only that every virus possesses a common structural domain, but also that the variation of the polypeptide folding in each virus is important in the function of the viral shell (2-4). We have been initiated crystal structural studies of TNV to elucidate its structure-function relationship. Propagation, purification and crystallization of the virus have been reported (5). TNV is crystallized into the space group of  $P4_232$  with the unit cell dimension  $a = 338 \text{ \AA}$ .

Cytochrome *c* oxidase is the key enzyme catalyzing the reduction of dioxygen to water in the mitochondria (6). It is an integral protein of the inner membrane, where it receives electrons from a reduced cytochrome *c*, converts  $O_2$  to a water on the inside surface, and pumps protons from inside to outside (7). The heart protein consisting more than six polypeptide subunits was isolated from bovine heart muscle by using the detergent (8). A detail understanding of enzyme structure is required for adequate elucidation of structure-function relationship. The enzyme was crystallized in the shape of hexagonal bipyramid. The crystals belong to the space groups  $P6_3$  or  $P6_4$  with cell dimensions,  $a=b=174.5 \text{ \AA}$ ,  $c=282.2 \text{ \AA}$ ,  $\alpha=\beta=90^\circ$ , and  $\gamma=120^\circ$  (8). X-ray diffraction experiment is described in the present paper.

Experimental

All the X-ray experiments were carried out at the BL6A2 by using Weissenberg camera of which radius is 430mm. Diffraction intensities were recorded on the imaging plate of  $40 \times 20 \text{ cm}^2$  (Fuji Film Co. Ltd.). The wave length of X-ray was  $1.488 \text{ \AA}$ .

**TNV** A crystal was mounted in a capillary to rotate about [111] axis and total of  $31.5^\circ$  was collected by 21 serial Weissenberg photographs with an oscillation range of  $1.62^\circ$ . Individual plates were overlapped by  $0.12^\circ$ . Exposure period for each shot was 65 sec. and the crystal was translated after every seven exposure to avoid deterioration of diffraction pattern. Intensities were processed by a program of Higashi (9). Total of 5,695 reflections, 85% of the data in the range of  $8 \text{ \AA}$  resolution, were obtained at the accepting criteria,  $F^2 > 3\sigma(F^2)$  and whole reflection.

**Cytochrome *c* oxidase** A crystal sealed in a glass capillary was visually aligned under the microscope to rotate about the *c* axis. The crystal was exposed for 400 sec. and oscillated through  $4^\circ$ .

Results and Discussions

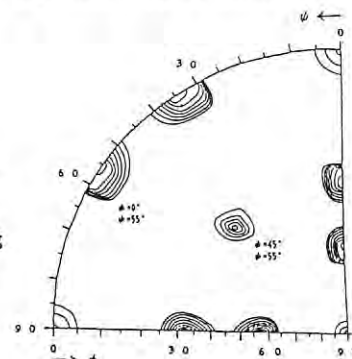
**TNV** Fast rotation function (10) was calculated to confirm orientation of the virus in the unit cell. The unit cell contains two virus particles, 120 icosahedral asymmetric units, and the space group has 24 equivalent points. Thus, all the crystallographic 2- and 3- fold axes must coincide with the icosahedral 2- and 3- fold axes, respectively. A stereographic projection of the rotation function corresponding to  $\chi=72^\circ$  is given in Fig.1, where contours are drawn at an equal interval of 2 beginning at 5 in an arbitrary scale. The rotation function elucidates the orientations of 5-fold axes, which consistent with those expected from the packing of the icosahedral particles in the unit cell.

**Cytochrome *c* oxidase** A clear diffraction pattern was observed as far as  $8 \text{ \AA}$  resolution. It is the highest resolution among crystals of membrane proteins from eukaryotes.

References

- (1) R.E.F. Matthews (1979). *Intervirology*, **12**, 252
- (2) M.G. Rossmann, C. Abad-Zapatero, M.R.N. Murthy, L. Lijas, T.A. Jones & B. Strandberg (1983). *J. Mol. Biol.*, **165**, 711-736
- (3) J.M. Hogle, M. Chow & D.J. Filman (1985). *Science*, **229**, 1358-1365.
- (4) M.M. Roberts, J.L. White, M.G. Grutter & R.M. Burnett (1986). *Science*, **232**, 1148-1151
- (5) K. Fukuyama, S. Hirota & T. Tsukihara (1987). *J. Mol. Biol.* **196**, 961-962
- (6) W.S. Caughey, W.J. Wallace, J.A. Volpe & S. Yoshikawa (1976). in *The Enzymes*, ed. P.D. Boyer (Academic press, New York), 3rd Ed., Vol. 13C, pp. 299-344
- (7) M. Wikstrom, K. Krab & M. Saraste (1981). *Cytochrome Oxidase - A Synthesis* (Academic press, New York)
- (8) S. Yoshikawa, T. Tera, Y. Takahashi, T. Tsukihara & W.S. Caughey (1988). *Proc. Natl. Acad. Sci. USA*, **85**, 1354-1358
- (9) T. Higashi (1986). *J. Crystallogh. Soc. Japan* (in Japanese), **28**, 356-363
- (10) R.A. Crowther (1972). in *The Molecular Replacement Method*, ed. M.G. Rossmann, Gordon & Breach, New York, pp. 173-178

Fig.1 Stereographic projection of the rotation function of TNV corresponding to  $\chi=72^\circ$ .





## DIFFRACTION EXPERIMENTS OF HYDROGENASE AT TWO WAVELENGTHS II

Yoshiki Higuchi, Kiyoshi Fujimoto, Yukio Morimoto, and Noritake Yasuoka

Basic Research Laboratory, Himeji Institute of Technology,  
2167 Shosha Himeji Hyogo 671-22INTRODUCTION

Hydrogenase is an enzyme which catalyzes reversible dehydrogenation of molecular hydrogen. All the hydrogenases so far isolated and characterized are iron-sulfur proteins, but flavin, nickel, copper, and/or selenium have been reported to be detected in some hydrogenases. The hydrogenase (hydrogen : ferricytochrome c3 oxidoreductase, EC 1.12.2.1) from *Desulfovibrio vulgaris* Miyazaki F (DvMF) solubilized by trypsin digestion and purified has molecular weight of 89000 (subunits:59000+28000) and is reported to have two or three [4Fe-4S] type clusters as unique cofactors. An anomalous dispersion of X-ray by heavy atoms in protein molecules may give useful information to locate these atoms, because the anomalous scattering power depends on the wavelength of X-ray used. X-ray from synchrotron radiation (SR) is suitable for this purpose, since any X-ray of desired wavelength is easily obtained. Here we described the our attempt to determine the active centers of hydrogenase crystal from (DvMF) by multi-wavelength diffraction study.

Experimental and Results

Membrane-bound hydrogenase was solubilized by trypsin digestion from the wet cells of DvMF bacterium. The protein was isolated<sup>1</sup> and purified<sup>2</sup> as described before. Single crystals ( $P2_12_12_1$   $a=102.1$ ,  $b=126.8$   $c=66.9\text{\AA}$ ) of freshly prepared hydrogenase were obtained by sitting-drop vapor diffusion method from 20% (w/w) polyethylene glycol 1000 buffer solution (25mM Tris-HCl, containing 0.05%  $\text{NaN}_3$  pH=7.5). X-ray intensity data were collected at 10°C using a Weissenberg camera designed for macromolecular crystallography by Sakabe et al<sup>3</sup> ( $r=430.5\text{mm}$ ) installed in BL-6A2. The wavelengths of x-ray used were 1.74Å (this is a wavelength near absorption edge of Fe atom) and 1.20Å ( $f' = 0$ ) from SR of National Laboratory for High Energy Physics. The diffraction patterns were recorded on Fuji Film 'Imaging Plate' (20 X 40cm), and read out by a Fuji Film BA-100. The hydrogenase crystal of 0.4X0.3X1.0mm was sealed in glass tube, and mounted on goniometer head, being crystal c-axis parallel to the spindle axis of the camera. Two sets of intensity data using two wavelengths of X-ray were collected from the different position of the same crystal moving the crystal by 0.5mm along the spindle axis. The experimental conditions are listed in Table I. The diffraction patterns on Imaging Plate were processed by program WEIS developed by Higashi et al.<sup>4</sup> in order to obtain indexed intensity data. 22018 of Bijvoet pair data ( $h k l$  and  $h k -l$ ) have been collected from 7 Weissenberg photographs using x-ray of 1.74Å. On the other hand, 42094 of data have been obtained from 10 photographs at 1.20Å. In order to reduce erroneous measurement of the reflections,

intensity data which have the relative difference with  $(F - \langle F \rangle) / \langle F \rangle > 0.2$  were rejected during the merging process. R-factors of merging ( $R_{\text{MERG}}$ ), anomalous difference between data from 1.74Å and 1.20Å ( $R_{\text{ANO}}$ ), and Bijvoet difference ( $R_{\text{BIP}}$ ) are shown in Table II. Patterson map calculated at 6Å with coefficient of  $(F(1.74\text{\AA}) - F(1.20\text{\AA}))^2$  reveal six candidates of the positions of the active centers, which satisfy the consistency among three Harker sections. Phasing process using these candidates of the positions of Fe-S clusters is now in progress.

Table I  
Experimental Condition of Data Collection

Wavelength(Å)	1.74	1.20
Beam current(mA)	225-203	135-126
Crystal rotation axis	$c^*$	$c^*$
Oscillation angle( $\omega$ :deg)	16.05	10.80
Film moving distance(d:mm)	10.7	7.2
Ratio of $\omega$ and d	1.5	1.5
Repeat of oscillation	30	5
Rotation speed of $\omega$ (deg/s)	2.0	2.0
Exposure time (s)	481.5	54
Number of film	7	10

Table II  
Some R-factors for intensity data (%)

	$R_{\text{MERG}}$	$R_{\text{BIP}}$
1.20 Å	6.61	4.15
1.74 Å	6.54	4.27
$R_{\text{ANO}}(1.74\text{\AA} - 1.20\text{\AA})$	6.46	

$$R_{\text{BIP}} = \sum |I(+)-I(-)| / \sum \langle I \rangle \quad \text{Bijvoet pairs}$$

$$R_{\text{ANO}} = \sum |F(1.74\text{\AA}) - F(1.20\text{\AA})| / \sum \langle F \rangle$$

$$R_{\text{MERG}} = \sum |I - \langle I \rangle| / \sum \langle I \rangle \quad \text{merged data}$$

We are indebted to Prof. Noriyoshi Sakabe, Mr. Atsushi Nakagawa Dr. Kiwako Sakabe and Dr. Tsuneyuki Higashi for their technical advice and use of computer programs. We also thank Dr. Keiichi Namba in Houtani Project, ERATO, for use of a Fuji Film BA-100 system.

References

- 1) T. Yagi, K. Kimura, H. Daidoji, F. Sakai, S. Tamura and H. Inokuchi, *J. Biochem.* (Tokyo), **79**, 661 (1976)
- 2) Y. Higuchi, N. Yasuoka, M. Kakudo, Y. Katsube, T. Yagi and H. Inokuchi, *J. Biol. Chem.*, **262**, 2823 (1987)
- 3) N. Sakabe, *J. Appl. Cryst.*, **16**, 542 (1983)
- 4) T. Higashi, N. Sakabe, *The report for a Grant-in-Aid for Scientific Research from Ministry of Education*, **52** (1984)

# PHASE DETERMINATION OF CYTOCHROME *c553* BY MULTI-WAVELENGTH ANOMALOUS DISPERSION METHOD

Atsushi NAKAGAWA<sup>1)</sup>, Yoshiki HIGUCHI<sup>2)</sup>, Noritake YASUOKA<sup>2)</sup>,  
Yukiteru KATSUBE<sup>3)</sup>, Tatsuhiko YAGI<sup>4)</sup>

<sup>1)</sup>Photon Factory, National Laboratory for High Energy Physics, Oho, Ibaraki 305

<sup>2)</sup>Basic Research Laboratory, Himeji Institute of Technology, Shosha, Himeji, Hyogo 671-22

<sup>3)</sup>Institute for Protein Research, Osaka University, Yamada-oka, Suita, Osaka 565

<sup>4)</sup>School of Education, Shizuoka University, Ohya, Shizuoka, Shizuoka 422

## Introduction

Cytochrome *c553* is an electron transfer protein in the metabolism of sulfate-reducing bacterium<sup>1)</sup>. Cytochrome *c553* from *Desulfovibrio vulgaris* Miyazaki F contains one polypeptide chain including 79 amino acid residues and one *c*-type heme group.

The crystal system of this protein belongs to tetragonal,  $a=b=42.7\text{\AA}$ ,  $c=103.4\text{\AA}$  and its space group is  $P4_32_12$ . It contains one molecule per asymmetric unit<sup>2)</sup>. This crystal diffracts higher than 1.5 Å resolution using SR-ray. But according to the condition of crystallization, it had been very hard to get good isomorphous derivatives.

In this experiment, we have tried to solve the "PHASE PROBLEM" by multi-wavelength anomalous dispersion method(MAD).

## Experiment

All data sets for MAD phasing method were collected at BL-6A2. The light source of this beamline is a normal bending magnet. And SR-ray is focused and monochromatized by cylindrical-curved fused quartz mirror and cylindrical-bended asymmetrical cut Si(111) monochromator. All diffraction data were collected by the Weissenberg camera for Macromolecular Crystallography<sup>3)</sup> and Imaging Plate. Data reduction was performed using the program system WEIS<sup>4)</sup>.

F-data sets of native crystals were collected at four different wave length X-rays.

1.  $F_P(\lambda_1)$  :  $\lambda_1=1.040\text{\AA}$  ( $\Delta f'=0.197$ ,  $\Delta f''=1.664$ )
2.  $F_P(\lambda_2)$  :  $\lambda_2=1.380\text{\AA}$  ( $\Delta f'=-0.440$ ,  $\Delta f''=2.678$ )
3.  $F_P(\lambda_3)$  :  $\lambda_3=1.743\text{\AA}$  ( $\Delta f'=-9.211$ ,  $\Delta f''=3.951$ )
4.  $F_P(\lambda_4)$  :  $\lambda_4=1.746\text{\AA}$  ( $\Delta f'=-6.299$ ,  $\Delta f''=0.469$ )

Five crystals, including both *a*- and *c*-axis rotation, were used to get F-data at 1.38Å. Other three data sets were collected using only one crystal at each wavelength, rotating along *a*-axis. But for later cases, rotation angle of each crystal was more than four times rotation range of independent region to reduce some statistical errors. To reduce other systematic errors, absorption and so on, each data set was corrected by absorption correction described by Katayama *et.al.*<sup>5)</sup> or local scaling method.

## Result and Discussion

Atomic parameters corresponding to  $\lambda_3$  and  $\lambda_4$  data were refined by centric refinement method, same as isomorphous replacement technique. Assuming that  $F_P(\lambda_1)$  was native and  $F_P(\lambda_3)$ (or  $F_P(\lambda_4)$ ) was derivative, and  $\Delta f'$  term was treated just same as isomorphous difference. As each measurement wavelength was determined by using absorption of Au, Ni and Fe foil, we tried to determine  $\Delta f'$  value from centric refinement method. Atomic parameters of  $\lambda_2$  data were refined using large  $\Delta F_P(\pm)$  reflections<sup>6)</sup>.

Calculation of phases by this experiment was according to Blow and Crick's best phase method<sup>7)</sup>. Average value of figure of merit was 0.597 for 2.2Å resolution data(4421 refln.).

The electron density map calculated by this method has good quality to trace main chain folding.

## Acknowledgment

The authors thank to Dr. K.Namba in ERATO for using BA-100, the Imaging Plate reading system.

The authors also thank to Prof. N.Sakabe in Photon Factory for his helpful suggestion.

## Reference

- 1) T.Yagi (1979)  
*Biochim. Biophys. Acta*, 548, 96
- 2) A.Nakagawa *et.al.* (1986)  
*J. Biochem.*, 99, 605
- 3) N.Sakabe (1983)  
*J. Appl. Cryst.*, 16, 542
- 4) T.Higashi (1989)  
*J. Appl. Cryst.*, in press
- 5) C.Katayama, N.Sakabe, K.Sakabe (1972)  
*Acta Cryst.*, A28, 293
- 6) W.Hendrickson, M.Teeter (1981)  
*Nature*, 290, 107
- 7) D.Blow, F.Crick (1959)  
*Acta Cryst.*, 12, 794

## X-RAY SOLUTION SCATTERING STUDIES ON SOLUBILIZED BACTERIORHODOPSIN III.

Mikio KATAOKA<sup>1</sup>, Masayoshi NAKASAKO<sup>1</sup>, Fumio TOKUNAGA<sup>1</sup>  
Tatzuo UEKI<sup>2</sup>, Yuzuru HIRAGI<sup>3</sup> and Katsumi KOBAYASHI<sup>4</sup>

1. Faculty of Science, Tohoku University, Sendai, Miyagi 980
2. Faculty of Engineering Science, Osaka University, Toyonaka, Osaka 560
3. Institute of Chemical Research, Kyoto University, Uji, Kyoto 611
4. Photon Factory, National Laboratory for High Energy Physics, Oho-machi, Tsukuba, Ibaraki 305

## INTRODUCTION

Bacteriorhodopsin (bR) is a sole integral membrane protein in purple membrane (PM) of *Halobacterium halobium*. As well as other membrane proteins, bR also solubilized with non-ionic detergents in order to investigate several properties and the experiments needs the information about the aggregation state of bR after solubilization. We studied the aggregation state of solubilized bR(sol-bR) by Small-Angle X-ray Scattering (SAXS) technique with contrast variation method and the extended one; combination method of heavy atom labeling and contrast variation<sup>1)</sup>. Obtained structure parameters strongly suggested that bR existed as a trimeric form in the solubilized state, and also that the trimer orientation was distorted during the solubilization process<sup>1,2)</sup>.

To examine these results in higher resolution, we recorded the Moderate-Angle X-ray Scattering (MAXS) from sol-bR.

have some 'undulation' around  $S=0.1\text{\AA}^{-1}$  because of 3-fold symmetry in trimer. However, the observed maximum was single one; the maximum indicated the existence of monomer rather than trimer in solubilized state. We think this inconsistency about aggregation state as follows. Structure parameters (square of first moment of electron density fluctuation and average distribution of bound iodine atoms in solubilized iodinated bR<sup>1)</sup>) suggests that hydrophobic interactions between protomers are weakened and their orientation in bR trimer loses the 3-fold symmetry with maintaining the hollow cylindrical structure during the solubilization. Thus, the orientation between secondary structures also loses the character of trimer and the maximum do not have any 'undulation'.

Through SAXS and MAXS experiments, we concluded the bR trimer in solubilized state as a distorted and swelled one.

## EXPERIMENTAL

Sol-bR was prepared according to the previous issue<sup>3)</sup>. The sample was concentrated by ultra-filtration membrane up to 30 mg/ml to record the MAXS with better S/N ratio.

X-ray scattering experiment was performed with SAXES diffractometer at BL-10C. Sample-to-detector distance was about 80 cm and exposure time was 900 sec. Detector was off-seted to record the higher scattering angle region.

## RESULTS

Fig. 1 shows a MAXS profile from sol-bR. The characteristic two scattering maxima were observed around  $S=0.025\text{\AA}^{-1}$  and  $S=0.10\text{\AA}^{-1}$ .

As is usually the case of oligomeric proteins, scattering maxima in the region of  $S<0.05\text{\AA}^{-1}$  are caused by the interference between subunits<sup>4)</sup>. Thus, we thought the first maximum as that caused by the hollow cylindrical arrangement of protomer in bR trimer, according to the results from SAXS experiments. However, the peak position suggested swelling of bR trimer in comparison with the native one.

In the region of  $0.05<S<0.15\text{\AA}^{-1}$ , scattering maxima originate from the interferences between secondary structures;  $\alpha$ -helix and  $\beta$ -sheet. For example, globin folding in myoglobin and haemoglobin exhibits a characteristic scattering maxima in this region<sup>4,5)</sup>.

bR monomer has 7 rod like structure considered to be  $\alpha$ -helices and these rods oriented in parallel with each other, so the second scattering maximum is interpreted as a interference of secondary structure in bR trimer. If bR trimer in solubilized state is perfectly the same as in PM, the scattering maximum should

## REFERENCES

- 1) Kataoka et al. J.Appl.Cryst., 21, in press
- 2) Kataoka et al. PF Activity Report #5, 255
- 3) Kataoka et al. PF Activity Report #4, 213
- 4) Ueki et al. J.Biochem., 99, 1127 (1986)
- 5) Ibel & Stuhmann. J.Mol.Biol., 93, 255 (1975)

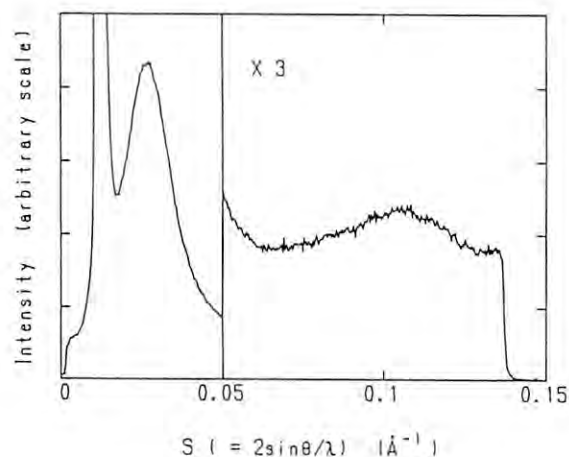


Fig. 1

Net Moderate-Angle X-ray Scattering profile of solubilized bR.



## QUARternary STRUCTURE CHANGE OF TRYPTOPHANASE OBSERVED BY SMALL-ANGLE X-RAY SCATTERING

Eui Ho KIM<sup>1)</sup>, Yuzuru HIRAGI<sup>1)</sup>, Tsuneo ODA<sup>2)</sup>, Masanobu TOKUSHIGE<sup>2)</sup>, Kanji KAJIWARA<sup>3)</sup>, Hiroshi URAKAWA<sup>3)</sup>, Yoh SANO<sup>4)</sup>, Tatsuo UEKI<sup>5)</sup>, Mikio KATAOKA<sup>6)</sup> and Katsumi KOBAYASHI<sup>7)</sup>

- 1) Institute for Chemical Reserch, Kyoto University, Uji, Kyoto 611
- 2) Faculty of Science, Kyoto University, Sakyo-ku, Kyoto 606
- 3) Faculty of Engineering and Design, Kyoto Institute of Technology, Masugasaki, Sakyo-ku, Kyoto 606
- 4) National Institute of Agrobiological Resources, Yatabe, Ibaraki 305
- 5) Faculty of Engineering Science, Osaka University, Toyonaka, Osaka 560
- 6) Faculty of Science, Tohoku University, Sendai, Miyagi 980
- 7) Photon Factory, National Laboratory for High Energy Physics, Tsukuba, Ibaraki 305

## INTRODUCTION

Tryptophanase is an enzyme which catalyses the decomposition of L-tryptophane,  $\alpha$ ,  $\beta$ -elimination and  $\beta$ -replacement reaction. The enzyme requires a pyridoxal phosphate (PLP) and monovalent cations such as  $K^+$ ,  $NH_4^+$  for its activity. It is composed of four identical subunits with the molecular weight of 55,000. In this report, the investigation was made on the effect of temperature, potassium ion and PLP on the quarternary structure of tryptophanase by means of small-angle X-ray scattering (SAXS).

## EXPERIMENTAL

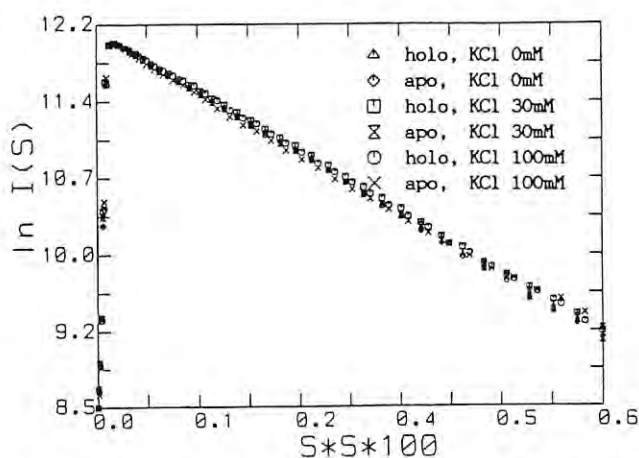
Tryptophanase was from *Escherichia coli* B/1t7-A. The concentration of protein was 10mg/ml and the pH of the solution was adjusted to 7.8. 0.67mM PLP was added to the holoenzyme samples. The concentrations of KCl were 0, 30, 100 and 500mM and the temperature was changed from 5°C to 20°C. The SAXS measurements were performed with a SAXES installed at the BL-10C.

## RESULTS AND DISCUSSION

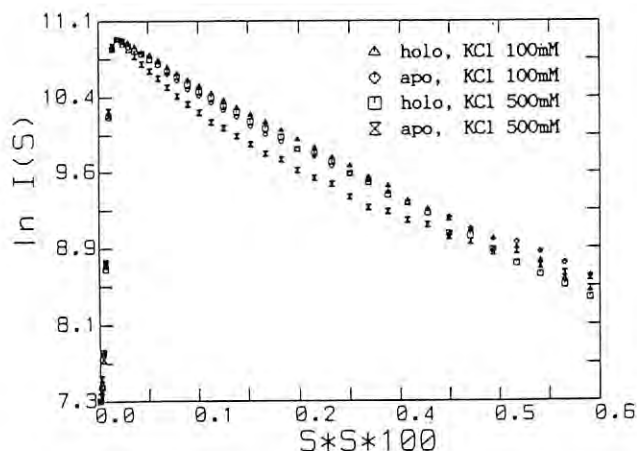
When the concentration of KCl is below 30mM, the radii of gyration ( $R_g$ ) of tetramer are evaluated as  $38.0 \pm 1.0 \text{ \AA}$  from Guinier approximation in either case with or without PLP. The  $R_g$  value of the holoenzyme is almost independent of the solution condition. On the other hand, Guinier plots of the apoenzyme exhibit that the system is polydisperse when increased the KCl concentration at 5°C. (Fig.1 (a), (b))

These results suggest that high concentration potassium ion make the quarternary structure of the apoenzyme instable and that the dimer and the aggregate of the tetramer are formed. Therefore cation works in two ways, i.e., activation and

instabilization of the enzyme. The structure of holoenzyme is rarely affected from potassium ion, suggesting that PLP binds to the enzyme and stabilizes its structure.



(a) 20°C, KCl concentration below 100mM.



(b) 5°C, KCl concentration above 100mM.

Fig.1 Guinier Plots of Tryptophanase



CONFORMATIONAL ANALYSIS OF BROKEN RODLIKE CHAINS: II.  
CONFORMATIONAL ANALYSIS OF POLY(D-GLUTAMIC ACID) IN AQUEOUS  
SOLUTION BY SMALL ANGLE X-RAY SCATTERING

Yoshio MUROGA<sup>1</sup>, Hiroyuki TAGAWA<sup>2</sup>, Yuzuru HIRAGI<sup>3</sup>, Tatzuo UEKI<sup>4</sup>,  
Mikio KATAOKA<sup>5</sup>, Yoshinobu IZUMI<sup>6</sup> and Yoshiyuki Amemiya<sup>7</sup>

- 1) Faculty of Engineering, Nagoya University, Chikusa-ku, Nagoya, Aichi 464
- 2) Faculty of Science and Technology, Nihon University, Chiyoda-ku, Tokyo 101
- 3) Institute for Chemical Research, Kyoto University, Uji, Kyoto 611
- 4) Faculty of Engineering Science, Osaka University, Toyonaka, Osaka 560
- 5) Faculty of Science, Tohoku University, Sendai, Miyagi 980
- 6) Faculty of Science, Hokkaido University, Sapporo, Hokkaido 060
- 7) KEK, National Laboratory for High Energy Physics, Oho, Tsukuba, Ibaragi 305

### Introduction

The conformation of poly(glutamic acid), PGA, in a helix-to-coil transition region is supposed to consist of a mixture of helical rods and random coils, but the detail has not yet been clarified. In this study, the conformations in three conformational regions are analyzed by small angle X-ray scattering (SAXS), by comparing observed scattering curves with theoretical ones.

2. (1) The deg. of neutralization (*i*) of PGA (Sample-A, -B and -C) for SAXS were adjusted so that the sample may take different conformations: helix form (Sample-A), a mixture of helix and coil forms (-B) and a random-coiled form (-C). The helix content of Sample-B was estimated to be 56 % according to the analysis of the potentiometric titration curve<sup>1</sup>, and the polymer concentrations were 0.53 (g/dL).

### Experimental

The SAXS was carried out using a synchrotron radiation as an X-ray source, set up in the Photon Factory of the National Lab. for High Energy Phys. at Tsukuba.

### Results and Discussion

The observed scattering behaviors of PGA are the one characteristic of ordinary polyelectrolytes solutions: a maximum appears in a low angle region. Therefore, the discussion is given to the data above *ca.*  $0.08 \text{ \AA}^{-1}$  in *h*. After the observed scattering intensities were corrected for the cross section of a polymer chain, they are compared with corresponding theoretical curves, which have been derived in the reference 2. The observed scattering curve of Sample-A is compared with a theoretical one for a freely hinged rod (Fig.1). The rod number and the rod length can be estimated to be 12 and *ca.* 45 Å, respectively. Here, an arrow indicates the value of *h*, above which the normalized function becomes insensitive to the molecular weight. In a similar way, it is shown that the conformation of Sample-B can be well represented by a model of several rods joined by flexible coils (Fig.2), whereas the scattering curve of Sample-C is far from the Debye function.

### References

- 1) M. Nagasawa, A. Holtzer, JACS, 86, 538 ('64).
- 2) Y. Muroga, Macromolecules, in press, 1988.

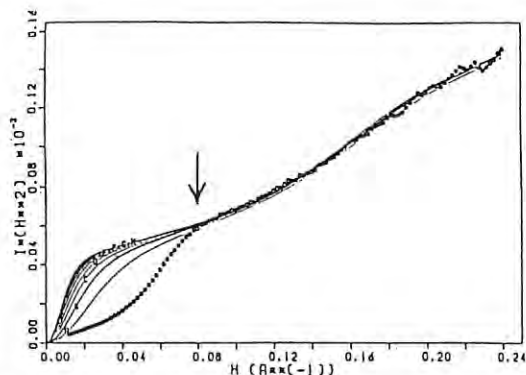


Fig. 1 Comparison between the observed Kratky plot of Sample-A and the normalized theoretical ones for freely hinged rods of contour length, *L*. *L* increases from 658 (A) to 5260 Å (H) with an increment of 658 Å. The rod length, *A*<sub>0</sub> = 45 Å.

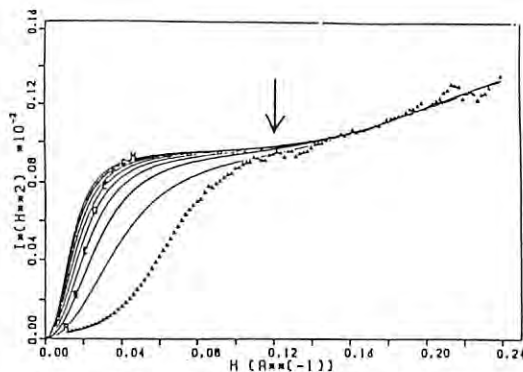


Fig. 2 Comparison between the observed Kratky plot of Sample-B and the normalized theoretical ones for broken rods joined by flexible coils with contour length *L*. *L* increases from 658 (A) to 5260 Å (H) with an increment of 658 Å. The rod length, *A* = 25 Å, *a* = 8 Å.

## MOLECULAR SHAPE OF 114-KILODALTON PEA PHYTOCHROME STUDIED BY X-RAY SOLUTION SCATTERING

Satoru TOKUTOMI<sup>1</sup>, Masayoshi NAKASAKO<sup>2</sup>, Jun SAKAI<sup>3</sup>,  
Mikio KATAOKA<sup>2</sup>, Fumio TOKUNAGA<sup>2</sup> and Masaki FURUYA<sup>3</sup>

<sup>1</sup>Division of Biological Regulation, National Institute for Basic Biology, Okazaki, 444

<sup>2</sup>Department of Physics, Faculty of Science, Tohoku University, Sendai, 980

<sup>3</sup>Plant Biological Regulation Laboratory, Frontier Research Programs, RIKEN, Wako, Saitama, 351-01

### Introduction

We have started the structural study of phytochrome, a photoreceptor chromoprotein in green plant for a variety of photomorphogenic responses, by small angle X-ray scattering (SAXS) and have reported a preliminary results in the Previous Report as follows. 114-kilodalton (kDa) pea phytochrome exists in a dimeric form with the molecular mass of 228 kDa. The radius of gyration ( $R_g$ ) of the molecule was determined as 53.8 Å by Guinier analysis, which is by far greater than the value calculated from a sphere with the molecular mass of 228 kDa. There are three possible explanations for this big discrepancy, (1) the molecular shape deviates from sphere greatly, (2) the average electron density is lower than that of standard soluble proteins, (3) the electron density is higher in the shell than in the core. In the present study, we examined these possibilities using the contrast variation technique. Furthermore, we have succeeded in figuring out the molecular shape of the 114-kDa phytochrome dimer.

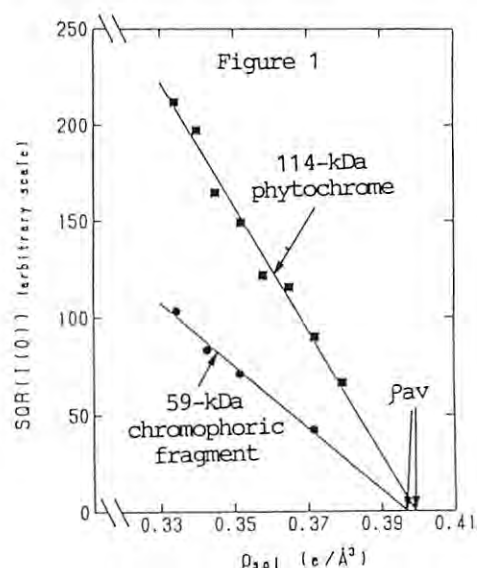
### Experimental and Results

SAXS was measured with SAXES at BL-10C. The details of the experimental conditions were described elsewhere (Biochim. Biophys. Acta 953 297-305, 1988). The contrast of the sample solution was varied by changing the concentration of sucrose in its solvent. The 114-kDa pea phytochrome consists of a 59-kDa chromophoric fragment domain and the remaining 55-kDa nonchromophoric fragment domain. The 59-kDa chromophoric fragment domain was obtained as a monomer fragment by tryptic digestion of the 114-kDa phytochrome dimer. The average electron densities ( $P_{av}$ ) of the 114-kDa pea phytochrome and its 59-kDa chromophoric fragment were obtained from the  $I(0)^2$  vs.  $\rho_{sol}$  plot, where  $I(0)$  was scattering intensity at 0 angle and  $\rho_{sol}$  was the electron density of the solvent.  $P_{av}$ 's were determined as shown in Figure 1 and were  $0.398 \pm 0.002$  and  $0.398 \pm 0.001$  e/Å<sup>3</sup> for the phytochrome and the chromophoric fragment, respectively, indicating that they have similar  $P_{av}$  to those of standard soluble proteins.

To obtain the informations regarding the spacial fluctuation of the electron density in the molecules, the results were analysed by the methods of Stührmann.  $R_g^2$  can be written as,

$$R_g^2 = R_c^2 + \alpha/\Delta\rho - \beta/(\Delta\rho)^2,$$

where  $\Delta\rho$  are the difference between  $P_{av}$  and  $\rho_{sol}$ .  $R_c$ ,  $\alpha$  and  $\beta$  are the radius of gyration of the molecular shape, the second and the square of the first moment, respectively.  $\alpha$ 's were calculated as  $-5.1 \pm 0.5$  and  $-12.7 \pm 0.5$  e/Å for the phytochrome and the chromophoric fragment, respectively. These negative values indicate that



the core of the molecules has higher electron density than the shell.  $R_c$ 's of the phytochrome and the fragment were calculated as  $53.7 \pm 0.2$  and  $38.1 \pm 0.3$  Å, respectively.  $R_c$  of the phytochrome was almost the same with its  $R_g$  at water contrast. These result showed that the molecular shape of the 114-kDa phytochrome dimer deviated from a sphere greatly, and that the size of the molecule is very large.

The molecular shapes of the 114-kDa phytochrome dimer and the 59-kDa chromophoric fragment were studied by constructing a model which gives the  $R_g$  of 54 Å and the best fit set of a  $\ln(I(S)/I(0))$  vs.  $S$  curve and a pair correlation function with those of the observed results, and also satisfies the requirements from the biochemical data. The molecular shape of the 59-kDa chromophoric fragment was best simulated by the oblate with the axial ratio of 1 : 5 (11Å, 55Å, 55Å) among the ellipsoids of revolution. Using this result and assuming the 2-fold axis in the dimer, the molecular shape of the 114-kDa phytochrome dimer was well simulated with two oblates (59-kDa chromophoric fragment domain) and two discs with the diameter of 65Å and the height of 20Å (55-kDa nonchromophoric fragment domain) shown in the Figure 2.

Figure 2



## IMPROVEMENT OF "SAXES" AND DEVELOPMENT OF DATA TREATMENT SOFTWARE

Tatzuo UEKI & Yoji INOKO	Faculty of Engineering Science, Osaka University, Toyonaka, Osaka 560
Mikio KATAOKA	Faculty of Science, Tohoku University, Sendai, Miyagi 980
Mamoru SATOH	Institute for protein Research, Osaka University, Suita, Osaka 565
Shuichi NOJIMA	Faculty of Engineering, Nagoya University, Nagoya, Aichi 454
Katsumi KOBAYASHI & Yoshiyuki AMEMIYA	Photon Factory, National Laboratory for High Energy Physics, Oho, Ibaraki 305

In the past few years, several improvement have been made on the small-angle X-ray scattering equipment for solution (SAXES) by the working group, mainly on the optics and the software of data acquisition and treatment. In the following, we will describe such work and the result (performance) in the present report.

Optics and beam transport

1. The monochromator (silicon crystal) on the upstream side has been attached with a cooling device, keeping the temperature of the circulating water at about 18 C. This device resulted in the thermal stability of the monochromator, i.e., the stability of the incident intensity flux upon specimen and hence contributed to the reduction of time for starting measurement after opening the BBS, to about one minute from about 15 minutes without the device.
2. We have put a new slit system about 200 cm upstream of the specimen guard slit system, at about 28 m from the X-ray source. This contributed drastically in two respects. The first is that it has reduced the level of the parasitic scattering from the guard slit in front of the specimen, to about 1/5 in the very small-angle region. Such a reduction made the measurement in small-angle region up to  $S$  ( $2\sin\theta/\lambda$ ) of better than  $0.001 \text{ \AA}^{-1}$ , that was not yet reached by any other SAXS equipment by SR over the world. In addition, this system resulted in very important aspect. We have suffered from the change of the parasitic scattering level when the X-ray source changes its position/direction in time. This change frequently made the data useless, sometimes up to two thirds of the total. The new system eliminated such a trouble and the measurements are presently proceeding efficiently than before.
3. The vacuum pipe system, between specimen and detector system, was replaced from the thick pipes of stainless steel to very light and thin pipes of aluminum alloy. As a result, the SAXES offers three settings of specimen-detector distance of 1,900, 850 and 500 mm, which can be rearranged easily by two persons with less time.
4. The extra beam line shutter has been installed in front of the specimen, outside the hutch. This may contribute to the thermal stability of the monochromator system in the occasion the hutch is opened without closing BBS. This is not presently controoled under the inter-lock system.

Specimen chamber

A temperature-jump specimen chamber was completed and has been used by the measurement of the structure of TMV particle. The stopped-flow chamber, which was completed in the early stage of SAXES development, has also been under service.

The data acquisition and treatment softwares

The data acquisition software, originally developed by one of the authors (M. K.), is now being remodelled mainly in the aim of easier use for the beginner. This will be used in the beam time starting January, 1989. The data treatment software, by using graphic terminal (Tamaha YGT 100), has also been developed, that provide the analysis of SAXS profiles in its first stage.



## STRUCTURAL ANALYSIS OF OLIGOMERIC PROTEINS IN SOLUTION

Tatzuo UEKI, Yoji INOKO, Mikio KATAOKA\*, Katsumi KOBAYASI\*\* and Shinji NITANI

Faculty of Engineering Science, Osaka University, Toyonaka, Osaka 560

\* Faculty of Science, Tohoku University, Aoba, Sendai, Miyagi 980

\*\* Photon Factory, National Laboratory for High Energy Physics, Oho, Ibaraki 305

## INTRODUCTION

Small-angle X-ray scattering (SAXS) provides structural information of an overall structure of particle in solution and, in this sense, SAXS is taken as one of physico-chemical techniques. In higher scattering angles, the scattering is much weaker, by a factor of 1/100 to 1/1000, as compared with the weak SAXS intensity. However, the scattering profile in this region has a very characteristic feature, not monotonous as SAXS. This scattering is pronounced for oligomeric proteins, and has been proved to be related to the arrangement of subunits in the particles, by the comparison of scattering profiles from myoglobin and hemoglobin (approximately taken as a tetramer of myoglobin) (1). From the profile, the spatial arrangement of subunits in particle may be deduced, and hence this method is taken as the structure analysis "in the level of molecule, not atom."

The present report describes a quantitative analysis of the method by using the scattering from monomer and tetramer of muscle aldolase.

## THEORETICAL BACKGROUND

The electron density  $\rho(\vec{r})$  of a particle can be written, if consists of single species, as

$$\rho(\vec{r}) = \rho_s(r) * \sum_i \delta(\vec{r} - \vec{r}_i)$$

where  $\rho_s(r)$  is the electron density of subunit and  $\vec{r}_i$  the position of the  $i$ -th subunit.

The scattering intensity from the particle is

$$I(S) = [f_s(S)]^2 \sum_i \sum_j \sin(2\pi S |\vec{r}_i - \vec{r}_j|) / (2\pi S |\vec{r}_i - \vec{r}_j|)$$

This expression is valid in the scattering range where subunits are taken as spherically symmetric. The first term in  $I(S)$  is the form factor of the subunit and the second the interference function that is related to the spatial arrangement of subunits in the particle.

Thus, if, by some way, we could extract the values of  $|\vec{r}_i - \vec{r}_j|$ , we may be able to reconstruct the arrangement of subunits in the particle, in the case of simple oligomers.

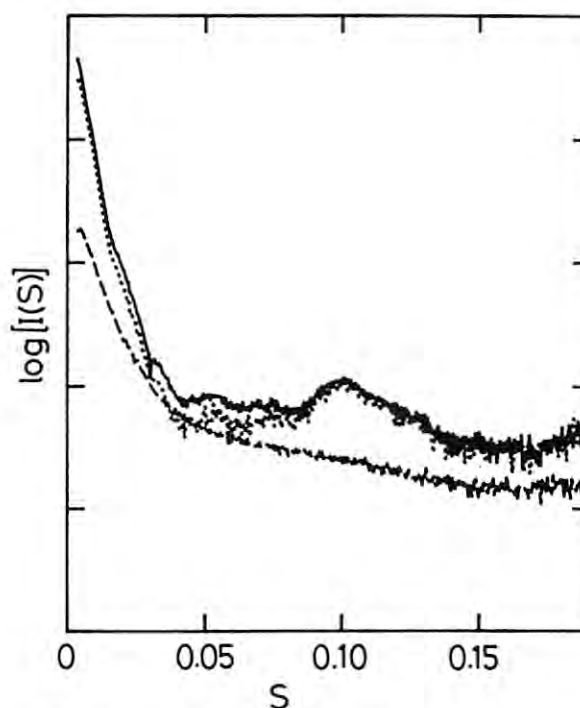
This analysis may be very important in the understanding of the structure-function relation of biological macromolecules, in the sense of movement of subunits in a particle if we carry out a time-resolved scattering experiments.

To apply this method, we have to measure the scattering profiles of whole particle,  $I(S)$ , and that of constituent subunit, the form factor. An enzyme, aldolase from muscle, was taken as a good example to testify such an analysis, since it consists of four subunits that are almost equal, and moreover, we can measure the profiles from native enzyme and subunit, separately, under different pH conditions.

## EXPERIMENTS AND RESULTS

The aldolase, one of important enzymes in the course of sugar metabolism in muscle, exists as a tetrameric form at pH higher than 5. It dissociates into subunits below pH 3. Such a behavior of the enzyme made the scattering experiments possible to obtain scattering profiles separately, needed for the analysis.

The X-ray scattering measurements were performed by the SAXES installed on BL-10C. The contrast variation experiments were carried out to yield the scattering of the "form" component from the total scattering by eliminating "internal" term. The scattering profiles from tetrameric and monomeric particles are shown in the figure. A preliminary analysis, as presented here, by using the total scattering profile, gives an approximate structure of aldolase in solution. It consists of four subunits, locating at the apexes of a deformed tetrahedron: the inter-subunit distances are 42 Å and 58 Å. This form suggests that the subunits are not in equivalent interaction in the molecule, as visualized by the crystal structure analysis (2).



solid line: aldolase (pH 5.4) 0% sucrose.  
dotted line: " (pH 5.4) 10% sucrose.  
broken line: subunit (pH 2.4) 0% sucrose.

1. Ueki et al. (1986) J. Biochem., 99, 1127.
2. Sygusch et al. (1987) PNAS, 84, 7846.



## STRUCTURAL BEHAVIOR OF TROPONIN-C UPON CALCIUM ION BINDING

Tetsuro Fujisawa, Tatzuo Ueki, Yoji Inoko, Mikio Kataoka<sup>+</sup>, Katsumi Kobayashi<sup>++</sup>

Faculty of Engineering Science, Osaka University, Toyonaka, Osaka, 560

<sup>+</sup> Faculty of Science, Tohoku University, Sendai, Miyagi, 980<sup>++</sup> KEK National Laboratory for High Energy Physics, Tsukuba, Ibaraki, 305

## INTRODUCTION

Troponin-C(Tn-C) is a calcium binding protein, which has four calcium binding sites. Two of these sites are high affinity sites, which also bind magnesium ion competitively. The other sites are calcium specific low affinity sites. We have already reported the calcium-induced structural change in the absence of magnesium ion (1,2). In order to clarify the change in physiological condition, we made SAXS experiments in the presence of magnesium ion.

Since Tn-C is believed to dimerize with increasing calcium concentration, we employed a series of dilute protein concentrations (below 10 mg/ml) of Tn-C for SAXS experiments for the purpose of minimizing the dimerization effect.

## RESULTS AND DISCUSSION

Fig. 1 shows the concentration dependency on forward scattering,  $I(0)/C$ , obtained by Guinier approximation. Circle and square designates data points for in the absence and presence of calcium ion, respectively. In the presence of calcium ion  $I(0)/C$  increases with increasing calcium ion, which suggests the existence of Tn-C dimer, while no aggregation was observed in the absence of calcium. In comparison to the scattering from lysozyme, we estimated molecular weight of 23,000(700) for Tn-C in the absence of calcium ion, which is analogous to that of 22,000(700) for Tn-C in the absence of magnesium ion.

Fig. 2 shows the concentration dependency on radius of gyration,  $R_g$ , of Tn-C. Symbols are used in same way as in Fig. 1. On extrapolation to zero concentration,  $R_g$  for Tn-C in the absence of calcium ion, was determined to be 24.3(0.2) Å, which is almost identical to  $R_g$  of 23.8(0.2) Å for Tn-C at pCa 6.5 in the absence of magnesium ion.

These facts supports the idea that the structure of Tn-C with two calcium ions does not deviate from that of Tn-C with magnesium ions.

## REFERENCES

- 1) T. Fujisawa, T. Ueki, Y. Inoko, & M. Kataoka (1987) in Photon Factory Activity Report, pp.263, KEK, Tsukuba.
- 2) T. Fujisawa, T. Ueki, S. Iida (1988) J. Biochem. to be submitted.

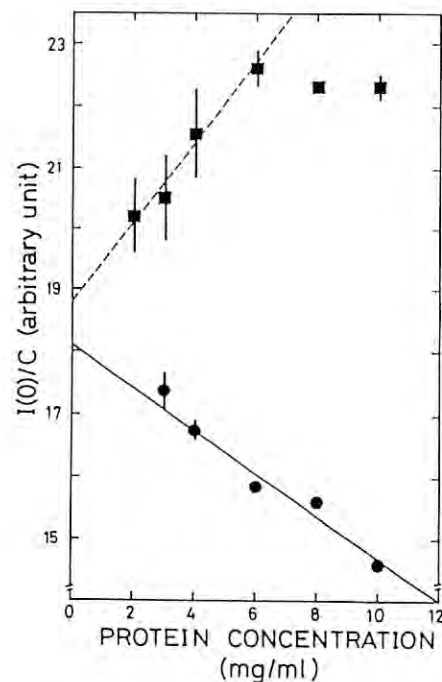


Fig. 1 Concentration dependency on forward scattering in the presence of magnesium ion.

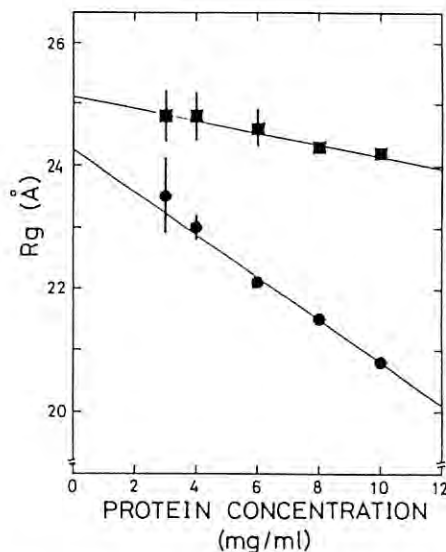


Fig. 2 Concentration dependency on radius of gyration of Tn-C.

INACTIVATION OF *BACILLUS SUBTILIS* SPORES BY MONOCHROMATIC X RADIATION  
WITH THE RESONANCE ENERGY OF PHOSPHORUS K-SHELL ABSORPTION

Nobuo MUNAKATA<sup>1)</sup>, Kotaro HIEDA<sup>2)</sup>, Hiroshi MAEZAWA<sup>3)</sup>, and Katsumi KOBAYASHI<sup>4)</sup>

1) Radiobiology Division, National Cancer Center Research Institute, Tokyo 104

2) Department of Physics, Rikkyo University, Tokyo 171

3) Department of Radiation Oncology, Tokai University, Isehara 259-11

4) Photon Factory, National Laboratory for High Energy Physics, Tsukuba 305

### Introduction

We have been engaged in a project to obtain the action spectra for inactivation and mutagenesis of *Bacillus subtilis* spores in the entire wavelength range of X and UV radiation<sup>1,2)</sup>. One of the aim of the project is to find out and focus upon particular wavelength regions where unique changes of the efficiency might occur. One of such regions of interest is around phosphorus K-shell absorption, since phosphorus atoms in the sugar phosphate linkage constitute the backbone of DNA strands. We therefore asked if the absorption by phosphorus K-shell electrons causes DNA damages which lead to inactivation of bacterial spores.

### Experimental

Experiments reported here were performed on two occasions in 1988. The beam line was equipped with a monochromator and a sample chamber designed for in vacuo irradiation. Suspension of three types of the spores, UVR (wild-type repair capability), UVS (*uvrA ssp*), and UVP (*uvrA ssp polA*) was spotted on membrane filter in a circle of 2mm diameter carrying  $5 \times 10^6$  spores per sample. The pieces of filter were attached to a metal holder which can carry up to 30 samples. The holder was moved vertically to assure the uniformity of fluence received by the samples. After irradiation, the spores were resuspended in water and colony-forming survival was determined as described<sup>1)</sup>.

### Results and Discussion

Survivals of three types of the spores were determined with monochromatic X radiation at three wavelengths, one of the energy corresponding to the peak resonance absorption (0.5763nm), of the lower energy (0.5779nm) and of the higher energy (0.5747nm). Survival curve was obtained by plotting the survival ( $N/N_0$ ) in log versus the exposure in kR. In all cases, exponential inactivation was observed in a whole range of the exposure (10kR-150kR). The curves were extrapolated to 1.2 at 0kR. Thence, the inactivation constants (k) were obtained from an equation  $N/N_0 = 1.2 \exp(-kD)$  (D=exposure in kR, N and  $N_0$  = c.f.u. of unirradiated and irradiated spores) and they are listed in the table.

Table

Summary of inactivation constants (k)

Wavelength (nm)	Spore type		
	UVS	UVP	UVR
0.5779	0.0206 (1.00)	0.0214 (1.00)	0.0168 (1.00)
0.5763	0.0400 (1.94)	0.0445 (2.08)	0.0328 (1.95)
0.5747	0.0242 (1.17)	0.0279 (1.30)	0.0241 (1.43)

In the table, the ratio of the inactivation constants are shown in the parenthesis to indicate the relative efficiency (those for 0.5779nm irradiation are taken as 1.00). For all three types of the spores, the efficiency of the radiation with the energy corresponding to the peak resonance absorption is the highest and amounts to 2.0-2.1 times of that of the radiation with the lower energy. The radiation with the higher energy is the next efficient and the efficiency amounts to 1.2-1.4 times of that of the lower energy. Thus, these results clearly demonstrate that resonance absorption by phosphorus K-shell electron leads to the inactivation of the spores. The differences among the three types of the spores are modest, indicating major parts of DNA damages produced by the radiation in this energy range are not subjected to repair mechanisms defined by the genes, *uvrA*, *ssp* or *polA*.

Several experiments performed in the same irradiation system indicate that this enhancement of sporocidal action at the peak energy is smaller than the case of strand scissions produced in dried plasmid DNA<sup>3)</sup>, but larger than the cases of the inactivation of bacterial<sup>4)</sup> or yeast cells<sup>5)</sup>. This possibly reflects the relative contribution of the direct versus indirect DNA absorption in producing the lethal DNA damages, which seems to be the largest in the bacterial spores among the cellular systems examined.

### References

- 1) N. Munakata et al., Photochem. Photobiol., **44**, 385 (1986)
- 2) N. Munakata et al., J. Radiat. Res., **29**, 44 (1988)
- 3) A. Azami et al., J. Radiat. Res., **29**, 43 (1988)
- 4) H. Maezawa et al., J. Radiat. Res., **29**, 43 (1988)
- 5) K. Kobayashi et al., J. Radiat. Res., **29**, 42 (1988)

ANALYSIS OF MUTATIONAL SPECIFICITY IN lacZ GENE ON PLASMID pUC19

Fumio Yatagai, Sumiyo Hachiya\*, Kazushiro Nakano, and Yoshimasa Hama\*

The Institute of Physical and Chemical Research, Saitama 351-01

\*Waseda University, Tokyo 162

To elucidate the specificity of mutagenesis induced by soft X-ray,  $\alpha$  part of lacZ gene on plasmid pUC19 was selected as a target. In the preliminary experiment, we determined the transformation efficiency of pUC19 following the 2.15 keV X-ray irradiation using Beam Line BL-11B.

Ten  $\mu$ l of the DNA suspension (150  $\mu$ g/ml) spread on 3 X 10 mm filter (Millipore Type HA), and this thin DNA film was exposed to 2.5keV X-ray at room temperature with the dose rate,  $\sim$ 4 kR/min. Following the exposure, each filter was placed in 200  $\mu$ l of TE (10 mM TrisHCl, 1mM EDTA) to recover the DNA from the filter. Competent cells of E. coli JM105 (0.2 ml of  $\sim 10^8$  cells/ml) were mixed with recovered DNA (0.1ml,  $\sim$ 40 ng), and this mixture was kept on ice for 30 min, heated up to 42C for 2 min, and finally supplemented with 1 ml of 2 X TY medium. The number of Amp<sup>R</sup> transformants were determined on 2 X TY (Amp 100  $\mu$ g/ml) plate after one hour incubation of the above mixture at 37C.

The rate of decrease in the transformation efficiency (Fig. 1) was extremely small compared to the data obtained with  $^{60}\text{Co}$   $\gamma$ -rays irradiation of the sample in TE (Fig. 2). Probably, the indirect effect of radiation was reduced by the relatively dry condition of thin DNA film during the X-ray exposure.

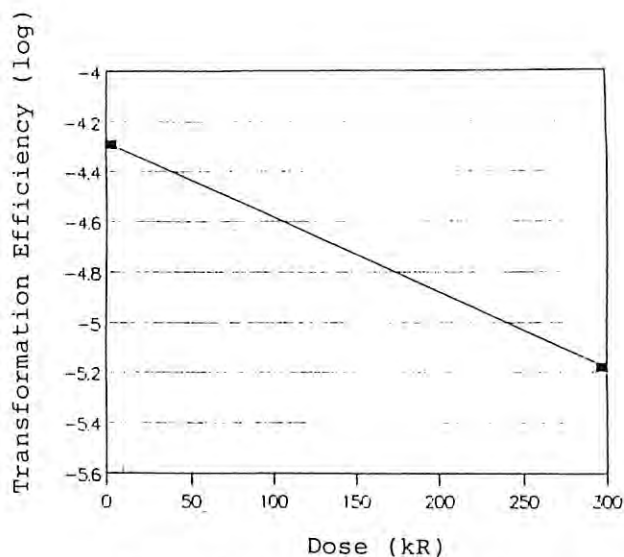


Fig.1 Soft-X-Ray Irradiation

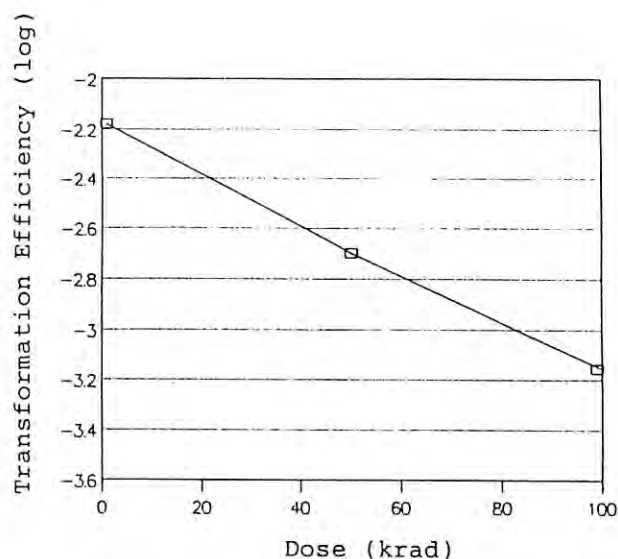


Fig.2 Co-60 Gamma Irradiation

CRYSTAL STRUCTURAL ANALYSIS OF A FERREDOXIN FROM *MYCOBACTERIUM SMEGMATIS* BY THE NATIVE ANOMALOUS DISPERSION METHOD#

Tomitake TSUKIHARA, Keiichi FUKUYAMA and Yoshinori SATOH\*

Faculty of Engineering, Tottori University, Koyama-cho, Tottori 680, and \*KEK, National Laboratory for High Energy Physics, Oho-machi, Tsukuba, Ibaraki 305

Introduction

Ferredoxins are typical iron-sulfur proteins containing clusters consisting of iron and inorganic sulfur atoms. The iron-sulfur active centers are linked to protein molecule by covalent bonds between iron and S<sub>y</sub> atoms of cysteinyl residues. They are classified into several groups according to their cluster structures such as [2Fe-2S] and [4Fe-4S]. A ferredoxin from *Mycobacterium smegmatis* Takeo is composed of 106 amino acid residues, where eight residues are cysteins (Hase *et al.*, 1979). The amino acid sequence of the ferredoxin from *M. smegmatis* is so similar to a ferredoxin I of *Azotobacter vinelandii* that both main chains are expected to fold in the same manner. The crystal structural analysis of *A. vinelandii* ferredoxin I showed us a unique structure of [3Fe-4S] cluster together with [4Fe-4S] cluster (Stout *et al.*, 1988). We are currently engaged in the crystal structural analysis of *M. smegmatis* ferredoxin to confirm the unique [3Fe-4S] structure found in the crystal structure of *A. vinelandii* ferredoxin I. We, however, have not successfully prepared a heavy atom derivative. Since this protein contains at least seven iron atoms as anomalous scatterers within the molecule, the native anomalous dispersion method can be applied to the phase determination.

The ferredoxin from *M. smegmatis* was crystallized into the space group of *C222*<sub>1</sub>, with cell dimensions *a*=172.0, *b*=56.3 and *c*=102.4 Å. Seven data sets of intensity data for the native crystal have been collected beforehand on a four-circle diffractometer by using Ni-filtered Cu-Kα radiation.

Experimental

Experiment has been performed at BL-14A. Intensity data for (*hkl*) and (*-hkl*) up to 7Å resolution were collected at room temperature on a four-circle diffractometer by using monochromatized X-ray of which wave length was 1.7534 Å. Integrated intensities were collected by the *w*-scan technique. Scanning range and speed in *w* were 0.18° and 1.0° per minute, respectively. Scanning was repeated to three times when the signal to noise ratio of the structure amplitude was less than 6.67. Measurements for four monitor reflections were repeated at every 100 reflections. Total of 1726 reflections were obtained and corrected for intensity change of incident beam and for deterioration of the crystal. Absorption correction was carried out by the method of North *et al.* (1968).

#X-ray experiment was not carried out in 1987, because of lack of crystal. Present paper is essentially same as the previous report of 1986.

Results and Discussion

Observed structure amplitudes of the present work are compared with the native data sets 1, 2 and 3 obtained previously by using Ni-filtered Cu-Kα radiation. Correlation coefficients of  $\Delta F$ ,  $\Delta F = F(hkl) - F(-hkl)$ , were evaluated among these data sets and listed in Table 1. The correlation of  $\Delta F$  are shown in Fig.1, t00. The observed structure amplitudes of the present work poorly correlate to the other data sets. Although anomalous difference Patterson map was composed for the data set of the present work, the map did not successfully show up vectors between iron-sulfur clusters in the crystals. The failure is probably due to deterioration of the crystal.

References

- Hase, T., Wakabayashi, H., Matsubara, H., Imai, T., Matsumoto, T., & Tobari, J. (1979). *FEBS Lett.*, **103** 224-228
- North, A.C.T., Phillips, D.C., & Mathews, F.S. (1968). *Acta Crystallogr.*, **A.24**, 351-359
- Stout, G.H., Turley, S., Sieker, L.C., & Jensen, L.H., *Proc. Natl. Acad. Sci. USA*, **85**, 1020-1022

TABLE 1 CORRELATION COEFFICIENT OF  $\Delta F$ 

	Native 1	Native 2	Native 3	Native 4
Native 1	1.000 ( 770)	0.364 ( 739)	0.388 ( 744)	0.106 ( 559)
Native 2		1.000 ( 891)	0.572 ( 851)	0.145 ( 575)
Native 3			1.000 (1994)	0.170 ( 578)
Native 4				1.000 ( 587)

Figures in parentheses are numbers of reflections included in the calculations. Native 4 is obtained in the present work.

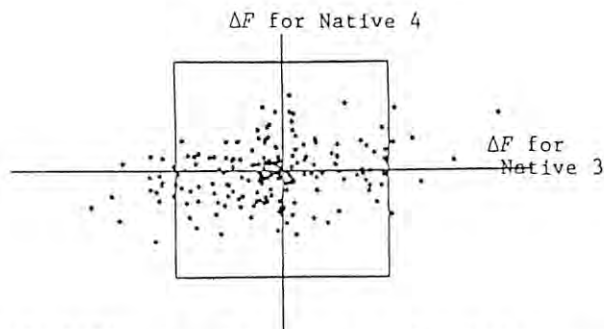


Fig.1. Difference of structure amplitude between Bijvoet pair for Native 3 and Native 4 (present work).



# Intensity Measurements with Short Wave-Length X-Rays; Structure Refinement of Ilmenite

Masataka OHGAKI<sup>1</sup>, Yasuyuki TAKENAKA<sup>1</sup>, Kiyooki TANAKA<sup>1</sup>, Fumiyuki MARUMO<sup>1</sup>, Hideki MORIKAWA<sup>1</sup>,  
Yoshinori SATO<sup>2</sup>, Fumihiko TAKEI<sup>3</sup>

1. Research Laboratory of Engineering Materials, Tokyo Institute of Technology,  
Nagatsuta 4259, Midoriku, Yokohama 227
2. Photon Factory, National Laboratory for High Energy Physics,  
Oho, Tsukuba, Ibaraki, 305
3. Institute for Solid State Physics, The University of Tokyo,  
Roppongi, Minato-ku, Tokyo

## Introduction

By recent studies of electron-density distributions in inorganic crystals with the X-ray diffraction method, qualitative knowledges have been much accumulated. However, it is required to increase accuracy of observed structure factors to obtain quantitative information.

The present study was undertaken with the intention to obtain diffraction data of ilmenite with reduced extinction effects. The authors have already measured diffraction intensities with shorter wavelength X-rays, and also studied electron density distributions in ilmenite by making use of the conventional X-ray sources.

## Experimental

The crystal used was synthesized with an infrared-heating floating-zone furnace. A piece of crystal shaped into a sphere of 0.145 mm diameter was used in the present study as in the previous experiments.

The data collection was carried out on a four-circle diffractometer at BL-14A. The wavelength was set to 0.4199(1) Å using Si(422) double crystal monochromator. The correction for incident beam fluctuation was performed by monitoring the intensity of incident beam with an ion-chamber. The following experimental conditions are adopted: collimator, 0.5 mm; scan mode,  $\omega$ -scan; scan speed, 8°/min; max of 2 $\theta$ , 50.0°; scan width, 0.5°. Scanning was repeated five times, and 746 reflections were measured of which 604 were  $|F_o| > 3\sigma(|F_o|)$ . By excluding the reflections unsatisfying this condition and those which show large variations among the five measurements,

467 (360 independent) reflections were used in the subsequent calculations.

The refinement was carried out with a modified version of the full-matrix least-squares program LINKT, which includes the extinction corrections after Becker and Coppens<sup>1,2)</sup>. Least-squares calculations assuming the type II extinction effects with the Gaussian mosaic-spread distribution was adopted. The site occupancies were refined on the assumption of partial disorder of the cations. The final R and Rw values reduced to 0.0236 and 0.0234, respectively. The atomic parameters are compared in Table 1 with those obtained with X-rays of different wavelength.

## Results

The positional parameters in the present study are partially identical with those obtained from the data collected with other wavelength X-rays. The obtained chemical formula for the present crystal is as  $(\text{Fe}_{0.97}\text{Ti}_{0.03})(\text{Ti}_{0.92}\text{Fe}_{0.07}\square_{0.01})\text{O}_3$ .

Since X-rays with a short wavelength are used, the isotropic extinction correction factor Y is close to one ( $Y_{\text{min}} = 0.930$ ). The value of Y is plotted as a function  $|F|^2/|F_{\text{max}}|^2$  in Fig. 1 compared with those obtained with the other wavelength X-rays. When a spherical specimen is used, Y is given in the following form<sup>1)</sup>:  $Y = [1 + Cx + \{A(\theta)x^2 / (1 + B(\theta)x)\}]^{-1/2}$ , where the functions A( $\theta$ ) and B( $\theta$ ), and the value C depend on the crystal examined. The extinction parameter x is expressed as  $x = c \cdot \lambda^2 \cdot |F|^2$  in the type II extinction effect. In Fig. 2, Y is plotted against  $\lambda^2$  on some reflections for the respective measurements. As seen in Fig. 2, the shorter wavelength X-rays receive smaller extinction effects, and the stronger reflections are affected by larger extinctions.

Table 1 Positional and thermal parameters (Å<sup>2</sup>).

	This work	$\lambda = 0.35\text{Å}$	AgK $\alpha$	MoK $\alpha$
Fe z	0.35548(4)	0.35548(2)	0.35542(1)	0.35542(1)
U <sub>11</sub>	0.00546(16)	0.00677(9)	0.00795(5)	0.00645(3)
U <sub>33</sub>	0.00538(24)	0.00614(12)	0.00805(6)	0.00626(4)
Ti z	0.14640(5)	0.14648(3)	0.14640(1)	0.14641(1)
U <sub>11</sub>	0.00400(16)	0.00488(10)	0.00652(5)	0.00502(3)
U <sub>33</sub>	0.00430(26)	0.00512(13)	0.00690(6)	0.00514(4)
O x	0.31742(35)	0.31720(24)	0.31723(13)	0.31715(8)
Y	0.02392(34)	0.02326(24)	0.02372(13)	0.02358(9)
z	0.24497(10)	0.24483(7)	0.24499(4)	0.24503(4)
U <sub>11</sub>	0.0046(5)	0.0049(3)	0.0067(2)	0.0053(1)
U <sub>22</sub>	0.0043(5)	0.0052(4)	0.0076(2)	0.0062(1)
U <sub>33</sub>	0.0063(6)	0.0063(3)	0.0083(2)	0.0070(1)
U <sub>12</sub>	0.0019(5)	0.0019(3)	0.0030(1)	0.0023(1)
U <sub>13</sub>	0.0001(5)	0.0007(3)	0.0002(1)	0.0003(1)
U <sub>23</sub>	0.0012(5)	0.0017(3)	0.0015(1)	0.0016(1)
R-factor	0.0236	0.0206	0.0192	0.0150
Y <sub>300</sub>	0.930	0.959	0.914	0.871

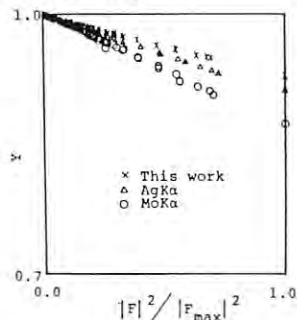


Fig. 1 The value of Y plotted as a function  $|F|^2/|F_{\text{max}}|^2$ .

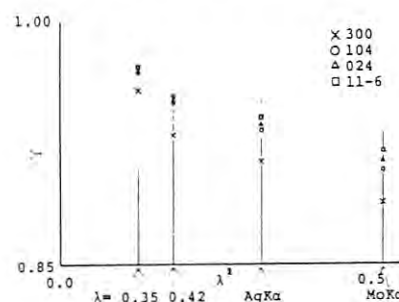


Fig. 2 The value of Y against  $\lambda^2$  for reflections.

- 1) Becker, P.J. & Coppens P. (1974) Acta Cryst., **A30**, 129, 148.
- 2) Becker, P.J. & Coppens P. (1975) Acta Cryst., **A31**, 417.

DEVELOPMENT OF SPECIMEN CHAMBER FOR LIGHT IRRADIATION AT LOW TEMPERATURE  
AND ITS APPLICATION TO BACTERIORHODOPSIN PHOTOCYCLE IV

Fumio TOKUNAGA, Mikio KATAOKA, Masayoshi NAKASAKO, Tatsumi SAKANAKA and Yoshiyuki AMEMIYA\*

Department of Physics, Faculty of Science, Tohoku University, Sendai, Miyagi 980

\*Photon Factory, National Laboratory for High Energy Physics, Oho-machi, Tsukuba, Ibaraki 305

# INTRODUCTION

bacteriorhodopsin(bR) is a typical membrane protein and its trimer arranged in a two-dimensional hexagonal lattice in purple membrane (PM) of *H. halobium*. bR has a spectroscopically well-defined photoreaction cycle and translocates  $H^+$  during the cycle. The most important photoreaction intermediate for the function is M412, judging from several investigations. Some structural studies on M412 have been performed but the results were not consistent<sup>1),2)</sup>. We also started X-ray diffraction experiment on M412 at low temperatures where the life-time of the intermediate was elongated.

At low temperature, any reproducible and significant structural change was not observed. Moreover, it was a positive nuisance for Fourier analysis with phases from electron microscopic study that the lattice constant became slightly smaller below 0°C<sup>3)</sup>.

On the other hand, we found another condition for life-time elongation of M412 where the lattice constant was maintained. Here we report the preliminary results of X-ray diffraction experiment on M412 performed under the new condition.

# EXPERIMENTAL

Isolated PM was suspended in Arg-HCl solution (0.75M pH 10) and dried. After this preparation, M412 was sufficiently accumulated under intense yellow light (wavelength>510 nm) even at room temperatures and the decay of the M412 was remarkably slow.

X-ray diffraction experiment was performed at BL-15A with light irradiation chamber, which was developed specially for the MUSCLE diffractometer<sup>3)</sup>. X-ray wavelength was 1.50 Å. Sample-to-detector distance was ca. 40 cm and the exposure time was 900 sec. Sample temperature

was maintained at ca. 7°C with temperature controlled  $N_2$  gas flow. Diffraction patterns were recorded for trans state and M412 one after the other.

# RESULTS

Background-subtracted diffraction patterns from M412 and trans state of PM are shown in Fig. 1. These patterns are addition of 5 data sets, respectively. The Bragg reflections caused by hexagonal packing of bR trimer were observed up to 7 Å resolution in the case of unirradiated PM. Moreover, the lattice constant and the intensity ratio of Bragg reflections of PM in Arg-HCl were the same as native PM in water. These facts indicate that Arg-HCl condition has no effect on the structure of PM.

Although the S/N ratio of diffraction pattern was still low due to high concentration of  $Cl^-$  ion, the change in diffraction intensity between M412 and trans is clear, and the lattice constant was not changed in M412. Fig. 2 shows the difference of diffraction intensities. Especially, (11), (32) and (43) reflections were decreased and (20), (21) and (41) reflections were increased in M412. These facts suggest that some structural changes would occur not in the lattice arrangement but in bR trimer and/or protoomer during the formation of M412. The change is now under analysis with use of difference Fourier method and R-factor research.

To obtain better S/N ratio data, we now refine the condition and experimental procedure. Final goal of this experiment is a trace of M412 decay on the basis of structure by time-resolved measurement.

# REFERENCES

- 1) Frankel et al., Biophys.J., **47**, 387 (1985)
- 2) Glaeser et al., Biophys.J., **50**, 913 (1986)
- 3) Tokunaga et al., PF Activity Report#5, 327(1987)

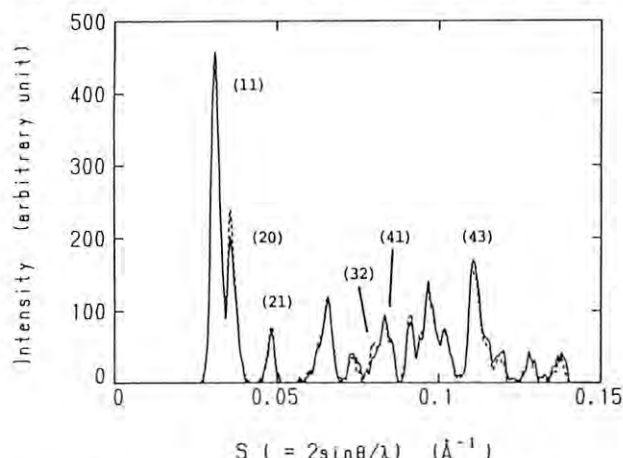


Fig. 1 X-ray Diffraction Patterns from trans state (solid line) and M412 (broken line). Brackets indicate Miller indices of two-dimensional hexagonal lattice.

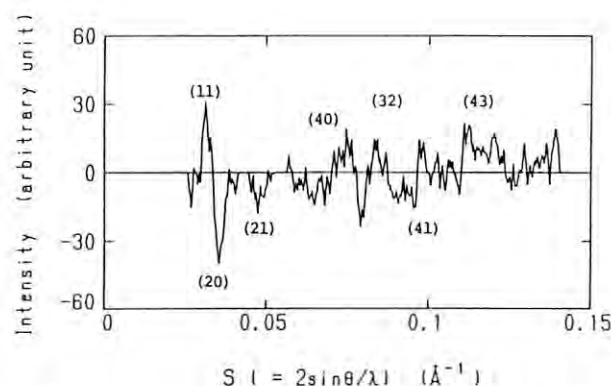


Fig. 2 Difference of diffraction intensity between trans state and M412. Data was obtained by the subtraction of M412 data from trans state one.

# EFFECTS OF X-RAY IRRADIATION ON MURINE HEART MUSCLE

I. MATSUBARA, N. YAGI, Y. SAEKI\*

M. ENDOH<sup>†</sup> & Y. AMEMIYA<sup>‡</sup>

Department of Pharmacology, University of Tohoku School of Medicine, Sendai.

\* Department of Physiology, Tsurumi University School of Dental Medicine, Yokohama.

† Department of Pharmacology, Yamagata University School of Medicine, Yamagata.

‡ Photon Factory, National Laboratory for High Energy Physics, Tsukuba.

## INTRODUCTION

Low doses of ionizing radiation are known to damage the organization of myofilaments in skeletal muscle (1). The primary damage appears to occur to high molecular-weight proteins (titin or connectin) which contribute to the passive tension as well as to the active tension of skinned skeletal muscle. We have studied whether a similar damage occurs to heart muscle during X-ray diffraction experiments.

## METHODS

Papillary muscles were isolated from the right ventricle of the rat to make two types of preparations. One is an intact preparation; the isolated muscle was held at a constant length in a specimen chamber which was continuously perfused with an oxygenated Tyrode solution at 20 °C. The muscle was stimulated at 2-sec intervals with an electrical pulse given through a pair of parallel electrodes.

The second type of preparation was a chemically skinned papillary muscle; the muscle was soaked in a saponin solution (250 µg/ml) for 1 hr to make the membrane permeable to the solutes of the bathing medium. This preparation was held isometrically in the specimen chamber and was activated by perfusing the chamber with a solution containing 0.04 mM  $\text{Ca}^{2+}$ , 10 mM ATP and an ATP regenerating system.

These preparations were mounted on the low-angle diffraction camera (2) at the beam line 15A and were irradiated with monochromatic X-rays ( $\lambda = 0.15$  nm). The ring current was approximately 100 mA.

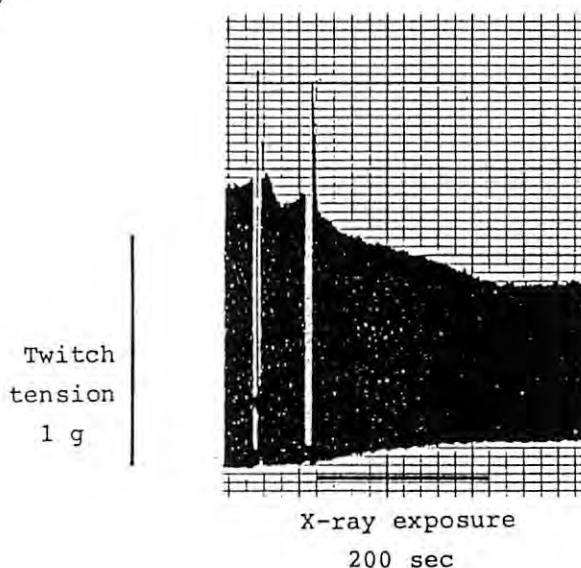
## RESULTS

The twitch tension of the intact preparation fell gradually during exposure to X-rays. At the end of a 5-min exposure, the active tension became almost a half of that before the exposure (Figure 1). The diastolic (resting) tension increased gradually during the exposure, suggesting that some fibres went into rigor. On the contrary, in the skinned preparation a 5-min exposure during a sustained contraction did not cause a significant fall of the tension.

## DISCUSSION

Our data have shown that X-rays used for diffraction studies do cause a significant damage to intact heart muscles. The fall of active tension accompanied by an increase in the resting tension suggests a deficiency of ATP. It is probable that X-rays damage the ATP-regenerating enzymes which constitute a part of the sarcomere structure such as the M-line. Such a damage is not expected to affect the skinned preparation since ATP is supplied sufficiently from the bathing medium.

Figure 1



## REFERENCES

- (1) Horowitz, R., E. S. Kempner, M. E. Bisher & R. J. Podolsky (1986). *Nature* 323, 160-164.
- (2) Amemiya, Y., K. Wakabayashi, T. Hamanaka, T. Wakabayashi, T. Matsushita & H. Hashizume (1983). *Nucl. Instr. Meth.* 208, 471-477.

# EFFECTS OF 2,3-BUTANEDIONE-2-MONOXIME ON THE STRUCTURAL CHANGES OF THE THIN FILAMENT DURING ACTIVATION OF FROG SKELETAL MUSCLES

Naoto Yagi, Keisuke Horiuti\*, Shigeru Takemori\*, Masaru Watanabe\*,  
Yoshiki Umazume\*, Ichiro Matsubara & Yoshiyuki Amemiya†

Department of Pharmacology, Tohoku University School of Medicine, Sendai, Japan.

\*Department of Physiology, The Jikei University School of Medicine, Minato-ku, Tokyo, Japan.

†Photon Factory, National Laboratory for High Energy Physics, Tsukuba, Japan.

## INTRODUCTION

BDM (2,3-butanedione-2-monoxime) inhibits contraction of skeletal muscle. Freyer et al.<sup>[1]</sup> that, in rat soleus muscle, BDM inhibits contraction by reducing the amount of calcium release from sarcoplasmic reticulum. On the other hand, Horiuti et al.<sup>[3]</sup> found that, in frog skeletal muscles, BDM suppresses the amount of calcium release only slightly.

We used X-ray diffraction technique to investigate the effects of BDM on calcium release. It is known that the second layer-line from the thin filament is sensitive to its structural changes caused by calcium<sup>[3]</sup>. Therefore it is expected that if calcium release is reduced, the intensity change of this layer-line is also reduced.

## METHODS

Semitendinosus muscles from bullfrogs (*Rana catesbeiana*) were used at a sarcomere length of  $4.0\mu\text{m}$ . At this length, there is very little overlap between the thick and thin filaments and only very small tension is developed. This helps to measure the intensity of the second layer-line which may be changed if the specimen moves during measurement. The muscles were stimulated isometrically by a 2-sec train of electrical pulses for 20 times at 2-min intervals. They were soaked either in a normal Ringer solution (control experiments) or in a Ringer solution containing 3mM BDM (test experiments) for 2 hr before the second series of stimulations was started. All experiments were made at  $5-6^\circ$ . X-ray experiments were done at the beam line 15A of Photon Factory, Tsukuba, using the camera and detector described in Amemiya et al.<sup>[4]</sup>. Ring currents were 100-300mA.

## RESULTS

The intensity of the second layer-line increases markedly during electrical stimulation (Figure 1). In the control experiments (Figure 1a), the increase in the second series of stimulations was 43% of that in the first series. In the presence of 3mM BDM (Figure 1b), the increase in the second series was about 65% of that in the first series. This value is not significantly different from the control value of 43%. The smaller increase in the second series may be due to a radiation damage by the strong X-rays from the synchrotron source rather than fatigue of specimens because no fatigue was observed in similar laboratory experiments using a rotating anode X-ray generator. The radiation damage may also explain the large scatter of data.

## DISCUSSION

Muscle contraction is regulated by the cytoplasmic calcium concentration. In frog skeletal muscles, calcium binds to the troponin molecule on the thin filament. Binding of calcium leads to a structural change in the thin filament which enables myosin heads to bind to actin and develop tension. The intensity of the second layer-line is affected by this structural change in the thin filament. Thus the present finding that BDM does not affect the intensity change of this layer-line during stimulation indicates that, in frog muscles, BDM does not have an inhibitory effect on the calcium release mechanism or the regulatory system of the thin filament.

## REFERENCES

- [1] Freyer, M.W., P.W. Gage, I.R. Neering, A.F. Dulhunty & G.D. Lamb (1988) *Pflügers Arch.* **411** 76-79.
- [2] Horiuti, K., H. Higuchi, Y. Umazume, M. Konishi, O. Okazaki (1988) *J. Muscle Res. Cell Motility* **9** 156-164
- [3] Kress, M., H.E. Huxley, A.R. Faruqi & J. Hendrix (1986) *J. Mol. Biol.* **188** 325-342
- [4] Amemiya, Y., K. Wakabayashi, T. Hamanaka, T. Wakabayashi, T. Matsushita & H. Hashizume (1983) *Nucl. Instr. Meth.* **208** 471-477

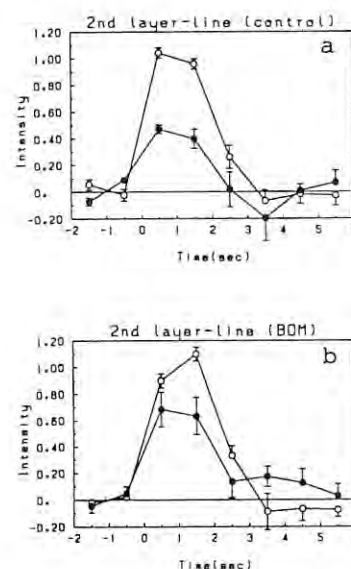


Figure 1

Intensity of the second layer-line from the thin filament. (a) Control experiments. The open circles represent intensities in the first series of stimulations while the solid circles represent those in the second series. The intensity during rest is taken as zero, and that averaged during stimulations is taken as 1.0%. (b) Test experiments in which the second series was done in the presence of 3mM BDM.



## TEMPERATURE DEPENDENCE OF THE RIPLE STRUCTURE IN DMPC-CHOLESTEROL MULTIBILAYER SYSTEM

Sinzi MATUOKA, Satoru KATO, Morio AKIYAMA<sup>#</sup>, Yoshiyuki AMEMIYA<sup>\$</sup>, Ichiro HATTADepartment of Applied Physics, School of Engineering, Nagoya University  
Furo-cho, Chikusa-ku, Nagoya 464<sup>#</sup>Department of Physics, Sapporo Medical College  
Minami 1-jo, Nishi 17-choume, Chuo-ku, Sapporo 060<sup>\$</sup>Photon Factory, National Laboratory for High Energy Physics Oho 1-1, Tsukuba, Ibaragi 305Introduction

DMPC (Dimyristoylphosphatidylcholine) multibilayer undergoes well defined thermal phase transitions. In its  $P_\beta'$  phase which appears between  $L_\alpha$  phase (liquid-crystalline phase) and  $L_\beta'$  phase (gel phase), the undulating bilayer structure (ripple) appears<sup>1)</sup>.

It is well known that cholesterol affects the properties of the multibilayer for example fluidity, phase transition temperature and so on. It has been reported using freeze fracture electron microscopy that the ripple repeat structure is also affected by cholesterol<sup>2)</sup>.

In this report we study the temperature dependence of the ripple repeat distance for the DMPC multibilayer system and how cholesterol changes the temperature dependence of the ripple structure.

Experimental

The multilamellars composed of DMPC and cholesterol were prepared by the conventional methods. Water content was about 60% in any cases. The sample was set in the aluminium cell. The temperature was controlled by the circulating water supplied from a temperature controlled water bath.

A small angle X-ray diffraction measurement was performed at BL-15A station, in which the sample to detector length was about 1300 mm.

Results and Discussion

Figure 1 shows the temperature dependence of the ripple repeat distance for DMPC containing various concentration of cholesterol measured in the cooling process (temperature scanning rate was about 0.2 °C/min). In pure DMPC multibilayer system the ripple repeat distance becomes larger from 120 Å to 140 Å at lower temperature.

The ripple repeat distance of DMPC-cholesterol system is larger than that of pure DMPC system at every temperatures. This fact is basically consistent with that observed by Copeland and McConnell using freeze fracture electron microscopy<sup>2)</sup> although they did not observe the temperature dependence of the ripple repeat distance.

In pure DMPC system the ripple peak was not detected below 13 °C. This is consistent with the fact that the pretransition appears at this temperature. On the other hand the ripple peak was observed even at 8 °C in DMPC-cholesterol system indicating that the cholesterol lowers the pretransition temperature.

In the middle temperature range of the ripple phase (about 10 - 20 °C), the slope of the ripple repeat distance vs temperature curve

for cholesterol-DMPC system is almost similar to that for the pure DMPC system. This fact suggests that the change of the ripple repeat structure is caused by the same mechanism in both systems.

Below 10 °C the ripple repeat distance becomes significantly large. This result is in good agreement with that obtained from freeze fracture electron micrographs<sup>3)</sup>.

Near 22 °C the ripple repeat distance significantly increases only when cholesterol is added. However this enlargement of the ripple repeat distance was not detected by freeze fracture electron microscopy<sup>3)</sup>. It is likely that the relaxation time of the ripple structure in these temperatures is faster than quenching rate.

References

- 1) A. Tardieu, V. Luzzati and F. C. Reman, J. Mol. Biol., **75**, 711 (1973)
- 2) B. R. Copeland and H. M. McConnell, Biochim. Biophys. Acta, **599**, 95 (1980)
- 3) T. Ishihama, S. Kato and I. Hatta, In Abstr. 26th Meet. Biophys. Soc. Jap., S 78 (1988)

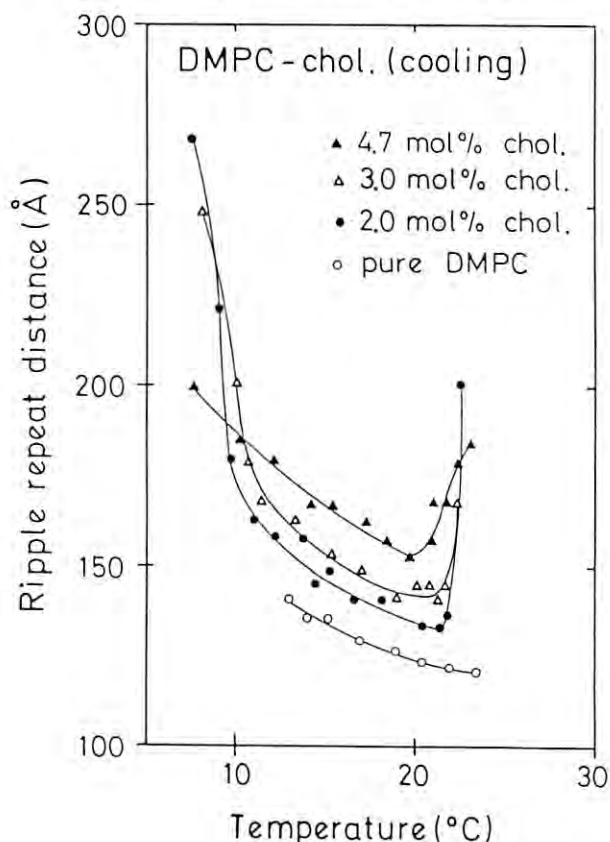


Fig. 1 Temperature dependence of the ripple repeat distance for DMPC-cholesterol multibilayer system.

## RADIAL MOVEMENTS OF MYOSIN HEADS IN MURINE HEART MUSCLE DURING CONTRACTION

Y. SAEKI, Y. AMEMIYA\*, N. YAGI<sup>†</sup> & I. MATSUBARA<sup>†</sup>

Department of Physiology, Tsurumi University School of Dental Medicine, Yokohama.

\* Photon Factory, National Laboratory for High Energy Physics, Tsukuba.

<sup>†</sup> Department of Pharmacology, University of Tohoku School of Medicine, Sendai.

## INTRODUCTION

The movements of myosin heads in heart muscle during contraction were previously studied with a time resolution of 60 msec using a rotating-anode X-ray generator (1). It revealed that the radial movement of myosin heads from the thick to the thin filaments roughly parallels the isometric tension. However, to clarify whether this molecular event precedes the tension development as is the case in skeletal muscle, a finer time resolution is needed. The use of strong X-rays contained in synchrotron radiation has enabled us to investigate this problem.

## METHODS

A papillary muscle was isolated from the right ventricle of the rat. The muscle was held isometrically in a specimen chamber which was perfused continuously with an oxygenated Tyrode solution at 37 °C. The muscle was stimulated at 2-sec intervals with an electrical pulse given through a pair of parallel electrodes. The muscle length was adjusted to produce the maximum isometric force.

The low-angle diffraction camera (2) combined with the beam line 15A was used at a specimen-to-detector distance of 2 m. A linear position sensitive counter was used to record the equatorial diffraction patterns. The 2-sec cycle of contraction was divided into 10-msec periods and the diffraction data were accumulated for each period over 200 contractions. From the data the integrated intensities of the two main equatorial reflections,  $I_{10}$  and  $I_{11}$ , were obtained for each period.

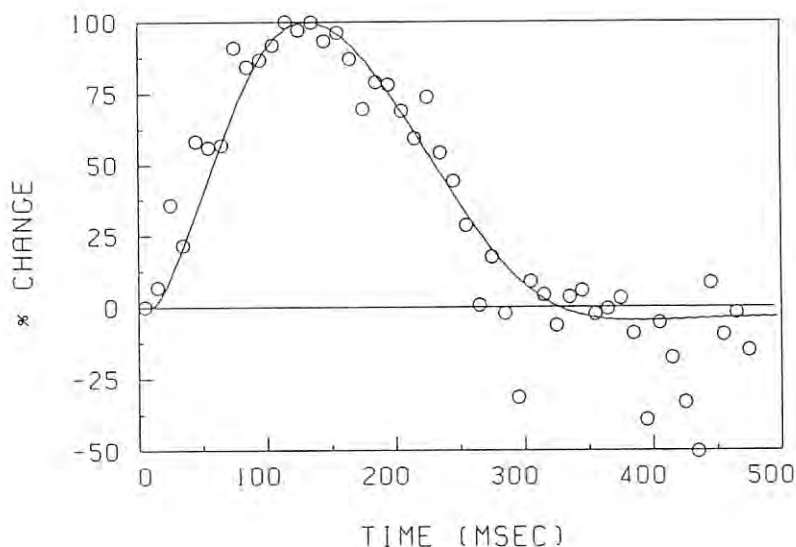
## RESULTS

The open circles in Figure 1 show the time course of the intensity ratio,  $I_{11}/I_{10}$ , expressed as percentages of the maximum change. The continuous line represents the isometric force. The figure suggests that, at the beginning of contraction, the radial movement of myosin heads from the thick to the thin filaments precedes the tension development by 10-20 msec. After the peak tension, the return of myosin heads to the thick filaments appears to parallel the fall of tension.

## DISCUSSION

Brady (3) has found, from mechanical experiments in which the contractile component of heart muscle was controlled to keep a constant length, that the intensity of the active state at the beginning of contraction increases prior to the force development. He interpreted this result as indicating that the intensity of the active state may represent the formation of cross-bridges between the thick and the thin filaments. Our observation that the change in the intensity ratio precedes the isometric tension development by 10-20 msec agrees with this view.

Figure 1



## REFERENCES

- (1) Matsubara, I., N. Yagi & M. Endoh (1979). *Nature* 278, 474-476.
- (2) Amemiya, Y., K. Wakabayashi, T. Hamanaka, T. Wakabayashi, T. Matsushita & H. Hashizume (1983). *Nucl. Instr. Meth.* 208, 471-477.
- (3) Brady, A. J. (1968). *Physiol. Rev.* 48, 570-600.

# EQUATORIAL X-RAY INTENSITY CHANGES DURING CONTRACTION OF FROG SKELETAL MUSCLES UNDER THE INHIBITORY ACTION OF 2,3-BUTANEDIONE-2-MONOXIME

Shigeru Takemori, Masaru Watanabe, Naoto Yagi\*, Keisuke Horiuti,  
Yoshiki Umazume, Ichiro Matsubara\* & Yoshiyuki Amemiya†

Department of Physiology, The Jikei University School of Medicine, Minato-ku, Tokyo, Japan.

\*Department of Pharmacology, Tohoku University School of Medicine, 2-1 Seiryō-machi, Sendai, Japan.

†Photon Factory, National Laboratory for High Energy Physics, Tsukuba, Japan.

## INTRODUCTION

BDM (2,3-butanedione-2-monoxime) inhibits contraction of skeletal muscle to a degree depending on its concentration. We studied the equatorial intensity changes during contraction of frog skeletal muscles at different tension levels using various concentrations of BDM.

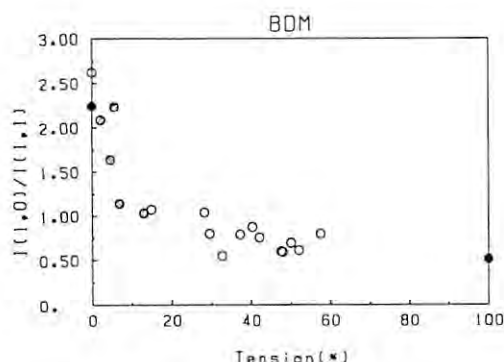
## METHODS

Thin sartorius muscles from frog (*Rana nigromacrata*) were used at a sarcomere length of  $2.4\mu\text{m}$ . First the muscles were isometrically stimulated by a 2-sec train of electrical pulses in a normal Ringer solution during which the equatorial pattern was recorded. Then the solution was changed to the one containing 3-6mM BDM. Muscles were left for 1 hr to equilibrate before the equatorial pattern was recorded again. All experiments were made at  $5-6^\circ$ . X-ray experiments were done at the beam line 15A of Photon Factory, Tsukuba, using the camera and detector described in Amemiya et al.<sup>[1]</sup>. Ring currents were 100-300mA.

## RESULTS

In a normal Ringer solution, the equatorial intensity ratio ( $I_{1,0}/I_{1,1}$ ) was 2.2 during rest and decreased to 0.50 during contraction (Figure 1, filled circles). In the presence of 3mM BDM, the average tetanic tension was 41% of the control and the intensity ratio was 2.6 during rest, 0.76 during contraction (Figure 1, open circles).

At higher (4.5 - 6mM) concentrations of BDM (Figure 1, hatched circles) the contractile tension was further reduced to less than 20%. The equatorial intensity ratio during contraction increased monotonically as the tension decreased, until the tension became about 5% of control. When the tension was smaller than this, the change in the intensity ratio upon stimulation was very small.



## DISCUSSION

There can be two mechanisms by which BDM reduces contractile tension. One is inhibition of the binding of myosin heads to actin and thus decrease the number of myosin heads which are attached to actin. The other is inhibition of the tension development of attached myosin heads. Using rapid cooling contracture, Yu et al.<sup>[2]</sup> changed the contractile tension of frog muscles. This is expected to lower the number of attached myosin heads. They showed that, at the tension level of 40% of the maximum, the intensity ratio was 1.1. The present value (0.76) is much lower than this, suggesting that the number of attached myosin heads is less affected than tension. Therefore it seems likely that BDM does not inhibit tension development by simply reducing the number of attached myosin heads: BDM probably affects the tension generation of the attached myosin heads.

The present X-ray diffraction results agree with those from biochemical studies which showed that BDM inhibits ATP hydrolysis by myosin. It seems likely that BDM reduces a rate constant of a certain step (or steps) of actin-activated myosin ATPase cycle after attachment of myosin heads to actin.

The relationship between tension and the equatorial intensity ratio shows rather abrupt deflection at a tension of about 5% of control. This may be because BDM affect calcium release at higher concentration. Although we found that BDM does not affect calcium release at 3mM (see Proposal No.87-038 in this report), there is a report suggesting it may affect it at high concentration<sup>[3]</sup>.

## REFERENCES

- [1] Amemiya, Y., K. Wakabayashi, T. Hamanaka, T. Wakabayashi, T. Matsushita & H. Hashizume (1983) Nucl. Instr. Meth. **208** 471-477
- [2] Yu, L.C., J.E. Hartt & R.J. Podolsky (1979) J. Mol. Biol. **132** 53-67
- [3] Fryer, M.W., P.W. Gage, I.R. Neering, A.F. Dulhunty & G.D. Lamb (1988) Pflugers Arch. **411** 76-79

## X-RAY DIFFRACTION OF THE LIVE SQUID RETINA

Toshiaki HAMANAKA\*, Yuji KITO\*\*, Masatsugu SEIDOU\*\*, Katsuzo WAKABAYASHI\*  
and Yoshiyuki AMEMIYA\*\*\*

- \* Department of Biophysical Engineering, Faculty of Engineering Science, Osaka University, Toyonaka, Osaka 560  
\*\* Department of Biology, Faculty of Science, Osaka University, Toyonaka, Osaka 560  
\*\*\* National Laboratory for High Energy Physics, Tsukuba, Ibaraki 305

### Introduction

The initial step of the visual process is the absorption of light by the visual pigment. The squid visual pigment is located in microvilli which are cylindrical extensions of the cell membrane, arranged hexagonally within the rhabdomes. Until now, only a few papers have been published on the structural study of invertebrate rhabdomes by x-ray diffraction. In those, however, the retina fixed by glutaraldehyde was used, because this tissue disintegrated within 1 hour of dissection. In the present study, we could succeed in recording the x-ray diffraction pattern from unfixed retina by the use of the synchrotron radiation and a storage phosphor screen, the imaging plate. The result suggests that it will be possible to investigate the structural response of photoreceptors to the light stimulation.

### Experimental

Living, active specimens of the squid, *Watasenia scintillans* were captured at Toyama Bay of the Japan Sea and brought to Tsukuba within several hours. The squids were decapitated and their retinas dissected in dim red light. For the x-ray experiments, 1-mm thick slices of retina were kept in an artificial seawater chamber with Mylar windows at 4 °C. Schematic diagram of a slice of squid retina was shown in Fig. 1.

X-ray experiments have been performed with a mirror-monochromator optics (the Muscle Diffractometer) at BL-15A1.<sup>1)</sup> The wavelength of the radiation was 1.50 Å. The sample-to-detector distance was 2196 mm. X-ray scattering intensity was recorded on the imaging plate and stored on magnetic tape after converting to the digital signals with the image reader and the image processor.<sup>2)</sup> The exposure time was 5-10 minutes and each recording finished within 30 minutes after the decapitation.

### Results

Figure 2 shows the x-ray diffraction pattern from outer segments of live squid retina, which was reproduced and photographed from the stored image with the image writer. The low angle x-ray diffraction spots are due to the 570-Å hexagonal lattice of microvilli. The six diffuse maxima centered around  $1/40 \text{ Å}^{-1}$  may originate from the bilayer structure of microvillar membranes. The intensities are different among equivalent Bragg reflections and stronger near the vertical axis of the pattern. This result suggests that rhabdomes are variously oriented around the vertical axis of retina in the sample as a whole.

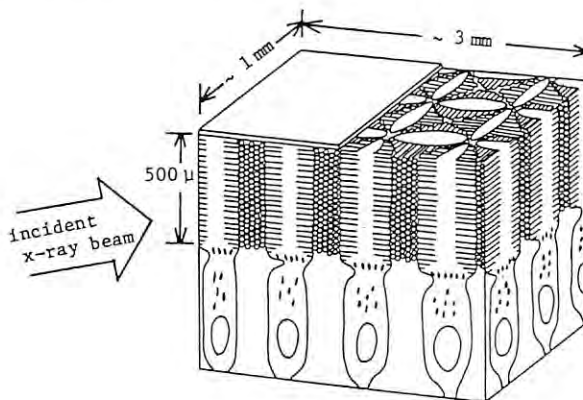


Figure 1. Schematic diagram of a vertical slice of squid retina. The retina consists almost entirely of photoreceptor cells, which are vertically separated into inner and outer segments. The photoreceptive outer segments are in the upper layer and consist of microvilli, which are cylindrical extensions of the cell membrane, packed hexagonally in the rhabdomes. The microvilli are 600 Å in diameter and 1 μm long.

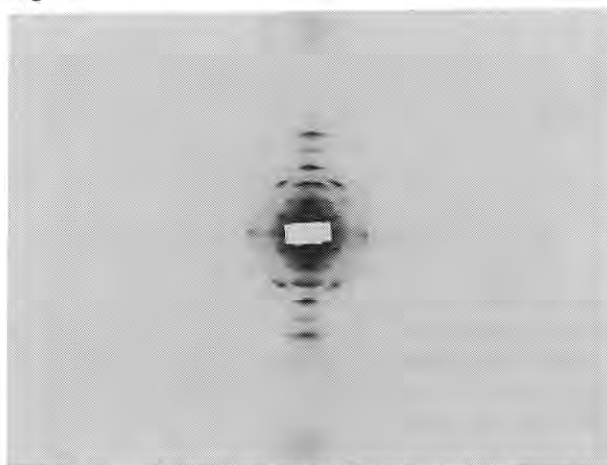


Figure 2. The x-ray diffraction pattern from a slice of live squid retina in artificial seawater. The storage ring was operated at 2.5 GeV with a beam current of 188 mA. The exposure time was 5 minutes.

### References

- 1) Y. Amemiya et al., Nucl. Instrum. Methods, **208**, 471 (1983)
- 2) Y. Amemiya et al., Nucl. Instrum. Methods, **A266**, 645 (1988)



# CHANGE IN THE SMALL-ANGLE DIFFUSE SCATTERING FROM A FROG SKELETAL MUSCLE DURING AN ISOMETRIC CONTRACTION

Katsuzo WAKABAYASHI\*, Katsumi NISHIMURA\*, Sinichiro NISHIDA\*,  
Hidehiro TANAKA\*\* and Yoshiyuki AMEMIYA\*\*\*

\* Department of Biophysical Engineering, Faculty of Engineering Science, Osaka University, Toyonaka, Osaka 560

\*\* Department of Physiology, School of Medicine, Teikyo University, Itabashi-ku, Tokyo 173

\*\*\* Photon Factory, National Laboratory for High Energy Physics, Tsukuba, Ibaraki 305

## Introduction

It is known that the strong small-angle diffuse scattering is observed in the central region of the muscle X-ray pattern. The change of the scatterings from the resting, isometrically contracting and rigor frog muscles was analysed. It was found that the scattering changes during contraction, suggesting a preferred orientation of myosin heads along the actin filaments [1].

## Methods and Results

The diffraction patterns of the resting, isometrically contracting and rigor muscles recorded with an imaging plate from the same muscle [2] were used for the analysis. In the intensity tracings of the pattern at intervals of  $10^\circ$  between the equator and the meridian, the diffuse scatter under each diffraction peak was derived by the standard fitting routine. After the removal of the peak, the whole background function was determined using the background data by the interpolation procedure using the spline function and/or by the Fourier-Bessel expansion method [3].

Figure 1 shows the perspective view of the resulting background function of the contracting pattern. The scattering decayed around  $1/5\text{nm}^{-1}$ . Our analysis indicated that the strength of the diffuse scattering was in order of the resting, contracting and rigor state. Figure 2 shows the comparison of the two-dimensional distributions of the scattering between the resting and contracting muscles. During contraction the scattering expanded in the meridional direction and compressed in the equatorial direction. This change was very different from that in the rigor state, where it was much compressed in the meridional direction. The plots of  $\ln I$  vs  $2\theta^2$  in the meridional and the  $45^\circ$  directions shows two straight lines, respectively and their slopes gave values similar to the radius of gyration of the myosin head in solution [4], apart from slight difference of the values in the different directions and in the states of muscle. Figure 3 shows the pseudo-color image of the difference pattern of the scatterings together with the original difference pattern made between the contracting and resting states. The red-colored region where the scattering increased during contraction appears in an elliptic shape that is longer in the meridional direction. Within this region the most intense scattering existed in about  $30^\circ$  direction from the meridian.

These results suggests that the myosin projections are staggered and align more perpendicularly along the actin filaments during contraction.

## References

- 1) J. Lowy and F. R. Poulsen, *J. Mol. Biol.*, **194**, 595 (1987)
- 2) Y. Amemiya, K. Wakabayashi, H. Tanaka, Y. Ueno and J. Miyahara, *Science*, **237**, 164 (1987)
- 3) R. Millane and S. Arnott, *J. Appl. Cryst.*, **18**,

419 (1985)

- 4) R. A. Mendelson and K. M. Kretzchmar, *Biochem.*, **19**, 4103 (1980)

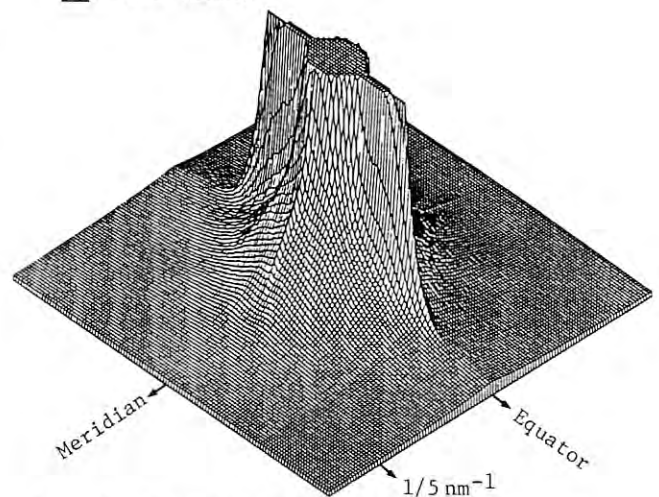


Fig. 1 The perspective view of the diffuse scattering in the contracting muscle.

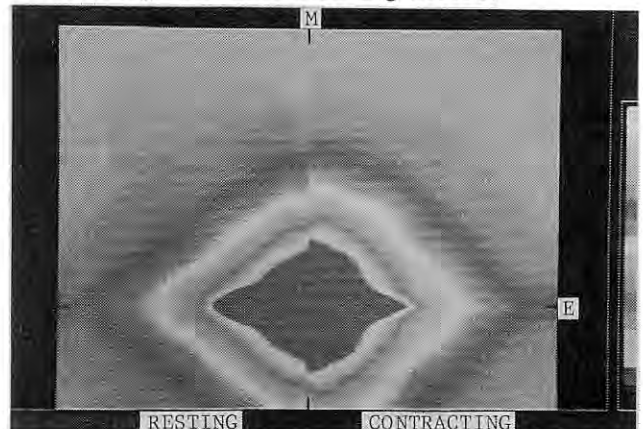
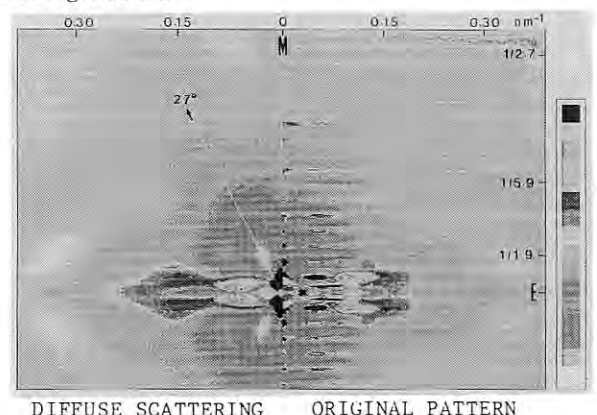


Fig. 2 Comparison of the distribution of the diffuse scatterings between the resting and contracting states.



DIFFUSE SCATTERING ORIGINAL PATTERN  
Fig. 3 Difference patterns between the resting and contracting states.

## CHANGES IN EQUATORIAL X-RAY DIFFRACTION INTENSITIES FROM SKELETAL MUSCLE OF THE FROG STRETCHED AT THE ONSET OF TWITCH

Hiroyuki IWAMOTO, Takakazu KOBAYASHI, Katsuzo WAKABAYASHI\*, Yoshiyuki AMEMIYA\*\* and Haruo SUGI

Department of Physiology, School of Medicine, Teikyo University, Itabashi-ku, Tokyo 173

\*Department of Biophysical Engineering, Faculty of Engineering Science, Osaka University, Toyonaka, Osaka 560

\*\*Photon Factory, National Laboratory of High Energy Physics, Tsukuba, Ibaraki 305

### Introduction

A quick stretch of a muscle applied at the onset of a twitch results in an instantaneous rise of force reaching its full tetanic value (Hill, 1949)<sup>1)</sup>. Hill has concluded from the results that the contractile component is fully activated immediately after stimulation but the force rises slowly because the component shortens at the expense of series elastic element during normal contractions. Later studies have shown that the series elasticity of the muscle is much smaller than expected, and Hill's observation may be understood as the recruitment of force-producing myosin crossbridges by the stretch. The present study was undertaken to obtain information about the structural basis of the phenomenon.

### Materials and Methods

A small fiber bundle was excised from the ileofibralis muscle of the frog, *Rana japonica*. This material showed better fiber orientation than the semitendinosus muscle<sup>2)</sup>. A ramp stretch (2% bundle length, duration = 20 ms) was applied at 20 ms after a single pulse stimulation. Sets of 10 contractions with and without stretches were repeated alternately. Diffraction measurements ( $\lambda = 1.5 \text{ \AA}$ , camera length = 2.5 m) were done at a time resolution of 5 ms.

### Results and Discussion

Fig. 1a shows the time course of the intensity changes of the equatorial reflections together with the force. When the bundle was stretched, much larger peak force was attained and the relaxation was delayed. The increase in the muscle stiffness is greatly accelerated by stretch<sup>3)</sup>, indicating that the number of force-producing crossbridges is increased. On the other hand, the difference between the reflection intensities of the stretched and isometric bundles was small, although the drop of the 1,0 reflection during activation tended to be faster in stretched bundles. No marked change in the 1,1 reflection was observed either. Provided the changes in the equatorial reflections reflect the radial movements of myosin heads towards actin filaments, the results may be taken to show that the stretch facilitates the conversion from non-force-producing crossbridges (which have already been in the vicinity of actin

filaments) to force-producing bridges, but has little effect on the radial distribution of the myosin heads. The reciprocal lattice spacing of 1,1 plane showed a change expected from the constant-volume behavior (Fig. 1b). There was no marked change in the half width of each reflection (Fig. 1c).

### References

- 1) Hill, A.V. (1949) Proc. R. Soc. Lond. B, 136; 399-420.
- 2) Iwamoto, H. et al. (1987) Photon Factory Activity Report, 5; 333.
- 3) Haugen, P. and Sten-Knudsen, O. (1987) J. Muscle Res. Cell Motility, 8; 173-187.

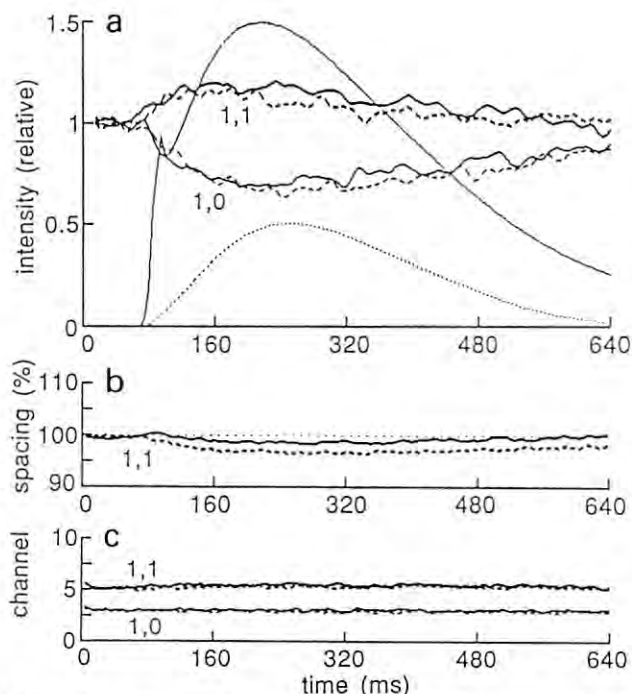


Fig. 1. a, Time course of the intensity change of the equatorial reflections and the force during a twitch of the fiber bundle of frog ileofibralis muscle. Mean of the data from 6 bundles. The reflection intensities are normalized with respect to the values immediately before stimulation. The solid line shows data from stretched bundle, and the broken line from isometric bundle. b, Reciprocal lattice spacing of 1,1 plane. The data are expressed relative to the value before stimulation. c, Half widths of the equatorial reflections.

## TIME-RESOLVED X-RAY DIFFRACTION STUDIES OF EQUATORIAL REFLECTIONS FROM FROG SKELETAL MUSCLE DURING SEGMENTAL LENGTH CLAMP

Takakazu KOBAYASHI, Hiroyuki IWAMOTO, Katsuzo WAKABAYASHI\*, Yoshiyuki AMEMIYA\*\* and Haruo SUGI

Department of Physiology, School of Medicine, Teikyo University, Itabashi-ku, Tokyo 173

\*Department of Biophysical Engineering, Faculty of Engineering Science, Osaka University, Toyonaka, Osaka 560

\*\*Photon Factory, National Laboratory of High Energy Physics, Tsukuba, Ibaraki 305

The changes in the intensities of the equatorial reflections during activation of a skeletal muscle is generally believed to reflect the radial movements of myosin heads toward actin filaments. These changes have been reported to occur ca. 50 ms ahead of rise in force<sup>1)</sup>. However, the rate of rise in force may be affected by nonuniform behavior of segments along the muscle, which is observed under a fixed-end condition<sup>2)</sup>. Especially an internal shortening has an effect to retard the force development. In order to eliminate the internal shortening, we introduced a technique to hold the length of a segment of the muscle constant during contraction (segmental clamp).

Two film markers were attached to a sartorius muscle of a bullfrog, *Rana catesbeiana*. The distance between the two markers was sensed by a photodiode array (Reticon) and its signal was fed back into the servo amplifier so as to control the segmental length. The muscle was stimulated by a train of three electrical pulses to produce a brief tetanus. The contractions were repeated every 30 s at 4°C. Diffraction measurements were made using a PSPC with a time resolution of 5 ms.

Fig. 1 shows the changes in the position of the length driver, segmental length and force in a muscle during ordinary fixed-end contractions (Fig. 1a) and contractions under segmental clamp (Fig. 1b). During segmental clamp, the internal shortening was virtually eliminated and the rise in force was somewhat faster. The intensity changes in the equatorial reflections are shown in Fig. 2 together with force. Although the rise in force during segmental clamp was about 20 ms faster, there was no appreciable difference in the changes in 1,0 and 1,1 reflections. The results may indicate that a part of the advance of the reflection change over the rise in force is accounted for by the presence of internal shortening but the remaining part represents the time required for the myosin heads to develop force after moving toward actin filaments.

## references

- 1) Wakabayashi, K., Tanaka, H., Amemiya, Y., Fujishima, A., Kobayashi, T., Hamanaka, T., Sugi, H. and Mitsui, T. (1985) *Biophys. J.*, 47; 847-850.
- 2) Kobayashi, T. and Sugi, H. (1982) *Jpn. J. Physiol.*, 32; 817.

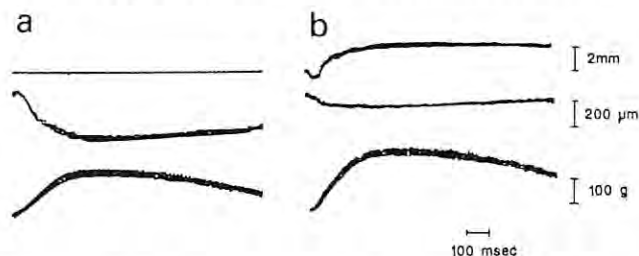


Fig. 1. Time courses of the position of the length driver, segmental length and force (from above) during brief tetani. a, fixed-end condition, b, segmental clamp. Traces of 10 contractions are superposed. Muscle length = 52 mm, segmental length = 5 mm at rest.

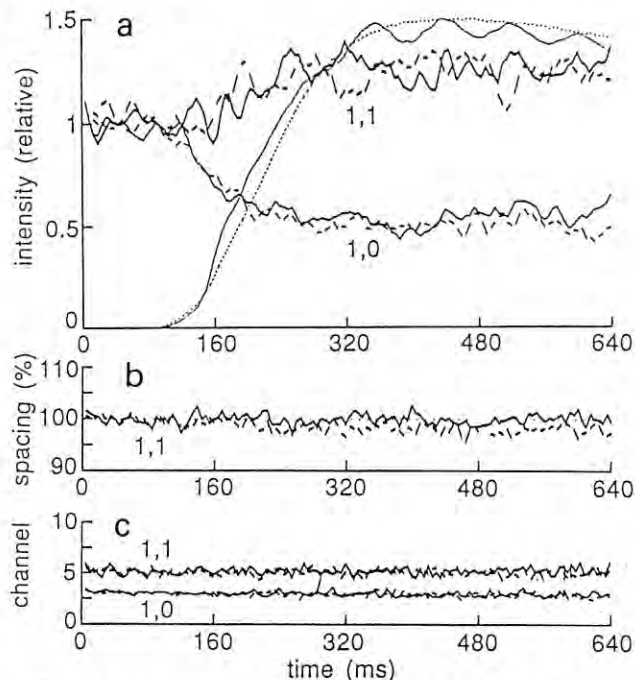


Fig. 2. a, Time courses of the intensity change of the equatorial reflections and the force during brief tetani. Mean of the data from two muscles. The reflection intensities are normalized with respect to the values immediately before stimulation. The solid line shows data from the muscles under segmental clamp, and the broken line from the muscles under fixed-end condition. b, Reciprocal lattice spacing of 1,1 plane. The data are expressed relative to the value before stimulation. Note the constancy of the spacing for the segment-clamped muscles. c, Half widths of the equatorial reflections.



# EFFECT OF THE SLOW SINUSOIDAL LENGTH CHANGE (2Hz) ON THE INTENSITY OF MYOSIN MERIDIONAL REFLECTIONS FROM ISOMETRICALLY TETANIZED FROG SKELETAL MUSCLES

Katsuzo WAKABAYASHI\*, En-Zhong WANG\*, Hiroyuki IWAMOTO\*\*, Takakazu KOBAYASHI\*\*, Hidehiro TANAKA\*\*, Toshiaki HAMANAKA\*, Yoshiyuki AMEMIYA\*\*\*, Haruo SUGI\*\* and Toshio MITSUI\*

\* Department of Biophysical Engineering, Faculty of Engineering Science, Osaka University, Toyonaka, Osaka 560

\*\* Department of Physiology, School of Medicine, Teikyo University, Itabashi-ku, Tokyo 173

\*\*\* Photon Factory, National Laboratory for High Energy Physics, Tsukuba, Ibaraki 305

## Introduction

We have studied the effect of sinusoidal length changes on the X-ray diffraction pattern from isometrically tetanized frog skeletal muscles by varying frequencies (5Hz, 10Hz and 20Hz), amplitudes (1% and 3%) and temperatures (4°C and 17°C).

In this report we show the effect of slow sinusoidal length change (2Hz) on the myosin meridional reflections.

## Experimental

Sartorius muscles of the bullfrog (*Rana catesbeiana*) with the sarcomere length of 2.4μm were isometrically stimulated with a train of 3 ms pulses at 20~40Hz to produce a maximum tetanic tension of 1.2s. When the tension reached a steady maximum level, the sinusoidal length changes of amplitude 1% and 3% at frequency 2Hz were applied to the muscle. This was repeated ten times for each muscle. Experiments were done at 4°C and 17°C. Intensities of the 14.3nm and 7.2nm myosin meridional reflections together with the tension were measured with a time-resolution of 20ms. The data from several muscles were added and averaged.

## Results

The effects of 3% amplitude of the sinusoidal length change on the intensities of the 14.3nm and 7.2nm reflections are shown in Fig. 1, where the comparison between 4°C and 17°C is made. The intensity change of these reflections in the 3% amplitude oscillation was generally more distinct than that in 1%. At 17°C there exist two low and high peaks and troughs in  $I_{14.3nm}$  within each cycle of the tension changes as was observed in the other frequencies [1,2]. At 4°C the small trough and peak became smaller, resulting in a shoulder and the intensity drop in the stretching phase became much bigger than at 17°C.  $I_{7.2nm}$  behaved similarly to  $I_{14.3nm}$  as in the case of the 5Hz oscillation [2]. Although the small shift of the positions of intensity minima and maxima seemed to be observed, the change of these reflections as a whole was very similar to those occurred in 5Hz and 10Hz oscillations. The 1,0 and 1,1 equatorial reflections also responded similarly to the 5Hz oscillation, but the change of  $I_{1,0}$  seemed to be much smaller than that of  $I_{1,1}$  (not shown here).

The present result indicates that the molecular motion of myosin heads follows properly to the low frequency sinusoidal length change.

## References

- 1) K. Wakabayashi et al., Biophys. J., 47, 471 (1986); H. Tanaka et al., Photon Factory Activity Report, 3, 176 (1985)
- 2) K. Wakabayashi et al., Photon Factory Activity Report, 5, 332 (1987)

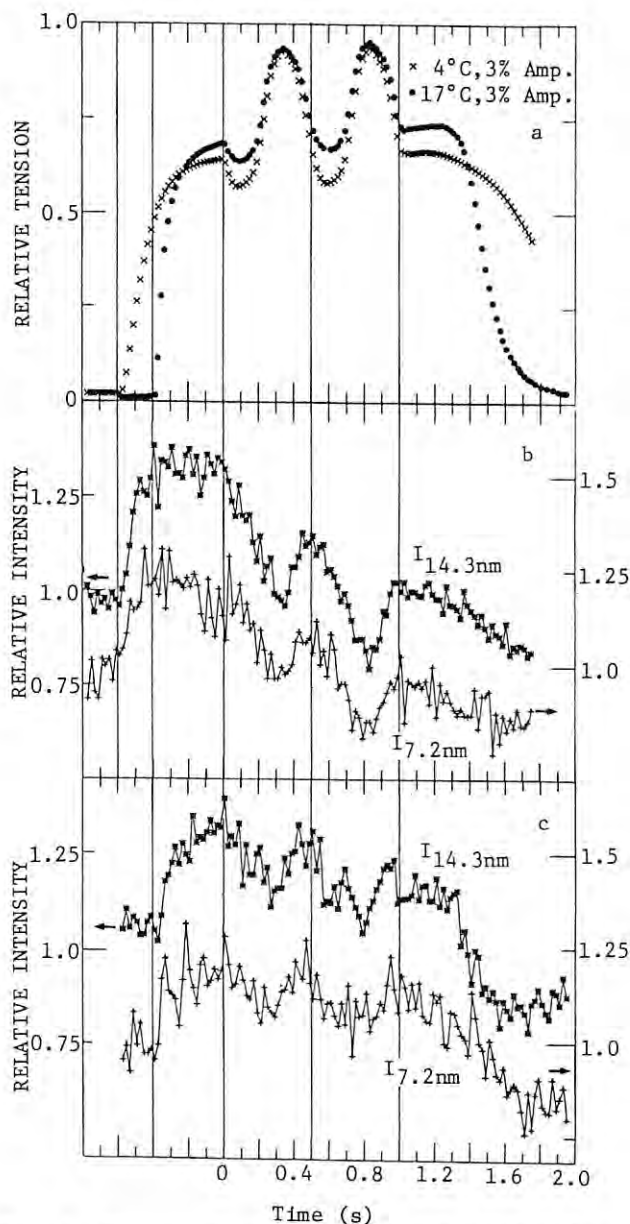


Fig. 1 Changes in tensions (a) and intensities of the 14.3nm and 7.2nm reflections during sinusoidal length changes of frequency 2Hz and 3% amplitude at 4°C (b) and 17°C (c).



# X-RAY DIFFRACTION STUDIES OF THE MODIFIED PURPLE MEMBRANE DURING ITS PHOTOCYCLE

Tomoya URUGA, Toshiaki HAMANAKA, Katsuzo WAKABAYASHI,  
Yoshiyuki AMEMIYA\* and Toshio MITSUI

Department of Biophysical Engineering, Faculty of Engineering  
Science, Osaka University, Toyonaka, Osaka 560, Japan

\* Photon Factory, National Laboratory for High Energy Physics,  
Oho, Tsukuba, Ibaraki 305, Japan

## Introduction

The purple membrane (PM) from *Halobacterium halobium* consists of a sole protein, bacteriorhodopsin (bR), and lipids. bR trimer with lipids form a well-ordered two-dimensional hexagonal arrays. Upon absorbing light, bR undergoes a photochemical reaction cycle through several spectroscopically distinct intermediates (K, L, M, O etc.). During the photocycle, bR transports protons across the membrane.

Under continuous light irradiation, bR exists as a mixture of light-adapted form and the photo-intermediates. In native PM at room temperature, the intermediates have a very short lifetime, so that their amounts are quite small compared with that of the light-adapted form. We have tried to lengthen the lifetime of M intermediate by modifying PM as described below and examined the effects of light upon the structure of the modified PM by X-ray diffraction methods.

In previous report 1), we have shown the structural changes of bR in glutaraldehyde and Triton X-100 treated PM due to light irradiation. In this report, we show the further characterization of above structural changes and the experimental results about another modified PM.

## Materials and methods

Glutaraldehyde treated PM (G-PM), glutaraldehyde and Triton X-100 treated PM (T-G-PM), sodium deoxycholate (DOC) PM (D-PM) and glutaraldehyde and DOC treated PM (D-G-PM) were prepared as described 2,3). X-ray diffraction studies were performed at BL15A. Experimental procedures were the same as described in previous report 1).

## Results

Figure 1 shows the diffraction patterns from T-G-PM suspension before and under irradiation. Under light irradiation, the lattice constant enlarged from 59.0 Å to 60.0 Å and the crystalline order of bR became worse and rather large intensity changes were observed for each Bragg reflection. However, such changes in diffraction due to irradiation were not observed in G-PM, D-PM and D-G-PM suspension. Since spectroscopic experiments showed that, under the present experimental conditions, most of bR in these modified PM were converted to M state, any measured differences between the diffraction patterns reflect the conformational changes of bR during the photocycle. In T-G-PM suspension, the interaction between bR and Triton X-100 seems to enhance the mobility of bR

molecules within the membrane. This may cause the conformational changes in bR during the photocycle to alter the unit cell dimension and lattice order.

Some of changes in diffraction patterns from T-G-PM suspension due to light irradiation remained for more than 20 min after stopping the irradiation. This suggests that, while the conformation in the vicinity of retinal reverted to that of the light-adapted form, the major altered conformation of bR molecules was rather stable in T-G-PM.

In the dried or glucose-embedded samples of T-G-PM, in contrast with suspension, significant changes were not observed, indicating that dehydration of the membrane protein restricts the major conformational changes.

## References

- 1) T. Uruga et al., Photon Factory Activity Report, 5, 326 (1987)
- 2) E. Lam and L. Packer, Archives of Biochem. Biophys., 221, 557 (1983)
- 3) S.B. Hwang and W. Stoeckenius, J. Membr. Biol., 33, 325 (1977)

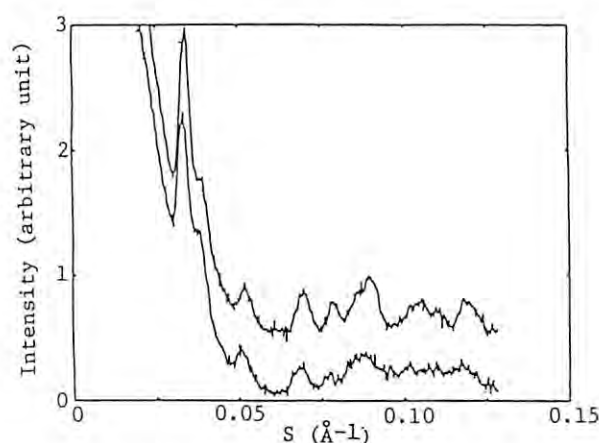


Fig. 1 X-ray diffraction patterns from T-G-PM suspension. The upper curve is for sample before light irradiation and the lower curve is for irradiated sample. Temperature, 5°C; pH, 7. The total counting time was 20 min for each curve.

## MEDIUM ANGLE X-RAY DIFFRACTION OF A TONICALLY CONTRACTING MOLLUSCAN SMOOTH MUSCLE

Yoshiko TAJIMA, Kazuyuki OKADA, Osamu YOSHIDA, and Yoshiyuki AMEMIYA\*

Department of Physics, Tokyo Metropolitan University, Setagaya-ku, Tokyo 158

\* Photon Factory, National Laboratory of High Energy Physics, Oho, Tsukuba-shi, Ibaraki 305

Introduction

The anterior byssus retractor muscle of *Mytilus edulis* (ABRM) shows a clear X-ray diffraction pattern from the thin filaments consisting of actin and tropomyosin. Many layer line reflections from the thin filaments are observed by small and medium angle diffractions. Small angle diffraction studies of skeletal muscles have indicated structural change of actin-containing filaments during contraction, and model presentation of the structure change have been attempted.<sup>1,2)</sup> Similar structure change of the thin filaments has been suggested by small angle X-ray diffraction studies of the tonically contracting ABRM.<sup>3,4)</sup> In this work we attempted to observe change in the medium angle diffraction pattern induced by tonic contraction for the purpose of studying the structure change of the thin filaments at a higher resolution.

Experimental and Results

Tonic contraction was produced by stimulation with acetylcholine by the same method as in the previous work.<sup>3,4)</sup> X-ray diffraction patterns were taken by point-focusing camera at BL15A-1 with Fuji imaging plates. The muscles were exposed to X-rays for 1 min in the tonically contracted state after stimulation with acetylcholine. The X-ray wave length was 1.540 Å and the camera length was 60 cm. The X-ray patterns were reconstructed on a display system from the digital intensity data read out from

the imaging plates, and photocopied on 35 mm roll films.<sup>5)</sup>

Figure 1 shows layer lines from the thin filaments observed in the relaxed state. The axial periods of the layer lines range from 380 Å to 7 Å. In the tonically contracted state all the layer lines in the relaxed state and a new layer line with an axial period of 190 Å were observed. Figure 2 shows a medium angle part of a diffraction pattern magnified on the display. A strong arc at the lower part of the pattern is from a polymer film at the window of the evacuated path between the sample and the imaging plate. The third layer line on the meridian with the 0th Bessel order is very strong both in the relaxed and in the tonically contracted state. Although new layer lines did not appear in the medium angle part, relative intensity changes among the layer lines were observed. The 112th layer line became weak, and off-meridional peak of the 69th layer line moved away from the meridian. Estimation of the integral intensities of the layer lines from the digital intensity data are in progress for comparison with the data in the relaxed state.

References

- 1) E. H. Egelman, *J. Muscle Res. Cell Motility*, **6**, 129 (1983).
- 2) K. Wakabayashi, Y. Ueno, Y. Amemiya, and H. Tanaka, *Molecular Mechanism of Muscle Contraction*. H. Sugi and H. Pollack. Eds. (Plenum Press, New York), 353 (1988).
- 3) Y. Tajima, K. Okada, O. Yoshida, and Y. Amemiya, *Photon Factory Activity Report*, 338 (1987).
- 4) Y. Tajima, K. Okada, O. Yoshida, T. Seto, and Y. Amemiya, *J. Appl. Crystal.*, to be published.
- 5) Y. Amemiya, T. Matsushita, A. Nakagawa, Y. Satow, J. Miyahara, and J. Chikawa, *Nuclear Instrum. Methods*, **A266**, 645 (1988).

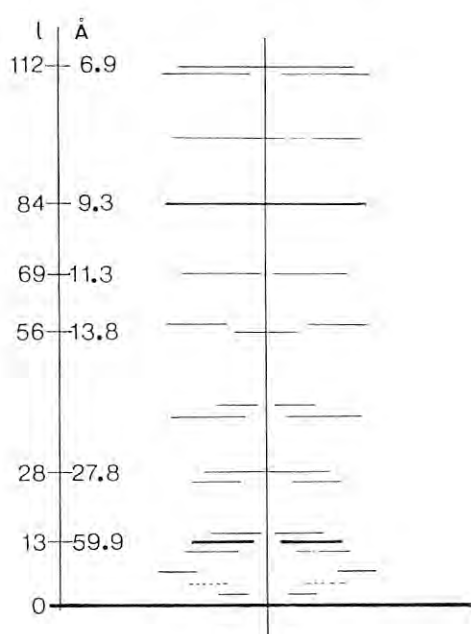


Fig. 1

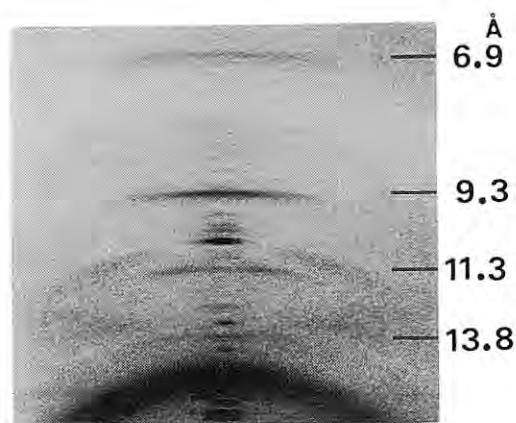


Fig. 2

DISSOCIATION AND ASSOCIATION KINETICS OF *E. coli* RIBOSOME.  
STOPPED-FLOW X-RAY SCATTERING STUDY AT SUBZERO TEMPERATURE

Hirotsugu Tsuruta<sup>1)</sup>, Akira Ishihama<sup>2)</sup>, Nobuyuki Fujita<sup>2)</sup>,  
Yoshiyuki Amemiya<sup>3)</sup>, and Hiroshi Kihara<sup>4)</sup>

- 1) Faculty of Science, Hiroshima University, Hiroshima 730, Japan
- 2) Department of Molecular Genetics, National Institute of Genetics, Mishima 411, Japan
- 3) Photon Factory, National Laboratory for High Energy Physics, Tsukuba 305, Japan
- 4) Jichi Medical School, School of Nursing, Tochigi 329-04, Japan

*E. coli* ribosome (70S,  $M_w = 2.5 \times 10^6$ ), protein synthesis factory, consists of two subunits: 50S and 30S. Both of them are complexes of proteins and rRNAs [1]. At physiological condition, ribosome exists as 70S, and it dissociates into subunits by removing  $Mg^{2+}$ . We observed dissociation and association kinetics induced by  $Mg^{2+}$  concentration jump with stopped-flow X-ray scattering method.

Ribosome was prepared as 70S at high  $Mg^{2+}$  concentration by density gradient ultracentrifugation. Purified ribosome was dissociated into subunits for association study just before the X-ray measurement by taking  $Mg^{2+}$  away with EDTA. All X-ray measurements were carried out at BL-15A1 of PF, using the monochromator described elsewhere [2].

Radii of gyration and zero-angle intensities for associated and dissociated forms were estimated respectively from the Guinier plots of static small angle X-ray scattering patterns (Table 1). Dissociated and associated fractions at certain  $Mg^{2+}$  concentration can be calculated with them.

Dissociation kinetics of which rate is dependent upon final  $Mg^{2+}$  concentration was monitored at 5°C (Fig. 1). On the other hand, association rate was too fast to be measured at 5°C. With using the stopped-flow device newly designed for the measurement at subzero temperature [3], we could observe association kinetics at -10°C in the presence of antifreeze, owing to slowdown of association at low temperature (Fig. 2). This fact demonstrates the efficiency of the stopped-flow X-ray scattering at subzero temperature [3].

- [1] Moore, P. B., *Nature* **331**, 223 (1988)
- [2] Amemiya, Y., Wakabayashi, T., Hamanaka, T., Wakabayashi, K., Matsushita, T., and Hashizume, H., *Nuclear Inst. Methods* **208**, 471-477 (1983)
- [3] Tsuruta, H., Nagamura, T., Kimura, K., Igarashi, Y., Kajita, A., Wang, Z.-X., Wakabayashi, K., Amemiya, Y., and Kihara, H., submitted to *Rev. Sci. Instr.*

Table 1. radii of gyration and zero angle intensities of *E. coli* ribosome.

$Mg^{2+}/mM$	$R_g/\text{\AA}$	$I(0)$
0.5	83.71	3017
0.47*	86.11	2804
5	86.61	3119
20	93.45	3406
20*	97.89	3434

0.708% ribosome, 5°C.

\*: at -10°C, in the presence of 30% ethylene glycol.

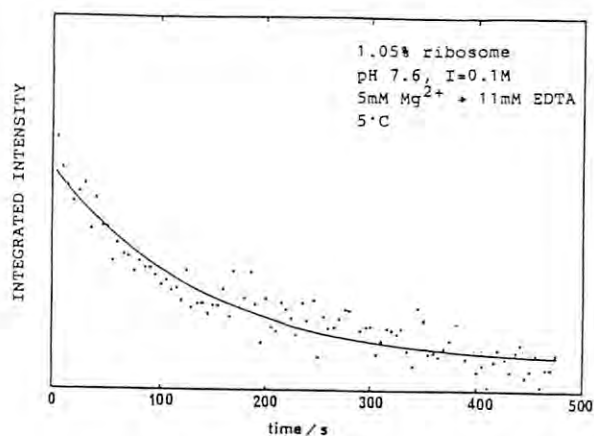


Figure 1. Dissociation kinetics of *E. coli* ribosome.

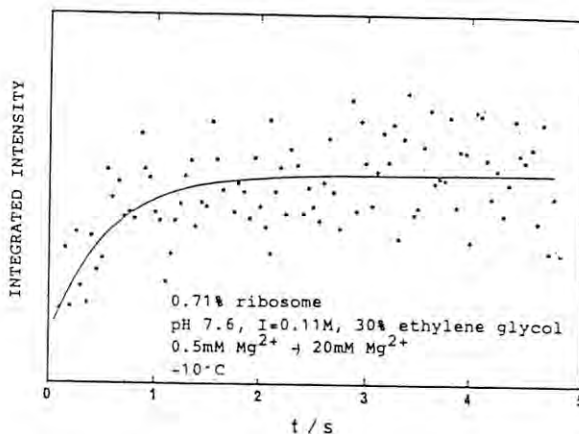


Figure 2. Association kinetics of *E. coli* ribosome at subzero temperature.

STRUCTURAL DYNAMICS OF ALPHA-2-MACROGLOBULIN AND FATTY ACID  
SYNTHETASE STUDIED BY TIME-RESOLVED X-RAY SMALL ANGLE SCATTERING  
EXPERIMENT

Atsushi IKAI<sup>1</sup>, Hideo ARAKAWA<sup>1</sup>, Hirayuki KYUSHIKI<sup>1</sup>,  
Hiroshi KIHARA<sup>2</sup>, Hirotsugu TSURUTA<sup>3</sup>, Katsuzo WAKABAYASHI<sup>4</sup>  
and Yoshiyuki AMEMIYA<sup>5</sup>

1) Univ. of Tokyo, 2) Jichi Medical School, 3) Hiroshima Univ., 4)  
Osaka Univ., 6) Natl. Lab. for High Energy Physics, Tsukuba, Japan

### Introduction

The structural change of alpha-macroglobulin upon complex formation with chymotrypsin was studied by time resolved X-ray small angle scattering experiment. Alpha2-macroglobulin is a serum proteinase inhibitor with a surprisingly wide specificity and is expected to function in the body defence mechanism against microbial invasions and in keeping the chemical homeostatic balance by modulating the activity of a large variety of vital proteinases in the body. The protein has been known to undergo a large structural change upon interacting with proteinases such as chymotrypsin and this conformational change is considered to be of fundamental importance in its inhibitory action. We decided to study the kinetics of this reaction using time resolved X-ray small angle scattering method and determine the time constant for the conformational change of macroglobulin.

Fatty acid synthetase is a large multifunctional enzyme which is capable of synthesizing long chain fatty acids from acetyl- and malonyl CoA. It is a good example of organized enzyme system which serves as a model for the understanding of organized metabolic systems in the cell as well as for the future development of molecular device based on designed macromolecules.

### Method

A stopped flow cell built for small angle scattering was used and two solutions, one containing macroglobulin and the other containing chymotrypsin were mixed within the dead time of the apparatus. The X-ray scattering curve from the mixed solution was recorded every hundred milli-seconds after mixing was completed.

### Results

The scattering curve of alpha2-macroglobulin had a definite shoulder reflecting the internal structure of its porous quaternary structure. The reaction with chymotrypsin reduced the intensity of the shoulder as has been reported by Osterberg and his coworkers (1). The decrease in intensity was successfully followed by stopped flow small angle scattering apparatus and we found that the half-time of the reaction was independent of the protein concentration within the limit of our experimental conditions. The result indicated that the structural change was slower than the association reaction between macroglobulin and chymotrypsin and we were able to obtain the time constant for the large scale structural change of macroglobulin for the first time. When combined with the data from the fluorescence stopped flow kinetics, our result gave the value of activation energy for this reaction, too.

The scattering curve of fatty acid synthetase was taken and the structure of the enzyme was analyzed with the help of electron micrographs of the enzyme. The electron micrograph showed that the enzyme has a rectangular structure with two large holes which are very likely the active centers of the enzyme. We simulated the scattering curve by several multibody models with reasonable success. The structure of the enzyme is expected to change during the enzymatic reaction and we are trying to detect the change by small angle scattering and follow the reaction to determine the type of structural change involved in the organized multifunctional enzyme.

### References

1. Branegard, B., Osterberg, R. and Sjoberg, B. (1982) Eur. J. Biochem., 122, 663-666



DISSOCIATION OF *Limulus polyphemus* (HORSESHOE CRAB) HEMOCYANIN  
MONITORED BY STOPPED-FLOW X-RAY SCATTERING METHOD

Kazumoto Kimura<sup>1)</sup>, Yoshihiko Igarashi<sup>2)</sup>, Akihiko Kajita<sup>2)</sup>, Zhi-Xin Wang<sup>3)</sup>,  
Hirotugu Tsuruta<sup>4)</sup>, Yoshiyuki Amemiya<sup>5)</sup>, and Hiroshi Kihara<sup>6)</sup>

- 1) Division of Medical Electronics, and 2) Department of Biochemistry, Dokkyo University School of Medicine, Mibu, Tochigi 321-02, Japan  
3) Institute of Biophysics, Academia Sinica, Beijing 100080, China  
4) Faculty of Science, Hiroshima University, Hiroshima 730, Japan  
5) Photon Factory, National Laboratory for High Energy Physics, Tsukuba 305, Japan  
6) Jichi Medical School, School of Nursing, Tochigi 329-04, Japan

*Limulus polyphemus* hemocyanin is an oxygen carrier protein of 3,600kDa molecular weight. This hemocyanin consists of 48 subunits, which are assembled to build 8 submultiples composed of 6 subunits each. The hemocyanin dissociates into 24mer (4 submultiples) by taking  $\text{Ca}^{2+}$  away at physiological pH. In addition, it dissociates into 12mer at pH 5.0 [1].

#### Model analysis of the scattering pattern

Static X-ray scattering patterns were measured for 48mer, 24mer, and 12mer states. Figure 1a shows a scattering pattern of 48mer state, giving a deep cleft at  $h=0.03(\text{\AA}^{-1})$ . This cleft was not observed for 24mer state. The scattering pattern of 48mer was calculated based on the model with an assumption that eight spheres of 60Å diameter (as models of submultiples) are arranged in two layers. Each layer has 4 submultiples, whose relative configurations are rotated at 45 degree (Fig. 2). The calculated pattern (Fig. 1b) agrees well with the experimental result.

#### Stopped-flow X-ray scattering

We have observed dissociation processes from 48mer to 24mer and to 12mer (depending on final pH) by stopped-flow X-ray scattering (Fig. 3). Prior to the dissociation, there observed a time-lag which was independent of final pH. Tentatively we ascribe the lag phase to the  $\text{Ca}^{2+}$  release induced by EDTA. The dissociation rate decreased with the increase of pH.

[1] Brenowitz, M., Bonaventura, C., and Bonaventura, J., *Biochemistry* 23, 879-886 (1984)

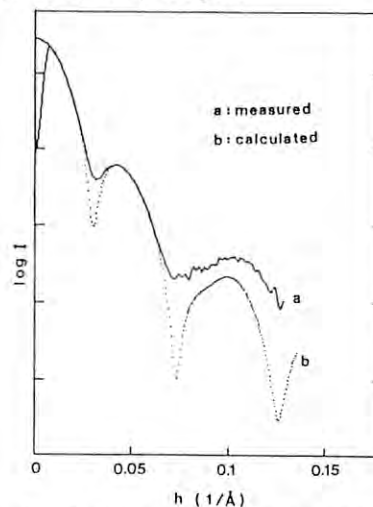


Figure 1. X-ray scattering pattern of *L. polyphemus* hemocyanin.



Figure 2. Submultiple assembly in *L. polyphemus* hemocyanin.

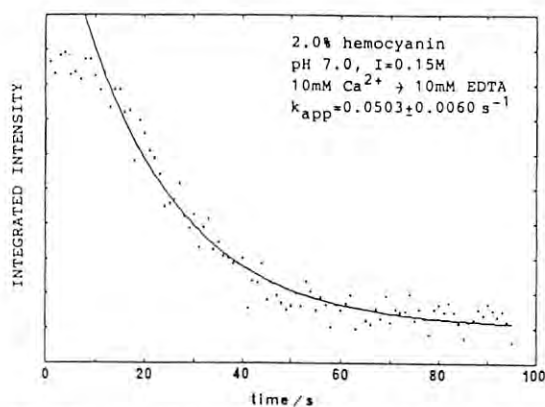


Figure 3. Dissociation kinetics of *L. polyphemus* hemocyanin.

DISSOCIATION OF *Eisenia foetida* (EARTHWORM) HEMOGLOBIN  
MONITORED BY STOPPED-FLOW X-RAY SCATTERING COMBINED  
WITH TIME-RESOLVED IMAGING PLATE AS DETECTOR

Yoshihiko Igarashi<sup>1)</sup>, Kazumoto Kimura<sup>2)</sup>, Akihiko Kajita<sup>1)</sup>,  
Hirotsugu Tsuruta<sup>3)</sup>, Yoshiyuki Amemiya<sup>4)</sup>, and Hiroshi Kihara<sup>5)</sup>

- 1) Department of Biochemistry, and 2) Division of Medical Electronics, Dokkyo University School of Medicine, Mibu, Tochigi 321-02, Japan  
3) Faculty of Science, Hiroshima University, Hiroshima 730, Japan  
4) Photon Factory, National Laboratory for High Energy Physics, Tsukuba 305, Japan  
5) Jichi Medical School, School of Nursing, Tochigi 329-04, Japan

*Eisenia foetida* (earthworm) hemoglobin is a giant oxygen carrier protein having a molecular weight of 3,800kDa (60S). It consists of 144 subunits, which is grouped into 12 submultiples. Six submultiples are assembled in a plane, and two planes are superimposed to make a native hemoglobin molecule. At alkaline pH, the hemoglobin dissociates into 10S, 3.6S, and 2.3S, depending on the final pH. It is reported that these dissociation processes finished within 1s [1]. We have combined a stopped-flow apparatus for X-ray scattering (dead time, 10ms). with a time-resolved imaging plate system and applied it to the dissociation study of *E. foetida* hemoglobin.

Figure 1 shows a static X-ray scattering pattern of the native hemoglobin and that taken one hour after changing pH to alkaline region. The scattering pattern of native hemoglobin shows a subpeak which suggests an ordered structure in the molecule, while the alkali-treated molecule does not. The fact indicates that the whole molecule may be dissociated into 10S, 5.6S, and 2.3S.

We have measured the pH-induced dissociation process (from pH 7.4 to 9.3) by means of stopped-flow X-ray scattering. We obtained a kinetic signal at 25°C, of which amplitude was very small. Judging from the static X-ray scattering data, it is probable that the reaction might be almost finished within the dead time of the stopped-flow apparatus. The signal amplitude became larger when the reaction was measured at 5°C (Fig. 2). Stopped-flow X-ray scattering study below 0°C will contribute to elucidation of dissociation mechanism of the earthworm hemoglobin in more detail, which will be tested at the next run.

[1] Chiancone, E., Veccini, P., Rossi Fanelli, M.R., and Antonini, E., J. Mol. Biol. 70, 73-84 (1972)

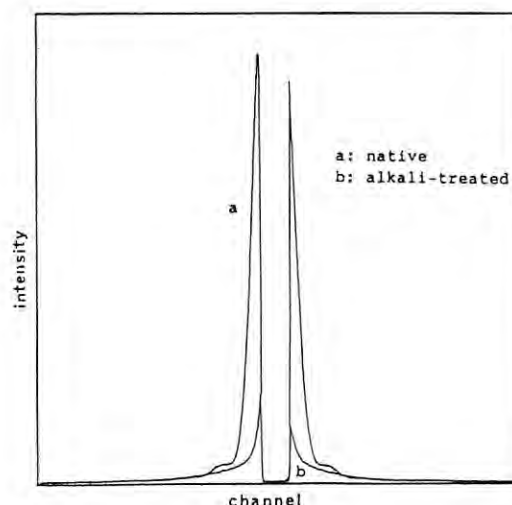


Figure 1. X-ray scattering pattern of *E. foetida* hemoglobin measured with imaging plate detection system.

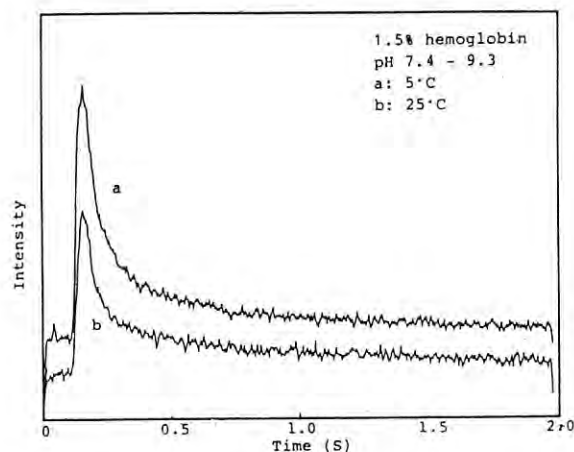


Figure 2. Dissociation kinetics of *E. foetida* hemoglobin as monitored by stopped-flow X-ray scattering combined with imaging plate.

# TIME RESOLVED SMALL-ANGLE X-RAY SCATTERING STUDY OF AGGREGATION PROCESS OF CUCUMBER GREEN MOTTLE MOSAIC VIRUS PROTEIN

Yoh SANO<sup>1</sup>, Hideo INOUE<sup>2</sup>, Yuzuru HIRAGI<sup>3</sup>, Kanji KAJIWARA<sup>4</sup>,  
Hiroshi URAKAWA<sup>4</sup>, Syoji ISODA<sup>3</sup>, Euiho KIM<sup>3</sup>, Sakumi  
MORIGUCHI<sup>3</sup> and Tatzuo UEKI<sup>5</sup>

1 National Institute of Agrobiological Resources, Yatabe, Ibaraki 305

2 Shimadzu Corporation, Kyoto 604

3 Institute for Chemical Research, Kyoto University, Uji, Kyoto 611

4 Kyoto Institute of Technology, Kyoto 606

5 Faculty of Engineering Science, Osaka University, Toyonaka, Osaka 560

## Introduction

Cucumber green mottle mosaic virus (CGMMV) is a rod-shaped virus and is morphologically similar to tobacco mosaic virus (TMV). The biophysical and biochemical properties of CGMMV are also similar to those of TMV. The homology of the amino acid sequence of both proteins is also very high.

It has been known from sedimentation velocity runs, standard light scattering and small-angle X-ray solution scattering (SAXS) using synchrotron radiation that the coat protein of TMV self-associates to form several kinds of aggregates depending on pH, temperature, ionic strength and protein concentrations<sup>1</sup>. The self-association of CGMMV protein has also been made by static SAXS<sup>2</sup>. We have continued the time-resolved SAXS measurements of CGMMV protein self-association process by temperature jump.

## Results and Discussion

CGMMV coat protein was dialyzed against 5mM, 50mM and 100mM phosphate buffer (PB) at pH 7.2. Time-resolved SAXS experiments were performed with the Enzyme Diffractometer BL-10C. Temperature jump from 5°C to 20°C or 25°C were performed with a sample cell whose pathlength is 1mm and its window is composed of a pair of quartz plates in thickness of 50  $\mu$ m. The dead time is less than 0.1sec.

The logarithm of scattered intensities  $I(h)$  was plotted against squares of the scattering vector  $h$ . In the present case protein solutions are mixtures of 4S (A-protein, around trimer of subunits), 8S, 20S disk (34 subunits) and multilayer disks, although their existing ratio varies by the condition of the solution.

In the most cases the above plots at each reaction time could be approximated by two components over the wide range of  $h$  which is the same as in the static SAXS<sup>2</sup>. A radius of gyration ( $R_g$ ) of the particle and a scattered intensity at  $h=0$ ,  $I(0)$ , are calculated from Simplex curve fitting method.

The time courses of CGMMV protein association are shown in Fig.1. Temperature jump is done from 5°C to 25°C where 20S disk predominantly elongates to multilayer disks. The  $R_g$

shows constant values at each time, whose values are 7nm for multilayer disk and 2.8nm for A-protein. The  $I(0)$  value for A-protein obtained shows no appreciable change. However, the  $I(0)$  for multilayer disk increases gradually with the reaction time. These data suggest that the disk formation is completed within 10 sec, that the elongation process is very slow and that the CGMMV protein elongates to a triple- or quadruple-layered double disk by jumping from 5°C to 25°C.

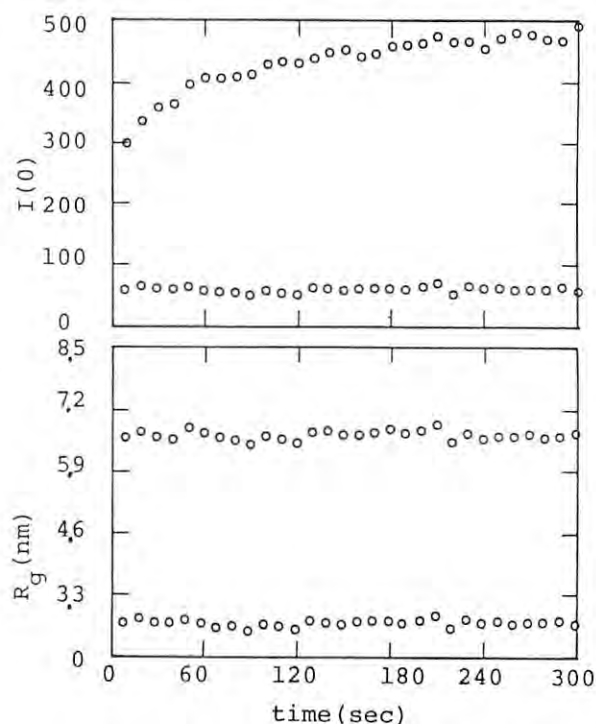


Fig.1. Time courses of the change of  $I(0)$  (upper) and  $R_g$  (nm) (lower) in 50mMPB at pH 7.2. Temperature jump is from 5° to 25°C. Protein concentration is 13mg/ml. The time interval is 10 sec.

1) Y.Hiragi et al:J.Mol.Biol.in press.

2) Y.Sano et al:Photon Factory Activity Report 5(1987)262.

## CONFORMATION CHANGE OF AMYLOSE AND AMYLOPECTIN INDUCED BY COMPLEXATION WITH IODINE-IODIDE

T. HIRAI\*, M. HIRAI\*\*, S. HAYASHI\*, and T. UEKI\*\*\*

\*Faculty of Textile Science and Technology, Shinshu University, Ueda 386

\*\*Department of Liberal Art, Kanagawa Institute of Technology, Atsugi 243-02

\*\*\*Department of Biophysical Engineering, Osaka University, Osaka 560

## INTRODUCTION

Complex formation of amylose with iodine has been known extensively.<sup>1,2</sup> Although the structure of the complex has been investigated from various points of view, it still remains some ambiguity. It has been suggested that the complex is considered to be a cluster compound in which polyiodide, a coloring matter of the complex, is occluded in the helical cavity of the amylose  $\alpha$ -helix.<sup>3,4</sup> It was also speculated that the structure of amylose changes with the complex formation.<sup>2,5</sup> In order to clarify the dynamic process of the conformation change accompanied with the complex formation, the authors started investigation by the use of small-angle X-ray scattering instrument using SOR at KEK. In this report, some preliminary results derived from scattering data of the iodine complex will be shown.

## EXPERIMENTAL

Amylose-A and amylopectin were guaranteed grade and extra pure reagent, respectively, and were purchased from Nakarai Chemicals Ltd. Some of the amylose samples were purified from potatoes according to Schoch's method.<sup>6</sup> Partially formalized poly(vinyl alcohol) (PFV) was prepared by acetalization of poly(vinyl alcohol). Other reagents were guaranteed grade purchased from Wako Chemical Industries Ltd.

Small-angle X-ray scattering experiments were carried out with small-angle scattering equipment SAXES installed at BL10C line in the Photon Factory of KEK. The wavelength used was 1.49 Å, and the sample-detector distance was 65 cm. Sample solutions were put into sample cells of 1 mm path-length. The time of exposure of samples to the X-ray beam was 900 sec.

## RESULTS AND DISCUSSION

In Fig. 1 and 2, distance distribution curves were shown on amylose and amylopectin with their iodine complexes, respectively. As shown in Figure 1, the center of scattering density and maximum length of intramolecular vector of amylose were changed drastically, compared with the case of amylopectin in Figure 2. It means that amylose changed its conformation from compact structure to extended one in this complexation process. Conformation change accompanied with the complexation was much bigger in amylose than in amylopectin. As the effect of ionic strength did not seriously affect on the conformation of amylose and amylopectin, the changes shown in the figures are attributed to the conformation change accompanied with the complexation. In the case of amylose of high molecularweight, the conformational change was not observed as just like to the case of amylopectin. The iodine complex of PFV did not show conformation change by the complexation, either, being consistent with the results of circular dichroism spectra on poly(vinyl alcohol).<sup>7</sup>

If the conformation change accompanied with the complexation reflects the conformational change from worm-like conformation to extended rod-like one as has been suggested,<sup>5,8</sup> the results shown in this report can be con-

sidered to be a first evidence that directly elucidates the conventional idea.

## REFERENCES

- 1) J. Szejtli, M. Richter, and S. Augustat, *Biopolymers*, **5**, 5-16(1967).
- 2) J. Szejtli, S. Augustat, and M. Richter, *Biopolymers*, **5**, 17-26(1967).
- 3) M. Noltemeyer and W. Saenger, *J. Am. Chem. Soc.*, **102**(8), 2710-2722(1980).
- 4) M. Noltemeyer and W. Saenger, *Nature*, **259**, 629-632(1976).
- 5) T. Handa and H. Yajima, *Biopolymers*, **20**, 2051-2072(1981).
- 6) T. J. Schoch, *Adv. Carbohydr. Chem.*, **1**, 247-277(1945).
- 7) M. K. Pal and P. K. Pal, *Makromol. Chem.*, **188**, 1735-1742(1987).
- 8) A. Cesaro, J. C. Benegas, and D. R. Ripoll, *J. Phys. Chem.*, **90**, 2787-2791(1986).

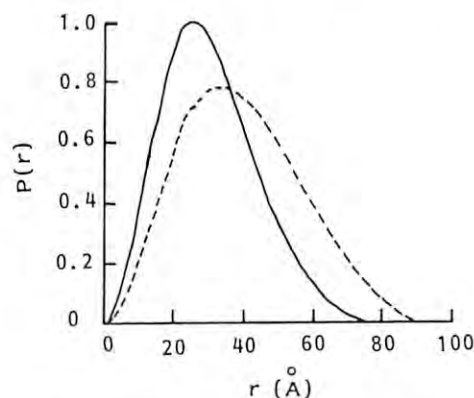


Fig.1 Comparison of the length distribution functions of amylose (—) and amylose-iodine-iodide complex (---). Molecular weight of amylose was 2900, [amylose]=0.2 unit-mol/l, [I<sub>2</sub>]=0.02 mol/l, [I<sup>-</sup>]=2×10<sup>-3</sup> mol/l, measured at 15°C.

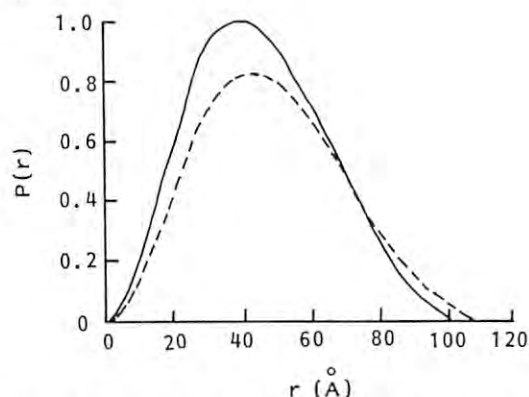


Fig.2 Comparison of the length distribution functions of amylopectin (—) and amylopectin-iodine-iodide complex (---). Molecular weight of amylopectin was >9000, [amylopectin]=0.2 unit-mol/l, [I<sub>2</sub>]=0.02 mol/l, [I<sup>-</sup>]=2×10<sup>-3</sup> mol/l, measured at 15°C.



# DETECTION CHARACTERISTICS OF MICROCHANNEL PLATES FOR PLASMA X-RAY DIAGNOSTICS

Naohiro YAMAGUCHI, Teruji CHO, Takashi KONDOH, Sadao AOKI\*,  
Hideki MAEZAWA\*\*, Masaharu NOMURA\*\*, and Yoshinori SATOW\*\*

Plasma Research Center, University of Tsukuba, Tsukuba, Ibaraki 305

\* Institute of Applied Physics, University of Tsukuba, Tsukuba, Ibaraki 305

\*\* Photon Factory, National Laboratory for High Energy Physics, Tsukuba, Ibaraki 305

## Introduction

X-ray measurement is an important method to diagnose high temperature plasmas. In general, spatial and spectral resolutions are required together with temporal resolution for plasma X-ray measurements. Therefore, two-dimensional or position-sensitive detectors become an important component of X-ray diagnostic instruments. Microchannel plates (MCPs) have often been used in X-ray imaging system<sup>1)</sup> or XUV spectrometer<sup>2)</sup>. We have performed the calibration measurement by using synchrotron radiation to investigate the X-ray detection characteristics of MCPs for a wide energy range and various angle of incidence<sup>3)</sup>.

## Experimental and Results

The specification of the MCP (Hamamatsu F1943-22MX) is listed as follows: Its channel diameter is 15  $\mu\text{m}$ , length to diameter ratio 40, open area ratio 57 %, and channel bias angle 13'. The surface of MCP is coated with normal electrode materials (Fe and Cr). The MCPs are operated under the condition of the unsaturated current detection mode. The calibration measurements have been performed by using synchrotron radiation from two beamlines. The beamlines are the undulator radiation beamline with an InSb(111) double crystal monochromator (1.8 to 8 keV) and the vertical

wiggler branch beamline with a Si(553) double crystal monochromator (23.4 to 82.5 keV). The incident photon flux has been calibrated by using a gold photodiode and a silicon surface barrier (SSB) detector at the former beamline, and by an ionization chamber with Kapton windows at the latter beamline.

The current response obtained in this experiment is shown in Fig.1. Some structures in the response are observed at the energies corresponding to the absorption edges of the MCP glass materials, Si and Pb. The current response as a function of incident angle to the channel axis,  $\theta$ , is also investigated for different X-ray energies. The results are shown in Fig.2 along with the previous data<sup>3)</sup>. In the lower energy ( $h\nu < 2\text{--}3\text{ keV}$ ), the response is proportional to  $\cot\theta$ , which agrees with the photoelectric response of a single cylindrical photocathode. On the other hand, in the higher energy range ( $h\nu \sim 7\text{--}20\text{ keV}$ ), a weak dependence on  $\theta$  is observed, and for very high energy photons ( $h\nu > 60\text{ keV}$ ) the response becomes proportional to  $\sec\theta$ . This is explained as follows: High energy X-rays can penetrate through the channel walls, then multiple channels contribute to produce photoelectrons. The number of channels increases as the angle of incidence increases, which is proportional to  $\sec\theta$ .

## References

- 1) N. Yamaguchi et al., Jpn. J. Appl. Phys. 24, 1065 (1985).
- 2) R. K. Richards, H. W. Moos, and S. L. Allen, Rev. Sci. Instrum. 51, 1 (1980).
- 3) T. Kondoh et al., Rev. Sci. Instrum. 59, 252 (1988).

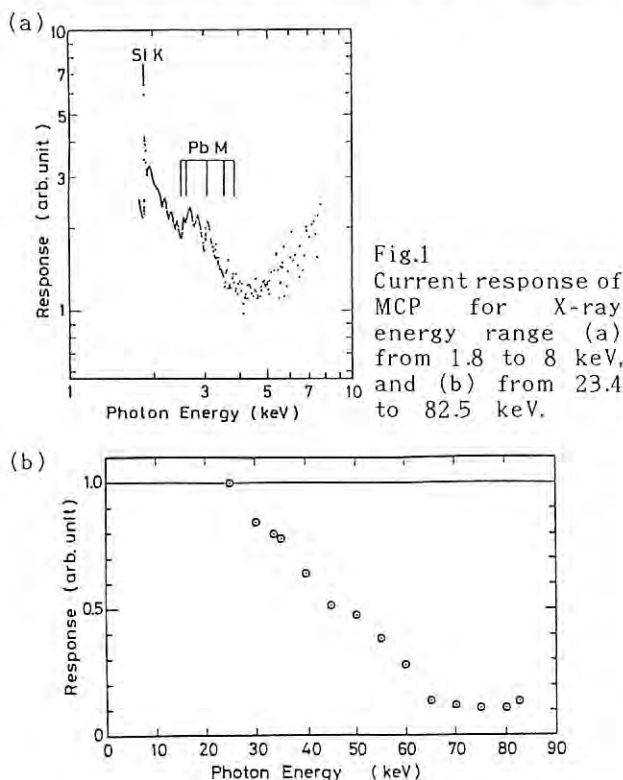


Fig.1  
Current response of  
MCP for X-ray  
energy range (a)  
from 1.8 to 8 keV,  
and (b) from 23.4  
to 82.5 keV.

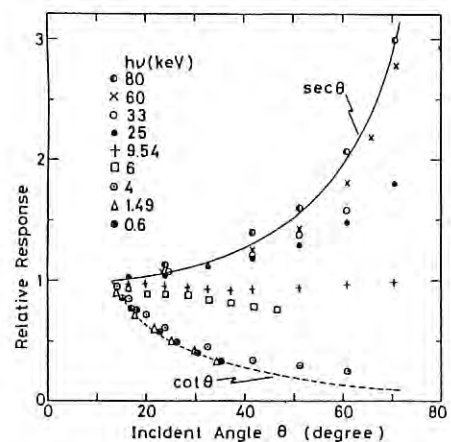


Fig.2 Relative X-ray detection efficiency of  
MCP vs. incident angle to the channel  
axis,  $\theta$ . Parameter is X-ray energy.  
Each curve is normalized at  $\theta = 13'$ .

## QUANTUM EFFICIENCY OF GOLD PHOTOCATHODES (2-8 keV)\*

T. Cho, N. Yamaguchi, T. Kondoh, M. Hirata, S. Miyoshi, S. Aoki<sup>1</sup>,  
H. Maezawa<sup>2</sup>, and M. Nomura<sup>2</sup>

Plasma Research Centre, University of Tsukuba, Ibaraki 305

<sup>1</sup>Institute of Applied Physics, University of Tsukuba, Ibaraki 305

<sup>2</sup>National Laboratory for High Energy Physics, Tsukuba, Ibaraki 305

## ABSTRACT

The quantum efficiency of gold photocathodes is investigated by using undulator radiation from 2 to 8 keV; in particular its detailed structure near the M absorption edge region is obtained. The secondary electron conversion efficiency of gold is calculated using the mass absorption coefficient given by a relativistic Hartree-Slater model and by the semiempirical values of Henke et al., respectively. These data are compared with the published data at some discrete energies, and we add several new data points, especially for the gold edge region (2-4 keV). Also, EXAFS is observed in the secondary electron current of the gold photocathode.

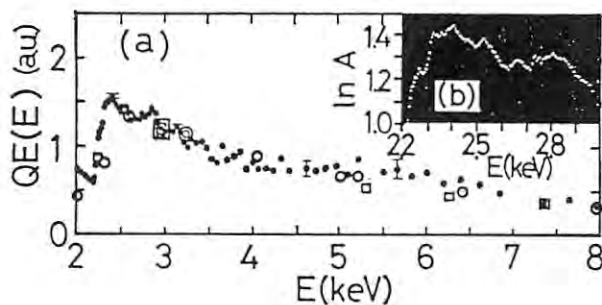


Fig. 1

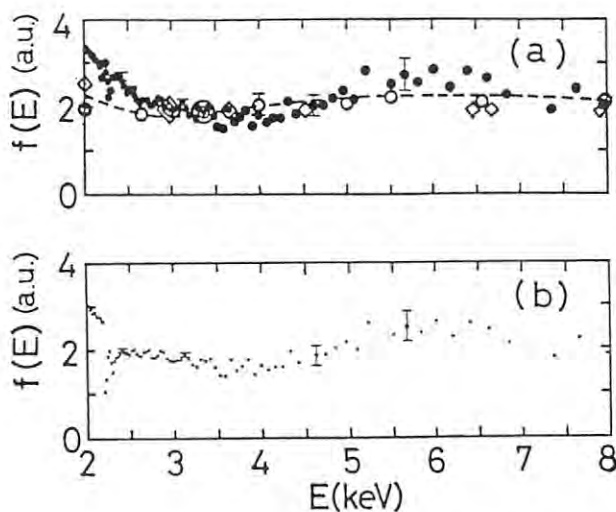


Fig. 2

## I QUANTUM EFFICIENCY OF GOLD PHOTOCATHODES

Figure 1 shows the relative values of  $QE(E)$  of gold as a function of photon energy; this efficiency is calculated from the following process: The experimental results of the normalized detection currents of  $I_{Au}/I_M$  and  $I_{SSB}/I_M$  give the energy response of  $I_{Au}/I_{SSB}$  for the normalized incident photon intensity. Since  $QE(E)$  of gold is proportional to the normalized energy response of  $I_{Au}$  by the incident photon intensity, the values of  $QE(E)$  is calculated from  $I_{Au}/I_{SSB}$  multiplied by the photon energy response of  $I_{SSB}$ ; this response is obtained by its parameters of the depletion layer, the dead layer and the entrance window thickness. In Fig. 1(a),  $QE(E)$  is plotted along with the data points from Henke et al. ( $\square$ ) and Day et al. ( $\circ$ ), where the relative values of the data are normalized at the points shown by  $\boxplus$  and  $\odot$ . It is noted that the jumps of  $QE(E)$  are seen at the  $M_V$  edge (2.29 keV) and the  $M_{IV}$  edge (2.21 keV). In Fig. 1(b), its detailed structure near the edges is presented in the form of  $I_{Au}/I_{SSB}$ . An oscillatory structure (EXAFS) above the energy of the  $M_V$  edge is found.

## II SECONDARY ELECTRON CONVERSION EFFICIENCY OF GOLD

The efficiency of converting primary photon energy into secondary electrons is described as  $f(E) = QE(E) / (\mu(E) \times E)$ . Here, the values of  $\mu(E)$  for gold are summarized by Saloman, Hubbell and Scofield. Two values of  $\mu(E)$  for each  $E$  are given by using (I) a relativistic Hartree-Slater model, and (II) the semiempirical values of Henke et al. Figures 2(a) and (b) correspond to each value of (I) and (II) described above, respectively. The data obtained by Day et al. ( $\circ$ ) and Eliseenko et al. ( $\diamond$ ), are also plotted in Fig. 2(a), along with the data fit by Day et al. (dotted curve). The symbols of  $\odot$  and  $\boxplus$  are the normalized points of their data to Fig. 2(a).

\* T. Cho et al., to be published in Rev. Sci. Instrum. (Nov. 1988)

# X-RAY DIFFRACTOMETRIC DETERMINATION OF LATTICE MISFIT BETWEEN $\gamma$ AND $\gamma'$ PHASES IN NI-BASE SUPERALLOYS

Katsumi OHNO, Hiroshi HARADA, Toshihiro YAMAGATA and Michio YAMAZAKI  
National Research Institute for Metals, Meguro-ku, Tokyo 153, JAPAN

Kazumasa OHSUMI

National Laboratory for High Energy Physics, Tsukuba-shi Ibaragi-ken 305, JAPAN

## Introduction

Nickel-base superalloys (so called single crystal Ni-base superalloys) for gas turbine blades have  $\gamma'$  precipitates, an ordered FCC phase based on  $\text{Ni}_3\text{Al}$ , in  $\gamma$ -matrix having a disordered FCC structure. The mechanical property of the alloys depends on the following factors<sup>1</sup>: 1) the volume fraction and size of  $\gamma'$  precipitate, 2) the composition of the  $\gamma$  and  $\gamma'$  phases, and 3) the coherency strains due to the lattice misfit between both phases.

The first factor can be easily analyzed by electron microscopy combined with image processing<sup>2</sup>. The second factor is to be determined by electron probe X-ray micro-analysis<sup>2</sup>.

On the third factor, the measured lattice misfits in the alloys by powder X-ray diffractometry were not reliable, because the misfit values are usually so small that most of the main diffraction lines overlap in the patterns obtained with a conventional X-ray tube focusing diffractometer (CTFXRD)<sup>3</sup>. In addition, the super lattice lines were usually very weak. This report describes the outline of the measurements of the diffraction patterns and their numerical analysis for resolving the overlapped peaks into individual peak

## Experimental and Results

Single crystal alloys having various lattice misfit values ( $\delta = (a_{\gamma'} - a_{\gamma})/a_{\gamma}$ ), from negative to positive, were provided by means of an alloy design system<sup>4,5</sup>. The single crystal rod was prepared for each alloy by directionally solidification method. The rods were heated to dissolve  $\gamma'$  precipitates and homogenize  $\gamma$  structure. These rods were then aged to complete  $\gamma'$  precipitation. Powder specimens, which were filed from the alloys and completely annealed, were measured with the Synchrotron radiation parallel beam X-ray diffractometer (SRPXRD)<sup>6</sup> on the 4B-beam line.

Synchrotron powder data were analyzed by applying a profile fitting method. The lattice misfits between  $\gamma$  and  $\gamma'$  phases were detected 0.06% by the fitting method.

The (311) reflection peak profiles obtained from both  $\gamma'$  phases electrochemically extracted from sample rod and the filings specimens were significantly different as shown in Fig. 1. However, it was difficult to detect these small changes of the peak position and shape by using CTFXRD.

Fig. 1 shows that the lattice parameter of  $\gamma'$  phases extracted from the alloys and that of in  $\gamma$ -matrix were completely different due to the elastic coherency strains between both phases. In the case of NASAIR-100 alloy having negative misfit,  $\gamma'$  phase was considered to be tense by  $\gamma$ -matrix because the lattice parameter of  $\gamma'$  phase extracted from

the alloys was smaller than that of  $\gamma'$  phase in  $\gamma$ -matrix.

Conversely, it seems that  $\gamma'$  phase in TMS-19 alloy having positive misfit was compressed by  $\gamma$ -matrix since the lattice parameter of  $\gamma'$  phase extracted was larger than that of  $\gamma'$  phase in  $\gamma$ -matrix as shown in Fig 1.

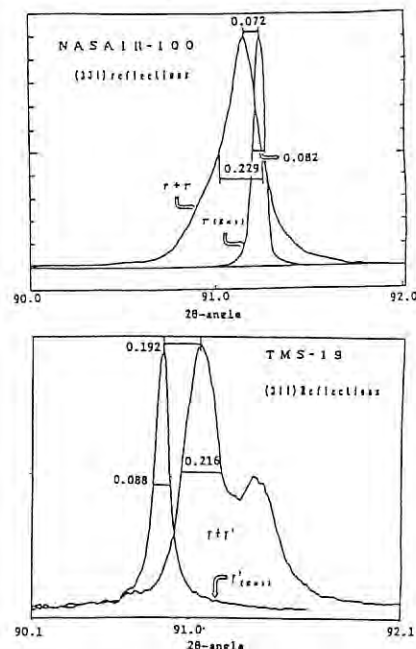


Fig. 1 Comparison of peak profile reflected from extracted  $\gamma'$  phases and from filing specimens

SRPXRD was a powerful tool for understanding the relation between the lattice misfit of  $\gamma$ - $\gamma'$  phases and the composition, the volume fraction, the morphology of  $\gamma'$  phase and etc.. The calculation of in situ misfit values will be made possible in the next step by taking the interaction factor into account by using Poisson's ratio and shear modules of  $\gamma$  and  $\gamma'$  phases.

## References

- 1) P. Caron and T. Kahn, Met. Sci. Eng., **61**, 173, (1983).
- 2) K. Ohno, and M. Yamazaki, Adv. X-Ray Anal., **30**, 67, (1987).
- 3) K. Ohno, H. Harada, T. Yamagata and M. Yamazaki, Tran. ISIJ, **28**, 219, (1987)
- 4) H. Harada, M. Yamazaki, Tesu-to-Hagane, **65**, 1059, (1979).
- 5) T. Yamagata, H. Harada, S. Nakazawa and M. Yamazaki, 5th Inter. Sympo. on Superalloys, 157, (1984).
- 6) W. Parrish, M. Hart, T. C. Huang and M. Bellotto, Adv. X-Ray Anal., **30**, 373, (1987).



## POWDER DIFFRACTION-PROFILES OF THE MONOCLINIC SUPERSTRUCTURE OF TRIDYMITE

Kuniaki Kihara, Hiroki, Okudera, Hirokazu Nakae, Tsuyoshi Motoyama, Hideyuki Sugaya, Masayuki Okuno, Takeo Matsumoto, Masanori Matsui\*, Takamitsu Yamanaka\*\* and Toshibumi Ashida\*\*

Department of Earth Sciences, Faculty of Science, Kanazawa University, Kanazawa 920

\* Chemical Laboratory, Kanazawa Medical University, Uchinada, Kahoku-Gun 920-02

\*\*College of General Education, Osaka University, Toyonaka, Osaka 560

### Introduction

Tridymite, a silica polymorph, is a typical example of minerals, showing successive transitions as temperature changes. One of the room temperature forms of this mineral has a monoclinic superstructure with twelve times of the cell of the hexagonal prototype structure. Since this mineral crystallizes at high temperatures, the lower temperature phases usually appear in complicated twins, as the results of the transitions.

In this research project, we aim at establishing the method of structural study of superstructures by the analysis of powder-diffraction profiles taken with SR. The twinning must not affect the powder diffraction, but the most serious problem may arise, not only from the superposition of peaks, but also from poor intensities of superstructure reflections. In this regard, X-rays of SR may have great advantages in the intensity and resolution.

The study is still in progress. We, nevertheless, describe about the experimental conditions and the comparison between the diffraction patterns obtained from SR X-rays and from Cu K $\alpha$  in our laboratory.

### Experimental

The experiment was performed at the BL-4 station of the Photon Factory, using the diffractometer PFPD<sup>1</sup>, which is equipped with a silicon monolithic double-monochromator, an X-ray monitor, a collimation-slit system and a scintillation counter. The goniometer has the radius of 300 mm and is scanned vertically. The cell constants of the sample at room temperature were previously determined as  $a=25.86$ ,  $b=4.99$ ,  $c=18.50$  Å and  $\beta=117.7^\circ$ . The sample crystals grown up on the surface of silica brick, supplied by K. Sakai of Asahi Glass Research Laboratory, were ground in ethanol and only suspended particles were gathered a few minutes later. The wave length of X-rays were determined as 1.5415(2) Å by the least-squares fitting of five reflections from Si. The measurements of the diffraction profiles were repeated several times in different conditions for the  $2\theta$  range from 22 to  $24^\circ$ . A condition described below was chosen as the best, and a full scan from 20 to  $100^\circ$  in  $2\theta$  was carried out.

### Results and discussion

Fig.1 shows the diffraction profile recorded under the conditions; slit system 0.5-0.3-0.2mm and  $2^\circ$  for the soller slit, scanning step  $0.02^\circ$ , measuring time

15 seconds per step and maximum counting rate 667 cps. Fig. 2 is the profile obtained from a goniometer, Rigaku 2171B, with Ni-filtered Cu K $\alpha$  radiation for the same sample as used in the SR experiment. In this case, a very narrow slit system,  $DS=SS=1/6$  and  $RS=0.15$ mm, and slow scanning speed as  $0.25^\circ/\text{min}$  in  $2\theta$  was inevitable even in obtaining such a less comparable profile. It is obvious that the resolution of the peaks is highly improved for the profile in the SR experiment.

Even in the diffraction pattern from the present SR experiment, many superstructure reflections were too weak to detect, or detectable only with low certainty, and also some crowded reflections appear as apparent single peaks. It remains obscure, until the whole pattern fitting is completed, whether our first measurement was successful or not.

### Reference

- 1) R. Uno, H. Ozawa, T. Yamanaka, K. Ohsumi, and A. Nukui, Photon Factory Activity Report, No.5(1987)

Fig. 1

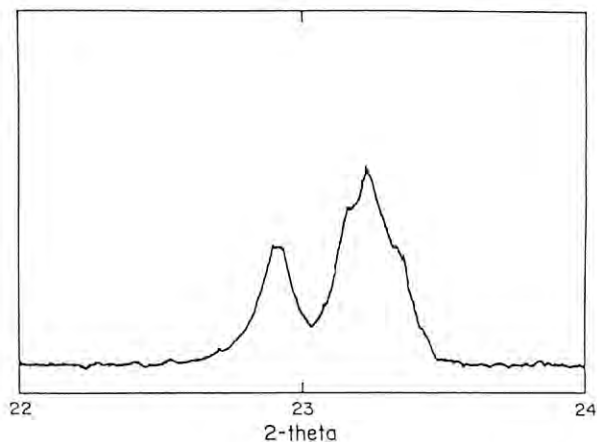
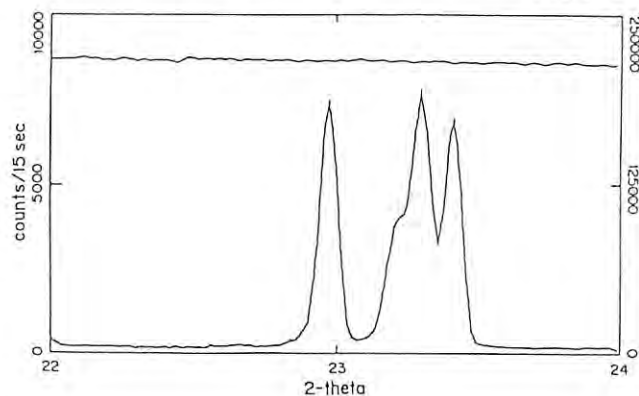


Fig. 2



# CHEMICAL STATE IMAGING OF ROCK SAMPLE BY X-RAY FLUORESCENCE SPECTROSCOPY USING CHEMICAL SHIFT OF Fe-K ABSORPTION EDGE

Izumi NAKAI, Yoshio SUZUKI\*, and Atsuo IIDA\*\*

Department of Chemistry, The University of Tsukuba, Ibaraki 305

\*Institute of Geoscience, The University of Tsukuba, Ibaraki 305

\*\*Photon Factory, National Laboratory for High Energy Physics, Tsukuba, Ibaraki 305

## Introduction

Knowledge of the chemical states of elements in a mineral is important to study its formation condition or metamorphic process. Mössbauer spectroscopy and optical absorption spectra have been often used for this purpose. However, it was difficult to obtain two dimensional data through these methods. Recently, Sakurai et al. have established a new technique which enables us to carry out chemical state mapping by X-ray fluorescence using absorption edge shifts.<sup>1)</sup> The present study is the first application of their method to practical problems in Earth Science.

## Experimental

Sample used in the imaging was fayalite from Hirukawamura, Gifu, Japan (Fig. 1 (a) & (b)).

X-ray absorption measurement near Fe K-edge was made at the XRF facilities at BL-4A at PF. Incident X-ray with beam size of 600x600  $\mu$  was obtained by a set of vertical and horizontal slit. The sample was placed on a XZ stage perpendicular to the orbital plane of SR and scanned by stepping motor. The intensity of the fluorescent X-ray was measured by Si(Li) detector. Details of data analysis is described in the literature<sup>1)</sup>.

## Results and Discussion

Fe K-edge absorption spectra of fayalite( $\text{Fe}_2^{2+}\text{SiO}_4$ ) and franklinite( $\text{ZnFe}_2^{3+}\text{O}_4$ ) are shown in Fig. 2, where the intensity of Fe K fluorescence X-ray is plotted as a function of the incident energy. Figure 2 shows that the energy of the absorption edge of franklinite ( $\text{Fe}^{3+}$ ) is higher than fayalite( $\text{Fe}^{2+}$ ). Consequently, when sample is excited by X-ray of 7.11 keV, divalent iron is mainly excited but with X-ray of 7.61 keV, both divalent and trivalent irons are excited.

Figures 3 (a) and (b) show two dimensional Fe images of the sample detected by Fe K fluorescence X-ray: (a) and (b) are excited by X-ray at 7.11 keV and 7.61 keV, respectively. Fig. 3 (b) indicates distribution of total iron ( $\text{Fe}^{2+} + \text{Fe}^{3+}$ ), while Fig. 3(a) represents an area rich in divalent iron. The sample rock is mainly composed of fayalite(Fa), greenalite(Gr), quartz(Qz) and contains a small amount of magnetite and grunerite. The white area in Figs. 3 (a) and (b) is lacking in iron and corresponds to the part of quartz. A simple arithmetical treatment of these data (see Ref. (1)) produces independent images of divalent and trivalent iron and the results are given in Figs. 3 (c) and (d). It is found that dark part in Fig. 3(c) correspond well with the distribution of fayalite where iron is divalent, while dark part in Fig. 3(d) corresponds well with that of greenalite and magnetite which contain trivalent iron.

The present study has demonstrated the capability of chemical state imaging of rock

samples with complicated textures. This method is truly nondestructive and it is therefore possible to analyze precious rock samples without any pre-treatment.

## Reference

- 1) K. Sakurai, A. Iida, M. Takahashi and Y. Gohshi, Jpn. J. Appl. Phys., 27, L1768(1988).

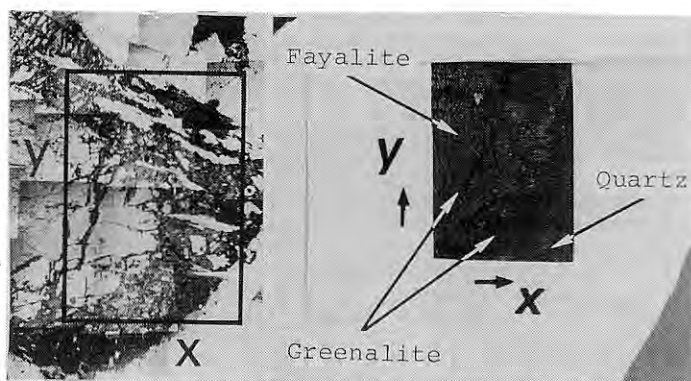


Fig. 1.(a) photomicrograph of sample (transmitted light) (b)analyzed area (reflected light).

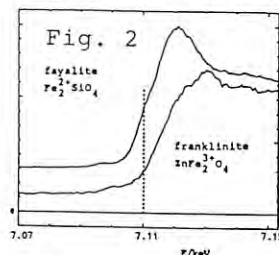
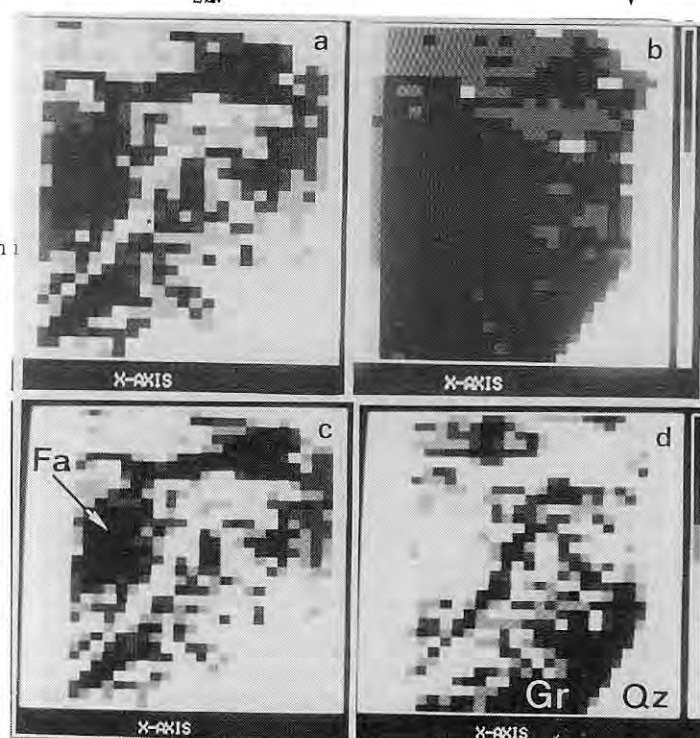


Fig. 2. Near edge absorption spectra.

Fig. 3. Fe K $\alpha$  image excited at (a) 7.11 keV and (b) 7.61 keV.

Distribution of (c) divalent Fe and (d) trivalent Fe.



## APPLICATION OF SYNCHROTRON RADIATION TO ARCHAEOLOGICAL OBJECTS (III)

Izumi NAKAI, Akihiko MOCHIZUKI, Takuji KAWASHIMA, Yoichi GOSHI\* and Atsuo IIDA\*\*

Department of Chemistry, The University of Tsukuba, Ibaraki 305

\* Department of Industrial Chemistry, Faculty of Engineering, University of Tokyo, Hongo, Tokyo 113

\*\* Photon Factory, National Laboratory for High Energy Physics, Tsukuba, Ibaraki 305

Introduction

We have demonstrated the potential advantages of SR-XRF in the analysis of archaeological objects in our previous reports. Here, we describe further application of this technique: Exp. 1 - two dimensional chemical imaging of artistic pattern in ancient artifacts; Exp. 2 - chemical state analysis of colorant elements of archaeological objects by measuring chemical shift of X-ray absorption edge by detection of XRF.

Experimental

Experiments 1 and 2 were carried out at BL-4A using the energy dispersive XRF system with a Si(Li) detector. Samples were excited by monochromated X-ray using Si(111) double crystals.

Exp. 1. Samples were placed on a remote controlled X-Z stage perpendicular to the orbital plane of SR. Fine parallel beam of desirable size was obtained by a simple set of vertical and horizontal slits. Two dimensional intensity data were obtained by step scanning.

Exp. 2. Absorption spectra were measured by X-ray fluorescence mode. Intensity of incident beam was monitored by an ionization chamber placed in front of the sample and that of the fluorescent X-ray was measured by the Si(Li) detector.

Results and Discussion

1. Chemical Imaging Figure 1(a) shows a photograph of the sample, which is a fragment of a broken core glass made in Egypt 18 dynasty (ca. 1500 B.C.). It was probably used for a perfumed oil bottle. The analysis was made for the area indicated by the frame in Fig. 1(a). The results are given in Figs. 1(b), (c), (d) indicating the Ni, Cu, and Zn images of the sample. The Cu distribution corresponds well with the sky blue glass, hence the colorant of the glass is found to be Cu. It was also found that zinc is abundant at the striped pattern of light brown color. The white striped pattern contains little transition metal elements, while the cobalt glass base is rich in the transition metals.

Figure 2(a) shows a photograph of the mosaic glass in Ptolemies dynasty (305 - 30 B.C.). This sample was excavated at a site of the Eastern Mediterranean area. Two dimensional imaging was made for Mn, Cu, Pb and the results are given in Figs. 2(b), (c), and (d), respectively. The frame in Fig. 2(a) indicates the analyzed area. It is found that Mn is responsible for the brown color of the glass. It is noteworthy that the white glass also contains significant amount of Mn. Mn is probably used as achromatic reagent of coloration of iron, which may be contained as an impurity in the raw material. It is found from Fig. 2(c) that the blue color of the glass is due to Cu. Figure 2(d) indicates that the base is lead glass and lead is particularly abundant at the red glass. Thus, coexistence of Cu and Pb is responsible for the red coloration.

2. Chemical State Analysis Fig. 3 shows Cu K-edge absorption spectra of several Cu containing substances. The intensity of Cu K fluorescent X-ray was plotted as a function of the energy of the incident X-rays. The energy of the absorption edge of CuO (divalent Cu) is higher than that of Cu<sub>2</sub>O (monovalent Cu). We can use such a chemical shift to predict the oxidation state of elements. Thus, it is found that the red glass contains monovalent copper and sky blue glass contains divalent one. Since this

measurement is truly nondestructive, we can apply the technique to the analysis of precious cultural assets such as potteries, glass ware, etc. Knowledge of the oxidation state of coloring elements in pigments, glaze etc. will provide useful information on the technology of the production of artifacts.

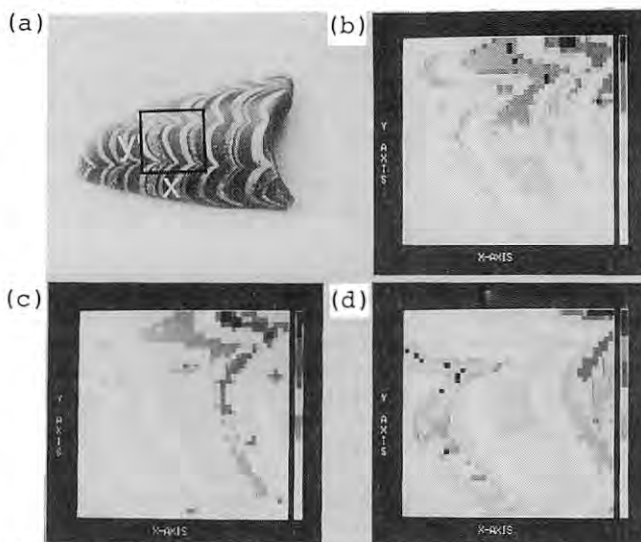


Fig. 1. Sample (a) and its Ni K $\alpha$  image (b), Cu K $\alpha$  image (c), and Zn K $\alpha$  image (d).

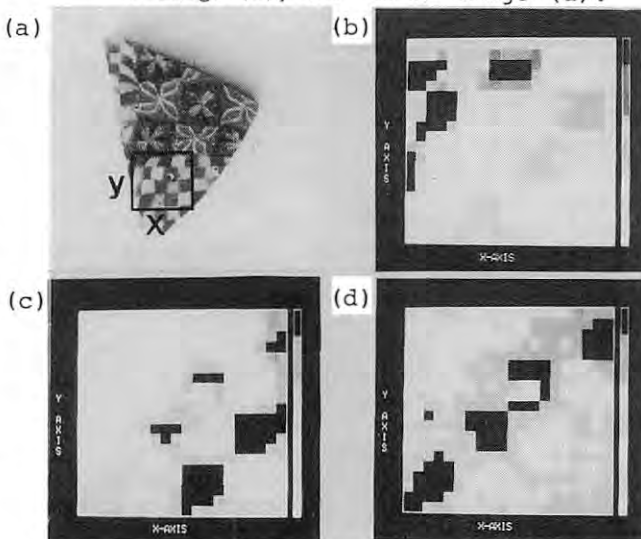


Fig. 2. Sample (a) and its Mn K $\alpha$  image (b), Cu K $\alpha$  image (c), and Pb L $\alpha$  image (d).

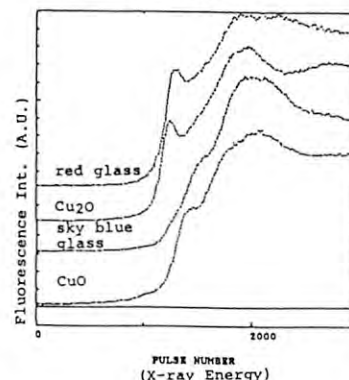


Fig. 3 Near edge absorption spectra.

## Non-destructive chemical state analysis of Cu oxide compounds

Naoki SAITOH, Takao SUZUKI, Yohichi GOHSHI\*

National Research Institute of Police Science, 6 Sanbancho,  
Chiyoda-ku, Tokyo 102, Japan\*Department of Industrial Chemistry, Faculty of Engineering,  
University of Tokyo, 7-3-1 Hongo, Bunkyo-ku, Tokyo 113, JapanIntroduction

It is important to analyze the chemical state of Cu in the Cu oxide sample from a fire scene because the chemical state of Cu may indicate the cause of the fire and the place where the fire was occasioned in an electric fire hazard. That is, in general when Cu oxide is CuO, an oxidation of Cu is likely occurred before the fire and when it is Cu<sub>2</sub>O, an oxidation may be occurred after the fire. In order to analyze amorphous samples non-destructively, an x-ray fluorescence method is usually used. But as for Cu oxide samples, there is little difference in profiles of Cu K $\alpha$  spectra(see Fig.1). Therefore in actual cases, it is not easy to distinguish the chemical state of Cu by means of the x-ray fluorescence spectroscopy. However when an absorption edge shift exists between two different chemical states of the same atom, there is a possibility to distinguish a chemical state by a selective excitation using an appropriate excitation energy. The method utilizing the shift of the absorption edge is expected to be useful to clarify the chemical state of Cu atom in Cu oxide compounds. We examined this method for the analysis of Cu oxides chemical state.

Experimental and Results

A SR beam is monochromated with a Si single crystal and is collimated to 50 $\mu$ m\*50 $\mu$ m through a slit. The collimated x-ray beam was irradiated on a sample and a fluorescence emission was detected with a solid state detector. The sample on a x-y stage was moved in a 2-dimensional space to measure x-ray fluorescence emission from each point and to obtain the chemical state mapping of Cu. At first, the Cu K absorption spectra of Cu compounds were measured to select an excitation energy for chemical state analysis. In Fig.2, Cu K absorption spectra of CuO and Cu<sub>2</sub>O are shown. There is a significant discrepancy between these two absorption profiles. At an excitation energy pointed to A in Fig.2, Cu K $\alpha$  fluorescence emission was measured.

In Fig.3, a mapping result for a test sample consisting of CuO and Cu<sub>2</sub>O is shown. In this figure, an area with larger intensity includes a larger concentration of Cu<sub>2</sub>O. This figure indicates that the x-ray fluorescence spectroscopy using the absorption edge shift makes it possible to perform a non-destructive chemical state analysis for various actual samples.

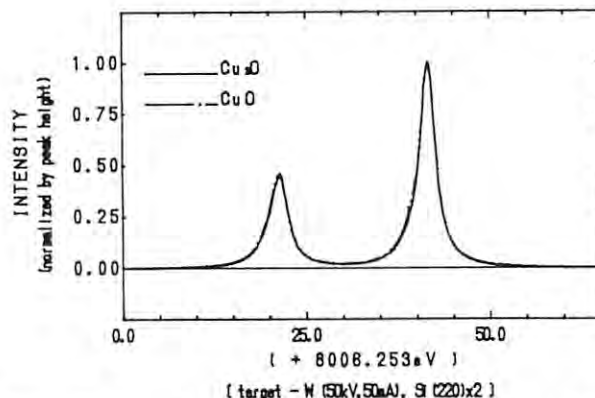


Fig.1 Cu K $\alpha$  emission spectra of CuO(dashed line) and Cu<sub>2</sub>O(solid line).

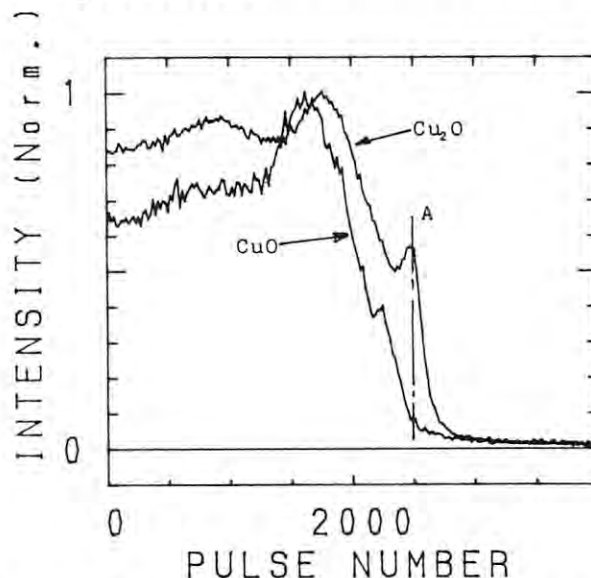


Fig.2 Cu K absorption spectra of CuO and Cu<sub>2</sub>O.

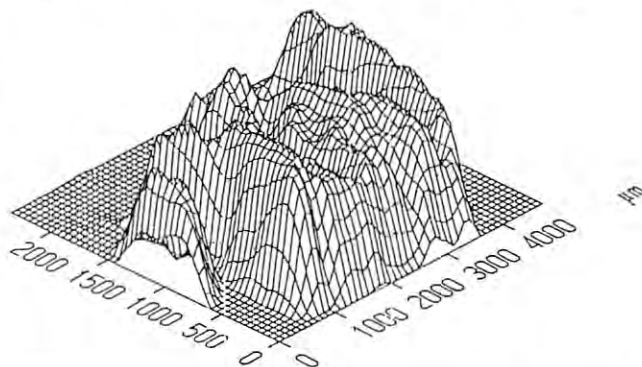


Fig.3 Cu K $\alpha$  fluorescence emission intensity distribution of a test sample.



## MICRO X-RAY FLUORESCENCE ANALYSIS USING ENERGY TUNABLE SR X-RAY MICRO ANALYZER

S. Hayakawa, A. Iida\*, S. Aoki\*\*, K. Sakurai, T. Onuki\*\*\*, O. Mitomi\*\*\* and Y. Gohshi

Department of Industrial Chemistry, Faculty of Engineering, University of Tokyo, Hongo, Bunkyo-ku, Tokyo 113

\*Photon Factory, National Laboratory for High Energy Physics, Tsukuba, Ibaraki 305

\*\*Institute of Applied Physics, University of Tsukuba, Tsukuba, Ibaraki 305

\*\*\*Nikon Co., Nishi-ohi, Shinagawa-ku, Tokyo 140.

Introduction

Focusing of SR has been expected to give the new dimensions to the various kinds of X-ray analyses both in the sense of the beam intensity and the spatial resolution. We have developed and characterized a SR X-ray micro analyzer(SRXMA) with Wolter type 1 mirror system<sup>1,2</sup>. In this report, the present performance of the SRXMA is described.

Experimental

Experiments were performed on the BL-4A. A schematic beam line layout is shown in Fig. 1. Two Pt coated Wolter type 1 mirrors(condenser and focusing mirror) were used. X-rays up to 10 keV were reflected and focused. A newly installed Si(111) double crystal monochromator upstream the condenser mirror has enabled the monochromatic micro beam analysis.

Samples were placed at F2 and scanned in x,y,z directions with stepping motors. An energy dispersive X-ray fluorescence(EDXRF) system was used to analyze the sample.

Results and Discussion

Improvements in the mechanism for the alignment have realized the reduction in the beam size and the enhancement of the intensity. With 8 keV monochromatic X-rays, the photon flux of  $4 \times 10^6$  photons/sec:100 mA was obtained at the final focal point(F2).

To characterize the focusing mirror exclusively, the pinhole of  $16 \mu\text{m}$  at F1 was illuminated with 8 keV X-rays without using the condenser mirror system. To estimate the beam size, a knife edge was scanned across the beam spot and intensities of transmitted X-rays were measured. The numerical derivatives of the edge scan profiles represent the beam profiles, which are shown in Fig. 2. The beam size of  $1.6 \mu\text{m}$  in one direction was almost the same as the designed value( $1.2 \mu\text{m}$ ). However, the beam size perpendicular to the former direction was blurred by scattered X-rays. These results show that the present focusing mirror has high figure accuracy but considerable surface roughness.

Sensitivities with the SRXMA for 100 sec measurements were summarized in Table 1. Minimum detection limits(MDL) were estimated by the measurement of a reference sample. For Mn, the MDL in relative concentration and in absolute amount were 1 ppm and about 0.02 pg, respectively with white beam excitation.

Most important feature of the present system is its energy tunability with the fixed focus position. With the monochromatic micro beam, an absorption edge spectrum in a micro

region of a sample can be obtained. Our preliminary experiments show that chemical speciation in micro region can be realized using the shift of the absorption edge<sup>3</sup>.

References

- 1) Photon Factory Activity Report, 130(1987).
- 2) Y. Gohshi et al., Adv. in X-ray Anal. 31, 495(1988).
- 3) K. Sakurai et al., Anal. Sci., 4, 37(1988).

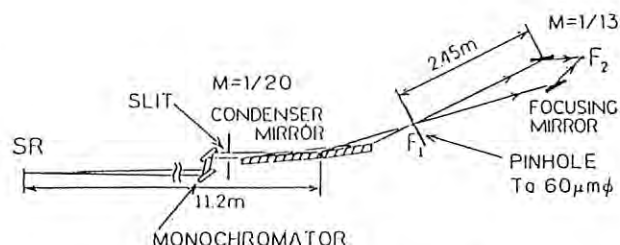


Fig. 1 a: A schematic beamline layout.

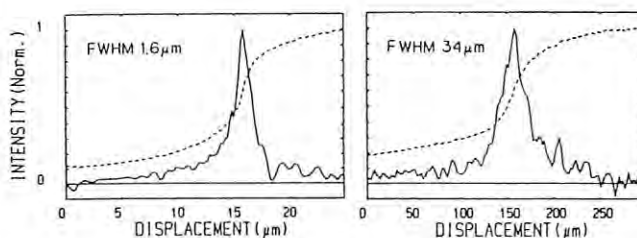


Fig. 2 The beam profile(solid line) obtained from the numerical derivative of the edge scan image(dotted line). vertical profile(left) and horizontal one(right).

Table 1. MDL obtained using a SRXMA for 100 sec measurement. Irradiation area was  $300 \mu\text{m}^2$ 

Excitation mode	MDL in		MDL in
	Mn	relative conc. Ca	abs. amount Mn
White	1 ppm	3 ppm	0.02 pg
Monochromatic (7.5 keV)	8 ppm	29 ppm	0.16 pg



## SR X-RAY FLUORESCENCE IMAGING BY IMAGE RECONSTRUCTION TECHNIQUE

Mamoru Takahashi, Kenji Sakurai, Atsuo Iida\*, Yohichi Gohshi

Department of Industrial Chemistry, Faculty of Engineering,  
University of Tokyo, Hongo, Tokyo 113, Japan\*Photon Factory, National Laboratory for High Energy Physics,  
Oho, Tsukuba-shi, Ibaraki 305, Japan

## INTRODUCTION

X-ray fluorescence (XRF) imaging can be made by the image reconstruction technique.<sup>1)</sup> A line-shaped incident X-ray beam is used with rotational and translational scanning of the sample in this imaging technique. A two dimensional elemental distribution of the sample is then obtained by the numerical processing. The advantages of using the image reconstruction technique in XRF imaging are the high signal to background ratio and the reduction of the measurement time due to the increased irradiation area at a step compared with the point-shaped beam technique. The chemical state imaging using the chemical shift of the absorption edge has been demonstrated by this technique.

In this report, we show that the XRF imaging with the high spatial resolution can be made with a sagittal focusing double crystal monochromator in combination with an asymmetric reflection.

## EXPERIMENTAL

The experiment was carried out on the beam-line 4A. A schematic arrangement is shown in Fig.1.

To achieve the high resolution XRF imaging, it is necessary to obtain the narrow line-shaped X-ray beam with the sufficient photon flux. We use a sagittal focusing double crystal monochromator and an asymmetric Si crystal for the beam demagnifier. A triangular-shaped ribbed crystal was used for the second crystal of the double crystal monochromator. An intensity gain of more than 10 was obtained by the sagittal focusing.

An asymmetric factor ( $b$ ) of the asymmetric crystal is given by  $b = \sin(\theta - \alpha) / \sin(\theta + \alpha)$ , where  $\theta$  is the Bragg angle and  $\alpha$  is the angle between the crystal surface and the reflecting plane. By using the asymmetric reflection as shown in Fig.1, the beam height is reduced by a factor of  $b$  with the intensity loss of only a factor of  $\sqrt{b}$ . We used the asymmetric crystal of  $1/70$  asymmetric factor at  $8.33$  keV. The height of the slit before the asymmetric crystal was  $160 \mu\text{m}$ . The distance between the slit and the sample was  $10$  mm.

A sample was mounted on the translational and rotational stage. The XRF from the sample was detected by a Si(Li) detector under the atmospheric condition.

## RESULTS AND DISCUSSION

We examined the beam height by scanning a

Ni 2000 mesh per inch grid ( $12.5 \mu\text{m}$  period,  $4.6 \mu\text{m}$  line width,  $1 \mu\text{m}$  thick). We estimated the beam height at about  $4 \mu\text{m}$ , which agrees with the designed one considering the broadening due to the angular divergence of X-rays. The incident X-ray intensity was more than  $1 \times 10^7$  cps ( $4 \mu\text{m}$  (h)  $\times$   $200 \mu\text{m}$  (w) beam size) at the SR beam current of  $200$  mA.

The XRF imaging by the image reconstruction technique was made with the same grid sample. The measurement carried out under the following conditions;  $90$  rotational steps ( $2^\circ$ /step),  $80$  translational steps ( $0.5 \mu\text{m}$ /step), and  $2$  sec measurement time at a step. The highest counts of Ni  $K\alpha$  intensity was more than  $1 \times 10^3$  cps. Fig.2 shows the reconstructed Ni XRF image of the Ni grid. It is clearly demonstrated that the high resolution (less than  $10 \mu\text{m}$ ) XRF imaging was achieved.

## REFERENCES

- 1) N. Gruker, X-Ray Spectrom. **8**, 149 (1979)

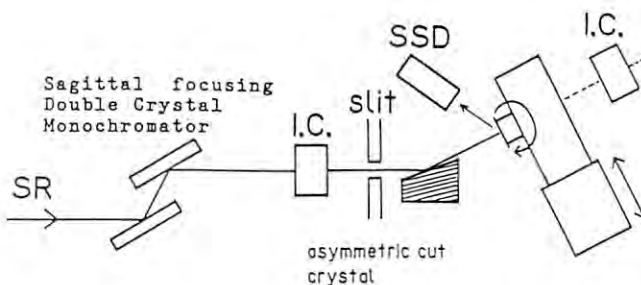


Fig.1 Experimental arrangement for the XRF image reconstruction.

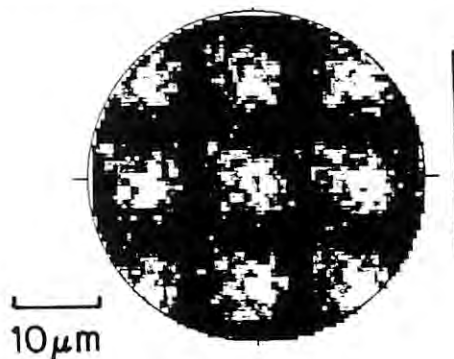


Fig.2 Ni  $K\alpha$  Fluorescence reconstructed image of a Ni 2000 mesh per inch grid.

DETERMINATION OF TRACE SIDEROPHILE AND LITHOPHILE ELEMENTS  
IN METEORITIC MINERAL CRYSTALS BY MICROFOCUS X-RAY FLUORESCENCE SPECTROMETER  
WITH REFERENCE TO THEIR FORMATION CONDITIONS

Osamu Hidaka, Hiroshi Takeda, Kazuhiro Toyoda, Jun Saito, Haruhiko Sato  
Mineralogical Institute, Faculty of Science, University of Tokyo  
Atsuo Iida

Photon Factory, National Laboratory for High Energy Physics  
Oho-machi, Tsukuba City, Ibaraki 305

### Introduction

Meteoritic minerals provide us with information on formation conditions and evolution of meteoritic and planetary materials in the early solar system. Major element abundances and crystallographic data of coexisting minerals have been employed for this purpose and trace element analyses have been performed on the separate samples by the INAA technique. It is ideal, if we could analyse trace elements within a localized area of the coexisting minerals. Thus, a microfocus X-ray fluorescence (XRF) spectrometer employing SOR is a powerful tool in earth and planetary sciences. We performed preliminary experiments on such unit constructed by Dr. A. Iida. Because we are interested in metal-silicate relationship, we tried to analyse some siderophile and lithophile elements in synthetic standards, meteoritic minerals and terrestrial mantle rocks. The purpose of these experiments were to find a sample preparation method to minimize contamination and to find possible sets of elements which can be analysed by this unit.

### Experimentals and Results

Samples used for microfocus XRF experiments include single crystal olivines and pigeonites about 1 mm in diameter coexisting in differentiated achondrites (PCA82506 and Y791538 ureilites) coexisting chromites and orthopyroxenes in terrestrial ultramafic rocks and achondrites (Y74013 diogenite). The samples are placed on a silicon wafer and fixed with Wevo Plastic (Tecnisco). Standard samples used are Ge metal, Pt alloy with 10.06% Ir, and Li borate glass beads doped by 5 REE (Yb, Ho, Eu, Nd, La) with three concentrations of each REE on the level of ca. 100, 20, 5 ppm, and those by Cu, Co, Cr, Y, Zr, of ca. 40 ppm. Standard rock samples JB-1 and JG-1 diluted with Li borate glass were also prepared as reference samples. The microfocus XRF unit on BL-4A was used for the XRF intensity measurements, irradiated in air by X-ray of exciting energies of 10, 20, 23.0 KeV, respectively. The beam size was adjusted to 0.5 X 2 and 2 X 3 mm. The intensities were counted for 400 sec. Results obtained are summarized below for each item of our proposal.

#### Trace elements in silicates-metal assemblages.

Perturbation of Ga, Ge, Ir between coexisting olivine, pyroxene and NiFe alloy in ureilites (Sample PCA82506) are useful data to trace their differentiation trends. We tried to determine Ge, but the more intense X-ray of Zn (8.28 KeV, 601.7 cps) was detected and interferes with weak Ge line. Because a single crystal was used, diffraction effect of fluorescent X-ray was detected, but avoided by rotating the crystal. Ir was also not detected because of interference

with other lines. However, weak lines of Ru (20.79 KeV, 350; 21.76 keV, 570 cps) were detected in the Ir-Pt standard, for an excitation energy of 23.60 KeV, which is the upper limit for BL-4A.

#### Ni in coexisting chromite and orthopyroxene.

Ni Ka and KB lines from orthopyroxenes and chromites from terrestrial ultramafic rocks have been well resolved by the XRF equipment. The Ni concentration in chromites from Y74013 diogenite is below 42 ppm. A chromite from Hidaka, Hokkaido, gives 0.44 wt. % Ni, which is high. The detection limit for samples containing Fe and Cr will be about 100 ppm. The errors by a microprobe analyses are greater than 0.1 wt. %. The XRF method may be useful for Ni.

#### REE determination for the Standard Specimens.

L-series characteristic XRF lines have been detected for the REE mixture samples. The intensities decrease in the order of atomic number from Yb, Ho, Eu, Nd to La. The intensity ratios for Yb=1 is 0.75 (Ho), 0.30 (Eu) and 0.10 (Nd). No La line has been detected for a 100 ppm La sample. Yb and Ho lines have been detected for 5 ppm samples.

X-ray intensities above the detection limits have been recognized for Cu, Co, Cr in the samples doped with Cu, Co, Cr, Y, and Zr. Heavy metals and REE have not been detected in JB-1 and JG-1, because of increase of background influenced by strong peaks of Ca, Ti and Fe. Weak peaks of Cu and Zn have been observed in JB-1. The Cu contents is estimated to be 50 ppm employing the doped standard. This is close to 56 ppm analysed by Japan Geol. Survey.

By increasing the beam size to 2 X 3 mm and the exciting energy to 20 keV, we could detect Ka lines of Y and Zr for the above doped standard. Approximately 40 ppm Sr and 158 ppm Zr (reported value is 153 ppm by JGS) were also detected in JB-1, but Y has not been detected (less than 25.5 ppm).

### Discussion

By employing Si wafer and Wevo plastic, we could minimize contamination of elements for the microfocus XRF. However, because of the interference of major elements in silicates, chromites and FeNi metals, many geochemically interesting elements such as Sc, Ge, Ga, Ir and REE could not be measured. Ni, Zn, Cu and Zr can be analyzed. Since Ru K line was detected for excitation energy of 23.0 keV, higher energy X-ray will be useful for Ru, Rh, Pd and REE K lines measurements.

We thank Drs A. Iida and K. Ohsumi at KEK and I. Nakai at Tsukuba Univ. for help, and Tanaka Precious Metal Co. for Pt-Ir.

## FABRICATION AND CHARACTERIZATION OF MULTILAYER ZONE PLATE FOR HARD X-RAYS

Kazuya SAITOH, Konosuke INAGAWA, Kazutake KOHRA, Chikara HAYASHI, Atsuo IIDA\* and Norio KATO\*\*

Institute for Super Materials, ULVAC JAPAN Ltd., 5-9-7 Tohkohdai, Tsukuba, Ibaraki 305

\* Photon Factory, National Laboratory for High Energy Physics, 1-1 Oho, Tsukuba, Ibaraki 305

\*\* Faculty of Science and Technology, Meijo University, Nagoya, Aichi 468

Introduction

A zone plate for soft X-ray region has been successfully fabricated by lithographic techniques and applied to the X-ray microscopy using synchrotron radiation<sup>1)</sup>. Though the zone plate for hard X-rays was expected to be promising for the focusing element of microanalysis and other applications of X-ray optics, it was difficult to fabricate a usable structure. Since the mass absorption coefficient becomes small for hard X-rays, the thickness of the zone plate should be more than a few tens of micron meters and aspect ratio of the zones also should be an order of one hundred. Recently, the authors could succeed in making the two-dimensional zone structure for X-rays of the Å region with a sputtering and slicing techniques. Bionta et al. reported liner zone plate with the similar techniques<sup>2)</sup>. In this report, the fabrication process and some characteristics of the multilayer zone plate are described.

Experimental

The zone plate was fabricated by using the DC planar magnetron sputtering. WSi<sub>2</sub> and C were coated alternatively around a gold wire substrate of 18  $\mu\text{m}$  diameter. The wire was stretched vertically and rotated during the deposition. The thickness of each layer was controlled automatically by the use of a quartz thickness monitor. The zone plate had 20 zones and the diameter was about 45  $\mu\text{m}$ . The thickness of the outer layer was about 0.3  $\mu\text{m}$ . After the deposition of all layers, a Ag layer (>100  $\mu\text{m}$ ) was coated around the specimen. Then the specimen was sliced into the plate perpendicularly to the wire axis, and both surfaces of the plate were polished mechanically down to 50  $\mu\text{m}$  thick. The plate was mounted to a holder.

The characterization of the zone plate was carried out on BL-4A at the Photon Factory. The synchrotron radiation of 8 keV was picked up through a double-crystal monochromator and impinged on the zone plate. An interference pattern of X-ray transmitted through the zone plate was obtained with an emulsion plate (Ilford L4). The intensity distribution of the X-ray pattern was also obtained by scanning a 10  $\mu\text{m}$  diameter pinhole which was inserted between the zone plate and a scintillation counter.

Results and Discussion

A scanning electron micrograph of the fabricated zone plate is shown in Fig. 1. Transmitting and obstructing layers appear to be black and white respectively. At the boundary between the transmitting and the obstructing layers, there seems to be no appreciable interdiffusion, while the roughness at the boundary increases with increasing radius.

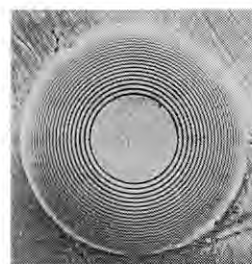


Fig. 1. Scanning electron micrograph of the zone plate which has 20 zones. Black and white rings correspond to carbon and WSi<sub>2</sub> layers respectively.

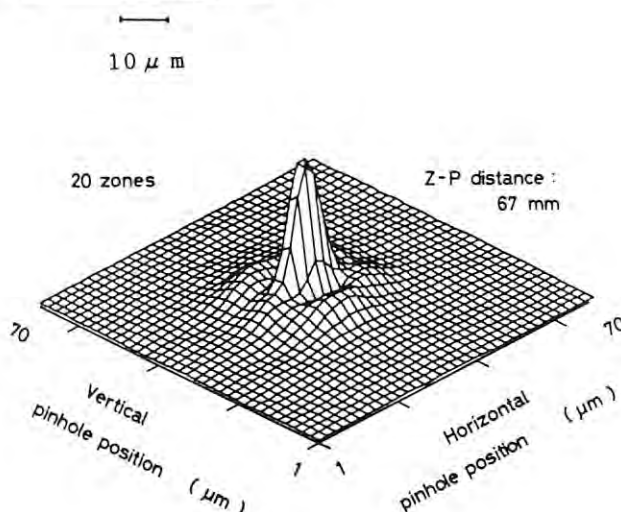


Fig. 2. The interference pattern of X-rays through the zone plate. The distance between the zone plate and the pinhole was 67 mm.

According to the X-ray spot image taken by the nuclear emulsion plate, the spot size is less than 3  $\mu\text{m}$  and 10  $\mu\text{m}$  in vertical and horizontal directions respectively. The spot size is larger than that by the calculation (0.3  $\mu\text{m}$ ). It is considered that the spot size of focused X-rays is essentially determined by the size of the synchrotron X-ray source and that the difference in the spot size in two directions is due to the difference in the dimension of the synchrotron radiation source. Figure 2 shows the obtained X-ray interference pattern. It is clear that the 8 keV X-rays transmitted through the zone plate are focused into a spot. The focal length was determined by measuring the X-ray peak intensity and the profile as a function of distance between the zone plate and the pinhole, and was about 67 mm. This value agrees with the theoretically estimated one (65 mm).

References

- 1) J. Kirz, H. Rarback: Rev. Sci. Instrum. **56** (1985) 1.
- 2) R. M. Bionta, A. F. Jankowski, D. M. Makowiecki: in X-Ray Microscopy, Springer-Berlin, 1988



# ANALYSIS OF ULTRA TRACE ELEMENTS IN MARINE ECOLOGICAL SAMPLES BY SR MONOCHROMATIZED X-RAY

Masafumi ISHIKAWA<sup>\*1</sup>, Atsuo IIDA<sup>\*2</sup>, Shinjiro HAYAKAWA<sup>\*2</sup>  
and Toshiaki ISHII<sup>\*1</sup>

<sup>\*1</sup> National Institute of Radiological Sciences, Division of Marine Radioecology, Isozaki 3609, Nakaminato-shi, Ibaraki-ken, 311-12, Japan

<sup>\*2</sup> National Laboratory for High Energy Physics, Oho 1-1, Tsukuba-shi, Ibaraki-ken, 305, Japan

## INTRODUCTION

To represent the natural feature of trace element in the marine environment particularly for sea water, elemental analyses were carried out using synchrotron radiation monochromatized X-ray. However, the elemental distributions over organs and tissues were also indispensable to supply further detail characterization of trace elements on the confirmation of physiological behaviour.

Therefore, this paper discusses the possibility of the synchrotron monochromatized X-ray scanning microbeam newly developed at BL-4A to analyse marine environmental samples, and demonstrates its distributional results from the radioecological points of view.

## I. EXPERIMENTAL

1) Sea water Preparation, Bombardment and X-ray Analysis: These can be referred to our previous paper.<sup>(1)</sup>

2) Target Preparation: A red snapper, *Chrysophrys major* was the sample for this scanning analysis. The size was 36cm in total length and 730g in weight. The scales were collected around the lateral line of the fish(A: above the lateral line, B: on the lateral line, C: below the lateral line), then passed through EtOH, and ultra pure water. After dryness, the scales were fixed on a quartz plate, then the surface was coated with carbon.

3) Beamline Layout, Scanning system and X-ray Measurement: The system Y. Gohshi et. al.<sup>(2)</sup> designed was the tool. The X-Z scanner was controlled by the program XYSCAN, then data was processed by the program XYDISP3B.

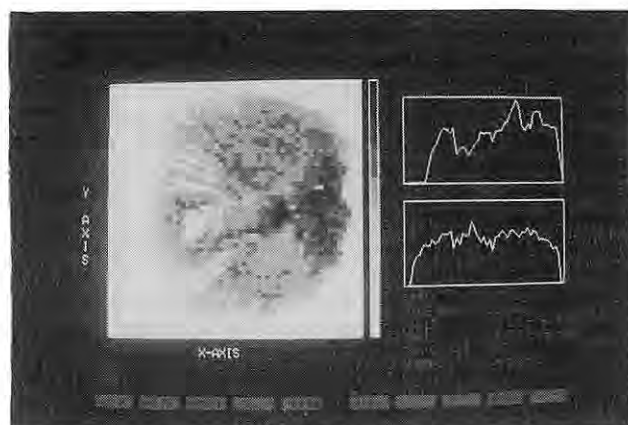
## II. RESULTS AND DISCUSSION

Environmental sea water samples were collected from Jan. 1987 to May 1988, at Nakaminato(Ibaraki) and at 100m off Takeno-ura, Onagawa(Miyagi). Target were prepared through the procedure using Na-DBDTC, then exposed by monochromatized X-ray for 2000 sec. with a 1.0x1.0mm beam under  $10^{-3}$  torr. Quantitative determination was made through the external standard method.<sup>(1)</sup> As it was pointed out in the previous report<sup>(1)</sup>, respective elemental amounts are higher in Nakaminato sea water.

Geographical characteristics were observed for these three elements of Ni, Cu, Mo. They are higher than the other sea water levels reported before. In particular Mo was rich in Nakaminato sea water, while Hg and Se were remarkable in the Onagawa' one. Detailed discussion are still being processed.

The fish scale scanning was implemented by a microbeam of  $150 \times 200\mu\text{m}$ . Between the three

Fig. 1 Ca Distribution on a Fish Scale



scales, no significant observation was obtained, concerning the elemental distribution and the quantity. Scale B is appropriate when discussing the characterization of elements, because it is on the lateral line, which acts as a sensor for the outer stimulus.

Fig. 1 shows Ca distribution for the scale B. Ca accumulated highly at the position of focus, where radiated channels gather under the front scales, and it is a border between body and the environmental sea water.

Generally speaking, the sea water contacting area was higher in Ca concentration. Also higher Ca accumulation was observed along the edge of the lateral line pore. These observations were effective for elements of Zn, Mn, and Fe. Since the lateral line pore is regarded to have physiological sensitivity on pressure etc., the higher elemental concentrations may role a part in these activities.

Particular interest is given to Ca at the radiated channel from the focus. Using this size of microprobe, higher Ca line patterns emerged intervally as rather narrow channels. Separate analysis of SEM image indicated that this narrow one correspond to the bottom(lower) between the two radiated channels(higher). Finally, average Sr:Ca observed ratio over the scale B was 4.66, which is greater than the value of 0.2, recognized as normal O.R.

## REFERENCES

- 1) M. Ishikawa and A. Iida; Photon Factory Activity Report, 5, 133(1987)
- 2) Y. Gohshi, S. Aoki, S. Hayakawa and K. Sakurai; Photon Factory Activity Report, 5, 130(1987)



## Photoacoustic EXAFS for the Analysis of Layered Materials

Tsutomu Masujima<sup>1</sup>, Hideaki Shiwaku<sup>1</sup>, Hisanobu Yoshida<sup>1</sup>, Hideo Imai<sup>2</sup>, Taro Toyoda<sup>3</sup>,  
Mikio Kataoka<sup>4</sup>, Takayuki Sano<sup>5</sup>, Atsuo Iida<sup>6</sup>, Atsushi Koyama<sup>6</sup>, Masaharu Nomura<sup>6</sup>,  
Hiroshi Kawata<sup>6</sup>, and Masami Ando<sup>6</sup>

- 1.Inst. Pharmaceutical Sci., Hiroshima Univ. School of Medicine, Kasumi, Hiroshima 734
- 2.Faculty of Pharmaceutical Sci., Fukuyama Univ., Higashimura-cho, Fukuyama 729-02
- 3.Dept. of Optoelectronics, Tokyo Kogakuin College of Technology, Tokyo 151
- 4.Dep. of Physics, Faculty of Sci., Tohoku Univ., Sendai, Miyagi 980
- 5.Faculty of Sci., Hiroshima Univ., Higashi-senda, Hiroshima 730
- 6.KEK, National Laboratory for High Energy Physics, Oho-machi, Ibaraki 305

It was found that X-ray photoacoustic spectra show fine structure like EXAFS, and the Fourier analysis of the spectra reveals the identical radial dispersion to that of conventional absorption spectra.<sup>1)</sup> This method, we call "Photoacoustic EXAFS" method, has unique potential to be applied to depth profiling at tens micron order with no sample pretreatment. The spectra of Cu K-edge region of a Ni-plated Cu (10  $\mu\text{m}$  thick) foil was analysed as a model to investigate the potential to reveal the structure of materials of sublayer.

**Experimental** Monochromatic X-rays were obtained by silicon(111) double crystal monochromator installed at Beam Line 4A. Current experimental setup for this photoacoustic EXAFS study was detailed previously<sup>1)</sup>. Data taking system of this setup was totally automatized by microcomputer and averaging after data accumulations of several scanning was also possible. The photoacoustic cell was detailed elsewhere.<sup>2)</sup> The ion chambers were set close to both sides of the photoacoustic cell, in order to compare the photoacoustic and absorption spectra, simultaneously.

### Results and Discussion

Figure 1 is the PA-EXAFS spectrum of Ni-plated Cu and its absorption spectrum at chopping frequency of 8 Hz. Although the fine structure at Ni K-edge region was not detected due to its small quantity, the fine structure at Cu K-edge region was found even in the photoacoustic spectrum which comes from the sublayered Cu. Quite corresponding structure between both photoacoustic and absorption spectra shows that the information of atomic structure of sublayer can be also obtained by photoacoustic method. Figure 2 shows the first spectrum of sublayered materials by the Fourier transform of the X-ray photoacoustic data. Analyzed area of the spectrum was narrowed to

preclude noisy area at high photon energy and this treatment make the result to be broad atomic radial dispersion. Main peak centered close to the nearest neighbor atomic distance of 2.6  $\text{\AA}$  is consistent with the data from the absorption method. Second peak centered at about 4.2  $\text{\AA}$  should split two peaks. It is also due to the narrow region of analyzed data. When the target materials locates deeper, the less signal can be obtained. Thus, the improvement in sensitivity is most important to get well defined data analysis. This success promises the unique application of the PA-EXAFS method and various samples are under study.

### References

- 1) T. Masujima, H. Kawata, et al., PF Activity Report, 5, 139 (1987).
- 2) T. Masujima, H. Kawata, et al., Review of Sci. Instrum., in press.

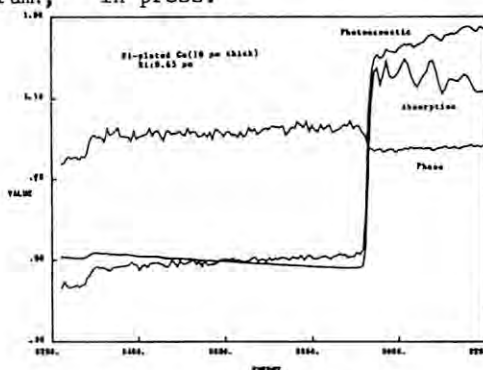


Figure 1. Photoacoustic EXAFS spectrum and absorption spectrum of Ni-plated Cu foil (10  $\mu\text{m}$ ). (Chopping Freq. 8 Hz)

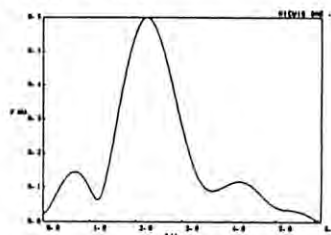


Figure 2. Fourier transform of the PA-EXAFS in Fig.1 in Cu K-edge region.

## Applicability of Photoacoustic EXAFS Method to Various Samples

Hideaki Shiwaku<sup>1</sup>, Tsutomu Masujima<sup>1</sup>, Hisanobu Yoshida<sup>1</sup>, Hideo Imai<sup>2</sup>, Taro Toyoda<sup>3</sup>,  
Hideo Yamakoshi<sup>4</sup>, Tetsuya Ikeda<sup>4</sup>, Hiroshi Makihara<sup>4</sup>, Atsushi Koyama<sup>5</sup>, Masaharu Nomura<sup>5</sup>,  
Atsuo Iida<sup>5</sup>, Hiroshi Kawata<sup>5</sup>, Masami Ando<sup>5</sup>

1. Inst. Pharmaceutical Sci., Hiroshima Univ. School of Med., Kasumi, Hiroshima 734
2. Factory of Pharmaceutical Sci., Fukuyama Univ., Higashimura-cho, Fukuyama 729-02
3. Dept. of Optoelectronics, Tokyo Kogakuin College of Technology, Sendagaya, Tokyo 151
4. Technical Headquarters, Mitsubishi Heavy Industries, Ltd., Sachiura, Yokohama 236
5. Photon Factory, National Laboratory for High Energy Physics, Oho, Tsukuba 305

The heat generation by X-ray absorption was found to be detected by photoacoustic method. It was found that the spectra of heat generation include the fine structure, EXAFS, in K-edge absorption region<sup>1</sup>). In previous study, metal foils were extensively studied as model systems. In this report, practical materials such as inorganic and biological materials and thick solids of optically opaque.

### Experimental

The experiments were performed at the Beam Line 4A with installed monochromator. The apparatus of the photoacoustic EXAFS was detailed elsewhere<sup>2</sup>). As a sample of inorganic materials, nickel sulfate powder was measured. Prior to measurement, the sample was ground down and dried at 130°C for about 10 hours. As a sample of biological materials, chlorophyllin was chosen. These powder samples were piled on the sticky paper. Furthermore, as a thick solid of optically opaque, the high temperature superconductor was measured. This superconductor was a compressed pellet. Modulation frequency for X-ray chopping was 9Hz.

### Result and Discussion

Figure 1 shows the photoacoustic EXAFS of dried nickel sulfate powder and its Fourier transform. The distance between the nearest neighbor atoms were estimated to be about 1.7Å by the photoacoustic method. The distance was estimated about 1.6Å by the absorption method. Figure 2 shows the photoacoustic EXAFS of chlorophyllin and its Fourier transform of chlorophyllin. Because of the low contents of Cu, the spectrum was very noisy and was hard to analyze. Figure 3 is the photoacoustic EXAFS of superconductor. In the absorption spectrum, fine structure was hardly seen in Cu K-edge region. On the other hand, the spectra of photoacoustic signal amplitude and phase showed distinguished changes in that region. Furthermore, EXAFS-like fine structure is perceived in the spectrum of photoacoustic signal amplitude. These results

indicated that this method can be successfully applied to the variety of optical opaque materials without sample preparation. However, for the practical application, it is necessary to improve sensitivity of detector system more than 10 times.

### References

- 1) T. Masujima, H. Kawata et al., Photon Factory Activity Report, 5, 139 (1987).
- 2) T. Masujima, H. Kawata et al., Rev. Sci. Instrum., (1988) in press.

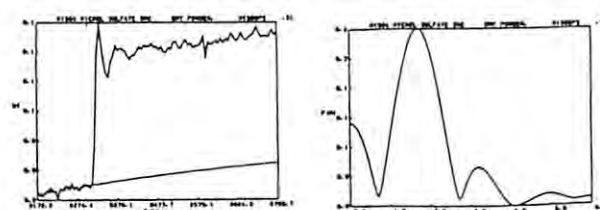


Figure 1. PA-EXAFS and its Fourier transform of dried  $\text{NiSO}_4$ .

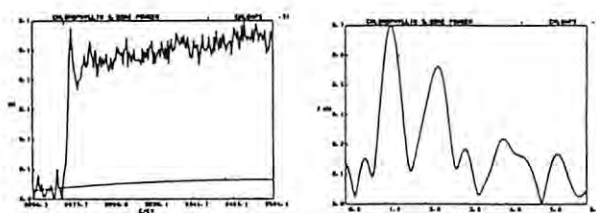
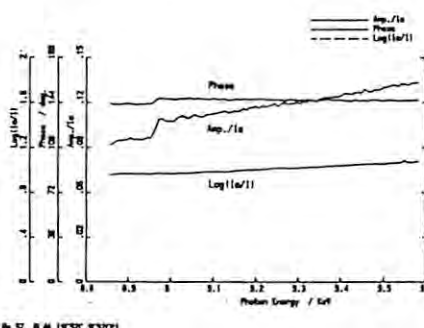


Figure 2. PA-EXAFS and its Fourier transform of Chlorophyllin.



Superconductor No. 37, 8.46 (KSCC, KSCOP)

Figure 3. X-ray photoacoustic spectrum of a high temperature superconductor.

## X-ray Photoacoustic Imaging by Computer Tomographic Method

Tsutomu Masujima, Hideaki Shiwaku, Hisanobu Yoshida, Atsuo Iida\*, Mamoru Takahashi\*\*, Kenji Sakurai\*\*, Yoichi Gohshi\*\*, Chieko Nagoshi\*\*\*, Hiroshi Kawata\*, Masami Ando\*

Inst. of Pharmaceutical Sci., Hiroshima Univ. school of Medicine, Kasumi, Hiroshima 734

\*Photon Factory, National Laboratory for High Energy Physiscs, Oho-machi, Tsukuba 305

\*\*Department of Industrial Chemistry, Faculty of Engineering, Univ. of Tokyo, Hongo, Tokyo 113

\*\*\*Inst. for Nuclear Study, Univ. of Tokyo, Tanashi, Tokyo 188

X-ray imaging analysis has been developed in various field, especially by the X-ray fluorescence study. Our new method, X-ray photoacoustics, also has a potential of imaging analysis and studied using focused X-ray beam. As a different approach for imaging, computer tomographic(CT) method can be applied using line-beam with  $\theta$ -Z axis rotation and translation scanning. Iida et al. has recently succeeded in this method to apply X-ray fluorescence imaging<sup>1)</sup>. Using the same system, X-ray photoacoustic CT imaging was investigated.

Simultaneous imaging of the amplitude and phase of photoacoustic signal will reveal the three dimensional atomic dispersion. Not only for this goal but also for the improvement of resolution, the sensitivity of this detection system should be improved and X-ray source with much more flux should be necessary.

## Reference

- 1) A.Iida, M.Takahashi, K.Sakurai, Y.Gohshi, Rev.of Sci. Instrum.,(1988) in press.

Experimental

Monochromatic X-ray at the Beam Line 4A was cut by 2 sets of slits to get a line beam at dimension of 0.8mm x 12mm. A X-ray photoacoustic cell was mounted on the  $\theta$ -Z stage which was insulated from the vibration through base optical bench by use of laminated rubbers. X-ray chopping frequency was 9 Hz. The original experimental setup and data analyzing system are detailed elsewhere<sup>1)</sup>.

Results and Discussion

Figure 1 shows a primitive model sample for the first trial of this experiment. Metal foils which gave high signal in the X-ray photoacoustic measurement was used. Figures 2a) and b) show the photoacoustic amplitude images at the X-ray wavelength above Cu K-edge and that below the edge respectively. The difference between these two images is the highlight region in Fig 2a) where Cu foil locates. This result shows that the analysis of atomic dispersion is also possible by the X-ray photoacoustic method. However, phase images was not obtained due to insufficient S/N ratios.

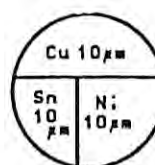


Figure 1 A scheme of the primitive model sample.

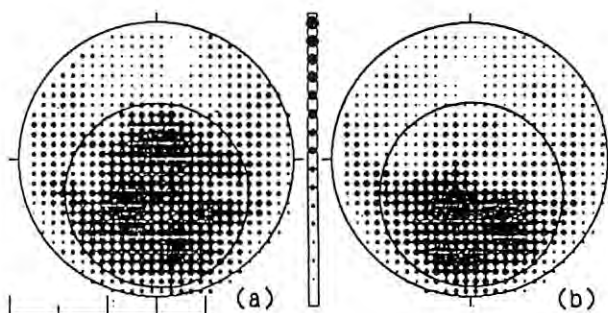


Figure 2 Reconstructed images of the sample in Fig.1. Wavelength; a) above Cu K-edge, b) below Cu K-edge.



X-RAY PHOTOACOUSTIC ABSORPTION SPECTRA OF  $\text{CuInSe}_2$  AND PHOSPHOR BRONZE

Taro Toyoda<sup>1</sup>, Tsutomu Masujima<sup>2</sup>, Hideaki Shiwaku<sup>2</sup>, Hisayuki Nakanishi<sup>3</sup>,  
 Saburo Endo<sup>4</sup>, Taizo Irie<sup>4</sup>, Ikuyo Shiozaki<sup>5</sup>, Atsuo Iida<sup>6</sup>,  
 Hiroshi Kawata<sup>6</sup>, and Masami Ando<sup>6</sup>

1. Dept. of Optoelectronics, Tokyo Kogakuin College of Technology, Shibuya-ku, Tokyo 151
2. Inst. Pharmaceutical Sci., Hiroshima Univ., School of Medicine, Kasumi, Hiroshima 734
3. Dept. of Electrical Engineering, Science University of Tokyo, Noda, Chiba 278
4. Dept. of Electrical Engineering, Science University of Tokyo, Shinjuku-ku, Tokyo 162
5. Dept. of Physics, Tokyo Metropolitan University, Setagaya-ku, Tokyo 158
6. KEK, National Laboratory for High Energy Physics, Oho-machi, Ibaraki 305

Recently, the heat generation by X-ray absorption has been found to be detected by photoacoustic method using synchrotron radiation in the case of Cu metal.<sup>1)</sup> It is the purpose of this Report to present the results of photoacoustic spectra by X-ray absorption applied to two samples,  $\text{CuInSe}_2$  and phosphor bronze which are Cu compound and alloy, respectively. The ternary compound semiconductor  $\text{CuInSe}_2$  has a chalcopyrite structure, and the electrical and optical properties have been studied actively because of the use as solar cells.<sup>2)</sup> Phosphor bronze,  $\text{Cu}(\text{Sn})$ , which contains 8 wt.% Sn and small amount of phosphor in Cu, is popular for use as strength material in mechanical applications.

**Experiments** Single crystals of  $\text{CuInSe}_2$  were prepared by melting the elements in an evacuated quartz ampoule followed by directional freezing.<sup>2)</sup> Then the crystals were made into powder as samples for the measurements. Phosphor bronze was mechanically polished to be 84  $\mu\text{m}$  thickness for the measurements. The experiments were carried on at the Beam Line 4A. The apparatus was the same as that explained in Reference 1). In order to get the absorption spectra simultaneously, the ion chambers were set at the both sides of photoacoustic cell. The photoacoustic signal was normalized by the preset count value of the first ionization chamber current. Chopping frequency was 9 Hz. The photoacoustic spectrum of Cu foil (5  $\mu\text{m}$ ) were measured as a reference sample.

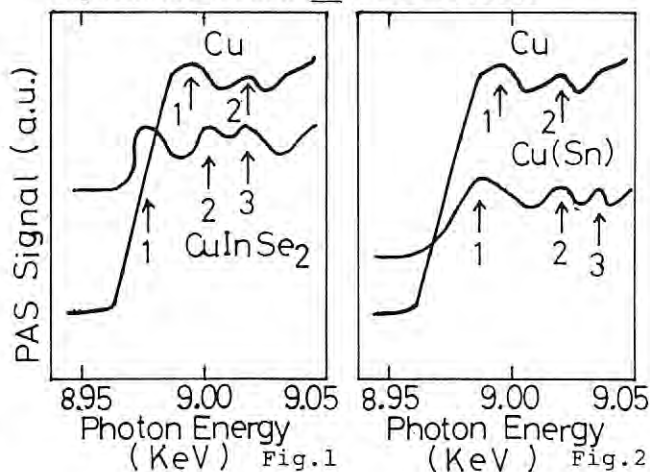
**Results and Discussions** Figures 1 and 2 show the X-ray photoacoustic spectra of  $\text{CuInSe}_2$  and phosphor bronze, respectively, with that of Cu. Both cases show the fine structures like XANES near Cu K-edge region. Figure 1 shows that the relative increase of the X-ray photoacoustic signal of  $\text{CuInSe}_2$  and the peaks of XANES like structures are different from those of Cu. The 1st peak energy value of  $\text{CuInSe}_2$  in Figure 1 is approximately 11 eV smaller than that of pure Cu, and we can observe the 2nd peak in  $\text{CuInSe}_2$ , which is not observed in the case of Cu. The 3rd peak energy value of  $\text{CuInSe}_2$  is the same as the 2nd one of Cu. Same tendency is observed in the case of phosphor bronze,  $\text{Cu}(\text{Sn})$ ,

shown in Figure 2. The 1st peak energy value of  $\text{Cu}(\text{Sn})$  in Figure 2 is approximately 6 eV smaller than that of Cu. The 2nd peak energy value of  $\text{Cu}(\text{Sn})$  is the same as that of Cu, and the 3rd peak is observed only in the case of  $\text{Cu}(\text{Sn})$ . However, the peak energy values of XANES like fine structures of  $\text{CuInSe}_2$  show the same as those for Cu in the case of absorption spectrum. Also, those of Cu in Figure 1 are identical with those of absorption spectrum within the experimental accuracy.

Unified explanations of these experimental results, especially the XANES like fine structures and the difference between the X-ray photoacoustic absorption and the absorption spectra by ion chambers, are left to future experimental and theoretical investigations. The XANES like fine structures in X-ray photoacoustic spectra might reflect the electronic structures of  $\text{CuInSe}_2$  and phosphor bronze. The detailed X-ray photoacoustic measurements and the investigation of heat production by microscopic theory<sup>3)</sup> are desirable for future investigations. These information should be useful for the use of X-ray photoacoustic absorption spectroscopy as a new experimental technique.

## References

- 1) T. Masujima, H. Kawata, et al., PF Activity Report 5, 139 (1987).
- 2) S. Endo and T. Irie, Solar Cells 16, 1 (1986).
- 3) M. E. Garcia, G. M. Pastor, and K. H. Bennemann, Phys. Rev. Letters 61, 121 (1988).





SYNCHROTRON X-RAY RIETVELD ANALYSIS OF  $\alpha$ -HAFNIUM PHOSPHATE  $\text{Hf}(\text{HPO}_4)_2 \cdot \text{H}_2\text{O}$ , AN INORGANIC ION EXCHANGER

Izumi NAKAI, Katsuhiko IMAI, Takuji KAWASHIMA, Kazumasa OHSUMI\*,

Fujio IZUMI\*\* and Isao TOMITA\*\*\*

Department of Chemistry, The University of Tsukuba, Ibaraki 305

\* Photon Factory, National Laboratory for High Energy Physics, Tsukuba, Ibaraki 305

\*\* National Institute for Research in Inorganic Materials, Ibaraki 305

\*\*\*Department of Chemistry, Faculty of Science, Ochanomizu University, Otsuka, Tokyo 112

### Introduction

An inorganic ion exchanger,  $\alpha$ -hafnium phosphate  $\text{Hf}(\text{HPO}_4)_2 \cdot \text{H}_2\text{O}$  (hereafter abbreviated as  $\alpha$ -HP), is regarded as a Hf analogue of  $\alpha$ -zirconium phosphate ( $\alpha$ -ZP). However, ion exchange behavior of  $\alpha$ -HP is slightly different from that of  $\alpha$ -ZP<sup>1)</sup>. Since the crystal structure of  $\alpha$ -ZP is known<sup>2)</sup>, it is expected that the structure analysis of  $\alpha$ -HP will help to understand the difference in ion exchange behavior between the two substances. Single crystal structure analysis of  $\alpha$ -HP could not be made because the sample was synthesized as fine powder. Therefore, Rietveld analysis using SR data was applied to the structure determination.

### Experimental

A powder sample of  $\alpha$ -HP was prepared by the direct precipitation method<sup>3)</sup> and used in the subsequent structure analysis. The measurement was performed at BL-4B station by using powder diffractometer, PFPD<sup>4)</sup>. The sample was loaded into a quartz glass capillary of 0.3mm diameter and was mounted on the diffractometer. The capillary was kept rotating by spinner during the data collection.

Intensity data were collected by using step-scan method: step width =  $0.02^\circ$  in  $2\theta$ , measuring time = 10sec, D.S. = 0.5mm, R.S. = 0.3mm. The wavelength of the radiation was adjusted by Si(111) monolithic monochromator with fixed exit beam position and was determined as  $1.54331(2)\text{\AA}$  by a calibration using the NBS standard Si powder. Absorption correction for a cylindrical crystal was applied to the intensity data. Rietveld analysis was made using a program RIETAN<sup>5)</sup>. Atomic parameters of  $\alpha$ -ZP<sup>2)</sup> were used as the initial model of the refinement.

Intensity measurement using conventional X-ray tube was also performed to compare with the SR data. The conditions of the data collection are: graphite monochromatized CuK $\alpha$  radiation, step-scan,  $0.02^\circ/\text{step}$ , 40sec/step, D.S. = S.S. =  $0.5^\circ$ , R.S. = 0.15mm, quartz-plate sample holder.

### Results and Discussion

Figure 1 shows a comparison of the Rietveld analysis patterns for the SR data (a) with that for the conventional X-ray data (b). The SR data give sharp pattern with high resolution because the SR beam is highly collimated and lacking in

the Ka2 component. For example, FWHM of the 200 peak ( $2\theta = 20^\circ$ ) is  $0.084^\circ$  for pattern (a) while it is  $0.120^\circ$  for pattern (b). On the other hand, Gaussian fraction of the profile function is 0.75(4) and 0.37(1) for patterns (a) and (b), respectively. This indicates that the diffraction profile of the SR data is close to a Gaussian peak shape.

Since  $\alpha$ -HP has a plate-like crystal form, 00l reflections have remarkably high intensity because of the preferred orientation effect when plate-type sample-holder was used in the measurement (see Fig.1(b)). On the other hand, the effect of preferred orientation was negligible in the SR data owing to the rotation of the capillary holder during the measurement (Fig.1(a)). Further, as the effective area of X-ray irradiation does not depend on the diffraction angle in the case of capillary method, it is another advantage of this method that low angle intensity-data can be used in the analysis.

The crystal structure of  $\alpha$ -HP obtained in this study is given in Fig.2. It is found that  $\alpha$ -HP and  $\alpha$ -ZP are basically isostructural, namely,  $\alpha$ -HP has a monoclinic unit cell with space group  $P2_1/n$  and has a layered structure composed of  $\text{PO}_4$  tetrahedra and  $\text{ZrO}_6$  octahedra stacked parallel to the ab-plane. The two adjacent layers are weakly linked by the hydrogen bonds. The bond distances between the metal atoms and oxygen in the structure of  $\alpha$ -HP are shorter and those between phosphorus and oxygen are longer than the corresponding distances in the structure of  $\alpha$ -ZP. Compared with the unit cell of  $\alpha$ -ZP, that of  $\alpha$ -HP contracted in the a and b directions and expanded in the c direction. However, the interlayer distance is approximately the same between the two substances. These structural features may account for the differences in ion exchange behavior between the two.

### References

- 1) I. Tomita et al., *Anal. Sci.*, **3**, 35(1987).
- 2) J. M. Troup et al., *Inorg. Chem.*, **16**, 3311(1977).
- 3) I. Tomita et al., *Bull. Chem. Soc. Jpn.*, **57**, 3281(1984).
- 4) R. Uno et al., *PF Activity Report*, No.5, 141(1987).
- 5) F. Izumi, *J. Cryst. Soc. Jpn.*, **27**, 23(1985).

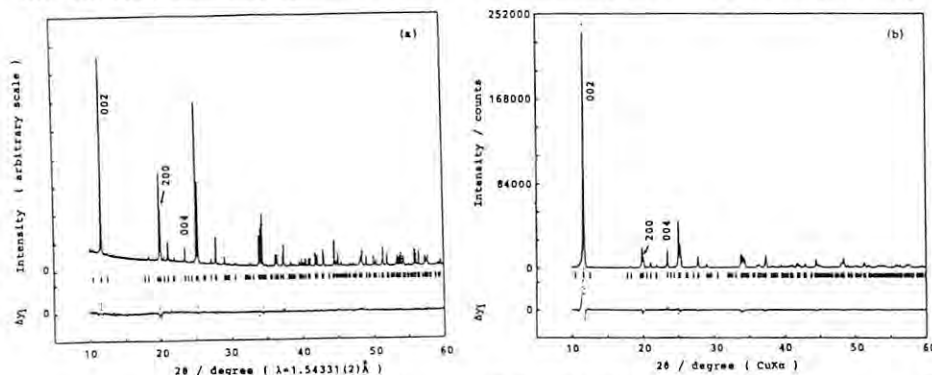


Fig.1. Rietveld refinement patterns of  $\alpha$ -HP obtained by using (a) synchrotron radiation and (b) conventional X-ray tube.

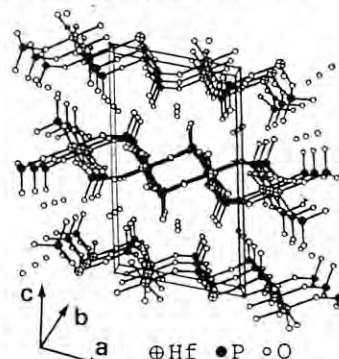


Fig.2. Crystal structure of  $\alpha$ -HP viewed along the b-axis.

## MEASUREMENT OF X-RAY DIFFRACTION FROM MICROMETER-SIZE SIALON

Masaaki.OHMASA, Kazumasa.OHSUMI\*, Kenji.HAGIYA and Hitoshi.KAMIMATSUSE

Institute of Materials Science, University of Tsukuba, Japan

\*Photon Factory, National Laboratory for High Energy Physics, Japan

Introduction

It is still necessary for us to use crystals of at least some tens micrometers in diameter for determination of their crystal structure, though recent progress in instrumentation for X-ray diffraction is remarkable. Therefore, structures of many natural and synthetic substances whose dimensions are around ten micrometers or less have been left unknown or studied by Debye-Scherrer method when amount of the samples was enough for the measurement. Besides, Debye-Scherrer method has an essential weak point, because three dimensional information in reciprocal space is reduced to one dimension, and it has been desired to develop a new method by which we can measure intensity of micrometer-size single crystals.

In the field of materials science, many compounds are synthesized by sintering by which crystals grow up to ten micrometers. Alpha-sialon having a wide solubility range of yttrium is one of such compounds, and larger crystals have not yet been synthesized to ascertain actual content of yttrium in a sialon single crystal. Present studies have consequently been undertaken to establish a method of structural studies on micrometer-size crystals and to determine yttrium content of an alpha-sialon single crystal.

Experimental

For the present purpose, an X-ray camera was constructed as described below. Since intensity of diffracted beam from a micrometer-size crystal is very weak, special attention was paid to reduce background level, that is, a fine (50  $\mu$ m) collimation system and a carefully designed shield were used to the camera. As the fine collimation system was used, Laue method was employed to avoid error in motion of the specimen. The camera was also put in He atmosphere during the experiment. Diffraction was recorded on the Polaroid films, and high speed and high contrast industrial X-ray films, or on the Imaging Plates.

The crystals were mounted on glass fibers of several micrometers in diameter by electrostatic attraction. The size of crystals used was 2.5 micrometers. The specimens of alpha-sialon having a formula,  $Y_{0.6}(Si_{9.3}Al_{2.7})(O_{0.9}N_{15.1})$ , were kindly supported by Dr. K.Ishizawa, Shinagawa Refractories Co., Ltd.(Fig.1).

Results

A Laue photograph of alpha-sialon is shown in the Fig.2. Most of all spots observed are elongated on the photographs. The phenomena are now examined whether they are caused by movement of the crystal during exposure time, by optical system or properties of the crystal itself. The spot on Laue photographs were indexed by a new developed computer program<sup>1)</sup>. Development of a data reduction program for Laue method is in progress.

References

- 1) K.Ohsumi, K.Miyahara & M.Ohmasa, Acta Cryst. A43, c-269, 1987.



Fig.1 Alpha-sialon crystals

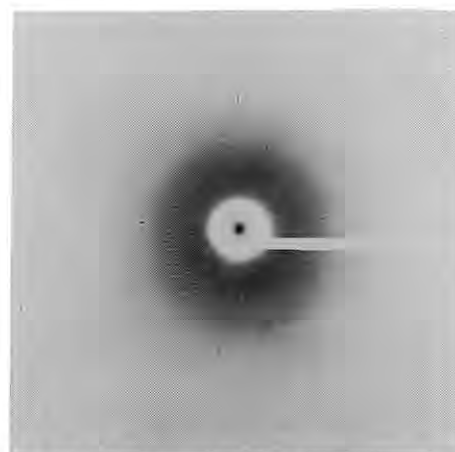


Fig.2 Laue photograph

## BASIC CHARACTERISTICS OF A POWDER DIFFRACTOMETER FOR THE PHOTON FACTORY

Haruo OZAWA, Ryosei UNO, Takamitsu YAMANAKA<sup>1</sup>, Kazumasa OHSUMI<sup>2</sup> and Akihiko NUKUI<sup>3</sup>

College of Humanities and Sciences, Nihon University, Setagaya-ku, Tokyo 156

1.College of General Education, Osaka University, Toyonaka-shi, Osaka 560

2.Photon Factory, National Laboratory for High Energy Physics, Tsukuba-shi, Ibaragi 305

3.National Institute for Research in Inorganic Materials, Tsukuba-shi, Ibaragi 305

Introduction

Investigation of basic characteristics of a powder diffractometer<sup>1)</sup> built for the Photon Factory in 1987 was almost completed. The characteristics show that the diffractometer is highly accurate in measurements of X-ray wavelength and of intensity of diffracted beams.

Experimental and Results

## (1) Accuracy obtained with the diffractometer

## (a) Wavelength of X-rays

The wavelength of X-rays at the Cu K absorption edge, which was determined as the center of XANES spectrum, was measured by diffraction angles of high angle lines from NBS standard Si powder 640b. It was  $1.380619 \pm 0.000012$  Å. Since the reported value of the absorption edge is  $1.38059$  Å, the wavelength was accurate within  $\pm 0.00003$  Å.

## (b) Monitoring

In order to examine the accuracy of monitoring the 111 reflexion of the NBS Si was measured for different widths of the incident slit with a constant receiving slit of  $0.2$  mm at  $1.38062$  Å. The integrated intensities obtained from data normalized by smoothed monitor intensity and those obtained from unnormalized data are

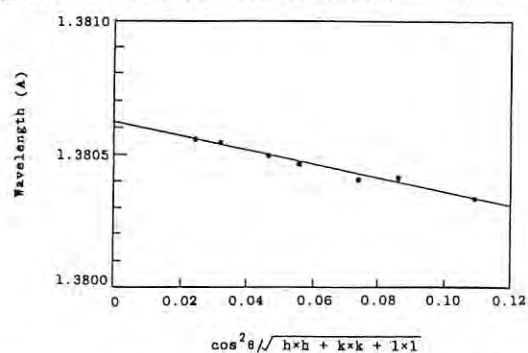


Fig. 1. Wavelength of X-rays at Cu K edge.

Table I. Ratios of integrated intensities normalized and unnormalized by the smoothed monitor intensity for each incident slit in a receiving slit ( $0.2$  mm).

Incident slit(mm)	Ratio of Integrated Intensity	
	unnormalized	normalized
0.1	0.243	1.015
0.2	1.000	1.000
0.3	1.515	1.002
0.5	2.454	1.020
1.0	2.251	0.983

shown in Table I. The normalized integrated intensities for  $0.2$  and  $0.3$  mm slits agreed within  $\pm 0.2$  %.

## (2) Profile of reflexions

Intensity measurements were carried out on reflexions from the NBS Si at  $1.38062$  Å. To fit the experimental data points, 8 profile functions were tested; those are a Gaussian, a Lorentzian, the Pearson 7th, 4th and 6th order rational functions, pseudo-Voigt and sum of 2 or 3 Gaussians. The fitted profile functions of 3 Gaussians and of pseudo-Voigt function are shown in Fig.2. The Gaussian Lorentzian ratio in pseudo-Voigt function was  $0.84$  at  $25.42^\circ$  and decreased to  $0.37$  at  $130.38^\circ$ .

Conclusions

The high accuracy of wavelength measurement is very useful in applications of anomalous dispersion. Since the accuracy of monitoring is comparable with the stability of an ordinary X-ray diffractometer, it is sufficient for the Rietveld analysis.

Reference

- 1) R.Uno et al: Photon Factory Activity Report 5 (1987) 141  
R.Uno et al: Australian J. Phys. 41(1988) 133

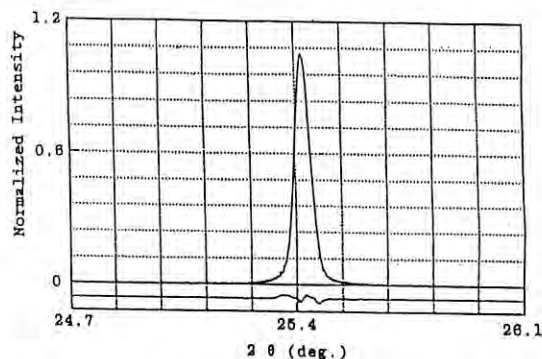
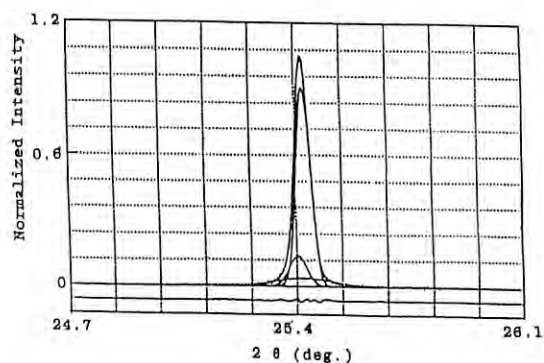


Fig. 2. Profile of 111 reflexion from Si.



# KINETIC STUDY UNDER HIGH PRESSURE BY ENERGY DISPERSIVE POWDER DIFFRACTION SPECTRA

Takamitsu Yamanaka<sup>1)</sup> and Kazumasa Sugiyama<sup>2)</sup>

<sup>1)</sup> College of General Education, Osaka Univ. Toyonaka Osaka 560, Japan

<sup>2)</sup> The Res. Inst. Min. Dress. Metal. Tohoku Univ. Katahira, Sendai 980, Japan

An in situ observation of the polymorphic transition of  $\text{GeO}_2$  under 30kb at 220, 315 and 380°C has been performed using energy dispersive (ED) spectra observed for every 15 min. A profile fitting based on the ED spectra elucidated the transition rate from  $\alpha$ -quartz form ( $P3_221$ ,  $z=3$ ) to rutile form ( $P4_2/mmm$ ,  $z=2$ ).

The smooth polychromatic x-ray of SR having a great number of photons provides a high resolution of peak profiles of ED spectra. Then a small amount of sample in the diamond anvil can be detected. The strong source intensity is also capable of shortening the measuring period, which is advantage for the kinetic studies of phase transition through the time-shared analysis.

A new X-ray powder diffractometer was designed for multiple uses of SR source at BL-4B. A diamond anvil pressure cell was set on the spinner with 1/20 rad/sec, which was attached on the goniometer. The spinner was simultaneously oscillated within 5° around the  $\omega$  axis, which was prepared for the randomization of the sample orientation and for reducing an effect of the grain growth. A platinum ring heater around the diamond anvil and another heater are installed in the pressure apparatus. The latter was prepared for a sub-heater because the pressure cell is built of a good heat conductor.

A profile decomposition method of the ED spectra can separately assign integrated intensities to the superposed diffraction peaks. The energy positions  $E_H$  of the ED diffraction peaks  $H_j$  can be determined from the energy conversion equation. Integrated intensity  $I_H$  of the reflection  $H$  can be derived by structure factor  $F_H$ , when the SSD is set at  $2\theta$ ;

$$I_H = I_0(E_H) p[(1 + \cos^2 2\theta) / \sin^2 2\theta \cos \theta] |F_H|^2 \cdot \exp(-2B \cdot E_H^2 \sin^2 \theta / h^2 c^2) A(E_H)$$

Diffraction intensity  $Y_0(E_j)$  at each energy is derived from the sum of integrated intensities of hexagonal and tetragonal phases. When reflections  $H_j$  of the former phase and  $h_j$  of the latter, the intensity is expressed by the following formula;

$$Y_0(E_j) = B(E_j) + \sum Y(2\Delta E_{iH}) I_H + \sum Y(2\Delta E_{ih}) I_h$$

where  $B(E_j)$  is a background, and  $Y(2\Delta E_{iH})$  is a profile function.

A new FORTRAN 77 program EDSYSTEM introduced the pseudo-Voigt profile function to ensure higher accuracy. The function is expressed by the sum of Gaussian function and Lorentzian function. The program takes into account many intensity-correction parameters of source intensity distribution, background, escape efficiency, asymmetry peak, absorption in terms of energy. The structure parameters were optimized by the least-squares method using EDSYSTEM, on the basis of the diffraction intensity  $Y_0(E_j)$  of each energies observed in 4096 ch of multichannel analyzer.

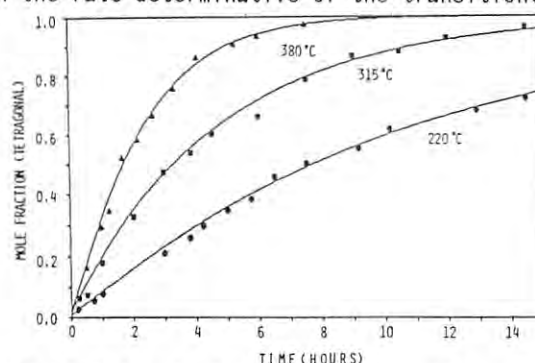
Profile fitting after the intensity corrections brought an intensity ratio of the decomposed spectra of the original and transformed phases. The mass ratio  $x(t)$  as a function of heat-up time ( $t$ ) was derived from the scale parameters of the profile fitting using the program EDSYSTEM. The mass ratio  $x(t)$  of the tetragonal phase be represented by

$$x(t) = 2c_{\text{tetr}} / \{3c_{\text{hex}} + 2c_{\text{tetr}}\}$$

in consideration of  $F(000)_{\text{tetr}} = 2/3 \cdot F(000)_{\text{hex}}$ .

A time-shared measurement of the mass ratio can derive the transition rate. The transition curve of  $\text{GeO}_2$  based on the massfraction indicates a "S" shape, which is composed of three stages; firstly a considerably long inductance period, secondly an initiation period of the rapid growth of the transformed phase and finally the conversion tail of the slow growth.

The transition rate from  $\alpha$ -quartz type to rutile type structure was confirmed by the transition-curve fitting to several solid-solid reaction models of Jander, Avrami-Erofeev and Prout-Tompkins equation. The transition mechanism was estimated from the fact that the Avrami-Erofeev model was best fitted to the curve excluding the inductance period (Fig. 1). The growth rate rather than nucleation rate resulted in the rate determinative of the transition.



Rate determination of the transition was confirmed to be a growth rate of non one-dimensional propagation rather than the nucleation rate. An apparent activation energy calculated by the Arrhenius equation was 13.7 kcal/mol. The considerably good fitting of the core-shrinking propagation supports the assumption that a large volume difference of 32% less than  $\alpha$ -quartz type structure prefers an exfoliation mechanism the core-shrinking propagation.

Zeto and Roy (1969) and Brar and Schlossin (1981) took no account of the inductance period and showed an apparent activation energy of 29 kcal/mole regardless of given pressures and 19.92 kcal/mole at 20GPa and 330~530 °C, respectively. The present in situ measurement of the mass fraction  $x(t)$  excluding those in the inductance period exhibited a considerably small activation energy. The transition based on diffusion process has a considerably long inductance period for a sort of the driving force reservoir. The period is an inevitable state for the premonitory phenomenon in the transition.

N.S. Brar and H. H. Schlossin, High temp. High Press. 13, 313-320 (1981)

R. J. Zeto and R. Roy, Proceeding of the 6th International Symposium on the Reactivity of Solid, 803-813. (1969)



EXAFS AND RDF STUDIES OF  $\text{Ge}_{27}\text{S}_{53}\text{I}_{20}$  GLASS

Hiroyuki NASU, Seigo MAKIDA

Department of Electrical Engineering, Faculty of Engineering,  
Hiroshima University, Higashi Hiroshima 724Introduction

Chalcohalide glasses seem to have a great potential for ultimate infrared transmitting glass material with high water durability<sup>1,2</sup>. As shown in Table 1, there are several known glass-forming chalcohalide systems, and Ge-S-I is one of the chemically and thermally stable glass systems among them.<sup>1</sup> However, the structure of Ge-S-I glasses has been controversial. From Raman spectroscopy, Koudelka et al.<sup>3</sup> concluded no detectable Ge-I bonds have been formed, although Heo et al. found the new peak formation by the addition of I and it has been tentatively assigned to Ge-I bonds. To clarify the structure, radial distribution function (RDF) calculated from X-ray diffraction and extended X-ray absorption fine structure (EXAFS) have been applied to  $\text{Ge}_{27}\text{S}_{53}\text{I}_{20}$  glass as a typical stable Ge-S-I glass in this study, and applied to  $\text{GeS}_2$  glass as a standard.

Experimental Procedure and Results

The raw materials, Ge powder, sulfur powder and iodine chips of analytical grade were mixed to obtain  $\text{Ge}_{27}\text{S}_{53}\text{I}_{20}$  and  $\text{GeS}_2$ , and put into silica ampoules. After evacuated and sealed, they were melted in a electric furnace and quenched in air. The detailed description can be found elsewhere<sup>1,2</sup>. The obtained glasses were ground for the following measurement.

Our measurements were carried out at the Photon Factory in National Laboratory for High Energy Physics on 10-b and 4-b line, and also at Faculty of Engineering, Chiba University (Dr. Igarashi).

Fig.1 (a) and (b) show the RDF estimated from X-ray diffraction measurements for  $\text{GeS}_2$  and  $\text{Ge}_{27}\text{S}_{53}\text{I}_{20}$  glass, respectively. In (a), the

peaks of the mean distance = 2.25 Å and 3.65 Å are ascribed to  $\text{Ge-S}$  bond and  $\text{Ge-S-Ge}$  bond, respectively. In (b), the peaks of the mean distance = 2.30 Å and 3.60 Å are assignable to  $\text{Ge-S}$  bond and  $\text{Ge-S-Ge}$  bond, respectively. From the consideration of all possible bonds and their distances, the peak of 2.71 Å can be ascribed to  $\text{Ge-I}$  bonds, and that of 3.10 Å to  $\text{S-Ge-I}$ .

Fig.2 (a) and (b) show the Fourier transform  $[F(r)]$  of the EXAFS oscillations for Ge K-edge of  $\text{GeS}_2$  and  $\text{Ge}_{27}\text{S}_{53}\text{I}_{20}$ , as a function of  $R-\alpha$ , where  $R$  is the distance to the first neighbor and  $\alpha$  is the constant, depending on the kind of elements. In (a), the first neighbor can be considered as S, and the mean  $R-\alpha$  between Ge and S is 1.88 Å. The shoulder can be noticed in (b) in the peak of the first neighbor. Dotted lines represent the deconvoluted peaks. The mean  $R-\alpha$  for the first peak is 1.84 Å, and those of the second and the third are 2.55 Å and 3.25 Å, respectively. Each of them can be assigned to  $\text{Ge-I}$  bonds (2.55 Å) and  $\text{Ge-S-Ge}$  (3.25 Å), respectively.

The dependence of  $\alpha$  on the elements next to Ge has been evaluated in detail for alloys containing Ge<sup>4</sup>), and thus one can confirm these assignments using it. The  $\alpha$  calculated from the difference in the atomic distance between RDF and EXAFS for S, Ge and I are nearly 0.4 Å, 0.3 Å and 0.16 Å, respectively, and those well agree with the data or extrapolated values in ref 4).

References

- 1) J. Heo, H. Nasu and J. D. Mackenzie, SPIE 683 (1986) 85-91.
- 2) J. Heo, J. S. Sanghera, H. Nasu and J. D. Mackenzie, Mat. Sci. Forum 19&20 (1987) 55-62.
- 3) L. Koudelka and M. Pisarcik, J. Non-Cryst. Solids 64 (1984) 87-94.
- 4) K. Tsunetomo, Master Thesis, Hiroshima University, 1988.

Table 1 Known Glass-forming  
Chalcohalide Systems

As-based systems	Ge-based systems	other systems
As-S-I	Ge-S-I	Sb-S-I
As-Se-I	Ge-Se-I	Sb-Se-I
As-Te-I	Ge-Te-I	Sb-S-Br
As-S-Br	Ge-S-Br	Si-S-I
As-Se-Br		P-S-I
As-Te-Br		P-Se-I
		Al-Cs-S-Cl
		Te-S-Cl, Br, I

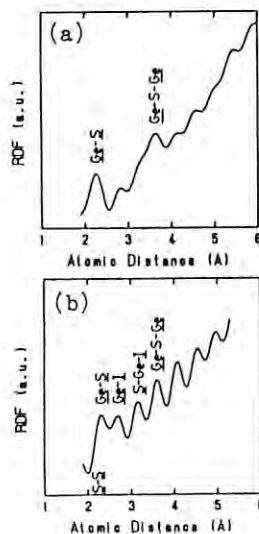


Fig.1

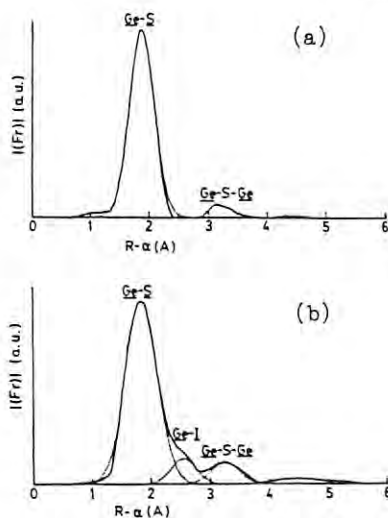


Fig.2

THE STRUCTURE STUDY OF  $\text{GeO}_2\text{-P}_2\text{O}_5$  GLASSES WITH THE ANOMALOUS X-RAY SCATTERING

Yutaka SHIMIZUGAWA, Katsuhisa ITOH, Satoru YAMAZAKI, Hideki MORIKAWA, Fumiyuki MARUMO, Akihiko NUKUI\*, Haruo OZAWA\*\*, Ryousei UNO\*\* and Kazumasa OHSUMI\*\*\*

Research Laboratory of Engineering Materials, Tokyo Institute of Technology, Yokohama 227

\*National Institute for Research in Inorganic Materials, Ibaraki 305

\*\*College of Humanity and Science, Nihon University, Setagaya, Tokyo 156

\*\*\*Photon Factory, National Laboratory for High Energy Physics, Tsukuba, Ibaraki 305

## INTRODUCTION

In radial distribution function (RDF) analysis of polyatomic non-crystalline solids, serious overlapping of peaks occurs frequently, which makes interpretation of the function ambiguous. The  $\text{GeO}_2\text{-P}_2\text{O}_5$  system is one of these materials; Ge-O and P-O nearest-neighbor pairs contribute to the same peak in RDF. To obtain more detailed structural information on such a materials, the differential anomalous X-ray scattering technique has been developed.<sup>1)</sup> The method requires to use the strong continuous X-rays such as synchrotron radiations. In the present study, we have performed two set of X-ray scattering measurement of  $\text{GeO}_2\text{-P}_2\text{O}_5$  glasses, using two different energy X-rays just before the Ge-K absorption edge.

## EXPERIMENTAL AND RESULTS

Three kinds of  $\text{GeO}_2\text{-P}_2\text{O}_5$  glasses were prepared by quenching melts. The raw materials were mixtures of reagent grade  $\text{GeO}_2$  and  $\text{NH}_4\text{H}_2\text{PO}_4$ . A flat plates were prepared from the obtained glasses for X-ray scattering measurement. The chemical composition of the obtained glasses are given in Table 1.

The intensity measurements were performed on a powder diffractometer installed on BL-4B in the Photon Factory.<sup>2)</sup> With this diffractometer, a monochromatic beam is selected out by utilizing a Si (111) monochromator. The energies of the X-rays were determined from the diffraction angles of high-angle diffraction lines (331, 422, 531, 620) of NBS standard Si powder. The energies of the used X-rays are listed in Table 2 with the anomalous scattering factors of Ge. A 0.5mm receiving slit and divergence slit of the same size were employed in the measurement.

Intensity data were collected by  $\theta$ - $2\theta$  step scan with  $0.4^\circ$  step width and 30 sec. fixed-time counting in  $2\theta$  range. The scanning was repeated three times with X-rays of the same energy. To eliminate fluorescence rays and higher order harmonics, a flat counter monochromator (graphite) was used. The sample room and the most of beam path were held at high vacuum during data collection. Intensity data after correction for absorption and normalization is shown in Fig.1. The intensity of incident beam is monitored by the scattered and fluorescent X-rays from an Al foil placed in the out-going beam path of the Si(111) monochromator.

After corrections variation of incident beam by the monitor counts, RDF was derived from the observed data. An example of RDF is shown in Fig.2. The first peak of RDF is not separated to Ge-O and P-O pairs. The final goal of the study is to sepa-

rate these pairs by using the difference of anomalous scattering factors. Fig.1 shows the energy dependence of the modified intensity data. Since energy dependence is observed in normalized intensities given in Fig.1, the separation of the peaks seems to be feasible.

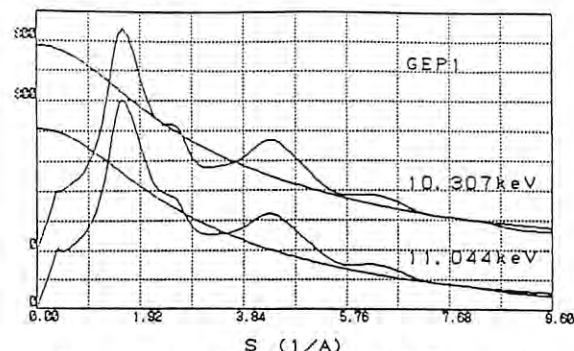


Fig. 1 Modified intensity data of GEP1 sample.

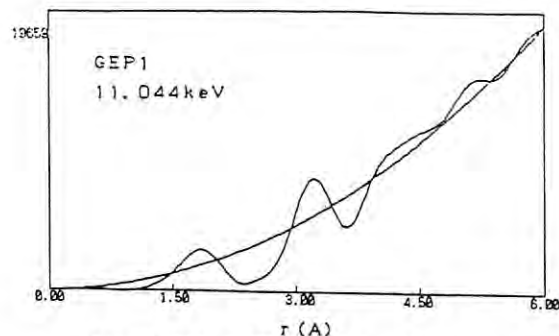


Fig. 2 RDF of GEP1 sample at 11.044 keV.

Table 1. The chemical composition of samples

sample	$\text{GeO}_2$ (mol%)	$\text{P}_2\text{O}_5$ (mol%)
GEP1	60.8	39.2
GEP2	66.0	34.0
GEP3	79.6	20.4

Table 2. X-ray energy and anomalous scattering factors of Ge atom

ENERGY(keV)	$f'$	$f''$
11.044	-4.876	0.498
10.307	-2.236	0.565

## REFERENCES

- 1) P.H.Fuoss, W.K.Warburton and A.Bienenstock, J. of Non-Cryst. Solids, **35 & 36** (1980) 1233.
- 2) R.Uno, H.OZAWA, T.Yamanaka, K.Ohsumi and A. nukui, P. F. Activity Report, **5** (1987) 141.

## Structure Analysis of Organic Compounds by X-ray Powder Diffraction

Masayasu KURAHASHI, Kazumasa HONDA, Midori GOTO, Isao KOJIMA, Yoshinori KOBAYASHI,  
Kenji KATO, Natsuo FUKUMOTO, Ryosei UNO\*, Haruo OZAWA\*, and Kazumasa OHSUMI\*\*

Analytical chemistry Division, National Chemical Laboratory for Industry, Tsukuba, Ibaraki 305

\*College of Humanities and Sciences, Nihon University, Setagaya Tokyo 156

\*\*Photon Factory, National Laboratory for High Energy Physics, Tsukuba, Ibaraki 305

### Introduction

It would be highly desirable if the structure could be determined by the first principle by using X-ray powder diffraction data. For this purpose high angle-resolution and accurate intensity data (no preferred orientation) are required. In order to collect such data we carried out preliminary experiments by using the advantages of synchrotron radiation.

### Experimental

The PFPD<sup>1)</sup> (Powder Diffractometer for the Photon Factory) installed at BL-4B was used for the high resolution measurement. The samples used were amino-carboxylic acids such as L-alanine, 6-aminocaproic acid, 5-aminovaleric acid and 7-aminoheptanoic acid, the structures of the latter two being unknown. Intensity data were collected by  $\theta$ - $2\theta$  step scan method with  $0.02^\circ$  (in  $2\theta$ ) step width for 5-10 seconds using 0.5-0.2 mm slits. During the data collection, the samples were kept rotating by spinner. The wavelength of radiation was set at 1.5406 Å.

The other experiment was performed to check the usefulness of Sakabe's camera<sup>2)</sup> at BL-6A for the powder diffractometry. The powder sample in a glass capillary was mounted on the camera. The wavelength was set to 1.040 Å. A powder pattern of L-alanine was taken at a normal setting of the cylindrical cassette with the radius of 28.65 cm. The imaging plate with the dimensions of 40x20 cm was mounted in the film cassette.

### Results and Discussion

Fig. 1. shows the powder diffraction spectra of L-alanine obtained by PFPD. The angle-resolution was so high that the lattice parameters for the amino-carboxylic acids could be determined by Ito's method easily. However, preferred orientation was observed in the data.

Fig. 2. shows the powder pattern of L-alanine obtained by using Sakabe's camera. The recorded signals on the imaging plates were digitized on a scanner using a 100  $\mu$ m raster step size. Fig. 3 shows the powder spectra processed by averaging the whole data of IP. The spectra thus obtained agree well with that calculated from the single crystal diffraction data. Accordingly, Sakabe's camera is very useful even if the size of powder sample is so large that the spotty diffraction pattern is produced.

We thank Prof. N.Sakabe and Dr. A.Nakagawa, PF KEK and Dr. A.Takenaka, Tokyo Institute of Technology for their kind help and suggestions in the data collection with the camera.

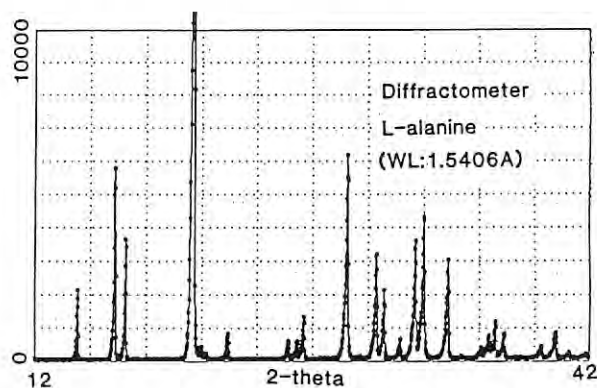


Fig.1. Powder diffraction spectra obtained by PFPD ( $\lambda=1.5406$  Å).

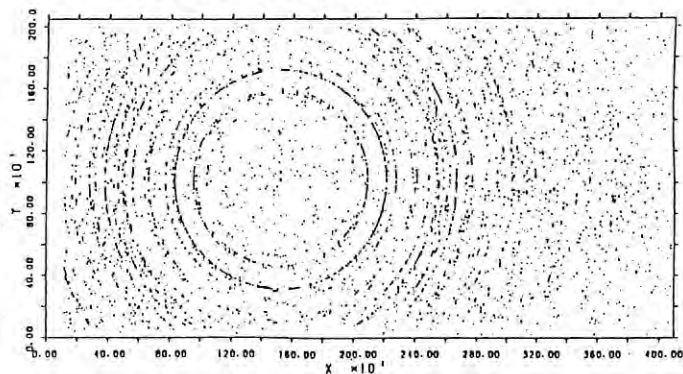


Fig.2. Powder diffraction pattern obtained by SAKABE's camera ( $\lambda=1.040$  Å).

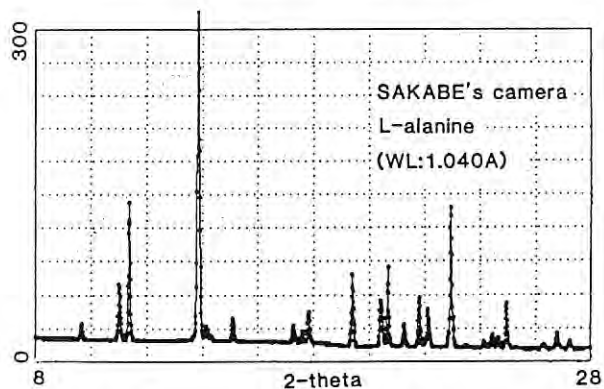


Fig.3. Powder diffraction spectra processed by using whole data of IP.

### References

- 1) R.Uno, T.Yamanaka, K.Ohsumi, and A.Nukui, PF Activity Report 1987, p. 141
- 2) N.Sakabe, PF Activity Report 1987, p. 87



SPATIALLY MODULATED STRUCTURES OF  $[\text{N}(\text{CH}_3)_4]_2\text{MnCl}_4$ 

Nozomu HAMAYA, Susumu SHIMOMURA, Yasuhiko FUJII, Noriko SHINGAKI  
Yoshihiro KUROIWA<sup>+</sup>, and Hiroyuki KONISHI<sup>++</sup>

Faculty of Engineering Science, Osaka University, Toyonaka, Osaka 560

<sup>+</sup>Institute of Applied Physics, University of Tsukuba, Tsukuba, Ibaraki 305

<sup>++</sup>Division of Synchrotron Radiation Research, JAERI, Tokai, Ibaraki 319-11

Spatially modulated structures are quite common in condensed matter. The periodicity may vary sensitively with external parameters, such as temperature, pressure, magnetic or electric field. A resulting sequence of long-period phases is often surprisingly complex. For example, the phase diagram of  $\text{CeSb}$  consists of, at least, fourteen commensurate phases<sup>1)</sup>. To describe such experimental findings, simple statistical models with competing interactions have been developed and studied extensively<sup>2)</sup>. Despite of their simplicity, complicated behaviors observed in real systems are reproduced successfully to some extent and, further, a particular study by Aubry<sup>3)</sup> led to novel concepts like the devil's staircase.

In our previous work<sup>4)</sup>, we observed a staircase behavior of the modulation wave vector along the  $c^*$  direction as a function of pressure in  $[\text{N}(\text{CH}_3)_4]_2\text{MnCl}_4$ , a member of the ferroelectric  $\text{A}_2\text{BX}_4$  family. It is rather surprising that many features found in its  $P$ - $T$  phase diagram can be exhibited by a very simple model with competing interactions (e. g. the ANNNI model). The purpose of this study is to disclose hidden properties of such a devilish system using a sophisticated high resolution x-ray diffraction technique.

A single crystal was mounted in a beryllium pressure cell so as to allow for scans in the  $(h0l)$  plane. The cell was mounted on a four-circle diffractometer installed at BL-4C. The transverse resolution was measured to be  $0.00018 \text{ \AA}^{-1}$  ( $\Delta\omega \sim 10''$ ) in FWHM, corresponding to  $0.00023c^*$ , at the 400 fundamental reflection using both a  $\text{Si}(111)$  double crystal, sagittally-focusing monochromator and a  $\text{Si}(111)$  analyzer.

Figure 1 shows diffraction profiles of the  $40q$  satellite reflection at the lock-in of the

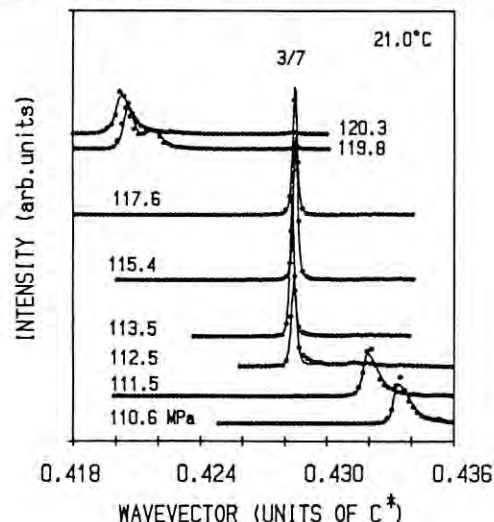


Figure 1. X-ray diffraction profile of the  $40q$  satellite reflection, showing the lock-in transition to  $q=0.4286$  ( $3/7$ ) for increasing pressure.

modulation wave number to a rational value of  $q=0.4286 (= 3/7)$ . This lock-in transition is always accompanied with a pressure-hysteresis of the wave number and, thus, is of first order. The symmetric satellite reflection at  $q=3/7$  has a resolution limited width (Fig. 2). In contrast, the peak width observed in the incommensurate phases is much broader. This fact together with the asymmetric peak shape are taken as evidence for the presence of disordered structure in the incommensurate phases. One may also notice in Fig. 2 that there is a tendency for the peak width to narrow with increasing pressure and that some data points of the width are scattered. The latter result seems to be associated with the existence of high-order commensurate phases in the nominally incommensurate region. In fact, the scattering of data, that is, the peak broadening occur at the wave numbers that correspond to those of long-period phases found above  $21.0^\circ\text{C}$ . To account for comprehensively these results, it is crucial to establish a microscopic picture of the devilish system both theoretically and experimentally.

## References

- 1) J. Rossat-Mignod et al., J. Mag. Mag. Materials, **31-34**, 398 (1983).
- 2) A recent review is P. Bak, Rep. Prog. Phys. **45**, 587 (1982).
- 3) S. Aubry, in Soliton and Condensed Matter Physics, eds. A. R. Bishop and T. Schneider (Springer, Berlin, 1978) p. 264.
- 4) N. Hamaya et al., Solid State Commun. **67**, 329 (1988); N. Hamaya et al., unpublished.

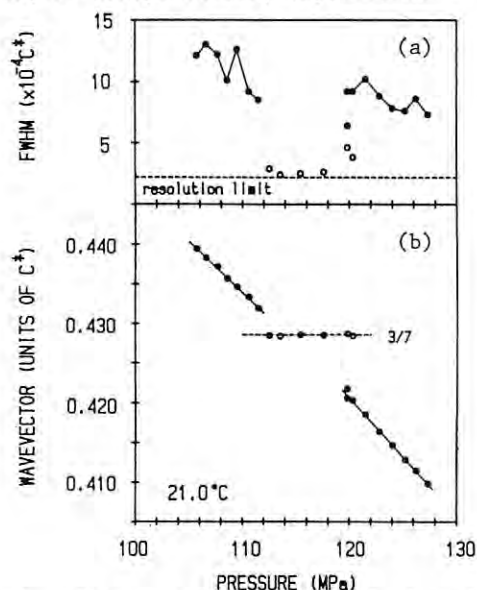


Figure 2. Pressure dependence of the width of the  $40q$  satellite reflection (a) and of the modulation wave number along the  $c^*$  direction (b).



## DIFFRACTION PATTERN OF AN ENVIRONMENTAL FIBONACCI LATTICE

Hikaru TERAUCHI, Kousei KAMIGAKI, Yasuo NISHIHATA, Shuichi HAYASE, Hiroyuki MASHIYAMA\*, Kenichi OHSHIMA\*\*, Jimpei HARADA\*\*\*, Shunji KISHIMOTO\*\*\*\* and Hiroshi IWASAKI\*\*\*\*\*

Faculty of Science, Kwansei-Gakuin University, Nishinomiya 662; \*Faculty of Science, Yamaguchi University, Yamaguchi 753; \*\*Institute of Applied Physics, Tsukuba University, Tsukuba 305; \*\*\*Faculty of Engineering, Nagoya University, Nagoya 464; \*\*\*\*Photon Factory, National Laboratory for High Energy Physics, Tsukuba 305

### Introduction

The recent discovery of a quasi-crystal with icosahedral symmetry has created strong interest in new class of solids. The icosahedral symmetry can be explained in terms of a three dimensional quasi-periodic lattice which gives sharp diffraction peaks.

A one-dimensional quasi-periodic lattice can be also obtained by the technique of the molecular beam epitaxy (MBE). We reported the diffraction patterns of the one-dimensional quasi-periodic lattices, in which the species of atoms are changed in each layer with the same spacing.<sup>1,2)</sup> The golden mean of the width ratio of alternating layers is not essential for the lattices. We called the lattices as "configurational Fibonacci lattices".

Here we present the diffraction pattern of the environmental Fibonacci lattice with a hexagonal(h)-cubic(c) Fibonacci sequence;  $S_1=h$ ,  $S_2=hc$ ,  $S_3=hch$ ,  $\dots$ ,  $S_r=S_{r-1} \cdot S_{r-2}$ . The real atomic sequence is

$$\begin{aligned} &hchhchhchhchc \dots \\ &ABCBCACBCBABAC \dots \end{aligned} \quad (1)$$

where the thickness is the same in each layer.

### Experimental

Environmental Fibonacci lattices were grown by Riber MBE 2300R&D on the (001) GaAs substrate following the sequence given in eq. (1). The layer species are  $A=Al_{0.5}Ga_{0.5}As$ ,  $B=GaAs$ ,  $C=AlAs$ . The thickness of each layer is designed as  $5a$ , that is, five times of the lattice constant of the zinc-blende structure. The length of the Fibonacci sequence  $r$  is 14.

The x-ray measurements were carried out using the beam line 4C. Radiation ( $\lambda=1.5400\text{\AA}$ ) was monochromatized by a pair of Si(111) and focused by a sagittal focusing mechanism. A four-circle diffractometer with horizontal  $2\theta$ - $\omega$  axes was employed.

Figure 1 shows the diffraction pattern of an environmental Fibonacci lattice. The inset in the figure gives the diffraction pattern around the (004) reflection, which is observed by the conventional set-up with Cu K $\alpha$  radiation (50kVx100mA). Many fine peaks are observed in the high resolution measurement using synchrotron radiation.

### Discussion

The diffraction pattern of the environmental Fibonacci lattice shows many fine peaks but is different from that of the configurational Fibonacci lattice.<sup>1,2)</sup> The difference between these two Fibonacci lattices is due to the correlation functions. The real atomic sequence in

the environmental Fibonacci lattice is not the Fibonacci sequence.

One notices that the environmental Fibonacci sequence contains a lot of 10H local structure.<sup>3)</sup>

### Acknowledgments

The authors wish to express their thanks to staff of the MBE group of Kwansei-Gakuin University and the crystal physics group of Photon Factory for their discussions. The useful comments of Y. Noda, Y. Yamada and Y. Kitano are greatly appreciated.

### References

- 1) K. Kamigaki, H. Sakashita and H. Terauchi: PF Activity Report 5, 145 (1987).
- 2) H. Terauchi, Y. Noda, K. Kamigaki, S. Matsunaka, M. Nakayama, H. Kato, N. Sano and Y. Yamada: J. Phys. Soc. Jpn. 57, 2416 (1988).
- 3) Y. Kitano: Dr. Thesis, Faculty of Engineering Science, Osaka University (1980).

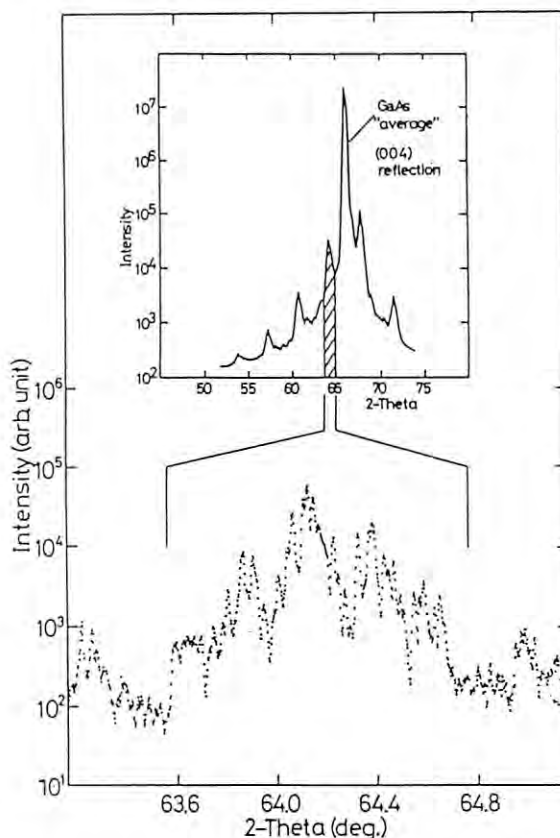


Fig. 1. X-ray diffraction pattern of an environmental Fibonacci lattice. An inset shows the diffraction pattern at lower resolution.

PHASE TRANSITIONS OF BLACK PHOSPHORUS AND BLACK PHOSPHORUS-ARSENIC  
ALLOY AT VERY LOW TEMPERATURES AND HIGH PRESSURES

Ichimin SHIROTANI, Kazuhiko TSUJI<sup>+</sup>, Haruki KAWAMURA<sup>++</sup>, Osamu SHIMOMURA<sup>+++</sup>,  
Kazuhiko TSUBURAYA, Keiichi OKUYAMA, Shigemitsu SHIBA, Osamu ENDO<sup>+</sup>,  
Takumi KIKEGAWA<sup>++++</sup>, and Tetsuo NAKAJIMA<sup>++++</sup>

Muroran Institute of Technology, 27-1, Mizumoto, Muroran 050

<sup>+</sup> Faculty of Science and Technology, Keio University, Hiyoshi, Yokohama 223

<sup>++</sup> Himeji Institute of Technology, 2167, Syosya, Himeji 671-22

<sup>+++</sup> National Institute for Research in Inorganic Materials, Sakura, Tsukuba,  
Ibaraki 305

<sup>++++</sup> Photon Factory, National Laboratory for High Energy Physics, Oho, Tsukuba,  
Ibaraki 305

Black phosphorus (black P) transforms an orthorhombic structure to a rhombohedral one and then further to a simple cubic one with increasing pressure at room temperature(1). The P-T phase diagram of black P has already been determined above room temperature by means of X-ray study with synchrotron radiation(2). As the phase diagram has not yet been studied below room temperature, the structure of black P has been investigated at liquid helium temperature and high pressure using synchrotron radiation.

A new diamond-anvil cell was developed for X-ray diffraction measurement which makes possible a continuous change of pressure at low temperatures. The diffraction patterns of black P and NaCl were recorded at  $2\theta = 21^\circ$ . The diffraction lines of NaCl were used to determine the pressure value according to Decker's scale.

The transition from the orthorhombic form to the rhombohedral one begins to occur at about 4.6 GPa at room temperature. Both phases coexist in wide pressure range under quasi-hydrostatic condition. X-ray diffraction profiles of black P have already been studied at 77 K and high pressures(3). Some diffraction lines of the rhombohedral structure at about 6 GPa are observed in addition to lines of the orthorhombic one. Black P transforms from the rhombohedral structure to the simple cubic one at about 10 GPa under room temperature and 77 K.

The pressure-induced phase transitions in black P were studied at around liquid helium temperature. The transition from the orthorhombic phase to the rhombohedral one began to occur at about 10 GPa under 11 K. The transition pressure risen from about 6 GPa at 77 K to 10 GPa at 11 K. The reversible transformation from rhombohedral to simple cubic form was observed at about 16 GPa under 11 K. The transition pressure increased abruptly in the very low temperature region.

Figure 1 shows the P-T phase diagram of black P below room temperature. Since the rate of attainment of equilibrium between orthorhombic and rhombohedral phases is very sluggish, the two phases coexist in wide pressure region under quasi-hydrostatic condition. The phenomena are more remarkable in the lower temperature range. Thus, it is very difficult that the boundary between orthorhombic and rhombohedral phases determines exactly. The dashed line shows the pressure which is started the phase transition.

Black phosphorus-arsenic alloys with  $P_{1-x}As_x$  ( $x$ : 0.05, 0.1, 0.2, 0.3, 0.4, 0.5, 0.6) were prepared at high temperature and pressure. X-ray

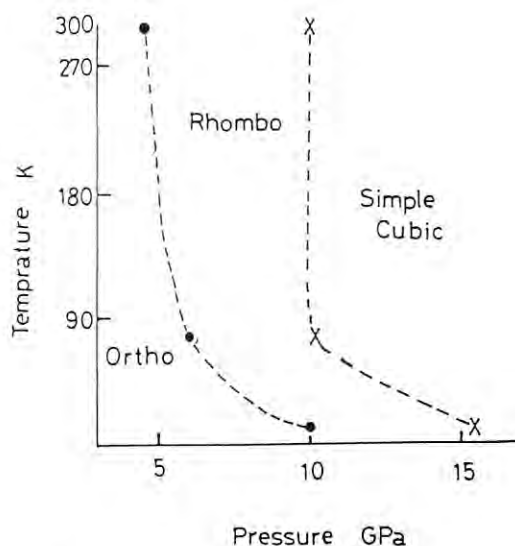


Fig. 1 P-T phase diagram of black P below room temperature

diffraction profiles in the alloys were similar to those of black P. The alloys are isostructural with black P. The orthorhombic form of alloys underwent transformation to successively denser rhombohedral and simple cubic forms at room temperature and high pressure(4). The transition from the orthorhombic form to the rhombohedral one for  $P_{0.95}As_{0.05}$  began to occur at about 6 GPa. This is about 1.5 GPa higher than that of black P. The alloy transformed from the rhombohedral structure to the simple cubic one at about 14 GPa. This transition pressure of  $P_{1-x}As_x$  increased with increasing  $x$  at room temperature.

1. J. C. Jamieson, Science, 139, 129 (1963).
2. T. Kikegawa et al., J. Appl. Cryst., 20, 406 (1987).
3. I. Shirotnani et al., Bull. Chem. Soc. Japan, 62, 211 (1988).
4. I. Shirotnani et al., Synthetic Metals, in Press.

DETERMINATION OF THE ENVIRONMENTAL STRUCTURE AROUND A SPECIFIC ATOM  
IN CRYSTALLINE MATERIALS BY THE ANOMALOUS X-RAY SCATTERING

Yoshio WASEDA, Eiichiro MATSUBARA, Kazumasa SUGIYAMA and Takashi SAKUMA\*

Research Institute of Mineral Dressing and Metallurgy (SENKEN),  
Tohoku University, Sendai 980, Japan.

\* Department of Physics, Faculty of Science,  
Ibaraki University, Mito 310, Japan.

There is a vast amount of research on new materials going on today and the utmost importance of the structure of such new materials at a microscopic level has been well recognized. The anomalous x-ray scattering (AXS) method for determining the environmental structure around a specific atom is also useful for crystalline materials in the variety of states<sup>1)</sup>. For this reason, this proposal includes to characterize the structural features of crystalline materials by the AXS method.

Fig. 1 shows the energy dependence in intensity of a  $\text{YBa}_2\text{Cu}_3\text{O}_{7-x}$  oxide superconductor as a function of the wave vector estimated from measurements at energies of 8.829 and 8.955 keV, which are -150 and -25 eV away from the Cu K absorption edge respectively. Here the difference,  $\Delta I_{\text{Cu}}(q)$  is taken from  $I(\text{at } -150 \text{ eV}) - I(\text{at } -25 \text{ eV})$  and the observed energy dependence is attributed to the anomalous dispersion effect of Cu. The sign of (+) and (-) in Fig.1 describe the values estimated from the crystallographic structure factor coupled with the model structure of Izumi et al.<sup>2)</sup>. The agreement in signs between calculation and experiment for the energy dependence arising from the anomalous dispersion effect of Cu is surprisingly good. The environmental radial distribution function around Cu is given in Fig.2. This result again implies that the model structure<sup>2)</sup> is quite feasible for describing the local atomic arrangement in a Y-Ba-Cu-O superconductor.

Copper selenide ( $\alpha\text{-Cu}_2\text{Se}$ ) is known to behave the solid fast ion conductors. The AXS method is useful in order to obtain insights into their structural features. Fig. 3 shows the variation of the intensity for  $\alpha\text{-Cu}_2\text{Se}$  measured at energies close to the K absorption edge of Cu and Se, respectively. The significant energy dependence of the intensity is detected at both

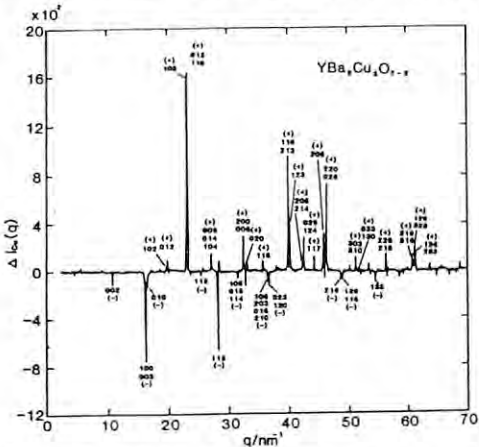


Fig.1 The energy dependence of the intensity  $\Delta I_{\text{Cu}}(q)$  for a  $\text{YBa}_2\text{Cu}_3\text{O}_{7-x}$  superconductor.

edges. These results are consistent with the conclusion that the space group  $O_h^5\text{-Fm}3m$  with a disordered arrangement of all copper ions is plausible for describing the structure of  $\alpha\text{-Cu}_2\text{Se}$ , although the detailed information is not obtained at the present time.

References

- 1) Y. Waseda, E. Matsubara and K. Sugiyama, Sci. Rep. RITU **34A**, 1 (1988)
- 2) F. Izumi, H. Asano, T. Ishigaki, A. Ono and F. P. Okamura, Japanese J. Appl. Phys., **26**, L611 (1987)

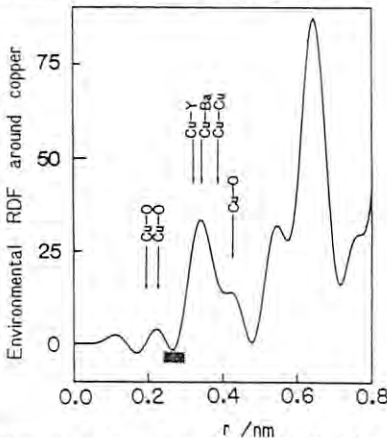


Fig.2 The environmental radial distribution function(RDF) around Cu in a  $\text{YBa}_2\text{Cu}_3\text{O}_{7-x}$  superconductor obtained from the measured energy dependence in intensity of Fig.1.

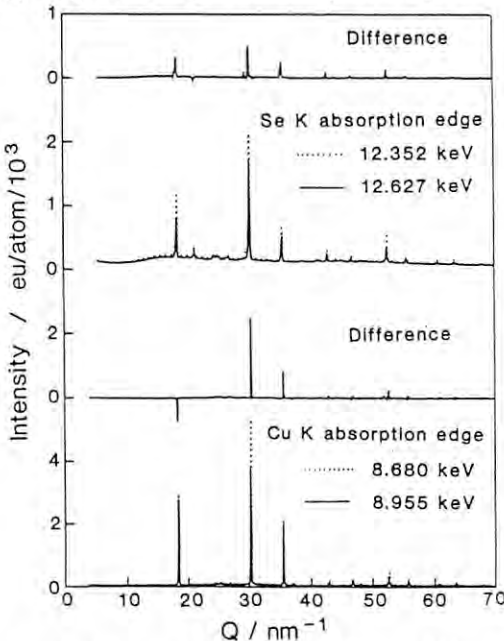


Fig.3 Differential intensity profiles of  $\alpha\text{-Cu}_2\text{Se}$  obtained from intensity data sets at the Se and Cu K absorption edge.

SPONTANEOUS DISTORTION IN ANTIFERROMAGNETIC TbCu<sub>5</sub>-TYPE COMPOUNDS

Kazuo KAMIGAKI, Tetsuo NAKAJIMA\*, Takejiro KANEKO, Shunya ABE,  
Hajime YOSHIDA and Hiroyuki YASUI

Institute for Materials Research, Tohoku University, Katahira, Sendai 980

\*Photon Factory, National Laboratory for High Energy Physics, Tsukuba 305

### Introduction

AuBe<sub>5</sub>-type cubic compounds TbCu<sub>5</sub> and its substitutions TbAgCu<sub>5</sub> and TbAuCu<sub>5</sub> are antiferromagnetic, and  $T_N$  are 16, 11.5 and 8 K, respectively. The magnetic spinstructure of them is similar: magnetic moments couple ferromagnetically in the (111) plane and antiferromagnetically in the adjacent (111) planes. However, the direction of the moment is different: along the 111-direction in TbAgCu<sub>5</sub>, in the (111) plane in TbAuCu<sub>5</sub>, and in the intermediate direction in TbCu<sub>5</sub>.<sup>1,2,3)</sup>

The similar situation was observed in the antiferromagnetic oxides of 3d-metals: FeO, MnO, NiO and CoO. In these oxides, some spontaneous distortion of lattice from the cubic structure was observed in the antiferromagnetic state.<sup>4,5)</sup>

The purpose of the present experiment is to detect the distortion of lattice from a cubic structure in TbCu<sub>5</sub>, TbAgCu<sub>5</sub> and TbAuCu<sub>5</sub> in the antiferromagnetic state.

### Experimental

A cryostat was prepared for the low temperature X-ray diffraction. The cryostat was made in a line: compact, easy to handle, simple in construction and easy to operation. The powdered specimen is glued on a copper plate, attached on a copper block fixed to the bottom of the liquid helium tank. The window for the X-ray beam is covered with a mylar film 0.1 mm thick.

X-ray diffraction experiment was performed in the beam line 6C-1. X-ray was collimated to 4

x4 mm<sup>2</sup> then narrowed to 1 x 1 mm<sup>2</sup> using crossed slits. The characteristic X-rays: CuK $\alpha$ , CuK $\beta$ , AgK $\alpha$ , and AgK $\beta$  originated from the specimen itself were used for markers in the energy scale.

### Results

Measurements were carried out at temperatures of liquid He, liquid N<sub>2</sub> and room temperature.

Profile of some diffraction peaks in TbAgCu<sub>5</sub> is shown in Fig. 1, at liq. N<sub>2</sub> and at liq. He temperature. Some splitting of (731) and (553) lines is observed at liquid helium temperature. However, the signal to noise ratio is not so high and the precise conclusion will be deduced after repetition of the experiment.

The authors would like to thank Mr. H. Nakazawa for his help in the experiment.

### References

- 1) T. Kaneko, K. Kamigaki, S. Abe and M. Ohashi: J. Appl. Phys. 53 (1982) 8088.
- 2) T. Kaneko, S. Abe, K. Kamigaki and M. Ohashi: J. Mag. Mag. Mat. 31-34 (1983) 253.
- 3) T. Kaneko, M. Ohashi, S. Abe, K. Kamigaki and H. Yoshida: J. Mag. Mag. Mat. 54-57 (1986) 469.
- 4) C. G. Shull, W. A. Strauser and E. O. Wollan: Phys. Rev. 83 (1951) 333.
- 5) W. L. Roth: Phys. Rev. 110 (1958) 1333.

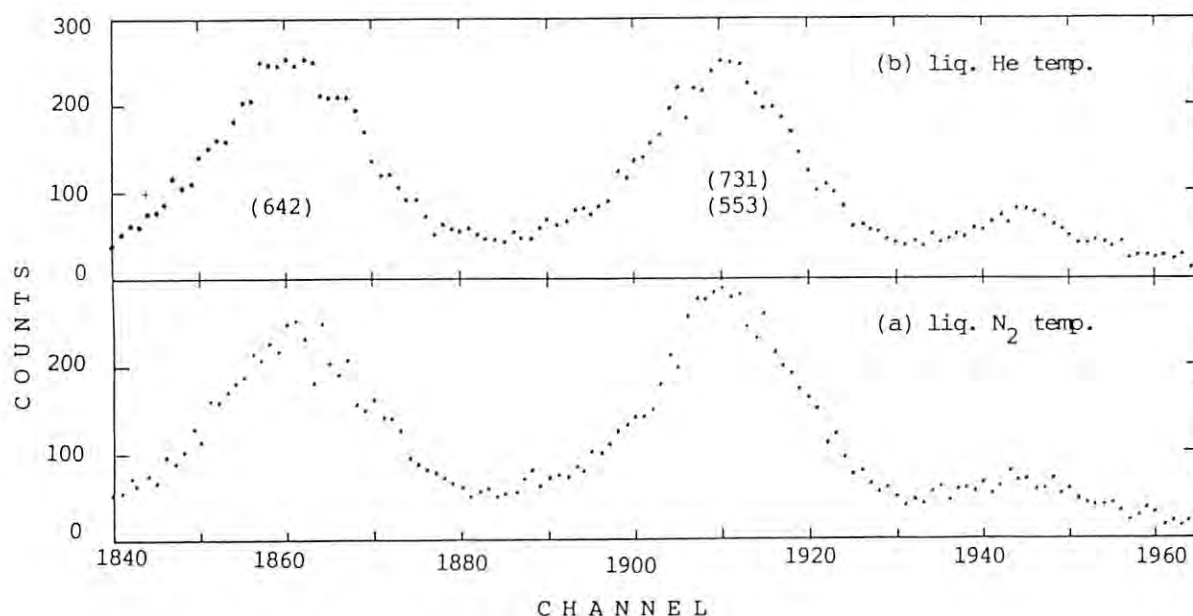


Fig. 1 Diffraction patterns for TbCu<sub>4</sub>Ag, 2-theta 29.0°, at (a) liq. N<sub>2</sub> (b) liq. He.



# Observation of Pendellösung fringe induced by X-ray resonant scattering using SR.

Masami YOSHIKAWA, Takaaki KAWAMURA<sup>†</sup>, Tomoe FUKAMACHI, Tetsuo NAKAJIMA<sup>††</sup>,  
Kenji EHARA, Fumito NISHI, Akira TAMURA, Hitoshi SUGAWARA and Kazunobu HAYAKAWA<sup>†††</sup>

<sup>†</sup>Samitama Institute of Technology, Okabe, Saitama 369-02

<sup>††</sup>Department of Physics, Yamanashi University, Kofu, Yamanashi 400

<sup>†††</sup>Photon Factory, National Laboratory for High Energy Physics, Tsukuba, Ibaraki 305

<sup>†††</sup>Advanced Research Laboratory, Hitachi Ltd., Kokubunji, Tokyo 185

Pendellösung fringe induced by the variation of the real part of anomalous scattering factor or X-ray resonant scattering has been observed by our group using an ordinary X-ray generator<sup>1)</sup>. In that experiment, the X-ray diffracted intensity was weak, so that the statistical error was still large for quantitative discussion.

The present paper describes experimental results of Pendellösung fringe due to X-ray resonant scattering just below the K absorption edge of the constituent atom in a crystal using the multi-purpose four-circle diffractometer with SSD at BL-6C1 (PF, KEK).

Two kinds of perfect crystals were used, one was GaAs and another was Ge. The former was GaAs single crystal which contained about 0.04 In atoms in a unit cell. The crystal perfection of the In-doped GaAs was much better than that of the undoped GaAs and the crystal was almost free from lattice defects. In the following, we denote the In-doped crystal as Ga(In)As.

Fig. 1 shows the observed intensities of the 200 reflection from Ga(In)As as a function of X-ray energy and (a)-(c) correspond to intensity profiles for sample thickness of 111  $\mu\text{m}$ , 155  $\mu\text{m}$  and 222  $\mu\text{m}$ , respectively. In Fig. 1 (a), one peak is observed, (b) has two peaks and (c) has three peaks. Fig. 2 shows the calculated results of the 200 integrated reflection

intensities in an energy dispersive mode from GaAs perfect crystal. The thickness of the crystal are 111  $\mu\text{m}$  (a), 155  $\mu\text{m}$  (b) and 222  $\mu\text{m}$  (c), respectively. Comparison Fig. 1 with Fig. 2, experimental results agree qualitatively with the theoretical results.

Fig. 3 shows the observed and calculated results of the integrated intensity of 844 reflection from Ge crystal just below the K absorption edge. The experimental results were shown clearly the intensity oscillation due to Pendellösung fringe induced by X-ray resonant scattering.

We observed satisfactorily Pendellösung fringe by changing the anomalous scattering factor just below the K absorption edge using SR. However, there still remain quantitative disagreements of the amplitude and the phase between theory and experiment. Further study should be necessary both in theory and experiment for quantitative discussion.

## References

- 1) M. Yoshizawa, T. Fukamachi, K. Ehara, T. Kawamura and K. Hayakawa, *Acta Cryst.*, **A44**, 433 (1988).
- 2) M. Yoshizawa, T. Kawamura, T. Fukamachi and K. Hayakawa, *Acta Cryst.*, **A42**, 113 (1986).

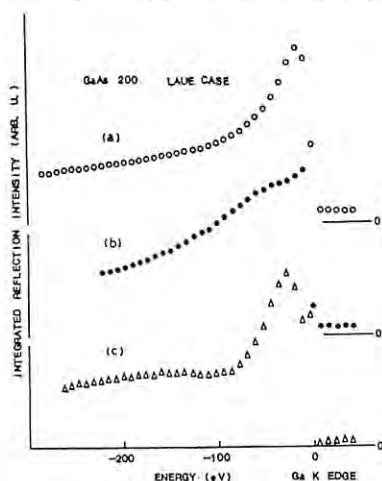


Fig. 1 Measured 200 reflection intensities for Ga(In)As in the Laue case across the Ga K absorption edge.

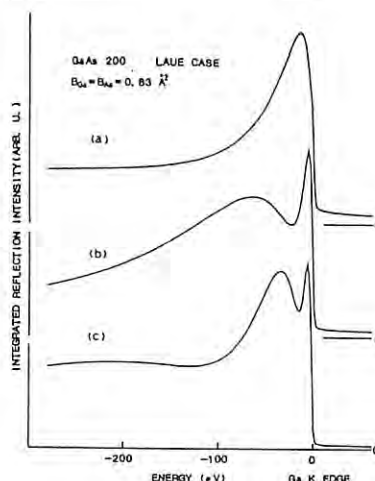


Fig. 2 Calculated values of 200 integrated reflection intensities by using a dynamical theory of X-ray diffraction.

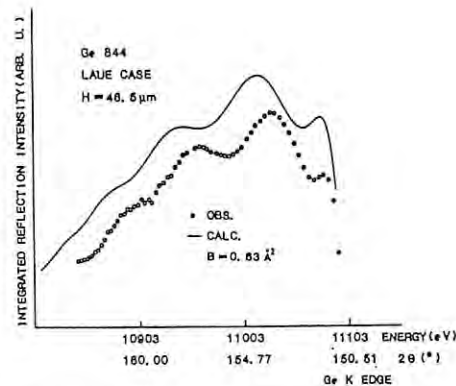


Fig. 3 The integrated reflection intensity of 844 from Ge near K absorption edge. The solid line is calculated value for  $B = 0.63 \text{ \AA}^2$ . Open circles are experimental values.

MAGNETIC SPONTANEOUS DISTORTION OF LATTICE IN  
ANTIFERROMAGNETIC COMPOUNDS

Kazuo KAMIGAKI, Tetsuo NAKAJIMA\*, Takejiro KANEKO, Shunya ABE,  
Hajime YOSHIDA and Hiroyuki YASUI

Institute for Materials Research, Tohoku University, Sendai 980

\*Photon Factory, National Laboratory for High Energy Physics, Tsukuba 305

### Introduction

Intermetallic compound  $\text{TbCu}_5$  has a cubic  $\text{AuBe}_5$ -type structure, and its substitution of one copper with Au, Ag, or Pd also has a cubic  $\text{MgSnCu}_4$ -type structure. These compounds are antiferromagnetic and spin structure has a rhombohedral symmetry 1,2,3). In these compounds a spontaneous magnetic distortion of the lattice is expected to occur from cubic to rhombohedral below the Néel temperature 4). The purpose of the present experiment is to detect the spontaneous distortion of the lattice in these compounds and to make analysis of the magnetic interaction.

### Experimental

To assure the precise detection of a tiny distortion, three specimens were fixed on one specimen holder at the separate positions: for instance,  $\text{TbAgCu}_4$  at the top,  $\text{NaCl}$  at the middle, and  $\text{TbAuCu}_4$  at the bottom. The specimen to be measured was selected by z-axis adjustment of the goniometer, and three patterns were obtained separately without any other change in the system. The incident X-ray beam is fine enough to irradiate one specimen at one setting position and no contamination was observed in the pattern.  $\text{NaCl}$  was used as a calibrant.

### Results

The diffraction patterns for  $\text{TbAuCu}_4$  obtained at liquid nitrogen temperature and liquid He are shown in Fig. 1. A slight change in the

peak shape is observed in the liquid helium pattern. The  $\text{MgSnCu}_4$ -type structure has a symmetry:  $T_2-F4m$ , and atomic positions: (4Mg: 0, 0, 0; 4Sn: 1/4, 1/4, 1/4; 16Cu: 5/8, 5/8, 5/8). The corresponding trigonal structure is  $C_3-R3$ , and atomic positions: (3Mg: 0, 0, -1/8; 3Sn: 0, 0, 1/8; 9Cu: 1/2, 0, 0; 3Cu: 0, 0, 1/2). According to the preliminary analysis, the angle between trigonal axes is greater than  $60^\circ$  in  $\text{TbAgCu}_4$  and smaller in  $\text{TbAuCu}_4$ . The magnitude of difference is less than  $0.5^\circ$  in two compounds.

The thermal expansion coefficient is deduced by taking the cubic cell, the value is  $18 \times 10^{-6}/\text{K}$  for  $\text{TbAuCu}_4$ . The value is close to the proper values in metallic compounds.

The precise analysis is now under way.

The authors would like to thank Messrs. H. Nakazawa and T. Komatsu for their assistance.

### References

- 1) T. Kaneko, K. Kamigaki, S. Abe and M. Ohashi: J. Appl. Phys. 53 (1982) 8088.
- 2) T. Kaneko, S. Abe, K. Kamigaki and M. Ohashi: J. Mag. Mag. Mat. 31-34 (1983) 253.
- 3) T. Kaneko, M. Ohashi, S. Abe, K. Kamigaki and H. Yoshida: J. Mag. Mag. Mat. 54-57 (1986) 469.
- 4) W. L. Roth: Phys. Rev. 110 (1958) 1333.

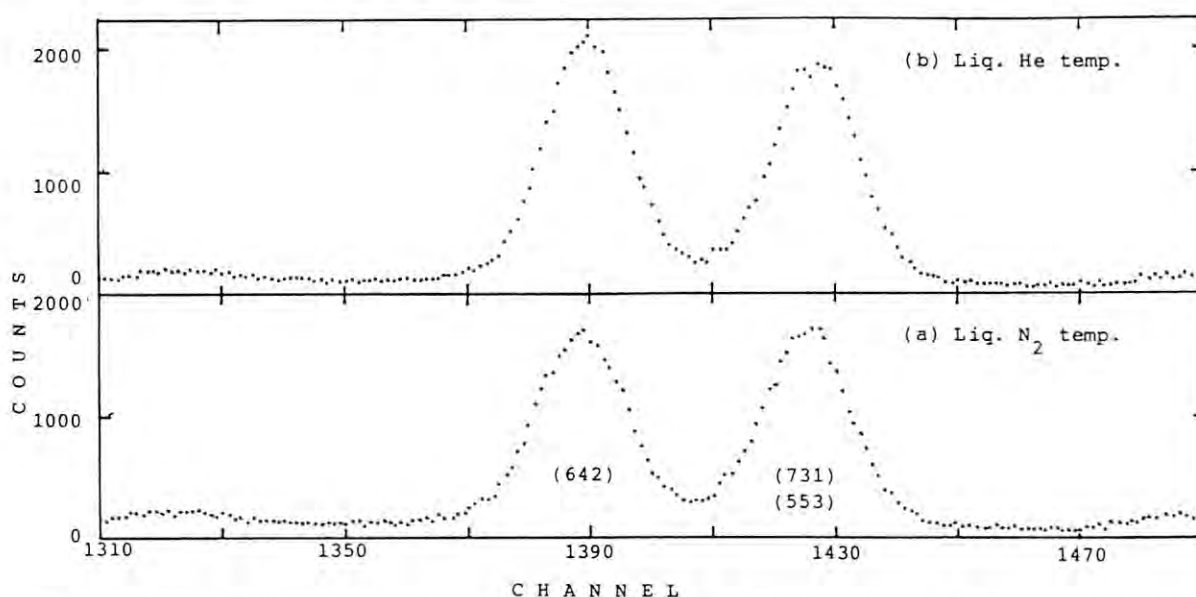


Fig. 1. Diffraction patterns for  $\text{TbAuCu}_4$ , 2-theta  $23.58^\circ$ , at (a) liq.  $\text{N}_2$  and (b) liq. He

## KINETICS OF PHASE TRANSITION IN GRAPHITE INTERCALATION COMPOUNDS

Naoto Metoki, Hiroyoshi Suematsu, Youichi Murakami, Yasuo Ohishi\*, Yasuhiko Fujii\*,  
Tadashi Matsushita\*\*, and Yoshiyuki Amemiya\*\*

Faculty of Science, University of Tokyo, Tokyo, 113

\* Faculty of Engineering Science, Osaka University, Toyonaka, Osaka, 560

\*\* Photon Factory, National Laboratory for High Energy Physics, Tsukuba, Ibaraki, 305

## Introduction.

Graphite Intercalation Compounds (GIC) exhibit various kinds of phase transitions, i.e. staging, in-plane (quasi-2D) melting, and stacking transitions. In the present study we have focused on the kinetics of the first-order-transition of the 1D nature in stage 1 Rb-GIC ( $C_8Rb$ ). The compound has the four-layer-stacking ( $\alpha\beta\gamma\delta$ ) phase at a low temperature[T] and the two-layer-stacking ( $\alpha\beta$ ) phase at a elevated T; both the phases have the same in-plane ( $2\times 2$ ) lattice commensurate with the graphite. The two phases are connected to each other by simple relation; the  $\alpha\beta$  phase can be obtained by a small lateral shift of the layers  $\gamma\delta$  in the  $\alpha\beta\gamma\delta$  phase. Thus the stacking transition corresponds to the ferromagnetic type structure ( $\alpha\beta\alpha\beta$ ) to the antiferromagnetic type structure ( $\alpha\beta\gamma\delta$ ) which are ordered in the 1D direction along the c-axis. The present work is the first investigation to study the kinetics in such a unique 1D-system.

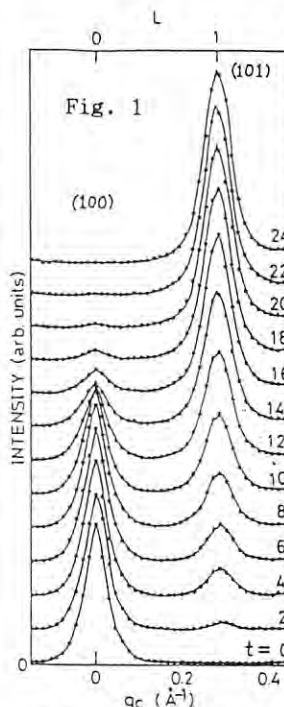
## Experiments.

The stacking transition can be controlled by sample temperature[T] and vapor pressure of Rb [ $P_{Rb}$ ]; the phase diagram have been determined by our previous work<sup>1</sup>. In this work we have observed the time dependence of the structure when changing  $P_{Rb}$  across the critical pressure  $P_{Rb}^c$  from the  $\alpha\beta\gamma\delta$ - to the  $\alpha\beta$ -side, and vice versa. X-ray diffraction measurements were carried out at PF-BL7C by using a vertical goniometer on which a double-furnace and a sample glass ampoule were placed, and a Si(111) monochromatized x-ray ( $\lambda=0.82164$  Å, immediately above the Rb K-absorption edge). The measurements were carried out from (100) to (101) Bragg-point in order to observe the stacking structure. It took 120 sec for a scan. SR x-rays provide us high time and momentum resolution.

## Results and Discussions

Fig. 1 shows the time dependence of the diffraction spectrum after a sudden increase of  $P_{Rb}$  ( $P_{Rb}=13.5$  to  $15.0$  Pa) at  $t=0$ . The sharp Bragg-peak (101) ( $\alpha\beta\gamma\delta$ ) grows and (100) ( $\alpha\beta$ ) shrinks as the phase transition proceeds. The spectrum shows no appreciable broadening of linewidth nor large diffuse scattering along  $c^*$ -axis. We conclude that this phase transition proceeds with domain growing by moving kink-type domain boundary within coexistence phase.

(1) The time dependence of the integrated intensity[I] of the diffraction peak can be normalized by the characteristic time  $t_{1/2}$ , which is determined experimentally as the time for I to grow to a half of the full intensity at the completion of the transition (Fig. 2). For the case of a large  $\Delta P_{Rb}$ , the observed time dependence is scaled by a unified function. The



results of phenomenological theory by Avrami<sup>2</sup> are also displayed for a comparison. The 1D case reproduces the experimental function in a good approximation. However for a small  $\Delta P_{Rb}$ , the experimental points shift from the theoretical prediction, and appear to have a much longer kinetics; the critical index may be much larger than the case of a large  $\Delta P_{Rb}$ .

(2) The characteristic time  $t_{1/2}$  has a steep function of  $\Delta P$  (Fig. 3). The feature indicates the remarkable slowing-down effect of the relaxation time around  $P_{Rb}^c$ .

(3) The time dependence of the linewidth of (100) can be clearly observed. The domain size grows from 60 Å in the nucleation to 400 Å at the completion of the phase transition. However (101) Bragg-peak shows no change in the linewidth. This discrepancy can not be understood now.

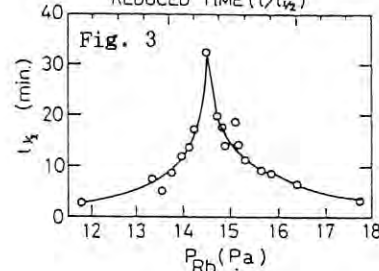
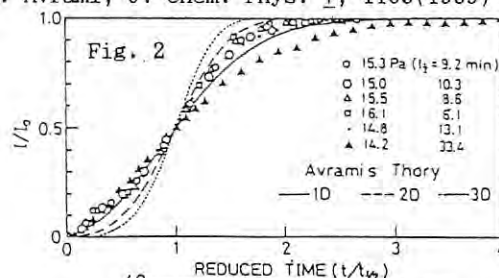
In order to elucidate interesting features of the kinetics in a low dimensional first-order-transition, we have still the intensive studies of the kinetics such as

- The time dependence of the domain size.
- The sample dependence of the phase transition.

We wish to thank A. Koyama for his technical advice.

## Reference

- N. Metoki and H. Suematsu, Phys. Rev. B38,
- M. Avrami, J. Chem. Phys. 7, 1103(1939)





DETERMINATION OF THE ENVIRONMENTAL STRUCTURE AROUND A SPECIFIC ATOM IN  
DISORDERED MATERIALS BY THE ANOMALOUS X-RAY SCATTERING

Yoshio WASEDA, Eiichiro MATSUBARA, Kazumasa SUGIYAMA and Takashi SAKUMA\*

Research Institute of Mineral Dressing and Metallurgy (SENKEN),  
Tohoku University, Sendai 980, Japan.

\* Department of Physics, Faculty of Science,  
Ibaraki University, Mito 310, Japan.

Recently, ternary Al-Ge-Ni alloys have been found to produce an amorphous phase over a wide range of composition by rapid quenching from the melt. Some interesting features were reported for these alloys; for example, a split first peak in the x-ray diffraction and the modulated pattern is also observed in the bright-image by transmission electron microscopy for  $\text{Al}_{60}\text{Ge}_{30}\text{Ni}_{10}$  alloy. In order to clarify the structural features of this ternary Al-Ge-Ni amorphous alloy, the AXS measurements<sup>1)</sup> have been done at the Ge and Ni K absorption edges.

Figs. 1 and 2 show the differential intensity profiles of amorphous  $\text{Al}_{60}\text{Ge}_{30}\text{Ni}_{10}$  alloy at the Ge and Ni edge, respectively. The energies used for the measurements were 10.8047 and 11.0795 keV for the Ge edge and 8.0316 and 8.3067 keV for the Ni edge. These energies correspond to energies 300 and 25 eV below each absorption edge. The differential intensity profile at the Ge edge in Fig.1 clearly indicates a non-crystalline pattern similar to the original one, although the relative intensity of the second peak decreases drastically in comparison with that of the first peak. This implies that most of the Ge atoms are contained in the non-crystalline region. The structure of this non-crystalline region can be estimated from the environmental radial distribution function (RDF) in Fig.3 together with the RDF of pure amorphous germanium. The profile of the environmental RDF around a Ge atom appears similar to the RDF of pure Ge and the coordination number was estimated to be 4.1 from the area of the first peak. Thus, it is plausible that the atomic arrangements around a Ge atom is similar to those in amorphous germanium. Small spikes overlapping with the diffuse profile indicated in Figs.1 and 2 may be understood as due to Ge-Ni pairs strongly correlated in the ordered phase.

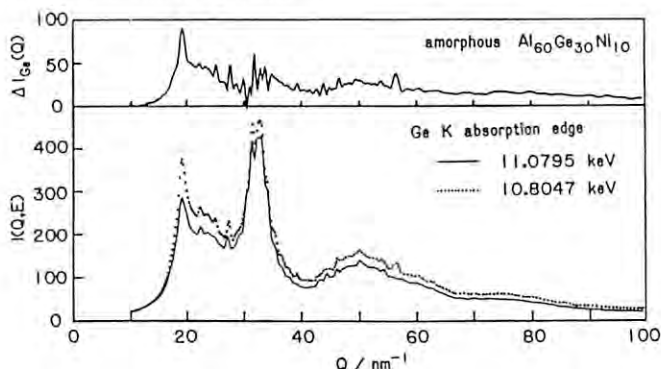


Fig.1 Differential intensity profile of  $\text{Al}_{60}\text{Ge}_{30}\text{Ni}_{10}$  alloy obtained from intensity data sets at the Ge K absorption edge.

On the other hand, it is imagined from the differential intensity profile at the Ni edge in Fig.2 that most of Ni atoms are in a crystal-like region and form a highly ordered structure, although a definite conclusion of the structure of this crystal-like region cannot be identified yet from the present results alone. The modulated region observed in the transmission electron microscope may be interpreted by harmony between the non-crystalline regions consisting of mainly Ge and Al and highly ordered crystal-like regions mainly related to the Ni atom correlations.

#### References

- 1) Y.Waseda, E.Matsubara and K.Sugiyama, Sci. Rep. RITU **34A**, 1 (1988)
- 2) J.B.Kortright, PhD thesis, Stanford University, SSRL Report **84/05**, 81 (1984)

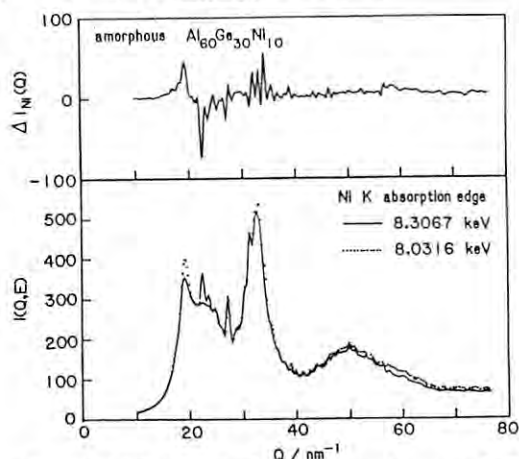


Fig.2 Differential intensity profile of  $\text{Al}_{60}\text{Ge}_{30}\text{Ni}_{10}$  alloy obtained from intensity data sets at the Ni K absorption edge.

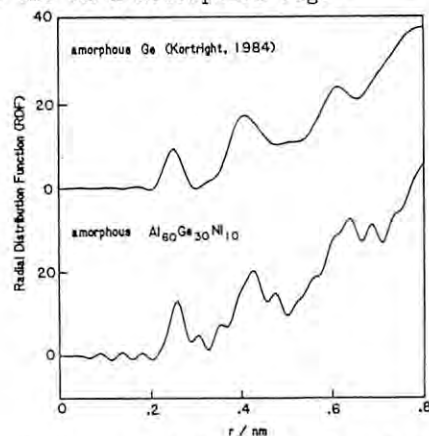


Fig.3 Environmental RDF obtained from the differential intensity profile of amorphous  $\text{Al}_{60}\text{Ge}_{30}\text{Ni}_{10}$  alloy in Fig. 1 and RDF of amorphous Ge<sup>2)</sup>.



# HIGH SPEED IODINE K-EDGE SUBTRACTION ANGIOGRAPHY IN THE ANIMAL EXPERIMENT

Tohoru Takeda<sup>1</sup> Masayoshi Akisada<sup>1</sup>, Izumi Anno<sup>1</sup> Teiichi Nakajima<sup>1</sup>,  
Ken Ueda<sup>2</sup>, Keiji Umetani<sup>2</sup>, Chiri Yamaguchi<sup>3</sup>

<sup>1</sup>Department of Radiology, The University of Tsukuba, Tsukuba-shi, Ibaraki-ken, 305 Japan.

<sup>2</sup>Central Research Laboratory, Hitachi Ltd. Kokubunji, Tokyo, 185 Japan.

<sup>3</sup>National Laboratory for High Energy Physics, Tsukuba-shi, Ibaraki-ken, 305 Japan

## Introduction

The selective coronary angiography is the final diagnostic modality for the ischemic heart disease. But this modality is invasive and costly. On the other hand, Rubenstein E. revealed that using the iodine K-edge energy subtraction angiography, coronary artery would be demonstrated with transvenous injection of the contrast material [1]. In Japan, two dimensional image acquisition system is now being constructed [2]. In this paper, the results of the animal experiment which was obtained by the high speed iodine K-edge subtraction angiographic system, will be described.

## Methods and Materials

The high speed K-edge subtraction system which was constructed at beam line of 8C of Photon Factory in Tsukuba, consisted of movable silicon (III) monocrystal, II-ITV and digital memory system. For the digital processing, X-ray TV images were digitized using a 8 bit AD converter, into 256x256 pixel matrices with an 8 bit depth. The 68000-IP computer was used for image processing and control of the system.

The slightly different energies of the beams are produced by diffracting the synchrotron radiation from rotating the silicon monochromator crystal ( $33.164 \pm 250$  eV). Asymmetric reflection at silicon planes expanded the beam size 25 times, produces  $50 \times 60$  mm<sup>2</sup> monochromatic X-ray beam. Photon energy between above and below iodine K-edge was changed within 16.7 msec. During the experiment the electron storage ring operated at 2.5 GeV with a typical current of approximately 200 mA. The incident monochromatized flux was about  $7.4 \times 10^7$  photons/second/mm<sup>2</sup> [3].

The rats were anesthetized with phenobarbital, and 24 G angiocatheter was inserted into tail vein. The rabbits were anesthetized with phenobarbital and 5F (0.8 mm) catheter was inserted into the inferior vena cava. 1.5 ml/Kg of contrast material (conraxon H 80%) was injected by the injector at the rate of 0.75 ml/Kg/sec [4,5,6]. Transvenous angiograms were carried out in a 40 degree left anterior oblique.

## Results

The clear K-edge subtracted images are obtained at thorax and abdomen of the rats. The common carotid arteries, subclavian arteries and both renal arteries can be seen.

The right coronary arteries and the main trunk of the left coronary artery can be

revealed clearly and dynamically in the rabbits (Fig.1). But the images of the coronary arteries show blur slightly. The contraction of the left ventricle and atrium is also demonstrated well. The structure of the right coronary artery can be demonstrated from proximal portion to distal portion in the systolic phase. But in the diastolic phase, the distal portion of the coronary artery can not be seen.



Fig.1 The coronary artery of the rabbit.

## References

1. Rubenstein E, Hughes EB, Campbell LE, et al: Synchrotron radiation and its application to digital subtraction angiography. SPIE 314: 42,1981
2. Akisada M, Ando M, Hyodo K, et al: An attempt at coronary angiography with a large size monochromatic SR beam. Nuclear Instruments and Methods in Physics Research A246:713-718,1986
3. Ueda K, Umetani K, Takeda T, Nakajima T, Anno I, Akisada M, Yamaguchi C: A high speed K-edge subtraction angiographic system for animal studies. SRI (submit)
4. Takeda T, Nakajima T, Anno I, et al: An approach to the high speed K-edge subtraction angiography: Animal experiment. Medical Imaging Technology 6:219-220,1988
5. Takeda T, Akisada M, Anno I, et al: High speed iodine K-edge subtraction angiography: A preliminary experiment with rats. Medical Imaging Technology (In press).
6. Takeda T, Akisada M, Nakajima T, Anno I, Ueda K, Umetaki K, Yamaguchi C: SR high speed K-edge subtraction angiography in the animal experiment with rabbits. SRI (submit)

# Al-Mn ALLOY ( $\phi$ PHASE) SHOWING THE DIFFRACTION PATTERNS SIMILAR TO DECAGONAL QUASICRYSTALS

Satoshi SASAKI, Akiji YAMAMOTO\*, Shigeto NISHITANI\*\* and Hideo SHINGU\*\*

Photon Factory, National Laboratory for High Energy Physics, Oho, Tsukuba 305

\*National Institute for Research in Inorganic Materials, Namiki, Tsukuba 305

\*\*Department of Metal Science and Technology, Kyoto University, Sakyo-ku, Kyoto 606

## Introduction

Soon after the discovery of icosahedral quasicrystals in Al-Mn alloys,<sup>1)</sup> decagonal quasicrystals<sup>2)</sup> were found in the same kinds of alloy by the observation of electron diffraction patterns. The decagonal phase is characterized by the diffraction patterns showing tenfold axes and one-dimensional periodicity along the axes. Because a single crystal of the  $\phi$  (AlMn) phase gives pseudo-tenfold axes in the X-ray diffraction,<sup>3)</sup> we examine the relationship between the  $\phi$  and decagonal phases.

## Results and discussion

The samples used for the quasicrystal study were synthesized by the rapid quenching method in the single roller apparatus with brass roll in a diameter of 300 mm. The nominal compositions of the mother alloy were Al-9at%Mn-9at%Cr-10at%Si and Al-8at%Mn-10at%Cr-9at%Si. The as-quenched films were 50-100  $\mu\text{m}$  in thickness for the rotation speed of 1750 to 1000 rpm. The grains with the dimension up to 50  $\mu\text{m}$  were extracted in ethanol with 3-5 vol% Br for 4-24 hours and used for X-ray studies. The observation by EM and SEM confirmed the existence of spherical grains of quasicrystals.

Although precession photographs were taken for 50 or more quasicrystals with monochromatized synchrotron X-rays ( $\lambda = 0.7 \text{ \AA}$ ; BL-10A), we could not observe any diffraction spots except those of the  $\phi$  phase. The minimum crystal size to detect the peak intensity was about 1-2  $\mu\text{m}$  in this system.

In such studies on quasicrystals, we incidentally found the pseudo-tenfold diffraction pattern of a crystal which was identified as  $\phi$  (AlMn) later. Figure 1 shows a series of X-ray diffraction patterns from the  $\phi$  phase where there are a pseudo-tenfold, sixfold and two fold axes with the zone-axis angles of 90, 18 and 90°, respectively. It suggests a high similarity to the selected-area electron diffraction patterns reported for the decagonal phase.<sup>2)</sup> We also have calculated powder diffraction patterns based on the atomic parameters obtained for the  $\phi$  phase (Fig. 2). It should be noted that the powder diffraction

patterns of  $\phi$  phase cannot be distinguished from those of the decagonal phase<sup>4)</sup> except one peak of the 103 reflection at  $2\theta = 37.1^\circ$ . Thus, our results imply that the local structure of cluster for the decagonal quasicrystal resembles to the crystal structure of the  $\phi$  phase.

1) Schechtman, D., Blech, I., Gratias, D. and Cahn, J. W. (1984) Phys. Rev. Lett., 53, 1951.

2) Bendersky, L. (1985) Phys. Rev. Lett., 55, 1461.

3) Sasaki, S., Yamamoto, A., Nishitani, S. and Shingu, H. (1988) in this Activity Report.

4) Takeuchi, S. and Kimura, K. (1987) J. Phys. Soc. Jpn, 56, 982.

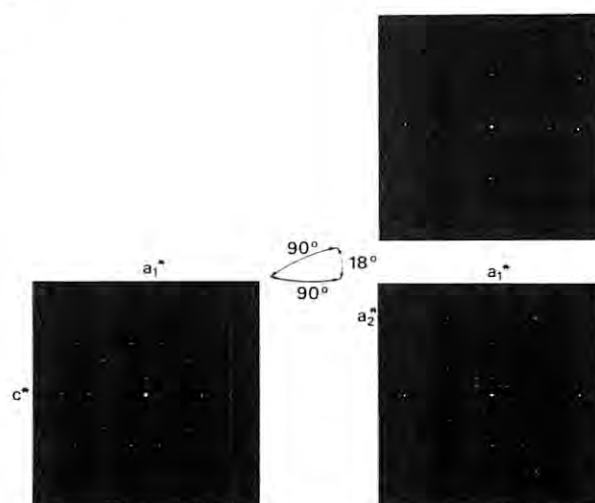


Fig.1, X-ray diffraction patterns of  $\phi$  (AlMn).

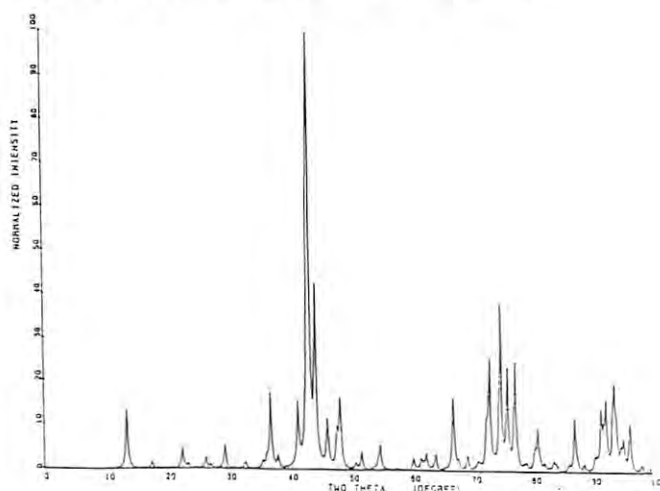


Fig.2, Calculated powder patterns of  $\phi$  (AlMn). Cu K $\alpha$

# ANOMALOUS TRANSMISSION OF THERMALLY SCATTERED X-RAYS IN A GERMANIUM CRYSTAL

Yasuji KASHIWASE, Masahiro MORI, Motokazu KOGISO, Katsutosi USHIDA, Masayuki MINOURA,  
Tetsuya ISHIKAWA\* and Satoshi SASAKI\*

Department of Physics, College of General Education, Nagoya University, Nagoya 464

\*National laboratory for High Energy Physics, Tsukuba, Ibaraki 305

## Introduction

Black diffraction lines <sup>1,2)</sup> which we call excess lines were observed across the 220 thermal diffuse scattering (TDS) spots on film photographs of perfect crystals of germanium in the Laue arrangement. Diffraction peaks corresponding to the lines were observed also by diffractometries using scintillation detector <sup>1,3)</sup>. We report a recent progress of the study on this lines.

## Experimental Method and Result

Experiment was performed with a vertical type four-circle goniometer at BL-10A. Parallel plates of germanium single crystals with the (111) surface of about 5x5 mm and the thickness 0.1~0.18 mm were used as specimens. The rocking curves of the 220 and 111 reflections in the Laue and Bragg arrangements, respectively, had profiles with FWHM close to the theoretical values for the absorbing perfect crystal. Synchrotron radiations of wavelengths 1.5405Å and 1.15Å monochromatized by the silicon 111 symmetric reflection were incident on the specimens in the Laue arrangement. The crystal orientations were fixed at the angular deviations  $\Delta\omega = \theta - \theta_B$  in the range  $-0.6^\circ \sim 0.6^\circ$  from the 220 Bragg position during the intensity measurement. Imaging plate <sup>4)</sup> as well as cosmic ray film was used to take diffraction photograph. Intensity profiles were also obtained by the imaging plate and diffractometry with a scintillation counter. A high angular-resolution diffractometry was performed to obtain rocking curve with FWHM of a few arc second for the excess line using a triple-crystal diffractometry system <sup>5,6)</sup> at BL-15C.

Figure 1 shows a typical diffraction pattern on an imaging plate for a crystal orientation at the angular deviation  $\Delta\omega = 0.4^\circ$  from the 220 Bragg position. Figure 2 shows a intensity profile of diffuse scattering on the dotted line in Fig.1. Long excess line EL and corresponding peak EL can be seen in Fig.1 and Fig.2, respectively. Figure 3 shows a measured intensity profile of diffuse scattering obtained by using the triple-crystal diffractometer. The relative intensity is plotted against  $\delta\theta$ , which is the angular deviation of the analyzer crystal from the intensity maximum position of the 220 Bragg peak when the specimen is just on the Bragg position. A diffraction peak corresponds to the excess line. Actual count at the maximum of the diffraction peak is about 800 per 20 seconds. Saturated peak is due to the Bragg reflection tail of the incident beam far from the 220 Bragg position.

The experimental result was compared with a calculation based on the dynamical theory <sup>2,3)</sup>. Agreement between the experimental profile and the calculation was obtained and gives an evidence of the anomalous transmission of X-ray TDS wave.

## References

- 1) Y.Kashiwase, M.Mori, M.Kogiso, M.Minoura, S.Sasaki: Photon Factory Activity Report 1987, p.199.
- 2) Y.Kashiwase, M.Mori, M.Kogiso, M.Minoura, S.Sasaki: J. Phys. Soc. Jpn. **57**, 524 (1988).
- 3) Y.Kashiwase, M.Mori, M.Kogiso, K.Ushida, M.Minoura, T.Ishikawa and S.Sasaki: to be published.
- 4) Y.Amemiya, T.Matsushita, A.Nakagawa, Y.Satow, J.Miyahara and J.Chikawa: Nucl. Instrum. Methods **A266**, 645 (1988)
- 5) T.Matsushita, T.Ishikawa and K.Kohra: J. Appl. Crystallogr. **17**, 257 (1984).
- 6) T.Ishikawa, J.Matsui and T.Kitano: Nucl. Instrum. Methods **A 246**, 613 (1984).

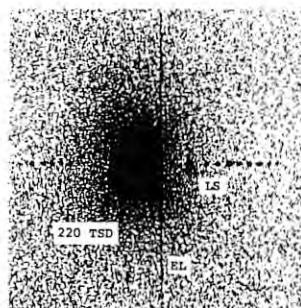


Fig.1. Diffraction pattern obtained by imaging plate,  $\lambda = 1.5405\text{\AA}$ ,  $\Delta\omega = +0.4^\circ$ , thickness 0.18 mm, EL; excess line, LS; Laue spot.

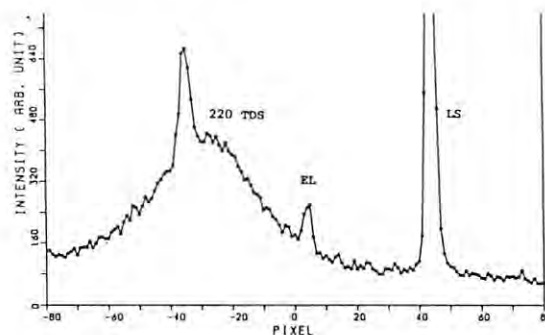


Fig.2. Intensity profile on dotted line in Fig.1.

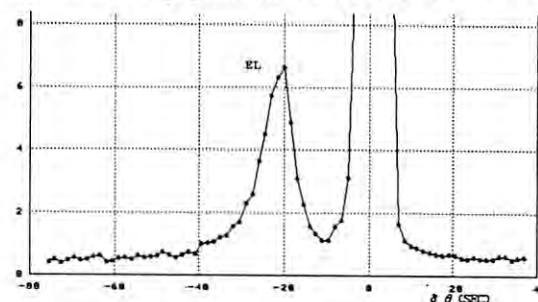


Fig.3. Intensity profile of the excess line obtained by triple-crystal diffractometer,  $\lambda = 1.5405\text{\AA}$ ,  $\Delta\omega = -20''$ , thickness 0.18mm.



## LOCAL ATOMIC ORDER IN THE SPIN-GLASS SYSTEM AU-Fe ALLOYS

Ken-ichi OHSHIMA, Hisakazu OKAJIMA<sup>+</sup>, Jimpei HARADA<sup>+</sup> and Satoshi SASAKI<sup>\*</sup><sup>+</sup>Institute of Applied Physics, University of Tsukuba, Tsukuba 305<sup>\*</sup>Department of Applied Physics, Nagoya University, Nagoya 464<sup>\*</sup>Photon Factory, National Laboratory for High Energy Physics, Tsukuba 305

## Introduction

Noble metal alloys containing 3d transition metals show peculiar magnetic behaviour, i.e. spin-glass and reentrant spin-glass, at low temperatures when their compositions are less than 20 at.%. It has been known that these properties are strongly affected by the local atomic

arrangements of 3d metals in alloys<sup>1)&2)</sup>.

Several diffuse scattering studies from Au-Fe alloy, which is one of the most typical spin-glass alloys, have been performed with the use of X-ray, electron and neutron sources, but there are no decisive conclusions on the local atomic arrangements of Fe atoms in this alloy. In the present study, we have performed the three dimensional diffuse intensity measurements in disordered Au-19.1 at.% alloy using the synchrotron radiation in order to determine the local structure more clearly.

## Experimentatl

A single crystal of Au-19.1 at.% Fe was grown by the Bridgman technique. Plate-like sample of about 10 mm in diameter and 2 mm thick was cut from the ingot. It was electrocally etched in a mixed  $\text{CaCl}_2\text{-HClO}_4\text{-CuNO}_3\text{-H}_2\text{O}$  solution to

remove the disordered surface layer. The sample was annealed for 2 days at 850°C, 5 days at 700°C and quenched into ice water.

Four-circle diffractometer was used to measure the diffuse scattering intensity from the sample at BL-10A of Photon Factory. Incident beam of 1.1 Å was selected with the use of Si 111 singly bent crystal.

## Results and Analysis

Intensity distribution on (hk0) rel. plane was shown in Fig. 1 in Laue units. The atomic size effect modulation causes asymmetrical intensity distribution. The component of local order diffuse intensity was separated from the total ones with the use of Borie-Sparks method. It is shown in Fig. 2 where diffuse streaks in  $\langle 210 \rangle$  directions and diffuse peaks at  $\langle 11/20 \rangle$  and  $\langle 000 \rangle$  positions were observed. By Fourier inversion of local order diffuse scattering intensity, the Warren-Cowley parameters  $\alpha_{1mn}$  were

determined up to the 49th shell. The sign

of the first neighbour parameter  $\alpha_{110}$  is

positive. This has an inclination to the clustering of Fe atoms. A possible local atomic arrangement was constructed on the local order parameters by the simulation program. Few [420] thin platelets with the size of about 2 unit cells exist on the simulated structure. The relationship between the local atomic order and magnetic behaviour in this alloy is now considering.

## References

- 1) H. Suzuki, J. Harada, T. Nakashima and K. Adachi: Acta Cryst. A38 (1982) 522
- 2) K. Ohshima, N. Iwao and J. Harada: J. Phys. F17 (1987) 1769

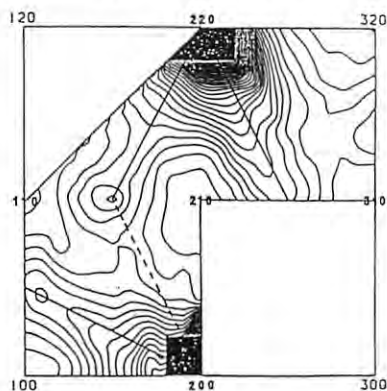


Fig.1. Contour map of the x-ray diffuse scattering distribution in the (hk0) rel. plane.

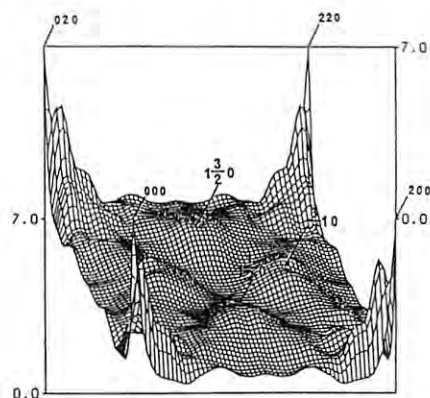


Fig.2. The component of local order diffuse intensity in (hk0) rel. plane in Laue units.



STUDIES ON THE PROCESS OF REACTION IN CRYSTALS BY SR.  
 --Dehydration of  $\alpha$ -AlOOH.--

Masaaki.OHMASA, Kenji.HAGIYA, Jiro.RYUTA, Sizuo.SAITO and Satoshi.SASAKI\*  
 Institute of Materials Science, University of Tsukuba, Japan  
 \*Photon Factory, National Laboratory for High Energy Physics, Japan

### Introduction

In order to study the process of reaction in crystals, it is necessary to observe decomposition of precursor and formation of the product during the transformation. Since such change is related to the structures of the both phases, X-ray diffraction is the most powerful method for this purpose. However, not only Bragg reflections but diffuse scattering or satellite reflections are observed occasionally in the early stage of the process and intensities of those scattering are extremely weak though they are important to analyze the process. Therefore use of synchrotron radiation is desirable to study those problems.

There are many compounds which show topotaxy during phase transformation. Since the product of such transformation is formed in an oriented manner under influence of the structure of precursor, diffraction patterns of the product are similar to those of a single crystal and anomaly of the diffraction can be easily detected. We have consequently studied the process of dehydration in  $\alpha$ -AlOOH which indicates topotaxy in the process of dehydration.

### Experimental

Single crystals from Shokozan, Hiroshima, Japan were selected for the investigation. Since preliminary results obtained by quenching method indicates that the intensity of satellites is too weak to measure on a conventional diffractometer and that the satellites shift towards the main reflection after longer heating, the process of dehydration

was observed at elevated temperatures by X-ray diffraction with strong SR beam of Photon Factory in KEK. The experiments have been done using the vertical four-circle diffractometer on the BL-10A. A small furnace was attached on the diffractometer to keep the specimen at a definite temperature.

### Results

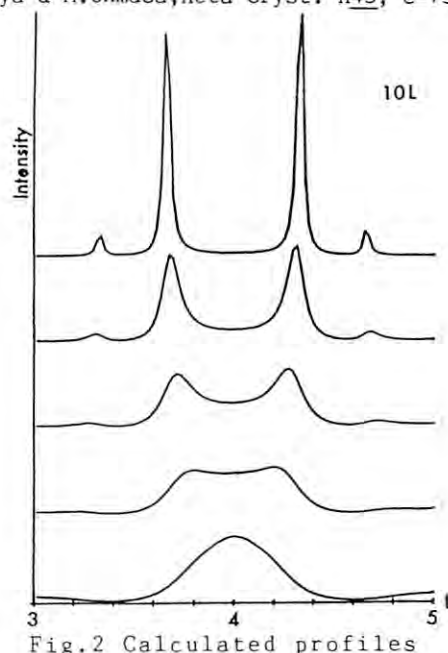
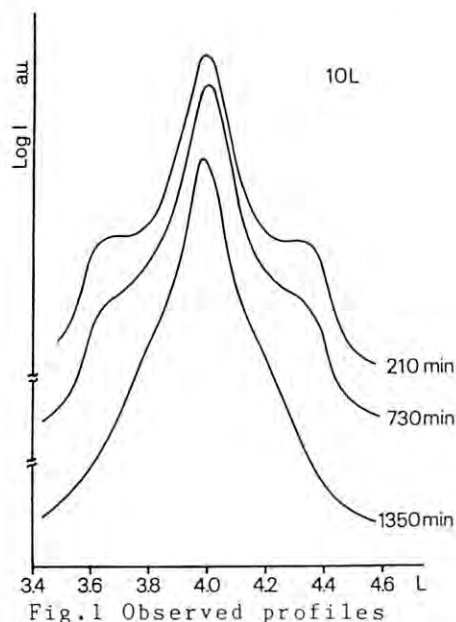
We have already clarified that the occupancy of Al in the product is less than 100% at early stage of the dehydration and that the modulation of the Al occupancy occur along c of the product (Ohmasa et al., 1984, 1987). By quenching method and by in situ observation, it was found that the satellites became diffuse and their maxima approached to the main reflections as the specimens were heated longer. Finally they coincided with the main. Since the arrangement of oxygen atoms in the product is hexagonal closest packing, we may regard the structure as a layer structure. The above observation can thus be interpreted as a one-dimensional stacking disorder. The intensity of the diffuse scatterings were calculated with the following formula:

$$I = \sum (N - |m|) \text{tr} V F P^m \exp(-2\pi i m s),$$

where N is number of fundamental layers, V a matrix of structure factors of the layers, F probabilities of existence of the layers, P sequence of the layers and tr a trace of a matrix. The observed profiles of the satellites and results of the calculations are illustrated in Fig.1 and Fig.2 respectively.

### References

- M.Ohmasa, et al., Acta Cryst. A40, c-256, 1984.  
 K.Hagiya & M.Ohmasa, Acta Cryst. A43, c-73, 1987.



## STUDY OF RUBBER-LIKE BEHAVIOR IN A Au-Cd ALLOY BY X-RAY DIFFRACTION

Takuya OHBA, Kazuhiro OTSUKA and Satoshi SASAKI\*  
 Institute of Materials Science, University of Tsukuba, Tsukuba, Ibaraki 305, Japan  
 \*Photon Factory, KEK, Tsukuba, Ibaraki 305, Japan

Introduction

Au-47.5at%Cd alloy shows an interesting property called 'rubber like behavior'. It appears in a stabilized state, i.e. after aging at room temperature for about one day in a martensitic phase. Birnbaum and Read<sup>1)</sup> showed that it is related to twin boundary motion, and they proposed a mechanism that is an interaction between order-faults and twinning dislocations. Stress-strain curve depending on time after transformation was examined<sup>2)</sup> and physical properties such as Young's modulus, internal friction and yield stress were also examined and reported to be changed. Lieberman et al.<sup>3)</sup> proposed the mechanism for the rubber-like behavior, i.e. twinning in a multiple lattice structure cannot occur only by a twinning shear; readjustments termed 'shuffles' in some atom positions are required. They proposed the model that the twinning shear occurs immediately and shuffling occurs gradually. In this paper, the model proposed by Lieberman et al. is examined.

Experimental

An ingot of Au-47.5at%Cd was prepared by melting from 99.99%Au and 99.9999%Cd in Ar filled quartz tube. The ingot was remelted in a cylindrical quartz tube with 4mm diameter. A single crystal was made by the Bridgman method in a carbon mould in Ar filled quartz tube. The sample was spark cut to a plate and electro-polished. It was set in a specially constructed equipment which gives tension to the sample on a goniometer of four circle diffractometer (BL-10A). The dimension of the sample was 0.8x4x50 mm<sup>3</sup>. The orientation of the sample was examined preliminary in a well-stabilized state in order to find reflections immediately after the transformation.

The sample was heated to a temperature above  $A_f$  (76°C) and then cooled to room temperature for producing martensitic phase,

i.e. fresh state. Measurements of Bragg reflection profiles were started just after producing martensite single crystal by applying tension in the equipment. Wave length utilized in the experiment was 0.7 Å. Scan mode used was  $-2$  scan. Scan range was  $2.0^\circ$  and an interval of the scan was  $0.04^\circ$  in  $\lambda$ . Change of incident beam intensity was monitored by dividing the incident beam. Counting time at each position was 1 s. Measurements were repeated every five minutes. Five reflections were measured in this short cycle up to about 3 hours after producing single crystal martensite. Ten reflections were measured in long cycle up to about 30 hours, i.e. reflections were measured about every one hour.

Results and Discussion

Peak profiles measured in a fresh state were compared with ones in a stabilized state for every reflection. We could not find any significant differences in the profile between two states.

If the shuffling of atomic positions occurs gradually, i.e. there is a structural change depending on time, intensities of Bragg reflection must be changed according to movement of atoms. The integrated intensities of measured reflections were obtained. They are shown in Fig. 1 as a function of time after the transformation. There is no change of the integrated intensity.

We are planning to measure peak profiles after moving twinning boundary in a stabilized state for further precise experiment.

References

- 1) H. K. Birnbaum and T. A. Read, Trans. AIME, 218, (1960) 662.
- 2) N. Nakanishi, T. Mori, S. Miura, Y. Murakami and S. Kaichi, Phil. Mag., 28, (1973) 277.
- 3) D. S. Lieberman, M. A. Schmerling and R. W. Karz, edited by Perkins, Shape Memory Effects in Alloys, Plenum, N.Y. (1957) 203.

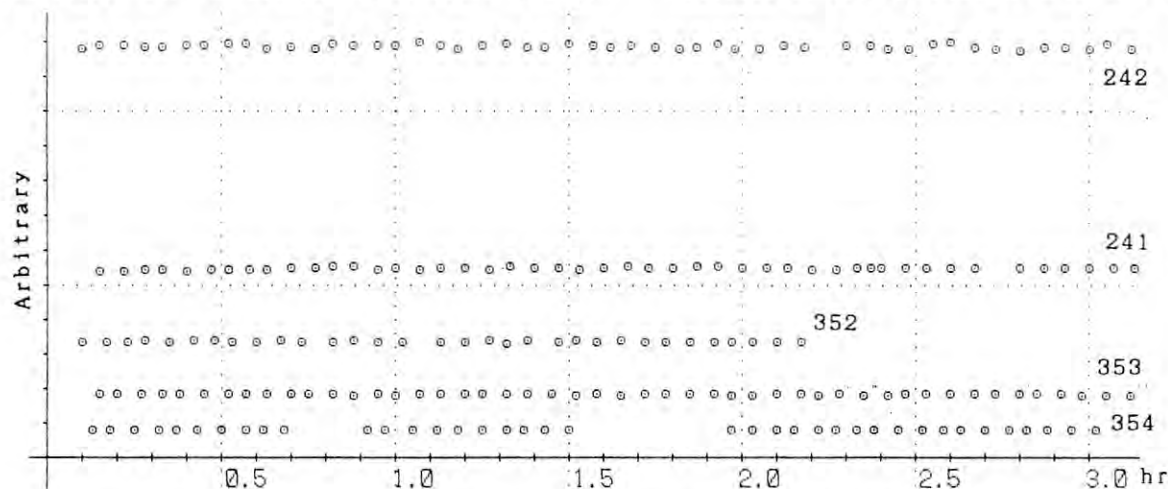


Fig. 1. Integrated intensities as a function of time.

# CRYSTAL-STRUCTURE DETERMINATION OF A SMALL SINGLE-CRYSTAL USING SYNCHROTRON X-RAYS: $\phi$ PHASE OF Al-Mn ALLOY

Satoshi SASAKI, Akiji YAMAMOTO\*, Shigeto NISHITANI\*\* and Hideo SHINGU\*\*

Photon Factory, National Laboratory for High Energy Physics, Oho, Tsukuba 305

\*National Institute for Research in Inorganic Materials, Namiki, Tsukuba 305

\*\*Department of Metal Science and Technology, Kyoto University, Sakyo-ku, Kyoto 606

## Introduction

Recent discovery of icosahedral quasicrystals<sup>1)</sup> in Al-Mn alloys has given great interest in studying the intermediate phase between glass and crystal. This phase was reported in rapidly cooled alloys and is characterized by noncrystallographic symmetry (fivefold axes). A single-crystal of  $\phi$  phase in Al-Mn alloys was incidentally found in the X-ray diffraction studies of the quasicrystals. It is noted that the crystal shows the diffraction patterns similar to those of the decagonal phase.

## Experimental

The crystal was grown at rapid quenching in a brass roller melt-quenching apparatus. The starting materials were Al with 7.8 at.% Mn, 10.3 at.% Cr and 9.1 at.% Si. Since the crystal used here is small (10 x 10 x 20  $\mu\text{m}$ ), all experiments including the precession and four-circle diffractometer works were made with synchrotron X-rays from a normal bending magnet at BL-10A. The storage ring was operated at 2.5 GeV and 300-150 mA with a life time of about 12 hours (Dec. 1986 - Feb. 1987). The X-rays were monochromatized with a Si(111) crystal ( $\lambda = 0.7 \text{ \AA}$ ).

The cell dimensions are  $a = 7.519(1)$ ,  $c = 7.827(1) \text{ \AA}$  and  $V = 383.2 \text{ \AA}^3$ . The intensity distribution indicates that the crystal is hexagonal and the Laue symmetry is  $6/mmm$ . The systematic absences are:  $l = 2n$  on  $hkl$  and  $l = 2n$  on  $00l$ . The crystal structure analysis suggests that the space group is most likely  $P6_3/mmc$  in the possible space groups. This crystal may be referred to as  $\phi$  (AlMn)<sub>2</sub> or  $\beta$  (AlMnSi).<sup>3)</sup> Intensity data were collected by the  $\omega$ -2 $\theta$  step-scan method up to  $\sin\theta/\lambda = 0.71$ . The intensity decay of the primary synchrotron beam could be reasonably well compensated for by referring to the intensity of a standard reflection. Of 500 measured and 253 independent reflections, 218 reflections having  $F \geq 3\sigma_F$  were used in the crystal structure analysis. Integrated intensities were corrected for Lorentz and polarization ( $p = 1$ ) factors and for absorption ( $\mu = 51 \text{ cm}^{-1}$ ) and anomalous scattering effects.

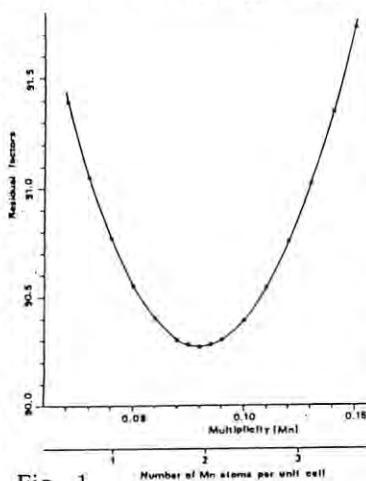


Fig. 1

## Results and discussion

As the first step of structure analyses, the three-dimensional Patterson function was calculated directly from the corrected  $F^2$  values. By a comparison of the Fourier and Patterson syntheses, Si and Mn/Cr atoms were placed on several of the largest peaks. Then, using the difference-Fourier method, the positions for Al atoms were found. All parameters were refined simultaneously using the full-matrix least-squares program, RADY,<sup>4)</sup> where the residuals of the function  $\sum w(|F_{\text{obs}}| - |F_{\text{calc}}|)^2$  were minimized. No extinction correction was applied because the crystal is enough small.

Both Mn and Cr atoms were found to distribute in the 6h sites together. After all parameters well converged in refinement, the separation of these two atoms was made by changing the fraction of atomic scattering factors of Mn and Cr atoms. The residual factors as a function of Mn/Cr ratio are schematically shown in Fig. 1 where there is a minimum very close to two Mn atoms per unit cell. The chemical formula thus obtained are  $\text{Al}_9\text{SiMnCr}_2$  in  $Z = 2$ .

The final positional and thermal parameters obtained in refinements are listed in Table 1. The refinement well converged to  $R = 0.024$  and  $R_w = 0.029$ . The atomic distances are: Si-Me =  $2.5019(2) \text{ \AA}$ , Si-Al(1) =  $2.6729(4)$ , Si-Al(2) =  $4.274(1)$ , Me-Me =  $2.7004(5)$ , Al(1)-Al(1) =  $2.808(1)$ ,  $2.918(2)$ , Al(1)-Al(2) =  $2.7929(9)$ ,  $2.969(1)$ , Al(2)-Al(2) =  $2.809(1)$ . Although we used a small crystal of 10-20  $\mu\text{m}$ , the maximum peak intensity was  $5 \times 10^4$  cps for the 301 reflection. Therefore, no extra procedure was needed to determine the crystal structure.

- 1) Shechtman, D., Blech, I., Gratias, D. and Cahn, J.W. (1984) Phys. Rev. Lett., 53, 1951-1953.
- 2) Taylor, M.A. (1960) Acta Metallur., 8, 256-262.
- 3) Robinson, K. (1952) Acta Cryst., 5, 397-403.
- 4) Sasaki, S. (1987) KEK Internal 87-3.

Table 1. Final atomic coordinates and thermal parameters.

	Al(1)	Al(2)	Si	Mn/Cr
x	0.2017(1)	0.5421(2)	0	-0.11972(8)
y	$= 2x$	$= 2x$	0	$= 2x$
z	0.0636(2)	1/4	0	1/4
$\beta_{11}$	0.0031(1)	0.0020(1)	0.0031(2)	0.00294(7)
$\beta_{22}$	0.0030(1)	0.0037(2)	$= \beta_{11}$	0.0025(1)
$\beta_{33}$	0.00172(6)	0.00302(9)	0.0012(1)	0.00104(5)
$\beta_{23}$	-0.00019(7)			
B(equiv)	0.49(2)	0.54(3)	0.45(2)	0.40(2)

Restrictions:

$y = 2x$ ,  $\beta_{22} = 2\beta_{12}$ ,  $\beta_{23} = 2\beta_{13}$  for 12k sites;  $y = 2x$ ,  $z = 1/4$ ,  $\beta_{22} = 2\beta_{12}$ ,  $\beta_{23} = \beta_{13} = 0$  for 6h sites;  $x = y = z = 0$ ,  $\beta_{11} = \beta_{22} = 2\beta_{12}$ ,  $\beta_{23} = \beta_{13} = 0$  for 2a sites.



THE DETECTION OF LOCALIZED EXCITED STATES IN CRYSTAL STRUCTURES BY  
THE SINGLE-CRYSTAL X-RAY DIFFRACTION METHOD (I)

Haruo SAWADA, Hiroshi IWASAKI, Kazumasa OHSUMI, and Satoshi SASAKI

Photon Factory, National Laboratory for High Energy Physics.

### Introduction

The trivalent chromium ion is known to have an energy level from which fluorescence and laser action to ground level can occur. The  $t_{2g}$  orbitals are occupied by 3 electrons in both levels, all of the same spin at ground level, one of them having opposite spin at the metastable level.

Since this metastable state has a long lifetime, in the order of milliseconds, an appreciable fraction of ions can be held constantly at this level by irradiation by sufficient flux of excitation energy. Detection with X-ray diffraction methods of the effect on crystallographic parameters brought on by the occupation of the metastable level is the final objective of this study.

The single-crystal X-ray diffraction stations at the Photon Factory facility are characterized by their very sharp and intense incidental X-rays which, in itself give results with high s/n ratios. There is a report<sup>(1)</sup> however, of an inferiority in the stability of P.F. X-rays compared to conventional generators and remaining problems in the correction of the collected data for decay of the synchrotron radiation.

Monitoring the temperature increase due to irradiation is especially important when using minute crystals onto which thermocouples cannot be attached, or the net heat evolved is too small to measure with them.

### Experiments and Results

The crystal used in the experiment is natural uvarovite (garnet);  $\text{Ca}_3(\text{Cr,Al,Fe})_2\text{Si}_3\text{O}_{12}$ , cubic cell dimension 11.9365 Å. It was ground into a sphere<sup>(2)</sup> with a diameter of approximately 0.3 mm. Intensity measurements were carried out with the automated four-circle diffractometer at beam line BL-10A of the P.F. A Si(111) crystal was used to monochromatize the X-ray to  $\lambda = 0.5625$  Å. Four reflexions with various  $2\theta$  values were chosen for the inspection of the reproducibility of the  $2\theta$  values. The data for the 16 16 16 reflexion gave the best result, in which the standard deviation of 10 successively measured  $2\theta$  values gave corresponding d-spacing deviation vs. d-spacing ratio  $\Delta d/d = 6.78 \times 10^{-5}$ . Assuming the linear expansion constant with temperature of this sample equal to that of YAG ( $7 \times 10^{-6}$  /deg, <sup>(3)</sup>), temperature change from about a few tens of degrees can be monitored by this method.

Reflection data were collected with the  $2\theta$ - $\omega$  step scan. Correction of data were made for Lorentz-polarization and decay of beam by interpolation of standard reflexion values. Only about 30% of the anticipated number of reflexions were measured. Preliminary results will be reported here.

Standard reflexion 12 10 6 was measured before every 24 reflexion data collected. The  $2\theta$  position of the standard reflexion showed 3 wild fluctuations of about 0.1° each during this experiment. The full duration of these fluctuations were about 10 to 20 reflexion data, and returned to normal by the next standard reflexion. No immediate cause could be pointed out, nor the effect on the processed structure data. The scan width was adjusted to accommodate the profiles of high angle reflexions should these fluctuations occur.

The largest observed structure factor of an extinct reflexion was chosen as the omission criterion for the preliminary analysis. 92 reflexions with  $2\theta/\lambda < 0.64$  were used for refinement. The converged  $R=8.75\%$ ,  $R_w=7.80\%$ . The difference Fourier map in the vicinity of the  $\text{Cr}^{3+}$  ion shows basically the same characteristic as that of the conventional generator (rotating anode MoK $\alpha$ ,  $2\theta/\lambda < 0.8$ , 384 used reflexions (equivalent-averaged, independent),  $R=2.06\%$ ,  $R_w=1.85\%$ ); the electron distribution around the  $\text{Cr}^{3+}$  ion is deficient in the direction of the  $e_g$  orbitals (Fig.1).

It is possible to consider reproducibility of reflexions measured in short time intervals high, and in making a comparison of very fine details between two structural data, those reflexions should be collected in that manner. If reflexions suspected to give significant intensity change upon irradiation could be deduced from data collected with a conventional generator, or from Fc's of reflexions with large contribution from the  $\text{Cr}^{3+}$  ion, a selected set of reflexions could repeatedly be measured with the synchrotron radiation.

### References

- (1) Ohgaki, M., Tanaka, K., Marumo, F., Takei, F., Satou, Y.: (1987) Proposal No.86-062 in Photon Factory Activity Report vol.5, 315.
- (2) Bond, W.L.: (1951) Making of small spheres. Review of Scientific Instruments. 52, 344-345.
- (3) Chronological Scientific Tables (1988). Ed. Tokyo Astronomical Observatory, Maruzen Co., Ltd.

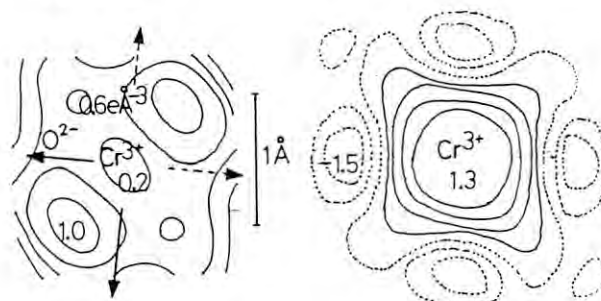


Fig.1. Synchrotron.  
Increment  $0.3e\text{Å}^3$

Conventional.  
 $0.4e\text{Å}^3$



## X-RAY RAMAN SCATTERING AS A SUBSTITUTE FOR SOFT X-RAY ABSORPTION

Yasuo UDAGAWA and Kazuyuki TOHJI

Institute for Molecular Science, Okazaki, Aichi 444

Introduction

For noncrystalline materials EXAFS (Extended X-ray Absorption Fine Structure) is now widely used as an established tool for the determination of local structure around a central atom. An application of EXAFS to elements with low atomic number is limited, however, because their K absorption edges lie in the soft x-ray region where the experiment is not feasible in air and no adequate window materials are available.

In order to evade this difficulty, a use of the inelastic scattering has been tried. Some preliminary results<sup>1,2)</sup> on graphite has been reported already. This report is an extension of the previous effort to diamond, an allotrope of graphite. It is confirmed for the first time that the inelastic scattering spectrum called x-ray Raman spectrum has an identical structure as the absorption spectrum of the compound<sup>3)</sup>.

Experimental and Results

The experiment was carried out at BL-10C. X-rays of about 8 keV were monochromatized by a double crystal Si(111) monochromator and was focused by a doubly focusing mirror. The scattered x-rays from sample were dispersed by a Johansson type Ge(333) crystal and detected by a proportional counter. The signal was accumulated in multichannel analyzer for at least 24 hours, and sometimes 3 days. To the lower energy side of the Compton scattering, Raman signal whose intensity is about one tenth of Compton scattering is observed. Fig.1(a) shows the Raman scattering spectrum of diamond after removing Compton contribution. It has very similar features as x-ray absorption spectra; a sharp edge followed by an oscillatory fine structure. As usual in the analysis of EXAFS, a smooth background indicated in the Fig. is assumed and subtracted. The extracted oscillation is shown in Fig.2(b). Also shown in Fig.2 (c) is the extracted EXAFS oscillation in the soft x-ray absorption spectrum from diamond reported by Comelli et al.<sup>4)</sup>. It will immediately be clear that these two are the same. Although not shown in Fig.2(c), fine structures near the edge also coincide exactly. Therefore, it is

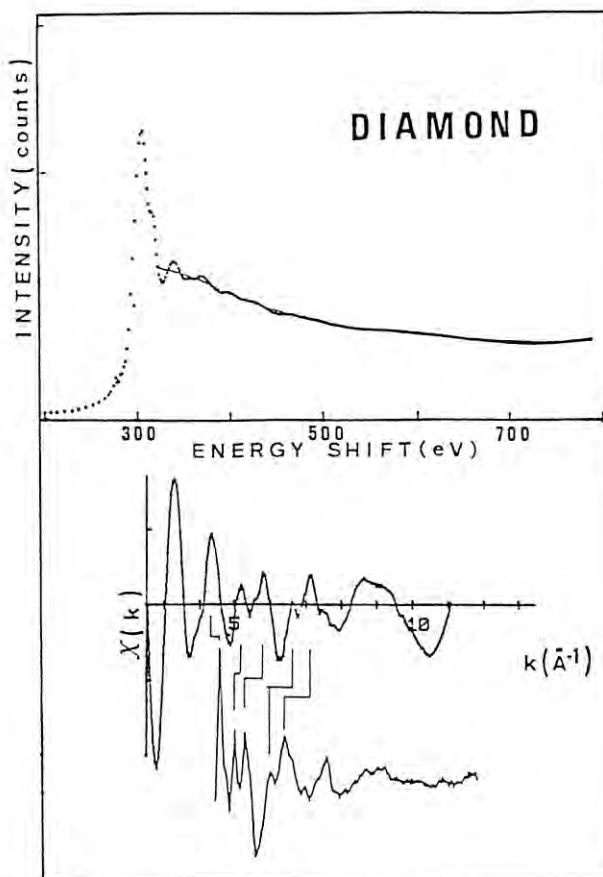


Figure 1. X-ray Raman scattering spectrum of diamond, extracted oscillation from the spectrum. Also shown is the extracted oscillation from the soft x-ray absorption spectrum of diamond reproduced from ref. 4.

experimentally confirmed for the first time that the x-ray Raman scattering can supply the same information as the soft x-ray absorption spectrum, and can be a substitute.

It should be mentioned that resonant effect in x-ray Raman scattering is also observed<sup>5)</sup>.

References

- 1) K.Tothji and Y.Udagawa, PF Activity Repost, #5, 266 (1987).
- 2) K.Tothji and Y.Udagawa, Phys.Rev. B36, 9610 (1987).
- 3) K.Tothji and Y.Udagawa, submitted to Phys.Rev.
- 4) G.Comelli, J.Stohr, W.Jark, and B.B.Pate, Phys.Rev. B37, 4383 (1988).
- 5) Y.Udagawa and K.Tothji, Chem.Phys.Lett. 148, 101 (1988).

## TERTIARY STRUCTURE OF CALMODULIN IN SOLUTION

Yoshinobu IZUMI<sup>1</sup>, Tomoyuki MATSUO<sup>1</sup>, Masayoshi WAKITA<sup>1</sup>, Hidenori YOSHINO<sup>2</sup>,  
Norio MATSUSHIMA<sup>3</sup>, Tatsuo UEKI<sup>4</sup>, Katsumi KOBAYASHI<sup>5</sup>, and Yasuhiro MIYAKE<sup>1</sup>

1. Faculty of Science, Hokkaido University, Sapporo 060
2. Department of Chemistry, Sapporo Medical College, Sapporo 060
3. Department of Physics, School of Allied Health Professions, Sapporo Medical College, Sapporo 060
4. Faculty of Engineering Science, Osaka University, Toyonaka, Osaka 560
5. Photon Factory Instrumentation Group, National Laboratory for High Energy Physics, Tsukuba 305

In this report, we describe the results of a solution X-ray scattering (SOXS) from calmodulin to examine the calcium-induced conformational change of this protein. The structural change of a calmodulin upon calcium binding is also studied in the presence of mastoparan which is one of the model polypeptides as a target-enzyme of calmodulin<sup>1</sup>.

### Experimental

Calmodulin was purified from pig brain according to the methods previously reported<sup>2</sup>. The SOXS profiles were recorded with synchrotron radiation from a storage ring at the Photon Factory of the National Laboratory for High Energy Physics, Tsukuba. The present analysis of the experimental data has been made on the basis of a dumbbell-shaped model constituted with two  $\text{Ca}^{2+}$ -binding domain (N- and C-domains) connected by a long central  $\alpha$ -helix.

### Results and Discussion

Fig. 1 shows SOXS profiles from calmodulin solutions with different amount of  $\text{Ca}^{2+}$  ions at moderate scattering angles. The change in the scattering profile can be clearly seen in which a hump at about  $10^2 s = 2.4 \text{ \AA}^{-1}$  and a broad peak at about  $10^2 s = 5.6 \text{ \AA}^{-1}$  increase depending on the increasing of  $\text{Ca}^{2+}$  concentration. These tendencies are almost complete upon the addition of 2.0 mol  $\text{Ca}^{2+}$ /mol of calmodulin.

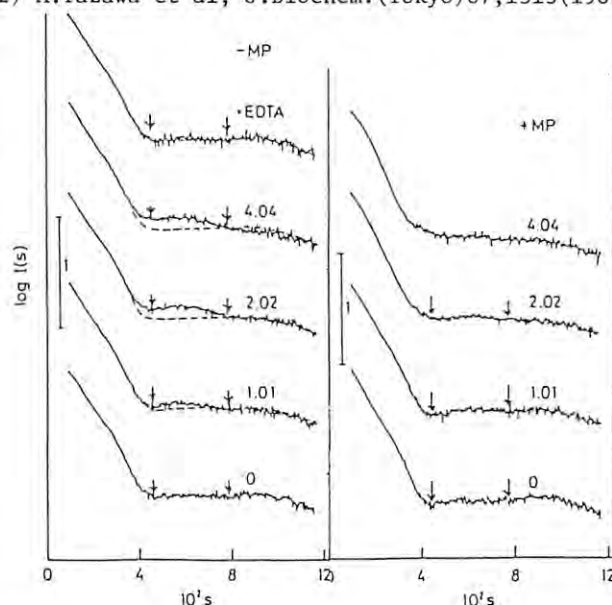
The radii of gyration  $R_g$  of calmodulin estimated from the initial slope of the Guinier plot of SOXS profiles are shown in Fig. 2 as a function of  $\text{Ca}^{2+}$  concentration. The  $R_g$  value increases as the  $\text{Ca}^{2+}$  concentration increases and is almost complete upon the addition of 2.5 mol  $\text{Ca}^{2+}$ /mol of calmodulin.

Fig. 3 shows the SOXS profiles from calmodulin solutions in the presence of mastoparan. The distinct change in the intensity profile can be seen in the figure with increasing  $\text{Ca}^{2+}$  concentration. From Fig. 3, it is noted that a hump at about  $10^2 s = 2.8 \text{ \AA}^{-1}$  disappears upon the addition of 2.0 mol  $\text{Ca}^{2+}$ /mol of calmodulin. These changes upon calcium binding in the presence of mastoparan are clearly different from those in the absence of mastoparan. The radii of gyration  $R_g$  of calmodulin in the presence of mastoparan estimated from the Guinier plots are shown in Fig. 2 as a function of  $\text{Ca}^{2+}$  concentration. The  $R_g$  value drastically decreases as the  $\text{Ca}^{2+}$  concentration increases and is almost complete upon the addition of 4.0 mol  $\text{Ca}^{2+}$ /mol of calmodulin.

Taken together, these results obtained with the presence of mastoparan suggest that the distance between two domains of calmodulin becomes to be so close by the binding of  $\text{Ca}^{2+}$  that  $R_g$

decreases drastically and the hump which would be characteristic of a dumbbell-shaped model disappeared.

- 1) H.Yoshino et al, in Calcium Signal and Cell Response, Ed. by K.Yagi and T.Miyazaki, Gakkai-Syuppan Center, Tokyo 1988, Y.Izumi et al, Rep.Prog.Polym.Phys.Jpn. 31 (1988) to be published.
- 2) M.Yazawa et al, J.Biochem.(Tokyo)87,1313(1980).



SOXS profiles of calmodulin in the absence (Left, Fig. 1) and presence (Right, Fig. 3) of mastoparan.

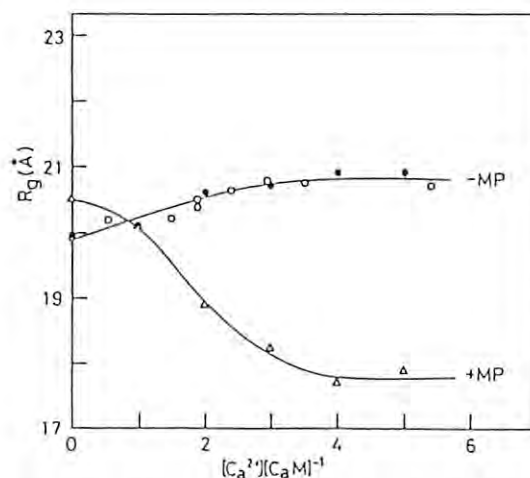


Fig. 2. Change in  $R_g$  of calmodulin as a function of  $\text{Ca}^{2+}$  concentration.

## Structural Study of Gelation of Branched Polyethylene in Solution

Yoshinobu IZUMI<sup>1</sup>, Tomoyuki MATSUO<sup>1</sup>, Yasuhiro MIYAKE<sup>1</sup>, and Tatsuo UEKI<sup>2</sup>

1. Faculty of Science, Hokkaido University, Sapporo 060

2. Faculty of Engineering Science, Osaka University, Toyonaka 560

Introduction

Polyethylene exhibits a thermoreversible gelation in a large number of solvents. The gelation occurs during the crystallization of polymer. Although the characterization of thermoreversible gelation in polyethylene solutions has been examined, only few diffractive studies have been made. The present work is concerned with the first observation of the static behaviors of the gelation and the melting of the gel of the system of a branched polyethylene-toluene by SAXES in stalled at Photon Factory of KEK.

Experimental

The branched polyethylene was supplied by Polysciences Inc., and the viscosity is 0.8132 dl/g in chloronaphtalene. The temperature of the sample holder was controlled by circulating water of constant temperature. The temperature fluctuation of the sample was within 0.1°C through the experiments. The details of the instrumentation and the procedure of SAXES are described elsewhere<sup>1</sup>. Five concentrations of polyethylene solution have been examined, i.e., 1(3%), 2(5%), 3(10%), 4(14%), and 5(20%).

Results and Discussion

The obtained results were analyzed using the invariant  $Q$  and the correlation length  $l_c$  defined by

$$Q = \int I(q) q^2 dq \quad \text{and} \quad l_c = \pi / \int I(q) q dq / Q,$$

where  $q$  is a scattering vector.

Fig. 1 shows the double logarithmic plots of  $Q$  and  $l_c$  versus reduced temperatures under the annealed condition, where  $\varepsilon$  and  $\varepsilon'$  are  $(T_m - T)/T_m$  and  $(T_{cr} - T)/T_{cr}$ , respectively,  $T_m$  is the melting temperature of gel and  $T_{cr}$  is the crystallization temperature. The results show that  $Q$  and  $l_c$  are an universal function of the reduced temperatures, respectively. The straight line in the plot of  $Q$  versus reduced temperature has a slope of 1.0, while that in the plot of  $l_c$  has a slope of about -0.1. As  $T_{cr}$  and  $T_m$  almost correspond to the temperatures of the appearance and the melting of gel phase, respectively, these exponents values may be directly related with the critical exponents of the gelation and the gel melting, i.e.,  $\beta \approx 1.0$  and  $\nu \approx 0.6$ .

Fig. 2 shows the corresponding plots of  $Q$  and  $l_c$  of the melting of the gel prepared under the quenched condition. From the slopes of the straight lines, we obtained the critical exponents of the gel melting, i.e.,  $\beta \approx 1.0$  and  $\nu \approx 0.6$ . It is noted that the exponents don't depend on the dilution effect and on the sample conditions. Furthermore, behaviors of (110) and (200) reflections observed in the wide-angle X-ray measurement correspond to those of the above results.

References

1. T. Ueki et al., Photon Factory Activity Report, VI-70(1982/83).

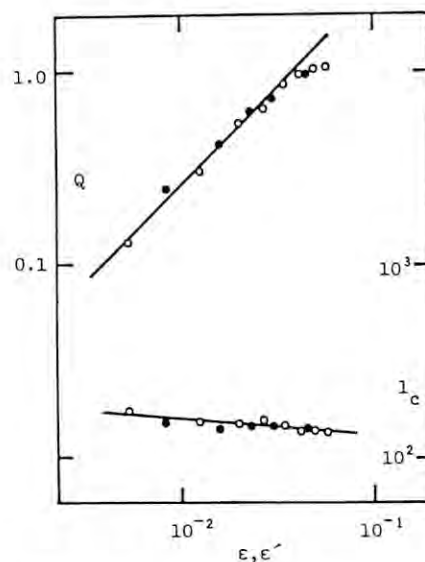


Fig. 1. Plot of  $Q$  and  $l_c$  versus reduced temperatures under the annealed condition.

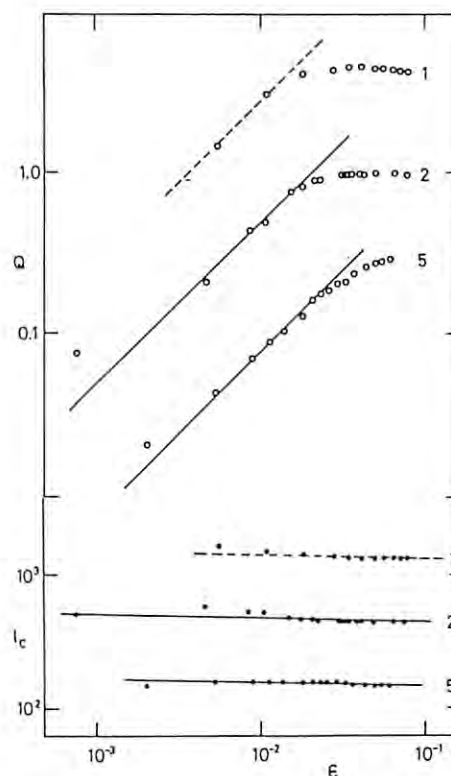


Fig. 2. Plot of  $Q$  and  $l_c$  versus reduced temperatures under the quenched condition.

STUDIES ON  $\text{Si}(111)\sqrt{3}\times\sqrt{3}\text{-Bi}$  AND  $\text{-Ag}$  SURFACES BY X-RAY DIFFRACTIONT. Takahashi, S. Nakatani, N. Okamoto, T. Ishikawa<sup>†</sup> and S. Kikuta<sup>††</sup>

Institute for Solid State Physics, University of Tokyo, Japan

<sup>†</sup> Photon Factory, National Laboratory for High Energy Physics, Japan<sup>††</sup> Faculty of Engineering, University of Tokyo, JapanIntroduction

Recently, X-ray diffraction has been applied to the structure analysis of crystal surfaces using synchrotron radiation. Hitherto, most of the works have been made under grazing incidence condition, and the surface structure projected on a plane parallel to the surface has been studied. In this work, X-ray intensity versus energy curves are measured under nearly normal incidence condition in order to measure the rod profiles, and the 3-dimensional surface structures of  $\text{Si}(111)\sqrt{3}\times\sqrt{3}\text{-Bi}$ <sup>(1)</sup> and  $\text{-Ag}$ <sup>(2)</sup> are investigated.

In these systems, the atomic scattering factor of adsorbed atoms is much greater than that of Si. Therefore the contribution of the reconstructed Si atoms to the diffracted intensities is small compared with that of the adsorbed atoms, and neglected in the first step of the analysis. Then the atomic arrangements of the adsorbed layer are easily determined from the intensity analysis of the fractional-order spots. Next, the adsorption sites of the adsorbed atoms are analyzed from the intensity changes along the integral-order rods especially near the Bragg points by utilizing the interference effect between the X-rays diffracted from the adsorbed layer and the bulk crystal. It is noted that the phase of the diffracted waves by the bulk crystal changes  $\pi$  on both sides of the Bragg points. Finally, the positions of the reconstructed surface Si atoms are obtained from the more detailed analysis.

Experimental and Results

Experiments were made at the beam-line 10C in the Photon Factory. Fig. 1 shows the result obtained for the  $\text{Si}(111)\sqrt{3}\times\sqrt{3}\text{-Bi}$  surface. Bi atoms forming a trimer are bonded with the first layer Si atoms, and the center of the trimer is on the second layer Si atoms. The distance between the Bi atoms is about 3.1 Å, and the distance between the Bi and first layer Si atoms is about 2.7 Å. These values are well explained from the atomic radii of the Bi and Si atoms.

In the case of the  $\sqrt{3}\times\sqrt{3}\text{-Ag}$  surface, the analysis shows that Ag atoms form honeycombed triangles as shown in Fig. 2. The distance between the nearest neighbor Ag atoms is about 3.4 Å, which corresponds to twice the van der Waals radius of Ag atoms. Fig. 3 shows the adsorption sites obtained from the integral-order rod profiles. The spacing between the Ag layer and the ideal first Si layer is about 2.9 Å. Since the rod profiles are not so sensitive to the reconstructed Si atoms near the Ag layer, it seems that Si atoms which are not shown exist near the surface below the Ag layer.

References

- 1) T. Takahashi et al.; Surf. Sci. 183 (1987) L302, 191 (1987) L825.
- 2) T. Takahashi et al.; Jpn. J. Appl. Phys. 27 (1988) L753.

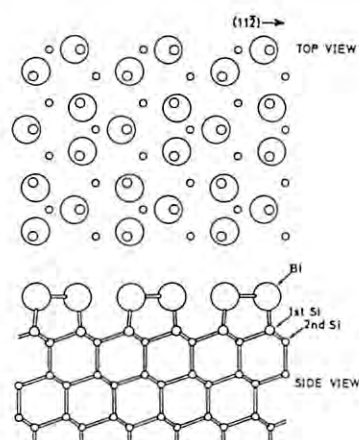


Fig. 1

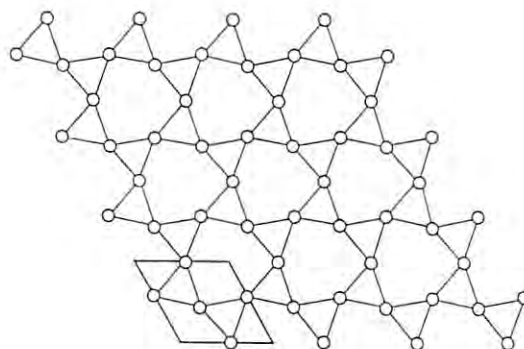


Fig. 2

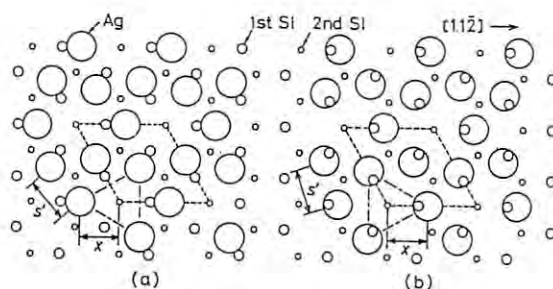


Fig. 3



## X-RAY CORRELATION PHOTOACOUSTIC MEASUREMENT OF LAYERED MATERIALS

Yoshinori SUGITANI<sup>+</sup> and Kenji KATO<sup>++</sup><sup>+</sup> Department of Chemistry, The University of Tsukuba,  
Tsukuba, Ibaraki 305<sup>++</sup> National Chemical Laboratory for Industry,  
Tsukuba, Ibaraki 305Introduction

Correlation photoacoustic measurement gives impulse response characteristics of heat generation in the sample caused by X-ray absorption without any use of pulsed X-ray source<sup>1,2)</sup>. The impulse response is referred to as the first kind of correlation photoacoustics<sup>3,4)</sup>, which gives information on thermal and structural properties of the sample material. Although conventional photoacoustic method gives similar informations by the use of phase delay or multi-frequency measurements, impulse response curve represents more detailed and visual information for understanding the layered samples than the conventional method.

Experimental and Results

The experiments was made at the beam lines BL10C (monochromated to 1.32-1.45Å) and BL15A (fixed at 1.504Å). The X-ray beam was modulated by a mechanical random chopper (containing 2 series of M-sequence,  $n=31$ ). The photoacoustic cell used was similar to that used in previous works<sup>1,2)</sup>. But the cell windows were enlarged (18.5mm diameter and 0.5mm thick) to avoid absorption of scattered beam in the cell space. The cell was placed on a pneumatic floating table. The preamplified photoacoustic signal and the reference signal from the chopper were introduced into FFT analyzer (ADVANTEST, TR9403), and the cross correlation between these signals was obtained by integration up to 1024 times.

Dependence of correlation photoacoustic spectra for copper foils (thickness 10, 50, 200, 1000µm) on the X-ray wavelength were measured

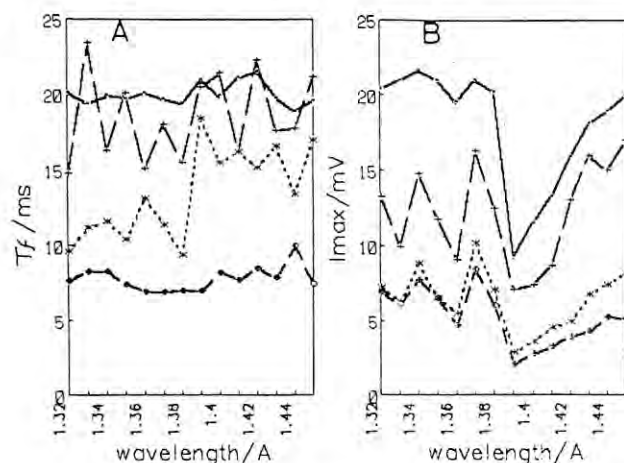


Fig.1. Dependence of correlation spectra versus X-ray wavelength. A:  $T_f$ , decay time, and B:  $I_{max}$ , peak intensity of heat pulse.  
•: 10µm, +: 50µm, \*: 200µm, o: 1000µm.

at wavelengths between 1.32 and 1.45Å. Although penetration depth of X-ray beam in the copper foil changed 4 to 28µm when the wavelength changed from 1.35 to 1.40Å across the point of the absorption edge,  $T_0$  showed no change. Figure 1 shows the change of  $T_f$  and  $I_{max}$  against X-ray wavelength.  $I_{max}$  shows sharp drop at absorption edge for each thickness, and  $T_f$  shows a rise at absorption edge for the samples with thicknesses of 50 and 100µm. These facts mean that 1)  $T_0$  and  $I_{max}$  were influenced by the heat generated near the surface, 2)  $T_f$  is influenced by depth of heat generation.

Laminated samples of aluminum and lead sheets were measured at 1.30 and 1.45Å. one to three sheets of aluminum foils (15µm thick) were adhered with polymer binder on both side of lead foil (50µm). Figure 2 shows correlation photoacoustic spectra obtained for the laminated sample with three aluminum layers. Two peaks are observed at  $T_0=10$  and 65ms. First and second peaks are considered to be related to the heat from the surface aluminum and that from the lead layers, respectively.  $T_0$  for the first peak shows no change with increase of number of aluminum layer, but  $T_0$  for second peak increased with number of aluminum layers (see Fig. 2 B).

References

- 1) Y. Sugitani and K. Kato, Photon Factory Activity Report 1987, p350
- 2) K. Kato and Y. Sugitani, Anal. Sci., **4**, 59 (1988)
- 3) K. Kato, S. Ishino and Y. Sugitani, Chem. Lett. 783 (1980).
- 4) Y. sugitani, A. Uejima and K. Kato, J. Photoacoust. **1**, 217 (1982).

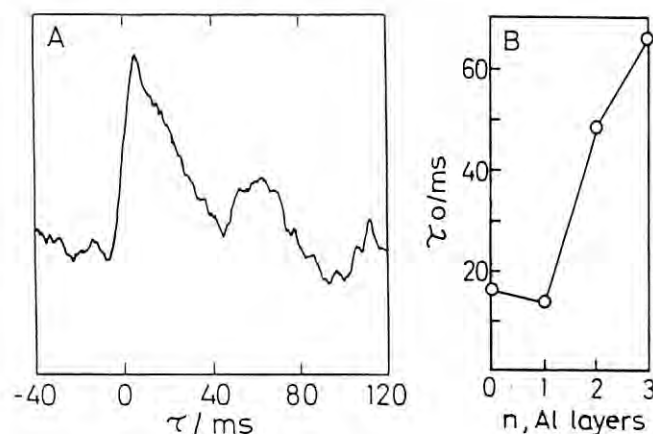


Fig.2. Photoacoustic spectra of laminated sample. A: Impulse response for the sample with 3 aluminum layers, B: dependence of  $T_0$  on number the aluminum layers.

## CRYSTALLIZATION OF POLY(VINYL ALCOHOL) ON HETEROGENEOUS NUCLEI

Seiji ISODA<sup>a</sup>, Sakumi MORIGUCHI<sup>a</sup>, Akiyoshi KAWAGUCHI<sup>a</sup>, Yuzuru HIRAGI<sup>a</sup>,  
Euiho KIM<sup>a</sup>, Kanji KAJIWARA<sup>b</sup> and Hiroshi URAKAWA<sup>b</sup>

a. Institute for Chemical Research, Kyoto University, Uji 611

b. Kyoto Institute of Technology, Kyoto 606

## INTRODUCTION

The crystallization of polymers was performed on heterogeneous nuclei not only to produce fine grained particles for improved optical and mechanical properties, but also to investigate the early stage of crystallization. Such a crystallization process may be traced with SAXS and also with electron microscope (EM).

In this report, the crystallization process of poly(vinyl alcohol) PVA was examined on poly(methyl methacrylate) PMMA particles of fine size in water solution.

## EXPERIMENTAL

PVA used was a commercial product of Unittika (viscosity averaged molecular weight is 1700) provided through Prof. Kaji and PMMA latex was prepared by Dr. Yamazaki<sup>1)</sup>. PVA was dissolved in hot water (100 °C), in which PMMA particles have been suspended, and after cooling down to 25°C was crystallized for 2 weeks. SAXS experiment was performed BL-10C at Photon Factory.

## RESULTS AND DISCUSSION

Figs.1-a and -b show the Guinier plots for PMMA/H<sub>2</sub>O and PVA/PMMA/H<sub>2</sub>O, respectively.

$R_g$  was estimated for PMMA as  $22.3 \pm 0.8$  nm from the Guinier plot for PMMA/H<sub>2</sub>O, and then the diameter of the PMMA particles was calculated to be 57.4 nm, assuming homogeneous density in PMMA spherical particles.

Fig.2-a shows an EM image of PMMA particles negatively stained with uranyl acetate and the mean diameter of the PMMA particles is estimated to be 52.0nm, though the diameter varies between 40 and 60 nm.

After the crystallization at 25 °C, SAXS in Fig.1-b yields the  $R_g$  value of  $27.7 \pm 1.0$  nm, which corresponds to 71.4 nm of spherical diameter. The value is larger than that of PMMA particle itself, suggesting that PVA is crystallized on PMMA particles.

Actually a shell structure was observed by EM for negatively stained specimens after the crystallization as shown in Fig.2-b, and the

shell thickness is about 4nm which corresponds roughly to the lamella thickness of PVA crystal. It seems that PVA crystal is grown on the PMMA particle.

Detailed mechanism of the formation of the shell structure is still in question and further experiments are needed with SAXS and EM.

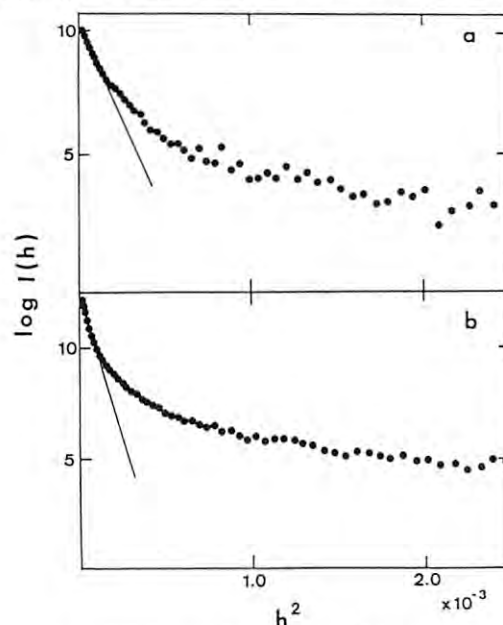


Fig.1-a.  $I(h)$  vs.  $h^2$  for PMMA/H<sub>2</sub>O,  
b. for PVA/PMMA/H<sub>2</sub>O.

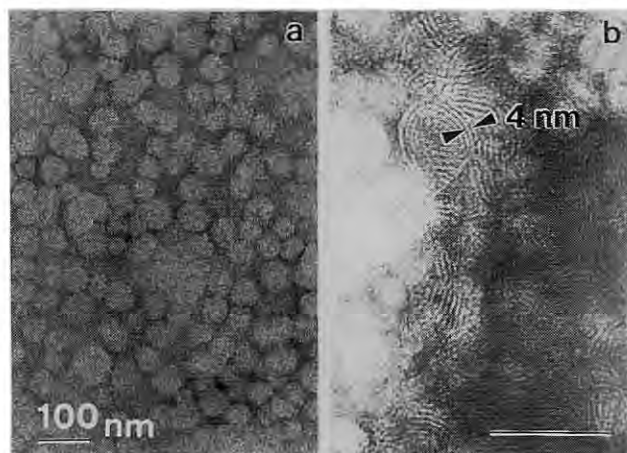


Fig.2-a. EM image of PMMA particles,  
b. of PVA crystallized on PMMA.

1) S. Yamazaki: Kobunshi Ronbunshu, 36, 729 (1979)

## Photoacoustic EXAFS Study at Beam Line 10C

Tsutomu Masujima<sup>1</sup>, Hideaki Shiwaku<sup>1</sup>, Hiroshi Kawata<sup>2</sup>, Hisanobu Yoshida<sup>1</sup>, Hideo Imai<sup>3</sup>,  
Taro Toyoda<sup>4</sup>, Mikio Kataoka<sup>5</sup>, Ikeda Tetsuya<sup>6</sup>, Hiroshi Makihara<sup>6</sup>, Takayuki Sano<sup>7</sup>,  
Katsumi Kobayashi<sup>2</sup>, Masami Ando<sup>2</sup>

1. Inst. Pharmaceutical Sci., Hiroshima Univ. School of Med., Kasumi, Hiroshima 734
2. Photon Factory, National Laboratory for High Energy Physics, Oho, Tsukuba 305
3. Faculty of Pharmaceutical Sci., Fukuyama Univ., Higashimura-cho, Fukuyama 729-02
4. Dept. of Optoelectronics, Tokyo Kogakuin College of Technology, Sendagaya, Tokyo 151
5. Faculty of Science, Tohoku University, Sendai, Miyagi 980
6. Technical Headquarters, Mitsubishi Heavy Industries, Ltd., Sachiura, Yokohama 236
7. Faculty of Science, Hiroshima Univ., Higashisenda, Hiroshima 730

The photoacoustic EXAFS method which was established by our group at the Photon Factory is an unique and new tool for analysis<sup>1)</sup>. However, in our application of this method to actual samples, it was found that sensitivity of our system should be improved. One of the way to overcome this problem is use of a high flux X-ray source. The Beam Line 10C is the station with installed double focusing system with tuneability of wavelength. We developed a system for X-ray energy scanning system to perform the PA-EXAFS study at higher S/N ratio.

**Experiments** Since the double crystal monochromator at BL10C was not designed to have a mechanical linkage between the two crystals, control of the monochromator was delicate. Thus we adopted feed back control with computer. A flow chart for the monochromator control by our microcomputer(NEC 9801 VM2) is shown in Fig.1.

## Results and Discussion

Figure 2 shows the spectra for Cu foil at 1  $\mu\text{m}$  thick. Very thin and thick Cu foil is known to give small photoacoustic signal<sup>2)</sup>. Corresponding fine structures were seen both in the absorption spectrum and in the photoacoustic spectrum even for this undesirable case. However, in the photoacoustic EXAFS, sharp decrease were also included at 9.1 and 9.15 keV. These spikes in this normalized spectrum were occurred when the photon flux was changed fairly drastic on the way of scanning. It seemed that the accumulated photoacoustic background noises were also depending on the pre-set accumulation times. Because the number of times for accumulation up to the preset value increases when the incident X-ray flux at the first ion

chamber decreased. Thus, it was finally considered that in order to get good quality of photoacoustic EXAFS through weak signal, the smooth change in the photon flux on scanning of the photon energy is quite important. In order to maintain the flux at similar level, learning system was also installed in the software. More desired energy scanning system for Beam Line 10C is under development.

## References

- 1) T.Masujima, H.Kawata, et al., Photon Factory Activity Report, 5, 139(1987).
- 2) T.Masujima, H.Kawata, et al., Chem. Lett., 1987, 973.

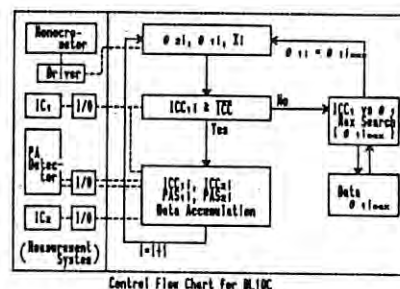


Figure 1. Control flow chart for the energy scanning system of BL10C with our microcomputer.

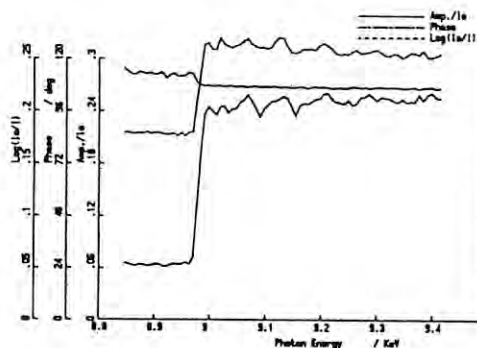


Figure 2. X-ray absorption spectra of Cu foil (1  $\mu\text{m}$  thick) by Photoacoustic and absorption method.



## NUCLEAR EXCITATION BY SYNCHROTRON RADIATION — BACKGROUND —

Takeshi MUKOYAMA, Harumi KAJI,<sup>†</sup> Kenji YOSHIHARA<sup>†</sup> and Tetsuo NAKAJIMA\*

Institute for Chemical Research, Kyoto University, Gokasho, Uji 611

<sup>†</sup>Department of Chemistry, Faculty of Science, Tohoku University, Aoba, Aramaki, Sendai 980

\*KEK, National Laboratory for High Energy Physics, Oho, Tsukuba 305

Introduction

In our preliminary reports,<sup>1,2</sup> we have shown that we succeeded to observe nuclear excitation for  $^{103}\text{Rh}$  and  $^{189}\text{Os}$  by synchrotron radiation. This process has been confirmed by observing x rays accompanying internal conversion from isomeric states, which are produced in course of de-excitation of higher-excited levels. However, due to narrow nuclear level widths the induced activity was so weak that the counting statistics was poor and the background contributions were important.

There have been performed extensive studies on the natural background in the  $\gamma$ -ray energy region ( $\geq 100$  keV), but to the authors' knowledge no systematic study in the x-ray energy region has been reported. This is because the x-ray background strongly depends on the surroundings. All materials around the detector can be a source of fluorescent x rays when they are hit by natural background radiations.

In order to estimate the contributions from the background to our x-ray spectra, we have attempted to measure the natural background for our experimental conditions in the previous work.

Experimental

The natural background in the energy region of rhodium K x rays and osmium L x rays were measured with a Ge low-energy photon spectrometer (LEPS). Two kinds of measurements were made with and without target foils in front of the detector, because the activity measurements were made with targets. The same Rh and Os foils used in the previous works<sup>1,2</sup> were used. The energy calibration of the detector system was performed by the use of  $^{57}\text{Co}$  and  $^{241}\text{Am}$  sources. The measuring period was chosen to be about  $5 \times 10^4$  sec.

Results and discussion

Figure 1 shows the background spectrum with the Rh targets. Two low-energy peaks at 8.8 and 10.3 keV correspond to the  $K\alpha$  and  $K\beta$  x rays of Ge. The fluorescent Rh K-x-ray peaks can be seen at 20.2 and 22.9 keV. Two high-energy peaks at 24.2 and 27.3 keV are K x rays from In.

The background spectrum without target is shown in Fig. 2. To see the high-energy part, the energy range is expanded. In the high-energy region, the  $K\alpha_1$  peaks of Pb (75.2 keV) and Bi (77.2 keV) are found. They are considered due to radioactive aerosols.

Figure 3 is the spectrum with the Os target. In addition to the In K x rays, there are three peaks corresponding to Re and Os K x rays. They are not seen in the spectrum without target in Fig. 4. The Os peaks come from the fluorescent x rays. On the other hand, the existence of the Re K-x-ray peak suggests that our Os target may contain long-life Os radioisotopes or radioactive impurities.

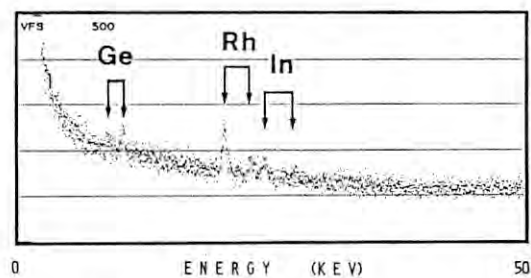


Fig. 1. Background with Rh foil.

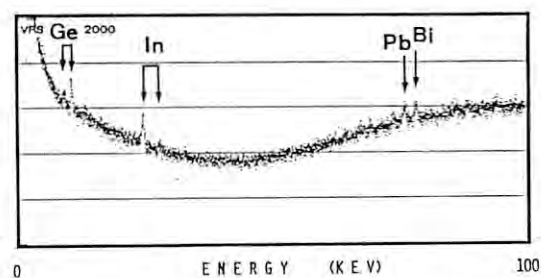


Fig. 2. Background without Rh foil.

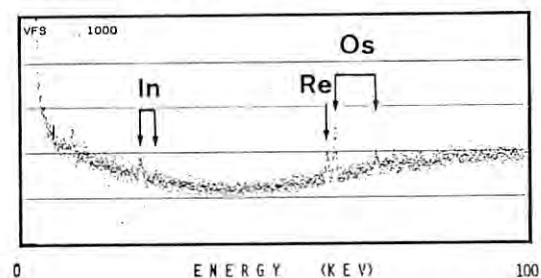


Fig. 3. Background with Os foil.

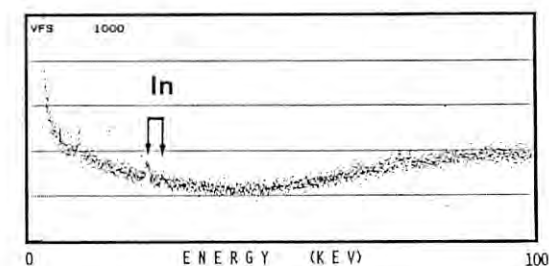


Fig. 4. Background without Os foil.

References

- 1) T. Mukoyama, H. Kaji, K. Yoshihara, T. Nakajima and H. Kobayakawa, Photon Factory Activity Report 1986, 283 (1986).
- 2) T. Mukoyama, H. Kaji, K. Yoshihara, T. Nakajima and H. Kobayakawa, Photon Factory Activity Report 1987, 322 (1987).



## DYNAMICAL DIFFRACTION OF X-RAY IN PERFECT CRYSTALS UNDER GRAZING-INCIDENCE CONDITIONS

H. Hashizume, O. Sakata, T. Nakahata, H. Sakuma and A. Aoshima

Research Laboratory of Engineering Materials, Tokyo Institute of Technology, Yokohama 227

Abstract

Dynamical X-ray diffraction during total external reflection has been studied by measuring rocking curves and fluorescence yield curves from a perfect germanium crystal under the grazing-incidence condition. The rocking-curve profiles observed from slightly asymmetric Bragg planes as a function of glancing angle were found to be quite different for both the diffracted and specular beams. These profiles show unusual features arising from the excitation or de-excitation of the wave fields in shallow surface layers of the bulk crystal. Furthermore, Ge K fluorescence signals measured during the Bragg reflection showed characteristic modulations, demonstrating the formation of X-ray standing waves inside the crystal with intensity modulations parallel to the surface. The work has been reported in details in refs. 1-3.

Rocking curve measurements

Experiments were conducted on a germanium (111) crystal with an optically flat surface. The polished surface was found to be inclined to the (111) plane by 3.3 mrad. The surface was etched in HF solution to remove the oxide layer and passivated by bromine. This specimen was horizontally mounted on a goniometer which allowed us to control independently the grazing angle  $\phi_0$  and the deviation angle  $\Delta\theta$  from exact Bragg incidence. For the specimen geometry, refer to our previous report [4]. The incident beam (photon energy 8.05 keV) obtained from the vertical-wiggler source was collimated by an asymmetric germanium 220 monochromator arranged in a non-dispersive position for the specimen (220) plane. The output beam had horizontal and vertical divergences approximating the plane-wave condition.

Figure 1 shows typical reflectivity curves observed at fixed  $\Delta\theta$  positions. The indicated  $\Delta\theta$  values are determined by comparing the experimental profiles with the theoretical ones. The two specimen orientations rotated by  $180^\circ$  around the surface normal gave surprisingly different curve profiles for both the specular and diffracted beams. Double steps are clearly visible in  $R_s(\phi_0)$  with one step at  $\phi_0 < \phi_c$  and the other step at  $\phi_0 > \phi_c$ , where  $\phi_c$  is the critical angle of total external reflection for off-Bragg conditions, which is equal to 5.4 mrad. The double steps are a direct consequence of wave dispersion during the Bragg reflection, which produces two wave fields in the crystal with different refractive indices. The observed profiles are largely in agreement with the calculations, indicating that the diffraction process is describable by the existing dynamical diffraction theory [1-3].

Standing-wave behaviors

More direct information on the X-ray wave fields has been gained by tuning the beamline optics now to 17.4 keV and recording fluorescence spectra from the specimen by a high-purity germanium detector. Figure 2 plots Ge K fluorescence signals,  $I_f$ , together with simultaneously measured specular and diffracted intensities,  $I_s$  and  $I_h$ , observed by rocking the specimen through the Bragg

position at three different values of  $\phi_0$  close to the off-Bragg critical angle  $\phi_c$ , which is now equal to 2.5 mrad. Clearly, the  $I_f$  signals confirm the formation of an X-ray standing wave (XSW) inside the crystal. This standing wave is intensity modulated along the  $h$  vector, which is directed nearly parallel to the specimen surface. For the Laue-case diffraction with which we are concerned, we have two possible standing waves, one with antinodes on the atomic planes and the other with nodes on the atomic planes. Most obvious in Fig. 2 is the variation of  $I_f(\theta)$  from a peaked profile at  $\phi_0 < \phi_c$  into a dipped profile at  $\phi_0 > \phi_c$  via a peak-valley profile at  $\phi_0 \approx \phi_c$ . This has been observed for the first time and demonstrates the specific dependences of the standing-wave amplitudes on  $\phi_0$ . These results show that new XSW experiments are feasible for the determination of interface structures parallel to the surface.

References

1. O. Sakata and H. Hashizume : Report RLEMTIT (Tokyo Inst. Tech.) 12, 45 (1987).
2. O. Sakata and H. Hashizume : Jpn. J. Appl. Phys. Part II, 27, No.11 (1988).
3. H. Hashizume and O. Sakata : SRI-88 Conference, Tsukuba, Aug.28-Sept.2, 1988; Proceedings to be published in Rev. Sci. Instrum.
4. O. Sakata *et al.* : Photon Factory Activity Report #5, 320 (1987).

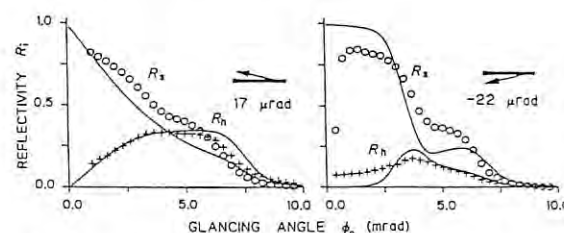


Fig. 1. Observed (open circles) and calculated (solid line) reflectivity curves at fixed  $\Delta\theta$  for two specimen orientations. The insets show the directions of the  $h$  vector with respect to the surface.  $R_s$ : specular beam,  $R_h$ : diffracted beam. The calculated curves include the incident-beam profile and the effects of the non-flat specimen surface.

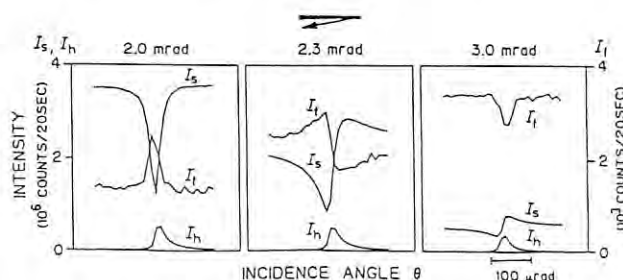


Fig. 2. Observed intensities for Ge K fluorescence  $I_f$ , specular beam  $I_s$  and diffracted beam  $I_h$  versus  $\theta$  for  $\phi_0 = 2.0, 2.3$  and  $3.0$  mrad.

## ANGLE-DISPERSIVE X-RAY DIFFRACTION BY WATER MOLECULES II.

Hiroshi TAKEUCHI, Makoto NAKAGAWA, Takayuki SAITO,  
Toru EGAWA, Toshiyuki MITSUHASHI<sup>+</sup>, Tetsuya ISHIKAWA<sup>+</sup> and  
Shigehiro KONAKA

Department of Chemistry, Faculty of Science, Hokkaido  
University, Kita-ku, Sapporo 060

<sup>+</sup>Photon Factory, National Laboratory for High Energy  
Physics, 1-1 Oho, Tsukuba, Ibaraki 305

### Introduction

Charge densities in the molecules can be studied by X-ray diffraction. In the previous work,<sup>1)</sup> we measured the energy spectra of the X-rays scattered by free water molecules and reported that there are systematic differences between the experimental and theoretical (SCF-MO) total intensities at small  $s$ -values ( $s = (4\pi/\lambda) \sin\theta$ ). In the present study, the total intensities,  $I_{\text{tot}}$ , at small  $s$ -values have been measured more precisely by using an angle-dispersive type diffractometer at the BL-14B experimental station.

### Experimental

The  $\omega$ - $2\phi$  horizontal type diffractometer and the sample cell constructed by Mitsuhashi et al.<sup>2)</sup> were used. The incident X-rays with the wavelengths of  $1.543/n$  Å ( $n=1,3,4,5$ ) were obtained by using a silicon (111) monochromator. The energy spectra of X-rays were observed by using a pure-Ge SSD with the energy resolution of 170 eV at scattering angles between  $10.5^\circ$  and  $75.7^\circ$ . The temperature of the sample cell was maintained to be about  $141^\circ\text{C}$ . A scintillation counter was used for monitoring the fluctuations of the scattered intensity at a fixed angle. The signals from the SSD were stored in a multichannel analyzer. The polarization factor was determined by measuring the scattered intensities by air with the scintillation counter mounted on a  $\chi$ - $\phi$  circle.

### Results

Experimental total intensities were obtained from the observed energy spectra by the following procedure: (1) absorption correction; (2) background correction; (3) normalization by using the monitor counts; (4) normalization regarding the effective scattering volume; (5) polarization correction. The limits of error were estimated from the statistical fluctuation of the counts of the SSD. The experimental total intensities were compared with the theoretical ones calculated from a CI molecular wavefunction, which is based on the [7s4p2d/5s2p] basis set and includes all singly excited configurations and selected doubly excited configurations.<sup>3)</sup> The experimental total intensities were normalized to the theoretical ones at  $s = 0.75$  Å<sup>-1</sup>. The experimental and theoretical results were compared in terms of the difference intensity,  $\Delta\sigma_{\text{ee}}(s) = I_{\text{tot}}^{\text{exp}} - I_{\text{tot}}^{\text{IAM}}$ , where  $I_{\text{tot}}^{\text{IAM}}$  is the theoretical intensity based on the independent atom model. As shown in Fig. 1, the theoretical values of  $\Delta\sigma_{\text{ee}}(s)$  are in fair agreement with the experimental data.

### References

- 1) H. Takeuchi et al., Photon Factory Activity Report 1987, p. 321.
- 2) T. Mitsuhashi et al., Photon Factory Activity Report 1983/1984, p. VI-172.
- 3) M. Breitenstein et al., Chem. Phys., **112**, 199 (1987).

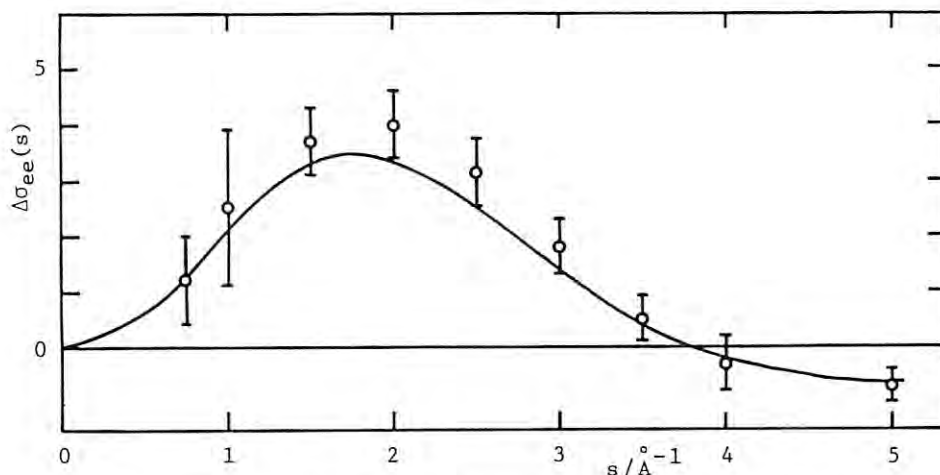


Fig. 1. Experimental ( $\circ$ ) and theoretical (—) difference intensities,  $\Delta\sigma_{\text{ee}}$ , for  $\text{H}_2\text{O}$ .

## The Bragg case Phase Plate

Keiichi HIRANO, Koichi IZUMI, Tetsuya ISHIKAWA\*  
Shoichi ANNAKA\*\* and Seishi KIKUTA

Department of Applied Physics, Faculty of Engineering,  
University of Tokyo, Hongo, Bunkyo-ku, Tokyo 113

\* Photon Factory, National Laboratory for High Energy Physics  
Oho, Tsukuba, Ibaraki 305

\*\* Tokyo University of Mercantile Marine, Etchujima, Koto-ku,  
Tokyo 135

Introduction

When the monochromatic and polarized X-ray is diffracted by a crystal in the Bragg-case, the polarization state of the forward diffracted beam changes from that of incident beam. This is mainly due to the difference of the phase velocity between the coherently excited  $\sigma$ -polarized and  $\pi$ -polarized waves in the crystal.

Using this dynamical effect, we have developed the Bragg case phase plate and experimentally verified the function of it.

Experimental

Fig.1 shows the experimental arrangement set up on BL-14B at the Photon Factory. The wavelength of the beam is 0.905Å. The first Si crystal with the asymmetric 220 Bragg case serves as a collimator. The second Si crystal is a polarizer producing the linearly polarized X-ray beam whose electric vector is inclined by  $45^\circ$  with respect to the horizontal plane. The polarization state of the beam from the polarizer was observed as shown in Fig.2. The third Si crystal with the symmetric 220 Bragg case serves as a phase plate. For the analysis of the polarization state of the forward-diffracted beam from the phase plate, an analyzer crystal with the symmetric 660-Bragg case was used and the integrated intensities were measured at each rotation angle of the analyzer around the incident beam direction.

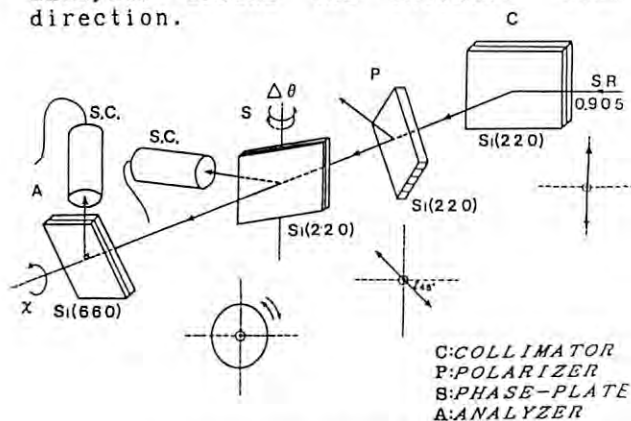


Fig.1 Experimental set up

Results and Discussion

In Fig.3, the experimental results are shown as solid circles with theoretical calculations (solid lines). The variation of the experimental integrated intensities coincides well with the theoretical value. Thus it is experimentally proved that a crystal plate adjusted in the Bragg-case condition serves as a X-ray phase plate. From the viewpoint of application the circularly polarized X-ray is useful. It is possible to obtain left-handed or right-handed circularly polarized X-ray from the linearly polarized synchrotron radiation by the use of this Bragg case phase plate.

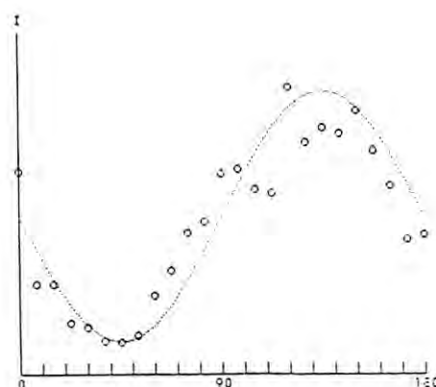


Fig.2 The polarization state from P

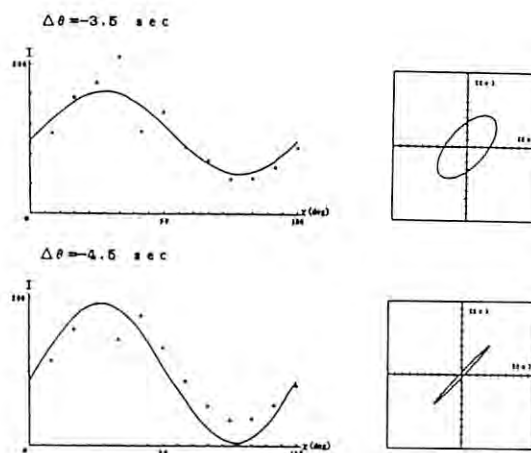


Fig.3 The polarization state from S

## X-RAY STANDING WAVE ANALYSIS OF GaAs/Si(100) INTERFACE

Tomoaki KAWAMURA, Masaharu OSHIMA, Yoshiro OHMACHI, Koichi IZUMI\*,  
Seishi KIKUTA\* and Tetsuya ISHIKAWA\*\*

NTT Applied Electronics Laboratories,  
Midori-cho, Musashino-shi, Tokyo 180

\*Department of Applied Physics, Faculty of Engineering,  
University of Tokyo, Hongo, Bunkyo-ku, Tokyo 113

\*\*Photon Factory, National Laboratory for High Energy Physics,  
OH, Tsukuba, Ibaragi 305

### Introduction

The X-ray Standing Method was known as the powerful tool for structure analysis of interfaces in semiconductor crystals<sup>(1)</sup>. In this report, this method was applied to the GaAs/Si(100) interface for the first time.

### Experimental

A GaAs/Si(100) sample was prepared by MOCVD method. The thickness of GaAs film was about 20Å. From the TEM image, the GaAs film was found to grow as islands on Si(100).

The experiments were carried out at BL-14B. Figure 1 shows the optical system of this experiment. The angle dispersion of an asymmetrically arranged monochromator was about 0.1 arcsec.

The wavelength was set about 0.85 Å (15keV). This value is about 5 keV higher than Ga and As K-absorption edges and the contamination of a Compton and Rayleigh scattering into the Ga and As K-edge was avoided. The Ga and As profile was measured by solid state detector with rotating the sample around Si(400) reflection.

### Result and Discussion

The fluorescence due to the X-ray standing wave method was expressed as follows;

$$I_f = 1 + \frac{|E_h/E_o|^2}{2f} \cos(2\pi D - \alpha), \quad (1)$$

where  $D (=d_z/d_{Si})$  is the relative position of Ga and As to Si.  $d_z$  is the distance between Ga or As atoms and the Si(400) net plane.  $d_{Si}$  is the lattice constant of Si.  $E_h$  and  $E_o$  is the complex amplitude of incident and reflected X-ray,

is related to the complex dielectric constant, which can be calculated analytically. Since the first and second terms of eq. (1) are independent of Ga and As position, only the

third term should be considered. Figures 3(a), (b) showed the third term of eq. (1). The solid lines indicate the curves of least square fitting. The broken lines mean the curves of Ga and As, relatively moved about 4% from original positions of Ga and As, respectively. Because of the difference of lattice constant of Si and GaAs about 4%, the position of Ga, As and Si would be different about 4%. Furthermore if As was positioned at the first layer and Ga was at second layer of GaAs film, the position of Ga and As should be different about 4%. However, the measured data was matched with original position of Ga and As rather than the position of Ga and As moved about 4% from the original position. The results indicate that the position of Ga and As was equivalent in the film. In this experiment, the Si(400) reflection was selected but this reflection is equivalent with respect to Ga and As. At the second step, GaAs/Si(111) sample will be tried because of the different position of Ga and As with respect to Si(111) plane in near future.

### Reference

- (1) K. Akimoto, T. Ishikawa and S. Kikuta; Jpn. J. Appl. Phys. **24**(1985), 1425.

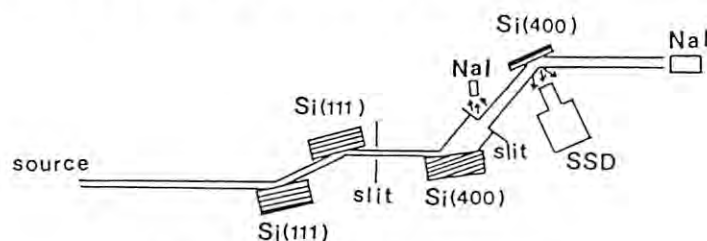


Fig. 1 Experimental arrangement

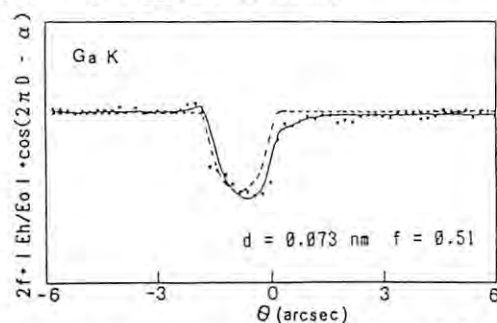


Fig. 2(a) Least square fitting of Ga K

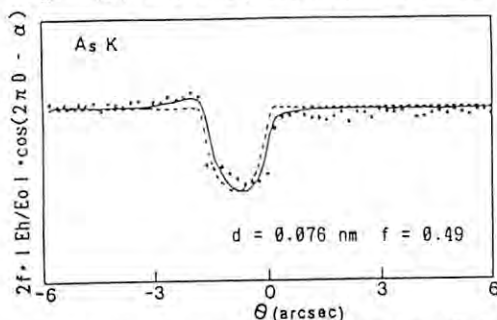


Fig. 2(b) Least square fitting of As K



# A STUDY OF SOLID-LIQUID PHASE TRANSITION FOR LITHIUM METAL BY HIGH RESOLUTION COMPTON SCATTERING MEASUREMENTS

Fumitake ITOH, Tomoki SUGAWA, Kenji SUZUKI  
Nobuhiro SHIOTANI\*, Nobuhiko SAKAI\*, Ou MAO\*  
Hiroshi KAWATA\*\*, Yoshiyuki AMEMIYA\*\* and Masami ANDO\*\*

Institute for Materials Research, Tohoku University, Sendai 980, Japan

\*Institute of Physical and Chemical Research, Wako, Saitama 351-01, Japan

\*\*Photon Factory, National Laboratory for High Energy Physics, Oho, Tsukuba, Ibaraki 305, Japan

## Introduction

A high resolution Compton spectrometer with momentum resolution of 0.084 atomic units(a.u.) has been successfully operated at BL14C of the Photon Factory at KEK using 29.5 keV X-rays. In this paper we report Compton profiles of lithium metal above and below its melting point(180°C).

## Experimental

The lithium sample with 5 mm thickness was sandwiched between two sheets of thin stainless-steel foil and was mounted in a vacuum chamber(  $5 \times 10^{-5}$  Torr). Compton profile measurements were done at 20 °C, 160 °C and 210°C, respectively.

## Results and Discussion

The Compton profile  $J(p_z)$  obtained are shown in Fig.1. It should be noticed that a fairly sharp cut-off is recognizable around  $p_z = 0.6$  a.u. in the Compton profile not only for the solid phases but also even for the liquid phase of lithium.

In order to see clearly the change of the electron momentum density upon melting, a difference Compton profile is defined as follows,

$$\Delta J(p_z) = J_T(p_z) - J_{20}(p_z), \quad (1)$$

where T indicates a temperature at which the measurement was done.

The results are shown in Fig.2 together with a corresponding theoretical difference profile based on the free electron model. The Compton profile by the free electron model was calculated with a Fermi momentum deduced from the mass density at each temperature and one free electron per lithium atom.

The experimental  $\Delta J(p_z)$ 's have positive sign around  $p_z = 0$  a.u. and negative around  $p_z = 0.5$  a.u., and then gradually approach to zero. This characteristic feature is well reproduced by the free electron model particularly for the difference profile between 160°C and 20°C(Fig.2(b)). However, the amplitudes of the experimental  $\Delta J(p_z)$  between 210°C and 20 °C are greater than the values predicted by the free electron model(Fig.2(a)). This fact suggests that the electron momentum distribution in liquid lithium metal is further modified by the disorder in the atomic arrangement due to melting.

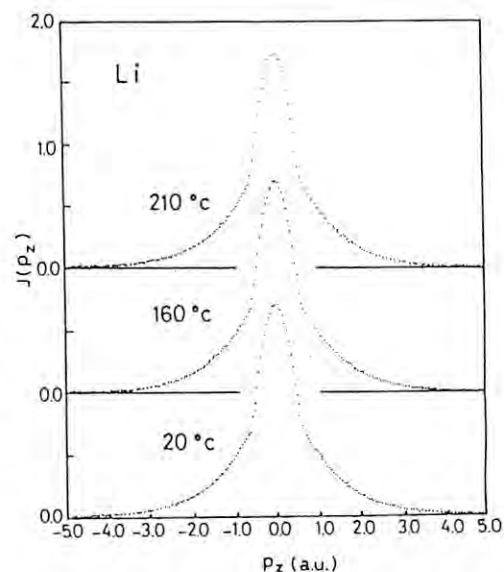


Fig.1. Compton profiles  $J(p_z)$  for lithium metal in the solid state(20°C and 160°C) and in the liquid state( 210 °C).

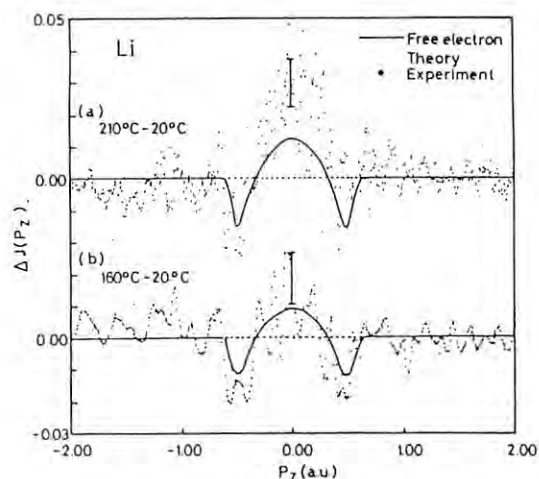


Fig.2. Difference Compton profiles  $\Delta J(p_z)$  between (a)210°C and 20°C, and (b) 160°C and 20°C (see text). The vertical bars indicate statistical uncertainties. The solid lines represent corresponding theoretical curves based on the free electron model.

## High resolution Compton profiles on Al-Li-Cu single quasicrystal.

Y.Tanaka, Y.Sakurai and S.Nanao, N.Sakai\*, M.Ito\*, O.Mao\* and N.Shiotani\*  
H.Kawata\*\*, Y.Amemiya\*\* and M.Ando\*\*

Institute of Industrial Science, University of Tokyo, Minato-ku, Tokyo 106

\*The Institute of Physical and Chemical Research, Wako, Saitama 351-01

\*\*Photon Factory, National Laboratory for High Energy Physics, Tsukuba, Ibaragi 305

## 1. Introduction

Since Al-Mn quasicrystal ( icosahedral phase ) was discovered by Shechtman et al.<sup>1</sup>, the formation of icosahedral phases (i-phase) has been found in many other alloys. And atomic structures of the i-phases have been studied extensively<sup>2,3</sup>. The i-phase of Al-Li-Cu system is obtained in equilibrium and can be made into a single i-phase. A single quasicrystal enables us to study anisotropy of the electronic structure of the i-phase.

In this report, we will present the electron momentum distribution in an Al-Li-Cu single i-phase by high resolution Compton scattering measurements.

## 2. Experimental

A master alloy of  $\text{Al}_{58.8}\text{Li}_{32.0}\text{Cu}_{9.2}$  was prepared by argon arc-melting. The master alloy was set in a boron-nitride crucible and was sealed in a quartz tube with argon gas. The single i-phase of Al-Li-Cu alloy was grown by Bridgman method at a rate of 0.5mm per hour. The size of the single quasicrystal phase was 18mm in diameter and 3mm in thickness. The composition measured by Inductively-Coupled-Plasma spectrometry was  $\text{Al}_{59.3}\text{Li}_{29.3}\text{Cu}_{11.4}$ . The point symmetry was checked by transmission Laue x-ray diffraction. The angles between the five-, three- and two-fold axes were consistent with the icosahedral symmetry.

Compton profiles were measured with an x-ray spectrometer installed at BL14C<sup>4</sup>. The raw profiles were corrected for the background, the energy-dependent Compton scattering cross-section and the detection efficiency of the analyzer and the detector.

## 3. Results

Dots in Fig.1 show the Compton profile  $J(P_z)$  with  $P_z$  (atomic unit) along the five-fold symmetry axis. A solid line in Fig.2 is a calculated Compton profile based on the free electron approximation. The number of free electrons is assumed to be three for Al, one for Li and Cu. The

contributions from the core electrons were assumed to be given by the free atom Hartree-Fock calculations by B.Menselsohn and J.B.Mann. The calculated profile agrees with the experimental results as seen in Fig.1. The experimental and theoretical values of cutoff at the Fermi surface are summarized in Table I.

Table I. The Fermi cutoffs of Compton profile and calculated one.

	$P_z$ (a.u.)
Experimental	$0.825 \pm 0.025$
Calculated	0.835

### [Reference]

1. D.Shechtman, I.Blech, D.Graitis and J.W.Cahn, Phys. Rev. Lett. 53, 1951 (1984)
2. Y.Sakurai, C.Kokubu, Y.Tanaka, Y.Watanabe, M.Masuda and S.Nanao, Mater. Sci. Engrg. 99 423 (1988).
3. S.Nanao, Y.Tanaka, Y.Sakurai, C.Kokubu, Y.Watanabe, M.Masuda, and I.Yasui, Mater. Sci. Engrg., 99 427 (1988).
4. F.Itoh, M.Sakurai, T.Sugawa, K.Suzuki, N.Sakai, M.Ito, O.Mao, N.Shiotani, Y.Tanaka, Y.Sakurai, S.Nanao, H.Kawata, Y.Amemiya, M.Ando, Rev. Sci. Instrum. To be published.

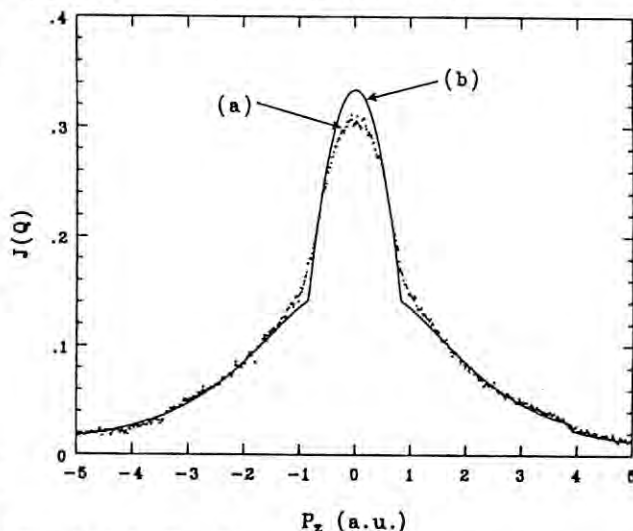


Fig.1 (a) The Compton profile  $J(P_z)$  along the five-fold symmetry axis, (b) The calculated Compton profile.

## Atomic Structure of Icosahedral Al-Mn-Ru-Si

Y.Sakurai, Y.Tanaka, S.Koshiba, O.Tsuda, Y.Watanabe, S.Nanao, #H.Kawata, #M.Ando

Institute of Industrial Science, University of Tokyo, 7-22-1 Roppongi, Minato-ku, Tokyo, 106 Japan

#National Laboratory for High Energy Physics, 1-1 Oho, Tsukuba-shi, Ibaragi-ken, 305 Japan

### 1. Introduction

It is known that the icosahedral phases (i-phase) with especially sharp diffraction peaks are fabricated with addition of Ru atom to Al-Mn-Si. Ru atoms in these i-phases play a role as good markers for the study of the icosahedral structure. In this study, the environmental atomic structures of Ru atom in  $i\text{-Al}_{76}\text{Mn}_{14}\text{Ru}_7\text{Si}_3$  and  $i\text{-Al}_{68}\text{Mn}_{20}\text{Ru}_8\text{Si}_4$  were investigated by X-ray diffraction measurements using the variation of the dispersion factors of Ru atom, and the validity of the model proposed by our group is checked by inquiring the location of Ru atoms in our model.

### 2. Experimental Procedures

The icosahedral single phases of  $\text{Al}_{76}\text{Mn}_{14}\text{Ru}_7\text{Si}_3$  and  $\text{Al}_{68}\text{Mn}_{20}\text{Ru}_8\text{Si}_4$  were fabricated by melt-spinning in a He atmosphere. The diffraction profiles, from  $0.4 \text{ \AA}^{-1}$  to  $20.0 \text{ \AA}^{-1}$ , of the powdered samples were obtained at two incident photon energies, 22.014 keV and 21.722 keV near the Ru K-absorption edge, in reflection geometry.

### 3. Results and Discussion

Figure 1 shows the differential profiles of scattering intensity at two different incident energies. Figure 2 illustrates partial pair distribution functions estimated by Fourier transforms of  $\Delta I(q)$  in Figure 1. The differential intensity profiles and the partial pair distribution functions are quite different between two samples. This fact indicates that the Ru atoms locate at different sites in two samples.

The actual structure model (Ideal model) for icosahedral Al-Mn phase was proposed by our group [1]. The structural framework of the Ideal model is three dimensional Penrose tiling (3DPT). The actual atomic configuration is obtained by decorating the 3DPT with the Mackay Icosahedron (MI) located at 12-fold vertices in 3DPT and the glue atoms

located between the MIs. The MI is  $\text{Al}_{42}\text{Mn}_{12}$  icosahedral cluster and made up of two (inner and outer) Al shells and one Mn shell with icosahedral symmetry. The experimental results are explained quite well by the ideal model where Ru atom occupies at the vertex of 3DPT in  $i\text{-Al}_{76}\text{Mn}_{14}\text{Ru}_7\text{Si}_3$  and the inner icosahedral shell of Mackay Icosahedron (M.I.) in  $i\text{-Al}_{68}\text{Mn}_{20}\text{Ru}_8\text{Si}_4$ .

### Reference

- [1] S.Nanao, Y.Tanaka, Y.Sakurai, C.Kokubu, Y.Watanabe, M.Masuda and I.Yasui, Mater. Sci. Eng. 99(1988)427.

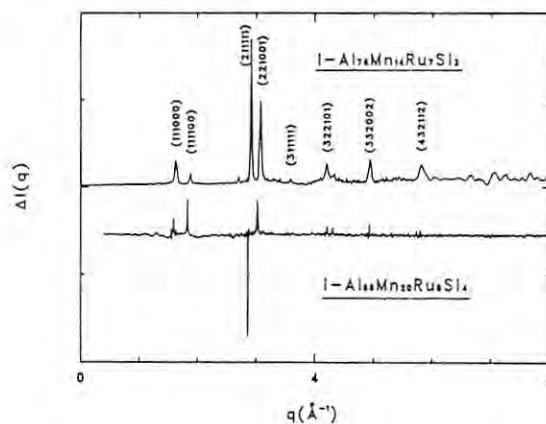


Figure 1

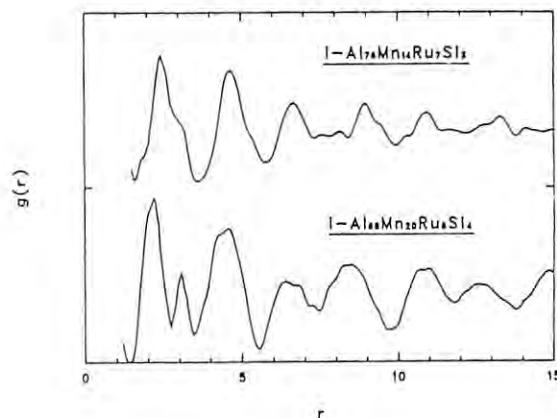


Figure 2

# CHEMICAL EFFECTS ON X-RAY INTENSITY RATIOS OF NUCLEI EXCITED BY SYNCHROTRON ORBITAL RADIATION

Kenji Yoshihara, Harumi Kaji, Tsutomu Sekine, Takeshi Mukoyama,\* Tetsuo Nakajima\*\*

Department of Chemistry, Faculty of Science, Tohoku University, Sendai  
980, \* Institute for Chemical Research, Kyoto University, Uji, Kyoto  
611, \*\* Photon Factory, National Laboratory for High Energy Physics,  
Tsukuba, Ibaraki 305

## Introduction

Chemical effects of X-ray intensity ratio were studied in cases of nuclear decay and particle induced X-ray emission (PIXE) in our laboratory [1, 2]. They can also be studied by synchrotron orbital radiation (SR). We have studied nuclear excitation by SR to apply it to generate X-rays and then to make comparison of their intensity ratios among various chemical states.

Our first approach to the problem is nuclear excitation of an isomer to its metastable state by resonance absorption of photons of suitable energy in SR beams. No positive results have been obtained except the preliminary work [3] of our research group. In this report nuclear excitation of  $^{103}\text{Rh}$  to its metastable isomer  $^{103\text{m}}\text{Rh}$  (half-life: 56m) is described and experimental and calculated integral cross sections are compared.

## Experimental

A disc of natural metallic rhodium (99.9%) with diameter of 13mm and thickness of  $1.18\text{g}/\text{cm}^2$  was irradiated with a white beam at the BL-14c line (Wiggler line) of Photon Factory of the National Laboratory for High Energy Physics (KEK). The target was irradiated for 4h, and then its induced radioactivity was measured with a low-energy photon spectrometer (LEPS) equipped with a pure germanium detector. The counting efficiency of the detector was determined using an  $^{241}\text{Am}$  standard source.

## Results and Discussion

Characteristic K X-ray spectra of the irradiated rhodium target (a) and nonirradiated one (b) are shown in Fig.1. Comparison of the irradiated sample with nonirradiated one leads us to the conclusion that  $^{103\text{m}}\text{Rh}$  is formed by irradiation of the SR beam. The integral cross section of  $^{103}\text{Rh}$  for metastable isomer production by resonance absorption of photons at 295 keV (Fig.2) was found to be  $(2.1 \pm 0.8) \times 10^{-28} \text{cm}^2 \cdot \text{eV}$ . The value was compared with  $(5.3 \pm 2.7) \times 10^{-26} \text{cm}^2 \cdot \text{eV}$  estimated from the previous experimental value  $(2.2 \pm 1.1) \times 10^{-25} \text{cm}^2 \cdot \text{eV}$  at the 1277keV level [4]. The lower value of the experimental integral cross section compared with the calculated one is probably ascribed to uncertainty of the branching ratio of transition from the 295keV level to the metastable level (40keV), which is estimated using a single particle model.

## References

- [1] K. Yoshihara and E. Lazzarini, "Hot Atom Chemistry" (ed. T. Matsuura) Kodansha, Tokyo, p.348 (1984).
- [2] K. Yoshihara et al. "Applications of Ion Beams to Materials Science" (ed. T. Sebe)

Hosei University Press, Tokyo, p.307 (1987).

[3] T. Mukoyama et al. Photon Factory Activity Report 1987, 322 (1987).

[4] K. Yoshihara, Isotopes and Radiation 3, 472 (1960).

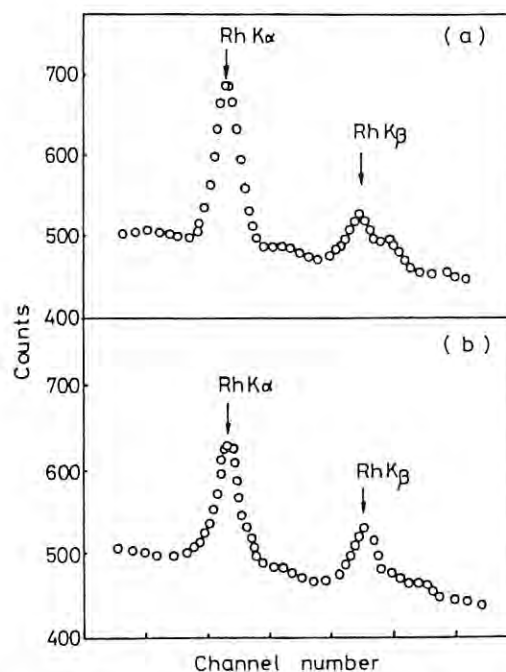


Fig.1. K X-ray spectra of (a) irradiated and (b) nonirradiated samples of Rh.

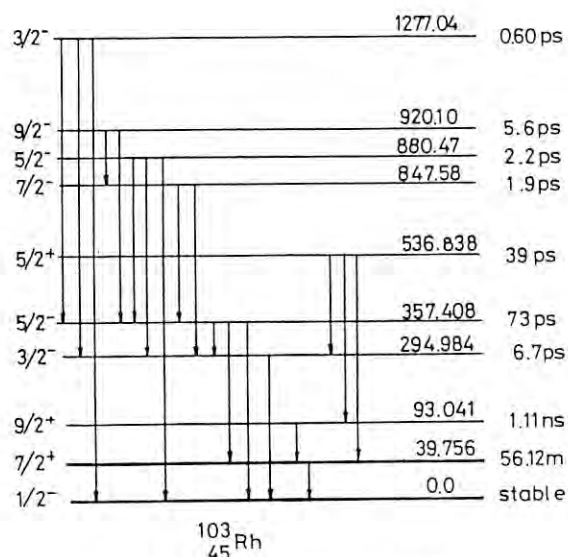


Fig.2. Energy levels of  $^{103}\text{Rh}$ .



## A NEW METHOD FOR DETERMINING DIFFUSION COEFFICIENTS OF POINT DEFECTS BY THE USE OF SR TOPOGRAPHY

Takeo HONDOH, Akira GOTO, Ryoji HOSHI, Takayuki ONO, Hidenori ANZAI and Ryota KAWASE

Department of Applied Physics, Hokkaido University, Sapporo 060, Japan

## I. INTRODUCTION

In the new method, climb motion of dislocations under supersaturation (or undersaturation) of the defects are observed in-situ by high speed X-ray topography. Since X-ray topography allows the use of a thick bulk specimen, a sufficient degree of supersaturation (or undersaturation) is made only by cooling (or heating) of the specimen at an elevated temperature. Although the method was first reported in our previous paper[1], advantage of the synchrotron radiation topography (SRT) is emphasized.

When a temperature of a perfect crystal changes suddenly to a lower one, point defects become supersaturated and move towards free surfaces to attain a lower equilibrium concentration of the defects. According to the theory on dislocation climb, the position of the dislocation  $L(t)$  can be expressed as

$$L_f - L(t) = (L_f - L_0) \exp(-\pi^2 D_x t / d^2) \quad (1)$$

where  $D_x$  is the diffusion coefficient of the point defects in the direction normal to the surface,  $d$  the specimen thickness,  $t$  the annealing time after cooling (or heating) and  $L_0$  and  $L_f$  are initial and final position of the dislocation [1]. Eq.(1) is very useful expression for the measurement; i.e.,  $D_x$  can be determined only from a specimen thickness and climb displacement data without any quantities depending upon minute mechanism of the dislocation climb. This is the most important advantage of the present method.

## II. EXPERIMENTAL RESULTS

The high speed X-ray topography system[2] installed at Photon Factory was used for the present experiments. A typical observation of the dislocation motion carried out using an ice single crystal is shown in Fig.1. The bottom topograph in the figure which was made by subtraction of the upper two topographs shows climb displacements clearly.

In order to obtain a value of  $D_x$  according to eq.(1),  $\ln(L_f - L(t))$  was plotted against time  $t$  in Fig.2. All three plots show straight lines as expected and their gradients are approximately the same. The diffusion coefficient of the self-interstitials in the direction of  $c_2$  axis at  $-4.1^\circ\text{C}$  is determined as  $(1.66 \pm 0.05) \times 10^{-9} \text{ m}^2/\text{s}$ . This value was given by averaging the data on five different dislocations and the error indicated is the mean error of the mean.

## III. DISCUSSION

In the present study, the SR topography was proved to be the powerful tool for determining the diffusion coefficients of point defects; i.e., rapid climb motion can be observed and the displacement can be easily measured by the use of TV system as shown in Fig.1. X-ray TV system is available for 60kW generator also, but it is not useful for the present method because of a long accumulation time for obtaining a topograph image and the poor image contrast. The advantage of the SRT is due to its white spectrum also because no readjustment of the TV camera position is necessary during the heat treatment in spite of a change in Bragg condition.

Although the present method was applied only to ice crystals so far, the method is available for any other crystals. Difficulties in application of the method must be in preparation of a single crystal with an appropriate density of dislocations. In addition, some preliminary experiments on behavior of dislocations should be made by various heat treatment to find out a suitable condition.

## References

- [1] K.Goto, T.Hondoh and A.Higashi: Jpn.J.Appl.Phys., 25(1986)351.
- [2] S.Suzuki, M.Ando, K.Hayakawa, O.Nittono, H.Hashizume, S.Kishino and K.Kohra: Nucl.Instr.Meth. Phys.Res., 227(1984)584.

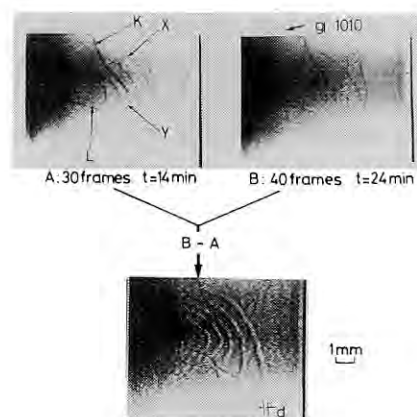


Fig.1 Climb motion of dislocations ; Two topographs, A and B, were reproduced by accumulation of 30 and 40 frames, respectively, from the tape recorded during heat treatment. The projection plane is a basal plane (0001) and the dislocations X and Y have the Burgers vectors  $\mathbf{b} = [0001]$  normal to the plane while the dislocations K and L have the vector  $\mathbf{b} = 1/3[11\bar{2}0]$  parallel to the plane. The bottom photograph shows the processed image subtracted A from B. It is clearly shown that the dislocations X and Y moved a distance  $d$  from a white line to a black one while the dislocations K and L did not move at all.

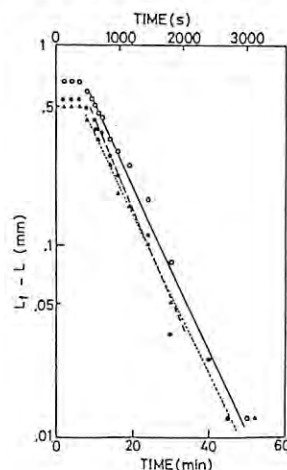


Fig.2  $\ln(L_f - L)$  vs. time plot.

## X-ray Photoacoustic Imaging for Depth Profiling

Tsutomu Masujima<sup>1</sup>, Hideaki Shiwaku<sup>1</sup>, Hideo Imai<sup>2</sup>, Hisanobu Yoshida<sup>1</sup>, Taro Toyoda<sup>3</sup>,  
Yoshiyuki Amemiya<sup>4</sup>, Hiroshi Kawata<sup>4</sup>, Masami Ando<sup>4</sup>

1. Inst. Pharmaceutical Sci., Hiroshima Univ. School of Med., Kasumi, Hiroshima, 734
2. Faculty of Pharmaceutics, Fukuyama Univ., Higashimura-cho, Fukuyama 729-02
3. Dept. of Optoelectronics, Tokyo Kogakuin College of Technology, Sendagaya, Tokyo 151
4. KEK, National Laboratory for High Energy Physics, Oho, Tsukuba, 305

**Introduction** X-ray photoacoustic imaging was proposed and studied with a model sample, i.e. patched metal foils, at 0.5 mm resolution<sup>1)</sup>. Through this study, this method seemed to be useful for a non-destructive 3-dimensional atomic analysis. Phase delay due to the heat diffusion from lower layer X-ray absorption point to the surface will be observed in photoacoustic signal. In order to analyze this phase data and signal amplitude simultaneously at each point of image, our software and apparatus were improved for precise depth profiling.

**Experimental** The focused beam at the Beam Line 15 A was utilized. In our apparatus for X-ray imaging, a X-Z stage and a vibration insulating mount was converted to new rigid one and to a laminated rubber sponge respectively in order to get less scanning noise than before. The phase data and the signal amplitude data at desired area were accumulated on a computer display with the accumulation request order through the console key of our microcomputer.

### Results and Discussion

Figure 1a) shows a scheme of model sample which consists of a Ni foil (20  $\mu\text{m}$  thick) base and two covering poly-ethylene terephthalates (PE) films (1.5-100  $\mu\text{m}$  thick). The photoacoustic image of signal phase was shown in Fig. 1b). The numbers, 1,2,3, attached in the image are the area where the data were accumulated and averaged, and the final averaged values are shown in upper left. The difference between area(2) and area(1) or (3) is the signal phase delay due to the covered PE films. A calibration curve (phase vs. thickness) showed linear relation below 100  $\mu\text{m}$  thickness. Above this region, the phase values showed saturation. Figures 2a,b) shows a scheme of the more practical model sample and its phase image. The

area 3 where 8.5  $\mu\text{m}$  PET film was glued on the Ni foil shows delay at about 14 degree. The thickness of PET layer can be estimated to be 10-16  $\mu\text{m}$  for this delay, and is consistent with the actual value under consideration of glue layer.

The precise photoacoustic images of phase and amplitude seems to disclose the three dimensional distribution of materials. Self-consistent data analysis is most important for fruitful future of this method and is under development.

### Reference

- 1) T. Masujima, H. Imai, et al., Photon Factory Activity Report, 5, 347 (1987).

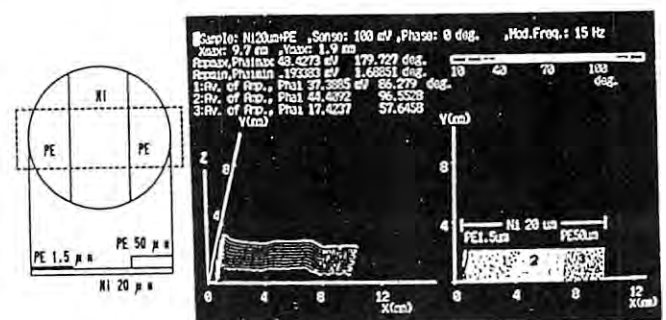


Fig.1 A scheme of a model sample for calibration and its photoacoustic phase image. Mod.freq. 13.5 Hz, 1.485 A X-ray

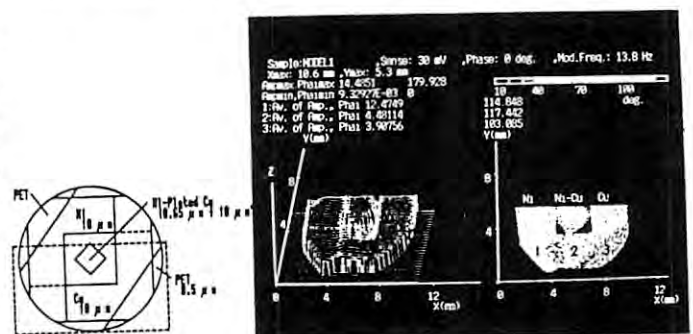


Fig.2 A scheme of a model sample for practice and its photoacoustic phase image. Same condition as in Fig.2.

## X-ray Semi-pulse Photoacoustic Method for Depth Profiling

Tsutomu Masujima<sup>1</sup>, Edward M. Eyring<sup>2</sup>, Hideaki Shiwaku<sup>1</sup>, Hisanobu Yoshida<sup>1</sup>, Hideo Imai<sup>3</sup>,  
Yoshiyuki Amemiya<sup>4</sup>, Hiroshi Kawata<sup>4</sup>, Tomotaro Katsura<sup>4</sup>, Katsumi Kobayashi<sup>4</sup>, Masami Ando<sup>4</sup>

1.Inst. Pharmaceutical Sci., Hiroshima Univ. School of Medicine, Kasumi, Hiroshima 734

2.Department of Chemistry, University of Utah, Salt Lake City, 84112, USA

3.Faculty of Pharmaceutical Sci., Fukuyama Univ., Higashimura-cho, Fukuyama 729-02

4.Photon Factory, National Laboratory for High Energy Physics, Oho, Tsukuba 305

Phase analysis was adopted for depth profiling in X-ray photoacoustic methods and fruitful results were obtained in the photoacoustic EXAFS and imaging<sup>1,2)</sup>. On the other hand, one more useful way is the pulse method which analyze the response of photoacoustic signal on a pulse-wise X-ray irradiation onto samples. The synchrotron radiation is essentially pulsed at psec or nsec order. However, it is so fast for the photoacoustic response that the synchrotron radiation X-ray was chopped pulse-wise by a rotating blade at audio frequencies. Thus we call this pulse hereafter as "semi-pulse". Fundamental studies were performed using focused beam at the Beam Line 15A and 10C.

**Experimental** An circle blade which has two slits( $12^\circ \times 2/360^\circ$ ) along its peripheral was rotated at 9 and 49Hz. The response signal was averaged by a digital storage oscilloscope. A layer sample consists of a Ni foil (20  $\mu\text{m}$  thick as base materials) and a glued polyethylene terephthalates(PET) film at various thickness on the Ni foil. The experimental setup was similar to that of imaging method<sup>2)</sup>.

### Results and Discussion

Figure 1 shows the signals at 9 Hz for base materials, Ni foil(20  $\mu\text{m}$  thick) and PET film(75  $\mu\text{m}$  thick). The signal for the Ni foil shows higher amplitude than that of PET, depending on their absorption coefficients, and shows slower decrease after the irradiation cut off. Since X-ray absorption length is close to its thickness, this slowness means the heat diffusion from the sub-layer of the Ni foil. In contrast, PET showed rapid decrease due to small amount of generated heat and slow heat conductivity in the sample. Figure 2 shows the coupled model layer sample, i.e. PET(75  $\mu\text{m}$  thick) coated Ni(20  $\mu\text{m}$  thick) foil. After a

sharp rise-up due to the surface PET, a broad shoulder is seen overlapping on the signal. This shoulder is due to the heat diffusion from lower layer, Ni foil. By the subtraction of the PET signal from this signal shape, 0.031 sec delay was observed for Ni signal. This delay due to the heat diffusion gives the estimation of 97  $\mu\text{m}$  thickness for the coated PET layer. It is consistent with the value of 75  $\mu\text{m}$  PET thickness under consideration of thickness of glue layer. This study shows that the heat conductivity or depth of surface layer can be analyzed by this method. Digitized data handling of data, and theoretical approaches are under development.

### References

- 1)T.Masujima, H.Kawata et al., Photon Factory Activity Report, 5,139 (1987), & 6 (1988) in press.
- 2)T.Masujima, H.Imai et al., Photon Factory Activity Report, 5,347 (1988), & 6 (1988) in press.

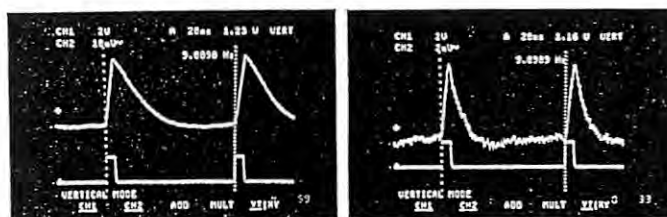


Figure 1. X-ray semi-pulse photoacoustic signals for a Ni foil (20  $\mu\text{m}$  thick) (left), and for a PET film (75  $\mu\text{m}$  thick) (right). Frequency 9 Hz; X-ray 1.485  $\text{\AA}$  (above Ni K-edge).

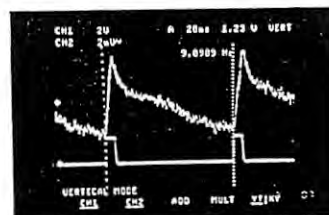


Figure 2. X-ray semi-pulse photoacoustic signal for PET(75  $\mu\text{m}$  thick) coated Ni foil (20  $\mu\text{m}$  thick). Same conditions as in Fig.1.



## FOCUSING OF SYNCHROTRON RADIATION BY A CYLINDRICAL MULTILAYER BRAGG-REFLECTOR

Hisataka TAKENAKA, Yasuji MURAMATSU, Hiroo HASHIZUME\*, Hidetoshi TAKAOKA, Yoshikazu ISHII, Hiroshi KAWATA\*\*, Osami SAKATA\*, Ichiro MINATO\*

NTT Applied Electronics Laboratories, Midori-cho, Musashino-shi, Tokyo 180

\*Research Laboratory of Engineering Materials, Tokyo Institute of Technology, Nagatsuta, Midori-ku, Yokohama 227

\*\*Photon Factory, National Laboratory for High Energy Physics, Oho-machi, Tsukuba-shi, Ibaraki 305

### I Introduction

Curved Bragg-reflectors for focusing Synchrotron Radiation (SR) are widely used in X-ray lithography and X-ray and X-UV analysis. Synthetic multilayered films are superior to bent crystals owing to their controllable structure parameters and wide band-passes in hard and soft X-ray regions. We report here the focusing of SR with a multilayered tungsten-carbon film prepared on a cylindrical surface.

### II Experiments

The Bragg-reflector consists of 40 pairs of 16 Å-thick tungsten and 24 Å-thick carbon layers deposited on a figured fused quartz substrate surface by RF magnetron sputtering. The substrate has an optically smooth 50 x 50 mm<sup>2</sup> surface with a 46 mm radius in one direction. Examinations using a surface profiler show that over the entire surface the film thickness is uniform within  $\pm 1$  %. Measurements with CuK $\alpha$  X-rays showed a first-order Bragg reflection from the multilayer with a 30 %, in good agreement with calculations including the affect of the film surface roughness evaluated by the surface profiler.

The focusing properties of the multilayered film were examined at beamline 15B of the Photon Factory. The experimental configuration is shown in Fig.1. SR from a normal bending magnet was reflected in the vertical plane by a silicon (111) monochromator to extract a beam of 1.5 Å from the source spectrum. The obtained beam was limited in size to 54 mm wide and 6mm high, and directed onto the multilayer Bragg-reflector located 38.7m from the light source point. X-ray films placed at various distances from the Bragg-reflector recorded images of the diffracted beam. The photon

flux in the beam was also measured using a scintillation counter.

### III Results

Figure 2 shows an image of the focused beam on a near-focal plane at 1.1 m from the Bragg-reflector. The lower image shows a diffracted beam, which is 4 mm wide and 8 mm high. This is slightly larger than the preeliction of a ray-tracing calculation, assuming a light-source size 10 mm wide and 1.36 mm high in  $4\sigma$ . The observed larger focus and unusual asterisk shape are thought to arise from the non-ideal surface figure of the fabricated Bragg-reflector, which causes focusing aberration. The focused beam intensity was found to be six times higher than the non-focused direct beam from the silicon monochromator. Furthermore, the observed variation of the beam size and shape over various distances are in qualitative agreement with the ray-tracing calculations.

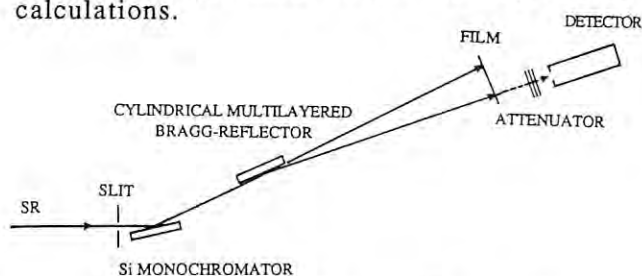


Fig.1. Experimental configuration.

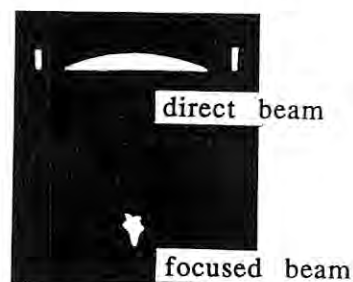


Fig.2. Observed images.



## X-RAY CHARACTERIZATION OF (1-x)InAs-xAlAs ALLOY FILMS GROWN ON InP SUBSTRATES

Osamu NITTONO, Masao IRIKURA, Hiroshi SUGIYAMA, Hiroyuki HOSHIYA and Saburo SHIMIZU\*

Department of Metallurgy, Tokyo Institute of Technology,  
O-okayama, Meguro-ku, Tokyo 152

\* ULVAC Corporation, Hagisono, Chigasaki, Kanagawa 253

Introduction

In the previous report, the features of lattice mismatches in the InAlAs/InP system alloy wafers prepared under various MBE growth conditions were investigated and discussed on the basis of the preparation conditions such as practical operating pressure of P(As<sub>4</sub>) and film compositions evaluated by a photoluminescence(PL) method at 77K. X-ray measurement of the lattice spacing was so effective that the film composition could be evaluated on the basis of the Vegard's law for the (1-x)InAs-xAlAs alloy system. This indicates that the X-ray method is a powerful tool for characterization of films grown on substrates, although X-ray transmission topographic observation was not successful for detection of misfit dislocations because of the use of thin film (0.4  $\mu$ m) and thick InP substrate (0.35mm). In the present study the features of reflection profiles are investigated in detail to characterize the lattice mismatches in the InAlAs films on the InP substrates, and film structure is discussed from the results obtained.

Experimental

InAlAs/InP specimens were the same as those in the previous study. Reflection profiles from both the substrate and the film were measured by means of X-ray double-crystal diffractometer with a nearly perfect InP monochromator. The (+,-) setting was usually used to measure X-ray reflection profiles from the specimens. In order to estimate the lattice distortion of films, the full width at half-maximum (FWHM) of the peak was evaluated from each rocking curve.

Experimental Results and Discussion

Figure 1 shows full widths at various peak heights of the rocking curve profile diffracted from the InP substrates for all the specimens. The film of the specimen A, which was prepared under a high As pressure, shows a small deviation from the lattice spacing of the InP substrate, and the InP substrate shows the widest FWHM of reflection profile among the specimens examined. From the previous study, it was found that this wide FWHM was due to mainly the wafer bending caused by a film epitaxially grown on the substrate. On the other hand, the films on the specimens (B, C and D) have smaller lattice spacings than that of the specimen A, and corresponding substrates show smaller FWHM's of reflection profile. If a film is grown epitaxially on the InP substrate without discontinuity of film, the film/substrate will be bent elastically to compensate a tensile stress due to the difference in lattice spacing. In the present case, the bendings of the specimens (B, C and D) will be larger than that of the specimen A. However, observed small FWHM's result in small bendings of the film/substrate. The above dif-

ference can be explained by a hypothesis that the films on the specimens (B, C and D) are not continuous and are grown locally on the InP substrates. Since epitaxially grown films having lattice mismatches are attributed to wafer bending, in the case of discontinuous film growth, a measurable amount of bending and thus the FWHM of reflection profile from the InP substrate are related with parts where films are grown epitaxially on the InP substrates. Observed small bending may be resulted from such a discontinuous film growth. This is consistent with the fact that the epitaxial films grown on the InP substrates, when they have larger lattice mismatches than  $4 \times 10^{-3} [(a_s - a_f)/a_s]$ , show no smooth surface under an optical microscope. As additional evidence, SR X-ray Laue topographic images taken from the specimen D showed partly discontinuous regions accompanied with some lattice distortions, although the InP substrate also contained a lot of dislocations. Based on the above results, we are now trying to improve growth conditions.

Table: X-ray Characteristics of InAlAs/InP wafers

specimen	x	spacing d (400)	FWHM	$(a_s - a_f)/a_s$
A	0.5532	1.4595	18.5"	$2.62 \times 10^{-3}$
B	0.6037	1.4544	13.7"	$4.30 \times 10^{-3}$
C	0.6579	1.4490	15.5"	$6.0 \times 10^{-3}$
D	0.6926	1.4456	12.5"	$8.0 \times 10^{-3}$
InP	—	1.46718	11.5"	—

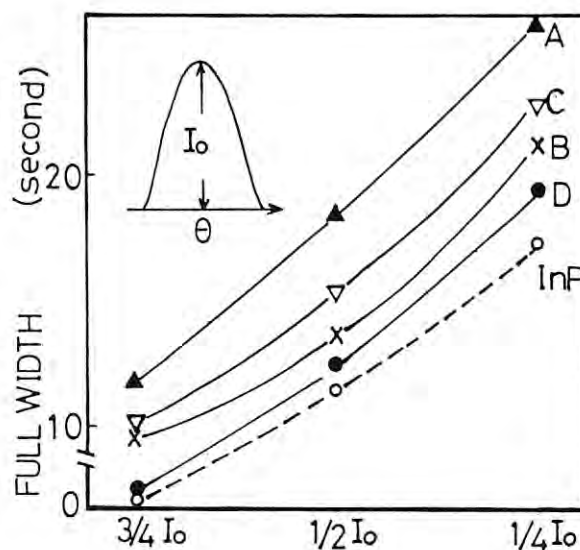


Fig. 1 FWHM's at various heights of the peak.

# EFFECTS OF GROWTH INTERRUPTION ON STRUCTURE OF MBE GROWN GaAs/AlAs HETERO-INTERFACES STUDIED BY X-RAY DIFFRACTION

S.KOSHIBA, S.NANAO, O.TSUDA, Y.WATANABE, Y.SAKURAI, H.SAKAKI  
and  
\*H.KAWATA, \*M.ANDO

Institute of Industrial Science, University of Tokyo,  
7-22-1 Minato-ku Roppongi, 106 Japan

\*National Laboratory for High Energy Physics,  
1-1 Oho, Tsukuba-Shi, Ibaraki-Ken, 305 Japan

## 1. Introduction

The quality of the hetero-interfaces has significant effects on the performance of the hetero-structure devices and the realization of good interfaces and precise periodicity has been one of the major targets for the molecular beam epitaxy (MBE). In this study, the precise X-ray diffraction measurements were carried out for GaAs/AlAs samples to investigate the effects of 'Growth-Interruption' which is reported by the photo luminescence study to improve the quality of the superlattice structure.

## 2. Experimental

Two superlattice samples (denoted as A and B) with the same  $(\text{GaAs}_6/\text{AlAs}_2)_{120}$  structure were prepared by MBE in a RIBER 2300 system under the monitor of in-situ RHEED oscillation. The sample A was made to undergo 'Growth-Interruptions' at every AlAs/GaAs and GaAs/AlAs hetero-interfaces with periods of 60 sec and 30 sec, respectively.

The (002) and (004) peaks, the +1st and -1st superlattice satellite peaks were measured for  $\langle 001 \rangle$  scanning direction.

## 3. Results and Discussions

Fig.1a and 1b show the profiles of the -1st peak for both of samples A and B measured at the X-ray energy of 10.15keV. There observed two effects of the 'Growth-Interruption'; 1) The distance between the +1st peak and the -1st peak of samples A and B are 0.0430 and  $0.0409\text{\AA}^{-1}$ , respectively. From these values, the periods of a superlattice for samples A and B are estimated to be 8.22 and 8.65 layers, respectively. The period of superlattice had been apparently shortened by the 'Growth-Interruption'. 2) The satellite peaks of sample B are split into several sub-peaks, as shown in Fig.1b, whereas those of sample A are not split.

The difference of an average superlattice period between samples A and B is probably attributed to the re-evaporation of Ga atoms during the waiting time in the 'Growth Interruption'[1]. Further investigation is necessary for this problem.

The satellite profiles were calculated for the model with multiple periods which had been decided by a Monte Carlo simulation, and also for the model with Ga and Al atoms

inter-diffused at the hetero-interfaces.

From the results of calculations, the model with inter-diffused Ga and Al atoms were denied and the cause of the splits of the satellite peaks is attributed to the existence of irregular distribution of superlattice periods[2]. The fluctuation of the period in a small domain was found to bring no splittings as long as the average period in each domain is kept constant. Thus, the actual superlattice structure of the present (Ga,Al)/As samples is pictured as a mosaic which is composed of multiple domains with different periods and the 'Growth Interruption' reduces the size of domain as well as the fluctuation of the period to improve the periodicity as a total.

## References

- [1] S.Koshiba, S.Nanao, H.Sakaki, M.Masuda, Y.Watanabe, O.Tsuda, H.Kawata and M.Ando : Proc. of JIMIS-5 1988 (The Japan Inst. of Metals), in press.
- [2] S.Koshiba, S.Nanao, H.Sakaki, O.Tsuda, Y.Watanabe, H.Kawata and M.Ando : MBE-V 1988, in press.

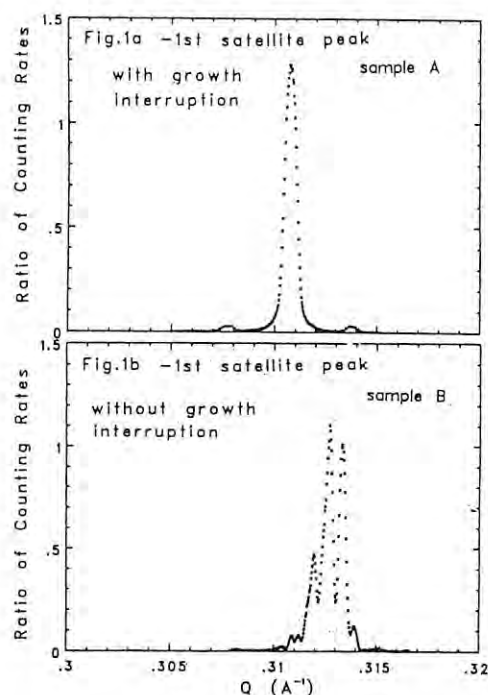


Fig.1 The -1th satellite peaks along the  $\langle 001 \rangle$  direction. (a) with and (b) without growth interruption.

## DIRECT OBSERVATION OF DISLOCATIONS IN SOLID HELIUM-4 BY X-RAY TOPOGRAPHY

Hideji SUZUKI, Izumi IWASA<sup>+</sup>, Tetsuo NAKAJIMA<sup>++</sup>, and Ichiro YONENAGA<sup>+++</sup>,

Tokyo Engineering University, Katakura, Hachioji, Tokyo 192

<sup>+</sup>Fundamental Technology Research Lab. Fuji-Xerox Co. Ltd., Ebina, Kanagawa 243-04<sup>++</sup>KEK, National Laboratory for High Energy Physics, Tsukuba, Ibaraki 305<sup>+++</sup>Institute for Materials Research, Tohoku University, Sendai 980Introduction

The dislocation image in X-ray topography of solid helium reported previously<sup>1,2)</sup> was very faint and ambiguous. We repeated observations using a slit in 0.017 mm width in order to improve the image contrast of dislocations. The other parts of equipment used in this experiment are the same as that reported in a previous activity report<sup>3)</sup>.

Results and Discussions

Figure 1 shows the change in low magnification topographs of bcc  $^4\text{He}$  during isothermal annealing. The topograph (b) was taken 1 minute after (a). The nearly horizontal white band is a small angle boundary. The misorientation at the boundary is about 5 minutes and the boundary did not move between (a) and (b). The oblique stripes are shadows of scratches at the edges of the slit. White or black narrow bands with varying width are small angle boundaries with the misorientation smaller than 1 minute or dislocation groups gathered to form small angle boundaries. These small angle boundaries or dislocation groups moved between (a) and (b). Irregular white patterns without sharp edges change the position and configuration considerably between (a) and (b). These white patterns can move and change the shape without change the surrounding structure. Therefore, we conclude that these patterns indicates high density dislocation groups.

As mentioned in the previous activity report, the image contrast of a dislocation in solid helium can be discussed by kinematical diffraction theory. Kinematical theory predicts white and black contrast of the dislocation image. This kind of contrast is observed in the vicinity of a small angle boundary, and an example is shown in Fig. 2. Vacancy concentration near a boundary is nearly in thermal equilibrium and a dislocation does not need to absorb or emit a large amount of vacancies. Therefore around the grain boundary dislocations are rather straight and the distance between neighboring dislocations is sufficiently large in comparison with the width of dislocation core, which scatters X-rays and does not contribute to the diffraction intensity. Meanwhile, dislocations in regions of whitish patterns are helical as mentioned previously, and dislocation cores are superposed to each others and only white contrasts are observed.

References

- 1) H. Suzuki, I. Iwasa and T. Nakajima: Proc. LT18, JJAP 26, Suppl. 26-3 (1987) 405.
- 2) H. Suzuki et al.: Photon Factory, Activity Report #5 (1987) 353.

3) I. Iwasa et al.: Photon Factory, Activity Report #4 (1986) 320.

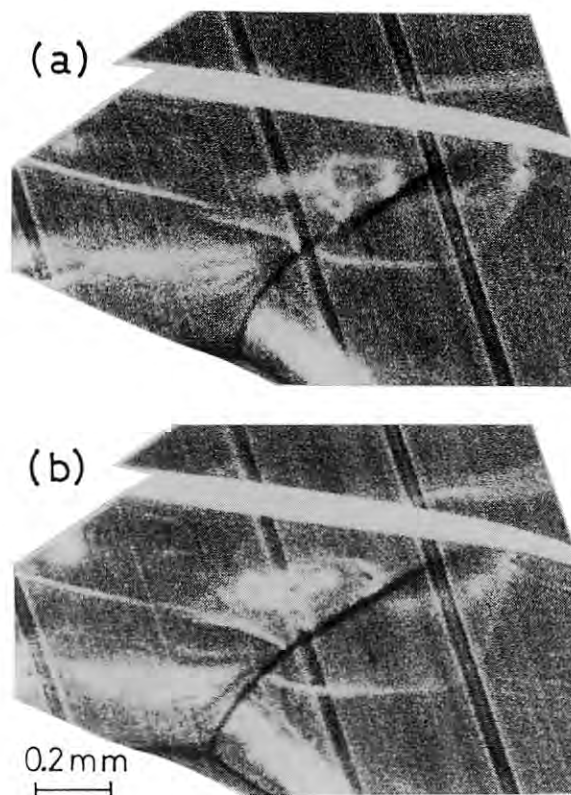
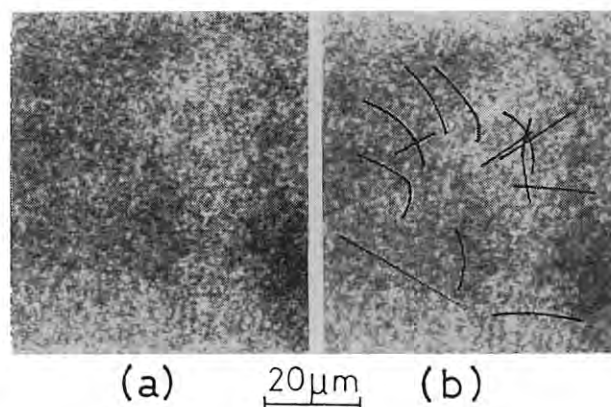
Fig. 1 Change of the topograph of bcc  $^4\text{He}$  by 1 minute annealing.

Fig. 2 Dislocation contrast of rather a straight dislocations. Curves drawn in (b) shows positions of dislocations.



SECTION TOPOGRAPHY USING A HIGH-ORDER REFLECTION AND ITS APPLICATION

Yoshimitsu SUGITA, Satoshi IIDA, Hiroshi TAKENO, Yasuyoshi YAGOU, and Hiroshi KAWATA\*

Department of Physics, Toyama University, 3190 Gofuku, Toyama 930

\*Photon Factory, National Laboratory for High Energy Physics, Tsukuba, Ibaraki 305

We have measured the static Debye-Waller factor (DWF) of silicon crystals by analyzing the Pendellösung fringes in a section topography.1)2)3) We tried in this investigation the section topography with an extremely large scattering vector, such as 18 18 0 or 24 0 0, using synchrotron radiation from a vertical wiggler.

Experiments were carried out using 0.4 Å x-ray beam monochromated with a triangle-shaped silicon bent monochromator in asymmetric 111 reflection. Section topographs were taken in the 440 to 18 18 0 and 800 to 24 0 0 reflections and recorded on a nuclear plate or imaging plate. (001) silicon crystals with 3.2 mm in thickness were used. The exposure times were varied from 0.5 min to 8 h for nuclear plate and from 1 s to 15 min for imaging plate, depending upon the reflection used, the width of the slit, and the degree of crystalline perfection of the crystals. Various silicon crystals were examined; as-grown FZ crystals, as-grown MCZ crystals, MCZ crystals heat treated at 650°C for 500 h, and as-grown and heat treated FZ crystals with D-defects which supposed to be vacancy agglomerates.

Fig.1 shows the dependence of the static DWF on the square of scattering vectors for samples, as-grown FZ, as-grown MCZ and heat treated MCZ crystals. For MCZ crystal heat treated at 650°C for 500 h, linear relationship was observed up to 18 18 0 reflection. Assuming precipitates to be of disc shape with 40 Å thick, it was concluded that precipitates with radius of 77 Å and density of  $2.5 \times 10^{13}/\text{cm}^3$  were formed. There was no substantial difference among as-grown FZ, as-grown MCZ and MCZ heat treated at 450°C for 750 h. Fig.2 represents the ratio of the kinematical to dynamical scattering intensity as a function of the square of the scattering vector.

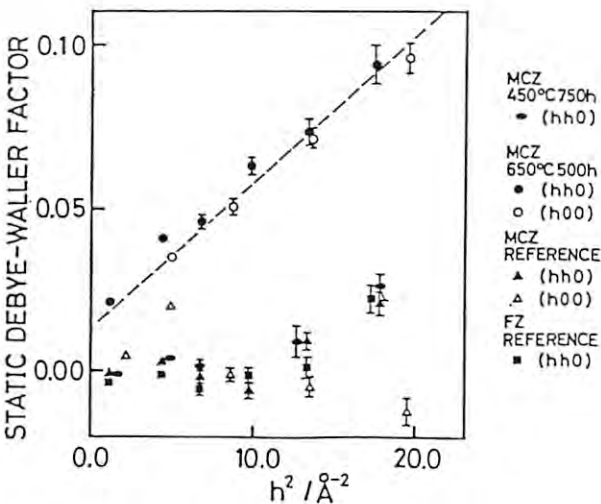


Fig.1 Static Debye-Waller factors of various silicon crystals

Fig.3 is a section topograph of the FZ crystal having V-region (D-defects). We can recognize the difference in the period of the Pendellösung fringes between V-region containing vacancy agglomerates and I-region (microprecipitates of oxygen remaining as a trace impurity) or A- and B-swirl regions. This finding indicates that V-region is more strained with respect to other regions.

References

- 1) Y.Sugita et al.:Jpn.J.Appl.Phys.26(1987)1903.
- 2) S.Iida et al.:Jpn.J.Appl.Phys.27(1988)1081.
- 3) Y.Sugita et al.:Photon Factory Activity Report (1987)p.354.

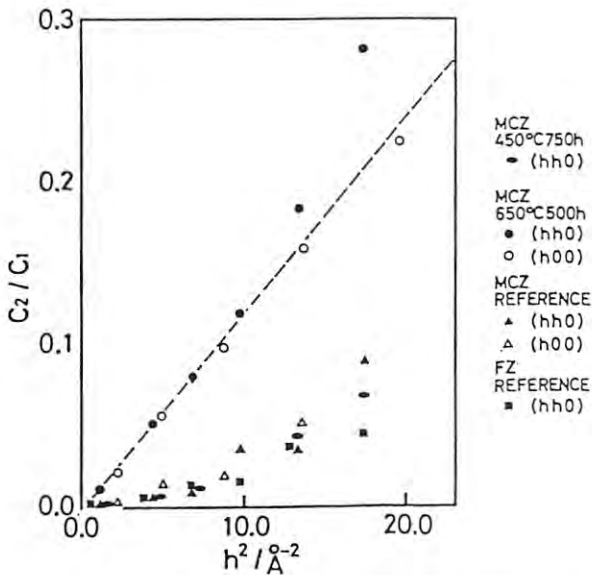


Fig.2 Ratio of kinematical to dynamical scattering intensity of various silicon crystals

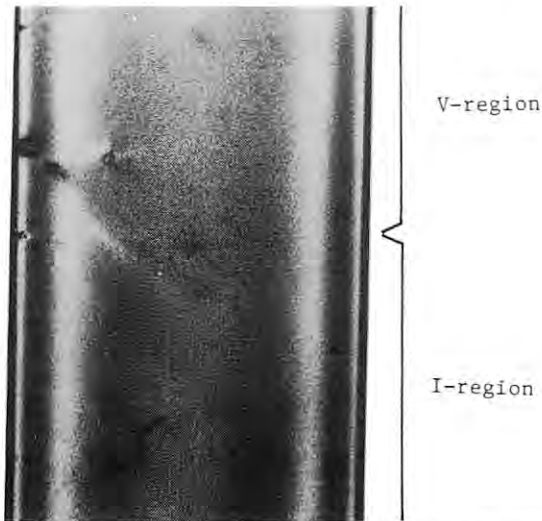


Fig.3 (14 14 0) topograph of as-grown FZ crystal



# DYNAMICAL OBSERVATION OF LATTICE DEFECTS IN NEARLY PERFECT ALUMINUM SINGLE CRYSTALS

Takao KINO, Kaoru MIZUNO\*, Kazuhiro TANAKA and Hiroshi KAWATA\*\*

Laboratory of Crystal Physics, Faculty of Science, Hiroshima University,  
Hiroshima 730

\* Department of Physics, Faculty of Science, Shimane University, Matsue 690

\*\* Photon Factory, National Laboratory for High Energy Physics Oho-machi,  
Tsukuba-gun Ibaraki 305

## Introduction

Thermal generation of vacancies in nearly perfect metal crystals has been studied by X-ray topography using a micro-focus X-ray apparatus, and a new generation mechanism was proposed. It is vacancy generation from interstitial type dislocation loops which were formed in nearly perfect lattice by a temperature rise. However, the origin of the interstitial loop is not clear, because it takes a long time to take a Lang topograph using a conventional X-ray source. Main purpose of this work is to make clear the formation mechanism of these interstitial type dislocation loops.

## Experimental

Specimens used in the present work were prepared from zone-refined aluminum (99.9999%) by a strain-annealing method in vacuum. The dislocation density of these crystals was decreased by a cyclic annealing between 270 and 100°C, and the final density was less than  $1 \times 10^3 \text{ cm}^{-2}$ . These specimens were mounted in an electric furnace settled on the goniometer head of Lang camera. The temperature of specimen was raised to 250°C by the heating rate of 500°C/h, and was kept at the temperature for 30 hours. During the heating procedure, the diffraction image was observed continuously, and several Lang topographs were taken at a suitable time interval.

## Results and Discussion

Topographs taken after the temperature rise are shown in Fig.1, and the denoted time below the picture is the time passed after the temperature rise. Black dots are not observed just after the temperature rise, and appeared several ten minutes later, and the number density arrives to the maximum value of  $3 \times 10^5 \text{ cm}^{-3}$  1 or 2 hours latter as seen in Fig.2. It should be emphasized that a fairly time is necessary for the appearance of interstitial type dislocation loops.

For the comparison a similar plots, which was obtained using a conventional X-ray source before, is shown in Fig.3. In this case, the temperature was raised to 200°C, and the number density of black dots holds at  $4-5 \times 10^5 \text{ cm}^{-3}$  for several hundred hours. From these experimental facts, the origin of interstitial loops seems to be due to the heterogenous nucleation mechanism.

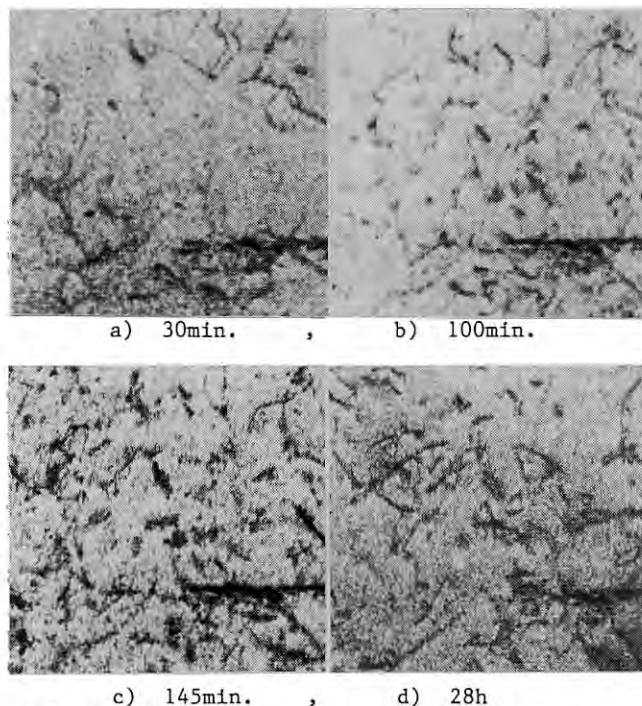


Fig.1

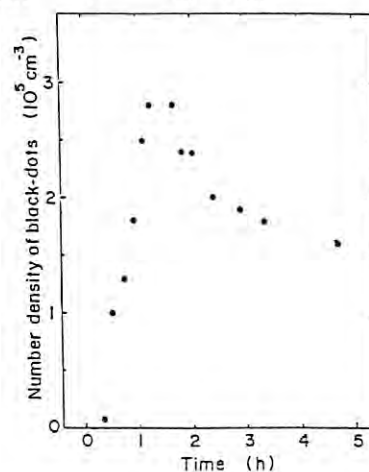


Fig.2

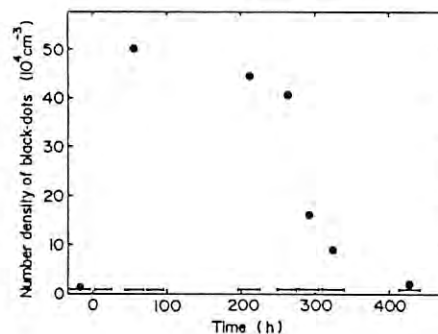


Fig.3

# ORTHORHOMBIC TO TETRAGONAL PHASE TRANSITION IN HIGH $T_c$ SUPERCONDUCTOR $YBa_2Cu_3O_{7-y}$ UNDER HIGH PRESSURE

Nobuo Mōri, Hiroki Takahashi, Yuuji Miyane, Junichi Susaki, Chizuko Murayama, Yutaka Ueda\*, Koji Kosuge\*, Osamu Shimomura\*\*, and Takumi Kikegawa\*\*\*

Institute for Solid State Physics, University of Tokyo, Roppongi, Minato-ku, Tokyo 106

\* Department of Chemistry, Faculty of Science, Kyoto University, Kitashirakawa, Sakyo-ku, Kyoto 606

\*\* National Institute for Research in Inorganic Materials, Sakura, Tsukuba 305

\*\*\* Photon Factory, National Laboratory for High Energy Physics, Oho, Tsukuba 305

## Introduction

It has been revealed that oxygen deficiency strongly affects not only the superconducting transition temperature of  $YBa_2Cu_3O_{7-y}$  but also the orthorhombic to tetragonal phase transition. For instance, the oxide with  $y=0.2$  shows the superconducting behavior below the temperature of about 92 K having an orthorhombic structure, though the oxide with  $y=1.0$  showing a tetragonal structure exhibits antiferromagnetic properties rather than superconductivity. In air the orthorhombic to tetragonal phase transition with  $y=0.2$  occurs near 700 C due to the disordering of oxygen atoms at the one-dimensional chains into the vacant sites (1,2). On the otherhand, the superconducting transition temperature increases with increasing pressure. In order to investigate the relation between the superconductivity and the structural phase transition, in situ X-ray powder diffraction measurements as functions of temperature and pressure have been done.

## Experimental and Results

The experiment was carried out on AR line using a cubic-anvil apparatus (MAX80). A powder sample of  $YBa_2Cu_3O_{7-y}$  was wrapped in a Pt sheet of 0.02 mm thick to avoid deoxidizing atmosphere. Temperature-dependent, X-ray powder diffraction data were collected using a Ge SSD at various pressures. Figure 1 shows diffraction patterns for the (033), (130) and (310), (303) lines at the pressure of 30 kbar as the temperature increases. Clearly a double peak was observed becoming a single peak at around 940 C with increasing temperature where the orthorhombic to tetragonal phase transition takes places. In Fig.2 the phase transition points obtained from the preliminary data are plotted tentatively as a function of pressure. The transition temperature increases with increasing pressure. This result is consistent qualitatively

with that expected from the difference in volume between the orthorhombic and tetragonal structures. It seems, however, that the phase transition is caused primarily by the disordering of oxygen atoms on the chain sites when one considers the change of atomic distances between the oxygen atoms under high pressure. Further experimental and analytical studies are in progress.

## References

- 1) J. D. Jorgensen et al., Phys.Rev.B 36, 3608 (1987)
- 2) Y. Nakabayashi et al., Jap. J. Appl. Phys. 27, L64 (1988)

Figure 1. Temperature-dependent, diffraction patterns for (033), (130), (310), and (303) lines at 30 kbar.

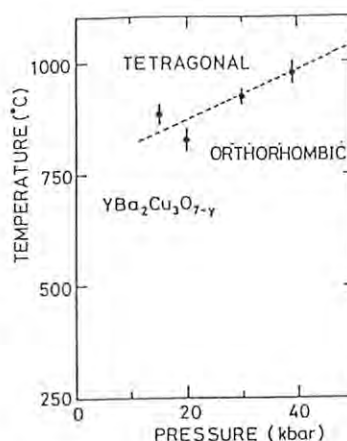
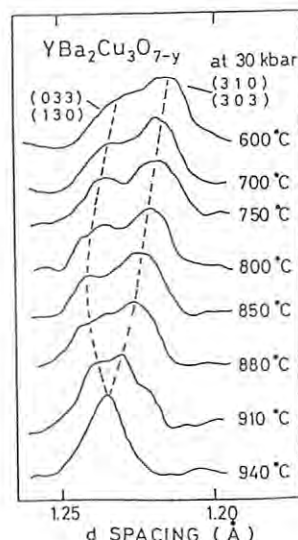


Figure 2. Orthorhombic to tetragonal phase transition as a function of pressure.

# HIGH PRESSURE AND TEMPERATURE GENERATION WITH A MULTIPLE ANVIL SYSTEM USING SINTERED DIAMOND ANVILS

E.Ohtani<sup>1</sup>, W. Utsumi<sup>2</sup>, O. Shimomura<sup>3</sup>, N. Kagawa<sup>1</sup>, T. Yagi<sup>2</sup>, M.Togaya<sup>4</sup>, A. Yoneda<sup>5</sup>, H. Sawamoto<sup>5</sup>, E. Ito<sup>6</sup>, T. Katsura<sup>6</sup>, A. Onodera<sup>4</sup>, K. Suito<sup>4</sup>, A. Matsumuro<sup>5</sup>, H.Hashizume<sup>5</sup>, S. Tanaka<sup>5</sup> and T. Kikegawa<sup>7</sup>

<sup>1</sup>Ehime University, Matsuyama 790, Japan

<sup>2</sup>ISSP Roppongi, Tokyo 106, Japan

<sup>3</sup>NIRIM, Tsukuba 305, Japan

<sup>4</sup>Osaka University, Osaka 560, Japan

<sup>5</sup>Nagoya University, Nagoya 464, Japan

<sup>6</sup>Okayama University, Misasa 682-02, Japan

<sup>7</sup>KEK-PF, Tsukuba 305, Japan

## Introduction

In order to extend the pressure range generated by the MA8 type multiple anvil device and to conduct *in situ* X-ray diffraction study at high temperature and above 20 GPa, it is essential to develop the multiple anvil device with sintered diamond anvils. In this project, we made reconnaissance work on high pressure and temperature generation by using sintered diamond anvil MA8/MAX80 system.

## Experiments

Sintered diamond cubes (4.85 mm cube, De Beers SYNDAX L555) were used for the anvils. The truncated edge lengths (TEL) of the anvils are 0.5 and 1.0 mm.

The configuration of the furnace is shown in figure 1. The pre-formed gaskets made of pyrophyllite were used for some high temperature runs. The twin plate heater and thermocouple were placed in the center of the pressure medium as shown in this figure. We tested various heating materials, such as graphite, nichrome metal, mixtures of TiC and diamond, and WC and diamond. Various materials were tested also for electrical leads; such as copper, molybdenum, stainless steel, and semi-sintered TiC. The Pt-Pt13%Rh and W3%Re-W25%Re thermocouples with a diameter of 0.1 mm was used for temperature measurements. The starting materials used are a mixture of gold and forsterite  $\text{Mg}_2\text{SiO}_4$ , and diopside  $\text{CaMgSi}_2\text{O}_6$ .

## Results

The pressure of 41 GPa was achieved with by the device with 0.5 mm edge-anvil; whereas pressures up to 28 GPa were generated by that with 1.0 mm edge-anvil in the press loads less than 100 tons. The high temperature generation was conducted at around 20-25 GPa. The temperature around 1000°C was achieved in the present furnace system at these pressures. Figure 2 shows the typical temperature versus power relationships in the present experiments.

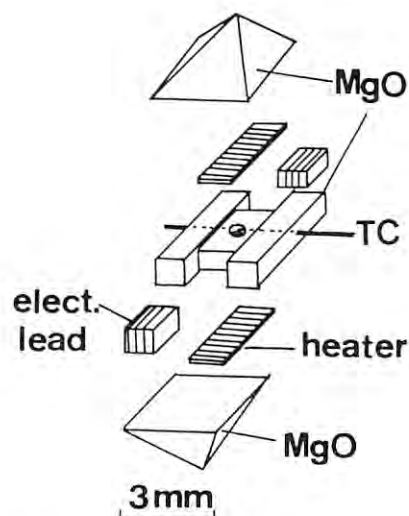


Figure 1. The furnace assembly

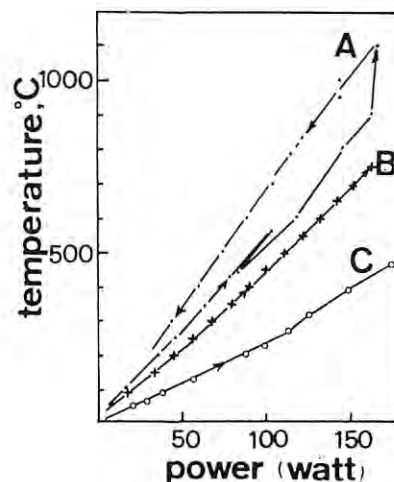


Figure 2. Power-temperature curves for heaters; A, Graphite heater; B, Nichrome heater; C, TiC and diamond mixture

## SEARCH OF LONG-PERIOD STRUCTURES IN RARE EARTHS

Nozomu HAMAYA, Kazuhiro FUCHIZAKI, and Takumi KIKEGAWA<sup>†</sup>

Faculty of Engineering Science, Osaka University, Toyonaka, Osaka 560

<sup>†</sup>Photon Factory, National Laboratory for High Energy Physics, Tsukuba, Ibaraki 305

Rare-earth elemental metals are known to exhibit the crystal structure sequence  $\text{hcp} \rightarrow \text{Sm-type} \rightarrow \text{dhcp} \rightarrow \text{fcc}$  for increasing pressure and decreasing atomic number. A similar but more complicated sequence involving longer-period structures can be found in the Mg-based Friauf-Laves alloys<sup>1)</sup>. They show unusual 'staircase' behavior of stacking sequence of close packed layer as a function of the average electron concentration. According to Bruinsma and Zangwill<sup>2)</sup>, a key mechanism giving rise to the 'devil's staircase' in the Mg-based alloys is the competition between the oscillatory Friedel potential and the elastic energy for lattice distortion induced by defects. They also pointed out that, in the case of rare-earth elemental metals, each of Fermi wave vectors for the d electrons and for the s electrons favors a different configuration of defects, and hence a different crystal structure. The purpose of this study is to seek previously undetected longer-period structures of gadolinium metal in the narrow pressure range between those with short periods.

In situ, energy-dispersive, powder x-ray diffraction measurements at high pressures and at high temperatures were carried out using MAX80 installed at the test beam line at Accumulation Ring, KEK.

We have first made a careful pressure scan up to 7 GPa at 250°C under hydrostatic condition using silicon oil as pressure medium. Figure 1 shows the change in diffraction patterns with increasing pressure along with calculated patterns for the hcp(2H), 8H, and Sm-type(9R) structures. The difference in stacking sequence between these structures can be represented more clearly by the use of the h-c notation instead of the ABC notation. Among various polytypes which may appear in the range of c concentration between hcp(h) and Sm-type(hhc), the 8H(hhhc) stacking has the shortest period of the c layer, and thus is expected the first to be stabilized. In Fig. 1, however, there are no reflections which indicate the presence of the 8H nor other long-period structures. All peaks are assigned to the hcp and Sm-type structures except for the reflections from a nickel metal sample container. This fact leads us to conclude that the hcp phase transforms directly to the Sm-type phase.

Figure 2 shows the P-T phase diagram for increasing pressure and temperature. Both the hcp-Sm-type and Sm-type-dhcp transitions were

observed to be associated with large pressure-hysteresis. In the latter transition, for instance, the hysteresis width was about 1 GPa at 500°C and about 2.5 GPa at 400°C. So far, on the basis of very limited experimental results, the Sm-type phase has been believed to extend to higher temperature until meeting the bcc phase which is located just below the liquid phase. The phase diagram shown in Fig. 2 differs from the previously reported one in presence of the triple-phase point. The present results indicate that the effect of temperature, thus, the entropy has to be evaluated properly in order to establish the crystal structure sequence in rare-earth elements.

## References

- 1) Y. Komura and Y. Kitano, *Acta Crystallogr.* **B33**, 2496 (1977).
- 2) R. Bruinsma and A. Zangwill, *Phys. Rev. Lett.* **55**, 214 (1985).

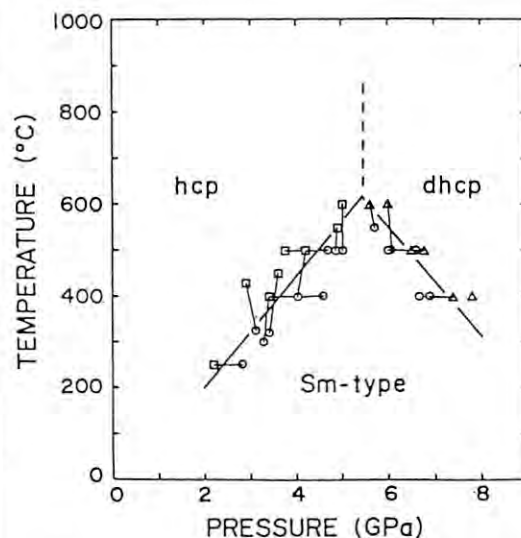
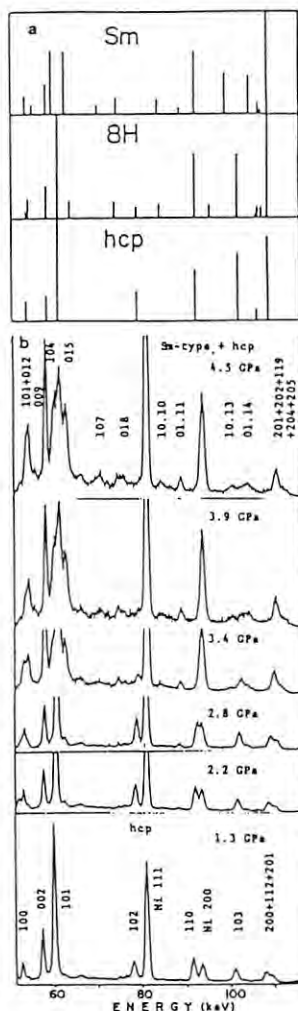


Figure 2. P-T phase diagram of Gd for increasing pressure and temperature.

Figure 1. Calculated diffraction patterns of the hcp, 8H, and Sm-type structures (a) and observed patterns for increasing pressure at 250°C (b).



## STRUCTURE OF LIQUID GALLIUM UNDER PRESSURE

Kazuhiko TSUJI, Kenichi YAOITA, Motoharu IMAI, Osamu ENDO, Osamu SHIMOMURA\* and Hirohisa ENDO\*\*

Department of Physics, Faculty of Science and Technology, Keio University, Yokohama 223

\*National Institute for Research in Inorganic Materials, Tsukuba 305

\*\*Department of Physics, Faculty of Science, Kyoto University, Kyoto 606

Introduction

The melting temperature of gallium decreases with increasing pressure<sup>1)</sup>. According to Clausius-Clapeyron's equation, liquid gallium is denser than GaI. To interpret the negative slope of melting curve, two species model<sup>2)</sup> was proposed where substance in liquid state consists of two species, the normal form and another form similar to the high pressure phases. In liquid selenium, the continuous phase transition to high pressure phase observed at lower pressure than the transition pressure of crystalline selenium<sup>3)</sup>.

At atmospheric pressure, gallium crystallizes to an orthorhombic structure consisting of a stacking of distorted hexagonal close packed layers, with the bonds within the layers considerably weaker than the bonds between the layers. The phase behavior of gallium at high pressure has been a subject of some confusion, because of the capricious appearance of metastable phases. The crystal structures of GaII and GaIII have been reported by several workers<sup>4-6)</sup>. The body centered tetragonal structure identical to the indium structure has been proposed for GaII and GaIII.

Experimental

X-ray diffraction measurements under high pressure and high temperature were performed using a cubic-anvil apparatus (MAX80). The specimen of gallium was put in a capsule of teflon. X-rays from AR were diffracted by the specimen and detected by a Ge SSD in the energy range of 40-120 keV. Structure factor  $S(Q)$  for liquid Ga was obtained from the diffraction intensity by taking into account the energy distribution of incident white x-ray, the absorption by the specimen and pressure-transmitting medium, the atomic scattering factor, etc..

Results and Discussion

In Fig. 1, an example of diffraction patterns of liquid gallium is shown. Obtained  $S(Q)$  for liquid gallium at various pressures are shown in Fig. 2. With increasing pressure, the peak positions shifted towards higher  $Q$ , and the position difference in  $Q$  of the principal peak and the subpeak decreased.  $S(Q)$  for liquid gallium are similar to the broadened diffraction pattern of the body centered tetragonal structure which was proposed for GaII or GaIII. The  $c/a$  ratio of the corresponding crystalline structure decreases with increasing pressure and it approaches to that of a face centered cubic structure.

References

- 1) A. Jayaraman, W. Klement, R. C. Newton and G. C. Kennedy: J. Phys. Chem. Solids **24** (1963) 7.
- 2) E. Rapoport: J. Chem. Phys. **46** (1967) 2891; *ibid.* **48** (1968) 1433.

- 3) K. Tsuji, O. Shimomura, K. Tamura and H. Endo: Z. Phys. Chem. Neue Folge **156** (1988) 465.
- 4) L. F. Vereshchagin, S. S. Kabalkina and Z. V. Troitskaya: Dokl. Akad. Nauk. SSSR **158** (1964) 1061.
- 5) C. E. Weir, G. J. Piermarini and S. Block: J. Chem. Phys. **54** (1971) 2768.
- 6) L. Bosio: J. Chem. Phys. **68** (1978) 1221.

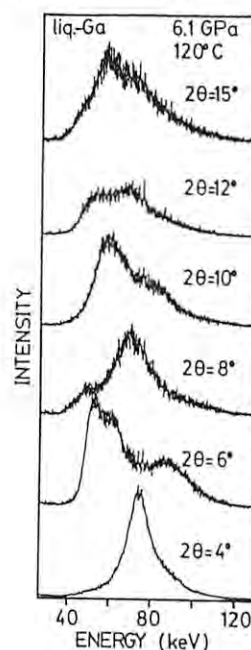


Fig. 1

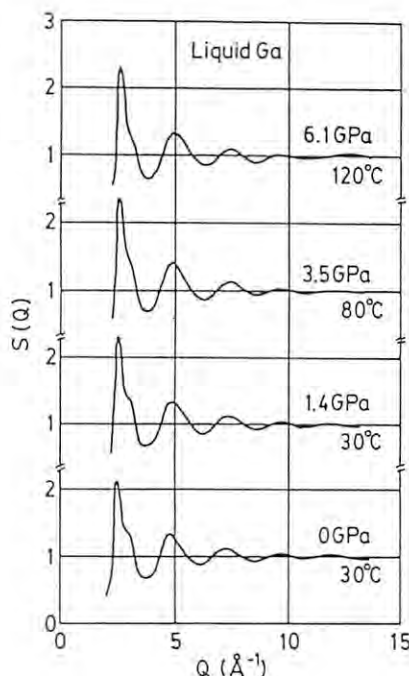


Fig. 2

## STRUCTURE OF LIQUID AND CRYSTALLINE BISMUTH UNDER PRESSURE

Kazuhiko TSUJI, Kenichi YAOITA, Motoharu IMAI, Osamu ENDO, Takumi KIKEGAWA\* and Osamu SHIMOMURA\*\*

Department of Physics, Faculty of Science and Technology, Keio University, Yokohama 223

\*Photon Factory, National Laboratory for High Energy Physics, Tsukuba 305

\*\*National Institute for Research in Inorganic Materials, Tsukuba 305

Introduction

At atmospheric pressure, bismuth crystallizes to a rhombohedral structure identical to that of arsenic, which is a distorted simple cubic structure. Four high pressure phases of bismuth have been known<sup>1)</sup>: Bi II has a monoclinic structure. The structures of Bi III and Bi IV have not been determined, and Bi V has a body centered cubic structure. As the x-ray absorption coefficient of bismuth is very large, it is difficult to obtain a diffraction pattern of good quality under high pressure by using a conventional apparatus. With high energy x-ray from SR, we have succeeded in measuring the x-ray diffraction for liquid bismuth under high pressure.

Experimental

X-ray diffraction measurements under high pressure and high temperature were performed using a cubic-anvil apparatus, MAX80. The specimen of bismuth was put in a capsule of BN. X-rays from AR were diffracted by the specimen and detected by a Ge SSD in the energy range of 40-120 keV. Structure factor  $S(Q)$  for liquid Bi was obtained from the diffraction intensity by taking into account the energy distribution of incident x-ray, the absorption by the specimen and pressure-transmitting medium, the atomic scattering factor, etc..

Results and Discussion

In Fig. 1, obtained diffraction patterns of several phases of bismuth are shown. In the patterns of Bi III and Bi IV there appeared several peaks which did not agree with the calculation based on the models proposed by Fedotov *et al.*<sup>2)</sup>.

An example of diffraction pattern of liquid bismuth at 3.6 GPa is shown in Fig. 2. Background peaks from the sample container are slightly observed only in the pattern taken at low diffraction angle.

Obtained  $S(Q)$  for liquid bismuth at 3.6 GPa and 300°C and  $S(Q)$  at atmospheric pressure and 293°C<sup>3)</sup> are shown in Fig. 3. The height of the subpeak which appears at the high- $Q$  side of the first peak of  $S(Q)$  increases with pressure. It is interesting that this is similar to the change of  $S(Q)$  at atmospheric pressure with decreasing temperature in the supercooled state<sup>4)</sup>.  $S(Q)$  of liquid bismuth both at atmospheric pressure and 3.6 GPa are similar to the broadened diffraction pattern of Bi III or Bi IV.

References

- 1) J. F. Cannon: J. Phys. Ref. Data 3 (1974) 781.
- 2) V. K. Fedotov, E. G. Ponyatovskii, V. A. Somenkov and S. Sh. Shil'shtein: Sov. Phys. Solid State 20 (1978) 628.
- 3) U. Dahlborg and M. Davidović: Phys. Chem. Liq. 15 (1986) 243.
- 4) M. Momiuchi: J. Phys. Soc. Jpn. 55 (1986) 200.

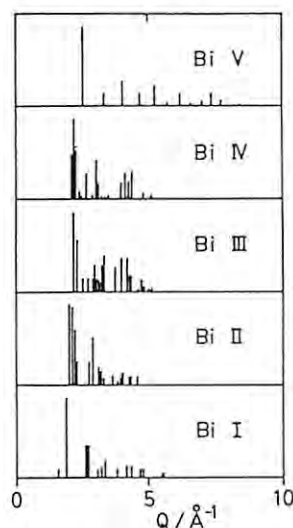


Fig. 1

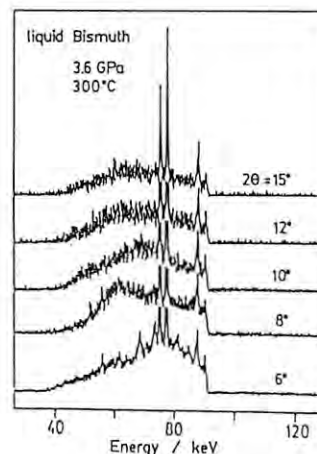


Fig. 2

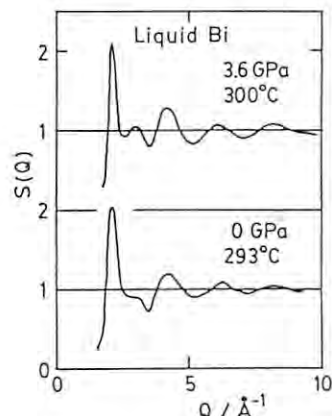


Fig. 3

## Accurate powder diffraction measurements under uniaxial stress

Yoshiko Sato Sorensen<sup>1</sup>, Osamu Shimomura<sup>2</sup>, Takehiko Yagi<sup>3</sup>,  
Kenichi Takemura<sup>2</sup> and Takumi Kikegawa<sup>4</sup>

<sup>1</sup>Univ. Washington, Seattle, WA 98195, U.S.A.

<sup>2</sup>NIRIM, Tsukuba, Ibaraki 305, Japan

<sup>3</sup>ISSP, Univ. Tokyo, Roppongi, Tokyo 106, Japan

## Objectives

There are many indications of substantial non-hydrostatic stresses in high pressure experiments. Since the existence of non-hydrostatic stresses can cause erroneous experimental results, it is important to characterize the stress conditions of the sample under high pressure. The goal of this experiment was to determine the non-hydrostatic stress condition by using synchrotron x-ray diffraction and the MAX80 system.

## Experimental Results

When a polycrystalline sample is compressed under non-hydrostatic conditions, with a hydrostatic pressure,  $p$ , and a uniaxial stress,  $t$ , the lattice spacing can be expressed as a function,  $F$ , of the variables:  $p$ ,  $t$  and elastic constants. For crystals with known elastic constants, we can obtain  $p$  and  $t$  by least square fitting observed d-spacings to function  $F$ .

Two sample configurations were chosen using sintered diamond pistons inside of the cubic boron epoxy pressure medium (Fig. 1a, 1b). It was assumed that the uniaxial stress is in the direction of the motion of the diamond pistons. Experiments were conducted on three samples: NaCl, Cu and SrO.

The hydrostatic pressure,  $p$ , and the uniaxial stress,  $t$ , obtained from the least square calculation for NaCl are plotted in Fig. 2 for two configurations: NACL-4-5 for configuration (a) and NACL-6 for configuration (b). These experiments can be summarized as follows:

(1) In configuration (a): The uniaxial stress is compressional, and increases with the increasing pressure up to about 3 GPa, and then remains constant above this pressure. In the pressure decreasing process, the uniaxial stress change from compression to tension.

(2) In configuration (b): There is initially tensile stress at the beginning of the pressurization, which changes to compression as the pressure is increased. In the pressure decreasing process, the uniaxial stress changes from compression to tension.

These results can be simply explained considering two sample configurations. The uniaxial stress in Cu with configuration (a) also showed similar behavior to that in NaCl with configuration (a). The effects of non-hydrostatic stress on the lattice plane compression were seen least in SrO because it has isotropic elastic properties.

## Future Plan

Our study demonstrated that the current MAX80 system can provide good determinations of the uniaxial stresses in the sample. The next step is to apply this technique to the determination of the strength of materials at high pressure and high temperature. This work will also have important consequence for the accurate determination of the equation of state of materials under real high pressure conditions.

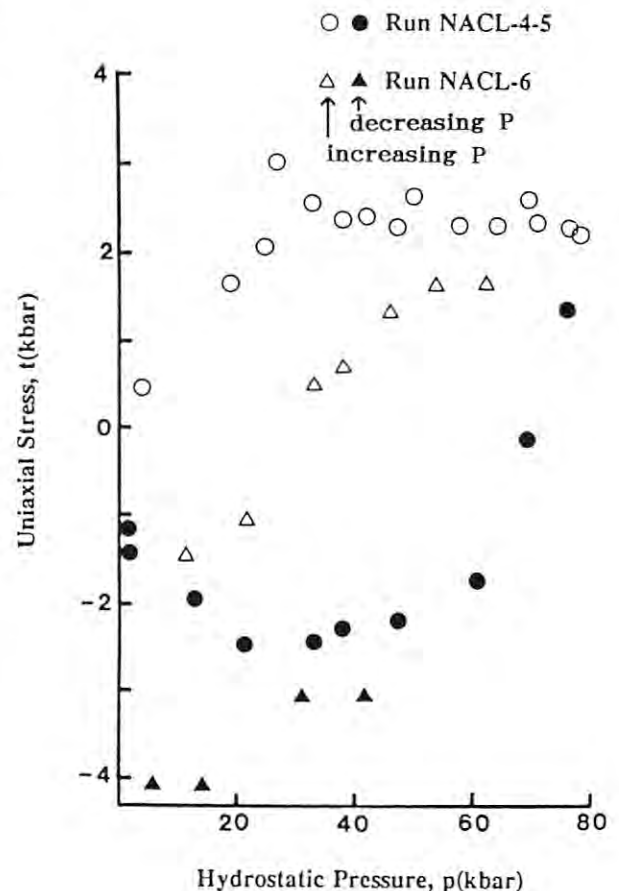
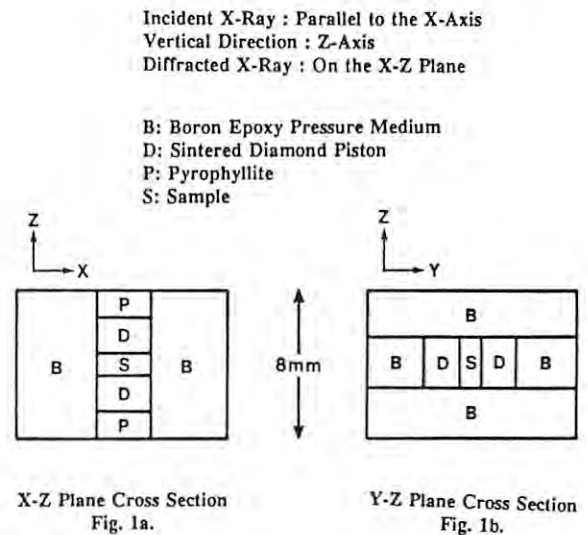


Fig. 2.

# High pressure X-ray diffraction Study Using an Imaging Plate

Osamu Shimomura<sup>1</sup>, Kenichi Takemura<sup>1</sup>, Yasuo Osishi<sup>2</sup>,  
Yuji Fujihisa<sup>2</sup>, Takumi Kikegawa<sup>3</sup>, Yasuhiko Fujii<sup>2</sup>,  
Yoshiyuki Amemiya<sup>3</sup> and Tadashi Matsushita<sup>3</sup>

<sup>1</sup>National Institute for Research in Inorganic Materials,  
Namiki 1-1, Tsukuba, Ibaraki 305, Japan

<sup>2</sup>Faculty of Science & Engineering, Osaka University,  
Toyonaka, Osaka 106 Japan,

<sup>3</sup>Photon Factory, National Laboratory for High Energy Physics,  
Oho, Tsukuba, Ibaraki 305 Japan

An imaging plate(IP) has been proved to be a powerful tool for powder X-ray diffraction study under pressure using a diamond anvil cell<sup>(1)</sup>.

We further investigated the X-ray diffraction system using a diamond anvil cell combined with an imaging plate in the following way.

## (1) check the linearity and accuracy of the reading apparatus

X-ray was impinged on IP through a 0.1mm slit by moving IP by 150mm from one edge of IP to other edge in horizontal and vertical directions. The movement was measured by a digital linear scale with accuracy of 0.01mm. The absolute value of 1 pixel was determined 101.1 ± 0.1 mm in vertical direction ( in lateral direction of the drum of the reading apparatus) and 100.7 ± 0.1 mm in horizontal direction ( in circumference direction ). These values are characteristic to the reading apparatus at the PF.

Standard deviation of the reading is about 0.1 pixel ( = 10 micron).

## (2) correction of the inclination of the IP

In order to treat the two dimensional data on the plate correctly, it is highly desirable that the plate should accurately be perpendicular to the incident X-ray beam. The inclination of the IP is illustrated in Fig. 1. By taking a powder diffraction profile of a standard sample (a mixture of micron size powder of Ag, Mo and Cu) and plotting against  $x^2$ , inclination angle and the actual beam center can be estimated. In this method, we can easily adjust the inclination of IP within 0.1deg.

## (3) evaluation of sample-to-film distance

Sample-to-film distance was measured by two method; a standard sample method and a double cassette method. In the former, the distance was determined by measuring the position of the diffraction peaks of a standard sample with well determined lattice constants. In the latter, the distance is determined by the ratio of two diffraction peak positions with same index recorded on IP at two film positions.

The former method is suitable for the precise compressibility measurement because the sample-to-film distance is strictly fixed, while the latter has an advantage that we need not know the lattice constant of the sample nor the x-ray wavelength.

The sample-to-film distances obtained by two methods are summarized in table 1. Agreement between two methods is very good. Slight deviation in these values are thought to be caused by a warping of IP. We are now making an IP cassette which reduce the warping less than 10 micron, which will give better accuracy in determination of film-to-sample distance.

(1)O.Shimomura et al., PF Act. Rep.#5 p161(1987)

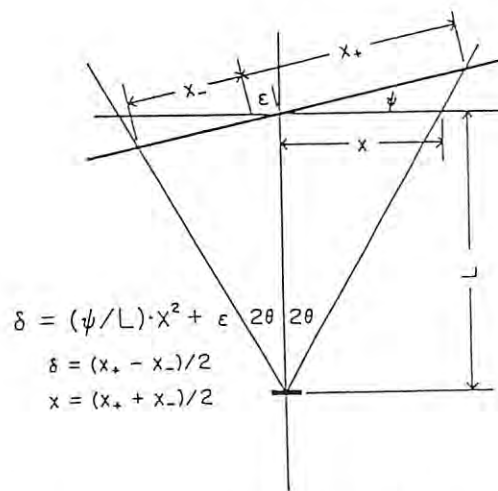


Figure 1. Diffraction geometry in case of flat film method. L denotes the film-to-sample distance,  $\psi$  the inclination of the film to the perpendicular plane to incident X-ray beam and  $\epsilon$  distance between an apparent and true beam centers.

Table 1. Film-to-Sample distances derived by a standard sample method and a double cassette method.  $L_S$  and  $L_I$  are estimated by the former method at short and long film position, respectively. The difference of two position was measured as 75.027mm, and  $L_I$  is the values after subtracting this distance from the measured long film distances.  $L_R$  is calculated by the latter method using the above distance between two film position.

#	desig.	$L_S$ (mm)	$L_I$ (mm)	$L_R$ (mm)
1	Ag 111	120.61	120.56	120.64
2	Mo 110	120.63	120.58	120.67
3	Cu 110	120.64	120.61	120.65
4	Ag 200	120.58	120.51	120.65
5	Cu 200	120.66	120.62	120.70
6	Mo 200	120.65	120.56	120.75
7	Ag 220	120.67	120.61	120.73
	mean	120.63	120.58	120.72
	S.D.	0.03	0.03	0.04



OBSERVATION OF ANTARCTIC METEORITES BY MONOCHROMATIC X-RAY CT  
BASED ON SYNCHROTRON RADIATION

Minoru Funaki,\* Katsuhisa Usami,\*\* Tatsumi Hirano,\*\* Takeshi Nagata\*  
and Isamu Taguchi\*\*\*

\*National Institute of Polar Research, Tokyo, 173

\*\*Hitachi Research Lab., Hitachi Ltd., Hitachi, Ibaraki 316-12

\*\*\*National Museum of Japan History, Sakura

X-ray computed tomography (X-ray CT) is a method to observe internal structures of objects, nondestructively. The images are obtained as two-dimensional distributions of X-ray linear absorption coefficients which depend on the used X-ray energy. A high resolution, tunably monochromatic X-ray CT based on synchrotron radiation have been developed and applied to observe internal structures of antarctic meteorites.

The schematic diagram of the developed CT scanner is shown in Fig.1. It was installed to BL-8C experimental station in the KEK Photon Factory 2.5 GeV electron storage ring. SR was monochromatized through Si(400) channel cut monochromator. The energy range is varied from 10 KeV to 40 KeV.

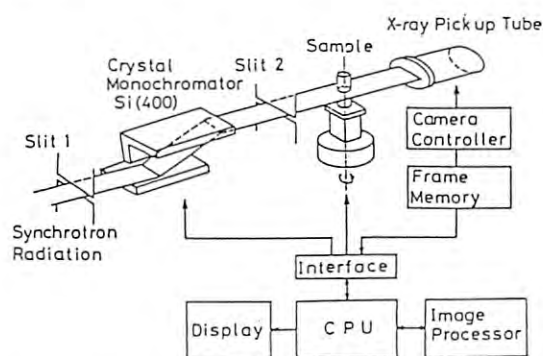


Fig.1 Schematic diagram of the monochromatic X-ray CT based on synchrotron radiation.

A high resolution X-ray pickup tube was used as a detector. Two-dimensional X-ray transmitted images of a sample was observed and a slice position was determined. A series of one-dimensional projection images corresponding to the slice position were measured by rotating the sample. The reconstructed image was displayed as a gray-scale image on a 512 x 512 pixel video display. The limiting spatial resolution was about 10  $\mu\text{m}$ .

An example of CT image of antarctic meteorite 769 is shown in Fig.2(a). X-ray energy was 21 keV. The brightness corresponds to the X-ray absorption coefficient. Brighter region reflects stronger absorption region. The slice thickness, which is determined by the accumulated line numbers in the image by pickup tube, about 20  $\mu\text{m}$ . The radial line patterns are artifacts from the existence of the strong absorption regions. In spite of these artifacts, fine structures such as bright regions seemed to be metal phases and some cracks, can be observed. For comparison, CT image of St. Séverin meteorite was taken and shown in Fig.2(b). Though the similar metal phases are recognized, no cracks are observed and the density seems to be higher than that of antarctic meteorite 769.

Quantitative evaluation of CT value is now under way.

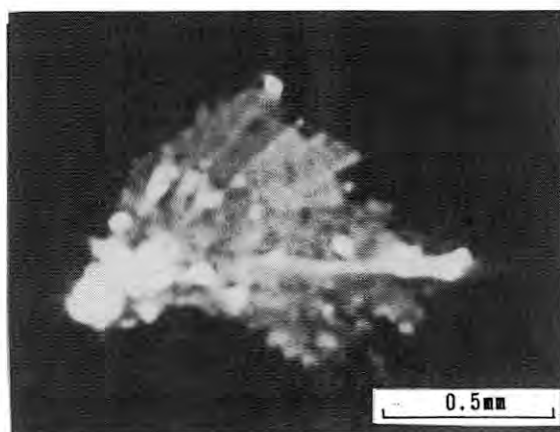


Fig.2(a) CT image of antarctic meteorite.



Fig.2(b) CT image of St. Séverin meteorite.

STRUCTURAL BEHAVIOURS OF  $\text{La}_2\text{CuO}_{4-y}$  AND  $\text{La}_{2-x}\text{Sr}_x\text{CuO}_4$ 

Ichiro HIROSAWA, Jun'ichiro MIZUKI, Masaaki MATSUDA\*, Eisuke KUDO\*, Kazuyoshi YAMADA\*, Yasuo ENDOH\* and Junji MATSUI

Fundamental Research Laboratories, NEC Cooperation

\*Department of Physics, Tohoku University

Since the discovery of high- $T_c$  superconductors, a number of studies were performed to understand the nature of high- $T_c$  superconductivity. Especially the properties on the  $\text{La}_2\text{CuO}_{4-y}$  and its family compounds are of interest as they seem to include essentials for the appearance of high- $T_c$  superconductivity. It has been found that oxygen deficiency and doped alkali earth metals (Sr, Ba and Ca) affect the various properties of these compounds<sup>1-4</sup>.  $\text{La}_2\text{CuO}_{4-y}$  has an antiferromagnetic ordering below about room temperature. Its Neel temperature is sensitive to oxygen deficiency. We will report here the studies on the influence of oxygen deficiency on the structural behaviours of  $\text{La}_2\text{CuO}_{4-y}$  and  $\text{La}_{2-x}\text{Sr}_x\text{CuO}_4$ .

Large single crystals of both doped  $\text{La}_{2-x}\text{Sr}_x\text{CuO}_4$  and pure  $\text{La}_2\text{CuO}_{4-y}$  with different thermal treatments were studied. Originally, all of them were grown with the flux method by NTT group<sup>5</sup>. One sample of  $\text{La}_2\text{CuO}_{4-y}$  was annealed in Argon atmosphere at 800°C for 10 hours (sample A), and the other was annealed in oxygen atmosphere at 1050°C for 5 hours (sample B). By these treatments, the oxygen deficiency in the sample A became more than that in the sample B.

Experiments were performed with 6-axis Huber diffractometer, which was installed at BL-9C. The monochromatized X-ray (1.5Å) reflected from Si(111), was used in this experiment. The sample was placed in an imaging furnace with a halogen lamp. It is well known that the crystal structure of  $\text{La}_2\text{CuO}_4$  and  $\text{La}_{2-x}\text{Sr}_x\text{CuO}_4$  with low Sr concentration is tetragonal at high temperature and undergoes an orthorhombic distortion at lower temperature. Since there are two equivalent displacement wave vectors, these crystals have a superposition of a and c axes in the low temperature phase. The space group of the orthorhombic phase was not identified clearly. There are three possibilities for the space group, namely Cmmm, Cmca and Pccn. Since we observed no reflections at 100, 001, 300 and 003 in the orthorhombic phase of these three samples, we could omit Cmmm and later we could reach the conclusion for Cmca<sup>6</sup>.

To study the influence of oxygen deficiency on the structural properties of  $\text{La}_2\text{CuO}_{4-y}$ , the temperature dependence of lattice constants was measured with the sample A and B. The temperature dependence of lattice constants with the diffractions at 200 and 002, was shown in Fig.1. The structural phase transition temperatures of the sample A and B were about 478K and 453K, respectively. Suppose that the superconducting phase appears only in the orthorhombic phase and that oxygen deficiency suppresses superconductivity<sup>1-4</sup>, the change in structural phase transition temperature with the oxygen deficiency seems to be curious.

There reported anomalies on the structural behaviours of these compounds at low temperatures. Another structural phase transition from orthorhombic to monoclinic phase was reported for

$\text{La}_{1.85}\text{Sr}_{0.15}\text{CuO}_4$ <sup>7</sup>). Also for  $\text{La}_{1.85}\text{Ba}_{0.15}\text{CuO}_4$ , anomalous structural instabilities at lower temperature were reported by Mck Paul<sup>8</sup>). Therefore, in the present study the structural behaviour of  $\text{La}_{1.9}\text{Sr}_{0.1}\text{CuO}_4$  was investigated with a Cryogenic refrigerator in the temperature ranging from 300K to 15K. Fig.2 shows the temperature dependence of lattice constants of a and c axes which were obtained by 200, 002, 400 and 004 diffractions. As can be seen, there was no anomaly in the temperature dependence of lattice constants in our  $\text{La}_{1.85}\text{Sr}_{0.15}\text{CuO}_4$  in this temperature range. Although the present data indicate that another phase transition<sup>7</sup>) does not exist, more detailed studies should be required for investigating the structural properties at low temperature. Since the sample studied in the present work does not show superconductivity, superconducting single crystals should be studied.

## References

- 1) F. Fujita et al. Jpn.J.Appl.Phys. 26, L368 (1987).
- 2) D. Jerome et al. J.Appl.Phys. 63, 4005 (1988).
- 3) S. Mitsuda et al. Phys.Rev. B36, 822 (1987).
- 4) K. Yamada et al. Solid State Comm. 64, 753 (1987).
- 5) Y. Hidaka et al. J. Crystal Growth 85, 581 (1987).
- 6) After these experiments, the space group was identified as Cmca with convergent-beam electron diffraction by M. Tanaka et al. Jpn.J.Appl.Phys. 26, L1502 (1987).
- 7) K. Kamigaki et al. Jpn.J.Appl.Phys. 26, L1642 (1987).
- 8) D. Mck Paul et al. Phys.Rev.Lett. 58, 1976 (1987).

Fig.1  $\text{La}_2\text{CuO}_4$

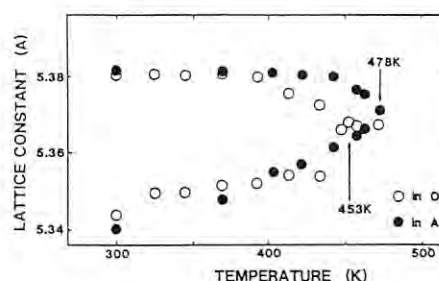
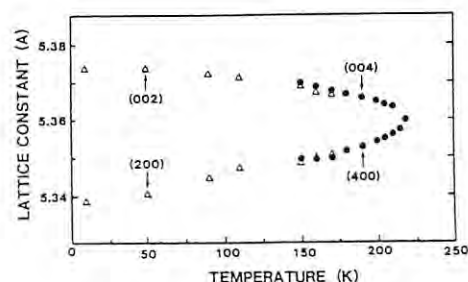


Fig.2  $\text{La}_{2-x}\text{Sr}_x\text{CuO}_4$



# COMPOSITION DEPENDENCE OF LATTICE PARAMETER FOR LEC GROWN GaAs CRYSTALS WITH DISLOCATIONS

Koji USUDA, Shigeru YASUAMI, Yasuo HIGASHI\*, Hiroshi KAWATA\* and Masami ANDO\*

Research and Development Center, Toshiba Corporation  
1, Komukai Toshiba-cho, Saiwai-ku, Kawasaki 210, Japan

\*Photon Factory, National Laboratory for High Energy Physics  
Ohomachi, Tsukuba-shi, Ibaraki 305, Japan

## Introduction

There are several mutually inconsistent reports (1-3) on the composition and defect dependence of the lattice parameter of undoped LEC-grown GaAs crystals. The variation in the lattice parameter is supposed to be in the  $|\Delta d|/d \sim 10^{-6}$  order. We hence carried out measurements using a 3-crystal diffractometer (4), which has a monolithic monochromator. The achieved resolution is  $|\Delta d|/d \sim 2 \times 10^{-6}$ .

## Experimental

The composition and defect dependence of the lattice parameter were examined for LEC (liquid encapsulated Czochralski)- and MLEC (magnetic field applied LEC)-grown crystals. Samples were  $7.5 \times 7.5 \text{ mm}^2$  chips diced from the crystal wafers.

## Results and Discussion

Figure 1 shows the EPD (etch pit density) dependence of the lattice parameter. Each point represents an averaged value over three central samples obtained from an undoped MLEC 3 in. diam wafers. The lattice parameter variation is within  $|\Delta d| \sim 2 \times 10^{-5} \text{ \AA}$ -wide band and shows no appreciable dependence on EPD.

Figure 2 shows across-a-diameter distribution of the lattice parameter and EPD for the wafer which exhibited the largest lattice parameter variation among the wafers in Fig.1. The lattice parameter seemingly varies with EPD. If this relation is genuine, the lattice parameter shown in Fig.1 should also vary accordingly. Hence, another kind of strain, residual strain, is suggested to exist. In the previous report (4), we already noticed that the magnetic field strength, one of growth parameters, is more influential than the composition. Then, we implied the existence of the residual strain.

Figure 3 shows the composition dependence of the lattice parameter. The crystals, 2 in. in diam, were grown by the MLEC (#1) and LEC (#2) method using one puller for each method. The lattice parameter increases as the As-fraction increases for #1 samples, while the almost invariable relation sags somehow at the stoichiometry for #2 samples. If this variation in the lattice parameter is principally due to the composition, the lattice parameter should vary uniquely with the composition. However, the lattice parameter shows the inconsistent tendencies among the two sets of crystals in Fig.3. It is hence concluded that residual strain varies the lattice parameter much more than composition.

For revealing the real composition dependence of the lattice parameter, a nearly residual-strain-free crystals are required.

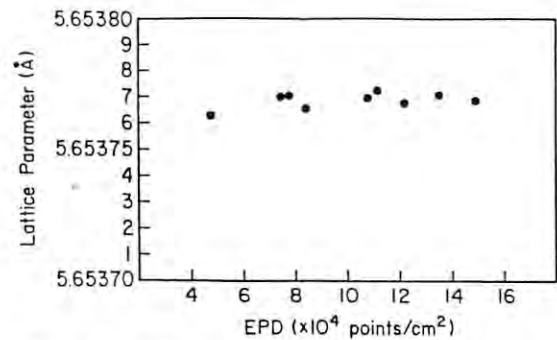


Fig.1 EPD Dependence of Lattice Parameter

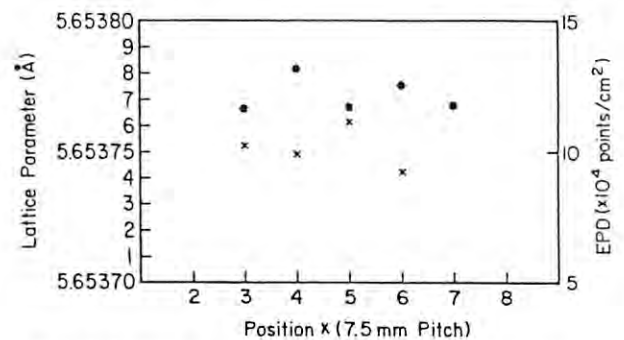


Fig.2 Lattice Parameter and EPD Variation across an undoped MLEC-GaAs Wafer

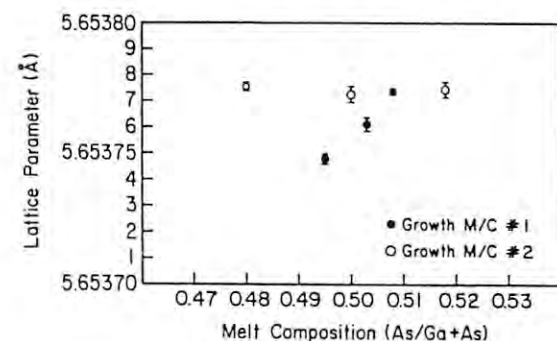


Fig.3 Composition Dependence of Lattice Parameter

## References

- 1) Y.Okada, Y.Kadota and Y.Tokumaru: Appl.Phys. Lett. **48** 975 (1986)
- 2) M.Nakajima, T.Sato, T.Inada, T.Fukuda and K.Ishida: Appl.Phys.Lett. **49** 1251 (1986)
- 3) H.Kuwamoto and D.E.Holmes: J.Appl.Phys. **59** 656 (1986)
- 4) K.Usuda, S.Yasuami, Y.Higashi, H.Kawata and M.Ando: Extended Abstracts of the 19th Conference on SSDM, Tokyo, 119 (1987)



# PHASE IDENTIFICATION IN OXIDIZED Hf/FE MULTILAYER FILMS BY USING ANOMALOUS SCATTERING

Muneyuki Imafuku, Yasuo Takagi and Satoshi Sasaki\*

R & D Laboratories-I, Nippon Steel Corporation, 1618 Ida, Nakahara-ku, Kawasaki 211, JAPAN

\*Photon Factory, National Laboratory for High Energy Physics, Tsukuba, Ibaraki 305, JAPAN

## INTRODUCTION

Interesting crystal and layer structures are formed in oxidized Hf/Fe multilayer films<sup>1)</sup>. It is not easy, however, to identify such structures by using "conventional" x-ray diffraction technique because many diffraction peaks of various different crystal structures appear in the patterns. By using anomalous scattering method, it becomes possible to know the partial contributions to each diffraction peak from different elements. The purpose of this study is to identify the oxide phases coexisting in the oxidized Hf/Fe multilayer films, which is an important step to clarify the mechanism of oxidation in the films.

## EXPERIMENTAL

The Hf(50 Å)/Fe(50 Å)(75 pairs of bilayers) multilayer films were prepared by ion-beam sputtering deposition<sup>1)</sup>. The BL 10A was used for the experiment. Two different wave length,  $\lambda_e=1.29850$  Å and  $\lambda_s=1.30814$  Å near (but longer than) the Hf  $L_{III}$  absorption edge were chosen for  $\theta-2\theta$  diffraction scan<sup>2)</sup>.

## RESULTS AND DISCUSSION

The diffraction patterns both by  $\lambda_e$  and  $\lambda_s$  from the films oxidized in different environments were shown in Figs. 1.(a) & (b).

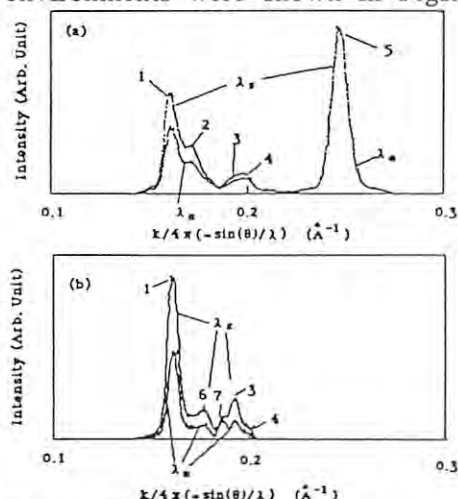


Fig. 1 The x-ray diffraction patterns of the films annealed at 500 °C for 30 min. in air of Michigan(a) & California(b).

If a peak consists of the contribution only from Fe atoms, there should not be any difference between the peak intensity by  $\lambda_e$  and that by  $\lambda_s$  (for example, No. 5 peak in Fig. 1(a)), while if a peak includes scattering from Hf, too, the intensity by  $\lambda_e$  should be smaller than that by  $\lambda_s$  because of negative contribution from  $f'$  (real part of anomalous scattering factor) to the intensity. The results of the peak identification were summarized in Table I.

Especially, the No. 6 peak could not have been identified as (222) of  $\beta\text{-Fe}_2\text{O}_3$ <sup>3)</sup> if the method had not been used, because the reflection overlaps with (002) of orthorhombic or tetragonal  $\text{HfO}_2$  almost completely.

## CONCLUSION

The crystal structures of the mixed oxide phases in the oxidized Hf/Fe multilayer films were successfully identified by using anomalous scattering method.

## REFERENCES

- 1) Y. Takagi, B. S. Chao, D. A. Pawlik, J. E. Keem and A. M. Kadin: *Proc. of MRS International Meeting on Advanced Materials, "Symposium K: Multilayer"*, Tokyo, May 30-June 3, 1988 (Materials Research Society, Pittsburgh) (in print).
- 2) M. Imafuku, Y. Takagi and S. Sasaki: Internal Report of Central R & D Bureau, Nippon Steel Corporation, 88-004, [in Japanese].
- 3) L. Ben-Dor, E. Fischbein, I. Felner and Z. Kalman: *J. Electrochem. Soc.* 124(1977)451.

Table I Peak identification in the oxidized Hf/Fe multilayer films.

Nos.	Compositions	Structures	Indices
1.	HfO <sub>2</sub>	monoclinic	(-111)
2.	HfO <sub>2</sub>	orthorhombic	(111)
3.	HfO <sub>2</sub>	monoclinic	(200, 020)
4.	HfO <sub>2</sub>	monoclinic	(002)
5.	Fe( $\alpha$ )	cubic(bcc)	(110)
6.	HfO <sub>2</sub>	monoclinic	(111)
7.	Fe <sub>2</sub> O <sub>3</sub> ( $\beta$ )	cubic(bcc)	(222)



# DEVELOPMENT OF A STEPWISE TEMPERATURE CONTROL DEVICE AND ITS APPLICATION TO TIME-RESOLVED SAXS MEASUREMENTS OF POLYMER BLENDS.

Toshiro Kojima, Hideo Nomura, Kazuhiro Chikaishi and Yoshiyuki Amemiya\*

Takatsuki Research Laboratory, Sumitomo Chemical Co. LTD.

Tsukahara 2-10-1, Takatsuki(569), Osaka

\*Photon Factory, National Laboratory for High Energy Physics,  
Oho 1-1, Tsukuba(309), Ibaraki

## Introduction

In some polymers, mechanisms of phase separation or crystallization are very important to control their physical properties. The characteristic length of these structural changes at the early stage is about 10-100Å. A Small Angle X-ray Scattering (SAXS) technique is a powerful tool for a analysis of structures which have these order of characteristic length. However, by using a conventional X-ray source, a time-resolved SAXS measurements cannot be carried out because of very weak SAXS intensity. By using a strong synchrotron radiation X-ray source, the time-resolved SAXS measurements can be carried out. We have developed a stepwise temperature control device for time-resolved SAXS measurements of some polymers in order to know the phase transformation mechanisms.

## Devices

For the dynamical measurements of phase separations or crystallizations of some polymers, the rate of temperature changing is required more than about 100C per minute. In order to achieve this rate, a blowing method of heated  $N_2$  gas was adopted. The block diagram of this device is shown in figure 1. And the features of this device is shown in table 1.

Table 1. Features of this device

Temperature Region	-20 - 500 C
Changing Rate	+150 C/min
	-150 C/min ( $T > 150$ C)
	-50 C/min ( $T < 150$ C)

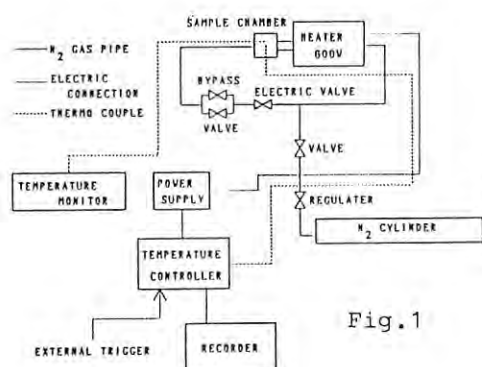


Fig. 1

## Application

The first application of this device was the time-resolved SAXS measurements of the phase separating process of a polymer blend of PMMA and SAN (PMMA=poly(methylmethacrylate), SAN=styrene-acrylonitrile copolymer). This polymer blend shows a phase separation at  $T=185$ C. It shows a uniform phase below this temperature. The temperature of this specimen is kept at below the phase boundary, then the temperature of the specimen is changed suddenly to the temperature above the phase boundary, we can observe the dynamical process of the phase separation. The temperature of this specimen was changed suddenly  $T=135$ C to  $T=220$ C in this experiment. The history of the temperature was shown in figure 2. The temperature change was completed within about 15sec. The profile of SAXS was changed as shown in figure 3. The wave length of this measurement was 1.504Å, the camera length was 2250mm, SAXS profiles were measured by PSPC(170mm) and the time resolution of these profiles was 2sec. From this figure, it is clear that the intensity of SAXS increased after the temperature change completed and the slope of the SAXS profile became steep with time. The time dependence of the integrated intensity was plotted in figure 4. In this figure, we can find out that the integrated intensity began to increase at  $t=16$ sec, and to decrease after  $t=60$ sec. This decreasing of the intensity was due to a direct beam stopper because the SAXS profiles sharpened and approached to the zero of the scattering angle. We can guess following mechanism from above experiments. The phase separation became distinctly and the characteristic length of the separating structure became larger according to the time. From these facts, the phase separating mechanism of this specimen is considered the nucleation growth process.

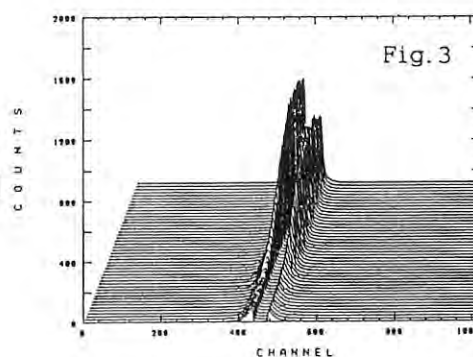


Fig. 3

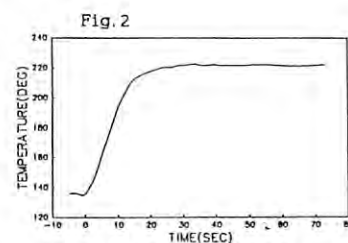


Fig. 2

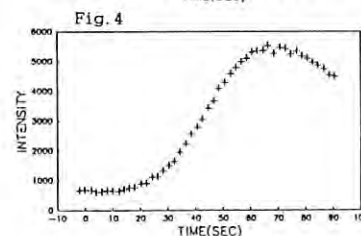


Fig. 4

# TIME-RESOLVED X-RAY MEASUREMENT OF SURFACE AND BULK STRAINS IN SILICON IRRADIATED BY A FREQUENCY-DOUBLED Nd:YAG LASER

Shigeru KOJIMA<sup>1)</sup>, Seiji KAWADO<sup>1)</sup>, Tetsuya ISHIKAWA<sup>2)</sup>,  
Toshio TAKAHASHI<sup>3)</sup>, and Seishi KIKUTA<sup>4)</sup>

- 1) Sony Corporation Research Center, Hodogaya-ku, Yokohama 240
- 2) Photon Factory, National Laboratory for High Energy Physics,  
Oho, Tsukuba, Ibaraki 305
- 3) The Institute for Solid State Physics, The University of  
Tokyo, Roppongi, Minato-ku, Tokyo 106
- 4) Department of Applied Physics, Faculty of Engineering,  
The University of Tokyo, Hongo, Bunkyo-ku, Tokyo 113

## Introduction

Using the time-resolved x-ray diffraction method, we have studied lattice deformation in silicon caused by YAG pulsed-laser irradiation.<sup>1,2)</sup> This report describes the time-change behavior of nearly intrinsic rocking curves of symmetric reflection and asymmetric reflection measured in order to differentiate between surface and bulk strains.

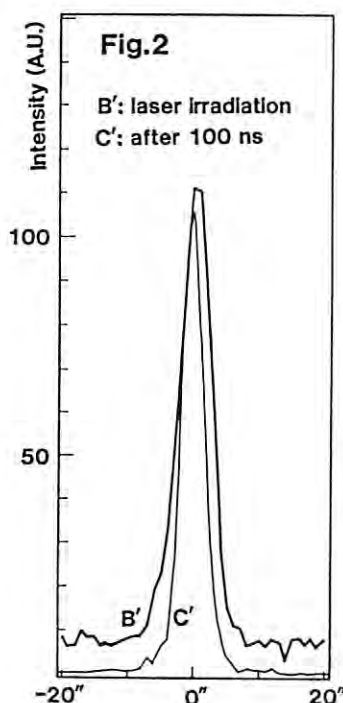
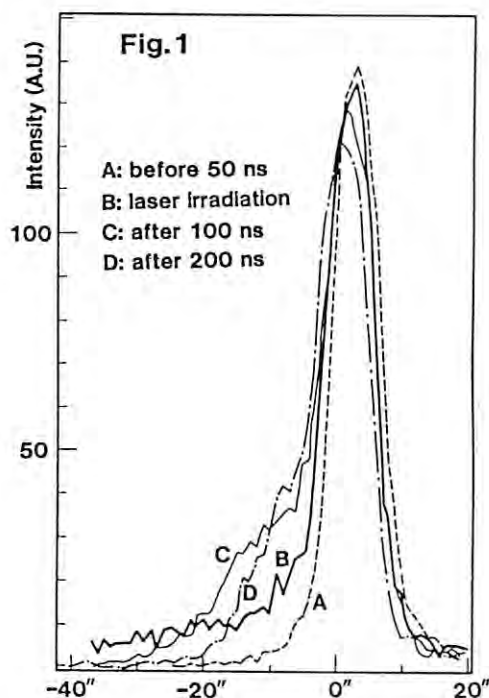
## Experimental

The experimental arrangement was the same as reported previously.<sup>1)</sup> The samples used were 10 mm-thick FZ silicon crystals with the (111) orientation for the symmetric reflection and (111)-12° off orientation for the asymmetric reflection (asymmetric factor 11.5). We irradiated the sample surface with a Q-switched Nd:YAG laser beam with a wavelength of 0.53  $\mu\text{m}$  and a pulse width of about 20 ns at a 10 Hz repetition rate. The power of the laser beam 7 mm in diameter was about 90 mJ/pulse. Time-resolved rocking curve measurements were carried out using the TAC technique described in Ref.1.

## Results

Figure 1 shows four time-resolved rocking curve profiles of the symmetric 111 reflection measured by changing the interval between the laser irradiation onto the sample surface and the gate pulse applied to the plastic scintillation counter. Each profile was normalized with the Bragg peak intensity of the profile observed 1 ms after the laser irradiation. The rocking curves of the asymmetric reflection were also measured in the same manner and are shown in Fig.2.

The enhancement of x-ray intensity was observed at the lower angle side of the rocking curve 100 ns after the laser irradiation using the symmetric reflection, but was not observed using the asymmetric reflection. Considering the difference in extinction distance between the symmetric reflection ( $\sim 20 \mu\text{m}$ ) and the asymmetric reflection ( $\sim 10 \mu\text{m}$ ),<sup>3)</sup> we suggest there is a displacement of the strained area accompanied by heat transfer. In addition, we found a rapid increase in the background intensity at the moment of the laser irradiation in the case of the asymmetric reflection, indicating the formation of a near-surface strain.



## References

- 1) S.Kojima et al., Jpn.J.Appl. Phys. **27**, L1377 (1988).
- 2) S.Kawado et al., SRI-88, Tsukuba, 1988, B-065.
- 3) K.Kohra and T.Matsushita, J.Jpn.Assoc.Cryst.Growth, **4**, 55 (1977) (in Japanese).

Fig.1. Time-resolved rocking curves measured with the symmetric 111 reflection.

Fig.2. Time-resolved rocking curves measured with the asymmetric 111 reflection.

# X-RAY FLUORESCENCE ANALYSIS OF TRACE METALS IN POLYMER USING SYNCHROTRON RADIATION

Eisaku SATOH, Yasunori YAMAMOTO, Toshiyuki TAKYU and Atsuo IIDA\*

Central Research Laboratories Idemitsu Kosan Co.,Ltd.  
Sodegaura, Kimitsu, Chiba 299-02

\* Photon Factory, National Laboratory for High Energy Physics  
Oho, Tsukuba, Ibaraki 305

## Introduction

Recently, polymers, such as polycarbonates (PC) which are transparent and heat-stable, have been used as optical materials. Trace metals in these materials are considered to affect their optical properties even at the ppb level<sup>1)</sup>. Conventional methods to determine the contents of trace metals in polymers, such as atomic absorption spectrometry, generally require ashing and other tedious sample preparations. In addition, the sensitivity of these methods are often insufficient to provide reliable data in the sub-ppm range.

In this experiment, sub-ppm level of transition metals (Cr, Mn, Fe, Co, Ni, Cu) in PC were analyzed by the method of X-ray fluorescence (XRF) using synchrotron radiation (SR), which is non-destructive and more sensitive.

## Experimental

Two grams of PC was desolved in high pure methylene chloride, and then 0-2 $\mu$ g (0-1ppm) of organic metal standards (Cr, Mn, Fe, Co, Ni, Cu) were added for quantitative analysis by the method of standard addition. Furthermore, 2 $\mu$ g (1ppm) of vanadium were added as internal standard. The solutions were poured into glass dishes and evaporated at room temperature to polymer film samples.

The film samples were excited by monochromated X-rays at 9.8keV with a Si double crystal monochromator. X-ray fluorescence were measured by a Si(Li) detector for 300 seconds of counting time.

## Results and Discussion

Table 1. shows detection limits and results in this measurements. Detection limit of each element was determined from the intensity of X-ray fluorescence and background of the samples added 0 and 1ppm of standards. The detection limits in analysis of metals in PC were found to be 0.15-0.67ppm. These values were higher than those by XRF using SR reported previously<sup>2)</sup>. This result was dependent on the high background from the polymer matrix.

Sub-ppm level of iron and nickel in PC were able to be determined and the values obtained were agree with those determined by instrumental neutron activation analysis (INAA), as shown in Table 1. Though the other elements were not detectable because of low concentration below the detection limit, this result was also comparable to that of INAA.

## References

- 1) T.Kaino et al, Prep. Chem. Soc. Jpn. 44th Meeting, 588(2M10), (1981)
- 2) A.Iida et al, Nucl. Instr. Meth. 228(1985)556

Table 1. Detection limits and results of determination of trace metals in polycarbonates by XRF using SR.

Element	Detection limit	Results (ppm)	
		XRF using SR	INAA
Cr	0.67	n.d.	0.052
Mn	0.58	n.d.	0.012
Fe	0.15	0.61	0.6
Co	0.21	n.d.	0.0013
Ni	0.18	0.24	0.12
Cu	0.20	n.d.	<0.03

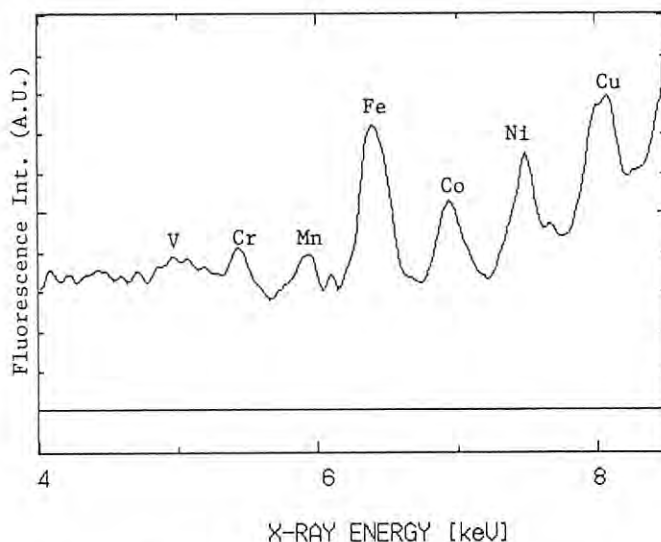


Fig.1. XRF spectrum of polycarbonates sample added 1ppm of metal standards.

## X-RAY DIFFRACTION STUDY OF Fe/MgO MULTILAYERED FILMS

Tamotsu KOYANO, Yoshihiro KUROIWA, Eiji KITA,  
Norio SAEGUSA\*, Ken-ichi OHSHIMA, and Akira TASAKI.

Institute of Applied Physics, University of Tsukuba,  
Tsukuba, Ibaraki 305.

\* On leave from Sumitomo 3M Ltd., Sagamihara, Kanagawa 229

### Introduction

Recently, we have reported that Fe atoms in Fe/MgO multilayered films prepared in the UHV condition have a magnetization larger than that of bulk Fe.<sup>1)</sup> According to the energy band calculation on bcc Fe, the magnetic moment increase with the increase of the atomic volume.<sup>2)</sup> It is speculated that the enhancement of magnetization originates in the lattice expansion at the Fe/MgO interface. In order to confirm this volume effect, we performed X-ray diffraction experiments at BL-4C.

### Experimental Procedure

The samples were prepared by alternate deposition in the UHV condition. The X-ray diffraction experiments were performed on BL-4C, where a four-circle diffractometer (Huber 5020-4) equipped with a graphite (00-2) crystal analyzer was used. A wavelength of  $1.00\text{\AA}$  was selected by the double-crystal Si(111) monochromator with sagittal focusing. The diffraction profiles were measured by the  $\theta-2\theta$  scanning method. The scattering vector is perpendicular to the plane of the sample.

### Results and Interpretation

An X-ray diffraction profile of Fe/MgO( $30\text{\AA}/15\text{\AA}$ ) multilayered film is presented in Fig.1. As the rocking curves of the diffraction lines have no peaks, it is concluded that the films have no texture structure.

Figure 2 shows the diffraction profiles of Fe/MgO( $x/15\text{\AA}$ ) films around Fe(110) line position. The three profiles are asymmetric and

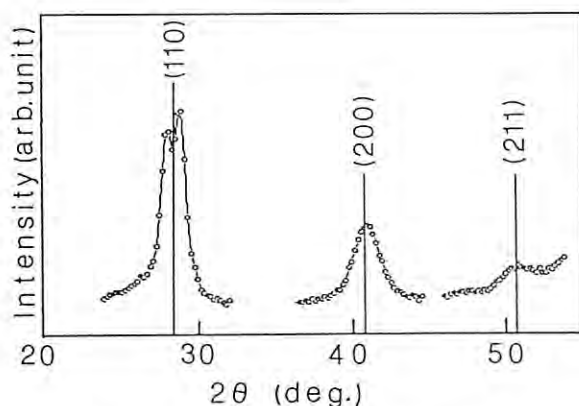


Fig.1 X-ray diffraction profile of Fe/MgO( $30\text{\AA}/15\text{\AA}$ ) film. Solid lines indicate the peak position of bulk  $\alpha$ -Fe.

seem to split into two peaks. If the splitting of these lines were due to the tetragonal deformation of bcc Fe, both Fe(110) and Fe(200) peak should split into two peaks of the intensity ratio of 2:1. In the present case, the intensity ratio of doublet Fe(110) line is nearly unity, and Fe(200) line seems to be unsplit. Thus, we can not conclude that the splitting is due to the tetragonal deformation. In order to obtain the lattice parameter of Fe atoms, treatment of the signal originating from the MgO layers is a critical problem. For the film of Fe  $16\text{\AA}$ , the calculated intensity ratio of Fe(110) line and MgO(200) line is not so large, which is 3:1, and the overlap of these lines is serious. Thus the lattice parameter of Fe atoms is not obtained from the present data. The X-ray diffraction experiment utilizing anomalous dispersion is necessary to obtain the lattice parameter of Fe atoms.

### References

- 1) T. Koyano, Y. Kuroiwa, E. Kita, N. Saegusa, K. Ohshima, and A. Tasaki, to be printed in J. Appl. Phys. (15 November 1988)
- 2) V. L. Moruzzi, P. M. Marcus, K. Schwarz and P. Mohn, Phys. Rev., **B34**, 1784 (1986)

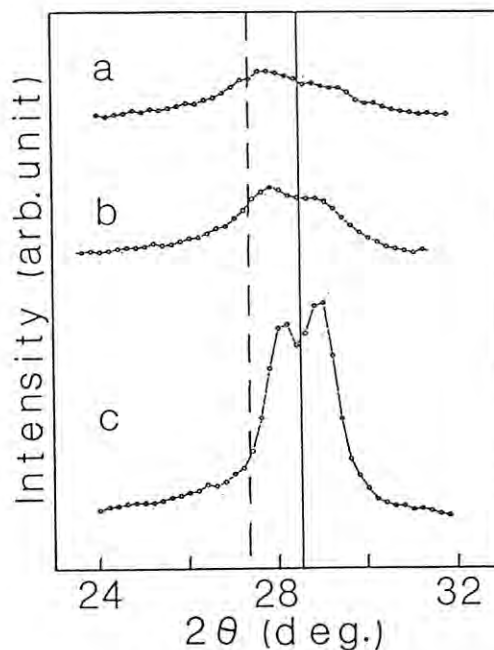


Fig.2 X-ray diffraction profile around Fe(110) peak of Fe/MgO( $x/15\text{\AA}$ ). (a)  $x=10\text{\AA}$ ; (b)  $x=16\text{\AA}$ ; (c)  $x=30\text{\AA}$ . Solid and dashed lines indicate the peak position of bulk  $\alpha$ -Fe(110) and MgO(200), respectively.



## SYNCHROTRON RADIATION LITHOGRAPHY SYSTEM IN AN ATMOSPHERIC ENVIRONMENT

Koichi OKADA, Eiichi KOUNO<sup>+</sup>, Eiichi NOMURA, Katsumi SUZUKI  
Kiyoshi FUJII, Yoshiharu TANAKA<sup>+</sup>, Joji IWATA<sup>+</sup> and Yutaka KAWASE<sup>++</sup>

Microelectronics Res. Labs.,<sup>+</sup>Production Engineering Dev. Lab.,

<sup>++</sup>R&D Planning and Technical Ser. Div., NEC Corporation, 1-1, Miyazaki Yonchome, Miyamae-ku, Kawasaki 213

### Introduction

Synchrotron radiation (SR) lithography is the most promising technology for replacing photolithography in future dimensions below 0.5  $\mu\text{m}$ . The high intensity and good collimation available with the SR appear to realize high throughput and highest resolution. Recently, the authors have developed an SR lithography system in an atmospheric environment, using the BL-9 beamline.

### System structure

The recently built SR lithography system, characterized by an atmospheric environmental exposure, provides a highly reliable beamline,<sup>1)</sup> an SR extracting chamber and a prototype SR stepper.<sup>2)</sup> The authors are deeply concerned with the exposure system in an atmospheric environment, since the system presents practical merits, such as lubricating material and vacuum chuck availability, mechanism simplicity and high throughput, due to eliminating the necessity for vacuum evacuation, as well as operation and maintenance ease.

Figure 1 shows the SR lithography system structure in an atmospheric environment. SR radiating from the Photon Factory storage ring is introduced into  $10^{-9}$  Torr ultrahigh-vacuum beamline (BL-9A branch beamline) with an oscillating mirror. In terms of system reliability, a fail-safe mechanism notion has been adopted, which is applicable to controlling any unforeseen vacuum breakdown, possibly due to a beryllium (Be) window rupture in the worst case. A 40 ms closing-time fast closing valve (FCV) and an acoustic delay line (ADL) are installed in the main beamline.<sup>3)</sup> In addition to the FCV and ADL, the authors have set up a <15 ms closing-time FCV and 40 ms delay-time ADL in the branch beamline, thus organizing a double vacuum protection system.

It is most essential that the SR extraction mechanism for atmospheric environmental exposure

be investigated. The SR extracting chamber consists of a Be window, a He chamber and an extraction window, as shown in Fig. 1. The He chamber is filled with flowing helium gas, whose pressure is precisely controlled within  $1 \text{ atm} \pm 10 \text{ mm aqua}$ , so as not to apply any extra pressure to the Be window. The extraction window, made of a 1  $\mu\text{m}$  thick silicon nitride film, has a 26 mm square area. Concerning a Be window, a high purity (99.8%) circular Be foil, vacuum-sealed by a Viton O-ring, was held mechanically onto a flange, using a stainless steel plate. A feasibility test was carried out in terms of pressure endurance.<sup>4)</sup> As a result, a Be window, 50  $\mu\text{m}$  in thickness and 35 mm in diameter, was preliminarily adopted, and, up to now, has operated successfully for the present purpose.

For attaining higher accuracy and throughput, a prototype SR stepper has been developed in an atmospheric environmental exposure mode. The stepper, connected with the beamline through the SR extracting chamber, consists of precision mechanical stages using piezoelectric actuators and DC servo motors, and a newly developed alignment system which can detect a 10 nm positioning error between a mask and a wafer during SR exposure.

### References

- 1) K. Okada, K. Fujii, Y. Kawase and M. Nagano: J. Vac. Sci. Technol. **B6**, 191(1988).
- 2) E. Kouno, Y. Tanaka, J. Iwata, Y. Tasaki and Ms. E. Kakimoto, and K. Okada, K. Suzuki, K. Fujii and E. Nomura: J. Vac. Sci. Technol. (to be published).
- 3) S. Sato, T. Koide, Y. Morioka, T. Ishii, H. Sugawara and I. Nagakura: Nucl. Instr. and Meth. **208**, 31(1983), and N. Kanaya, S. Sato, K. Nakajima and S. Hayashi: IEEE Trans. Nucl. Sci. **NS-33**, 1071(1986).
- 4) E. Nomura and K. Okada: in Digest 1988 1st MicroProcess Conf., 90(1988).

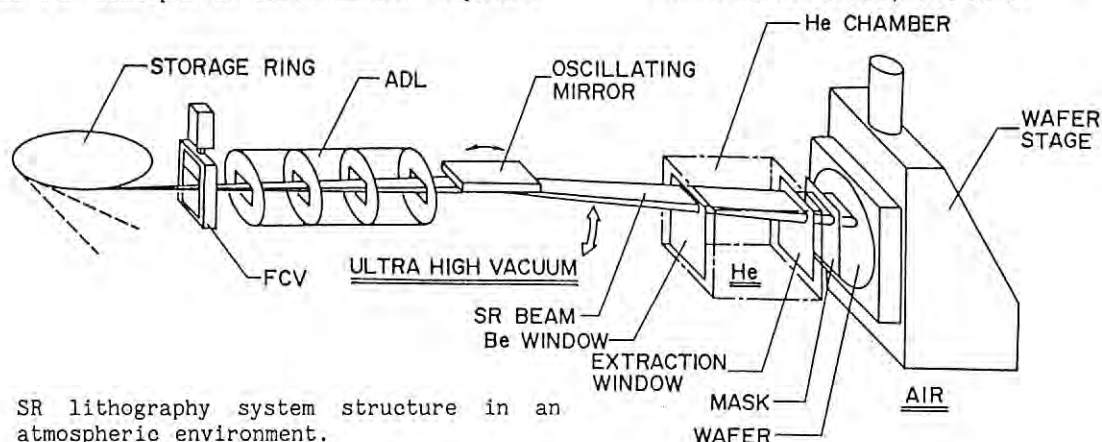


Fig.1 SR lithography system structure in an atmospheric environment.

# COMPUTER-CONTROLLED OSCILLATING MIRROR SYSTEM FOR SYNCHROTRON RADIATION LITHOGRAPHY

Kiyoshi Fujii, Koichi Okada, Masaharu Nagano\* and Hidehiko Kuroda\*

Microelectronics Res. Labs., R&D Planning and Technical Service div.\*,  
NEC Corporation, 1-1 Miyazaki 4-chome, Miyamae-ku, Kawasaki, Kanagawa 213

## INTRODUCTION

Synchrotron radiation lithography has a high potential for the quarter micron level high throughput lithography technique for ULSI fabrication. Since the SR beam has a narrow intensity distribution vertically, the SR beam should be scanned over the wafer to obtain a large exposure area.

The authors have adopted the oscillating mirror method<sup>1,2</sup> to enlarge the exposure area. Concerning the oscillating mirror system, the x-ray mirror reflectivity changes as a function of the glancing angle for the SR beam. Therefore, the x-ray intensity on the wafer depends on the beam height with reference to the light reflected from the mirror onto the wafer. In order to obtain high dose uniformity, a novel oscillating mirror system has been investigated, in which the SR beam scanning speed can be controlled as a function of the SR beam glancing angle with reference to the mirror.

## EXPERIMENTAL

Diagrams of the lithography beamline(BL-9A) and the oscillating mirror control system are shown in Fig.1 and Fig.2.<sup>3</sup> The driving force for the mirror was a combination of a DC servomotor and a cam. The DC servomotor was controlled by a microcomputer. In this system, the scanning speed of the reflected beam can be controlled as a function of the glancing angle by using the peculiarly-shaped cam and/or by controlling the angle velocity for the cam. In this work, an eccentric cam was employed and the DC servomotor was controlled to realize various scanning curves. The velocity data, prepared in the RAM of the microcomputer in advance, was sent to the motor according to the encoder count. The exposure shutter, situated upstream of the

oscillating mirror, was controlled in connection with the mirror motion. Shutter opening and closing was carried out to pass and stop the beam when the SR beam was overshooting the exposure area. The oscillating mirror was operated at a 1 scan per second rate.

The dose variation was obtained from the remaining resist thickness. The negative resist, MES-E, was coated about 1  $\mu\text{m}$  thick on Si wafers, and exposed without an x-ray mask in the vertical stepper. The number of scans was adjusted so as to obtain 70-80% remaining resist thickness after development. The resist thickness was measured by Nanospec/AFT along the vertical center line of the exposure area, and converted to x-ray dose, using the sensitivity curve, which was prepared in advance.

## RESULTS AND DISCUSSION

The experimental vertical dose variation, in case of constant velocity scanning, is shown in Fig 3(a). The dose difference between the upper and lower edges in the exposure field is approximately  $\pm 6\%$ . Next, the scanning speed was modified to improve the dose uniformity. Measurements were made on several velocity data, in which the scanning velocity at the vertically lower part of the exposure area was decreased. The best dose uniformity was obtained when the velocity curve was parabola and the ratio of the lower edge velocity to the upper edge velocity was 0.8. As shown in Fig.3(b), excellent vertical dose uniformity, better than  $\pm 3\%$  was obtained.

- 1) R.P. Haelbich et. al., J. Vac. Sci. Technol., B1, 1262 (1983)
- 2) M. Bieber et. al, ibid, B1, 1271(1983)
- 3) K. Okada et. al. ibid, B6, 191(1988)

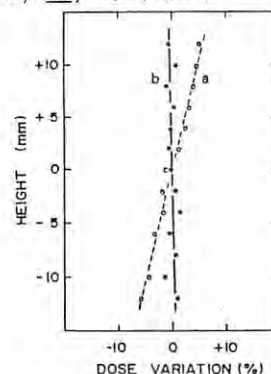
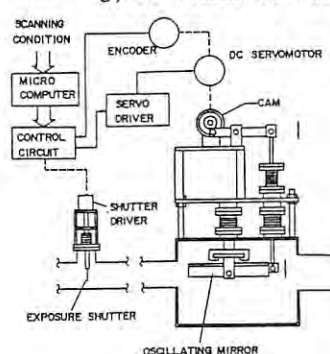
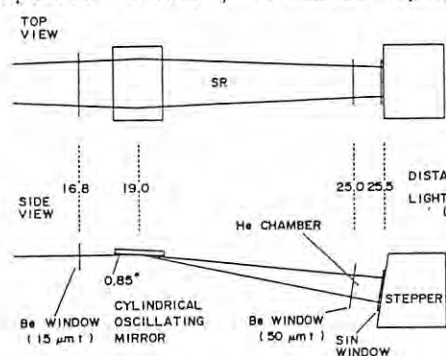


Fig.1 Lithography beamline optical system. Fig.2 Oscillating mirror control system. Fig.3 Vertical dose variation.

## MICROSTRUCTURE AND Schottky BARRIER HEIGHT OF Yb/GaAs INTERFACE

Kazuyuki HIROSE, Koichi AKIMOTO, Ichiro HIROSAWA,  
Jun'ichiro MIZUKI, Takashi MIZUTANI and Junji MATSUI

Fundamental Research Laboratories, NEC Corporation  
Miyazaki, Miyamae-ku, Kawasaki, Kanagawa, 213, Japan

### Introduction

Metal/semiconductor contact has been extensively studied due to both technological and scientific interest for over thirty years. Above all, the atomic structure at the interface and the mechanism for Schottky barrier (SB) formation are current topics. It was not until a couple of years ago that the atomic structure at a buried interface was directly observed for metal/semiconductor systems. It was significant that the superstructure was found at the Al/GaAs interface and likewise at  $a\text{-Si/Si}_{1-x}\text{Ge}_x$  interfaces. This result indicated the possibility that the relation between local electronic and structural properties would be clarified, even for conventional polycrystalline-metal/GaAs interfaces, similarly for an single crystalline-metal/semiconductor interface. Regarding Schottky barrier height (SBH), although it seems that a few models, such as unified defect model (UDM) and metal induced gap states (MIGS) model, can explain quite a few of the experimental results, new observations have appeared which are not explicitly involved yet in these models. The anomalous SBH changes were found for metal/GaAs contacts by inserting a chalcogen interlayer and a rare-earth metal interlayer. For contacts involving transition metal, peculiar SBH dependence on the physical properties, compared to other contacts, were considered to be due to rehybridization between transition metal d-band and either Si or GaAs sp-band. These observations indicated the importance of understanding the stage at which SBH was definitely determined during the interface evolution for various kinds of interfaces. This paper shows the existence of a superstructure at the Yb/GaAs interface observed by X-ray diffraction, using synchrotron radiation and the SBH difference for the interfaces with different atomic structures.

### Experimental

The sample structure used in this study consists of a 90 Å thick Al cap layer, a very thin Yb interlayer and a 0.7 μm thick Si-doped ( $1 \times 10^{17} \text{ cm}^{-3}$ ) GaAs epitaxial layer. Two kinds of samples were prepared for the present study; one had a 3 Å thick Yb interlayer (sample A), while the other had a 20 Å thick Yb interlayer (sample B). Yb and then Al were sequentially deposited at 30 °C in an MBE growth chamber, after a 4X6 surface superstructure was confirmed on the GaAs epitaxial layer surface by RHEED. The interface atomic structure was studied using a grazing incidence X-ray diffraction (GID) technique. The experiment was carried out with synchrotron radiation at BL-9C, installed at the Photon Factory (PF) in Tsukuba. SBH's were carefully determined from both I-V and C-V measurements.

### Results and Discussion

GID measurements revealed that the interface between Yb and GaAs(001) has a 4X1 superstructure and that the two diffraction patterns are obviously different from each other. Figures 1(a) and (b) show the partial pair-correlation function (partial Patterson function) calculated from the observed structure factors for fractional-order reflections for sample A and B,

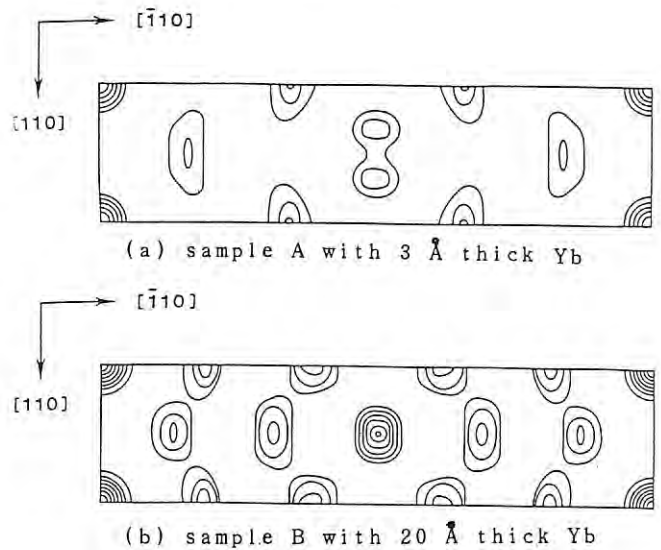


Fig. 1.

respectively. The difference between the two pair-correlation maps appears mainly in the center peak of the 4X1 lattice in Fig. 1(b). Because this peak intensity is very high, this pair-correlation comes from the correlation between the Yb atom (with a large atomic structure factor) and any other atoms. Therefore, it can be said that sample B has a new kind of ordered Yb structure which sample A does not have. Table I summarizes the  $\phi_b^{I-V}$ , ideality factor ( $n$ ) determined from I-V measurements and  $\phi_b^{C-V}$ , carrier concentration ( $N_D$ ) determined from C-V measurements. Since  $\phi_b^{I-V}$  and  $\phi_b^{C-V}$  are consistent with each other and since  $n$  values are close to unity, these data are sufficiently reliable. Note that the SBH value for sample B becomes larger than that for sample A by about 80 meV. It is observed that SBH values differ between Yb/GaAs interfaces with different interfacial superstructure caused by different Yb thicknesses. This observation leads us to the important conclusion that SBH is finally determined upon completion of metallization at a certain specific thickness and that the polycrystalline-metal/semiconductor interface is sufficiently homogeneous for SBH to reflect the interfacial structure difference.

Table I.

Sample	Yb thickness (Å)	ideality factor $n$	SBH I-V (eV)	SBH C-V (eV)	carrier concentration $N_D$ ( $\text{cm}^{-3}$ )
A	3	1.06	0.75	0.76	$2.24 \times 10^{17}$
B	20	1.07	0.84	0.82	$2.44 \times 10^{17}$



# INTERFACIAL SUPERSTRUCTURES OF AlN/GaAs AND AlN/InP SYSTEMS FABRICATED BY CHEMICAL VAPOR DEPOSITION WITH SURFACE PRETREATMENT OF GaAs AND InP SUBSTRATES

Shinji FUJIEDA, Koichi AKIMOTO, Ichiro HIROSAWA, Jun'ichiro MIZUKI, Yasunori MOCHIZUKI, Yoshishige MATSUMOTO and Junji MATSUI\*  
Fundamental Research Laboratories, NEC Corporation

\* R&D Group, NEC Corporation  
1-1 Miyazaki 4-chome, Miyamae-ku, Kawasaki, Kanagawa 213, Japan

## Introduction

The properties of III-V semiconductor surfaces should be controlled more precisely. We have developed a chemical vapor deposition of AlN on GaAs and InP, aiming at the high-quality passivation.<sup>1)</sup> It was found that the electrical properties of AlN/GaAs and AlN/InP interfaces are improved by the pretreatments which result in less As concentration at the GaAs surface<sup>2)</sup> and As-stabilized InP surface. In this report, we will show the structures of AlN/GaAs and AlN/InP interfaces, which are important for the understanding of the electrical properties of the interfaces.

## Experimental

60 Å-thick AlN films were deposited at 220°C on (100) GaAs and (100) InP substrates. Trimethylaluminum and hydrazine were used as precursors of AlN. The pretreatment was performed during the cooling after the epitaxial growth of GaAs with trimethylgallium and AsH<sub>3</sub> or the removing of the native oxides of InP in PH<sub>3</sub> ambient, prior to the AlN deposition. For GaAs case, AsH<sub>3</sub> was supplied throughout the cooling <G1>, or AsH<sub>3</sub>-introduction was stopped at 500°C and the GaAs was kept in pure H<sub>2</sub> at 500°C for 10 min <G2>. For InP case, PH<sub>3</sub> was supplied throughout the cooling <I1>, or the PH<sub>3</sub>-introduction was stopped at 450°C and the InP was thermally treated in AsH<sub>3</sub> ambient at 450°C for 10 min <I2>. The interfacial structures were characterized by the grazing incidence X-ray diffraction (GID) measurements. The details of the GID measurements utilizing synchrotron radiation were reported in the previous paper.<sup>3)</sup>

## Results and Discussion

1x4 and 1x6 interfacial superstructures were found for <G2>. A 2x1 superstructures were found for <I2>. It has been shown that n-type MIS diodes fabricated with <G2> and <I2> treatments have less density of interface states, respectively.<sup>2,5)</sup> No superstructures were found for <G1> and <I1>. The diffraction patterns<sup>4)</sup> for the 1x4 superstructure of AlN/GaAs<sup>4)</sup> and the 2x1 of AlN/InP<sup>5)</sup> are shown in Figs. 1 and 2, respectively. These are the first observation of superstructures for the samples fabricated by CVD.

The present results suggest that the electrical properties should depend strongly on interfacial structure. The fact that the AlN/GaAs sample <G1> has less interface states than the sample <G2> seems to indicate that the states are caused by excess As at the interface. The AlN/InP interface pretreated in AsH<sub>3</sub> flow at 450°C, however, showed 2x1 structure. The effect of the AsH<sub>3</sub> treatment on the electrical properties is the same as other As-related treatments, suggesting that the InP surface was terminated by As, which causes the 2x1 superstructures.

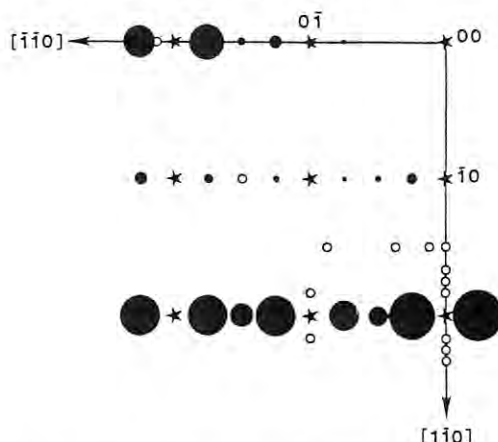


Fig.1 The 1x4 diffraction pattern of AlN/GaAs sample <G2>. In Figs.1 and 2, areas of the solid circles are proportional to intensities. At the reciprocal lattice points for the open circles, no diffraction peaks were observed. The fundamental reciprocal lattice points were indicated by the star marks.

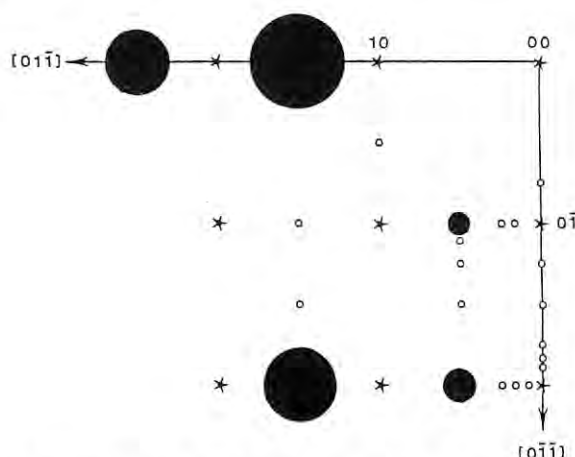


Fig.2 The 2x1 diffraction pattern of AlN/InP sample <I2>.

## References

- 1) M. Mizuta, S. Fujieda, Y. Matsumoto and T. Kawamura: Jpn. J. Appl. Phys. 25(1986)L945.
- 2) S. Fujieda, M. Mizuta and Y. Matsumoto: Jpn. J. Appl. Phys. 27(1988)L296.
- 3) K. Akimoto, J. Mizuki, T. Tatsumi, N. Aizaki and J. Matsui: Surf. Sci. 183(1987)L297.
- 4) K. Akimoto, I. Hirose, J. Mizuki, S. Fujieda, Y. Matsumoto and J. Matsui: Jpn. J. Appl. Phys. 27(1988)L1401.
- 5) S. Fujieda, K. Akimoto, I. Hirose, J. Mizuki, Y. Matsumoto and J. Matsui: submitted to Jpn. J. Appl. Phys.
- 6) R. Blanchet, P. P. Viktorovitch, J. Chave and C. Santinelli: Appl. Phys. Lett. 46(1985)761.



## MBE APPARATUS FOR IN SITU GRAZING INCIDENCE X-RAY DIFFRACTION

Koichi AKIMOTO, Jun'ichiro MIZUKI, Ichiro HIROSAWA and Junji MATSUI

Fundamental Research Laboratories, NEC Corporation  
1-1, Miyazaki 4-chome, Miyamae-ku, Kawasaki, Kanagawa 213, JapanIntroduction

In the field of fabrication process of semiconductor devices, it requires very sophisticated techniques to grow and control materials. A molecular beam epitaxy (MBE) techniques, for example, has become one of the popular techniques to satisfy these requirements. Recently, highly intense SR X-rays make it possible to realize the grazing incidence X-ray diffraction to study surfaces and also interfaces.

We constructed the MBE apparatus furnished with two E-gun evaporators, two Knudsen cells and RHEED, for in situ grazing incidence X-ray diffraction studies. We will describe a design of our apparatus and present its performance in the followings.

Description of the Apparatus

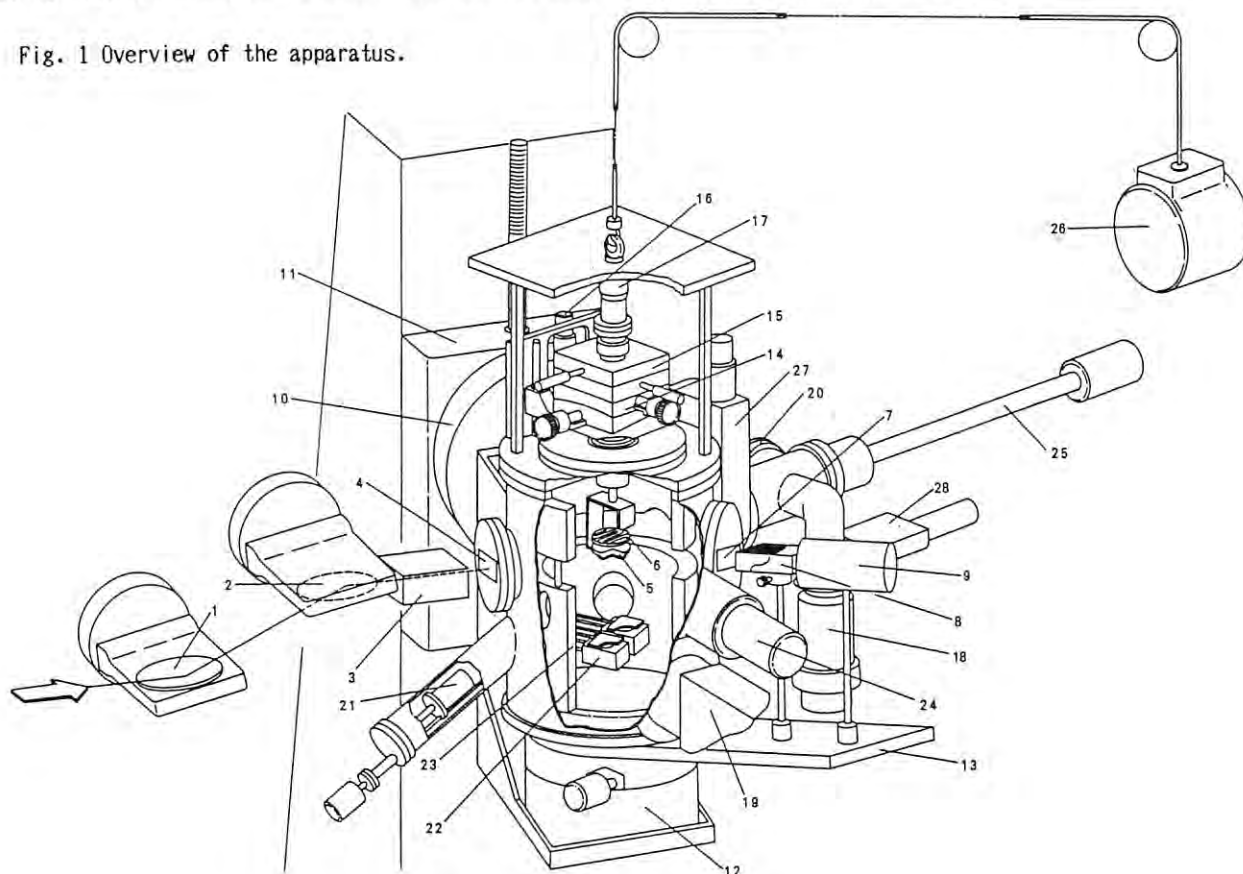
Figure 1 shows an overview of the apparatus. In our work, a sample (5) is mounted horizontally, and then the surface normal is nearly perpendicular to the X-ray polarization direction. In this geometry, a large active sample area is irradiated because of the shape of the incident synchrotron X-rays at BL-9C. This geometry also allows that the entire UHV chamber (318.5 mm in diameter and 300 kgw) is rotated simply with using a spring (26) of constant force (200 kgw) without compromising precision of the diffractometer (10,12). The UHV chamber is placed on a vertical two-axis goniometer (12). A two-theta arm (13) is used for moving the counter (9). The two-axis

goniometer (12) is set on a horizontal one-axis goniometer (10) for adjusting the grazing incidence angle. These goniometers (10,12) and the UHV chamber are installed on the Z-table (11), which can be moved along a vertical direction. Two 200  $\mu$ m thick Be windows (4) are located on the chamber walls for the incident beam. The diffracted beam is collected by a scintillation counter (9) through the Be window (7) and the 0.17° Soller slits (8). By the combination of three Be windows, two-theta angle can be changed from 0° to 126° without any blind angle. The sample, which can be heated up to 1000 °C by a Ta heater (6), is mounted on the top of the rotating manipulator (17) with a precisely tilting mechanism (14). The chamber is equipped with the RHEED apparatus (24). For the crystal growth or evaporation, two 2cc PBN Knudsen cells (21) and two E-gun evaporation sources (22) are prepared so as to make in situ X-ray diffraction measurements without changing the sample position. The sample is transferred by the magnetic transfer rod (25) from a preparation chamber (20). The base pressure in the MBE chamber is  $2 \times 10^{-10}$  Torr.

Performance

A chemically precleaned (111)Si wafer was heated up at 850 °C, on which we observed the 7x7 superstructure by X-ray diffraction. Moreover, the intensity at the (1/7 6/7) reciprocal lattice point was still observable (1/10 of the initial intensity) even after 12 hour exposure to an air.

Fig. 1 Overview of the apparatus.



## ANALYSIS OF DIFFUSE X-RAY SCATTERING FROM THE OMEGA PHASE IN TITANIUM ALLOYS

Masahiko MORINAGA<sup>1</sup>, Masato KATO<sup>1</sup>, Naohisa TAKESUE<sup>1</sup>, Natsuo YUKAWA<sup>1</sup>,  
Ken-ichi OHSHIMA<sup>2</sup>, Jimpei HARADA<sup>3</sup>, Satoshi SASAKI<sup>4</sup> and Shuji HANADA<sup>5</sup>

- 1) Toyohashi University of Technology, Toyohashi, Aichi 440, Japan
- 2) Institute of Applied Physics, University of Tsukuba, Tsukuba, Ibaraki 305, Japan
- 3) Department of Applied Physics, Nagoya University, Chikusa, Nagoya 464, Japan
- 4) Photon Factory, National Laboratory for High Energy Physics, Oho, Tsukuba, Ibaraki 305, Japan
- 5) The Research Institute for Iron, Steel and Other Metals, Tohoku University, Sendai 980, Japan

### Introduction

The omega phase occurs metastably in certain b.c.c. alloys (e.g. Ti and Zr alloys) upon quenching from high temperatures. The diffuse scattering peaks appear near  $2/3, 2/3, 2/3$  type reciprocal positions. A variety of structural models have been proposed for the diffuse omega phase. There are co-operative displacements of atoms along the  $\langle 111 \rangle$  directions in this phase. However, the further detailed local structure still remains unclear. All previous models have been made on the basis of diffuse intensity distributions on the only one (110) b.c.c. reciprocal lattice plane. In order to determine the local structure more definitely, it is needed to measure diffuse intensities in a volume in reciprocal space and to analyze them in a conventional way. In the present study, such an experiment was first carried out using a single crystal of Ti-24 mass% V alloy quenched from 1273 K.

### Experimental

The diffuse X-ray scattering in a volume in reciprocal space was obtained in absolute units with monochromatic radiation (wavelength  $\approx 1.2 \text{ \AA}$ ). The measurements were performed at the beam line 10A. A total number of measured points was about 13000. The direct beam intensity was estimated to be  $1.0 \times 10^{10}$  counts/sec at 175 mA, 2.5 GeV. The details on the measurements will be seen in our previous paper<sup>1</sup>.

### Analysis

For the Ti-V alloy, contribution of the chemical short range order to the total measured intensities is negligibly small, because of the very similarity in the X-ray atomic scattering factor between Ti and V.

Then, the diffuse scattering is expressed as,

$$I_D (\text{e. u.}) / f_{av}^2 = I_{SE} + I_{TDS+Huang}$$

where,  $I_D (\text{e. u.})$  is the measured diffuse intensity in electron units per atom and  $f_{av}$  is the average atomic scattering factor.  $I_{SE}$  is the size effect scattering and  $I_{TDS+Huang}$  is the sum of the thermal diffuse scattering and the Huang scattering. Thus, the observed diffuse intensities arise mostly from static and dynamical displacements of atoms from the ideal b.c.c. lattice positions. Utilizing a least-square method, the observed intensities can be separated into each components.

### Results

Fig. 1 (a-d) are the contour maps of the diffuse intensities in the (011) reciprocal plane; (a) and (b) are  $I_{SE}$  and  $I_{TDS+Huang}$  respectively, (c) is the synthesized intensity (i.e. the sum of  $I_{SE}$  and  $I_{TDS+Huang}$ ), and (d) is the measured intensity. There is good agreement between (c) and (d).

$I_{SE}$  and  $I_{TDS+Huang}$  exhibit large positive or negative peaks near the  $2/3, 2/3, 2/3$  reciprocal positions.

The existence of large atomic displacements was also confirmed from an experiment of the conventional crystal structure analysis. The measured atomic displacement coefficient, B, was as large as  $1.92 \text{ \AA}^2$ .

Local displacement parameters of atoms were determined quantitatively from the analyses of diffuse scattering. Based on these parameters, a structural model of the diffuse omega phase is now constructing.

### Reference

- 1) K. Ohshima, J. Harada, M. Morinaga, P. Georgopoulos and J. B. Cohen, J. Appl. Cryst., **19**, 188 (1986).

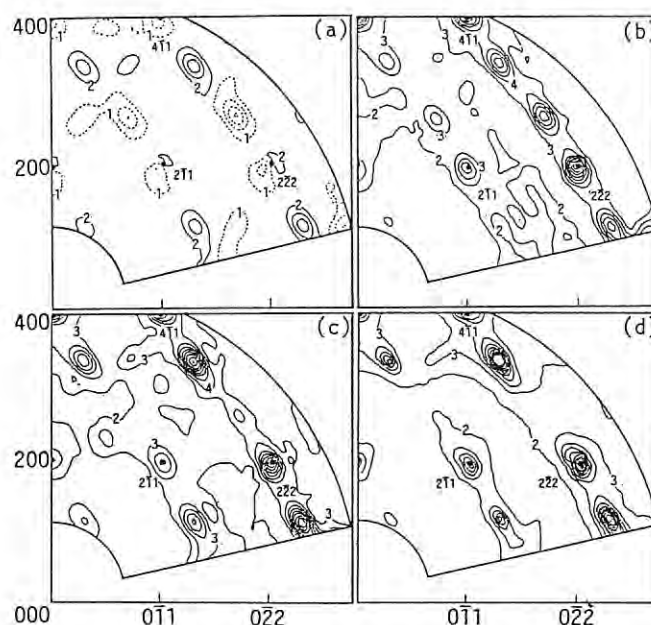


Fig.1 Contour maps of the diffuse X-ray intensity distribution in the (011) b.c.c. reciprocal lattice plane; (a)  $I_{SE}$ , (b)  $I_{TDS+Huang}$ , (c) synthesized and (d) observed intensities. The label of the curve 1,2,3,4 corresponds to the value of -0.5, 1.0, 2.5, 4.0, respectively and the contour interval is 1.5 (electron units per atom/  $f_{av}^2$ ).

## IMAGING SYSTEM WITH AN AMORPHOUS SILICON LINEAR SENSOR

Ken-ichi HASEGAWA,<sup>1</sup> Koh-ichi MOCHIKI,<sup>2</sup> Hiroyuki TAKAHASHI,<sup>2</sup>Cikaho IKEDA,<sup>3</sup> Ryouki KATO<sup>3</sup> and Yoshinori SATO<sup>4</sup>

1. Depart. of Electrical Engineering, Hosei University, Kajinocho, Koganei-shi, 184

2. Depart. of Nuclear Engineering, University of Tokyo, Bunkyo-ku, Tokyo, 113

3. Fuji Xerox Co., LTD., Hongo, Ebina-shi, Kanagawa, 243-04

4. Photon Factory, National Laboratory for High Energy Physics, Tsukubashi, 305

Introduction

Our group has been investigating characteristics of an a-Si linear image sensor (Fuji-Xerox, FIE-8B) for X-ray measurements[1]. We use a  $Gd_2O_3S$  phosphor sheet as an X-ray-to-light converter. This position-sensitive detector has a dynamic range of more than three decades and a spatial resolution of 0.5 mm(FWHM).

Following those results, we have developed a 2D position-sensitive detector in which the a-Si linear sensor is combined with an area-to-line converter using plastic optical fibers.

Area-to-line conversion

As shown in Fig. 1, a 2D image obtained with a  $Gd_2O_3S$  phosphor sheet is converted into 1D patterns at the fiber outlets. The plastic fiber used here is ESKA-CK10 (Mitsubishi Rayon Co., Ltd.) 50 cm long and 250  $\mu$ m in diameter. The a-Si linear sensor FIE-8B has 2048 elements 100 x 100  $\mu$ m<sup>2</sup> in each active area on 125  $\mu$ m centers, so that a long active length of 256 mm is usable. The 1024 fibers are aligned on the surface. The detective area is 8.0 mm x 6.9 mm (32 x 32 fibers). The optical fibers are aligned with a pitch of 250  $\mu$ m on the X-axis, while the fiber layout on the Y-axis has a zig-zag configuration as shown in Fig.1.

Performance

We reported in the previous paper that the minimum rms noise caused by switching noise and leakage currents in the sensor corresponds to 140 photons/s/element for 8 keV X-rays, therefore, the minimum rms noise can be estimated to be 270 photons/s/element.

Using collimated beam of 35  $\mu$ m diameter, spatial resolution of 500  $\mu$ m x 400  $\mu$ m (FWHM) was measured.

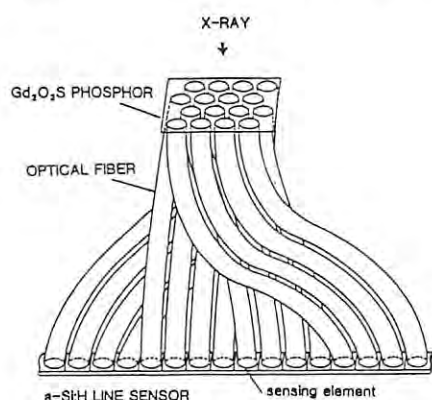


Fig.1 Schematic drawing of the area-to-line converter.

In order to apply the detector to synchrotron radiation experiments, we made a preliminary experiment for EXAFS measurements. The result is shown in Fig. 2. Between the output current from an ion chamber and output voltage of the a-Si sensor, good agreement can be observed. This result shows a possibility of EXAFS measurements of a local area in a sample.

Discussion

There is no technical limit to constructing a 2D detector with a larger sensitive area by this method. The biggest problem on the construction of area detectors, in general, is the cost which may be proportional to the number of channels. In the case of a 256 x 256 ch area detector, 64 image sensors are required. However, the estimated cost of the detector assembly seems to match well its associated signal processor including a large temporary memory.

We have also made another a-Si linear sensor with sensing elements 500  $\mu$ m high x 100  $\mu$ m wide for 1D measurements. As sensing elements with arbitrary shape can be fabricated, it is possible to construct a better a-Si sensor adapted well for 2D imaging.

The  $Gd_2O_3S$  phosphor sheet used here is 130  $\mu$ m in thickness, which is suitable to use for a much higher X-ray energy than 8 keV because it is mainly sold for medical use. Gas detectors was very low sensitivity in such an X-ray energy region, while our detector will become a powerful tool at high energy synchrotron radiation source facilities.

- 1) K. Mochiki, K. Hasegawa and S. Namatame, to be published in Nucl. Instr. and Meth.

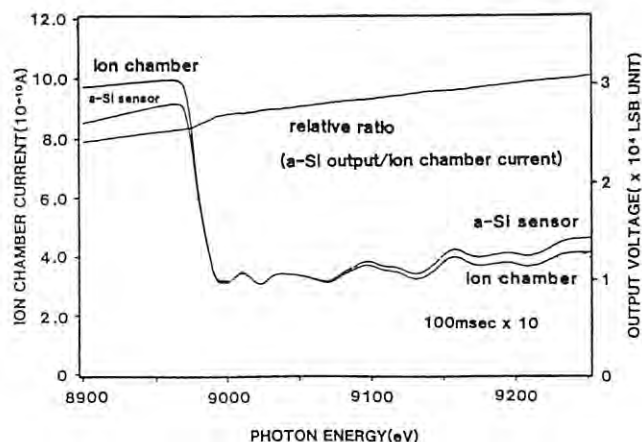


Fig.2 Comparison between outputs of the a-Si image sensor and an ion chamber.



## Real Time K-edge Subtraction X-ray Imaging

Hiroshi FUKAGAWA, Chousaku NODA, Katsuyuki NISHIMURA,\* Youichi SUZUKI  
Shin HASEGAWA, Masami ANDO,\*\* Kazuyuki HYODO,\*\* Masayoshi AKISADA,\*\*  
Fukae TOYOFUKU,\*\*\* Eiichi TAKENAKA\*\*\*\* and Ryosuke HOSAKA\*\*\*\*\*

The University of Electro-Communications, Chofu, Tokyo 182

\*Saitama Medical School, Moroyama, Saitama 350-04

\*\*National Laboratory for High Energy Physics (KEK), Tukuba, Ibaraki 305

\*\*\*University of Tsukuba, Tukuba, Ibaraki 305

\*\*\*\*Kyushu University, Fukuoka, Fukuoka 812

\*\*\*\*\*National Self Defence Medical College, Tokorozawa, Saitama 356

## K-edge Subtraction Imaging

An X-ray K-edge subtraction television system for noninvasive angiography utilizing synchrotron radiation is investigated.

The phantom, including contrast material (iodine), is irradiated by monochromatized dual energy X-ray flux, alternately, through a high speed beam expanding monochromator. The monochromator consists of a silicon crystal plate vibrating at 30Hz so that the phantom is irradiated by the X-ray flux of 150eV above and below the K-edge photon energy of iodine, 30 times per second, synchronizing to the television frame. As an X-ray detector, TV cameras optically coupled to an X-ray image intensifier (X.I.I.) are used and the video signal is processed to display the subtraction image of pairs of successive two images in real time.

Of the several types of processing schemes possible for the above mentioned system,<sup>1)</sup> the two cameras system shows the best result.

## System Implementation

The block diagram and the timing chart of the system are shown in Figs.1 and 2. The output image of X.I.I is divided into the same two images with the aid of a beam splitting prism of a special make. The two images are televised by the CCD cameras with electronic shutters on CCD chips. The timing of the shutter pulses is controlled so that the exposures for camera A and camera B correspond to the two kinds of X-ray

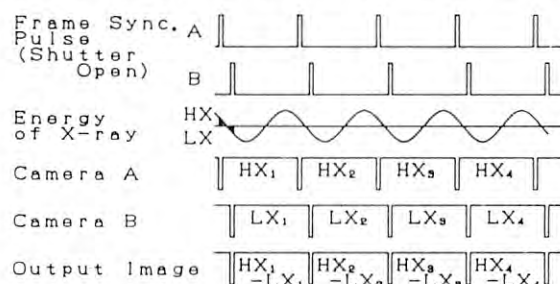


Fig.2 Timing Chart

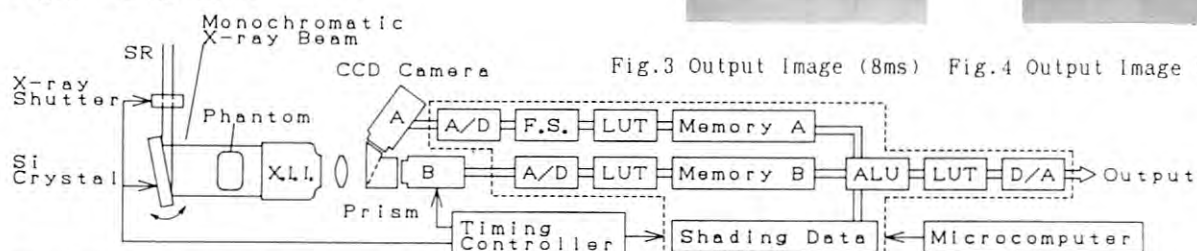


Fig.1 Block Diagram

irradiation. Each video signal is memorized in memory A (MA) and B (MB) as image data of higher photon energy (HX) and lower one (LX), respectively, after sampling ( $512 \times 256$  pixels) and quantizing (8 bits). The image data HX in MA and LX in MB are read out at the same time and fed to the digital calculation circuits simultaneously in order to obtain image difference signal.

## Experimental Results

Phantoms were examined with these imaging systems. One of the moving phantoms prepared for the experiments on fluoroscopy and the output images are shown in Figs.3 and 4. Exposure and interval times are 8ms (Fig.3) and 2ms (Fig.4), respectively.

1)Akio SUWA,et al:JJAP 27, No.10 (1988)(in press)

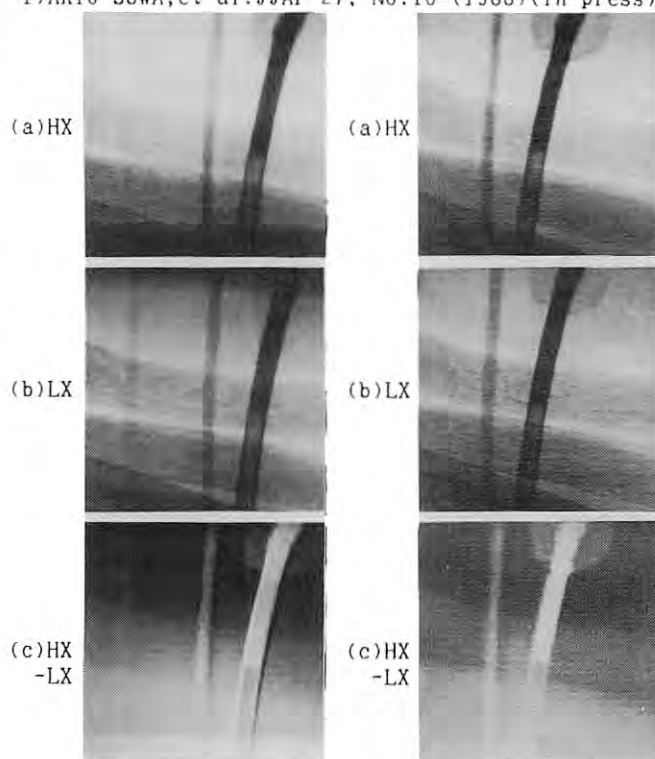


Fig.3 Output Image (8ms) Fig.4 Output Image (2ms)



# IN-SITU MEASUREMENT OF THE LATTICE CONSTANT OF WUSTITE SOLID SOLUTION UNDER HIGH PRESSURE

Toshimori Sekine<sup>1</sup>, Takumi Kikegawa<sup>2</sup>, Osamu Shimomura<sup>1</sup>, and Takehiko Yagi<sup>3</sup>

<sup>1</sup>National Institute for Research in Inorganic Materials, 1-1 Namiki, Tsukuba 305

<sup>2</sup>National Laboratory for High Energy Physics, 1-1 Oho, Tsukuba 305

<sup>3</sup>Institute for Solid State Physics, University of Tokyo, Roppongi, Minato-ku, Tokyo 106

## INTRODUCTION

There are four phases, metal, wustite, magnetite, and hematite, in the system Fe-Fe<sub>2</sub>O<sub>3</sub>. Wustite Fe<sub>x</sub>O is stable only at high temperatures above 570°C[1], and is in equilibrium with metallic iron or with magnetite, depending upon the oxygen fugacity. Although stoichiometric wustite FeO in rock salt structure is not stable[2], there is a controversy on the stability of stoichiometric wustite at high pressure. In-situ characterizations of wustite are required in order to know the detailed stability of wustite at high temperature and high pressure.

We have carried out in-situ measurements of the lattice constant of wustite coexisting with metallic iron or with magnetite using the MAX-80 apparatus.

## EXPERIMENTAL

The starting wustite and magnetite were prepared from hematite under controlled oxygen fugacity conditions at 1 atm with H<sub>2</sub>-CO<sub>2</sub> gas mixtures. The lattice constants are 4.312 Å and 8.395 Å, respectively. The wustite is mixed with metallic iron consisting of spherical particles of micrometer size, and with the magnetite. These two mixtures were used as starting materials.

High pressure experiments were carried out with MAX-80 using 6 mm anvils and sodium chlorite as pressure calibrant. Temperature was measured with chromel-alumel thermocouples, as shown in Fig. 1, without correction of the pressure effect on emf. The phase relations were investigated initially at an isobaric condition (about 3.5 GPa).

## RESULTS AND DISCUSSION

We collected data at several time intervals to check reaction rate, but the reaction was so

quick to observe the change of the wustite lattice constant in case of the mixture of wustite and metallic iron. However, in case of the mixture of wustite and magnetite, the reaction appears to be slow in the present high pressure cell. The cell keeps a lower oxygen fugacity, but the reaction in the mixture occurs at relatively high oxygen fugacity conditions. These competitive reactions were inevitable, and the observed lattice constant was not considered to be reasonable, as shown with a cross mark in Fig. 2. It is necessary to check the data also at relatively high oxygen fugacity conditions. Figure 2 gives a relationship between  $X$  of Fe<sub>x</sub>O and temperature for wustite quenched at various pressures. Our data for the wustite coexisting with metallic iron are consistent with that by Simons and Seifert[4]. The range of wustite in equilibrium with metallic iron extends towards the stoichiometric composition with increasing pressure.

There is another problem of the quenching effect of wustite from high temperature[6]. We could not collect data during quenching. It may be required to see the structure change during a slow cooling, especially for wustite coexisting with magnetite.

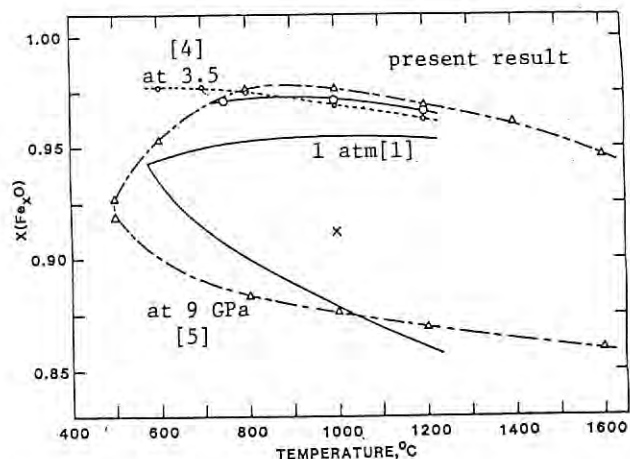


Fig. 2. Relationship between run temperature and  $X$  of wustite Fe<sub>x</sub>O determined from the lattice constant. A cross means one experimental point where wustite coexists with magnetite (see text for details).

## REFERENCES

1. L.S. Darken and R.W. Gurry, J. Am. Cer. Soc., **67**, 1398(1945).
2. R.M. Hazen and R. Jeanloz, Rev. Gophys. Space Sci., **22**, 37(1984).
3. C.A. McCammon and L. Liu, Phys. Chem. Mineral., **10**, 106(1984).
4. B. Simons and F. Seifert, Carnegie Inst. Year Book, **78**, 625(1979).
5. M. Kato, S. Urakawa and M. Kumazawa, 28th High Press. conf. Jap., 36(1987)(abstract).
6. B. Andersson and J.O. Sletnes, Acta Cryst., **A33**, 268(1977).

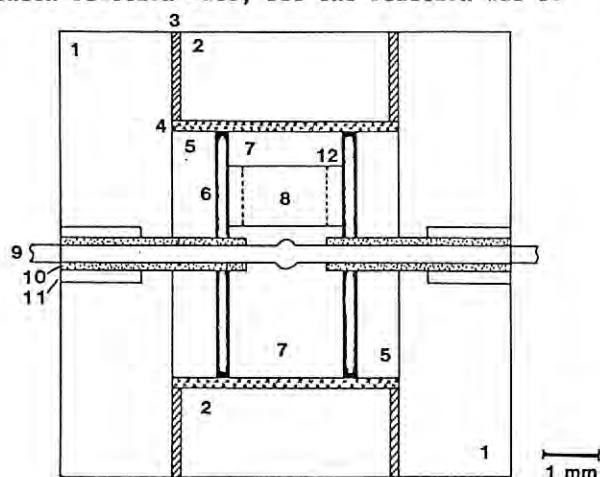


Fig. 1. Schematic cross section of furnace assembly used for the 6 mm anvil. 1. boron, 2. fired pyrophyllite, 3. gold tube, 4. molybdenum disk, 5. NaCl+10%boron, 6. graphite heater, 7. NaCl(orh-BN), 8. sample, 9. thermocouple, 10. alumina tube, 11. stainless steel tube, and 12. h-BN sleeve.

# THE ELECTRONIC PROPERTIES OF IONIC INSULATORS ON SEMICONDUCTOR SURFACES: ALKALI HALIDES ON GaAs

Ruth KLAUSER, Masakazu KUBOTA and Yoshitada MURATA

The Institute for Solid State Physics, The University of Tokyo,  
Roppongi, Minato-ku, Tokyo 106, Japan

Masaharu OSHIMA, Yasuko YAMADA, Tomoaki KAWAMURA and Tsuneaki MIYAHARA\*

NTT Laboratories, Musashino, Tokyo 180, Japan

\* KEK Photon Factory, Tsukuba 305, Japan

## Introduction

Alkali halides are excellent candidates to study the formation of insulator-semiconductor interfaces dependent on the lattice mismatch between the overlayer and the substrate.

In the first period of our beamtime at BL-1A of the Photon Factory we measured photoelectron core level spectra of the alkali halides: NaF and KF on the As-rich GaAs(100) and (111) surfaces and investigated adsorption and desorption behaviour by various annealing temperatures and different depositions.

## Experimental

Angle-integrated photoemission spectra were taken at a photon energy of 108.4 eV. Additionally X-ray photoelectron spectra were observed using a separate XPS source. The GaAs(100) and the As-terminated GaAs(111) were cleaned by Ar<sup>+</sup> sputtering and annealing. NaF and KF powders were evaporated from a tungsten basket.

## Results and Discussion

For initial monolayer deposition (about 0.5 ML) of NaF on GaAs(100) the F2p peak is shown in Fig. 1A. Heating up the sample to 460° C fluorine completely desorbs and only sodium remains on the surface (Fig. 1B). The fluorine desorption is combined with a decrease in the Ga3d/As3d peak intensity, but shows no significant shift of the substrate peak positions.

For multilayer deposition (about 8 ML) of NaF, substrate and overlayer core level peaks are shifted to higher binding energies (Fig. 1C), which are caused by a strong charging up of the uniform NaF film and in the case of the substrate peaks additionally by a band bending effect.

Reducing the amount of NaF to a monolayer, it is necessary to heat up the sample to 610° C (Fig. 1D), which is much higher than the fluorine desorption temperature in the initial monolayer case and no preferential desorption has occurred. There is also more fluorine deposited on the surface than for the initial thin adlayer. We explain this result as a separate deposition of Na and F at the initial monolayer coverage and the formation of a stable two-dimensional ionic NaF lattice from the monolayer obtained after annealing the initial multilayer. These behaviour is the same for the GaAs(111) surface.

For KF on GaAs(100) (Fig. 2) neither a preferential desorption of fluorine in the initial monolayer case nor a charging up effect in the multilayer case could be observed.

The reason for the fundamental difference of KF and NaF might originate in the different lattice constants. Contrarily to NaF, the KF lattice nearly matches the one of the substrate. We assume that KF islands are epitaxially grown on the surface.

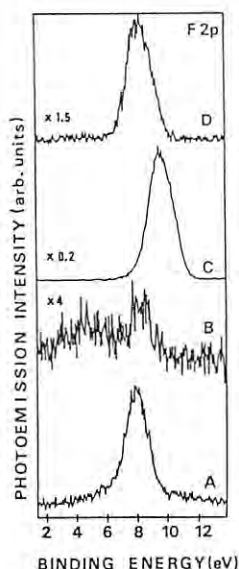


Fig. 1. Photoelectron spectra from the F2p core level of NaF on GaAs(100). A: monolayer deposition, B: after annealing the initial monolayer deposition up to 460° C, just below the fluorine desorption temperature, C: multilayer deposition, and D: after annealing the initial multilayer up to 610° C, the NaF amount is reduced to monolayer.

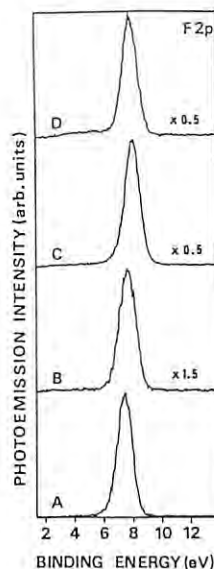


Fig. 2. Photoelectron spectra from the F2p core level of KF on GaAs(100). A: monolayer deposition, B: after annealing the initial monolayer deposition up to 400° C, C: multilayer deposition, and D: after annealing the initial multilayer deposition up to 500° C.

## OPTICAL PERFORMANCE AND APPLICATIONS OF A SOFT X-RAY MICROSCOPE

Yasushi KAGOSHIMA, Sadao AOKI, Masami KAKUCHI\*, Hideki MAEZAWA\*\*,  
Kazuyuki HYODO\*\* and Masami ANDO\*\*

Institute of Applied Physics, University of Tsukuba, Tsukuba,  
Ibaraki 305 Japan

\*NTT LSI Laboratories, Atsugi, Kanagawa, 243-01 Japan

\*\*Photon Factory, National Laboratory for High Energy Physics,  
Tsukuba, Ibaraki 305 Japan

## INTRODUCTION

Soft x-ray microscopes have been in operation or under construction in many synchrotron radiation facilities. The applications of the microscopes for biological specimens have been demonstrated with spatial resolution of better than 100 nm[1].

We developed a soft x-ray microscope using Fresnel zone plates as optical elements and the undulator radiation as a soft x-ray source at station BL-2B [2]. In this report are described the imaging performance of the microscope and its some applications.

## EXPERIMENT

Fig.1 shows the experimental arrangement of the soft x-ray microscope. The beamline diaphragm of 1 mm diameter limits the angular acceptance to the intrinsic divergence of the undulator radiation. The plane deflection mirror eliminates unwanted hard x rays. The main optical system which consists of a CZP, a pinhole, an OZP and a screen is designed so that the spatial resolution of 0.3  $\mu\text{m}$  and the magnification of around 200 can be achieved. A spatial filter is used in order to enhance the contrast of the image. An aluminum foil of 1.5  $\mu\text{m}$  thickness is used in order to protect the condenser zone plate from the high power of the undulator radiation.

The modulation transfer function (MTF) of the microscope was measured by making use of various pitch transmission gratings. Fig.2 shows the magnified image of 0.6, 0.4 and 0.3  $\mu\text{m}$  pitch gratings. Fig.3 shows the MTF, which was obtained from the contrast of the images of various pitch gratings. It was confirmed that the experimental performance was almost consistent with the theory.

As applications of the microscope, some biological specimens were observed. Fig.4 shows a magnified image of a red blood cell in its dry state. In this figure, the smoothed flattened shape of the cell can be recognized.

## CONCLUSION

Modulation transfer function of the soft x-ray microscope was measured. It was confirmed that performance of the microscope was almost consistent with the theory. Furthermore, the feasibility for practical observation of biological specimens was confirmed.

## References

- 1) X-Ray Microscopy-Instrumentation and Biological Applications, edited by P.C.Cheng and G.J.Jan (Springer, Berlin, 1987).
- 2) Y.Kagoshima et al., to be published in proceedings of X-Ray Microscopy '87 (Springer, Berlin)



Fig.2 Magnified Image of 0.6, 0.4 and 0.3  $\mu\text{m}$  Pitch Transmission Gratings.

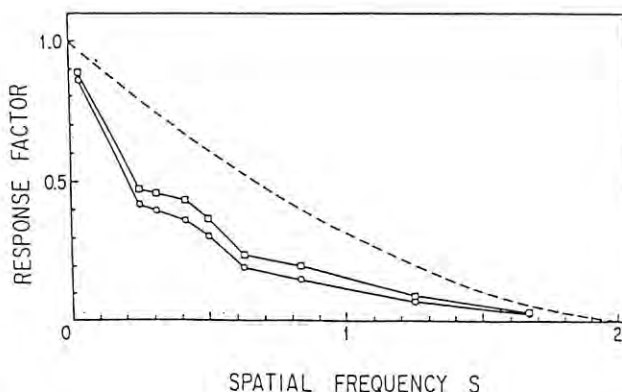


Fig.3 Modulation Transfer Function (MTF) of The Soft X-ray Microscope.  $S=0.50\mu\text{m}/\text{pitch}(\mu\text{m})$ .

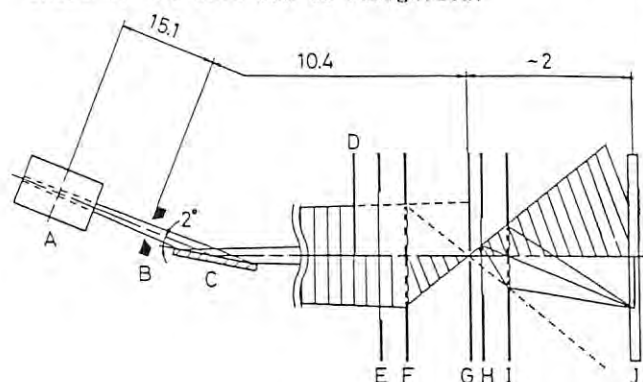


Fig.1 Experimental Arrangement of The Soft X-ray Microscope. A:Undulator, B:Beam Line Diaphragm (1mm $\phi$ ), C:Deflection Mirror, D:Spatial Filter, E:Al Foil(1.5 $\mu\text{m}$ ), F:CZP, G:Pinhole(10 or 20 $\mu\text{m}\phi$ ), H:Object, I:OZP, J:Screen.

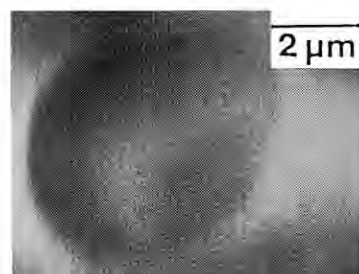


Fig.4 Magnified Image of Red Blood Cell.



SOFT-X-RAY  $\tilde{p}\tilde{A}$  SCATTERING BY LIGHT ELEMENT SOLIDS

Tadasu SUZUKI, Koichi MORI, Yasuo IGUCHI<sup>†</sup>, Kazumichi NAMIKAWA<sup>††</sup>,  
Hideki MAEZAWA<sup>†††</sup> and Akira YAGISHITA<sup>†††</sup>

Department of Physics, Sophia University, Kioi-cho, Chiyoda-ku, Tokyo 102

<sup>†</sup> Department of Systems Engineering, Toa University, Ichinomiya-gakuen-cho,  
Shimonoseki-shi, Yamaguchi 751

<sup>††</sup> Department of Physics, Tokyo Gakugei University, Nukuikita-machi, Koganei-shi, Tokyo 184

<sup>†††</sup> Photon Factory, National Laboratory for High Energy physics, Oho, Tsukuba-shi Ibaraki 305

The Transition probability ( $W$ ) of  $\tilde{p}\tilde{A}$  scattering increases as the scattered wavelength becomes longer. The theoretically estimated value  $W$  is about  $10^{-11}$  (/sr-atom-sec-photon) under the two conditions of  $k_0 \cdot a < 1$  and  $10 I \geq h\nu_0 \geq I$ , where  $k_0$  and  $h\nu_0$  are the wavenumber and the energy of the incident X-rays, and  $a$  and  $I$  are the radius and the ionization energy of inner-shell electron.<sup>1),2)</sup> The scattered photons might be detected if using intense radiation from an undulator.<sup>3)</sup>

The experimental arrangement is shown in Fig-1. The soft X-ray generated by an undulator and monochromatized with a grating incidence monochromator was guided onto a polycrystalline beryllium plate of 0.5 mm thick. The scattered radiation was detected at 90° from the polarization direction of incident rays, and was measured in the visible to infrared region by photomultiplier. Energy of the incident X-rays was 407 eV (30.5 Å) and flux was estimated as  $10^{12}$  (photons/sec-200 mA) with a resolution of 0.04 Å for 50 μm slits. Solid angle of observation was 15.8 (msr). The photo

cathode was cooled down to -45 °C with a cooling device for decreasing thermal noises.

Five interference filters were used as band-pass filters. The peak wavelength, transmittivity, bandwidth of the filters and sensitivity of the photomultiplier were summarized in Table 1, as well as transmittivity of viewing-port. These numerical values were used for the raw data corrections. Measurement time was 300 sec for each data. The relative cross section thus obtained is shown in Fig-2.

The corrected data disagreed with the theoretical prediction for the present, probably due in part to some noises not avoided yet. Thermal noise of the detector was much decreased than that in the last experiment, but background noise mostly due to the γ-rays still exists. Further reduction of electronic and γ-ray background noises is necessary.

## References

- 1) Y. Ohmura and T. Suzuki : J. Phys. Soc. Japan 53 (1984) 2801-2817
- 2) Y. Ohmura and T. Suzuki : J. Phys. Soc. Japan 55 (1986) 699-700
- 3) PF Activity Report, 1987 #5, p122

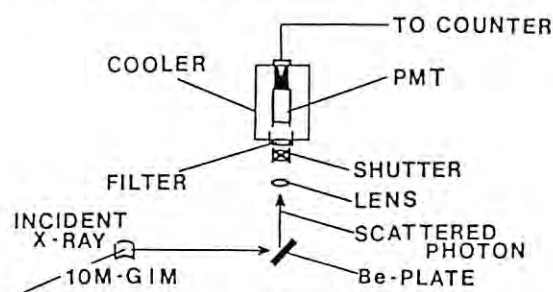


Fig-1 Experimental arrangement

peak w.l [nm]	tr <sub>f</sub> [%]	band w [eV]	tr <sub>w</sub> [%]	senp [%]
350	54	0.112	70	85
400	39	0.072	80	85
469	42	0.044	75	80
564	60	0.035	92	90
750	79	0.076	92	100

Table-1

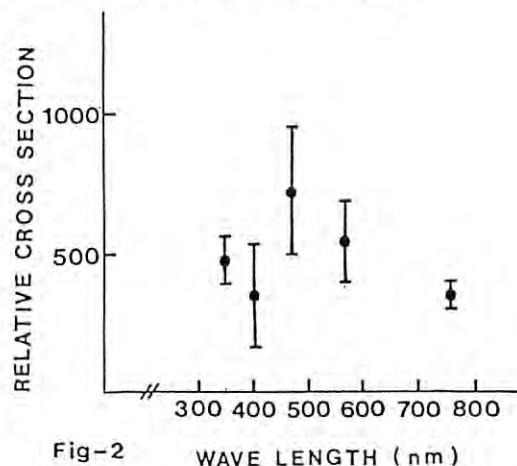


Fig-2



Photon Energy Dependence of Desorbed Ions from  $\text{H}_2\text{O}/\text{Si}(100)$  in the Valence Excitation Region

Hidetoshi NAMBA, Kousuke Ueyama\*, Mituo KOIZUMI\* and Haruo KURODA

Research Centre for Spectrochemistry and Department of Chemistry, Faculty of Science, the University of Tokyo, Hongo, Bunkyo-ku, Tokyo 113

\*Kuroda Solid Surface Project, Research Development Corporation of Japan, Tohokodai, Tsukuba, Ibaragi 300-26

Introduction

It can be considered that a fundamental research of photochemical reactions on well defined solid surfaces is a key feature for understanding surface chemical dynamics and for developing a new technique of surface material design. Detecting photo-reacted species by combining photon stimulated desorption(PSD) and surface analysis as a function of photon energy is an useful method to clarify an elemental process of surface photochemistry. It has been believed in PSI(=ion)D due to a core excitation that a formation of repulsive potential between a photon absorbed atom or ion and surrounding ones through an inter-atomic Auger transition has induced ion desorption(KF mechanism).<sup>1,2</sup> It implies that ion desorption is determined by only an internal state of the chemisorbed system. In this case a chemical shift due to chemisorption is only a selective parameter in photoexcitation. On the other hand, in a valence excitation region, more state selectivity or controllability in the photoexcitation can be expected. However a clear experimental evidence on surfaces suggesting the later mechanism has not yet been reported.

We briefly report results of PSD of  $\text{H}_2\text{O}$  adsorbed on  $\text{Si}(100)$  in the photon energy range from 4 to 60 eV. The experiments were performed at BL-7B in PF-KEK.

Experimental

Samples of  $\text{Si}(100)$  were cleaned by heating under UHV. Water admitted on a clean surface showing a  $2 \times 1$  LEED pattern at room temperature. Water molecule dissociatively chemisorbed with the same periodicity of the substrate. Detection of ion and neutral species by a quadrupole mass spectrometer were performed with measurements of UPS and AES.

Results and Discussion

Figure 1 and 2 shows the intensity distributions of  $\text{H}^+$  and  $\text{OH}^+$  as a function of photon energy above 16 eV. The  $\text{H}^+$  distribution has a threshold at about 22 eV and shows a broad peak extending to the photon energy above 50 eV. The  $\text{OH}^+$  peak begins from about 30 eV and also extends to 50 eV. The fact of the different fragmentation found in this energy range suggests that two kinds of photoexcitation cause each  $\text{H}^+$  desorption. Two different behaviours of  $\text{H}^+$  desorption must be resolved as shown by the dotted line in Fig.1.

In this energy range the substrate has no

absorption edge. UPS results indicate that thresholds corresponding to occupied energy levels of  $\text{Si-OH}$ ,  $\text{SiO-H}$  and  $\text{O } 2s$  are located about 4, 9 and 22 eV below the Fermi level, respectively. The smaller threshold energy shown in Fig.1 corresponds to the energy difference between  $\text{O } 2s$  and the Fermi level. The larger one is almost equal to the sum of the energies between  $\text{O } 2s$  and the Fermi level and between  $\text{SiO-H}$  and the Fermi level. The results suggest that the photoexcitations from  $\text{O } 2s$  to energy levels located near the Fermi level without and with a shake-up type excitation cause the different fragmentation under the present sensitivity of the detection. We measured a polarization dependence of  $\text{H}^+$  intensity as a function of the angle of incidence to the sample. The polarization dependence is quite similar in the energy range above 16 eV. The result fits with the explanation mentioned above that the same principal excitation is commonly included in both excitations. A shake up is generally polarization independent because that is due to an unipolar process.

In summary, we found the clear experimental evidence of PSD that does not fit with KF mechanism.

References

1. M.L. Knotek, Rep.Prog.Phys., 47(1984)1499.
2. "DIET I" ed. by N.H. Tolk et al. (Springer, Berlin, 1983).

Fig. 1  
 $\text{H}^+$  Yield

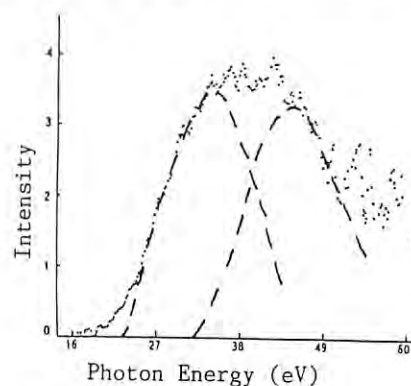
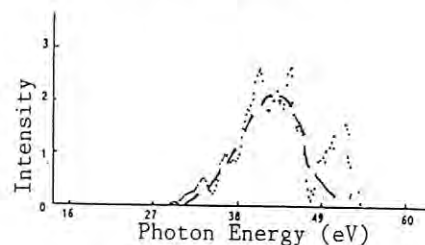


Fig. 2  
 $\text{OH}^+$  Yield



## CHARGE DISTRIBUTION OF Xe IONS PRODUCED BY MULTIPLE-PHOTOIONIZATION

T.MUKOYAMA<sup>1</sup>, A.YAGISHITA<sup>2</sup>, T.TONUMA<sup>3</sup>, T.KOIZUMI<sup>4</sup>,  
T.MATSUO<sup>5</sup>, H.SHIBATA<sup>6</sup>, K.SHIMA<sup>7</sup> and H.TAWARA<sup>8</sup>

- 1 Institute of Chemical Research, Kyoto University, Uji, Kyoto 611
- 2 Photon Factory, National Laboratory for High Energy Physics, Tsukuba 305
- 3 Institute of Physical and Chemical Research, Wako-shi 351-01
- 4 Department of Physics, Rikkyo University, Tokyo 171
- 5 Department of Pathology, Medical Research Institute, Tokyo Medical and Dental University, Tokyo 113
- 6 Research Center for Nuclear Science and Technology, The University of Tokyo, Ibaraki 319-11
- 7 Institute of Applied Physics and Tandem Accelerator Center, University of Tsukuba, Tsukuba 305
- 8 Institute of Plasma Physics, Nagoya University, Nagoya 464-01

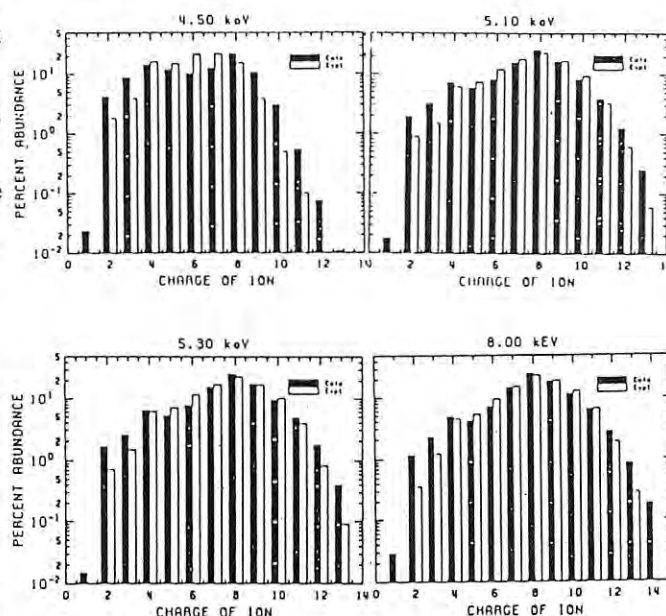
In a previous Activity Report #5, we reported our analysis of the mean charge of Xe ions produced by 4.1 - 8.0 keV X-ray impact<sup>1)</sup>. We observed that the mean charge of ions shows significant jumps at the  $L_1$ ,  $L_2$  and  $L_3$  edges of Xe which are found to be reproduced well through Monte Carlo simulation technique. This feature can be understood to be due to innershell vacancy cascade in photoionization. In this report we describe further analysis on the observed charge distribution of Xe ions produced through photoionization of X-rays in the energy range of 4 - 8 keV, based upon Monte Carlo technique. In Fig. 1 are shown some of examples of the charge distributions of Xe ions produced with 4.5, 5.45 and 6.8 keV photons. The present results indicate that the charge distributions show a peak around 8+ in the whole energy range investigated and relative abundances of ions with high charge increases with increasing photon energy, whereas that with low charge decreases with increasing the photon energy. It is also noticed that another peak shows up at the charge of 4+ for photons with the energy lower than the  $L_3$ -subshell edge. This peak can be understood to be originated from the initial vacancies produced in the  $M_4$ - and  $M_5$ -subshells. Generally speaking, the agreement between calculation and experiment seems to be good. However, more careful comparison suggests that the present Monte Carlo calculation tends to overestimate the intensities of ions with the charge lower as well as higher than the average or mean charges, compared with those obtained experimentally. These variations may be due to the assumptions in both calculation and experiment. In the present calculation, the atomic transition probabilities for multiply charged ions, as they are not available except for only a few cases, are assumed to be equivalent to those for singly charged ions. This assumed that vacancies in the outer shells, which are produced simultaneously are always filled up before vacancy cascades proceed from the innershells. Indeed it is not clearly known which vacancies are filled first. In the present calculation, we also neglect the increased binding energies of electrons due to multiple ionization during vacancy cascade. The use of the correct binding energies tends to decrease fractions of ions in higher charge because some Auger channels are energetically forbidden. On the other hand, experimentally, the detection efficiencies for lower charge ions might be lower than those for higher charge ions because the number of electrons emitted during collisions is smaller for lower charge ions than for higher

charge ions and, thus, probabilities of detecting these electrons, which are used as stop signal in our TOF spectrometer in the present experiment, may change. Another is the fact that, as these ions are less intense, their statistics obtained is not so good. Full detailed discussion of these results is given in our recent publication<sup>2</sup>.

## References

- 1) T.Tonuma et al., Photon Factory Activity Report #5 (1987) p.265.
- 2) T.Mukoyama et al., J.Phys. B 20 (1987) 4453.

Figure 1 Charge distributions of Xe ions produced in photoionization. (a) 4.50 keV, (b) 5.10 keV, (c) 5.30 keV and (d) 8.00 keV. The open columns show the experimental data, whereas the solid columns the calculated values.



## THRESHOLD PHOTOIONIZATION OF Xe SUBSHELL

Tatsuji HAYAISHI<sup>1</sup>, Akira YAGISHITA<sup>2</sup>, Eigorou MURAKAMI<sup>3</sup>, Eiji SHIGEMASA<sup>4</sup> and Yumio MORIOKA<sup>5</sup><sup>1</sup>Institute of Applied Physics, University of Tsukuba, Tsukuba, Ibaraki 305, Japan<sup>2</sup>National Laboratory for High Energy Physics, Tsukuba, Ibaraki 305, Japan<sup>3</sup>Chiba Institute of Technology, Narashino, Chiba 275, Japan<sup>4</sup>Tohoku University, Katahira, Sendai 980, Japan<sup>5</sup>Institute of Physics, University of Tsukuba, Tsukuba, Ibaraki 305, JapanIntroduction

Threshold electrons, having zero kinetic energies, can be ejected from atoms when the photon energy of irradiation is of the same level as the ionization energy of a shell of the atom. In inner-shell excitation, however, emission of threshold electrons has been observed by Heimann et al.<sup>1)</sup> in resonance states below the ionization limits. They proposed that resonance states decay primarily through shake-off in which the excited electron is ejected through Auger processes following the 4d hole. To investigate the decay processes on the resonance states in detail, it is desirable to observe not only the threshold electrons but also the accompanying ions. In this article we report the measurement of multiply charged ions in coincidence with threshold electrons near the 4d ionization limits of Xe.

Experiment

Experiments were carried out using a 2m grasshopper monochromator at BL-11A. The monochromator was equipped with a 600 lines/mm grating. The spectral resolution was about 0.85 Å (0.3 eV at 65 eV) with 100µm slit widths. The mass spectrometer used was of time-of-flight type accompanied with a threshold-electron energy analyzer<sup>2)</sup>. The resolution of the electron energy analyzer is roughly estimated to be about 0.03 eV on the basis of the FWHM measured at the Kr 4p ionization limits.

Results and Discussion

Figure 1 shows the yield spectra of Xe<sup>2+</sup> and Xe<sup>3+</sup> ions in coincidence with threshold electrons in the 64-72 eV photon energy region. In the coincidence method, no Xe<sup>+</sup> ions were detected throughout the photon energy region.

Two dominant peaks which appear somewhat above the 4d ionization limits are due to the 4d photoelectron. It becomes evident that Xe<sup>2+</sup> and Xe<sup>3+</sup> ions are produced through normal and double Auger processes following the 4d hole. The profiles show the effect of post-collision interaction, namely, shifts of peak positions and asymmetric shapes<sup>4)</sup>.

Many structures below the 4d ionization limits correspond to the Rydberg states, 4d<sup>-1</sup>np. It signifies that threshold electrons are ejected through decay on these resonance states even below the ionization limits. The same facts also have been observed near the Ar 2p and Kr 3d ionization limits.<sup>5,6)</sup> It is conceivable that shake-off<sup>1)</sup> and two-step autoionization<sup>5)</sup> take part in the decay process.

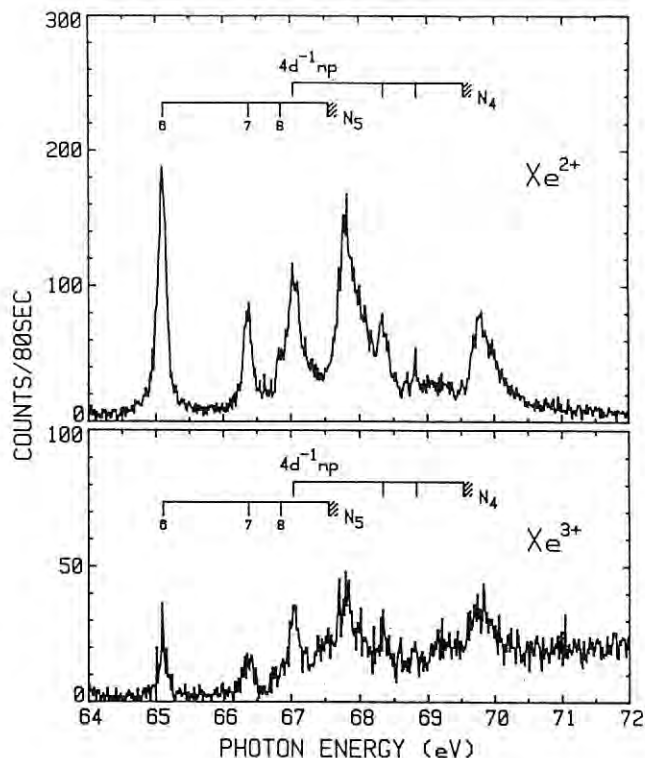


Figure 1. Yield spectra for Xe<sup>2+</sup> and Xe<sup>3+</sup> ions obtained in coincidence with threshold electrons as a function of photon energy. The photon energy scale was calibrated on the Xe 4d<sup>-1</sup>6p peak at 65.11 eV<sup>3)</sup>.

References

- 1) P.A. Heimann, D.W. Lindle, T.A. Ferrett, S.H. Liu, L.J. Medhurst, M.N. Piancastelli, D.A. Sherley, U. Becker, H.G. Kerkhoff, B. Langer, D. Szostak and R. Wehlitz, *J. Phys.* B20, 5005 (1987)
- 2) Y. Morioka, T. Akahori, T. Hayaishi, T. Namioka, T. Sasaki and M. Nakamura, *J. Phys.* B19, 1075 (1986)
- 3) G.C. King, M. Tronc, F.H. Read and R.C. Bradford, *J. Phys.* B10, 2479 (1977)
- 4) A. Niehaus, *J. Phys.* B10, 1845 (1977)
- 5) T. Hayaishi, E. Murakami, A. Yagishita, F. Koike, Y. Morioka and J.E. Hansen, *J. Phys.* B21 in press (1988)
- 6) T. Hayaishi, E. Murakami, A. Yagishita, Y. Morioka, G.P. Li, E. Shigemasa and T. Sasaki, *PF Acty. Rept.*, 270 (1987)



Research institute for Scientific Measurements, Tohoku University, Sendai 980

<sup>a</sup>Institute for Molecular Science, Myodaiji, Okazaki 444

<sup>b</sup>Photon Factory, KEK, Tsukuba 305

<sup>C</sup>Department of Science and Technology, Meisei University, Hino 191

<sup>d</sup>Institute of Applied Physics, University of Tsukuba, Tsukuba 305

eV, suggesting the ion-pair production such that

We have started systematic investigations on ionic fragmentation following the photoionization of the organometallic molecules in the soft X-ray region. We are mainly interested in investigating how fragmentation correlates with core-hole relaxation processes following the photoionization. We report here ionic photofragmentation studies on  $\text{Sn}(\text{CH}_3)_4$  (TMT) in the photon energy range 60–100 eV using time-of-flight (TOF) mass spectrometry.

$$\text{Sn}(\text{CH}_3)_4^{2+} \rightarrow \text{SnCH}_m^+ \text{ (or } \text{Sn}^+) + \text{CH}_3^+ + \text{neutrals.}$$

The experiments were carried out on BL11A at the Photon Factory. The monochromatized photon beam was focused onto the center of the ionization section of a TOF mass spectrometer. Sample gas (TMT) was introduced to the ionization section as an effusive beam through a nozzle of diameter 0.8 mm so that the molecular beam crossed the photon beam at right angles.

The doubly-charged ion would be produced by autoionization of the 4d-core hole state.

(b) Sn:4p photoionization

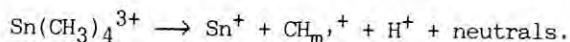
Figs. 1 and 2 give examples of photoelectron-photoion coincidence (PEPICO) and photoion-photoion coincidence (PIPICO) spectra.

The photoionization cross section of the 4p-subshell of atomic Sn is considerably smaller than that of 4d-subshell near the 4p threshold (80eV).<sup>1</sup> The effect of the Sn:4p-core photoionization of TMT is, however, clearly seen in the PIPICO spectra in Fig. 2: the ion-pair productions involving  $H^+$ , such as  $H^+-CH_m^+$  ( $m'=0-3$ ) and  $H^+-Sn^+$ , is enhanced significantly by the 4p-core photoionization above 80 eV.

(a) Sn:4d photoionization

It is known that the atomic 4d-subshell photoionization cross section of Sn increases from the threshold (34 eV) to its maximum peak at about 70 eV and then decreases to the Cooper minimum at about 150 eV.<sup>1,2</sup> The valence-shell photoionization cross section of TMT, on the other hand, decreases monotonically and is much smaller than the 4d-core cross section above 60 eV.<sup>3</sup> Thus, main fragment ions  $\text{CH}_3^+$ ,  $\text{SnCH}_m^+$ , and  $\text{Sn}^+$  seen in the PEPICO spectrum at 60 eV would be produced by the Sn:4d photoionization. These ions are also seen in the PIPICO spectrum at 60

The 4p-core photoionization would be predominantly followed by the Coster-Kronig transition which fills the 4p-core hole with one of the 4d electrons and ejects another electron. The TMT with two 4d-core holes would eject one more electron by autoionization. The observed PIPICO spectrum suggests the dissociation pathway of the triply-charged TMT:



- 1) J. J. Yeh and I. Lindau, At. Data Nucl. Data Tables 32 (1985) 1.
- 2) P. Gerad, M. O. Krause, and T. A. Carlson, Z. Phys. D 2 (1986) 123.
- 3) I. Novak, J. M. Benson, A. Svensson, and A. W. Potts, Chem. Phys. Lett. 135 (1987) 471.

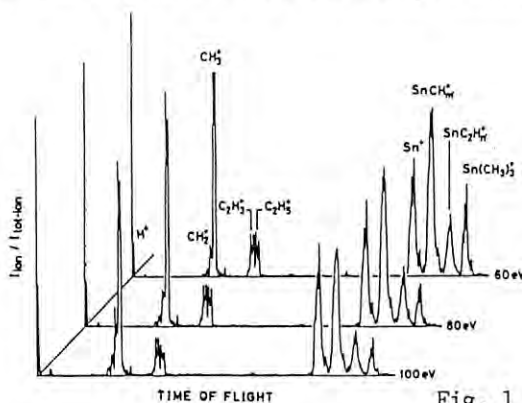


Fig. 1

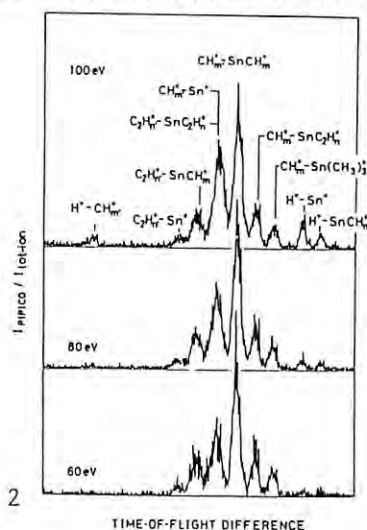


Fig. 2



IONIC FRAGMENTATION FOLLOWING THE C:1s AND Sn:3d PHOTOIONIZATION OF  $\text{Sn}(\text{CH}_3)_4$ 

Kiyoshi UEDA, Eiji SHIGEMASA, Yukinori SATO, Shin-ichi NAGAOKA<sup>a</sup>, Inosuke KOYANO<sup>a</sup>, Akira YAGISHITA<sup>b</sup>, Tetsuo NAGATA<sup>c</sup>, and Tatsuji HAYAISHI<sup>d</sup>

Research institute for Scientific Measurements, Tohoku University, Sendai 980

<sup>a</sup>Institute for Molecular Science, Myodaiji, Okazaki 444

<sup>b</sup>Photon Factory, KEK, Tsukuba 305

<sup>c</sup>Department of Science and Technology, Meisei University, Hino 191

<sup>d</sup>Institute of Applied Physics, University of Tsukuba, Tsukuba 305

### Introduction

We have extended the preceding study<sup>1</sup> on ionic photofragmentation of  $\text{Sn}(\text{CH}_3)_4$  to higher photon energy region between 260 and 600 eV, in which binding energies of C:1s (290 eV) and Sn:3d (500 eV) lie.<sup>2</sup> Our interest stems from how fragmentation pattern changes through the site-specific excitation of the C- or Sn-core. The experimental approach is the same as the preceding report.

### Results and discussion

#### (a) C:1s photoionization

Figs. 1 and 2 show examples of the photoelectron-photoion coincidence (PEPICO) spectra and photoion-photoion coincidence (PIPICO) spectra, respectively. In general, decomposition of  $\text{Sn}(\text{CH}_3)_4$  proceeds and small fragment ions such as  $\text{H}^+$ ,  $\text{C}^+$ , and  $\text{Sn}^+$  increase, as the excitation energy increases. Close inspection, however, reveals that relatively large ions  $\text{CH}_3^+$ ,  $\text{C}_2\text{H}_3^+$ , and  $\text{SnCH}_m^+$  increase from 260 eV to 300 eV, as seen in Fig. 1. This retardation of the fragmentation is due to the C:1s ionization starting from about 290 eV. The C:1s ionization is followed by the KVV Auger: the core-electrons originally belonging to Sn do not take part in the electronic relaxation of C:1s hole. The parent ion thus produced is doubly-charged. According the PIPICO spectra in Fig. 2, typical fragmentation patterns of the doubly-charged ion  $\text{Sn}(\text{CH}_3)_4^{2+}$  produced via C:1s ionization would be

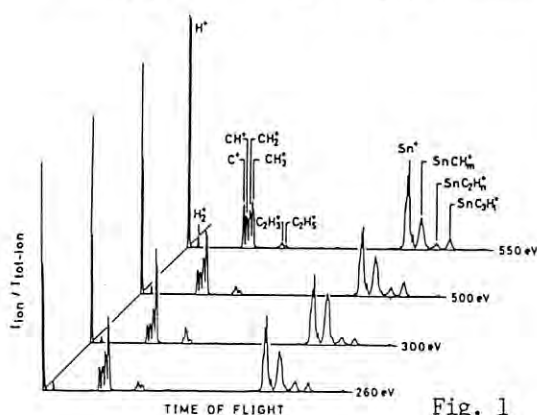
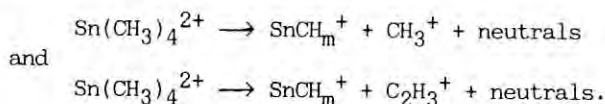


Fig. 1

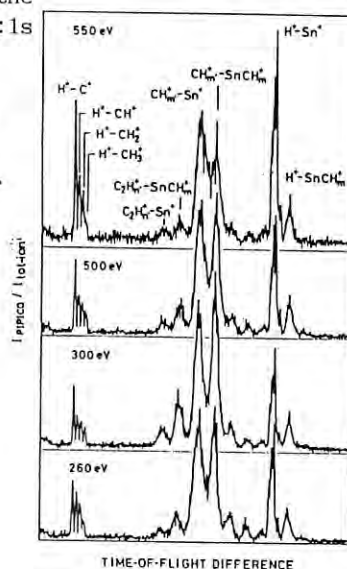
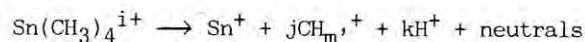


Fig. 2

#### (b) Sn:3d photoionization

Fig. 3 gives  $I_{\text{ion}}/I_{\text{photon}}$  for each ionic fragment near the Sn:3d edge.  $I_{\text{tot-ion}}/I_{\text{photon}}$  in fig. 3 increases above 500 eV owing to the Sn:3d ionization.<sup>2</sup> Ionic fragments whose production is effectively enhanced by the Sn:3d ionization are  $\text{Sn}^+$ ,  $\text{H}^+$ , and  $\text{CH}_m^+$ . Examining the PIPICO spectra of fig. 2, we find that each of  $I_{\text{PIPICO}}/I_{\text{tot-ion}}$  for  $\text{H}^+-\text{Sn}^+$  and  $\text{H}^+-\text{CH}_m^+$  with  $m'=0, 1$ , and 2 is enhanced by the Sn:3d ionization whereas that for  $\text{H}^+-\text{CH}_3^+$  is not.

The Sn:3d subshell in TMT is relatively deep and the Sn:4s, 4p, and 4d sub-shells exist as higher core-levels in TMT. Thus, the vacancy relaxation following the 3d ionization would occur to produce the multiply-charged TMT: the degree of the charge achieved would be 3-5. The observed features of the ionic fragmentation strongly suggest the dissociation pathway of the multiply charged TMT such as



with  $i=3-5$ ,  $j+k+1=i$ , and  $m'=0-2$ .

### References

- 1) K. Ueda et al., preceding report.
- 2) J. J. Yeh and I. Lindau, At. Data Nucl. Data Tables 32 (1985) 1.

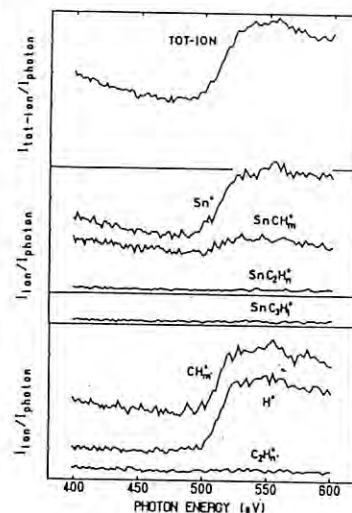


Fig. 3

# IONIC FRAGMENTATION FOLLOWING THE Ga:3p AND 3s PHOTOIONIZATION OF Ga(CH<sub>3</sub>)<sub>3</sub>

Kiyoshi UEDA, Eiji SHIGEMASA, Yukinori SATO, Shin-ichi NAGAOKA<sup>a</sup>, Inosuke KOYANO<sup>a</sup>, Akira YAGISHITA<sup>b</sup>, and Tatsuji HAYAISHI<sup>c</sup>

Research institute for Scientific Measurements, Tohoku University, Sendai 980

<sup>a</sup>Institute for Molecular Science, Myodaiji, Okazaki 444

<sup>b</sup>Photon Factory, KEK, Tsukuba 305

<sup>c</sup>Institute of Applied Physics, University of Tsukuba, Tsukuba 305

## Introduction

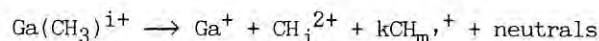
We have studied ionic photofragmentation of Ga(CH<sub>3</sub>)<sub>3</sub> in the photon energy region between 90 and 260 eV, in which binding energies Ga:3p (110 eV) and Ga:3s (160 eV) lie. We are especially interested in the fragmentation in which H<sup>+</sup> is produced via the site-specific excitation of the Ga-core far from H atoms. The experimental approach is the same as the preceding reports.<sup>1</sup>

## Results and Discussion

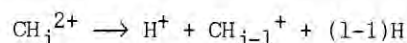
Fig. 1 gives I<sub>ion</sub>/I<sub>photon</sub> for each ionic fragment. The I<sub>tot-ion</sub>/I<sub>photon</sub> in Fig. 1 increases above 110 eV owing to the Ga:3p ionization.<sup>2</sup> Most of the ionic fragments are enhanced by the Ga:3p ionization whereas Ga(CH<sub>3</sub>)<sub>2</sub><sup>+</sup> is not. The H<sup>+</sup> yield increases above 160 eV again, owing to the Ga:3s photoionization. The effect of Ga:3s photoionization cannot be seen in the other ions, because the 3s photoionization cross section is very small.<sup>2</sup> The H<sup>+</sup> intensity normalized by the total-ion intensity, given in Fig. 1(d), clearly indicates the enhancement of the H<sup>+</sup> production by the

Ga:3p and 3s photoionization. The PIPICO efficiency curves in Fig. 2 indicate that the H<sup>+</sup>-Ga<sup>+</sup> pair production is enhanced by the Ga:3p or 3s ionization whereas the CH<sub>m</sub><sup>+</sup>-Ga(CH<sub>3</sub>)<sub>2</sub><sup>+</sup> pair production is not.

Let us consider how H<sup>+</sup> is produced via relaxation processes followed by the photoionization of the Ga:core-electron located far from H atoms. The Ga:3p photoionization will be followed by the Super-Coster-Kronig transition, which replaces the 3p hole with one of the 3d electrons and ejects another 3d electron. The parent ion with two-3d-hole will autoionize to become the triply-charged ion. The Ga:3s photoionization would produce the quartly-charged ion via similar vacancy cascade processes. The valence electrons participating the C-H bonds will not take part in these electronic relaxation processes of the Ga:core-hole. The effective production of H<sup>+</sup> would be reasonably understood by the two-step dissociation pathway:



followed by



with i=3 or 4 and k+j=i.

## References

- 1) K. Ueda et al., two preceding reports.
- 2) J. J. Yeh and I. Lindau, At. Data Nucl. Data Tables 32 (1985) 1.

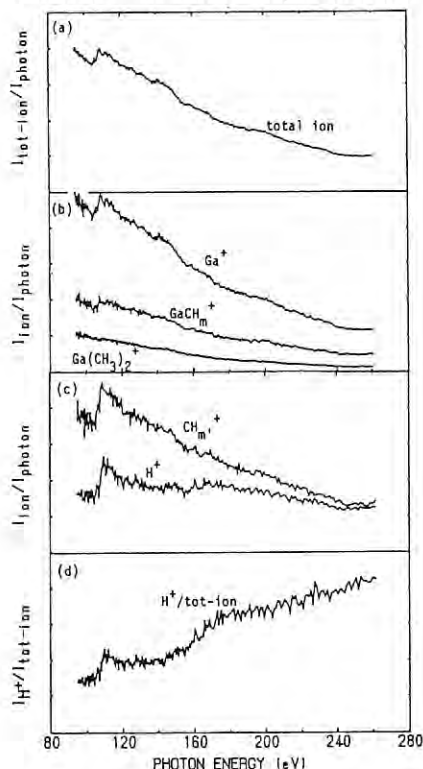


Fig. 1

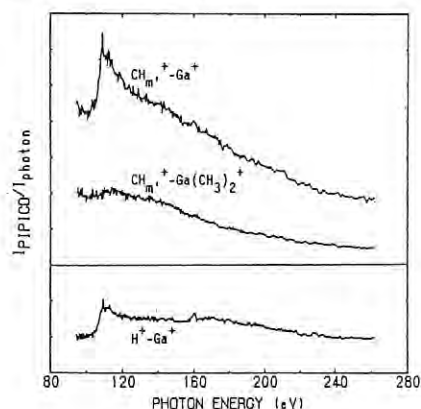


Fig.2

## OPTICAL CONSTANTS OF SUPERTHIN GOLD FILMS FOR SOFT X-RAYS

Mihiro YANAGIHARA, Jianlin CAO, Masaki YAMAMOTO, Akira ARAI,  
Shigeru NAKAYAMA, Hiroaki KIMURA, Tamaki MIZUIDE, and Takeshi NAMIOKA  
Research Institute for Scientific Measurements, Tohoku University, Katahira, Sendai, Miyagi 980

## Introduction

Soft X-ray multilayer mirrors have lately attracted considerable attention for their novel optical properties. In order to realize useful multilayer mirrors, it is required to have accurate optical constants of various materials for soft X-rays, especially in the form of a superthin film ( $< 100$  Å thick). Such data are, however, not available at present. Therefore, it is not clear how the optical constants of materials in a thin film form depend on the film thickness and structure. We studied the dependence of the optical constants of superthin gold films on the film thickness and deposition method in the soft X-ray region.

## Reflectance Measurements and Analysis

Superthin Au films of 39, 49, 55, 68, 94, 125, 145, 201, and 270 Å thick were prepared by ion-beam sputtering (IBS), and 89 and 211-Å thick Au films were made by electron-beam evaporation (EB). All the samples were deposited on bowl-feed polished BK7 substrates. A WYKO profilometer was used to measure the thickness and surface roughness of the deposited films (rms surface roughness  $\sim 5$  Å) as well as the surface roughness of substrates ( $\sim 5$  Å).

The reflectance measurements were carried out on BL-11A using a high-precision reflectometer. Reflectance vs incidence angle ( $R-\theta$ ) curves were measured at 10 to 26 photon energies between 60 and 900 eV by varying  $\theta$  stepwise 15 to 30 times from  $89^\circ$  to an angle at which the reflectance became immeasurable ( $\sim 10^{-3}$ ). At every angle of incidence, the intensity of reflected light was accurately determined from a series of intensity measurements done by rotating the detector at intervals of  $0.01^\circ$  through the reflection angle. The incident light intensity was constantly monitored by measuring the photocurrent from a gold mesh placed in the path of the incident beam.

The  $R-\theta$  curves derived in this way were analyzed in terms of the plane parallel slab model, in which the Fresnel reflection coefficients were corrected with a Debye-Waller factor for the surface roughness. The optical constants of the sample films was determined by fitting the calculated reflectance to the measured  $R-\theta$  curves by means of the least squares method.

## Results and Discussion

Figure 1 shows plots of the optical constants,  $\delta = 1-n$  and  $k$ , vs film thickness  $d$  for  $E = 100$  eV. The open (solid) circles and open (solid) triangles show  $\delta$  and  $k$  of the IBS (EB) samples, respectively. For comparison the data of Henke et al.<sup>1)</sup> are also shown in the figure at  $d = \infty$ .

As is seen,  $\delta$  and  $k$  of the IBS films show their dependence on the film thickness. The behavior of  $\delta$  and  $k$  for  $d \lesssim 60$  Å can be explained by taking into account the fact that the IBS

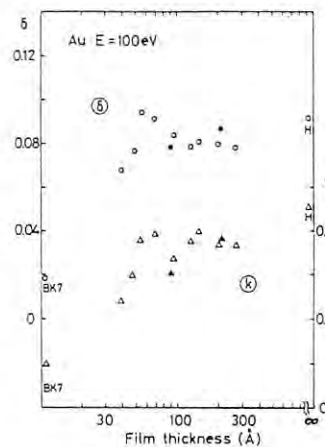


Fig. 1.  $\delta = 1-n$  (○: IBS, ●: EB) and  $k$  (△: IBS, ▲: EB) of superthin Au films vs film thickness measured at  $E = 100$  eV.

films prepared by our deposition system undergo a structural change from islands to a continuous film structure at  $d \sim 60$  Å. For a sample having an island structure, the incident soft X-rays are reflected not only from gold but also from the uncovered part of the BK7 substrate, whose  $\delta$  and  $k$  were estimated, in the present study, to be smaller than those of Au (their values are shown at  $d \sim 0$  Å in the figure). Consideration of these facts provides a qualitative explanation for the initial rise in the  $\delta-d$  and  $k-d$  curves.

As is noticed in Fig. 1,  $\delta$  and  $k$  show some variations in a range  $60 \lesssim d \lesssim 150$  Å. A similar behavior is observed also for other photon energies with a speculation that these variations might be due to a phase change in the crystal structure. To clarify this point we examined the crystal structure of the samples by means of X-ray and electron diffractions. However, we could not observe any sign of phase change in the diffraction patterns for the sake of their ambiguity.

It is also seen in Fig. 1 that  $\delta$  estimated for the 201-Å thick IBS film is lower by about 7% than that for the 211-Å thick EB film. According to the free electron theory a large  $\delta$  value means a high electron density, and this leads to a conclusion that the EB film is more tightly packed than the IBS film in the state of continuous film. The crystal structure may have something to do with this matter. Therefore, we measured X-ray diffractions from the EB and IBS films of about 1000 Å thick, and found that the FWHM of the diffraction peaks of the IBS film is wider by three times than that of the EB film. This result shows that the IBS film has crystal grains of small size. The IBS film may have porosities owing to the small grain. Besides precise observations for thin films using an X-ray or electron-beam diffractometer, measurements of mass density using a microbalance, for example, are now necessary to clarify this point.

## Reference

- 1) B. L. Henke, P. Lee, T. J. Tanaka, R. L. Shimabukuro, and B. K. Fujikawa: *At. Data Nucl. Data Tables* 27 (1982) 1.



## RE-EXAMINATION OF SOFT X-RAY REFLECTANCE OF MULTILAYER MIRRORS AFTER IRRADIATION OF SR

Masaki YAMAMOTO, Mihiro YANAGIHARA, Akira ARAI, Jianlin CAO,  
Shigeru NAKAYAMA, Tamaki Mizuide, Hiroaki Kimura, and Takeshi NAMIOKA

Research Institute for Scientific Measurements, Tohoku University, 2-1-1 Katahira, Sendai, 980

### Introduction

Soft x-ray multilayer mirrors of Mo/Si and Rh/Si have been designed and fabricated<sup>1)</sup> for dispersive elements to be installed as a reflection filter in the beamline 12C, PF-KEK, developed for experiments on Photo-assisted Chemical Vapor Deposition (Photo-CVD)<sup>2)</sup>. The present study is on an evaluation part to bring information to further improvement of the fabrication of multilayer mirrors.

### Reflectance before Irradiation of SR

Soft x-ray reflectances of multilayer mirrors were measured with a precision reflectometer<sup>3)</sup> installed at the beamline 11A, PF-KEK equipped with a grasshopper monochromator. For the Mo/Si multilayer, a peak reflectance of 42.5% was obtained for light of 100 eV at  $\sim 49^\circ$  angle of incidence with a resolving power of  $\sim 13$ . For the Rh/Si multilayer, the highest reflectance comparable to Mo/Si multilayer was obtained by only 21 layers, thus the multilayer filters fabricated were found to be quite efficient as the dispersive element for photo-CVD experiments<sup>4)</sup>.

### SR Irradiation at Beamline 12C

After the reflectance measurement, the multilayers were installed in the beamline 12C and were evaluated in respect to the radiation durability to the strong undispersed SR under the irradiation at  $45^\circ$  angle of incidence for 26 hours with an average ring current of 175 mA. The spot size on the filter was  $\sim 5 \times 5 \text{ mm}^2$ . The temperature of the filter was measured by a thermocouple pasted on the surface of the filter, and was found to be about  $100^\circ\text{C}$  after reaching an equilibrium. No cooling system was employed. The intensity of the light reflected from the filter was estimated to be  $10^{14}$ – $10^{15}$  photons/s from a measurement of photoelectrons emitted by a gold mesh placed in the reflected beam by assuming the photoelectron yield of gold to be 0.1.<sup>2)</sup> Visual examination of the Mo/Si filter after extended irradiation of SR showed a slight surface shade, which is quite likely to be caused by C layer deposition by decomposition of residual gas elements of hydro-carbon.

### Re-Examination of Soft X-Ray Reflectance

In the present experiment, the soft x-ray reflectance of the multilayer mirrors after the irradiation test is re-examined to study the irradiation damage. The same experimental system, the reflectometer at beamline 11A, was used to measure the reflectance. Reflectance spectra at various angles of incidence were measured at the center of the irradiated part and at the non-irradiated part. Figure 1 shows examples of the measured spectra at photon-energies of 65eV–110eV with a Be-filter for rejection of higher order

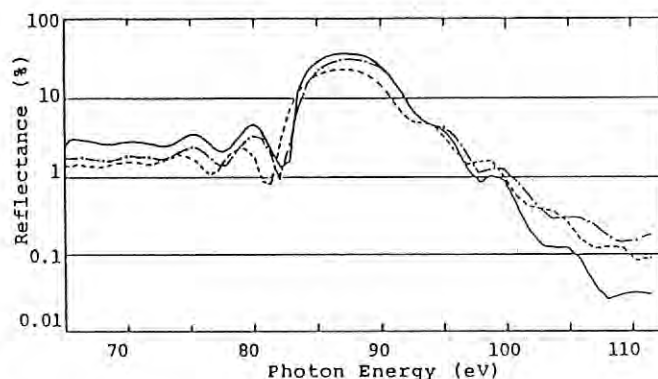


Fig. 1 Soft x-ray reflectance spectra of the Mo/Si multilayer filter. Angle of incidence was fixed to  $40^\circ$  from normal. The solid line - before irradiation. The dotted line - irradiated part. The dash-dott line - non-irradiated part.

components from the grasshopper monochromator. The solid line shows, in reference, the original spectrum measured before the SR irradiation. At the non-irradiated part, reflectance was reduced slightly but no shift in peak position was observed. At the irradiated part, a certain amount of peak shift was evident as well as the 30% reduction in peak reflectance.

At  $49^\circ$  angle of incidence at the non-irradiated part, the peak reflectance of 40% was observed, which was comparable to the original value. This showed that the multilayer filter withstood the temperature increase to  $100^\circ\text{C}$  by SR irradiation.

It was also found by inspection of the reflectance spectra around the K absorption edge of C in and out of the surface shade that a carbon layer exist at the surface of the shade. This suggest that the 30% attenuation in measured reflectance should be explained in some part by the surface contamination of C deposition. No deterioration was observed in surface roughness term by measurements of the WYKO profiler. Quantitative analysis is now in progress.

### References

- 1) M. Yamamoto, M. Yanagihara, A. Arai, J. Cao, S. Nakayama, T. Mizuide and T. Namioka, to appear in *Rev. Sci. Instrum.* (1989).
- 2) K. Tanaka, H. Kato, T. Kikuchi, and A. Yagishita, to appear in *Rev. Sci. Instrum.* (1989).
- 3) M. Yanagihara, M. Niwano, T. Koide, S. Sato, T. Miyahara, Y. Iguchi, S. Yamaguchi, and T. Sasaki, *Appl. Opt.*, **25** 4586 (1986).
- 4) M. Yanagihara, M. Yamamoto, A. Arai, J. Cao, and T. Namioka, *Proc. SPIE* **984** (1989) in print.



## MULTIPLE-PHOTOIONIZATION OF RARE-EARTH ATOMS; Sm, Eu AND Yb.

Masuihiro YOSHINO, Tatusji HAYAISHI<sup>+</sup>, Yukikazu ITIKAWA<sup>#</sup>, Yoh ITOH<sup>\$</sup>, Tetuso KOIZUMI<sup>\*</sup>,  
Takashi MATSUO<sup>\$\$</sup>, Tetuso NAGATA<sup>++</sup>, Yukinori SATO<sup>##</sup>, Yusuke TAKIZAWA<sup>\*</sup>  
and Akira YAGISHITA<sup>\*\*</sup>

Faculty of General Education, Shibaura Institute of Technology, Ohmiya, Saitama 330;  
+Institute of Applied Physics, University of Tsukuba, Tsukuba-shi, Ibaraki 305;  
#Institute of Space and Astronautical Science, Meguro-ku, Tokyo 153; \$Faculty of  
Science, Josai University, Keyaki-dai, Sakado, Saitama 350-02; \*Department of  
Physics, Rikkyo University, Toshima-ku, Tokyo 171; ++Department of Science and  
Technology, Meisei University, Hodokubo, Hino, Tokyo 191; ##Research Institute of  
Scientific Measurements, Tohoku University, Katahira, Sendai 980; \$\$Med. Res.  
Inst., Tokyo Med. Den. University Bunkyo, Tokyo 113; \*\*Photon Factory, National  
Laboratory for High Energy Physics, Oho, Tsukuba-shi, Ibaraki 305

In the course of experimental study for multiple photoionization of metal atoms, we present here the results for the rare-earth atoms; Sm, Eu and Yb.

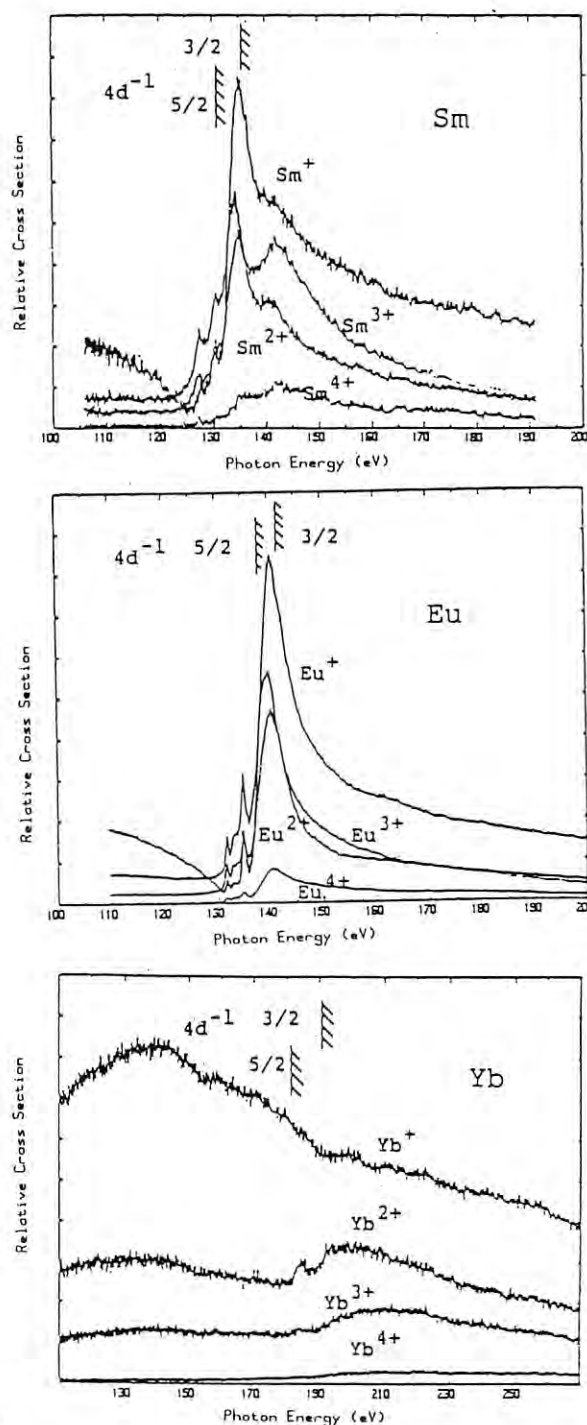
The details of experimental apparatus and procedure have been described previously<sup>1)</sup>. The synchrotron radiation emitted from 2.5 GeV storage ring in the Photon Factory was dispersed with a 2 meter Grasshopper monochromator, and crossed with a beam of target atoms from a furnace. The resultant photoions were mass-selected by a time-of-flight spectrometer. The relative intensities for the different charge state of the ion were measured as a function of photon energy in the region around 4d-ionization threshold of each target.

Figures 1, 2 and 3 show the ion yield spectra obtained for Sm, Eu and Yb respectively. For Sm and Eu, a pronounced peak which was attributed to the 4d-4f,  $\epsilon$ f giant resonance was seen in each ion yield spectrum at the position of 4d-ionization threshold of relevant atoms. On the other hand, no such structure was found for Yb whose 4f subshell was fully filled. As can be seen, the production of the singly-charged ion was dominant in this photon energy range, in contrast with the results for atoms just preceding the rare-earth atoms in the Periodic Table of which main products were doubly- and triply-charged ions<sup>2)</sup>. Though experimental results on rare-earth atoms are scarce, the determination of photoelectron partial cross sections have been reported for Sm<sup>3)</sup> and Eu<sup>4)</sup>. In both cases, 4f partial cross section is apparent to be dominant in the vicinity of the 4d-4f resonance, which indicate that singly-charged ion is exclusively produced via  $4d^9 4f^n 6s^2 \rightarrow 4d^{10} 4f^{n-2} 6s^2 \epsilon 1$  autoionization. The interference between the discrete excitation plus autoionization and the direct ionization causes the asymmetry in the Fano type profile of the singly-charged ion yield spectrum.

Detailed analysis of the results is still in progress.

## References

- 1) Y. Sato et al., J. Phys. B **18**, 225 (1985)
- 2) T. Nagata et al., PF Act. Rep. #5 268 (1987)
- 3) T. Precsher et al., J. Phys. B **19**, 1645 (1986)
- 4) U. Becker et al., Phys. Rev. A **34** 2858 (1986)



## POLARIZED XANES STUDIES OF POLYETHYLENE AND FLUORINATED POLYETHYLENES

T.Ohta, K.Seki, M.Taniguchi, T.Yokoyama, I.Morisada, H.Tanaka,  
T.Usami\*, S.Hashimoto\*\*

Dept.Mat.Sci., Fac.Science, Hiroshima Univ., Hiroshima 730

\*Plastics Lab. Mitsubishi Petrochemical Co.Ltd., Yokkaichi, Mie, 510

\*\*Research Lab. Japan Synthetic Rubber Co.Ltd., Tama-ku, Kawasaki, 214

XANES spectra are associated with electronic transitions from inner shell to vacant levels and give information on the electronic structures.

Especially, measurements of oriented samples with polarized synchrotron radiation yield detailed information via the polarization dependence of various transitions.

We performed XANES measurements using monochromatized SR for the C and F K-edges of

- (1) elongated polyethylene (PE) film
- (2) elongated poly(vinylidene fluoride) (PVDF) film
- (3) poly(tetrafluoroethylene) (PTFE) film
- (4) oriented evaporated film of  $\text{CH}_3(\text{CH}_2)_{34}\text{CH}_3$  as a model compound of PE
- (5) oriented evaporated film of  $\text{CF}_3(\text{CF}_2)_{18}\text{CF}_3$  as a model compound of PTFE.

Experiments were performed at the soft X-ray beam line BL 11A at the Photon Factory.

Absorption spectra for (1) and (2) were taken with the transmission mode, and for (3)-(5) with total electron yield mode.

Obtained spectra are shown in Figs.1-3. Distinct polarization dependence is observed, especially for model compounds (4) and (5).

From the polarization dependence of PE and its model compound (Fig.1), peak a is attributed to the transition to  $(\text{C-H})^*$ , while peak b is to  $\sigma(\text{C-C})^*$ .

In the case of PTFE and its model compound (Fig.2) peaks a, b and c are assigned to the transitions to  $\sigma(\text{C-F})^*$ ,  $\sigma(\text{C-C})^*$  and  $\sigma(\text{C-F})^*$  excited states, respectively. Similar polarization dependence was observed for the F K-XANES.

The spectrum of PVDF shows little polarization dependence due to the poor orientation. It can be analyzed by the superposition of the spectra of PTFE and PE, as shown in Fig.3. Above results indicate that the XANES spectra reflect a local electronic structure around the excited atom.

Further analysis of these spectra is now in progress.

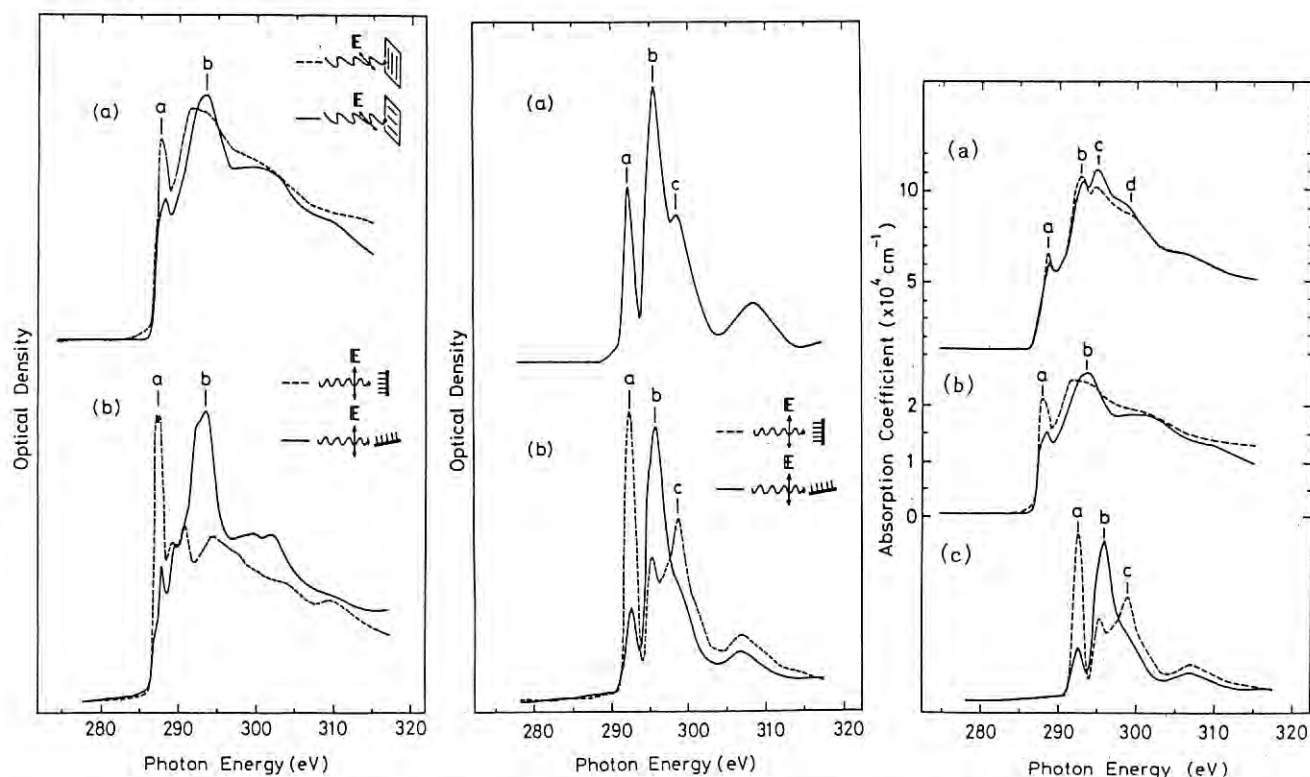


Fig.1 C K-XANES spectra of PE(a) and  $\text{CH}_3(\text{CH}_2)_{34}\text{CH}_3$  (b) Fig.2 C K-XANES spectra of PTFE(a) and  $\text{CF}_3(\text{CF}_2)_{18}\text{CF}_3$  (b) Fig.3 C K-XANES spectra of PVDF(a), PE(b) and  $\text{CF}_3(\text{CF}_2)_{18}\text{CF}_3$  (c)

## IN SITU DC OXYGEN-DISCHARGE CLEANING OF OPTICAL ELEMENTS

Tsuneharu KOIDE, Tetsuo SHIDARA, Kenichiro TANAKA, Akira YAGISHITA, and Shigeru SATO

Photon Factory, National Laboratory for High Energy Physics, 1-1 Oho, Tsukuba-shi, Ibaraki-ken 305

Degradation in the efficiency of optical elements due to carbon contamination has been an inevitable problem which has hindered spectroscopic studies since the initial stages of SR utilization. On the basis of our recent studies of dc oxygen-discharge cleaning,<sup>1</sup> we have performed *in situ* cleaning of optical elements in a Seya-Namioka beam line for gas-phase experiments (BL-12A) and a grasshopper beam line (BL-11A).<sup>2</sup>

The basic idea to achieve a high cleaning rate was to make a part of the vacuum chamber be an oxygen-plasma source by incorporating dc discharge electrodes (made of aluminum) in the mirror box or monochromator. To avoid any harmful effects from the discharge, we carefully chose an electrode and optical surface configuration which can prevent (or minimize) sputter deposition from both the electrode and the chamber wall onto the optical surfaces.<sup>2</sup> A pressure level acceptable for throughput measurements was attained without a bakeout within 5~10 hours after cleaning.

All of the optical elements were given cleaning procedures for the Seya-Namioka line in three steps: post-focusing mirrors ( $M_2$ ,  $M_3$  and  $M_4$ ), a grating (G) and pre-mirrors ( $M_0$  and  $M_1$ ). Figure 1 shows transmitted intensity curves over an energy range from 4 to 40 eV, taken before and after three cleanings. The detector was a photomultiplier coated with sodium salicylate. An increase in the intensity as much as factors of 10 ~ 50 was attained after cleaning all of the elements (3rd cleaning), except in the region between ~15 and ~20 eV. A series of treatments resulted in a progressive appearance of peaks at ~11, ~15, ~22 and ~32 eV; Au and Pt have

common features at these energies. Since the blazed energy of the grating nearly coincides with that of the main peak (~22 eV), the throughput improvement after the second cleaning can be attributed to a recovery of the grating blaze effect<sup>1</sup> as well as of the reflectance of a coating material (Au). A relatively low enhancement rate between ~15 and ~20 eV can be reasonably explained by the high reflectance of carbon, as compared with those of Au and Pt at near-normal incidence in this region.<sup>1</sup>

In the grasshopper line, cleaning was made for a second mirror ( $M_1$ ), a Codling mirror ( $M_2$ ) and a grating (G) in two steps. Figure 2 shows the throughput curves around the carbon K edge before and after each cleaning. An NBS  $Al_2O_3/Al$  photodiode detector and a 250-nm thick Ag filter were used. The spectrum before cleaning showed a large loss in intensity at the carbon K edge, with a main dip at ~288 eV and a satellite dip at ~282 eV. The feature at ~288 eV is attributed to a graphitic contaminant. The first cleaning resulted in a significant increase in flux at the K edge, although two dips still remained. The second cleaning was found to attain a dramatic improvement in the throughput at the K edge; a small dip only remained at ~288 eV. This achievement could be mainly ascribed to the removal of contaminants from the Codling mirror. The low energy dip (~282 eV) exhibited no change in depth after the two cleaning procedures. This suggests the presence of carbide species, possibly  $PtC_x$ , on the Pt-coated first mirror  $M_0$  which was not given a cleaning.

- 1) T. Koide et al., Nucl. Instr. and Meth. A246, 215 (1986); Phys. Scr. 35, 313 (1987); Appl. Opt. 26, 3884 (1987); Appl. Opt. 27, 4305 (1988).
- 2) T. Koide et al., Rev. Sci. Instrum. (to be published).

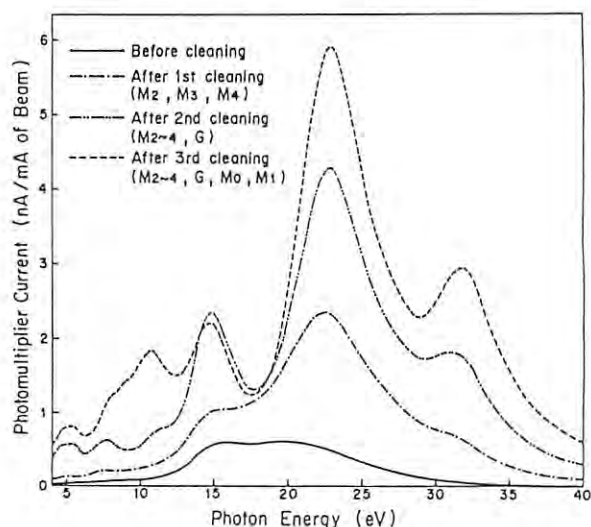


Fig. 1 Throughput curves of the Seya-Namioka beam line before and after cleaning. The first cleaning was made for three refocusing mirrors for 50 min, the second for a grating for 30 min, and the third for a first premirror for 90 min and for a second premirror for 20 min.

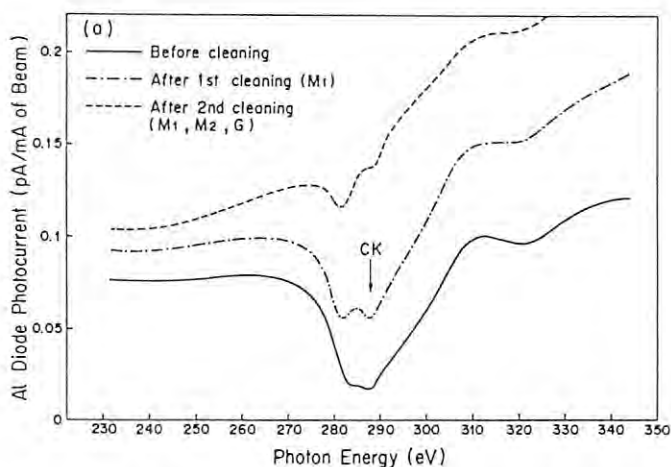


Fig. 2 Throughput curves of the grasshopper beam line around the carbon K edge before and after cleaning. The first cleaning was made for a second premirror for 210 min, and the second for the Codling mirror and a grating for 150 min.



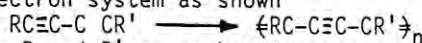
# STUDY OF THE POLYMERIZATION PROCESS OF DIACETYLENE LONG-CHAIN COMPOUND BY INNER SHELL POLARIZED ABSORPTION SPECTRA

Kazuhiko Seki, Ikuo Morisada, Hiroshi Tanaka, Kunishige Edamatsu, Masahiko Yoshiki, Yasutaka Takata, Toshihiko Yokoyama, Masaki Taniguchi, Toshiaki Ohta, Hiroo Nakahara<sup>+</sup>, Kiyoshige Fukuda<sup>+</sup>, and Munehisa Mitsuya<sup>++</sup>

Dept. Mat. Sci., Fac. Science, Hiroshima Univ., Hiroshima 730, Japan  
<sup>+</sup>Dept. Chem., Fac. Science, Saitama University, Urawa 338, Japan  
<sup>++</sup>Advanced Study Institute, Hitachi Ltd., Kokubunji, Tokyo 185, Japan

## Introduction

Various diacetylene compounds are known<sup>1</sup> to polymerize under UV irradiation to form extended  $\pi$ -electron system as shown



where R and R' are substituent groups. These reactions attracted much attention since

(1) In some cases, this reaction can proceed to change monomer single crystal to polymer single crystal.<sup>2</sup>

(2) The formed  $\pi$ -electron systems have large non-linear optical coefficients.

(3) The reaction can also proceed in Langmuir-Blodgett (LB) films<sup>3</sup> or evaporated films<sup>4</sup> of long-chain compounds, where  $R = CH_3(CH_2)_n$  and  $R' = (CH_2)_mCOOH$ .

The study of the change of the  $\pi$ -electronic structure shown above has been tried by many workers. However, most of them used compounds with  $\pi$  systems in R and R', and the overwhelming contribution from them covered the information on the system in the main chain. Recently, we succeeded in observing the change of the occupied state with UV photo-electron spectroscopy for the long-chain compound with  $n = 9$  and  $m = 8$  (tricoso-10,12-dienoic acid), in which side groups do not contribute to the spectrum in the low ionization energy region.<sup>4</sup>

On the other hand, X-ray absorption near-edge structure (XANES) is a useful technique for studying the unoccupied electronic states. In this study, we applied it to the examination of the change of electronic structure on the UV polymerization of the evaporated and LB films of the above-mentioned long-chain compound.

## Experimental

The experiments were performed at the soft X-ray beamline BL11A at the Photon Factory. The spectra were measured as the total electron yield, detected with a channeltron, for two angles of incidence of synchrotron radiation  $\alpha = 0^\circ$  and  $75^\circ$ . The samples were prepared on NESA glasses. In both the evaporated and LB films, the alkyl side groups are oriented roughly vertical to the substrate. Some samples were polymerized before measurements to various degrees of polymerization, and in-situ polymerization by UV irradiation in the measurement chamber was also performed using a D<sub>2</sub> lamp as the light source. No enhancement of polymerization by synchrotron radiation was observed.

## Results and Discussion

In Fig. 1, we show the change of the carbon

K-edge XANES spectra of an evaporated film of the monomer on in-situ polymerization for  $\alpha = 75^\circ$ . The peaks at the low-energy region correspond to the excitation from the C 1s orbitals to the unoccupied orbitals. We see a clear change on polymerization.

The peak A at 285.5 eV in the monomer spectrum corresponds to the transition to the  $\pi^*$  state of the monomer. At the early stage of polymerization (so called blue form), two new peaks B and C appear at 284.6 eV and 286.0 eV. They continue to grow at further irradiation leading to the so called red form, and the original peak A disappears. This change should correspond to either (i) the local change of geometry from two conjugated triple bonds to conjugated double and triple bonds, or (ii) the evolution of the density-of-states of extended 1-dimensional unoccupied  $\pi$  band.

Further studies including the polarization dependence of these transitions and the dependence on the way of sample preparation are under progress.

## References

- 1) G. Wegner, Z. Naturforsch. 24b, 824 (1969); Macromol. Chem. 145, 885 (1971).
- 2) B. Tieke, G. Wegner, D. Nagele, and H. Ringsdorf, Angew. Chem. Int. Ed. 15, 764 (1976).
- 3) Y. Tokura, T. Kanetake, K. Ishikawa, and T. Koda, Synth. Metals 17, 407 (1987).
- 4) H. Nakahara, K. Fukuda, K. Seki, A. Asada, and H. Inokuchi, Chem. Phys. 118, 123 (1987).

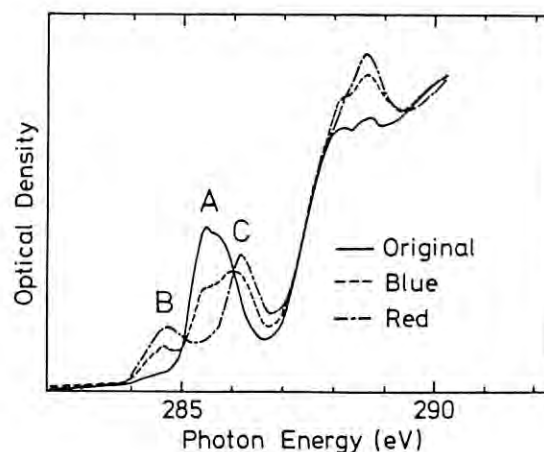


Fig. 1 Change of the C 1s XANES spectra of  $CH_3(CH_2)_9C\equiv C-C\equiv C(CH_2)_8COOH$  evaporated film with UV irradiation.



# SURFACE EXAFS AND X-RAY STANDING-WAVE PROFILES FOR $(\sqrt{3}\times\sqrt{3})R30^\circ$ Cl/Ni(111)

M.Funabashi[1], Y.Kitajima[2], T.Yokoyama[3], T.Ohta[3] and H.Kuroda[1,4]

[1]J.R.D.C., Tokodai, Tsukuba, Ibaraki 300-26, JAPAN

[2]KEK-PF, Oho, Tsukuba, Ibaraki 305, JAPAN

[3]Dept.Materials Science, Hiroshima Univ., Hiroshima 730, JAPAN

[4]Dept.Chemistry, Fac.Science, Univ.of Tokyo 113, JAPAN

## 1.Introduction

We present the results obtained by combining the surface EXAFS and the soft X-ray standing-wave (SW) methods for 1/3 monolayer chlorine adsorbed on a Ni(111) single crystal.

## 2.Experiments and Results

$(\sqrt{3}\times\sqrt{3})R30^\circ$  Cl/Ni(111) was prepared by dosing clean, (1x1)-ordered Ni(111) with Cl produced by the electrolysis of sintered silver chloride<sup>1,2</sup>.

Absorption spectra were taken at BL11B at ambient temperature with a UHV chamber. Cl K-edge surface EXAFS measurements were conducted by monitoring Cl-K fluorescence yield. Polarization dependence of the effective coordination numbers for the first nearest neighbor Ni atoms allows to determine the adsorption site. The results are given in table 1 and this indicates that the 3-fold hollow site is most preferred. The Cl-Ni distance is determined to be  $2.40\pm0.04$  Å and accordingly the Cl-Ni interlayer spacing is 1.92 Å.

The normal-incident SW profile corresponding to the (111) Bragg-reflection was observed in the vicinity of 3.05 keV, and the other profile was found when the incident angle of X-ray was about 70 degree to the surface normal and the X-ray energy was nearly the same as the (111) one. The latter is associated with the  $(\bar{1}\bar{1}1)$  normal reflection. These two SW profiles, shown in Fig.1, result that the displacement of the chlorine atoms is 1.94 Å relative to the (111) plane and is negligibly small relative to the  $(\bar{1}\bar{1}1)$  plane.

## 3.Conclusion

Fig.2 shows the proposed surface structure viewed along the  $[1\bar{1}0]$  axis. Two kinds of 3-fold hollow sites for Cl atoms are possible; the one is given as "site 1" in fig.2, which corresponds to the hcp site, while the fcc site is shown as "site 2". From the present SW analysis the adsorption site is exclusively determined to be "site 2". It should be noticed that the resultant value of the Cl-Ni interlayer spacing determined by the surface EXAFS is nearly equal to the one given by the

SW method.

## Reference

- 1) W.Erley et al., Surface Sci. 66(1977)371
- 2) N.D.Spencer et al., J.Vac.Sci.Technol., A, 1, 1983, 1554.

$\theta$	Result		Calculated $N^Z$		
	R(Å)	$N^*$	On-top	Bridge	3-fold
90°	2.41	1.85	0	0.87	1.73
45°	2.42	3.99	1.5	2.57	3.64
15°	2.38	5.25	2.8	4.04	5.29

Table 1 Results of SEXAFS

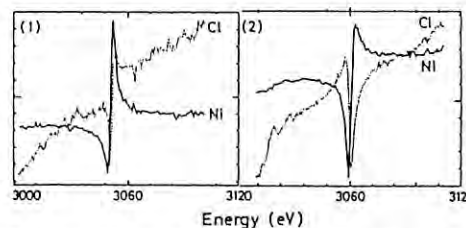


Fig.1 X-ray Standing Wave profiles of (1)(111) and (2)( $\bar{1}\bar{1}1$ ) Bragg reflection

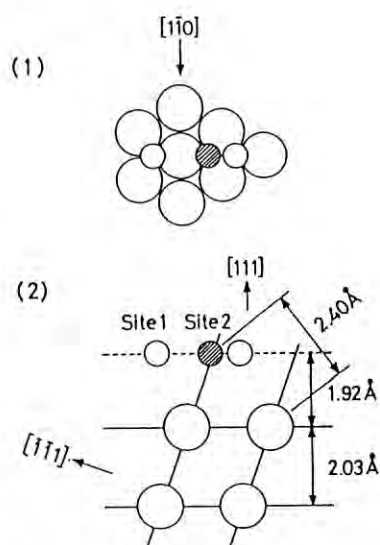


Fig.2 Top view (1) and side view (2) of the model structure

# STRUCTURE ANALYSIS OF c(2x2)Cl/Ni(100) BY SURFACE EXAFS AND SOFT X-RAY STANDING WAVE METHODS

Manabu Funabashi[1], Yasutaka Takata[2], Toshihiko Yokoyama[2],  
Yoshinori Kitajima[3], Haruo Kuroda[1,4], and Toshiaki Ohta[2]

- 1)Research Development Corp. Japan, Tokodai, Tsukuba, Ibaraki 300-26, JAPAN.
- 2)Dept.Materials Science, Fac.Science, Hiroshima Univ., Hiroshima 730, JAPAN.
- 3)Photon Factory, KEK, Oho, Tsukuba, Ibaraki 305, JAPAN.
- 4)Dept.Chemistry, Fac.Science, Univ.Tokyo, Hongo, Tokyo 113, JAPAN.

## Introduction

The determination of a surface structure is one of the most fundamental and important subjects to understand the properties of a solid surface. Especially, when the rearrangement of the substrate surface is induced by the adsorption of foreign atoms(surface relaxation or surface reconstruction occurs), it may be more interesting.

To the best of our knowledge, though the adsorbate structures of Cl atoms on Ni(111) and Ni(110) have been investigated preliminarily[1], no structural study on Cl/Ni(100) has been published so far. In this study we demonstrate the structure of Cl/Ni(100) by use of the surface EXAFS and the soft X-ray standing wave (SW) techniques. We also compare the structure of this system with that of c(2x2)S/Ni(100), and discuss the similarities and dissimilarities.

## Experimental

The experiment was carried out at the soft X-ray double crystal monochromator station (BL-11B). Single crystal Ni(100) was cleaned by the argon ion bombardment and annealing. The clean surface was dosed with Cl<sub>2</sub> produced by the electrolysis of sintered silver chloride. A very sharp c(2x2) LEED pattern was observed without further treatment. The Cl-K edge EXAFS spectra were taken for three polar angles,  $\theta=90^\circ$  (normal incidence),  $\theta=45^\circ$  and  $\theta=15^\circ$  (glancing incidence). The SW profiles associated with a normal incidence Ni(200) Bragg reflection were measured with the energy-scanning mode. Both of the EXAFS and SW absorption spectra were recorded by monitoring Cl-K fluorescence with a newly developed proportional counter[2].

## Results and Discussion

The EXAFS spectra of three polar angles were analyzed by use of the EXAFS data of NiCl<sub>2</sub> as a standard. From all the spectra, the nearest neighbor Cl-Ni bond length is estimated to be 2.43Å which is equal to the bulk value.

In order to determine the adsorption site, the polarization dependence of the experimental effective coordination number was compared with the calculated ones for three types of adsorption geometries. As exemplified in Table 1, the four fold hollow site is most probable.

The analysis of the SW absorption profiles was performed with the similar method to the hard X-ray SW analysis. After the background signal from clean Ni(100) is subtracted, the profiles were curve-fitted. The result indicates that the Cl atoms are located 1.75Å upward from the bulk

Ni(200) lattice plane. Combining the EXAFS result with the SW one, it is concluded that the spacing between the 1st and 2nd Ni layers is expanded by 4.5% of the Ni(200) bulk lattice spacing.

The surface structure of Cl/Ni(100) is compared with that of S/Ni(100)[3] (Table 2). In both systems, the adsorbate atoms are located on four fold hollow site, and the surface layer spacings are expanded. However, the degree of expansion in Cl/Ni(100) is only one third of that in the S/Ni(100) case. This indicates that the relaxation of the surface layer depends considerably on the species of the adsorbate atoms.

## References

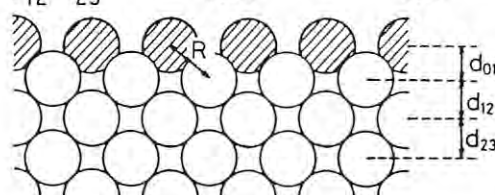
- [1]W.Erley et al, Surf. Sci., 66, 371 (1977).  
W.Erley, *ibid*, 114, 47 (1982).
- [2]M.Funabashi et al, submitted to RSI.
- [3]T.Yokoyama et al, in this issue.

Table 1. Experimental versus calculated coordination numbers  $N^*$  for c(2x2)Cl on Ni(100).

	Expt.	Calculated		
		hollow	bridge	atop
$N^*(90^\circ)$	2.60	3.15	0.79	0
$N^*(45^\circ)$	4.27	4.42	2.61	1.50
$N^*(15^\circ)$	4.01	5.52	4.18	2.80
$N^*(90^\circ)/N^*(15^\circ)$	0.65	0.57	0.19	0
$N^*(45^\circ)/N^*(15^\circ)$	1.06	0.80	0.62	0.54

Table 2. Bond lengths and spacings for c(2x2)Cl/Ni(100) and c(2x2)S/Ni(100). All values are expressed in angstroms.

	adsorbate atoms	
	Cl	S
R	2.43	2.23
$d_{01}$	1.67	1.37
$d_{12}$	1.84	1.97
$d_{23}$	1.76	1.76
$d_{12}-d_{23}$	0.08	0.21



SIDE VIEW

# SOFT X-RAY STANDING-WAVE ABSORPTION PROFILES OF $(5\sqrt{3}\times 2)\text{S}/\text{Ni}(111)$ : RECONFIRMATION OF SURFACE RECONSTRUCTION

Toshihiko YOKOYAMA[1], Yoshinori KITAJIMA[2], Manabu FUNABASHI[3]  
Haruo KURODA[3,4], and Toshiaki OHTA[1]

[1]Dept.Materials Science, Fac.Science, Hiroshima Univ., Hiroshima 730, JAPAN

[2]Photon Factory, KEK, Oho Tsukuba, Ibaraki 305, JAPAN

[3]Research Development Coop. Japan, Tokodai, Tsukuba, Ibaraki 300-26, JAPAN

[4]Dept.Chemistry, Fac.Science, Univ.Tokyo, Hongo, Tokyo 113, JAPAN

## Introduction

Sulfur-deposited Ni(111) systems are quite attractive since they provide various types of LEED patterns, some of which cannot be understood without taking surface reconstruction into account. Our previous surface EXAFS and XANES studies on  $(5\sqrt{3}\times 2)\text{S}/\text{Ni}(111)$ [1] suggested that the surface nickel layer loses its original 3-fold symmetry and is drastically reconstructed into a pseudo Ni(100) surface by the adsorption of sulfur atoms.

We have investigated the soft X-ray standing-wave (SW) absorption spectroscopy and proposed its usefulness for determining the surface local structure of adsorbates deposited on single crystal surface[2]. In the present study, we have measured and analyzed the SW absorption profile of  $(5\sqrt{3}\times 2)\text{S}/\text{Ni}(111)$  to reconfirm the reconstruction proposed previously.

## Experimental

A clean and ordered Ni(111) single crystal, which was prepared by repeated cycles of annealing and ion-bombardment in an ultra-high vacuum environment, was dosed with hydrogen sulphide and was subsequently pyrolysed at about 600K. This treatment leads to clear  $(5\sqrt{3}\times 2)$  complex LEED pattern which retains its sharpness for several days under UHV atmosphere.

Soft X-ray SW absorption profiles were measured with the normal-incident energy-scanning mode at the soft X-ray double crystal monochromator station beam line 11B[3]. Fluorescence-yield detection, which is necessary to improve signal-to-background ratio, was adopted by use of a newly-developed gas-flow proportional counter[4].

## Results and Discussion

Fig.1 shows the SW absorption profiles associated with S-K and Ni-L fluorescence yields. Curve-fitting analysis reveals that the sulfur atoms are located 1.17 Å upward from the bulk nickel lattice plane. This value might be too small to describe the surface structure within the non-reconstructed surface model. Even if we introduce the significant contraction between the top and the second nickel layers, the resultant layer spacing should be unacceptably small.

On the other hand, the full reconstruction model proposed previously is consistent with the present SW observation. In this model, whose top view is given in fig.2, the first layer nickel is rearranged to pseudo Ni(100) surface which has nearly 4-fold axis, and sulfur adsorbs on the resultant hollow site and forms chemical bonds with four equivalent nickel atoms. The spacing

between the sulfur and the nickel layer is 1.27 Å given by the surface EXAFS result[1]. Combining the SW result with the surface EXAFS one, we can estimate that the spacing between the first and the second is 1.93 Å, which implies occurrence of small contraction of the surface layer spacing. Fig.3 gives the side view of the determined model structure.

Through the present investigation, we can claim that the full reconstruction model is confirmed without any doubt and the more detailed structure is successfully deduced.

[1] Y.Kitajima et al. submitted to PRL.

[2] T.Ohta et al. JJAP 24 1475 (1985);

T.Yokoyama et al. to be published in PRL.

[3] T.Ohta et al. NIM A246 373 (1986).

[4] M.Funabashi et al. submitted to RSI.

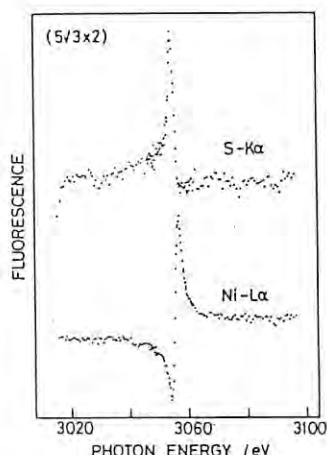


Fig.1. Soft X-ray SW absorption profiles of  $(5\sqrt{3}\times 2)\text{S}/\text{Ni}(111)$  measured with S-K and Ni-L fluorescence yields.

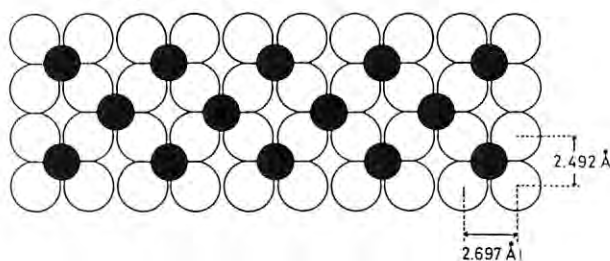


Fig.2. Model structure of  $(5\sqrt{3}\times 2)\text{S}/\text{Ni}(111)$  (top view)

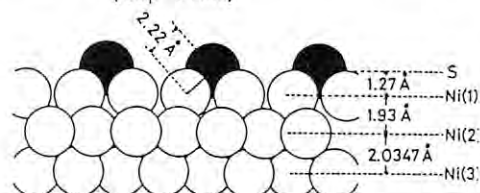


Fig.3. Model structure of  $(5\sqrt{3}\times 2)\text{S}/\text{Ni}(111)$  (side view).



# SOFT X-RAY STANDING-WAVE ABSORPTION PROFILES OF $p(2 \times 2)\text{S}/\text{Ni}(111)$ : USEFULNESS AS A SURFACE STRUCTURE ANALYSIS

Toshihiko YOKOYAMA[1], Manabu FUNABASHI[2], Yoshinori KITAJIMA[3],  
Haruo KURODA[2,4], and Toshiaki OHTA[1]

[1]Dept.Materials Science, Fac.Science, Hiroshima Univ., Hiroshima 730, JAPAN

[2]Research Development Coop. Japan, Tokodai, Tsukuba, Ibaraki 300-26, JAPAN

[3]Photon Factory, KEK, Oho, Tsukuba, Ibaraki 305, JAPAN

[4]Dept.Chemistry, Fac.Science, Univ.Tokyo, Hongo, Tokyo 113, JAPAN

## Introduction

Recently we demonstrated that the soft X-ray standing-wave (SW) method combined with the incident photon energy scanning technique is a promising tool to determine the surface local structure of adsorbates on single-crystal substrates[1]. This technique is quite useful since it is available in the same experimental condition as surface EXAFS spectroscopy and provides complementary information. Here we report the results of the SW absorption profiles for  $p(2 \times 2)\text{S}/\text{Ni}(111)$  and discuss the detailed model structure for this system with the help of the surface EXAFS result.

## Experimental

Commercially-available single crystal  $\text{Ni}(111)$  was cleaned in an ultra-high vacuum environment according to the well-established procedure. Surface cleanliness and order were checked by AES and LEED, respectively. Sulfur was deposited on the clean  $\text{Ni}(111)$  by dosing with hydrogen sulphide. Clear  $p(2 \times 2)$  LEED pattern was observed without further treatment.

Nearly normal-incident soft X-ray SW absorption profiles were measured with the energy-scanning mode at the soft X-ray double crystal monochromator station beam line 11B[2]. The energy resolution of the present monochromator (a pair of  $\text{Ge}(111)$  crystals) and the divergence of the incident X-ray beam are excellent enough to record SW spectra. It turned out necessary to adopt the fluorescence yield mode instead of the electron yield modes because the background signal ( $\text{Ni}$  LMM Auger electrons) dominates the SW profile quite significantly. We have developed a UHV-compatible soft X-ray detector for these purposes. This is a gas-flow type of proportional counter[3], and was successfully used for the present experiment.

Fig.1 shows the SW absorption profiles associated with S-K and Ni-L fluorescence yields for  $p(2 \times 2)\text{S}/\text{Ni}(111)$ . Distinct difference can be seen between the two spectra, indicating that the S-K profile may purely originate from adsorbate sulfur associated with little background contribution.

## Results and Discussion

Details of the analysis procedure will be described elsewhere[4]. The pure SW profile of S adsorbed atoms was extracted by subtracting weakly contributing background signal appearing in clean  $\text{Ni}(111)$  data (not shown) from the raw data (Fig.1). The resultant profiles are then curve-fitted according to the well-known formula[5] including Lorentzian convolution to

account for the effective energy resolution. The final result reveals that sulfur atoms are located 1.38 Å upward from the bulk  $\text{Ni}(111)$  lattice plane.

On the other hand, according to the surface EXAFS result, the interatomic distance between the sulfur and the first nickel layer is 2.20 Å, and hence, if we assume that sulfur is located at the three-fold hollow site which is the most probable site in such systems, the layer spacing between sulfur and nickel is estimated to be 1.66 Å. This value is quite different from the one determined by the SW analysis (1.38 Å), indicating that a significant lattice relaxation occurs due to sulfur adsorption. Fig.2 shows the side view of the detailed surface model structure, and the distance between the 1st and the 2nd nickel layers are contracted by as much as 15% compared with that of the bulk.

It should be emphasized that such detailed structure cannot be obtained until we use these two methods, which provide complementary information to each other.

[1] T.Ohta et al. JJAP 24 1475 (1985).

[2] T.Ohta et al. NIM A246 373 (1986).

[3] M.Funabashi et al. to be published in RSI.

[4] T.Yokoyama et al. to be published.

[5] D.P.Woodruff et al. SS 195 237 (1988).

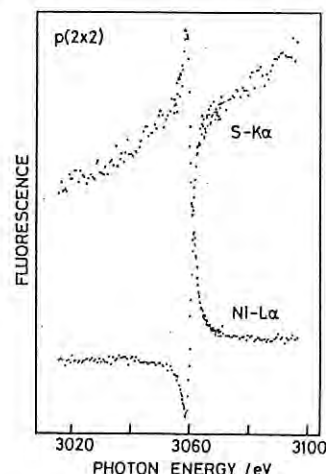


Fig.1. Soft X-ray SW absorption profiles for  $p(2 \times 2)\text{S}/\text{Ni}(111)$  measured with S-K and Ni-L fluorescence

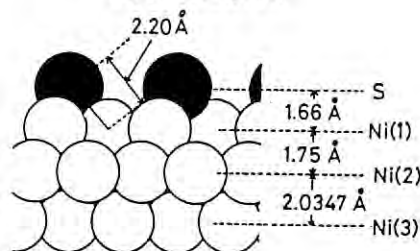


Fig.2. Model structure of  $p(2 \times 2)\text{S}/\text{Ni}(111)$  (side view).



# SOFT X-RAY STANDING-WAVE ABSORPTION PROFILES OF $c(2 \times 2)S/Ni(100)$ : DISCUSSION ON THE ANALYSIS METHOD AND COMPARISON OF THE DETECTION MODES

Toshihiko YOKOYAMA[1], Yasutaka TAKADA[1], Yoshinori KITAJIMA[2],  
Manabu FUNABASHI[3], Haruo KURODA[3,4], and Toshiaki OHTA[1]

[1]Dept. Materials Science, Fac. Science, Hiroshima Univ., Hiroshima 730, JAPAN

[2]Photon Factory, KEK, Oho, Tsukuba, Ibaraki 305, JAPAN

[3]Research Development Coop. Japan, Tokodai, Tsukuba, Ibaraki 300-26, JAPAN

[4]Dept. Chemistry, Fac. Science, Univ. Tokyo, Hongo, Tokyo 113, JAPAN

## Introduction

The soft X-ray standing-wave (SW) technique could be a powerful method to analyse the structures of surfaces and interfaces[1]. This method, however, has to be improved since there remain some ambiguities in the procedure of data analysis.

The first purpose of the present investigation is to confirm how one can evaluate the SW absorption correctly, especially how to estimate the imaginary parts of structure factors. The  $c(2 \times 2)S/Ni(100)$  system may be suitable for this purpose because the surface structure of this system was already known[2] except for its surface relaxation. The second purpose is to elucidate whether this relaxation actually occurs.

## Experimental

Normal-incident soft X-ray SW absorption profiles were measured with the energy-scanning mode at the soft X-ray double crystal monochromator station beam line 11B[3]. As the detection systems, the Auger electron yield (AEY) mode and the fluorescence yield (FY) mode were employed for comparison. In both measurements total electron yield (TEY) spectra were recorded simultaneously for energy calibration. In order to extract the pure profile from sulfur we have to measure a background spectrum which should be subtracted from raw data of adsorbate sulfur. In the FY mode the data of clean  $Ni(100)$  was adopted while in the AEY mode the spectrum which was measured on condition that the energy of collected electrons was shifted 50eV above the S-LVV signal was regarded as background. Fig.1(a)-(c) show the SW absorption profiles associated with S-K FY, S-LVV AEY and TEY, respectively.

## Results and Discussion

The pure SW profile of adsorbed sulfur atoms was extracted by subtracting background signals (not shown) from the raw data (Fig.1(a)-(b)). The resultant profiles are then curve-fitted according to the well-known formula[4] including Lorentzian convolution to account for the effective energy resolution. The FWHM used in the present analysis is 3eV. There remains, however, ambiguity for estimating the imaginary parts of X-ray structure factors denoted by  $\text{Im}[F(hkl)]$ . Here we have tried to deduce this value from the TEY spectrum which corresponds to the bulk nickel profile. If it is assumed that all the nickel atoms are located on the (200) lattice planes and that the value of  $\text{Im}[F(200)]$ , which is difficult to estimate theoretically, is equal to  $\text{Im}[F(000)]$ , then it is determined to be 14.5.

This is in fairly good agreement with the value of 9.5 which is simply evaluated from the linear absorption coefficient, and hence our estimation may be reasonable taking the present difficulties into account.

According to the analysis of the FY spectrum, the displacement of sulfur atoms relative to the (200) lattice plane is determined to be 1.58 Å, while the surface EXAFS results indicated that sulfur is located 1.37 Å upward from the surface nickel layer[2]. These facts reveals that the spacing between the first and the second nickel layers is expanded by 0.21 Å (12%) compared with the bulk spacing. The lattice expansion observed in the  $c(2 \times 2)S/Ni(110)$  system[5] is about 10% which agrees quite well with the present result. To the contrary, in  $p(2 \times 2)S/Ni(111)$  significant contraction (15%) occurs as shown in the other report of the present issue, and these observations will be an interesting topic in the surface theory.

On the other hand, the AEY spectrum leads to conclusion that the displacement of sulfur is 1.73 Å, which is equivalent to -0.03 Å. The large deviation between the FY result (1.58 Å) and the AEY one implies that in the AEY spectrum the background contribution which dominates the raw data cannot be subtracted in the computational data analysis. It can be concluded that the fluorescence detection method is indispensable in the measurements of SW absorption profiles.

- [1] T.Ohta et al. JJAP 24 1475 (1985).
- [2] S.Brennan et al. PR B24 4871 (1981).
- [3] T.Ohta et al. NIM A246 373 (1986).
- [4] D.P.Woodruff et al. SS 195 237 (1988).
- [5] T.Ohta et al. J.Physique 47 C8-503 (1986).

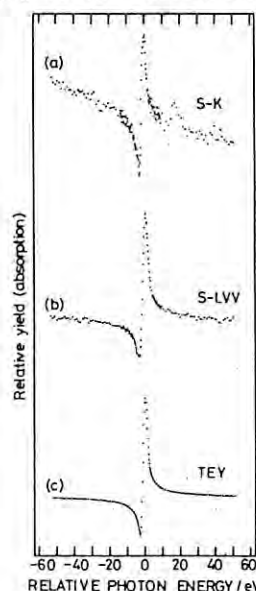


Fig.1 Soft X-ray SW spectra measured with S-K fluorescence yield mode (a), S-LVV Auger electron yield mode (b), and total electron yield mode (c).

## STUDY ON LOCAL STRUCTURE AROUND SULFUR OF IRON SULFIDE CATALYST

Nobuyuki MATSUBAYASHI, Hiromichi SHIMADA, Yuji YOSHIMURA, Toshio SATO,  
Akio NISHIJIMA, and Toshiaki OHTA\*

National Chemical Laboratory for Industry, Tsukuba, Ibaraki 305

\*Department of Physics, Faculty of Science, The University of Hiroshima,  
Higashisenda-cho, Nakaku, Hiroshima 730

### Introduction

Sulfide catalysts are being widely used for hydrotreating petroleum. However, the structure of active sites for each reaction has not yet been clarified. In these catalysts, sulfur atoms seem to be essential for the formation of active sites. Accordingly, surface X-ray absorption spectroscopy (XAS) was applied to the investigation of the local environment around S in the catalysts.

### Experimental

Two types of iron catalysts supported on HY zeolite and active carbon were prepared by impregnation with a solution of ferric nitrate. The catalysts were presulfided in a stream of 5 vol% of  $\text{H}_2\text{S}/\text{H}_2$  at  $400^\circ\text{C}$  for 1h.

The apparatus shown in Fig.1 was designed and developed for the measurements of both XAS and XPS spectra.<sup>1)</sup> This new apparatus was applied to measurements of S K-absorption XAS and XPS at the BL-11B of the Photon Factory. XAS can be measured by monitoring sample current, Auger electrons yield, total electrons yield, fluorescent X-ray, and transmitted X-ray using the apparatus. In this report, sample current method was used to obtain XAS spectra.

### Results and Discussion

Figure 2 shows the S K-edge XANES spectra for FeS,  $\text{Al}_2(\text{SO}_4)_3$ , and the two catalysts. The XANES spectra of FeS/HY zeolite and FeS/active carbon catalysts are quite different from that of  $\text{Al}_2(\text{SO}_4)_3$ . This result indicates that the chemical state of sulfur is not sulfate on these catalysts. Although these spectra resemble that of FeS rather than that of  $\text{Al}_2(\text{SO}_4)_3$ , they are not very similar. These results indicate that FeS particles are highly dispersed on HY zeolite and active carbon supports. Therefore the state of sulfur on the catalysts seems to be quite different from that of FeS. A little difference was found between XANES spectra obtained from the FeS/HY zeolite and FeS/active carbon catalysts. This result seems to show different interaction between FeS and two kinds of supports. More detailed studies including XPS are now progressing.

The authors would like to thank Dr. Ken-ichiro Tanaka, Dr. Masaharu Nomura, and Dr. Yoshinori Kitajima of the National Laboratory for High Energy Physics for their help and suggestion on measurements at BL11B in Photon Factory.

### References

- 1) N.Matsubayashi, I.Kojima, M.Kurahashi, A.Nishijima, A.Itoh, and T.Utaka, Rev. Sci. Instrum., submitted.

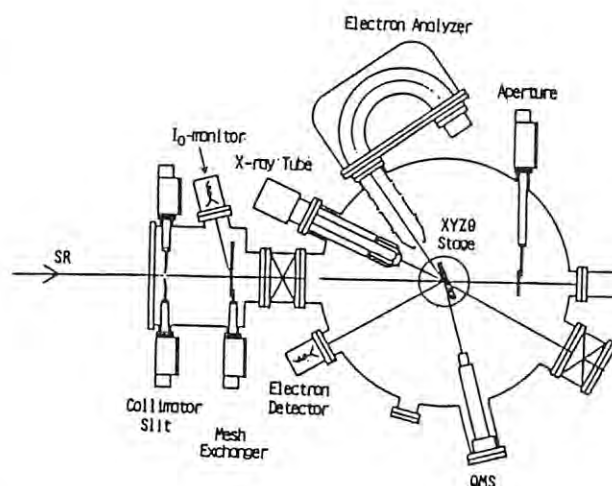


Fig.1 Schematic diagram of the apparatus used for the XAS measurements in the present report.

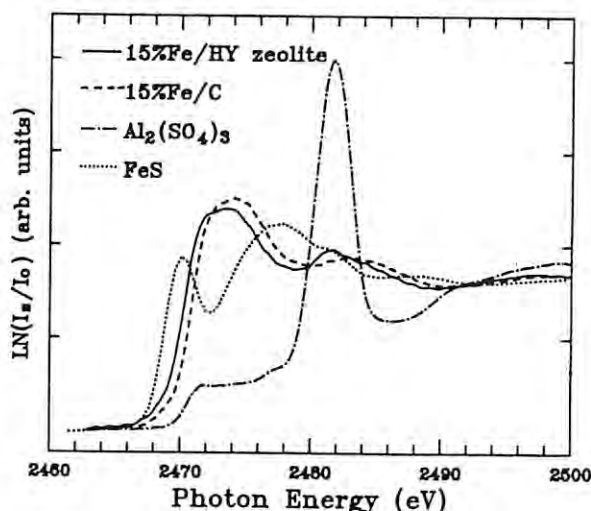


Fig.2 S K-edge XANES spectra obtained by monitoring sample currents.

TWO-DIMENSIONAL X-RAY PHOTOELECTRON DIFFRACTION MEASUREMENTS  
BY USE OF RETARDING FIELD TYPE ANALYZER

Shigeo KANAYAMA, Masanori OWARI, Eisaku NAKAMURA and Yoshimasa NIHEI

Institute of Industrial Science, University of Tokyo,  
7-22-1, Roppongi, Minato-ku, Tokyo 106

### Introduction

X-ray photoelectron diffraction (XPED) has been shown to be a promising method for surface structural and chemical state analysis.<sup>1,2)</sup> In order to obtain two-dimensional XPED pattern in a short time, Mizuno et al.<sup>3)</sup> constructed a direct observation system of photoelectrons using a retarding field type electron energy analyzer, microchannel plates (MCP), a video camera, and a real-time image processor. This system was combined with synchrotron radiation X-ray source.<sup>4)</sup> In this report, acquisition method and obtained data of two-dimensional XPED patterns are presented.

### Experimental

Details of the XPED direct observation system are described elsewhere.<sup>3)</sup> The retarding field type analyzer consists of four concentric grid meshes, at the center of which a sample is placed. Electrons with kinetic energy higher than the high-pass filter potential are allowed to pass the analyzer, multiplied by MCPs, and visualized by a phosphor-coated anode set behind the MCPs. The light spots are detected by a video camera, and the signals are accumulated in a real-time image processor controlled by PDP-11/23 minicomputer. An image of finite energy range can be got by subtraction of two images obtained at slightly different filter potentials. All the experiments were performed at BL-11B of Photon Factory in the National Laboratory for High Energy Physics. X-ray was monochromatized to 1764 eV by the InSb(111) double crystal monochromator. The beam was cut by slits and irradiated a 1 mm x 1 mm area of a GaAs(001) crystal.

### Results and Discussion

Figure 1 shows the image of Ga3d photoelectrons from GaAs(001) obtained with this system. In this raw image, clear XPED pattern was not observed, for most of the contrast was caused by Moire pattern of 4-grid meshes. In order to obtain net XPED contrast, pixel-by-pixel divisions were performed between images acquired from crystal GaAs and those from amorphous one set at quite the same position. Where, the two states of GaAs were obtained from the same sample before and after annealing without changing its position. Each image was accumulated for 45 minutes. The resultant image of Ga3d photoelectrons is shown in Fig.2. This pattern agrees well with calculated XPED pattern shown in Fig.3. It took about 10 hours to acquire the XPED pattern over the same solid angle range by a conventional point-by-point collection type analyzer.

### Conclusions

Ga3d and As3d XPED patterns were obtained from GaAs(001) rapidly with the XPED direct observation system. Through the experiments, it has been indicated that the XPED direct observation system is valid for rapid XPED measurements.

### References

- 1) Y. Nihei, M. Owari, M. Kudo, and H. Kamada: Jpn. J. Appl. Phys., 20, L420 (1981).
- 2) N. Koshizaki, M. Kudo, M. Owari, Y. Nihei, and H. Kamada: *ibid.*, 19, L349 (1980).
- 3) K. Mizuno, M. Owari, and Y. Nihei: Bunko Kenkyu 34, 233 (1985).
- 4) S. Kanayama, M. Owari, E. Nakamura, and Y. Nihei: Rev. Sci. Instrum., in press.

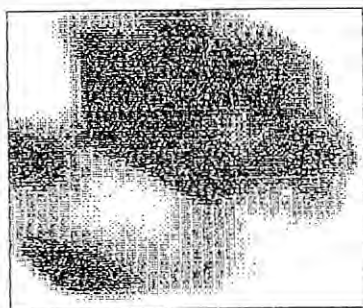


Fig.1 Raw image of Ga3d photoelectrons from GaAs(001)

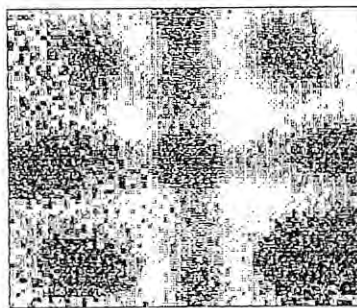


Fig.2 Extracted XPED pattern of Ga3d photoelectrons from GaAs(001)

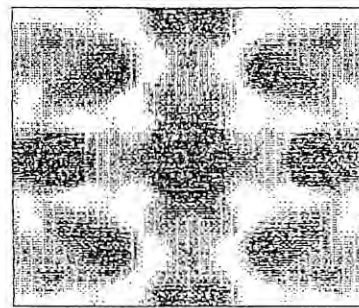


Fig.3 Calculated XPED pattern of Ga3d photoelectrons from GaAs(001)



THE OPTICAL SPECTRA OF  $\alpha$ - $\text{Al}_2\text{O}_3$  SINGLE CRYSTALS IN VUV REGION II

Tetsuhiko TOMIKI, Tomoyoshi FUTEMMA, Hiroo KATO\*, Tsuneaki MIYAHARA\*, Yoshihiro AIURA<sup>+</sup>  
and Hirohito FUKUTANI<sup>+</sup>

Department of Physics, University of the Ryukyus, Nishihara, Okinawa 903-01

\* Photon Factory, National Laboratory for High Energy Physics, Tsukuba, Ibaraki 305

+ Institute of Physics, University of Tsukuba, Tsukuba, Ibaraki 305

As a continuation to the report in 1987 [1], we present in Fig. 1 the reflectivity spectra of  $\alpha$ - $\text{Al}_2\text{O}_3$  single crystals at 299 K in the spectral regions further extended from 40 eV to 110 eV for  $\langle c \rangle \perp \vec{E}$ ,  $\vec{E}$  being the electric field vector of incident light. The measurements were performed at BL-11C (6 eV  $\sim$  40 eV) and BL-11C (30 eV  $\sim$  110 eV). In addition to the usual LiF filter for  $E \lesssim 11.85$  eV as before, an In filter was employed for  $11.6 \text{ eV} \lesssim E \lesssim 17.0 \text{ eV}$  to minimize the disturbances due to the 2nd order diffraction light. This induced changes in relative magnitudes of the reflectivity in comparison to the preceding result [1] in the region cited above.

The exciton peak lies at 9.05 eV. Assuming the onset of the inter-band transitions around  $E \sim 9.60$  eV, the transitions from  $0^{2-}2p^6$  valence bands to the ionization level of  $\text{Al}^{2+}1s_02p^6$  is expected to lie around  $E \sim (9.60 + 28.44) \text{ eV} = 38.04 \text{ eV}$ ,  $28.44 \text{ eV} = E(\text{IP})$  being the ionization potential of  $\text{Al}^{2+}2p^63s$ . The monotonously decreasing part of the spectrum beyond  $E \sim 40$  eV is thus conceived to be due mainly to the free electron absorptions with which the structures of sharp Al  $L_{2,3}$  exciton doublet followed by the broad bands are superposed up to  $E \sim 106$  eV.

Figure 2 shows the  $\epsilon_2$ -spectrum of Al  $L_{2,3}$  region obtained by the Kramers-Kronig analysis of the spectrum  $R(E)$  of Fig. 1. One may notice a clear splitting of the  $L_2$  and  $L_3$  components (78.31 eV and 78.73 eV) and the succeeding broad band structures. This is the first to report the doublet structure to our knowledge, though several workers have measured this part of the spectrum [e. g., 2, 3]. The intensity ratio  $L_2/L_3$  is found to be 1.43 or 1.79 according as the Gaussian or Lorentzian lineshape assumed for the analysis, indicating a strong exchange interaction [4] between the constituent electron and hole of exciton in a small orbit of the L shell. As regards the succeeding broad bands spectrum, excellent agreement is found between the present work and [2].

## References

- [1]. T. Tomiki, T. Futemma, H. Kato, Y. Aiura, H. Fukutani and T. Miyahara: Photon Factory Activity Report (1987) p. 289.
- [2]. A. Balzarotti, F. Antonangeli, R. Girlanda and G. Martino: Phys. Rev. 29 (1984) 5903.
- [3]. Works quoted in the article (Chapt. 10) by D. W. Lynch in the "Handbook on Synchrotron

Radiation" Ed. by G. V. Marr, Vol. 2 [North Holland, Amsterdam, Oxford, New York, Tokyo 1987].

- [4]. Y. Onodera and Y. Toyozawa: J. Phys. Soc. Japan 22 (1967) 833.

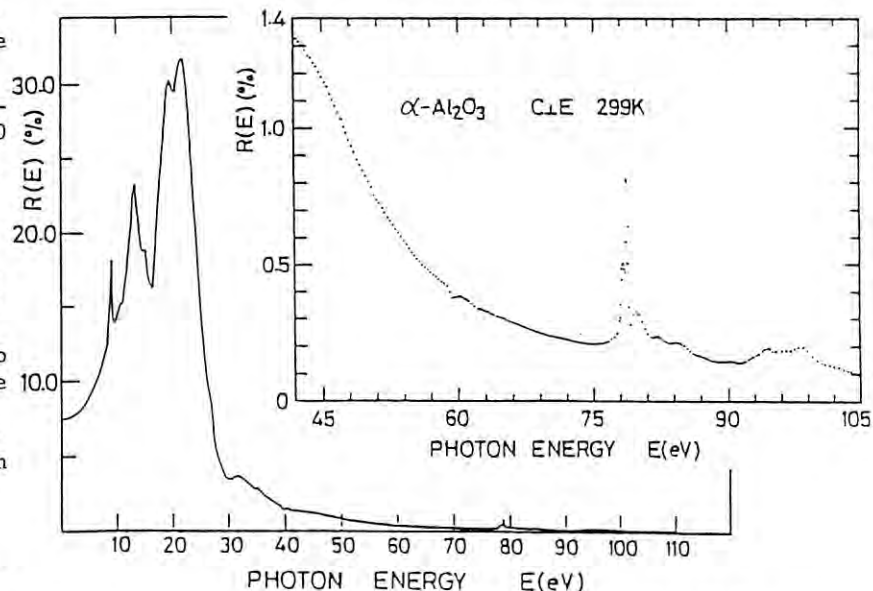


Fig. 1. The reflectivity spectra of  $\alpha$ - $\text{Al}_2\text{O}_3$  at 299 K for  $\langle c \rangle \perp \vec{E}$ .

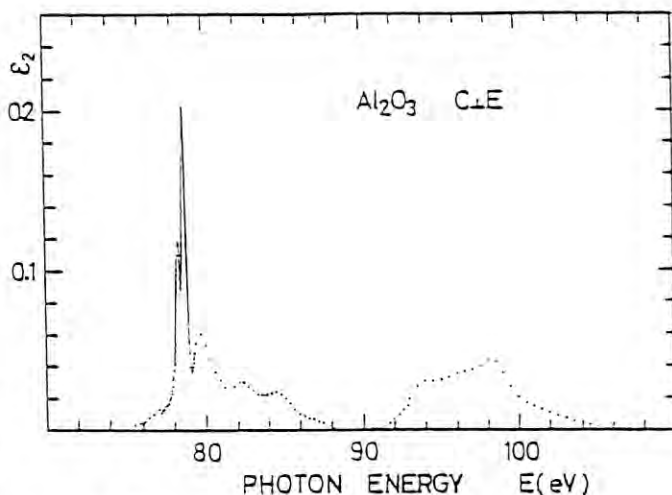


Fig. 2. The spectrum of  $\epsilon_2$  in the region of Al  $L_{2,3}$ . Dots stand for the measured points, and the thin curve traces them to elucidate the doublet structure.



PHOTO-STIMULATED DESORPTION OF  $H^+$  IONS FROM OXIDIZED SILICON SURFACES

Yuji TAKAKUWA, Michio NIWANO, Hiroo KATO<sup>+</sup>, Masafumi NOKAWA, Satoshi MATSUYOSHI,  
Naoki OHYAMA, Hitoshi KATAKURA, Hiroyuki ISHIDA, Motaharul Kabir MAZUMDER  
and Nobuo MIYAMOTO

Research Institute of Electrical Communication, Tohoku University, Sendai 980  
<sup>+</sup>Photon Factory, National Laboratory for High Energy Physics, Tsukuba, Ibaraki 305

Introduction

Photo-CVD (Chemical Vapor Deposition) is a promising technique for epitaxial crystal growth at low temperatures and is a key technology for fabrication of future VLSI devices. Photo-stimulated desorption (PSD) is considered to be one of the important processing steps in this photo-CVD. Exploring the mechanism of PSD, therefore, is of great importance for device fabrication. It should also be emphasized that PSD is an effective spectroscopic tool for surface analysis since it is extremely surface-sensitive.

In this report, we present a preliminary result of an analysis of oxidized Si(111) surfaces by PSD technique. We observed the desorption of  $H^+$  ions in the photon energy region above 20 eV. This work is a part of a series of studies on surface photo-chemical reactions on silicon surfaces.

Experimental

Samples used in the present experiment were a Si(111) wafer. The surface was cleaned in situ by annealing up to 1000°C, after which it was confirmed to have (7x7) structure using RHEED analysis. The base pressure of the experimental chamber was  $< 5 \times 10^{-10}$  Torr. The surfaces were oxidized by exposure to pure  $O_2$  gas (99.9%). Oxygen gas was introduced into the chamber via a variable leak valve with the ionization gauge switched on during admission. All exposures are given in Langmuir units (1L =  $10^{-6}$  Torr s).

Measurements were carried out at beam-line 11C with a 1m Seya-Namioka monochromator of the vertical dispersion type. The photon beam had an incident angle of 45° to the surface normal. A commercial quadrupole mass spectrometer was used to measure PSD ion yields. A filament in the ionization cell of the spectrometer was switched off to reduce ion signals due to the background gas. A bias voltage of 50 V was applied between the sample and the entrance slit of the spectrometer to extract ions from the surface. Ion signals were detected in the pulse-counting mode. PSD spectra were measured in the photon energy range from 10 to 40 eV. All measurements were made at room temperature.

Results

Only an extremely weak ion signal was detected from the Si(111)-(7x7) clean surface. A strong  $H^+$  signal was observed after oxidation. Desorption of other ion species, e.g.  $O^+$ , was hardly discernible in the present photon energy region. Figure 1 shows PSD spectra of  $H^+$  ions from surfaces after some different oxidation procedures. The spectrum of the surface oxidized at room temperature (R.T.) displays a

rising edge at 20 eV and a peak at 35 eV. On the other hand, the surfaces oxidized at a substrate temperature of 700°C, show a common spectral feature irrespective of the extent of oxygen-exposure; the  $H^+$  yield is peaked at 23 eV. It is interesting to notice that the surface treated with oxidation at R.T. followed by annealing at 700°C shows almost the same spectral profile as those oxidized at 700°C.

The present results show that the oxidation seems to play an important role for the  $H^+$  ion desorption. It is well known that the  $SiO_2$ -Si interface has a large density of unsaturated Si bonds which can capture hydrogen atoms.<sup>1)</sup> One possible explanation for the  $H^+$  desorption, therefore, is that during oxygen exposure hydrogen atoms from the ambient gas were co-adsorbed on the unsaturated-bonding sites at the  $SiO_2$ -Si interface. H atoms chemisorbed on Si(111)-(7x7) surface are known to be completely desorbed by annealing at 700°C.<sup>2)</sup> The peak observed at 23 eV remained after annealing at 700°C. This suggests that the peak is due to the desorption of H-atoms captured on the unsaturated-bonding sites characteristic of the  $SiO_2$ -Si interface. However, the origin of the observed peaks is still not entirely understood.

References

- 1) K.L.Brower and T.J.Headley: Phys. Rev. B34 (1986) 3610.
- 2) S.M.Gates: Surf. Sci. 195 (1988) 307.

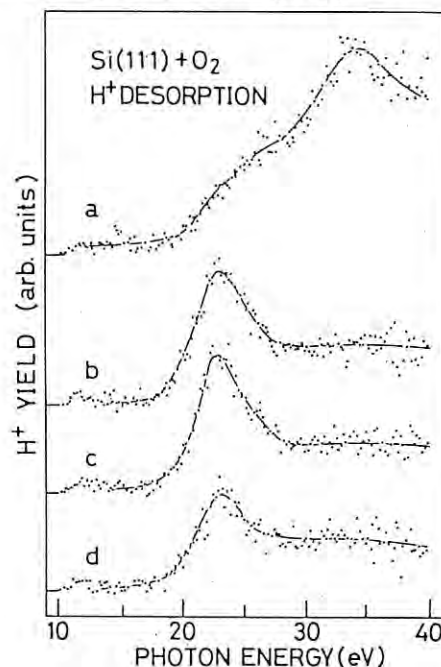


Fig. 1. Desorption spectra for  $H^+$  from oxidized silicon surfaces. (a)100L(R.T.), (b)100L(700°C), (c)500L(700°C), and (d)100L(R.T.)+annealing(700°C).

PIEZOREFLECTIVITY OF Na<sup>+</sup>2p CORE EXCITON IN NaCl

Masatada YURI, Shintaro SATO, Hirohito FUKUTANI and Hiroo KATO\*

Institute of Physics, University of Tsukuba, Ibaraki 305

\*Photon Factory, National Laboratory for High Energy Physics, Ibaraki 305

Piezorefectivity spectra of NaCl and NaF were measured in the photon energy region from 32 to 36 eV at room temperature. Measurements were made at BL-11C by using Seya-Namioka type monochromator installed with an Au-coated 1200 grooves/mm grating of 38 nm blazing wavelength. The band pass was approximately 0.08 eV. Piezorefectivity spectra were measured with a modulation method, the details of which were reported in previous papers.<sup>1)</sup>

Figure 1 shows the piezorefectivity spectra of sodium chloride under the [001] stress. In figure 1, the solid line and dotted line represent the piezorefectivity spectra,  $(\Delta R/R)_\perp$  and  $(\Delta R/R)_\parallel$ , respectively. The subscript  $\perp$  or  $\parallel$  denotes the polarization of light either perpendicular or parallel to the stress. The reflectivity spectrum, R, without the stress is also shown for comparison. The reflectivity spectrum shows a distinct peak at 33.5 eV. We can also find a weak shoulder at low energy side (33.15 eV). These structure can be ascribed to the doublet structure of excitons associated with the transition from Na<sup>+</sup>2p states to Na<sup>+</sup>3s states.<sup>2)</sup> Na<sup>+</sup>2p states are split into two states because of the spin-orbit interaction.

The piezorefectivity spectrum under the cubic strain,  $(\Delta R/R)_{\text{cub}}$ , is obtained as a linear combination of piezorefectivity spectra under the [001] stress. The  $(\Delta R/R)_{\text{cub}}$  spectrum is shown by the solid line in figure 2. This spectrum is normalized to the unit cubic strain.

The logarithmic energy derivative of the reflectivity spectrum,  $(1/R)(dR/dE)$ , is also shown the dotted line for comparison.

Generally, the line shape of piezorefectivity is a superposition of two parts; one is proportional to the  $(1/R)(dR/dE)$  spectrum caused by energy shift or level splitting and the other to the R spectrum induced by the level mixings.

In a usual case, the  $(\Delta R/R)_{\text{cub}}$  spectrum was shown to be the  $(1/R)(dR/dE)$  type spectrum because state was not split by the cubic strain.

Previously we reported that  $(\Delta R/R)_{\text{cub}}$  spectrum of almost alkali halide is proportional to  $(1/R)(dR/dE)$  at fundamental absorption region.<sup>1)</sup>

In the case of NaCl core exciton, the  $(\Delta R/R)_{\text{cub}}$  spectrum can not be described by only the  $(1/R)(dR/dE)$  term as is shown in figure 2; in the  $(1/R)(dR/dE)$  spectrum there is a sharp positive peak at 33.4 eV, whereas the corresponding peak can not be seen in the  $(\Delta R/R)_{\text{cub}}$  spectrum; the energy of the minimum of the  $(\Delta R/R)_{\text{cub}}$  spectrum (33.7 eV) does not coincide with that of the  $(1/R)(dR/dE)$  spectrum (figure 1). That means that intensity decrease caused by volume expansion contribute to the spectrum as well as the structure shifts to low energy side.

These features of piezorefectivity of core exciton in sodium chloride is different from those of excitons in fundamental absorption region in many alkali halides.

Analysis of the piezorefectivity data of sodium fluoride are being made but it seems that the change of intensity is nothing or a little compared to that of sodium chloride.

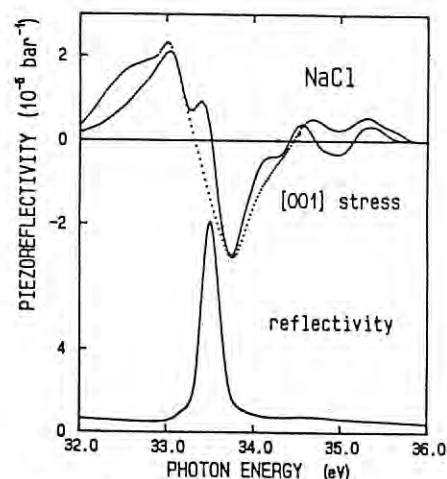


Fig.1

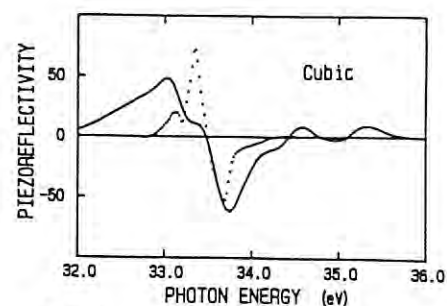


Fig.2

## References

- 1) H. Futani et al.:  
J. Phys. Soc. Jpn. **50** (1981) 1587.  
A. Yamada et al.:  
J. Phys. Soc. Jpn. **52** (1983) 4270.  
A. Yamada et al.:  
J. Phys. Soc. Jpn. **54** (1985) 4005.  
M. Miyabe et al.:  
J. Phys. Soc. Jpn. **56** (1987) 378.  
K. Yagi et al.:  
J. Phys. Soc. Jpn. **57** (1988) 1478.
- 2) S. Nakai et al.:  
J. Phys. Soc. Jpn. **30** (1970) 428.

## ANGLE-RESOLVED PHOTOEMISSION STUDY OF OXYGEN ADSORPTION ON W(110) AT 300K

Yoshihiro AIURA, Yasuo SAKISAKA\*, Kazuyuki EDAMOTO\*\*,  
Hirohito FUKUTANI and Hiroo KATO\*\*\*

Institute of Physics, University of Tsukuba, Tsukuba, Ibaraki 305, Japan

\*Department of Chemistry, Faculty of Science, Kyoto University, Kyoto 606, Japan

\*\*Department of Chemistry, Tokyo Institute of Technology, Ookayama, Meguro-ku, Tokyo 152, Japan

\*\*\*Photon Factory, National Laboratory for High Energy Physics, Tsukuba, Ibaraki 305, Japan

In order to understand an adsorption mechanism clearly, it is necessary to study both the electronic states and the geometrical structure of the surface. Concerning to the  $p(2 \times 1)$  oxygen overlayer formed on the W(110) surface, there have been few investigations of the electronic states, while many structural studies<sup>(1)</sup> such as Low Energy Electron Diffraction (LEED) have been performed. Angle-Resolved Photoelectron Spectroscopy (ARPES) is one of the best techniques to obtain the electronic properties of surface-adsorbate complex as the O/W(110) system. Here, we report the electronic structure of the W(110) $p(2 \times 1)$ -O surface using ARPES.

Measurements were performed at BL-11D using an apparatus for ARPES described elsewhere. The angular acceptance of the analyzer was  $\pm 1^\circ$  and total energy resolution was varied between 0.2 and 0.4 eV depending on the incident photon energy. The working pressure was less than  $2 \times 10^{-10}$  Torr during the measurements. The clean W(110) surface was prepared by heating to  $\sim 1700$  K in oxygen atmosphere of  $\sim 1 \times 10^{-7}$  Torr and by annealing in vacuum at  $\sim 2000$  K for a short period of time. The  $p(2 \times 1)$ -O structure was prepared by oxygen exposure of 6 L at room temperature and verified by LEED.

Figure 1 shows the off-normal emission spectra for the  $p(2 \times 1)$ -O surface measured along  $[1\bar{1}0]$  azimuth at a photon energy of  $h\nu = 40$  eV with incidence angle of  $\theta_i = 25^\circ$  (mainly s-polarized light). The normal-emission spectrum measured at  $\theta_i = 60^\circ$  (p-polarized light) is also shown at the bottom of the figure (solid line). The binding energy ( $E_B$ ) is referred to the Fermi energy ( $E_F$ ) of the clean W(110) surface. Two O2p-derived peaks, which are marked by A and B, are observed in fig. 1. From the angular dependence of these O2p-derived peaks we obtained the dispersion curves along  $[1\bar{1}0](\bar{\Gamma}\bar{N})$  azimuth as shown in fig. 2. In the figure, the surface Brillouin zones of the clean W(110) (solid line) and W(110) $p(2 \times 1)$ -O (dotted line) are also shown. The upper band corresponding to the peak A disperses upward by  $\sim 1$  eV along  $\bar{\Gamma}\bar{N}$  direction, and the dispersion is symmetric about  $\bar{N}$ . The lower band corresponding to the peak B appears only near  $\bar{N}$  and does not exhibit clear dispersion along the  $\bar{\Gamma}\bar{N}$  direction.

As shown in fig. 1, the intensity of the peak A measured with p-polarized light is higher than that with s-polarized light. Therefore, we assign the upper band to the emission from O2p<sub>z</sub>-level. This assignment is supported by the fact that the upward dispersion of the upper band can be explained by a simple tight-binding theory for an isolated oxygen monolayer. On the lower band, the intensity and position of the peak B measured along  $\bar{\Gamma}\bar{N}$  direction are not so different from those measured along  $\bar{\Gamma}\bar{H}$  direction. This

is derived from a simple tight-binding theory, which indicate that two O2p-levels parallel to the surface for the  $p(2 \times 1)$  structure mix each other along both directions. Therefore, we suppose that the lower band is ascribed to the O2p-levels parallel to the surface. It is interesting that the results and conclusion are similar to those for Cr(110) $p(4 \times 2)$ -O<sup>(2)</sup>.

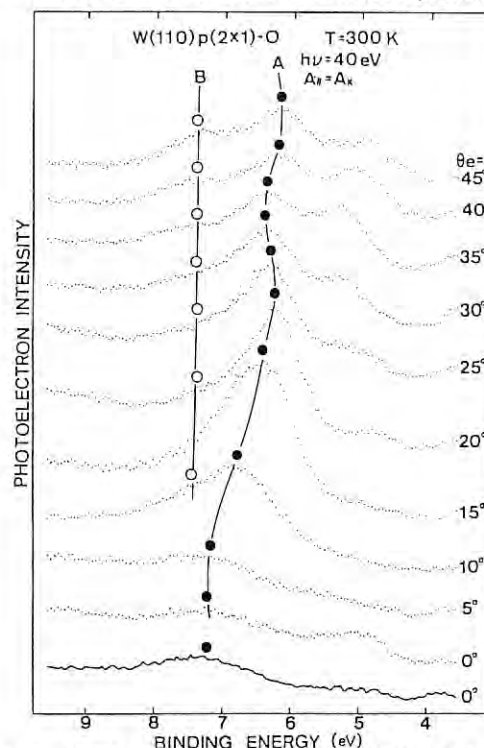


Fig. 1 ARPES spectra for the W(110) $p(2 \times 1)$ -O surface

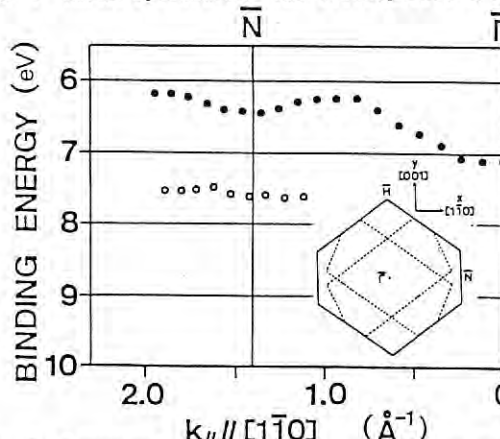


Fig. 2 Energy-dispersion curves of the O2p-derived bands for the W(110) $p(2 \times 1)$ -O surface

## REFERENCES

- 1) T. M. Lu et al., Surf. Sci., **92**, 133 (1980).  
N. J. Dinardo et al., Surf. Sci., **140**, L229 (1984).
- 2) T. Komeda et al., Phys. Rev., **B38**, 7345 (1988).



## Angle-resolved photoemission study of hydrogen-adsorbed Cr(110)

Tadahiro KOMEDA, Yasuo SAKISAKA, Masaru ONCHI, Hiroo KATO+, Shoji SUZUKI++, Kazuyuki EDAMOTO+++, and Yoshihiro AIURA++++

Department of Chemistry, Faculty of Science, Kyoto University, Kyoto 606, Japan

+Photon Factory, National Laboratory for High Energy Physics, Tsukuba-shi, Ibaragi 305, Japan

++Department of Physics, Faculty of Science, Tohoku University, Sendai 980, Japan

+++Department of Chemistry, Faculty of Science, Tokyo Institute of Technology, Ookayama, Tokyo 152, Japan

++++Institute of Physics, University of Tsukuba, Tsukuba-shi, Ibaragi 305, Japan

### Introduction

We made LEED and angle-resolved photoemission studies of hydrogen-adsorbed Cr(110) surfaces. For this system there has been quite a few investigations with modern analytical techniques, partly because of the difficulties of the sample preparation.

### Experiment

The experiments were made on BL-11D with a spherical analyzer. The clean Cr(110) surface, showing the p(1x1) LEED pattern, was prepared by repeated Ar<sup>+</sup> sputtering and annealing cycles. With liquid N<sub>2</sub> cooling, the crystal could be cooled to 80 K.

### Results and discussion

A p(2x2) LEED pattern was observed at the hydrogen exposure of 1-5 L. As the hydrogen exposure was increased to 7 L, streaks between the integral-order spots along [110] azimuth started to be observed and the streaked (1x1) LEED pattern was completed at ~10 L.

Figures 1 and 2 show off-normal spectra at  $h\nu=25$  eV along the [001] direction ( $\Gamma\bar{H}$  azimuth) for the p(2x2)-H and streaked (1x1)-H surfaces, respectively. The H-induced features are indicated by solid circles. The results are summarized as follows: (1) The feature at the binding energy of ~2.5 eV is observed only for small emission angles  $\theta_e$  for both surfaces. This feature can be considered to be the H-induced surface state. (2) For the p(2x2)-H surface, a feature at the constant binding energy of ~5.5 eV is observed for various  $\theta_e$ . This level lies over the projected Cr bulk bands for smaller  $\theta_e$ . The intensity of this peak increases for larger  $\theta_e$ . The variation of this peak intensity can be explained by a broadening effect due to the hybridization of H-derived level with the substrate band. (3) For the streaked p(1x1)-H surface, a H<sub>1s</sub>-derived state, which is split off from the Cr bulk bands, exists at the binding energy of 7.8 eV at  $\Gamma$  and shows considerable dispersion of ~2.8 eV in the [001] azimuth having the same periodicity of the substrate structure. (4) The upward shift of the H-derived state for smaller coverage is partly due to the removal of

dispersion in the H level. (5) The Cr-H bonding state is mainly d-like at around  $\bar{\Gamma}$  and mainly s-like near the zone boundary.

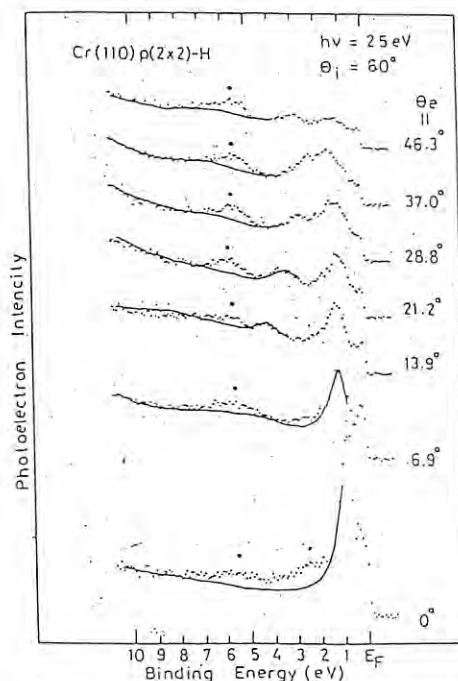


Figure 1

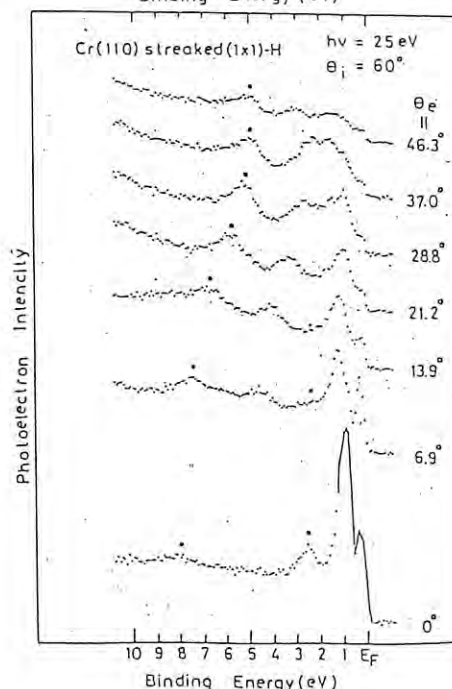


Figure 2



## Angle-resolved photoemission study of oxygen-adsorbed Cr(110)

Tadahiro KOMEDA, Yasuo SAKISAKA, Masaru ONCHI, Hiroo KATO<sup>+</sup>, Shoji SUZUKI<sup>++</sup>, Kazuyuki EDAMOTO<sup>+++</sup>, and Yoshihiro AIURA<sup>++++</sup>

Department of Chemistry, Faculty of Science, Kyoto University, Kyoto 606, Japan

<sup>+</sup>Photon Factory, National Laboratory for High Energy Physics, Tsukuba-shi, Ibaragi 305, Japan

<sup>++</sup>Department of Physics, Faculty of Science, Tohoku University, Sendai 980, Japan

<sup>+++</sup>Department of Chemistry, Faculty of Science, Tokyo Institute of Technology, Okayama, Tokyo 152, Japan

<sup>++++</sup>Institute of Physics, University of Tsukuba, Tsukuba-shi, Ibaragi 305, Japan

### Introduction

The interaction of oxygen with a Cr(110) surface has been studied by angle-resolved photoemission spectroscopy (ARUPS).

### Experiment

The ARUPS measurement were made on BL-11D with a spherical analyzer.

### Results and discussion

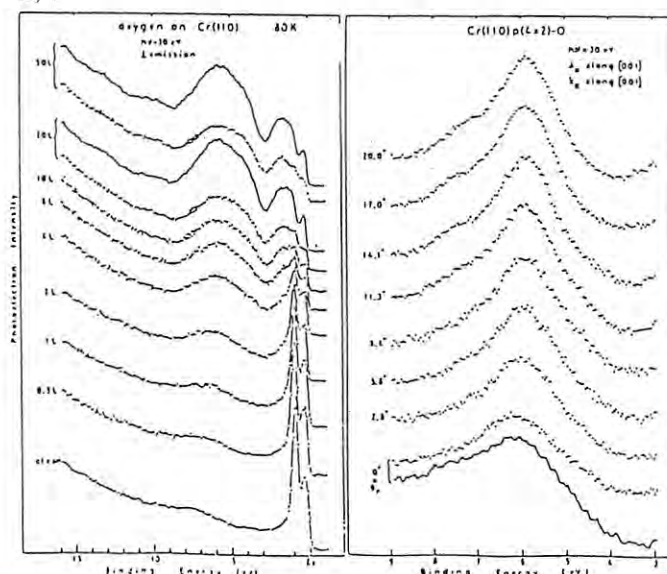
LEED studies showed that Cr(110)p(4x2)-O surface was obtained after  $\sim 1.5$  L exposure at 80 K and subsequent annealing at 300 K, and the well known faceted Cr(110)-O surface, showing streaked LEED pattern along [110] azimuth, was prepared by 10-20 L oxygen exposure at 80 K and subsequent heating  $\sim 770$  K.

Figure 1 shows normal emission spectra of Cr(110) at  $h\nu=30$  eV for various oxygen exposures at 80 K. The results are summarized as follows; (1) dissociative chemisorption for oxygen exposure less than 2L (2) oxidation above 4L. We note that 7.5 eV feature (shaded region) can be ascribed to the  $\pi_g$  orbital of chemisorbed molecular oxygen.

Figure 2 shows off-normal emission spectra of the p(4x2)-O surface measured at  $h\nu=30$  eV and  $\theta_i=25^\circ$  (dots) and  $60^\circ$  (line). Two  $O_{2p}$  derived feature are observed at  $\sim 6.2$  and  $\sim 7.4$  eV which is ascribed to the emission from  $O_{p_z}$  and  $O_{p_x}$  levels, respectively. The upper level at  $\sim 6$  eV disperses upward by  $\sim 0.3$  eV along  $\overline{1\overline{1}0}$  and the dispersion is symmetric about  $\overline{1\overline{1}0}$ .

Figure 3 shows off-normal emission spectra of the faceted Cr(110)-O surface along the [001] azimuth measured at  $h\nu=30$  eV and  $\theta_i=60^\circ$  (dots) and  $25^\circ$  (line). If the  $\theta_e=0^\circ$  spectrum is shifted uniformly by  $\sim 0.8$  eV towards higher binding energies ( $E_B$ ), energies of oxygen-induced features at lower  $E_B$  are in agreement with the values in the oxide spectrum obtained after 20-50 L oxygen exposure at 80 K. Two  $O_{2p}$ -derived features at  $\sim 5.3$  eV and  $\sim 6.6$  eV can be assigned to the  $p_x$  and  $p_z$  emissions, respectively. The energy dispersion  $E(k_{\parallel})$  of the  $O_{2p}$  derived bands along

the [001] azimuth (perpendicular to the streaks) are shown in Fig. 4. Note that the dispersion of the bands is symmetric about  $k_{\parallel}=1.09 \text{ \AA}^{-1}$  which is  $2\pi$  times the inverse streaking spacing. (i.e.,  $\pi/a$ , where  $a$  is the lattice constant of 2.884 Å).



## ELECTRONIC STRUCTURE OF NbC(100) SURFACE: ANGLE-RESOLVED PHOTOEMISSION STUDY

Kazuyuki EDAMOTO, Seiji MAEHAMA, Eizo MIYAZAKI, and Hiroo KATO<sup>†</sup>

Department of Chemistry, Tokyo Institute of Technology, Ookayama, Meguro-ku, Tokyo 152, Japan

<sup>†</sup>Photon Factory, National Laboratory for High Energy Physics, Tsukuba-shi, Ibaraki 305, JapanIntroduction

NbC possesses many interesting physical properties, which are known to be closely related to this electronic structure.<sup>1</sup> In this report, the electronic structure of NbC(100) is investigated by the use of angle-resolved photoemission study.

Experimental

The measurements were conducted on BL-11D with a spherical-sector-type analyzer. The clean NbC(100) surface was prepared by flashing at 1500°C.

Results and discussion

Fig. 1 shows normal emission spectra for the NbC(100) surface taken at various photon energies ( $h\nu = 25-50$  eV). The incidence angle of the light is 25°(a) and 60°(b). The resonance emission observed at just below  $E_F$  ( $h\nu > 35$  eV) is attributed to a Fano type resonance corresponding with the  $4p \rightarrow 4d$  excitation. Besides the resonance emission, six peaks labelled A-F are observed. According to the symmetry selection rules, the polarization dependencies shown in Fig. 1 indicate that peaks A and B originate from the initial states of  $\Delta_5$  symmetry and peaks C, D, E and F originate from those of  $\Delta_1$  symmetry. In Fig. 2 are plotted experimental points together with the calculated band structure along  $\Gamma$ -X direction.<sup>2</sup> The dispersions of peaks B, E and F are well reproduced by the theoretically calculated bulk bands. Together with considering the symmetric properties, these peaks are attributed to the direct transitions from the bulk bands. The sample used in this work possesses ~10 % carbon vacant sites, which are expected to have considerable influence on the electronic structure of NbC.<sup>1</sup> Theoretically, a vacancy induced state of NbC is expected to exist at 2.6 eV below  $E_F$  and to be totally symmetric ( $\Delta_1$  like). The non-dispersive peak C, which is observed at 2.3 eV and  $\Delta_1$  like, is thus attributed to the vacancy induced state. It is known that the surface state is important for the chemical properties of the surface. In order to resolve the surface state,  $O_2$  adsorption study has been performed (Fig. 3). It is clearly shown that the peak A, which is non-dispersive, is very sensitive to the  $O_2$  adsorption, indicating that this is due

to the surface state. Considering the symmetric property ( $\Delta_5$  like) and energy position, this is explained as a Tamm state which is pulled off from the bulk  $\Delta_5$  band.

References

- 1 L. E. Toth, Transition Metal Carbides and Nitrides (Academic Press, New York, 1971).
- 2 P. A. P. Lindberg, L. I. Johansson, J. B. Lindstrom, P. E. S. Persson, D. S. L. Law and A. N. Christensen, Phys. Rev. B36 (1987) 6343.

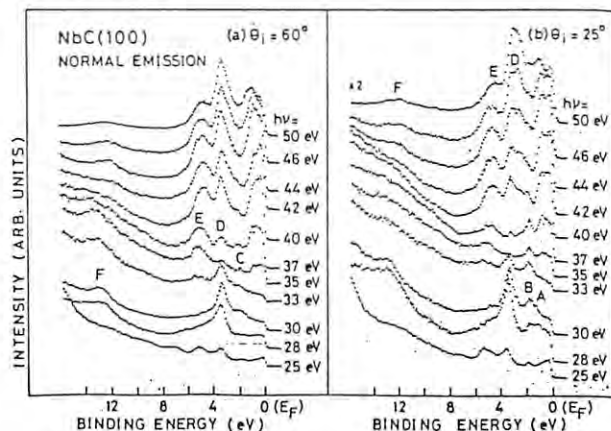
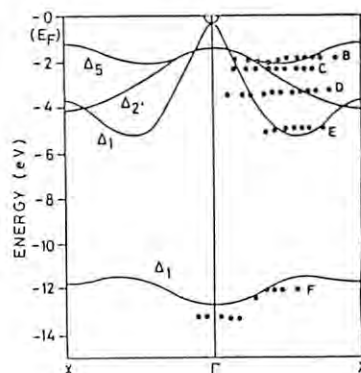


Fig. 1



← Fig. 2

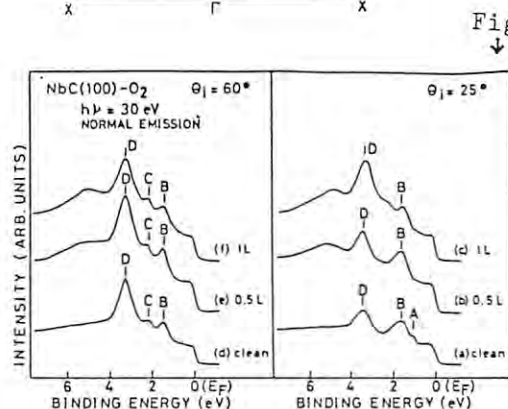


Fig. 3

ANGLE-RESOLVED PHOTOEMISSION STUDY OF  $O_2$  ADSORPTION ON NbC(100)Kazuyuki EDAMOTO, Seiji MAEHAMA, Eizo MIYAZAKI, and Hiroo KATO<sup>†</sup>

Department of Chemistry, Tokyo Institute of Technology, Ookayama, Meguro-ku, Tokyo 152, Japan

<sup>†</sup>Photon Factory, National Laboratory for High Energy Physics, Tsukuba-shi, Ibaraki 305, JapanIntroduction

The surface properties of the transition metal carbides are of interest because of their use as catalysis, coating materials, etc. We report here the angle-resolved photoemission study on the adsorbed state of  $O_2$  on the NbC(100) surface at 110 K.

Experimental

The measurements were conducted on BL-11D with a spherical-sector-type analyzer. The clean NbC(100) surface was prepared by flashing at 1500°C.

Results and discussion

Fig. 1 shows the change in the normal-emission spectra of the NbC(100)- $O_2$  surface. An incidence angle of the light is  $60^\circ$  and a photon energy is 30 eV. As the NbC(100) at 110 K is exposed to 10 L  $O_2$ , the spectrum is varied to that shown in Fig. 1b which corresponds to the chemisorbed phase. As the same surface is further exposed to  $O_2$  (30 L), the different adsorbed phase is formed (Fig. 1c). By heating this surface at 200 K, the surface is recovered by chemisorbed phase (Fig. 1d). Above results suggest that, for 30 L exposure, the condensed layer is formed on the chemisorbed phase, and by heating at 200 K, the condensed layer is reversibly removed and underlying chemisorbed phase reappears. The adsorbed state of  $O_2$  in the condensed layer is investigated by polarization dependent measurements. Fig. 2 shows the normal-emission spectra of the condensed layer taken at  $\theta_i = 25^\circ$  (dominantly s-polarized) and  $60^\circ$  (dominantly p-polarized). The correspondence between the peaks and the vertical ionization potentials of  $O_2$  molecule in the gas phase<sup>1</sup> is also shown. It is clearly shown that the  $1\pi_u$ -derived peak is enhanced as the p-polarized light is used. Considering the symmetry selection rules, this result indicates that the molecule lies with the O-O axis parallel to the surface. Details of the chemisorbed phase are also investigated by the temperature dependent and polarization dependent measurements together with the theoretical study using DV-X $\alpha$  method.<sup>2</sup> Some of the important results are as follows: (1) The chemisorbed phase is composed of chemisorbed atomic oxygen and molecularly chemisorbed species. (2) The atomic

oxygen is located on an atop site of the surface carbon atom. (3) The molecularly chemisorbed oxygen is the peroxide-like species.

References

- 1 M. S. Banna and D. A. Shirley, J. Electron Spectrosc. Related Phenom. 8 (1976) 255.
- 2 M. Orita, I. Kojima and E. Miyazaki, J. Chem. Phys. 87 (1987) 4162.

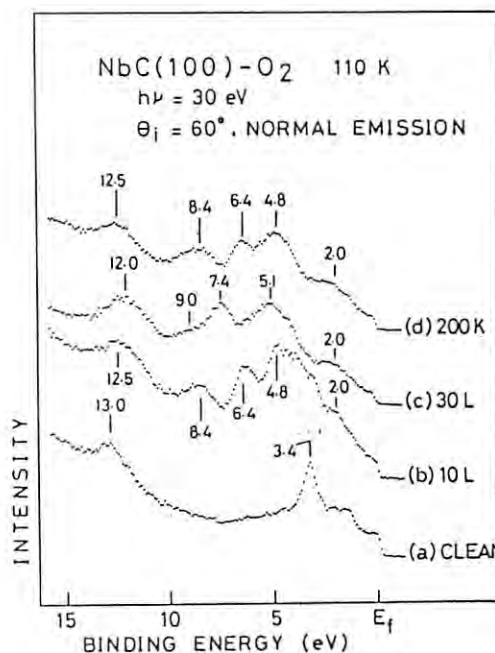


Fig. 1

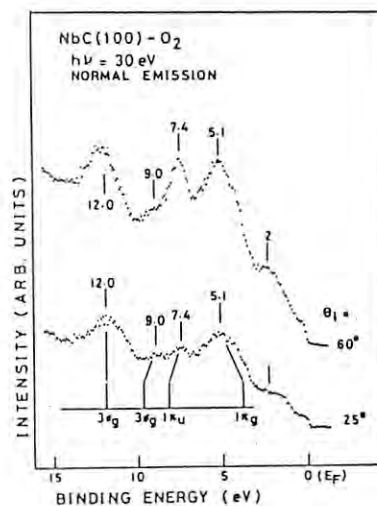


Fig. 2



PHOTOEMISSION FROM  $\text{SmRh}_3\text{B}_2$ 

Hidenao SUGAWARA, Hiromu ARAI<sup>a)</sup>, Tsutomu MITSUISHI<sup>b)</sup>, Tsuneaki MIYAHARA<sup>c)</sup>,  
Tomohiro KITAZUME, Hiroo KATO<sup>c)</sup>, Yuko ABE<sup>a)</sup> and Mitsuo KASAYA<sup>a)</sup>

Faculty of Education, Gunma University, Maebashi 371

a) Department of Physics, Faculty of Science, Tohoku University, Sendai 980

b) Faculty of Engineering, Utsunomiya University, Utsunomiya 321

c) Photon Factory, National Laboratory for High Energy Physics, Tsukuba 305

Recently, interesting magnetic properties have been reported for a series of rare earth ternary borides  $\text{RRh}_3\text{B}_2$  ( $R$  = rare earth)<sup>1-3)</sup>. Above all,  $\text{CeRh}_3\text{B}_2$  has anomalous magnetic properties; e.g. its saturated magnetic moment at low temperature is very small, and its magnetic ordering temperature is unusually high ( $T_C = 115\text{ K}$ ). For this material, photoelectron spectra have been reported<sup>4)</sup> and it has been found that the Fermi level is situated at the energy position where the density of states in the Rh 4d band is very low, contradicting the itinerant magnetism picture for  $\text{CeRh}_3\text{B}_2$ .

In the present study, photoemission measurements have been made on  $\text{SmRh}_3\text{B}_2$  in order to understand its electronic structure. The magnetic behavior of  $\text{SmRh}_3\text{B}_2$  is similar to that of  $\text{CeRh}_3\text{B}_2$ <sup>5)</sup>. The magnetic ordering temperature has been reported to be 100 K. Our measurements consist of two parts; the first is measurements of photoelectron spectra for the valence band region in the photon energy range from 30 eV to 140 eV, the second those for the Sm 3d core electrons at a photon energy of 1.9 keV with use of a double-crystal monochromator.

Figure 1 shows energy distribution curves of  $\text{SmRh}_3\text{B}_2$  up to 13 eV for the binding energy in the photon energy range from 30 eV to 140 eV. These spectra were normalized in such a way that all spectra have the same height at the binding energy of 1.8 eV, where spectra excited with low-energy photons show maximum intensities for the Rh 4d band appearing in the region from the Fermi level to 5 eV. The shape of the Rh 4d band is essentially identical with that of  $\text{CeRh}_3\text{B}_2$ . When photon energy is increased over 90 eV, photoelectron intensity at binding energies above 4 eV increases remarkably. It is due to 4f-electron emission from trivalent Sm. 4d-4f resonant photoemission is observed for photon energies above 130 eV. In the figure, the position of the Fermi level was determined by measuring that of gold. Spectra excited with photons of energies less than 120 eV display a clear step at the Fermi level, the intensity of which amounts to one third of maximum intensity of the Rh 4d band in spectra excited with low-energy photons, indicating the existence of the Fermi level in the Rh 4d band for this material. This suggests that the itinerant electron magnetism in the Rh 4d band occurs for  $\text{SmRh}_3\text{B}_2$ .

Any indication of 4f-electron emission from divalent Sm cannot be seen in the figure. However, measurements of the constant-initial-state spectra with initial state energies fixed on and just above the Fermi level showed resonant behavior above the Sm 4d-4f threshold, although intensities were very small. On the other hand, Sm-3d core spectrum revealed no discernible intensity from  $\text{Sm}^{2+}$ . These inconsistent observations may be ascribed to difference in surface sensitivity between excitation with low energy photons for the valence-band photoemission and excitation with

a high energy photon of 1.9 keV for the Sm 3d photoemission.

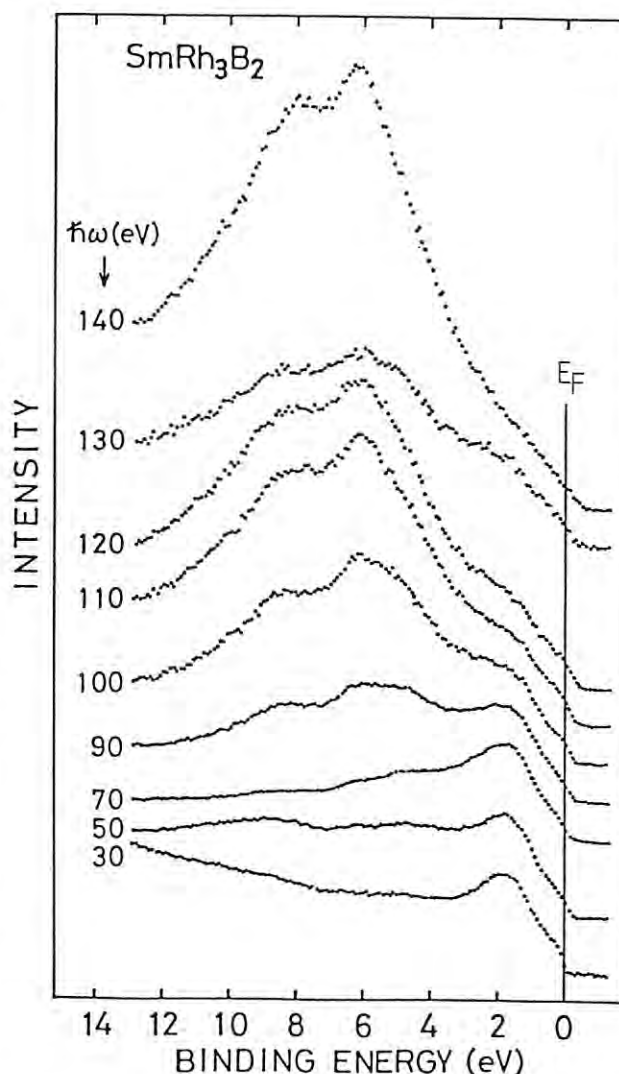


Fig. 1. Photoelectron spectra of  $\text{SmRh}_3\text{B}_2$ .

## References

- 1) D.K. Misemer, S. Auluck, S.I. Kobayasi and B.N. Harmon, *Solid State Commun.* **52**, 955(1984).
- 2) S.A. Shaheen and J.S. Schilling and R.N. Shelton, *Phys. Rev.* **B31**, 656(1985).
- 3) S.K. Malik, A.M. Umarji, G.K. Shenoy, P.A. Montano and M.E. Reeves, *Phys. Rev.* **B31**, 4728 (1985).
- 4) E.V. Sampathkumaran, G. Kaindl, C. Laubschat, W. Krone and G. Wortmann, *Phys. Rev.* **B31**, 3185(1985).
- 5) Y. Abe, M. Kasaya and T. Kasuya, to be published.



## PHOTOIONIZATION QUANTUM YIELD OF DIMETHYLETHER IN THE EXTREME-UV REGION

Masatoshi UKAI<sup>a, b)</sup>, Kosei KAMETA<sup>a)</sup>, Tetsu KAMOSAKI<sup>a)</sup>, Kyoji SHINSAKA<sup>a)</sup>,  
Hitoshi KOIZUMI<sup>c)</sup>, Yoshiro ITO<sup>d)</sup>, Ken-ichiro TANAKA<sup>b)</sup> and Yoshihiko HATANO<sup>a)</sup>

a) Department of Chemistry, Tokyo Institute of Technology, Meguro-ku, Tokyo 152

b) Photon Factory, National Laboratory for High Energy Physics, Oho, Tsukuba 305

c) Faculty of Engineering, Hokkaido University, Sapporo 060

d) Department of Mechanical Engineering, Nagaoka University of Technology, Nagaoka, Niigata 940-21

## Introduction

Photoionization quantum yield, which is the absolute probability of the photoionization on a single photoabsorption event, is the quantity of considerable importance to evaluate photoabsorption process above the ionization potential of a molecule in the VUV region, i.e., competition of direct photoionization and excitation to the superexcited states opening to autoionization, fluorescence emission, and predissociation. Although several efforts have been devoted to the study<sup>1)</sup>, serious confusions exist even for the simplest molecules. The problems were originated from lack of intense light sources and suitable window materials in the VUV region. By using a multiple-stage photoionization chamber and synchrotron radiation, the photoionization quantum yields for  $C_3H_6$ ,  $C_4H_8$ ,  $C_6H_{12}$ ,  $C_2H_6O$ , and  $C_3H_8O$  isomers<sup>2)</sup> have recently been shown for the first time in the region of wavelength from LiF cut-off (105nm) down to their respective ionization potentials.

We report the photoionization quantum yield of dimethylether (DME) in the region of wavelength of 54-92nm together with the fluorescence excitation spectra for the VUV emission.

## Experimental

Experimental details are similar to our previous works<sup>2)</sup>; in the present work, metal foil filters are employed as the window materials for incoming SR beam, which prevent sample gas effusion into the optical path and eliminate the higher order radiation from the VUV monochromator. In 52-80 nm and 74-94nm regions, Sn and In foils of about 1000Å thickness giving about 1% transmission are, respectively, used. The detection efficiency of the microchannel plate and the cutoff wavelength of  $MgF_2$  or  $BaF_2$  window determine the fluorescence band pass. Absolute photon flux is obtained by measuring photoionization current of Kr and Xe ( $\eta=1$ ).

## Results and Discussion

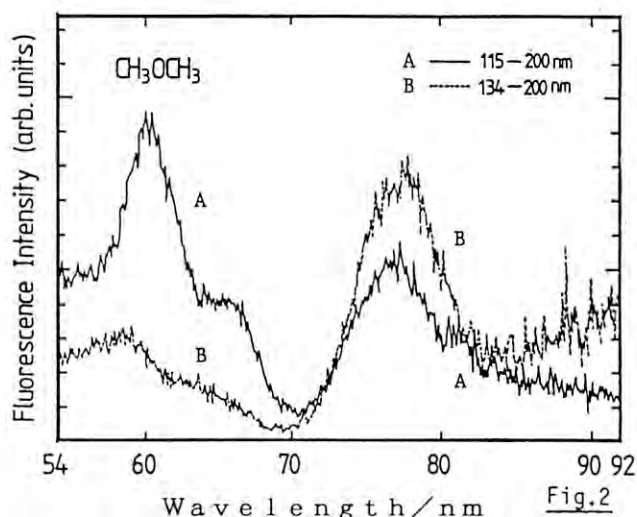
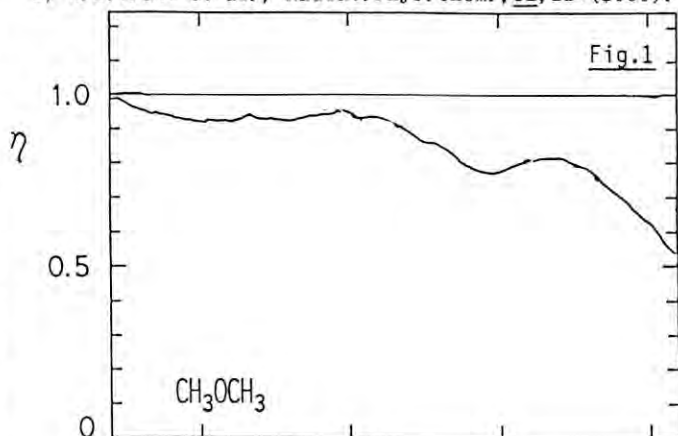
Figure 1 presents the photoionization quantum yield  $\eta$  for DME in 54-92nm. First, very strikingly, the present result clearly shows that the  $\eta$  value does not reach unity even at more than 10eV above its ionization threshold. Second, the  $\eta$  value increases with the increase in the photon energy. Third, two (or three) characteristic minima are observed. Finally, the value of  $\eta$  converges to unity at around 54nm. The minima should correspond to the ro-vibronic bands of the Rydberg series converging to the excited ionic states from such as  $\pi_{CH_3}$  and  $\sigma_{CO}$  orbitals or the MO corresponding to C-2s.

Excitation spectra of DME are presented in fig.2 for fluorescence of 115-200nm (A) and 134-200nm (B). Characteristic structures in the spectrum (A) around 60, 65, and 77nm coincide with those seen in fig.1, which are also observed in the

spectrum (B); the relative intensities are not identical, though. These excitation spectra clearly show dissociation channels of the superexcited states followed by fluorescence emission of fragments. In the spectrum (B), fluorescence from only molecular fragments can be detected; meanwhile, Lyman- $\alpha$  emission of hydrogen atom is accessible in the spectrum (A). Since the most probable pathway for dissociation is H atom emission, the noticeable difference between the two spectra is to be attributed to Lyman- $\alpha$  emission. The structures centered at the same excitation wavelength show the superexcited states predicted in fig.1 acting as the precursor for both fluorescent fragments. The envelop of the spectrum (B) shows excellent structural similarity with  $(1-\eta)\sigma$ , non-ionizing portion contributing to the total photoabsorption cross section.

1) A.W. Gallagher, C.E. Brion, J.A.R. Samson, & P.W. Langhoff, J. Phys. Chem. Ref. Data, **17**, 9(1988).

2) H. Koizumi et al., Radiat. Phys. Chem., **32**, 111(1988).



One of the authors (MU) thanks the JSPS fellowship for post-doctoral Japanese Junior Scientists.

## ROLE OF MOLECULAR SUPEREXCITED STATES IN THE PHOTOIONIZATION QUANTUM YIELDS

Masatoshi UKAI<sup>a, b)</sup>, Kyoji SHINSAKA<sup>a)</sup>, Kosei KAMETA<sup>a)</sup>, Tetsu KAMOSAKI<sup>a)</sup>, Ryo CHIBA<sup>a)</sup>  
 Hitoshi KOIZUMI<sup>c)</sup>, Yoshiro ITO<sup>d)</sup>, Ken-ichiro TANAKA<sup>b)</sup> and Yoshihiko HATANO<sup>a)</sup>

a) Department of Chemistry, Tokyo Institute of Technology, Meguro-ku, Tokyo 152

b) Photon Factory, National Laboratory for High Energy Physics, Oho, Tsukuba 305

c) Faculty of Engineering, Hokkaido University, Sapporo 060

d) Department of Mechanical Engineering, Nagaoka University of Technology, Nagaoka, Niigata 940-21

## Introduction

It is of great importance to show the role of the superexcited (autoionizing) states in the photoionization of polyatomic molecules in the energy range from VUV up to soft X-ray by evaluating quantitatively the initial photoabsorption product, i.e., absolute measurements of the total photoabsorption cross sections and the ionization quantum yields. These quantities are quite fundamental to understand not only the photoionization process itself, but also the radiation effects and the other ionized gas phenomena. Although several efforts have been devoted to the measurements of the photoionization quantum yields, very few reports are available even for the simplest molecules<sup>1)</sup>. Furthermore, serious conflicts exist in some cases.

Absolute measurements of the photoionization quantum yields are in progress for some simple, but chemically very important, molecules in the VUV region shortward of 105nm (LiF cutoff).

Fig.1 Ionization Chamber.

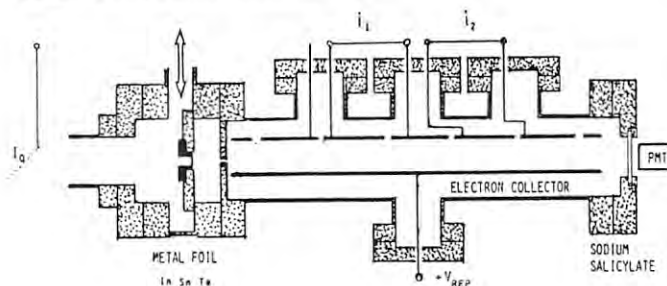
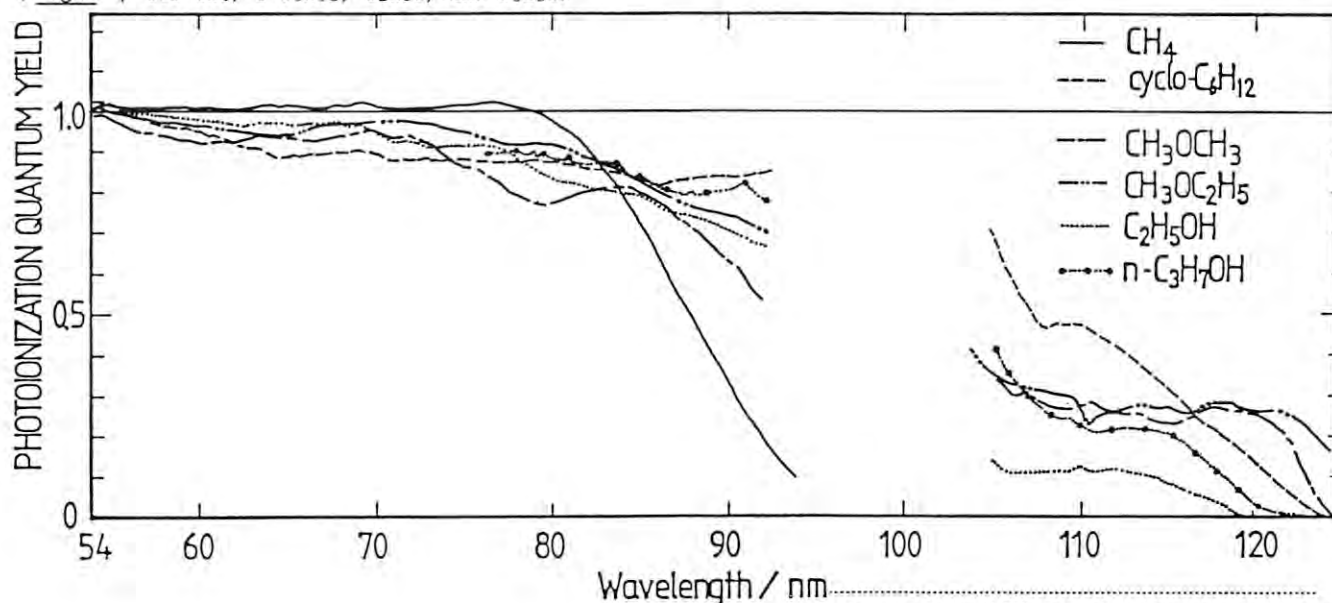


Fig.2  $\eta$  for  $\text{CH}_4$ ,  $\text{c-C}_6\text{H}_{12}$ ,  $\text{C}_2\text{H}_6\text{O}$ , and  $\text{C}_3\text{H}_8\text{O}$ .



## Experimental

Photoionization quantum yields are obtained at BL-12A using a multiple-staged photoionization chamber<sup>1)</sup> (fig.1). In the present work, metal foil filters are employed as the window materials for incoming SR beam. In 52-80nm and 74-94nm regions, Sn and In foils of about 1000Å thickness with about 1% transmittance are respectively, used. Measuring photo-currents,  $i_1$  and  $i_2$ , the photoionization quantum yield  $\eta$  is obtained as follows;

$$\eta = \frac{i_1/e}{I_0 \exp(-\sigma_T N L_1) \{1 - \exp(-\sigma_T N L)\}}$$

$$\sigma_T = \frac{\ln(i_1/i_2)}{L N}$$

where  $\sigma_T$  and  $N$  are the total photoabsorption cross section and gas density. Absolute photon flux  $I_0$  is obtained by measuring photo-current of Kr and Xe ( $\eta=1$ ).

## Results and Discussion

Figure 2 shows the obtained ionization quantum yields together with those in the previous measurements<sup>1)</sup>. A large discrepancy from unity in the  $\eta$  values is observed, which diminishes with the increase in the photon energy. A considerable portion of the superexcited states existing in this region is shown to undergo dissociation, fluorescence decay, and other non-ionizing channels, which is determined by the rate of autoionization in competition with dissociation and the density of superexcited states. Further analysis and interpretation are in progress.

1) H. Koizumi et al., Radiat. Phys. Chem., 32, 111(1988).

One of the authors (MU) thanks the JSPS fellowship for post-doctoral Japanese Junior Scientists.

## CHARACTERISTICS OF FLAT FIELD SPECTROMETERS FOR FUSION PLASMA DIAGNOSTICS

Hirotsuka Kubo, Akira Sakasai, Nobuhiro Nishino, Yoshihiko Koide, Hideaki Yokomizo, Tatsuo Sugie, Hiroshi Takeuchi, Kenichiro Tanaka \*, Hideaki Maezawa\*, Kenji Itoh\*, and Naohiro Yamaguchi \*\*

Japan Atomic Energy Research Institute, Naka-Machi, Naka-gun, Ibaraki 311-01

\*Photon Factory, National Laboratory for High Energy Physics, Oho, Tsukuba-shi, Ibaraki 305

\*\*Plasma Research Center, University of Tsukuba, Tennoudai, Tsukuba-shi, Ibaraki 305

### Introduction

In recent years, time-resolving multichannel spectrometers capable of observing many impurity radiation lines have become widely used for tokamak plasma spectroscopy<sup>1) 2)</sup>. Absolute intensity calibration of the spectrometer is needed for measurements of impurity density, radiative losses, and impurity transports. And the calibration is interesting in optics, because the theory of the diffraction efficiency with concave gratings has not been established.

In this report, we describe the sensitivity calibration of a flat-field spectrometer in the wavelength region 275-1200 Å.

### Multichannel Spectrometer

The spectrometer has been designed to have a flat field by means of a holographic grating, and a multichannel intensified photodiode array is placed in its focal plane. A 300-groove/mm grating coated with platinum is used, and the angle of incidence is 85°.

### Experimental

The experimental arrangement of the calibration is shown in Fig.1. The synchrotron radiation was dispersed with a 1-m Seya-Namioka monochromator at beam line 12A. All of the light which passed through the entrance slit of the spectrometer was dispersed with the holographic grating and detected with the multichannel detector. The absolute intensity of the light was monitored with a windowless far UV photodiode which had been calibrated at the National Bureau of Standards in USA<sup>3)</sup>. First- and higher-order contributions to the signal were estimated by using filters (tellurium, tin, and LiF). Since the synchrotron radiation is highly polarized in the plane of the electron orbit and the

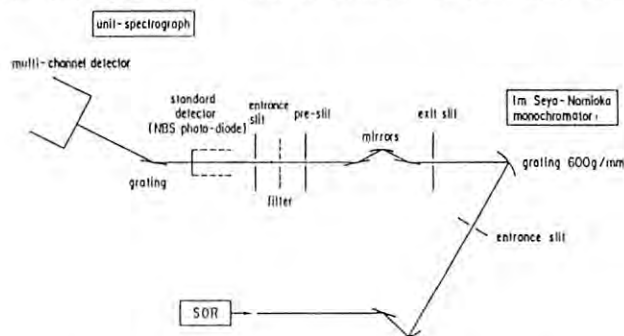


Fig. 1 Arrangement of the experiment.

grating acts as a partial polarizer, the spectrometer was calibrated in two positions; with the grating grooves perpendicular and parallel to the electron orbit.

### Result

The result of the calibration is shown in Fig.2. The sensitivity refers the output voltage of the detector per photon flux. The response at the each position of the grating is not constant, and it is estimated that this effect causes an error of 20%. The error of the sensitivity of the NBS photodiode had been estimated typically as 8%. As a result, the total error in the sensitivity of this spectrometer is estimated to be about 30%.

### References

- 1) H.Kubo, T.Sugie, A.Sakasai et.al., Rev.Sci. Instrum., to be published.
- 2) H.Nagata, M.Shiho, and T.Sugie, Japan Atomic Energy Research Institute Report, JAERI-M, to be published.
- 3) L.R.Canfield, R.G.Johnson, and R.P.Madden, Appl.Opt., **12**, 1611 (1973)

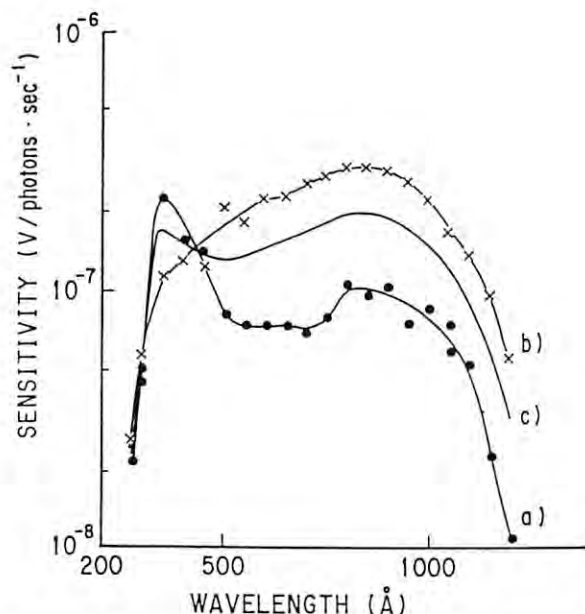


Fig. 2 Calibration curve of the spectrometer.  
a) the sensitivity using synchrotron radiation polarized perpendicular to the grating grooves, b) the sensitivity using synchrotron radiation polarized parallel to the grating grooves, c) the averaged sensitivity for two orientations.

THRESHOLD ELECTRON-ION COINCIDENCE MEASUREMENTS OF  $\text{CO}_2^+$ 

Yumio MORIOKA,<sup>1)</sup> Takahiro MATSUMOTO,<sup>1)</sup> Tetsuya ENDOW,<sup>1)</sup> Tatsuji HAYAISHI,<sup>2)</sup>  
Kenichiro TANAKA<sup>3)</sup> and Kenji ITO<sup>3)</sup>

- 1) Institute of Physics, University of Tsukuba, Tennodai, Tsukuba, Ibaraki 305, Japan  
2) Institute of Applied Physics, University of Tsukuba, Tennodai, Tsukuba, Ibaraki 305 Japan  
3) National Laboratory for High Energy Physics, Oho, Tsukuba, Ibaraki 305, Japan

## INTRODUCTION

Threshold electron-ion coincidence measurements of  $\text{CO}_2^+$  were performed by Frey et al. They determined the vibrational frequencies and the amount of spin orbit splitting of the X, A, B and C states of  $\text{CO}_2^+$ . They also studied the decay of the C state of  $\text{CO}_2^+$  using the mass analysis. Eland and Berkowitz<sup>2)</sup> studied the formation and predissociation of the C state of  $\text{CO}_2^+$ .

We reexamined their investigation by the use of the coincidence with ions which was better than only threshold electron spectroscopy in the point of the removal of the noise.

## RESULTS AND DISCUSSION

Threshold electrons of  $\text{CO}_2^+$  were measured from the ionization threshold to 400 Å. The vibrational frequencies of the X, A, B and C states of  $\text{CO}_2^+$  were determined in agreement with the previous investigations. The spectrum of the X, A, B and C states of  $\text{CO}_2^+$  are shown Fig.1, 2, and 4. In the Franck-Condon gap between the X and A states the resonant autoionization was observed as shown in Fig. 2.

It is found that the C state completely decays to  $\text{CO}^+ + \text{O}$  and  $\text{C}^+ + \text{CO}$  and that the ratios of  $\text{CO}^+ + \text{O}$  to  $\text{C}^+ + \text{CO}$  were varying with the vibrational levels. In the region of 450 Å, the broad peak was observed which was found in coincidence with  $\text{CO}^+$ .

## REFERENCES

- 1) R.Frey et al Chem. Phys. **21**, 89 (1977)  
2) J.H.D.Eland and J. Berkowitz J.Chem.Phys. **67** 2782 (1977)

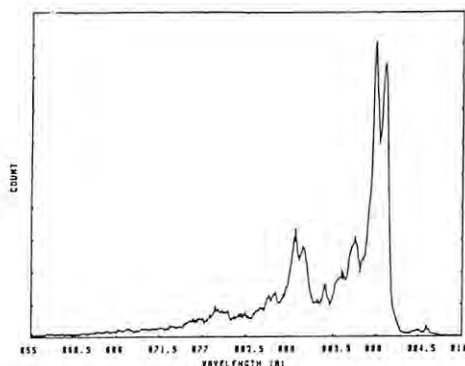


Fig. 1. Threshold electron spectrum of the X state of  $\text{CO}_2^+$

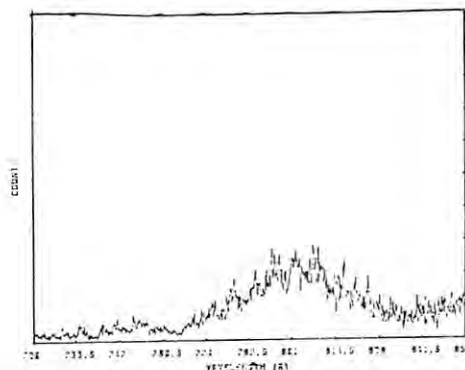


Fig. 2. Threshold electron spectrum in the region of 800 Å

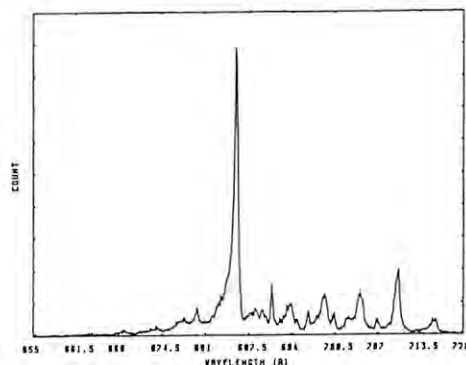


Fig.3. Threshold electron spectrum of the A and B states of  $\text{CO}_2^+$

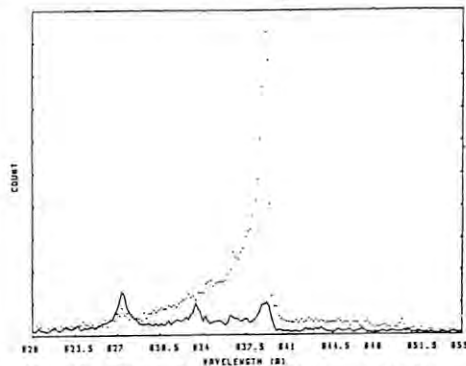


Fig.4. Threshold electron spectrum of the C state of  $\text{CO}_2^+$



NON-IONIZING DECAY OF SUPEREXCITED  $C_2H_2$  IN THE VACUUM ULTRAVIOLET REGION

Masatoshi UKAI<sup>a, b)</sup>, Kosei KAMETA<sup>a)</sup>, Kyoji SHINSAKA<sup>a)</sup>, Ryo CHIBA<sup>a)</sup>,  
Ken-ichiro TANAKA<sup>b)</sup>, Yoshiro ITO<sup>c)</sup>, and Yoshihiko HATANO<sup>a)</sup>

a) Department of Chemistry, Tokyo Institute of Technology, Meguro-ku, Tokyo 152

b) Photon Factory, National Laboratory for High Energy Physics, Oho, Tsukuba 305

c) Department of Mechanical Engineering, Nagaoka University of Technology, Nagaoka, Niigata 940-21

### Introduction

Although the photoionization of  $C_2H_2$  in the VUV region has been studied very extensively, quantitative investigations have been limited only for the recent few studies<sup>1, 2)</sup>. Especially, the photoionization quantum yield, i.e., the absolute photoionization probability on a single photoabsorption event, has been remained only in the preliminary fashion<sup>3)</sup>. This result showed a large deviation of the quantum yield from unity, in which a strong competition between autoionization and the nonionizing processes is expected. Ibuki et al. have obtained very recently the photoionization quantum yield and the optical oscillator strength distribution in the VUV-EUV region by means of the dipole (e, 2e) coincidence method<sup>4)</sup>.

In the present work, formation and destruction of the superexcited  $C_2H_2$  molecule have been studied by way of the measurements of a photoionization quantum yield and fluorescence excitation spectra in the extreme-UV region.

### Experimental

A VUV excitation source was obtained from a 1m Seya-type monochromator. Two kinds of experiments have been carried out. Using a multiple-plated photoionization chamber<sup>5)</sup> with an In or a Sn foil window at the entrance, photoionization quantum yields have been measured in the excitation region of 54-92nm. In another experiment, fluorescence excitation spectra have been recorded using a VUV detector (a microchannel plate coupled with a  $MgF_2$  filter) and an UV-visible detector (a visible photomultiplier with a band pass or a low pass filter) set perpendicular to the exciting photon beam.

### Results and Discussions

Figure 1 presents the photoionization quantum yield of  $C_2H_2$  in 52-92nm. The structure with double minima<sup>3)</sup> in the absolute scale at around 73 and 86nm is well reproduced, but the absolute value at the 73nm minimum is somewhat different from the recent dipole (e, 2e) measurement<sup>4)</sup>. The minima are due to the Rydberg band converging to  $3\sigma_g^{-1}(\sigma_{CC})$  and  $2\sigma_u^{-1}(C_{2s})$ .

Figure 2 shows excitation spectra of the fluorescence at UV-visible (280-800nm) and VUV (120-180nm) region. The UV-visible excitation spectrum shows a good agreement with the result by Metzger & Cook<sup>3)</sup> in the excitation region of 60-100nm, but the VUV excitation spectrum is not identical. The spectra for other fluorescence regions (not shown) are somewhat different from both spectra. It suggests that the above described structure in fig.1 is originated by superposition of separate non-ionizing processes coupled with distinct fragmentation.

In the UV-visible excitation spectrum, an individual Rydberg structure is observed below the ionization threshold. A remarkable VUV fluorescence recorded in the same excitation region is not

ascribed to the emission from dissociation fragments judging from the thermodynamic balance. It is due to direct fluorescence from the initial excited molecule, which has been regarded unlikely to be detected because of the extremely long fluorescence lifetime<sup>2, 6)</sup> ( $\mu s$ ) of the highly excited  $C_2H_2$  molecules in comparison with that for predissociation.

- 1) C. Y. R. Wu & D. L. Judge, J. Chem. Phys., **82**, 4495 (1985)
- 2) M. Suto & L. C. Lee, J. Chem. Phys., **80**, 4824 (1984).
- 3) P. H. Metzger & G. R. Cook, J. Chem. Phys., **41**, 642 (1964)
- 4) T. Ibuki, G. Cooper, Y. Iida, & C. E. Brion, to be published.
- 5) H. Koizumi, T. Yoshimi, K. Shinsaka, M. Ukai, M. Morita, Y. Hatano, A. Yagishita, & K. Ito, J. Chem. Phys., **82**, 4856 (1985).
- 6) H. Okabe, J. Chem. Phys., **62**, 2782 (1975).

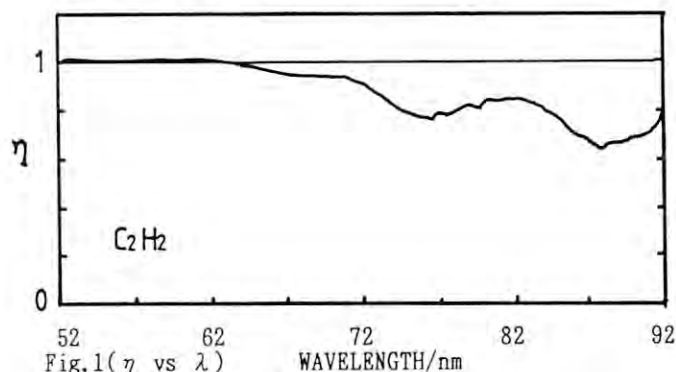


Fig.1 ( $\eta$  vs  $\lambda$ )

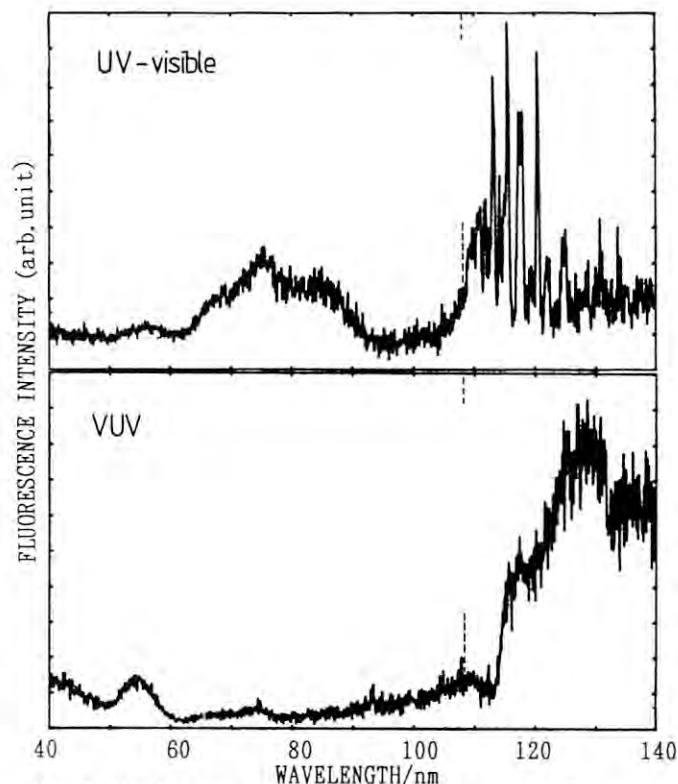


Fig.2 Fluorescence excitation spectra of  $C_2H_2$ .

One of the authors (MU) thanks the JSPS fellowship for post-doctoral Japanese Junior Scientists.

VACUUM ULTRAVIOLET FLUORESCENCE IN THE PHOTODISSOCIATION OF SUPEREXCITED  $N_2$  AND  $O_2$ 

Masatoshi UKAI<sup>a), b)</sup>, Ken-ichiro TANAKA<sup>b)</sup>, Kosei KAMETA<sup>a)</sup>, Kyoji SHINSAKA<sup>a)</sup>,  
Ryo CHIBA<sup>a)</sup>, Yoshiro ITO<sup>a)</sup>, and Yoshihiko HATANO<sup>a)</sup>

a) Department of Chemistry, Tokyo Institute of Technology, Meguro-ku, Tokyo 152

b) Photon Factory, National Laboratory for High Energy Physics, Oho, Tsukuba 305

c) Department of Mechanical Engineering, Nagaoka University of Technology, Nagaoka, Niigata 940-21

### Introduction

Among possible decay channels of the molecular superexcited states, dissociation into excited fragments is of significant importance to evaluate the non-ionizing portion as well as to identify energy or electronic states. Recently, we have successfully demonstrated the neutral dissociation of the doubly excited hydrogen molecule by Lyman- $\alpha$  detection<sup>1, 2)</sup>. Fluorescence measurements not only from neutral fragments but also from the excited molecular ions, or from the ionic fragments after autoionization will also supply a wealth of information about the decay dynamics of the superexcited molecules. Furthermore, fluorescence detection is quite advantageous to investigate time dependent behavior of the states<sup>3)</sup>. These remarks keeping in mind, we have developed a new instrument for fluorescence measurements to study the decay dynamics of superexcited states in the extreme-UV region. In this report, we show the atomic VUV fluorescence excitation spectra of  $N_2$  and  $O_2$ .

### Experimental

Figure 1 presents the schematic diagram of the present system. Briefly, monochromatized synchrotron radiation beam enters the gas cell through a tiny orifice, and the fluorescence photons are detected by a MCP (microchannel plate) or a visible photomultiplier (PMT-1). By combining with an appropriate optical filter (low pass, high pass, and narrow band pass), one can obtain monochromatic fluorescence proper for the decay channel of interest in the region from the VUV to the visible. PMT-2 is used for photon flux measurement together with the Au mesh at the upstream of the gas cell.

### Results and Discussion

Figure 2 shows the fluorescence excitation spectrum of  $O_2$  for visible emission (420-650nm) in the excitation wavelength of 40-90nm. The spectral resolution is 0.2nm band pass. The structure shortward of 68nm is due to  $O_2^+(b^4\Sigma_g^- \rightarrow a^4\Pi_u)$  emission and the small structure at the red side of the 68nm onset is  $O_2^+(A^2\Pi_u \rightarrow X^2\Pi_g)$  emission. By further choosing fluorescence band width, we can obtain individual excitation spectrum, i.e., the partial photoionization cross sections for the  $O_2^+(A$  or  $b)$  states.

Figures 3 and 4 present the VUV (115-200nm) fluorescence excitation spectra for  $O_2$  and  $N_2$ , respectively. Since VUV fluorescence is not available from ionic species for  $O_2$  and only a weak band is possible for  $N_2$ , these structures are attributed due to atomic VUV radiation such as  $O(^3S \rightarrow ^3P)$  and  $N(^4P \rightarrow ^4S)$ . A relatively good agreement is obtained with a previous measurement<sup>4)</sup>. Some distinct structures are seen in the present both spectra. Detailed analysis will be reported elsewhere.

One of the authors (MU) thanks the JSPS fellowship for post-doctoral Japanese Junior Scientists.

- 1) S. Arai, et.al., Z. Phys., **D4**, 65(1986).
- 2) S. Arai, et.al., J. Chem. Phys., **88**, 3016(1988).
- 3) K. Shinsaka et.al., J. Chem. Phys., **83**, 4405(1985).
- 4) L. C. Lee et al., J. Chem. Phys., **61**, 3261(1974).

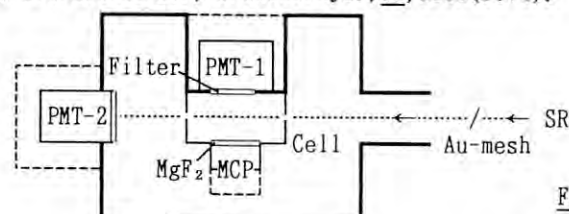


Fig. 1

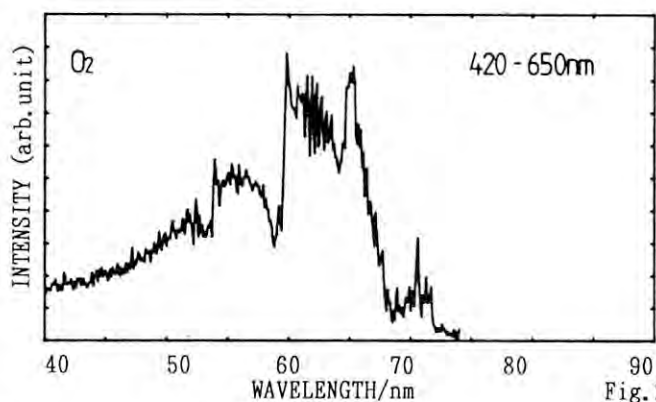


Fig. 2

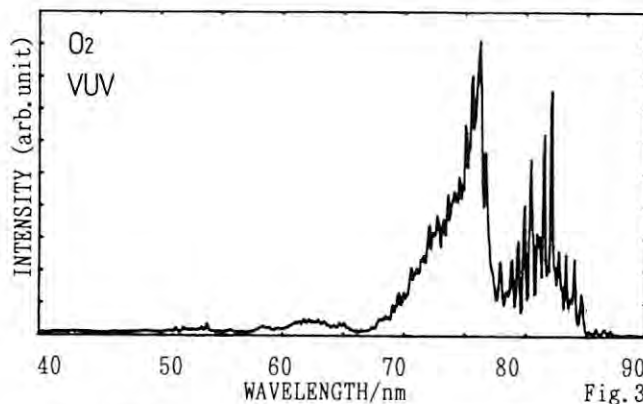


Fig. 3

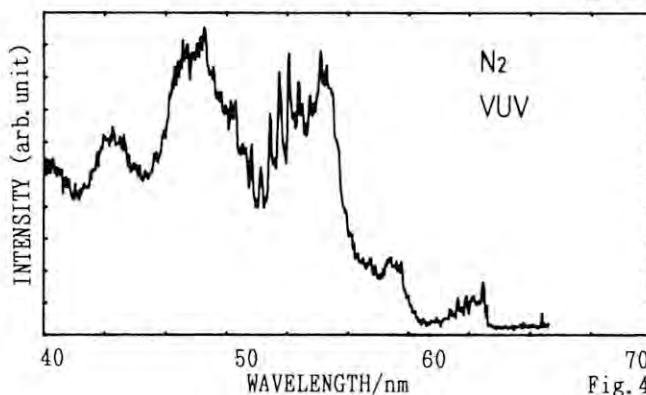


Fig. 4

HIGH-RESOLUTION ABSORPTION SPECTRUM OF CALCIUM NEAR THE  $4p\ ^2P_{1/2,3/2}$  EDGES

Kiyoshi UEDA, Kenji ITO\*, Hisashi CHIBA, Yukinori SATO, and Takeshi NAMIOKA

Research Institute for Scientific Measurements, Tohoku University, Sendai 980

\*Photon Factory, KEK, Tsukuba 305

Introduction

Near the  $4p\ ^2P_{1/2,3/2}$  edges of Ca, two Rydberg series  $4p(^2P_{1/2})ns[1/2]_1^0$  and  $4p(^2P_{1/2})nd[3/2]_1^0$ , in the J1 coupling notation, converge to the limit  $I_{1/2}=74494.341\text{ cm}^{-1}$  and three Rydberg series  $4p(^2P_{3/2})ns[3/2]_1^0$ ,  $4p(^2P_{3/2})nd[1/2]_1^0$ , and  $4p(^2P_{3/2})nd[3/2]_1^0$  converge to the limit  $I_{3/2}=74719.23\text{ cm}^{-1}$ . These five Rydberg series may interact mutually and also autoionize to several continuum states associated with the  $4s\ ^2S_{1/2}$  and  $3d\ ^2D_{3/2,5/2}$  states of  $\text{Ca}^+$ . We report observations of the absorption spectrum of Ca near the  $4p\ ^2P_{1/2,3/2}$  edges by use of the high-resolution facility 6VOPE<sup>1</sup> on BL-12B at the Photon Factory. The high-resolution spectrum is expected to provide new information about the channel coupling.<sup>2</sup>

Experimental

Calcium vapor was generated in a heat-pipe oven, specially designed<sup>3</sup> for metal-vapor experiments using SR and installed on BL-12B, at the oven temperature about  $950^\circ\text{C}$ . The absorption spectrum of Ca was registered on  $2 \times 10''$  Kodak SWR plates in the wavelength region of 1330-1410 Å using the 4th spectral order of a 6.65-m, 1200-grooves/mm, 5500-Å blaze, Os-coated grating. Exposure time was typically 60 min. at the ring current about 200 mA for the positron storage.

Results and Discussion

Figure 1 shows a portion of the absorption

spectrum of Ca near the  $4p\ ^2P_{1/2,3/2}$  edges. Between  $I_{1/2}$  and  $I_{3/2}$ , two autoionizing Rydberg series ① and ② can be seen in Fig. 1 and are tentatively assigned to  $4p(^2P_{3/2})ns[3/2]_1^0$  and  $4p(^2P_{3/2})nd[1/2,3/2]_1^0$ , respectively, on the basis of the assignments by Connerade et al.<sup>4</sup> for low-n members above 1350 Å: the two nd series are considered degenerate. The quantum defects for the two series  $ns[3/2]_1^0$  and  $nd[1/2,3/2]_1^0$  are about 2.7 and 1.2, respectively, at the absorption peaks. Just below  $I_{1/2}$ , the two series converging to  $I_{3/2}$  interact with the series ③ converging to  $I_{1/2}$ , showing the complicated absorption intensity modulation. The series converging to  $I_{1/2}$  is tentatively assigned to  $4p(^2P_{1/2})ns[1/2]_1^0$ . The quantum defect is about 2.5. The  $4p(^2P_{1/2})nd[3/2]_1^0$  series cannot be identified. Multi-channel quantum-defect analysis<sup>2</sup> is in progress.

References

1. K. Ito, T. Namioka, T. Morioka, T. Sasaki, H. Noda, K. Goto, T. Katayama, and M. Koike, *Appl. Opt.*, **25** (1986) 837.
2. M. J. Seaton, *Rep. Prog. Phys.* **46** (1983) 167; K. Ueda, *Phys. Rev. A* **35** (1987) 2484.
3. K. Ueda, W. T. Hill, and M. L. Ginter, *Rev. Sci. Instrum.* **57** (1986) 888.
4. J. P. Connerade, M. A. Baig, W. R. S. Garton, and G. H. Newsom, *Proc. R. Soc. Lond. A* **371** (1980) 295.

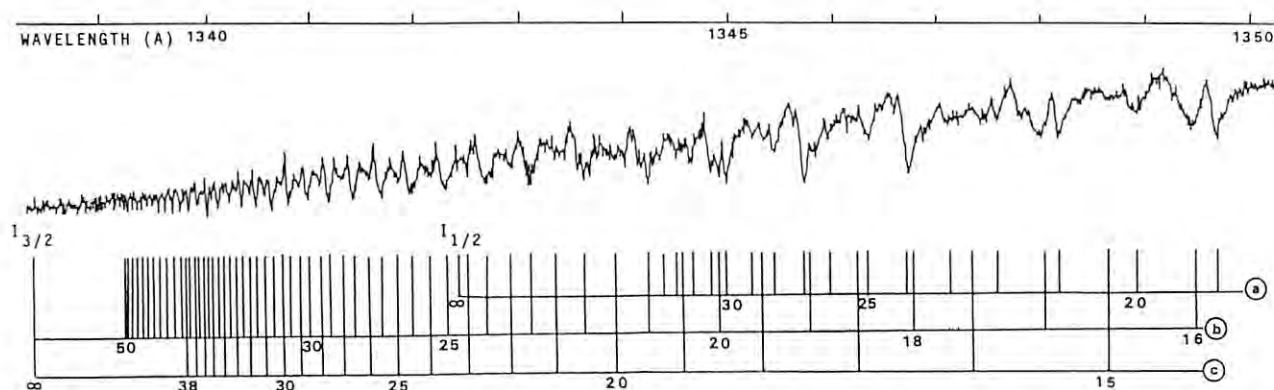


Fig. 1. Absorption spectrum of neutral calcium in the ground state  $4s^2\ ^1S_0$ : a,  $4p(^2P_{1/2})ns[1/2]_1^0$ ; b,  $4p(^2P_{3/2})ns[3/2]_1^0$ ; c,  $4p(^2P_{3/2})nd[1/2,3/2]_1^0$ .



## ABSORPTION CROSS SECTION OF KRYPTON ATOM IN ITS PHOTOIONIZATION THRESHOLD REGION

Kengo MAEDA<sup>1</sup>, Kenji ITO<sup>2</sup> and Takeshi NAMIOKA<sup>3</sup>

1)Faculty of Education, Kumamoto University, Kurokami, Kumamoto 860, Japan.

2)Photon Factory, National Laboratory for High Energy Physics, Oho, Tsukuba 305, Japan.

3)Research Institute for Scientific Measurements, Tohoku University, Katahira, Sendai 980, Japan.

## INTRODUCTION

The absorption spectra of rare gases in their photoionization threshold regions show typical Beutler-Fano profiles caused by autoionization. A high-resolution absorption cross section measurement is needed in order to compare with theoretical calculations of the cross sections/1/.

In this report is presented the photoabsorption cross section of krypton gas between the  $^2P_{1/2}^0$  and  $^2P_{3/2}^0$  ionization limits by using the high-resolution 6VOPE facility at BL-12B of the Photon Factory.

## EXPERIMENTAL

The 6.65 m, 1200 grooves/mm grating of the 6VOPE facility was used in the 6th spectral order. The resolution in its focal plane scanning mode was  $\sim 1.5 \times 10^5$  at  $\sim 88$  nm with the entrance and exit slit widths of 10  $\mu\text{m}$ . The main spectrometer tank containing krypton gas was used as an absorption cell. The sample gas pressure in the cell was  $2 \times 10^{-4} - 7 \times 10^{-4}$  Torr, and the effective optical path length,  $l$ , was 12.6 m. The uncertainty in the column density was estimated to be 2 %. The wavelength scanning has been done at a rate of 0.006 - 0.024 nm/min with the sampling time of 1 sec.

The photoabsorption cross section,  $\sigma$ , at wavelength,  $\lambda$ , can be calculated by using the following equation/2/:

$$I/I_0 = (1-A)\exp(-\sigma N l) + A\{(1-B)\exp(-\sigma_s N l) + B\},$$

where  $I$  or  $I_0$  is the light intensity measured with or without an absorbing gas,  $N$  the number of density of a sample gas,  $A$  the focused stray level,  $B$  the fraction of  $A$  that does not suffer from absorption,  $\sigma_s$  the effective absorption cross section of Kr gas for the stray light. These three parameters,  $A$ ,  $B$  and  $\sigma_s$ , were determined experimentally from  $I/I_0$  vs.  $Nl$  curve measured at 88.08 nm, which corresponds to the very diffuse  $6d'(3/2)_1^0$  peak.

## RESULTS

The photoabsorption cross section of krypton atom is shown in Fig.1 for the wavelength region of 84.45 - 88.60 nm. The uncertainty of the cross section in the present measurement is estimated to be less than 10 %. The wavelength in Fig.1 was calibrated with the results in photographic method/3/.

Carter and Hudson have also measured the photoabsorption cross section of Kr in this spectral region with a lower resolution (0.04 nm)/4/. Their cross sections are in agreement with ours except for the cross sections of the sharp  $ns'(1/2)_1^0$  peaks and those in the shorter wavelength region. For example, the present cross section for the  $8s'(1/2)_1^0$  peak is nearly twice of the result by Carter and Hudson.

An enlarged spectrum in the wavelength region of 84.5 - 84.8 nm is shown in Fig.2. As can be seen in Fig.2, the  $nd'(3/2)_1^0$  series is resolved up to  $n=58$ . With respect to this region, Carter et al. did not report the evidential cross section data because of the lower instrumental resolution.

A detailed analysis of spectrum and a comparison with theoretical calculation are under way. We are planning to extend the photoabsorption measurement in the focal plane scanning mode to other rare gases.

## REFERENCES

- /1/ R. D. Hudson and V. L. Carter, J. Opt. Soc. Am., 58, 227(1968).
- /2/ K. Ito, K. Maeda, Y. Morioka and T. Namioka, Appl. Optics, submitted.
- /3/ K. Yoshino and Y. Tanaka, J. Opt. Soc. Am., 69, 159(1979).
- /4/ V. L. Carter and R. D. Hudson, J. Opt. Soc. Am., 63, 733(1973).

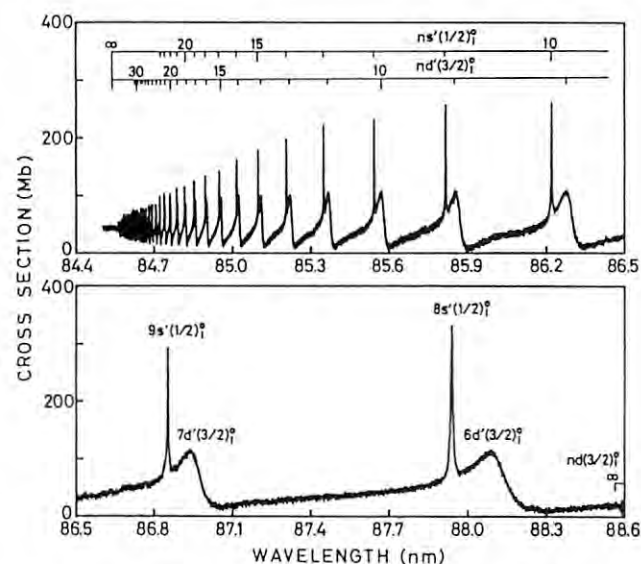


Fig.1 Absorption cross section of krypton atom in the wavelength region of 84.5 - 88.6 nm.

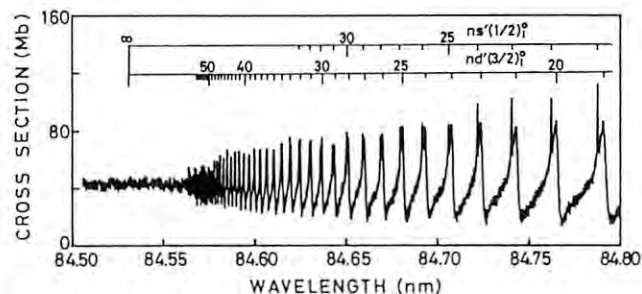


Fig.2 Enlarged spectrum of krypton atom near the 2th ionization limit.



# TEST OPERATION OF A VUV/SOFT X-RAY MONOCHROMATOR FOR UNDULATOR RADIATION AT THE PHOTON FACTORY.

Yasuji MURAMATSU and Hideki MAEZAWA\*

NTT Applied Electronics Laboratories, Musashino, Tokyo 180

\*Photon Factory, National Laboratory for High Energy Physics,  
Tsukuba, Ibaraki 305

## INTRODUCTION

The high brilliance of undulator radiation has paved the way for achieving compatibility of high resolution and high output flux in the grazing incidence optics of a synchrotron radiation monochromator<sup>1)</sup>. A VUV/soft X-ray monochromator<sup>2,3)</sup> for utilizing undulator radiation from a 26-period multipole wiggler/undulator<sup>4)</sup> has been developed at the Photon Factory. The aim of this monochromator is to achieve high resolution and high output flux. It is characterized by an optical system comprising an entrance slitless quasi-Rowland circle mounting. The monochromator was installed in a branch beamline of BL-16, and operated to measure undulator radiation spectra in order to evaluate its preliminary performance. This paper describes the result of these spectral measurements and the valuation of the preliminary performance.

## PRELIMINARY PERFORMANCE OF THE MONOCHROMATOR

During spectral measurements, positron beams with a beam current of about 250 mA were stored in the Photon Factory storage ring, and the magnetic gap of the 26-period multipole wiggler/undulator was set to about 70 mm. A piece of gold mesh mounted after the exit slit was used as a photocathode. A conventional replica grating with a groove density of  $1200 \text{ l}\cdot\text{mm}^{-1}$  was mounted on the monochromator for this preliminary test operation.

Figure 1 shows the measured spectral response of the monochromator over the photon energy range from 40 eV to 300 eV. Harmonics up to the fourth order were observed, the first being detected at 60 eV. This indicated that the entrance slitless quasi-Rowland circle mounting adopted for the monochromator had a possibility of achieving both high resolution and high output flux.

Scattering which was caused by radiation damage on the grating surface by the high power density of undulator radiation was observed in the higher photon energy region. Figure 2 shows SEM (Scanning Electron Microscopy) images of the irradiated and non-irradiated grating surfaces. This shows clearly that the scattering was caused by the broken grooves and rough surface in the irradiated area. Thus, it is confirmed that conventional replica gratings cannot withstand the high power density of undulator radiation. Therefore, thermally resistant gratings such as master gratings made of SiC should be developed to make full use of this

undulator monochromator. Development of thermally resistant optical elements for undulator radiation is now in progress.

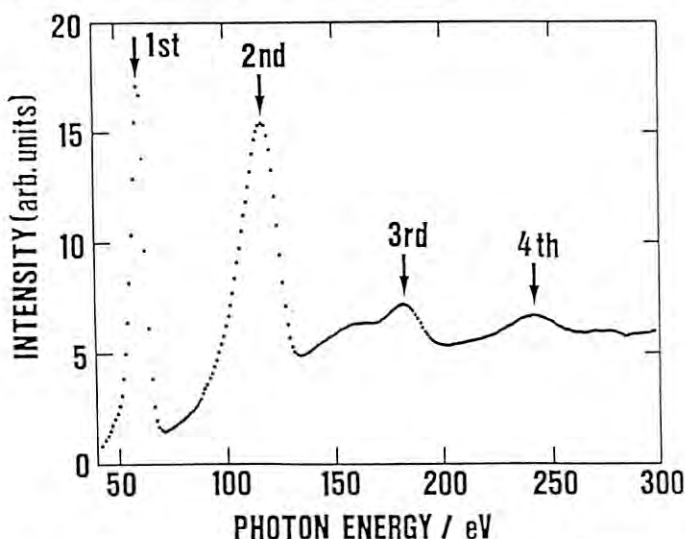


Fig. 1. Spectral response of the monochromator over the photon energy range from 40 eV to 300 eV. A replicated  $1200 \text{ l}\cdot\text{mm}^{-1}$  grating and a  $50 \mu\text{m}$  slit were used.

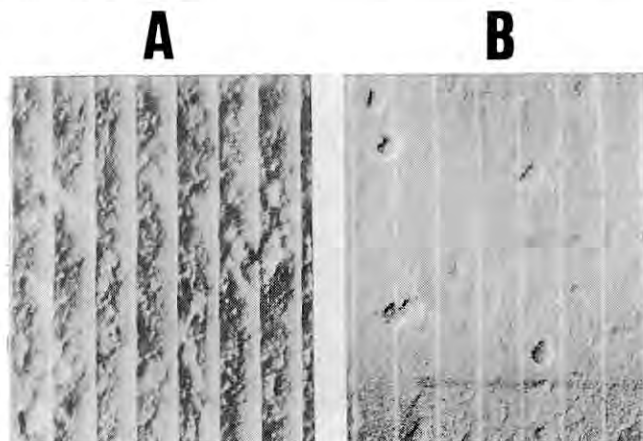


Fig. 2. SEM images of the grating surface. (A):irradiated area, (B):non-irradiated area.

## References

- 1) H. Maezawa, Y. Kagoshima, K. Mori and A. Toyoshima; Proceedings of SRI-88.
- 2) Y. Muramatsu and H. Maezawa; Photon Factory Activity Report, #5,362-364(1987).
- 3) Y. Muramatsu and H. Maezawa; Proceedings of SRI-88.
- 4) T. Shioya, S. Yamamoto, S. Sasaki, M. Katoh, Y. Kamiya and H. Kitamura; Proceedings of SRI-88.

# ANGLE-RESOLVED PHOTOEMISSION DETERMINATION OF THE BAND STRUCTURE OF $\text{YBa}_2\text{Cu}_3\text{O}_{7-x}$ (001)

Yasuo SAKISAKA, Tadahiro KOMEDA, Takahiro MARUYAMA, Masaru ONCHI, Hiroo KATO\*, Yoshihiro AIURA\*\*, Hiroyuki YANASHIMA\*\*, Takahito TERASHIMA\*\*\*, Yoshichika BANDO\*\*\*, Kenji IJIMA\*\*\*\*, Kazunuki YAMAMOTO\*\*\*\* and Kazuto HIRATA\*\*\*\*

Department of Chemistry, Faculty of Science, Kyoto University, Kyoto 606, Japan

\* Photon Factory, National Laboratory for High Energy Physics, Tsukuba-shi, Ibaraki 305, Japan

\*\* Institute of Physics, University of Tsukuba, Tsukuba-shi, Ibaraki 305, Japan

\*\*\* Institute for Chemical Research, Kyoto University, Uji 611, Japan

\*\*\*\* Research Institute for Production Development, Kyoto 606, Japan

## Introduction

The electronic structure of the 90-K YBCO ( $\text{YBa}_2\text{Cu}_3\text{O}_{7-x}$ ) superconductor is an interesting topic of research. Whether or not the band picture is valid in this oxide is a vital key factor concerned with the essence of the superconducting mechanism responsible for such a high  $T_c$ . Several angle-integrated photoemission studies on sintered pellets of this oxide concluded the breakdown of the band picture. However, the quality of their samples was poor and angle integration smears fine structures near the Fermi energy ( $E_F$ ). Thus, accurate and precise angle-resolved photoemission spectroscopy (ARUPS) study on carefully characterized specimens is highly desired for the correct electronic structure to be clarified. We present an ARUPS study of high-quality epitaxial YBCO(001) films at 300 K to elucidate the normal-state electronic structures. Our results favor a one-electron band picture.

## Experimental

The ARUPS experiments were made on BL-11D. The single-crystal YBCO(001) thin films (10 mm  $\phi$  x 1000 Å thick) were prepared epitaxially on  $\text{SrTiO}_3$ (100) [see Ref. 1]. In the ARUPS chamber, the samples were annealed at  $\sim 600^\circ\text{C}$  for  $\sim 20$  min in  $\sim 100$  Torr  $\text{O}_2$  and then cooled very slowly. The cleanness of the surface was confirmed by AES and their crystalline order by LEED [sharp (1x1) LEED patterns were observed]. After all the measurements, the superconducting transition was checked [ $T_c$  ( $R=0$ ) = 88K,  $\Delta T$  (10-90 %) = 1.5 K,  $R$  (290 K) = 200  $\mu\Omega$  cm].

## Results and discussion

Fig. 1 shows off-normal spectra of YBCO(001) along  $\Gamma\text{M}$  ( $h\nu=45$  eV and  $\theta_1=60^\circ$ ). The 5- and 7-eV features stay at almost fixed locations, while the 3-eV feature at  $k=0$  ( $\Gamma$ ) disperses to lower binding energy with increasing  $k$  from  $\Gamma$  to M ( $\sim 2$  eV at M). We found that along  $\Gamma\text{M}$  and  $\text{X-M}$  the dispersion of the 3-eV feature is periodic about the M point. Fig. 2 shows the off-normal spectra along  $\Gamma\text{X-M-}\Gamma$  in the  $E_F$  region ( $h\nu=40$  eV and  $\theta_1=25^\circ$ ). The important result is the observation of a clear Fermi edge in spectra (b), (f), (j), and (r). Furthermore, the fine structures disperse with  $k$  and some of them cross the Fermi level. We found that our results are in consistent with the band calculations of Ref. 2.

## References

- 1) T. Terashima et al., Jpn. J. App. Phys. 27, L91 (1988).
- 2) L.F. Mattheiss and D.R. Hamann, Solid State Commun. 63, 395 (1987); S. Massidda et al., Phys. Lett. A 122, 198 & 203 (1987).

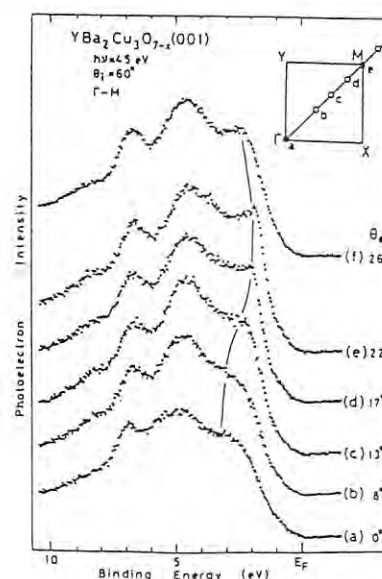


Fig. 1

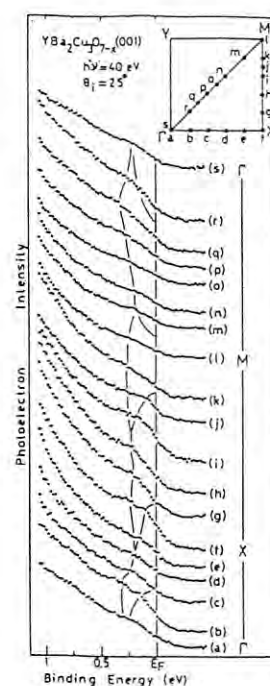


Fig. 2

## AN ATTEMPT AT PATTERN DEMAGNIFICATION BY ASYMMETRIC BRAGG REFLECTION

Shigeo SUZUKI, Jun-ichi NISHINO, Mitsuaki MORIGAMI, Mitsuaki HARADA,  
Shingo TERAOKA, Shun-ichi KOBAYASHI, Shuji FUJIWARA, Kazuhiro KANEDA,  
Takashi GOTO, Ryu SHIMIZU, Hideki MAEZAWA\* and Masami ANDO\*

Tsukuba Research Center, Sanyo Electric, Co. Ltd.  
Koyadai, Tsukuba-shi, Ibaraki 305

\*Photon Factory, National Laboratory for High Energy Physics  
Oho, Tsukuba-shi, Ibaraki 305

### Introduction

For X-rays in the energy region of a few keV, there is no material which acts as a refractive lens. Therefore 1 to 1 proximity printing technique has been studied in X-ray lithography. In this report we propose a new method of pattern demagnification in submicron scale using an asymmetric Bragg reflection of monochromatic X-rays<sup>1</sup> and show some experimental results.

### Experimental

Our method needs highly parallel, bright and monochromatic X-rays. We used X-rays from the undulator. X-ray beam emitted from the undulator was monochromatized by a double crystal monochromator of Si(111). The wavelength dispersion obtained by this monochromator was  $\Delta\lambda/\lambda < 10^{-3}$ . A mask was set in the incident beam. The reduction mirror and the second crystal of the monochromator were set in the (+,+) arrangement to restrict the range of wavelength and the beam divergence.

We have chosen wavelength  $\lambda = 3.5\text{\AA}$ , the offset angle  $\alpha = 22^\circ$  and 111 reflection ( $\theta = 34^\circ$ ). Then the reduction ratio  $n$  is 0.25. The distance from the resist film to the mask along the path of the X-ray beam was about 5mm.

A mask pattern used is a set of line and space whose width are  $5\mu\text{m}$ ,  $4\mu\text{m}$ ,  $3\mu\text{m}$  and  $2\mu\text{m}$  parallel to X and Y directions. A focused ion beam system and lift off technique was applied to prepare such mask patterns. The absorber was Au of  $8300\text{\AA}$  thick supported on SiN membrane and the expected contrast was 13 for  $\lambda = 3.5\text{\AA}$ .

Resist films used in this experiment were positive type EBR-9 (TORAY). Sensitivity of EBR-9

is about 10 times higher than that of PMMA in X-ray region for the same developing condition. The thickness of the resist film was  $2500\text{\AA}$ .

### Results and Discussion

The pattern was reduced only in one direction. Fig.2 shows optical photograph of the replicated image. A pattern size was reduced to 1/4 of original size only in vertical direction. Exposure was about  $100\sim 130\text{mA}\cdot\text{hours}$ . A scanning electron micrograph of the replicated image is shown in Fig.3. Line and space patterns whose width are  $5, 4, 3, 2\mu\text{m}$  were reduced to  $1.25, 1, 0.75, 0.5\mu\text{m}$  respectively. The first three replicated patterns were successfully resolved, but the resolution for a half micron pattern was not high enough in this experiment due to Fresnel diffraction from the mask and beam divergence.

There are some fringes at the end of the replicated lines, but there are no fringes parallel to replicated lines. Some X-rays diverge in various direction after passing through the mask pattern. But the Bragg condition of a perfect crystal is very strict, and the crystal accepts X-rays only within a very narrow angular range. The component which deviated in vertical direction can not be reflected by mirror. This phenomenon was confirmed by the similar experiment for  $n=1$  (offset angle =  $0^\circ$ ) and the calculation of Fresnel diffraction<sup>2</sup>.

If this procedure is repeated successively in two directions, two dimensional reduction will be realized.

This work was performed as a joint work between KEK-PF and SANYO Electric Co.Ltd.

### Reference

- <sup>1</sup>S. Suzuki et al. PF Activity Report #5, 312(1987)
- <sup>2</sup>J. Nishino et al. Rev. Sci. Instrument, To be published

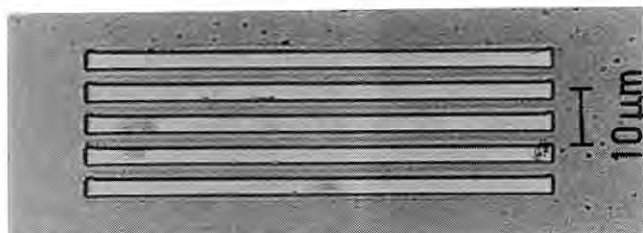


Fig. 1 The mask pattern ( $3\mu\text{m}$  L/s).

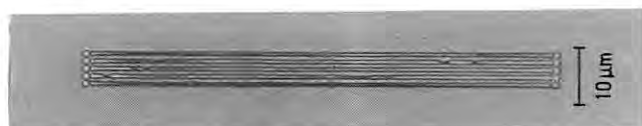
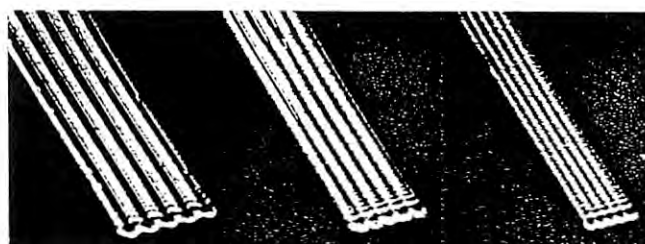


Fig. 2 The replicated image.



(a)  $4 \rightarrow 1\mu\text{m}$  (b)  $3 \rightarrow 0.75\mu\text{m}$  (c)  $2 \rightarrow 0.5\mu\text{m}$   
Fig. 3 Scanning electron micrographs of the replicated image.



OPTICAL CONSTANTS FOR COATED THIN FILMS IN THE SOFT X-RAY REGION  
 Naoto KIHARA, Hiroshi NAGATA, Nobuyuki NAKAGIRI and Hisao FUJISAKI  
 Yoshida Nano-Mechanism Project, JRDC  
 Nishi-ohi, Shinagawa-ku, Tokyo 140  
 Tsuneaki MIYAHARA  
 Photon Factory, National Laboratory for High Energy Physics  
 Oho-machi, Ibaraki 305

### Introduction

We determined optical constants for Ti, V and Ni thin films in the 2-4.5nm wavelength region, from the use of reflectance measurements.

Sample preparation in this region requires us to overlay the sample material with a stable protective film to prevent surface oxidization.

The 5-nm thickness of the protective carbon was found to be suitable to determine the optical constants of test materials and not to cause significant errors in those derived optical constants.

In this report, we present the obtained optical constants.

### Experiments and Results

Thin film materials of Ti, V and Ni were deposited onto 3-mm thick optically-polished glass (BK7) using an rf-sputtering apparatus. The protective carbon of 5-nm thick was deposited just after the 400nm deposition of the test material.

Reflectance measurements were done at beam line 11A with S-polarized 2-4.5nm radiation, filtered with Cu, Ag and C to reduce the higher-ordered diffraction for 2-3nm, 3-4nm and 4.5nm, respectively. Reflection data were taken at more than 30 angles of incident X-rays for each wavelength until the reflectance decreased to  $10^{-4}$  which corresponds to the S/N limit of a detector.

Our theoretical optical coating model<sup>1)</sup> includes Debye-Waller factors in the Fresnel coefficients of each interface to account for reflectance loss due to coherent surface roughness scattering.<sup>2)</sup> To estimate the model parameters corresponding to our experiment, we employed the least-squares method with 8 parameters.

The derived values of parameters are presented with the optical constants (solid line for real part, broken line for imaginary part respectively) calculated using the data of Henke et al.<sup>3)</sup> and bulk densities in Fig (a)-(c). In the figures the symbols  $\circ$  and  $\diamond$  denote  $\delta$  ( $=1-n$ ) and  $k$  for the test materials, and the symbols  $\bullet$  and  $\blacklozenge$  denote  $\delta$  ( $=1-n$ ) and  $k$  for the protective carbon, respectively.

### References

- 1) M. Born and E. Wolf, Principles of Optics (Pergamon, Oxford, 1980), p323
- 2) D.L. Windt, W.C. Cash, Jr., M. Scott, P. Arendt, B. Newnam, R.F. Fisher, A.B. Swartzlander, P.Z. Takacs and J.M. Pinneo, Appl.Opt. 27, 279(1988)
- 3) B.L. Henke, P. Lee, T.J. Tanaka, R.L. Shimabukuro and B.K. Fujikawa, AIP Conf. Pro. 75, 340(1981)

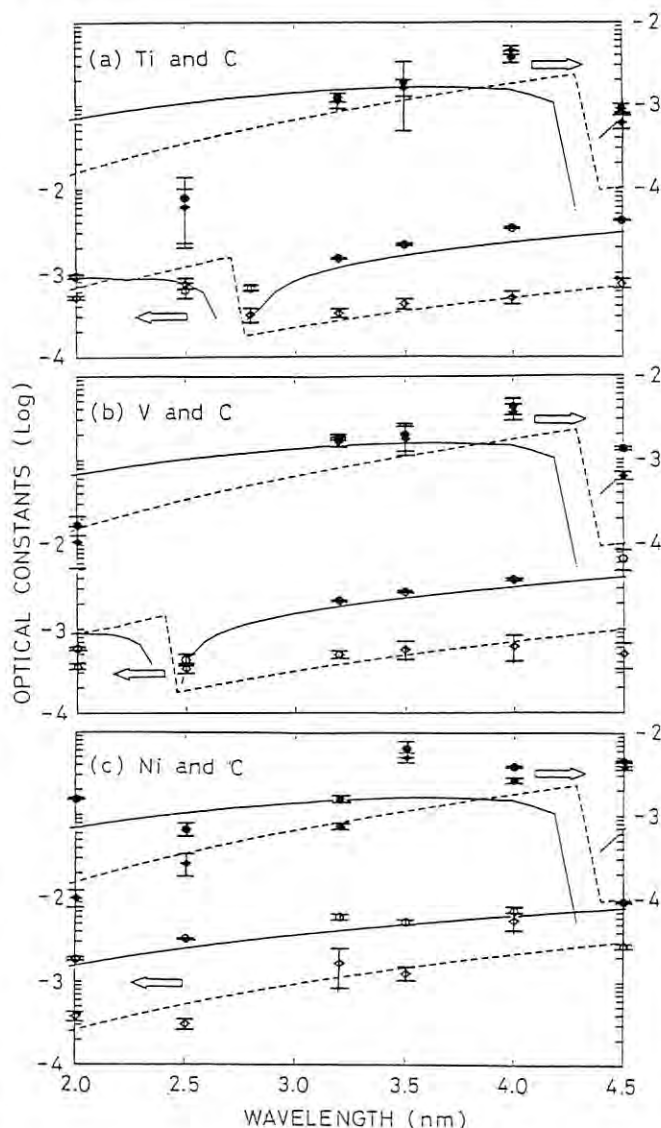


Fig.(a)-(c)  
 Optical constants as a function of  
 soft X-ray for (a) C/Ti, (b) C/V,  
 (c) C/Ni



## PHOTOCHEMICAL ETCHING OF GaAs AT LOW TEMPERATURE USING SYNCHROTRON RADIATION

Shingo TERAKADO, Jun-ichi NISHINO, Mitsuaki MORIGAMI,  
Mitsuaki HARADA, Shigeo SUZUKI and Kenichiro TANAKA\*

SANYO Tsukuba Research Center, 2-1 Koyadai, Tsukuba, Ibaraki 305

\*Photon Factory, National Laboratory for High Energy Physics, 1-1 Oho, Tsukuba, Ibaraki 305

### Introduction

The photochemical etching by synchrotron radiation (SR) is expected to be one of the most promising technique, because gases used in such etching process have large absorption cross sections in the vacuum UV (VUV) region. The gases excited by the VUV are immediately decomposed or ionized and begin to react with the substrate.

### Experimental

Experiments were carried out in the beam line BL-12A at the photon factory. The wave length region used in the experiment was longer than 105nm, because a lithium fluoride (LiF) window was set into the entrance of the reaction chamber. The LiF window was used to protect the high vacuum of the beam line from the gases in the reaction chamber. The base pressure of the reaction chamber was  $\sim 1.0 \times 10^{-6}$  Torr. Two kinds of gases were used in the experiment. One was 10%  $\text{Cl}_2$  reactive gas diluted with Ar, the other was pure Ar gas which was used for the protection of the LiF window. The total pressure in the reaction chamber was controlled at 0.6 Torr by a needle valve in the gas inlet lines. In that condition, the partial pressure of  $\text{Cl}_2$  was kept at 0.1 Torr. The temperature of Si-doped GaAs substrate was kept at  $-50^\circ\text{C}$  by controlling the flow rate of the liquid nitrogen. The substrate was set perpendicularly to the radiation beam.

### Results and Discussion

It has been shown in the previous experiment that the etching occurred on both the irradiated and the non-irradiated regions when the temperature of the substrate was above room temperature<sup>1)</sup>. It has been considered that  $\text{Cl}_2$  gas excited in gas-phase caused spontaneously the reaction everywhere on the substrate. In this experiment, we tried to set the substrate temperature to  $-50^\circ\text{C}$ . It is expected that the etching reaction on the non-irradiated region is greatly reduced by cooling the substrate, because in general this reaction has some activation energy and the reaction probability decreases with lowering the temperature of the substrate. The surface profiles of GaAs etched at  $-50^\circ\text{C}$  with  $\text{Cl}_2$  (0.1 Torr) are shown in Fig. 1. SR dose (etching time  $\times$  storage ring current) under this condition was  $\sim 40,000 \text{ min} \times \text{mA}$ . The surface profile of the non-irradiated region is shown in Fig. 1 (a) and that of the irradiated region is shown in Fig. 1 (b). It was found from Fig. 1 (a) that etching reaction by the excitation in gas-phase was scarcely observed on the non-irradiated region. On the contrary, as shown in Fig. 1 (b), the etching reaction of the irradiated region was

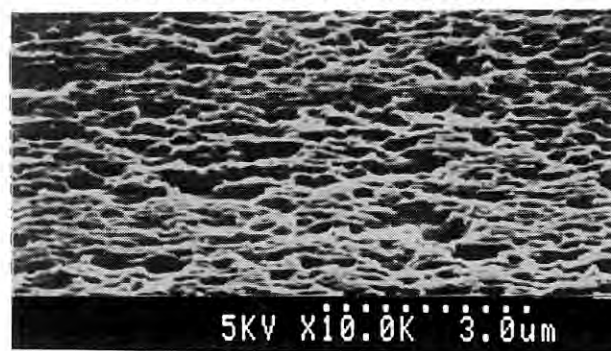
remarkable. This result indicates that the etching reaction is enhanced on the irradiated surface even at the low substrate temperature. The irradiated region shows rough surface (Fig. 1 (b)) probably due to the fact that the GaAs substrate was covered partially by oxide layer or something other deposited film. The boundary region between the irradiated and the non-irradiated regions shows diffused profile (Fig. 2) possibly due to diffraction effect at the photo mask or excitation in the gas-phase. As the irradiated region can be selectively etched, cooling of the substrate will become a most important candidate for a resist-less method.

### References

- 1) S. Terakado, M. Nakao, A. Mizukami, K. Tanaka and J. Chikawa, PF. Activity Rpt. #5, 305 (1987)



(a) The non-irradiated region



(b) The irradiated region

Fig. 1. GaAs surface etched at  $-50^\circ\text{C}$  by photochemical etching with  $\text{Cl}_2$  gas.

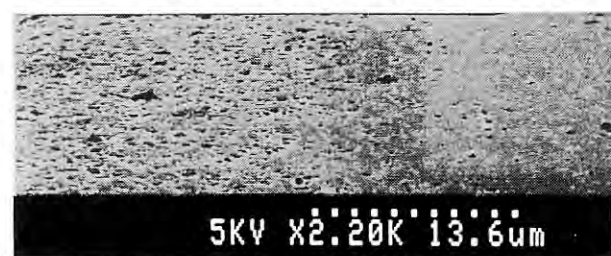


Fig. 2. The boundary between the irradiated and the non-irradiated regions.

## Synchrotron Radiation Excited Deposition of Silicon Film

Yasuo NARA, Yoshihiro SUGITA, Masaki OKUNO, Takashi ITO, Hiroo KATO\* and Ken-ichiro TANAKA\*

FUJITSU Laboratories LTD.

10-1 Morinosato Wakamiya, Atsugi City, Kanagawa, 243-01.

\*Photon Factory, National Laboratory for High Energy Physics.

1-1 Oho, Tsukuba City, Ibaraki, 305.

### Introduction

Synchrotron radiation is a promising light source for deposition and etching of semiconductor material.<sup>1)</sup> Vacuum ultra-violet(VUV) light involved in the synchrotron radiation can effectively excite the inner core energy level of source gas and decompose the source gas to produce radicals and ions that can not be obtained by using conventional light source such as Hg lamp.

In this paper, we will report the synchrotron radiation excited deposition of silicon films on the SiO<sub>2</sub> substrate by using SiH<sub>4</sub> gas and a result of a direct pattern transfer experiment.

### Results and discussion

We used the beam-line BL-12C, which has a multilayer mirror with 21 layers of Rh-Si films as a VUV monochromator and a differential pumping system.

First of all, we measured the spectra from the multilayer mirror. Energies of photo-electron from Ne gas were investigated by cylindrical mirror analyzer. By varying the incident angle from 39° to 47°, VUV light with peak energy of 83-97eV and HWFM value of 10eV is obtained.

The differential pumping system enables us to obtain more than 1 Torr at reaction chamber without any window material.

Silicon film deposition experiment under VUV light irradiation was performed at the condition of SiH<sub>4</sub> gas (5% diluted in He) of 1 Torr and substrate temperature of 500°C. Irradiation time was 1 hour. Incident angle of multilayer mirror was fixed at 47°. By using this incident angle, center photon energy of 97eV is available. A Ni mesh with 80x80 micron open area (100 micron pitch) was set about 1 mm above the substrate in order to monitor the effect of VUV light irradiation and to realize the selective film deposition on the substrate.

Figure 1 shows the micro-scopic photograph of the substrate surface. The mesh pattern is clearly transferred to the substrate surface. But the thickness difference between irradiated area(open area of mesh) and non-

irradiated area(shadow area of mesh) was too small to measure by stylus thickness measurement.

We have analyzed the top surface of the sample by Auger electron spectroscopy. The results show that much more metallic silicon signal is observed at the non-irradiated area than at the irradiated area. This means that the deposition of silicon film occurs mainly at the non-irradiated area. Direct irradiation of synchrotron radiation to the substrate surface seems to prevent photo-dissociated species(radicals and ions) from adsorbing on the substrate surface. Radicals and ions generated in the vapor phase drift towards the non-irradiated area and causes film deposition.

These reactions are not observed by the conventional photo-excited processes and are probably due to the activation of the surface reaction by the irradiation of high energy photon beam. Use of such a reaction to semiconductor micro-fabrication process can be expected as a new approach because control of the surface reactions is becoming important.

1) T. Urisu and H. Kyuragi, J. Vac. Sci. Tech., B(5), p.1436, 1987.

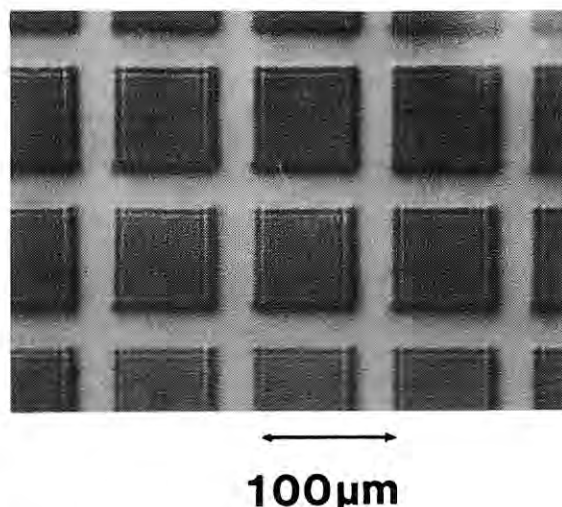


Fig.1 Micro-scopic photograph of substrate surface.

## RADIATION DAMAGE IN SILICON NITRIDE X-RAY LITHOGRAPHY MASK

Ichiro MORI, Masaru HORI, Yukiko KIKUCHI, Soichi NADAHARA, Masamitsu ITOH,  
Haruki KOMANO and Ken-ichiro TANAKA\*

ULSI Research Center, Toshiba Corporation

1 Komukai-Toshiba-cho, Saiwai-ku, Kawasaki 210, Japan

\*Photon Factory, National Laboratory for High Energy Physics  
1-1 Oho, Tsukuba 305, Japan

### Introduction

X-ray lithography using synchrotron radiation (SR) is a promising technology for finer microfabrication of VLSI with less than  $0.25\ \mu\text{m}$  feature sizes.<sup>1)</sup> The X-ray lithography mask is a key component in insuring the success of this technology. The recent investigation<sup>2)</sup> revealed that radiation damage effects in a BN:H mask, such as a geometrical distortion, were due to a modification in bonding configurations of the hydrogen. The purpose of this study was to evaluate the extent of radiation damage effects in silicon nitride (SiN) mask membranes prepared by a low pressure chemical vapor deposition (LPCVD).

### Experimental

The SiN films were deposited on Si substrates in a conventional LPCVD reactor using  $\text{SiH}_2\text{Cl}_2$  and  $\text{NH}_3$  as reactant gases at a total pressure of 40 Pa, at a temperature of  $850^\circ\text{C}$  and at a  $\text{SiH}_2\text{Cl}_2/\text{NH}_3$  ratio of 5. The film thickness was  $1.5\ \mu\text{m}$ . A typical stress value was  $2.5 \times 10^9\ \text{dyne/cm}^2$ .

The SR spectrum was selected so that its peak would be at 8 Å by using a SiC plane mirror with a grazing incidence of  $1^\circ$ . The exposure was performed continuously for 5 hours at a specimen chamber with a vacuum ranging from  $1 \times 10^{-5}$  to  $2 \times 10^{-6}$  Pa. The calculated cumulative absorbed dose for a  $1.5\ \mu\text{m}$  thick SiN film was  $4.3 \times 10^6\ \text{J/cm}^2$ .

### Results and discussion

The irradiated area of the SiN membrane was colored slightly in brown. Optical transmission decreased a few % for the irradiated area compared to an unirradiated one. In order to clarify the cause of coloration, ESCA analysis was performed on the irradiated and unirradiated area of the same film. The atomic ratios of O/N and Si/N were 1.4 and 1.3, respectively, and these values were not changed by irradiation. However, the C/N ratio increased from 0.78 to 4.3 by irradiation. These facts imply that a carbon film was formed on the irradiated area. The film thickness was too thin to be measured by a stylus method.

The geometrical distortions of the membrane were evaluated by measuring the pattern displacement of a regular array of crosses patterned onto a  $20 \times 20\ \text{mm}^2$  field before and after irradiation using an XY interferometric measuring system (Nikon 2I). The pattern displacements along Y-direction are shown in Fig.1. There was a relaxation in the membrane area corresponding to the irradiated area and this caused pattern displacement of  $0.1\ \mu\text{m}$ . According to a one-dimensional spring model, this value corresponded to a change in stress of  $7 \times 10^7\ \text{dyne/cm}^2$ .

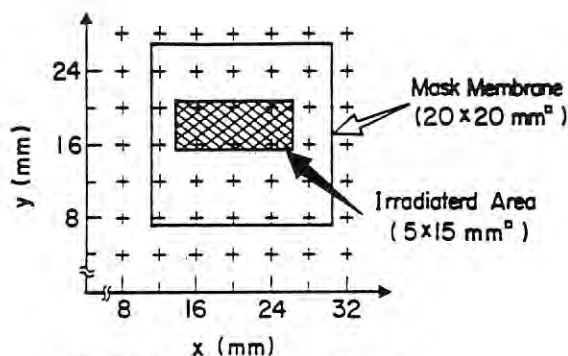
FTIR analysis showed that the SiN film did not

contain hydrogen bonds and no change in the atomic composition was caused by irradiation. A cross-sectional TEM photograph showed that any defects and voids, of which sizes were several 10 Å, were not induced in the film by irradiation.

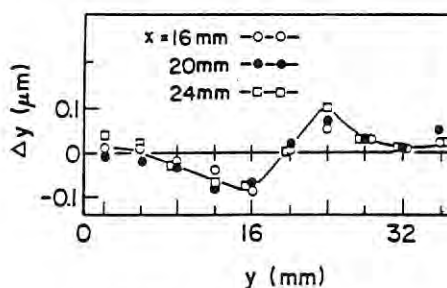
ESR analysis demonstrated that the dangling bond concentration increased about 3 times by irradiation for the film of which tensile stress was  $2.5 \times 10^9\ \text{dyne/cm}^2$  and a g-value was 2.004, which was attributed to the Si-N dangling bond. These facts indicate that the Si-N bonded structure was broken by irradiation. It is well known that the tensile stress varies with the atomic ratio of Si/N.<sup>3)</sup> In this study, the Si/N ratio was not changed by irradiation. Therefore, the breaking of Si-N bonded structure caused a slight displacement of atomic position, which corresponded to the change in tensile stress for the irradiated films.

### References

- 1) A.Heuberger, J.Vac.Sci.Technol.B, Vol.6, No.1, 107 (1988)
- 2) W.A.Jhonson et al., J.Vac.Sci.Technol.B, Vol.5, No.1, 257 (1987)
- 3) E.A.Irene, J.Electronic Materials, Vol.5, 237 (1976)



(a) Configuration of cross marks on SiN mask.



(b) Pattern displacements along y direction.

Fig.1. Geometrical distortions of SiN membrane.



# REALE TIME SURFACE ANALYSIS WITH SHYNSHROTRON RADIATION PHOTOEMISSION SPECTROSCOPY

Yasuko YAMADA MARUO, Masaharu OSHIMA, and Tomoaki KAWAMURA

NTT Applied Electronics Laboratories, Midoricho, Musashino, Tokyo 180

## Introduction

Real time surface sensitive analysis with synchrotron radiation photoemission spectroscopy (SRPES) is for the first time attempted to analyze the initial growth stage of thin films. Since solid surface are sensitive, it is difficult to keep the clean solid surface in the vacuum chamber with the heating system. Although real time SRPES was applied to the gas phase analysis, it has not been used for the solid surface analysis because of the reason mentioned above. In this work, real time SRPES analysis was done by using a K-cell cooling system.

## Experimental

The experiments were carried out at the Photon Factory BL-1A beam line. To obtain the good depth resolution (0.5 nm), radiation was tuned to a photon energy of about 130 eV. An ultrahigh vacuum system containing a sample, a photoelectron detector, and a K-cell was used as shown in Fig. 1. The samples were  $\text{CaF}_2/\text{GaAs}(100)$  system. Photoelectrons were detected at the same time when  $\text{CaF}_2$  was grown with the MBE method. The pressure in the chamber was maintained  $10^{-9}$  torr even during the  $\text{CaF}_2$  growth by using a K-cell cooling system. Each SRPES spectra were measured with in 0.5 min.

## Results and Discussion

Real time photoemission spectra were measured for Ga3d, As3d, Ca3p, and F2s. The changes in photoelectron spectra from Ga3d and As3d core levels are shown in Figs. 2 and 3. Both Ca3p and F2s core levels in SRPES were not clearly detected because of small quantity of  $\text{CaF}_2$  and small ionization cross sections. In Figs. 2 and 3, the both peak positions shift toward lower binding energy. These shifts are considered to be due to the evaporation of Ga oxide and elemental As from the GaAs substrate surfaces with  $\text{CaF}_2$  growth. Ga oxide comes from GaAs oxidation during substrate heating procedure. When substrates were heated, the pressure once up to  $10^{-7}$  Torr.

In the present work, when the GaAs substrates were used, it was found that As evaporation from GaAs substrates was very serious. However, we could check the possibility of real time SRPES analysis for the first time. We believe this method can give the important information about the initial growth stage of thin films by selecting suitable substrates and films.

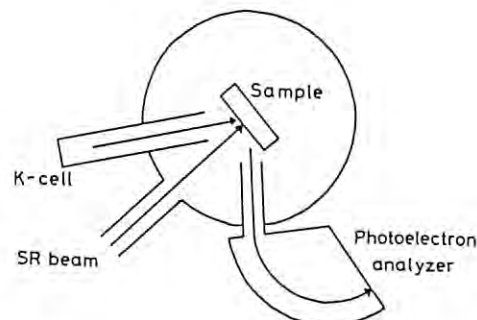


Fig. 1. Experimental apparatus for real time SRPES analysis.

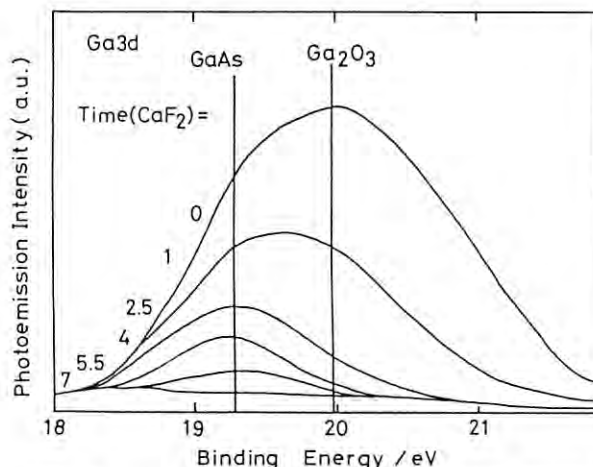


Fig. 2. The change of photoelectron spectra from Ga3d core level with  $\text{CaF}_2$  growth time.

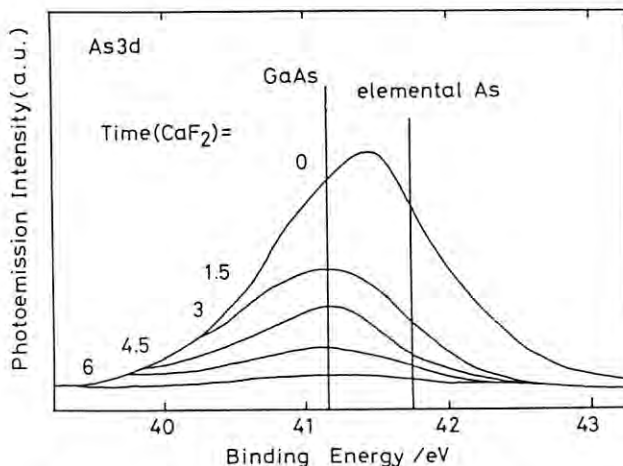


Fig. 3. The change of photoelectron spectra from As3d core level with  $\text{CaF}_2$  growth time.



SRPES AND RHEED STUDIES FOR THE  $\text{CaF}_2/\text{GaAs}(001)$  INTERFACE

Yasuko YAMADA MARUO, Masaharu OSHIMA, Takao WAHO\*, and Tomoaki KAWAMURA

NTT Applied Electronics Laboratories, Midoricho, Musashino-shi, Tokyo 180

\*NTT LSI Laboratories, Morinosato Wakamiya, Atsugi, Kanagawa 243-01

Introduction

$\text{CaF}_2$  is a good insulator. Its cubic fluorite structure makes it good candidate for epitaxy on zincblende GaAs substrates. To determine the dependence of bonding properties on substrate temperature, surface sensitive analysis with synchrotron radiation photoemission spectroscopy (SRPES) is performed for MBE-grown  $\text{CaF}_2$  films on GaAs(001) substrates. MBE-grown samples were used for the first time for SRPES analysis, because interfacial bonding properties are sensitive to surface structure and surface preparation methods. We measured RHEED pattern changes during  $\text{CaF}_2$  growth, then the differences in the bonding properties studied by SRPES were related to the RHEED pattern.

Experimental

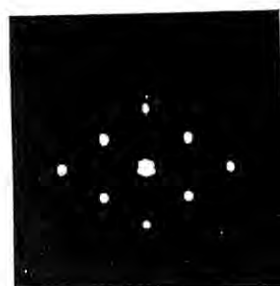
The experiments were carried out at the Photon Factory BL-1A beam line. To obtain the good depth resolution (0.5 nm), radiation was tuned to a photon energy of about 130 eV. The samples were grown by MBE. At first, GaAs was homoepitaxially grown on GaAs(001) substrates, then  $\text{CaF}_2$  films were grown on (2x4) As-stabilized GaAs(001) substrates. Substrate temperature were 580°C (high) and 420°C (low).

Results and Discussion

Figure 1 shows RHEED pattern obtained from the  $\text{CaF}_2/\text{GaAs}(001)$  sample with high and low substrate temperatures. At the high substrate temperature, the RHEED pattern changes from (a)-stage to (b)-stage by further  $\text{CaF}_2$  growth<sup>1)</sup>. The differences between Ca3p photoemission spectra from (a) and (b) stages are shown in Fig. 2. There are three binding states. Considering the values of chemical shifts, Ca atoms in Ca-1 state can be regarded as the Ca atoms which bonds to As atoms on GaAs substrate. The Ca-2 state corresponds to the Ca atoms which exit at the  $\text{CaF}_2/\text{GaAs}$  interface, and Ca-3 state corresponds to the Ca atoms in  $\text{CaF}_2$ . In the high substrate temperature case, the main state is Ca-1, indicating that there are Ca atoms with almost no-neighboring F atoms at the  $\text{CaF}_2/\text{GaAs}$  interface as a result of the  $\text{CaF}_2$  dissociation reaction. Since the RHEED pattern in (a)-stage is obtained only in the high substrate temperature case, these Ca atoms with almost no-neighboring F atoms can be related to this reconstructed pattern. In the low substrate temperature case, the main state was Ca-3. Therefore  $\text{CaF}_2$  does not dissociate and  $\text{CaF}_2$  grows directly on GaAs(001) substrates without the intermediate layer.



(a)



(b)

Fig. 1. RHEED patterns in the initial stage of  $\text{CaF}_2$  heteroepitaxy at 580°C (a) and 420°C (b) on GaAs(001) substrate. Incident electron energy is 13 keV in the  $[1\bar{1}0]$  direction.

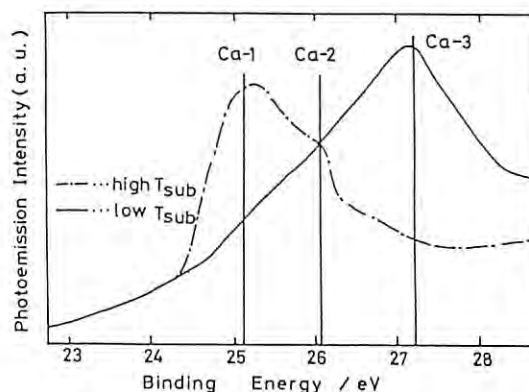


Fig. 2. Differences between photoelectron spectra from Ca3p core level with substrate temperature at the  $\text{CaF}_2/\text{GaAs}(001)$  interface.

1) Y. YAMADA, M. OSHIMA, T. WAHO, and T. KAWAMURA: to be published in Jpn. J. Appl. Phys.

BONDING PROPERTIES AT THE  $\text{CaF}_2/\text{GaAs}(111)$  INTERFACE

Yasuko YAMADA MARUO, Masaharu OSHIMA, Takao WAHO\*, and Tomoaki KAWAMURA

NTT Applied Electronics Laboratories, Midorocho, Musasino-shi, Tokyo 180

\*NTT LSI Laboratories, Morinosato Wakamiya, Atsugi, Kanagawa 243-01

Introduction

Calcium fluoride is an insulator which is lattice matched with GaAs to a high degree. These properties make  $\text{CaF}_2$  a technologically important material since it can be grown on GaAs as an epitaxial insulator. In this study, this system was studied using photoemission spectroscopy with synchrotron radiation to understand the bonding properties at the  $\text{CaF}_2/\text{GaAs}(111)$  interface.

Experimental

The experiments were carried out at the Photon Factory BL-1A beam line. To obtain the good depth resolution (0.5 nm), radiation was tuned to a photon energy of about 114 eV. N-type GaAs(111)B substrates were used. The in situ cleaning method of 3 keV Ar ion bombardment followed by 500 C annealing was adopted. The  $\text{CaF}_2$  was grown with the MBE method at a typical substrate temperature of 500 C. After samples were prepared in the MBE growth chamber, they were transferred in situ to the analysis chamber, where photoemission experiments were performed.

Results and Discussion

Photoemission spectra were measured for Ga3d, As3d, Ca3p, F2s, and valence band levels. The changes in photoelectron spectra from Ca3p with F2s core levels are shown in Fig. 1. In Ca3p, two binding states are found, Ca-1 and Ca-2. The Ca-1 binding state dominates the initial growth stage, and the Ca-2 binding state becomes dominant as the  $\text{CaF}_2$  thickness increases. From the time dependence of Ca-1 peak and Ca-2 peak appearance, and comparison with Ca3p peak position of standard  $\text{CaF}_2$  sample, the Ca-2 binding state is considered the Ca state of  $\text{CaF}_2$ , and Ca-1 binding state is regarded as an interfacial state. F2s also shows two

binding states, F-1 and F-2. For the same reason as the Ca3p case, the F-2 binding state is considered the F state in  $\text{CaF}_2$ , and the F-1 binding state is concluded to be an interfacial state.

From the peak synthesis results<sup>1)</sup>, an interfacial model is proposed in Fig. 2. Although component ratio Ca/F is 1/1, the interface is abrupt and  $\text{CaF}_2$  grows in layer growth mode.

1) Y. YAMADA, M. OSHIMA, T. WAHO, T. KAWAMURA, S. MAEYAMA, and T. MIYAHARA: Jpn. J. Appl. Phys. 27(1988)L1196.

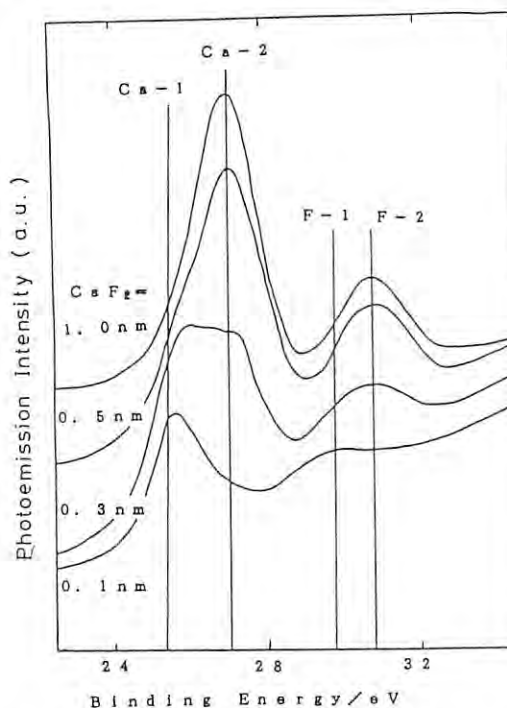


Fig. 1. The change of photoelectron spectra from Ca3p and F2s core levels with  $\text{CaF}_2$  thickness at the  $\text{CaF}_2/\text{GaAs}(111)$  interface.

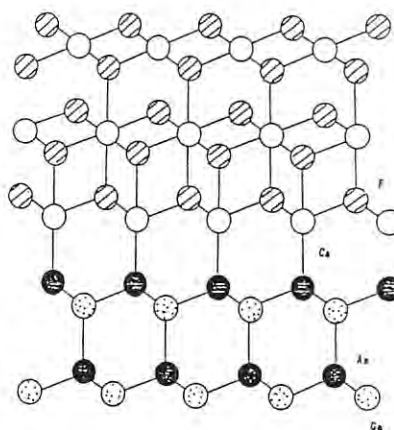


Fig. 2. Structural model for the  $\text{CaF}_2/\text{GaAs}(111)$  interface.

## FIRST OBSERVATION OF SYNCHROTRON RADIATION POST-IONIZATION EFFECT

Masaharu OSHIMA, Tomoaki KAWAMURA, Tetsuya MARUO and Yoshikazu HOMMA  
NTT Applied Electronics Laboratories, Musashino, Tokyo 180, JAPAN

### 1. Introduction

Various efforts<sup>1)</sup> have been devoted by the use of intense laser, plasma and electron irradiation to enhance secondary ion emission yield for more sensitive and more accurate compositional analysis with SIMS. In this study, synchrotron radiation has been successfully used for the first time for that purpose.

### 2. Experimental

Experiments were carried out at BL-1A of the Photon Factory by using the Multi-technique surface analysis system. In situ ion etching was performed using a differentially-pumped Ar<sup>+</sup> ion gun with 4.5 keV energy and 0.045  $\mu$ A ion current. The beam size was 3mm  $\phi$ . The zeroth order SR light from a Au-coated grating with  $\alpha$  of 83° was irradiated on the sample surface. Samples were GaAs, ZnSe, SiC, Al<sub>2</sub>O<sub>3</sub>, Ga, Si and Al. Secondary ions were detected with a quadrupole mass spectrometer with  $M/\Delta M$  of 300.

### 3. Results and discussion

When the SR was irradiated just onto the Ar-ion sputtered area of the GaAs sample, Ga<sup>+</sup> and As<sup>+</sup> secondary ion intensities decreased. The same tendency was observed in cases of other samples.

So, we moved the sample back and forth in order not to shine the SR directly onto the sputtered area. When the experiment set-up was like in Fig.1, a sharp increase was obtained for the GaAs sample. Figure 2 shows the Ga<sup>+</sup> mass spectra with and without SR. The mass spectra were measured in both cases of the lowest ring current just before electron injection and the highest ring current just after injection. A very clear SR irradiation effect on Ga<sup>+</sup> ion increase

which depends on the photon flux was observed. Up to about 80% increase of secondary ions can be attributed to the photoionization of sputtered neutrals, that is the post-ionization effect by SR irradiation just above the sample surface. This enhancement effect was also seen in cases of Al, Ga, and Si. However, when the SR was irradiated onto the insulating Al<sub>2</sub>O<sub>3</sub> surface, no secondary ions were detected, which is probably because of the positive charging of the insulator surface.

The dependence of the secondary ion intensity on the geometry between the SR irradiated area and the sputtered area was measured by changing the sample position in Y-axis. As shown in Fig.3, a sharp increase in the ratio of  $I(\text{SR})/I(\text{no SR})$  was obtained only when the SR went through just above the surface. On the contrary, when the SR shined the sputtered area, the ratio decreased drastically.

In conclusion, we observed the post-ionization phenomena of sputtered neutrals by SR irradiation which also implies a possibility of application to ion beam deposition processes.

### References

- 1) W.Reuter, Secondary Ion Mass Spectrometry SIMS V ed. A.Benninghoven et al. (Spring-Verlag, Berlin 1986) pp.94-102.

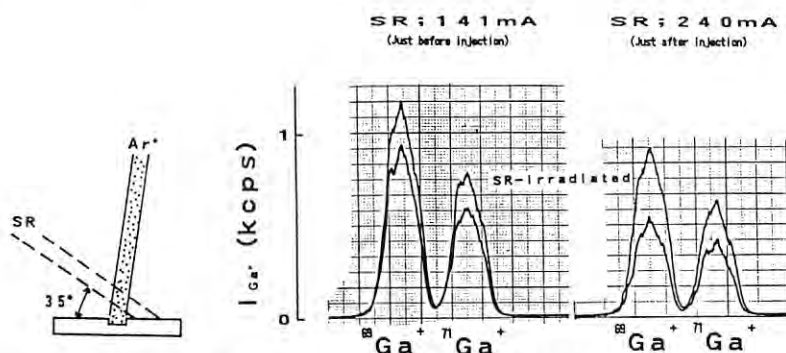


Fig.1 Configuration of experimental set-up.

Fig.2 Post-ionization effect by SR irradiation on the GaAs sample for the highest and lowest ring current cases. SR shined just above the surface, not on the surface.

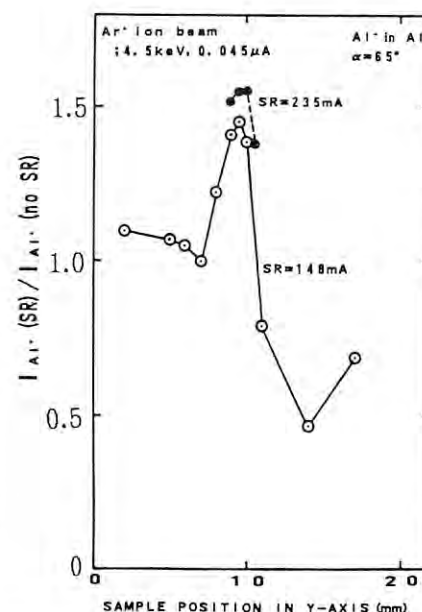


Fig.3 Dependence of SR post-ionization effect on the SR to sputtered area configuration. The sample was an Al metal.

SRPES ANALYSIS OF INTERFACE REACTIONS BETWEEN Si AND  $\text{YBa}_2\text{Cu}_3\text{O}_y$ 

Masaharu OSHIMA, Yasuko YAMADA, Tomoaki KAWAMURA, Satoshi MAEYAMA, and Tsuneaki MIYAHARA\*

NTT Applied Electronics Laboratories, Musashino, Tokyo 180, Japan

\* Photon Factory, KEK, Tsukuba, Ibaraki 305, Japan

### 1. Introduction

Interface characteristics between junction materials and oxide superconductors were analyzed with synchrotron radiation photoemission spectroscopy. This study can provide fundamental insights concerning the Josephson junction formation process with amorphous Si as well as the initial growth process of  $\text{YBa}_2\text{Cu}_3\text{O}_y$  thin films on Si substrates.

### 2. Experimental

Experiments were carried out at BL-1A of the Photon Factory. Samples were  $\text{YBa}_2\text{Cu}_3\text{O}_y$  ceramics ( $T_c=90\text{K}$ ). Surfaces were cleaned by scraping with a special file in UHV. Si was deposited on clean surfaces at room temperature at a deposition rate of about  $0.3\text{\AA}/\text{sec}$  measured by a quartz thickness monitor.

### 3. Results and discussion

The resonance photoemission with the incident photon energy of  $76\text{ eV}$  was found to be useful to evaluate whether or not the uppermost surface region is in the  $\text{Cu}^{++}$  state. If not, the superconducting state is possibly broken in the surface region.

The Josephson junction formation process was investigated using "amorphous Si deposition on a clean  $\text{YBa}_2\text{Cu}_3\text{O}_y$  surface". The resonance peak practically disappeared, when only about 1 monolayer of Si was deposited, as shown in Fig.1. At the first stage of Si deposition, a shoulder peak emerged at about  $1.2\text{ eV}$  higher binding energy than the  $\text{Cu}3d-02p$  hybrid band. This peak can be attributed to Si-O bonding. The drastic change in the resonance peak at the interface was also observed on Si-deposited  $\text{CuO}$  surfaces. Thus, Si

atoms play a role of withdrawing the oxygen from the Cu-O bondings to form the more energetically favorable Si-O bonds. An analogous phenomenon was observed by Hill et al.<sup>1)</sup> in the case of  $\text{Fe}/\text{LaSrCuO}$ .

Figure 2 shows  $\text{Si}2p$  spectra from Si-deposited  $\text{YBa}_2\text{Cu}_3\text{O}_y$  surfaces. Si was in the  $\text{SiO}$  state at the interface even in the first stage of Si deposition. At the second stage, a small Si peak in the metallic state also appeared in addition to the  $\text{SiO}$  peak. Then the metallic peak became dominant. The XPS  $\text{Cu}2p$  peak was found to change from the  $\text{CuO}$  state to the metallic state. Thus strong interfacial reactions take place even in the surface region detected by XPS. In other words, amorphous Si is not a good candidate for the junction material, because the XPS-detecting region which is deeper than the coherence length is not in the superconducting state, or even in the  $\text{Cu}^{++}$  state.

Judging from the XPS signal intensity change with Si deposition, the oxidation reaction of Si takes place only at the interface, and does not propagate into the whole Si layer. This is probably because the initially formed  $\text{SiO}$  layer might act as a protective layer against further reaction. These results imply that an appropriate thin oxide film is useful for junction formation, and that  $\text{YBa}_2\text{Cu}_3\text{O}_y$  film can be grown on Si substrates with the thin oxide film.

Based on these results, we constructed an interface formation model on rough  $\text{YBa}_2\text{Cu}_3\text{O}_y$  surfaces, as shown in Fig.3. A very strong reaction occurred even at the initial stage of Si deposition. Si was in the  $\text{SiO}$  state, and in the  $\text{YBa}_2\text{Cu}_3\text{O}_y$  surface region under  $\text{SiO}$ , Cu was reduced to the metallic state.

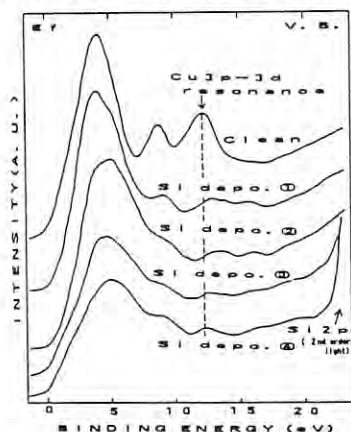


Fig.1 Valence band spectra of Si-covered  $\text{YBa}_2\text{Cu}_3\text{O}_y$  surfaces.  $h\nu=76\text{ eV}$ .

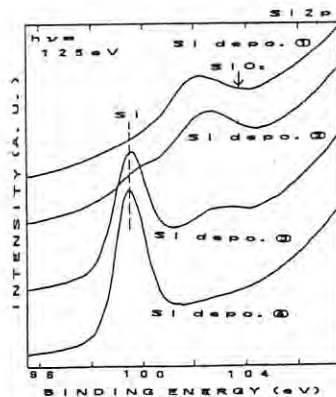


Fig.2  $\text{Si}2p$  spectra from Si-covered  $\text{YBa}_2\text{Cu}_3\text{O}_y$  surfaces.  $h\nu=125\text{ eV}$ .

### Reference

- 1) D.M.Hill, H.M.Meyer III, J.H.Weaver, B.Flander Meyer and D.W.Capone II, Phys. Rev., B36 (1987) 3979.

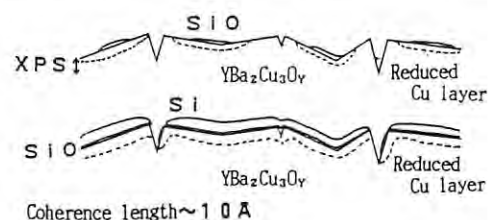


Fig.3 Si/  $\text{YBa}_2\text{Cu}_3\text{O}_y$  interface model.



# Synchrotron Radiation Photoelectron Spectroscopy of Single Crystal Bi-Sr-Ca-CuO

Fumihiko Maeda, Tomoaki Kawamura, Masaharu Oshima,  
Yoshikazu Hidaka\* and Akihiko Yamaji\*

NTT Applied Electronics Laboratories, Midoricho, Musashino, Tokyo, 180  
\*NTT Opto-Electronics Laboratories, 162 Tokai, Ibaraki, 319-11

## Introduction

Superconductivity has been reported for Bi-Sr-Ca-Cu-O system<sup>1)</sup>. This system has some different natures from the other high-Tc superconductor oxides,  $\text{YBa}_2\text{Cu}_3\text{O}_x$  and  $\text{La}_{2-x}\text{Sr}_x\text{CuO}_{4-d}$ . For example, this material shows a marked cleavage and can easily be separated into layers. So, this system would be expected to have different valence band structure. This report is the study for the valence band structure by the photoelectron spectroscopy with synchrotron radiation.

## Experimental

Photoelectron measurements have been carried out at BL-1A of the Photon Factory. The samples were  $\text{Bi}_2(\text{Ca}_{0.37}, \text{Sr}_{0.63})_3\text{Cu}_2\text{O}_x$  single crystals with almost single phase of low-Tc phase ( $T_c=80\text{K}$ ). The clean surface was obtained by cleaving with an adhesive tape in UHV. The energy resolution of the spectrometer was 0.2eV-0.4eV depending on the photon energies of 35eV-120eV.

## Result and Discussion

Figure 1 shows photoelectron spectra of single crystal  $\text{Bi}_2(\text{Sr}, \text{Ca})_3\text{Cu}_2\text{O}_x$  in the binding energies from 0eV to 20eV with various photon energies. Bands A and B are valence band and B has three structures. In this system, the valence band is consist of Cu-3d, O-2p and Bi-6p at least.  $B_2$  becomes larger with increasing photon energy. The photoionization cross section of Cu-3d is comparably larger than Bi-6p and O-2p. Therefore  $B_2$  was assigned Cu-3d band. The origin of the other structure is not clear now. The structure C is extrinsic because this structure depends on the sample. We didn't find this structure on the other samples. Owing to the difference of the photoionization cross section, the structure E was assigned Sr-4p and the structure F was assigned Ca-3p.

As to the structure D, we assigned this structure to be valence band satellite due to the two d-hole bound state<sup>2)</sup>. We paid much attention to the photon energy 76eV, a little above Cu-3p core threshold. There occurs resonance photoemission in copper. Utilizing this state and Cu-3d main band, we can obtain intra-atomic Coulomb energy between d electrons (Udd). The state D is located at 12eV (this is little smaller than  $\text{YBa}_2\text{Cu}_3\text{O}_x$ ) and  $B_2$  is located 3.6eV. So, Udd is about 5eV, which is almost the same as that in YBCO. But it's not clear this value is enough large or small valence band widths.

Figure 2 shows the photoelectron spectra around the Fermi level. There is a clear structure, A, at the Fermi level. Especially, in case of the photon energy 40eV and 76eV, Fermi edge was observed. But in the photon energy 95eV and 117eV the structure on the Fermi level does not indicate cut-off feature. This indicate that the band across the Fermi level appeared the photoelectron spectra has relatively small cross section in high photon energy. Therefore we suggest this band is not due to Cu-3d. But the origin is not clear now.

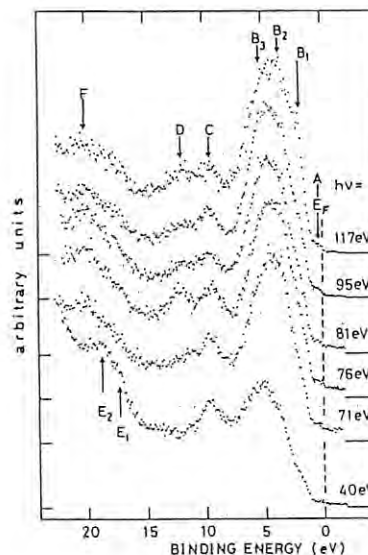


Fig.1 The photoelectron spectra of  $\text{Bi}_2(\text{Sr}, \text{Ca})_3\text{Cu}_2\text{O}_x$  with the photon energy from 40 to 117eV.

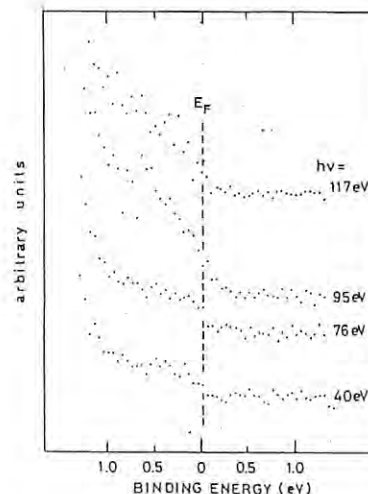


Fig.2 The photoelectron spectra of  $\text{Bi}_2(\text{Sr}, \text{Ca})_3\text{Cu}_2\text{O}_x$  near Fermi level measured at the photon energy of 40, 76, 95, and 117eV.

## References

- 1) H. Maeda, Y. Tanaka, M. Fukutomi and T. Asano  
Jpn. J. Appl. Phys. 27(1988)L209
- 2) T. Takahashi et al. Phys. Rev. B  
14(1987)5686

SRPES STUDIES OF HIGH  $T_c$  SUPERCONDUCTOR SURFACES AND INTERFACES FOR CONTACT FORMATION

Masaharu OSHIMA, Yasuko YAMADA, Tomoaki KAWAMURA, Satoshi MAEYAMA,  
 Kouji HOHKAWA\*, Yasuo TAZOH\*, and Tsuneaki MIYAHARA\*\*  
 NTT Applied Electronics Laboratories, Musashino, Tokyo 180, Japan  
 \* NTT LSI Laboratories, Atsugi, Kanagawa 243-01, Japan  
 \*\*Photon Factory, KEK, Tsukuba, Ibaraki 305, Japan

### Introduction

To fabricate devices using recently developed high  $T_c$  superconducting materials, interface characteristics between contact metals and superconductors should be clearly understood. In this study, synchrotron radiation photoemission spectroscopy was used to evaluate superconductor surfaces and interfaces. Furthermore, a new surface processing technique to realize very low contact resistance was developed based on these SRPES experiments.

### Experimental

Experiments were carried out at BL-1A of the Photon Factory. Samples were  $\text{YBa}_2\text{Cu}_3\text{O}_x$  bulk materials ( $T_c=90\text{K}$ ) and  $\text{YBa}_2\text{Cu}_3\text{O}_x$  thin films ( $T_c=76\text{K}$ ). Surfaces were cleaned by scraping with a special file in UHV ( $10^{-10}$  Torr). Au was deposited on clean surfaces at room temperature.

### Results and discussion

When the incident photon energy was tuned to about 76 eV, a peak which appeared only on  $\text{Cu}^{++}$  ( $3d^9$  configuration) materials came up at a binding energy of about 12 eV on the clean  $\text{YBa}_2\text{Cu}_3\text{O}_x$  surface. This peak is regarded as a  $\text{Cu}3p-3d$  resonance photoemission. When the clean surface was Ar-sputtered, this peak disappeared completely and  $\text{Cu}^{++}$  was reduced to the metallic state.

On the other hand, O-sputtering was found to effectively clean the surface while maintaining the resonance peak as shown in Fig.1. Although XPS  $\text{O}1s$ ,  $\text{Y}3d$  and  $\text{Cu}2p$  peak remained unchanged after O-sputtering, only  $\text{Ba}4d$  peak showed a significant change as shown in Fig.2.

Next, Au/ $\text{YBa}_2\text{Cu}_3\text{O}_x$  interfaces were analyzed using this resonance photoemission technique for contact formation. Even though up to 30 Å of Au was deposited, the resonance peak was almost unchanged, as shown in Fig.3. This means that no interfacial reaction took place. Thus good contact properties may be obtained by this "O-sputtering and in situ Au deposition" process. In fact, contact resistance of  $5.5 \times 10^{-7} \Omega \text{cm}^2$  at 77K was obtained with the  $\text{YBa}_2\text{Cu}_3\text{O}_x$  film. This is the lowest ever reported. However, the I-V characteristics suggested that a semiconductor region still remains at the Au/ $\text{YBa}_2\text{Cu}_3\text{O}_x$  interface. This may be correlated to the change of the  $\text{Ba}4d$  chemical state.

In conclusion, a practical dry cleaning procedure was developed to obtain very low contact resistance by using the resonance photoemission technique.

### References

- 1) Y.Tazoh, K.Aikawa, K.Miyahara, K.Hohkawa, S. Miyazawa and M.Oshima, Applied Superconductivity Conference, 1988(Los Angeles)

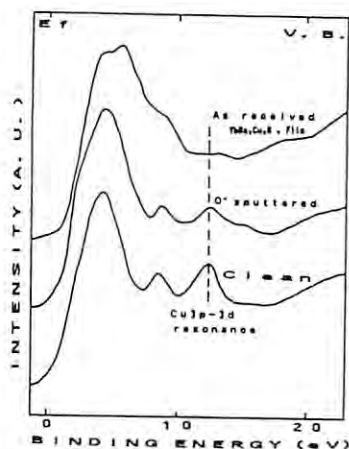


Fig.1 Valence band spectra of O-sputtered  $\text{YBa}_2\text{Cu}_3\text{O}_x$  thin films.  $h\nu=76$  eV.

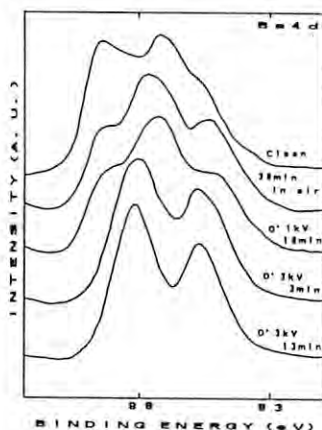


Fig.2 XPS  $\text{Ba}4d$  spectra from scraped and O-sputtered  $\text{YBa}_2\text{Cu}_3\text{O}_x$  surfaces.

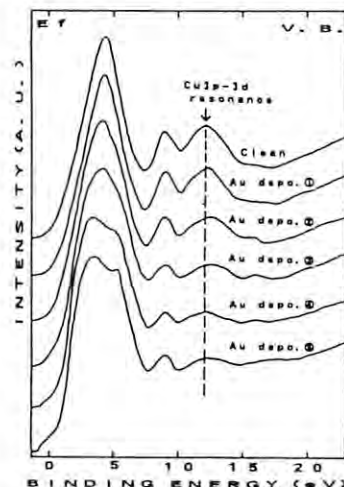


Fig.3 Valence band spectra of Au-covered  $\text{YBa}_2\text{Cu}_3\text{O}_x$  surfaces.

Reaction Mechanism Study with SR-Stimulated Etching of SiO<sub>2</sub>

Jun-ichi Takahashi, Yuichi Utsumi, and Tsuneo Urisu  
NTT LSI Laboratories, Atsugi-shi, Kanagawa 243-01, JAPAN

### Introduction

In recent years, several unique characteristics have appeared in SR excited semiconductor processes. In particular, unique etching selectivity between Si and SiO<sub>2</sub> etching was found.<sup>1)</sup> We have investigated detailed reaction mechanisms with SR-stimulated etching of SiO<sub>2</sub>.<sup>2)</sup>

### Results and Discussions

The apparatus was set in the beam line BL-1C. The incident beam was focused by a Pt coated toroidal mirror and wavelength was selected by varying incident angles for a pair of Pt coated plane mirrors. Reaction gas was 100% SF<sub>6</sub>.

The etching reaction was observed only in the SR irradiated area, as shown in Fig.1, indicating that a surface excitation mechanism is dominant.

The etching rate increased with increasing SF<sub>6</sub> pressure and gradually saturated at higher pressures, suggesting that the Langmuir-type adsorption process plays an important role in the reaction.<sup>2)</sup>

The dependence of the etching rates on the substrate temperature (Fig.2) indicates that the effective activation energy of the reaction is negative, as opposed to plasma etching cases, indicating that the etching reaction is induced by photoexcitations, and not by thermal effects.

The dependence of the reaction on exciting wavelength was studied by varying the incident angles for the plane mirrors. The results indicate that photons in 20 - 200 Å range are effective for the etching reaction, suggesting core or valence electron excitation of substrate Si atoms.

Referring to the fact that SiF<sub>4</sub> is a stable product in plasma etching, it is assumed that the etching proceeds through the SiF<sub>4</sub> desorption induced by the reaction between substrate Si and adsorbed F atoms.

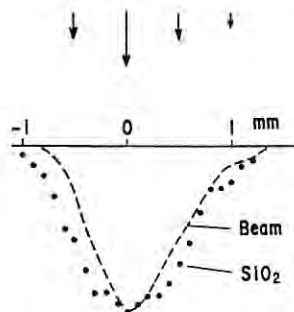
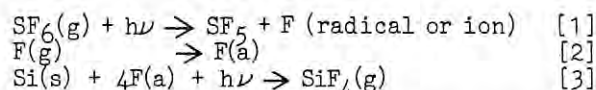


Fig.1 Beam profile and SiO<sub>2</sub> etching profile.

Based on these experimental results and considerations, we estimate the main reaction mechanism for the present etching as follows:<sup>2)</sup>



Here, (g), (a), and (s) indicate gas phase molecules, adsorbed atoms, and substrate atoms, respectively. By using a mass spectroscopic study reaction [1] was confirmed to be a main process in SR photolysis of SF<sub>6</sub>. Reaction [3] is a main etching process, that is, surface reaction between photoexcited Si atoms and adsorbed F atoms resulting in SiF<sub>4</sub> desorption.

### References

- 1) T.Urisu and H.Kyuragi. J.Vac.Sci.& Technol. B5 (1987) 1436.
- 2) J.Takahashi, Y.Utsumi, and T.Urisu. Extended Abstracts of the 20th Conference on Solid State Devices and Materials, Tokyo, 1988, p.73.

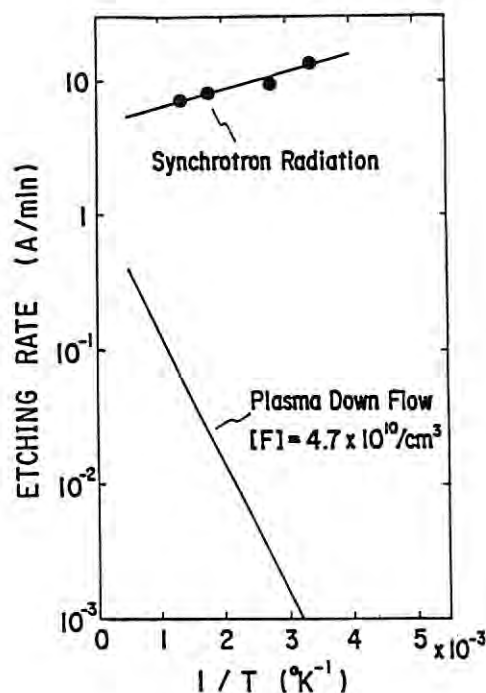


Fig.2 Dependence of the etching rate on substrate temperature. Ring current is normalized to 100 mA. Plasma down flow etching rate estimated for similar gas phase F atom concentration [F] to the present SR etching case, is given as a comparison.

## PHOTOREMISSION AND XANES STUDIES OF Si(100) SURFACE OXIDATION

Masatoshi NAKAZAWA, Hideo SEKIYAMA and Susumu KAWASE

Central Research Laboratory, Hitachi Ltd., Kokubunji, Tokyo 185

Introduction

An understanding of the properties of the SiO<sub>2</sub>/Si interface is very important for device technology. Thus, the oxidation of a Si(100) surface has been extensively studied to further understand its properties. High resolution ( $\Delta E < 0.3$  eV) photoemission spectroscopy and XANES with synchrotron radiation were used.

Experimental

The experiments were carried out with soft X-ray monochromatized by a grazing incidence monochromator at the BL-8A at the Photon Factory.<sup>1)</sup> A double-pass-type CMA (cylindrical mirror analyzer) was used for analyzing photoelectrons. The total energy resolution of the photoemission analysis system, including the electron analyzer and the monochromator, was evaluated from the Fermi edge of gold to be higher than 0.3 eV (see Fig. 1). The oxidation of a Si(100) surface was studied in-situ using this analysis system. Sample cleaning and oxygen exposure were performed in the spectrometer chamber with the base pressure less than  $5 \times 10^{-8}$  Pa. A clean surface was obtained by repeated Ar ion sputtering and annealing.

Results and Discussion

Si 2p photoelectron spectra for the Si(100) surface exposed to an oxygen pressure of  $1 \times 10^{-4}$  Pa at different temperatures are shown in Fig. 2. The spectra were measured at  $h\nu = 130$  eV. The oxidation of the clean surface was carried out by successive oxygen exposures, as indicated in Fig. 2.

Three intermediary components are formed at the initial oxidation stage ( $20\text{--}10^3$  L oxygen exposures at room temperature). Those Si 2p 3/2 peak energy shifts from the bulk component are 0.9, 1.8, and 2.7 eV, respectively. These are attributed to Si atoms bonded to 1, 2, and 3 oxygen atoms (Si<sup>1+</sup>, Si<sup>2+</sup>, and Si<sup>3+</sup>), as suggested by Hollinger and Himpsel.<sup>2)</sup>

Surface oxidation proceeds much faster when the surface is heated to 300–400 °C during oxygen exposure. In this case, the intensity of the SiO<sub>2</sub> peak increases with the increase in the intensities of intermediary oxidation states. A SiO<sub>2</sub> thin layer is formed by further oxidation ( $10^4$  L oxygen exposure) at 700 °C.

The spectra in Fig. 2 were decomposed to estimate the intensities of different intermediary components. The results exhibit that the proportion of Si<sup>3+</sup> state at the SiO<sub>2</sub>/Si interface increases with the formation of the 0–1 nm thick SiO<sub>2</sub> layer. However, in the oxidation phase where a SiO<sub>2</sub> layer is formed over 1 nm, the three intermediary states at the interface are distributed with ratios of Si<sup>3+</sup>:Si<sup>2+</sup>:Si<sup>1+</sup> = 7:2.5:1.

Oxygen K-XANES spectra for the Si(100) surface exposed to oxygen are shown in Fig. 3.

The intensity of peak B increases with the surface oxidation. In addition, the peak energy becomes higher. These results indicate that, as the oxidation at the surface proceeds, the effective coordination number of Si atoms around an oxygen atom increases and/or the Si–O bond becomes stronger.

References

- 1) Photon Factory Activity Report 3, 59 (1984/85).
- 2) G. Hollinger and F. J. Himpsel, Appl. Phys. Lett. 44, 93 (1984).

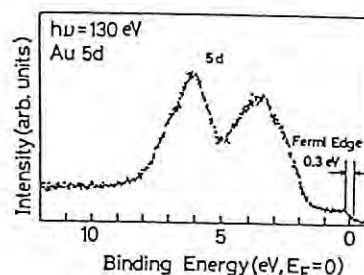


Fig. 1. Valence band spectrum of Au.

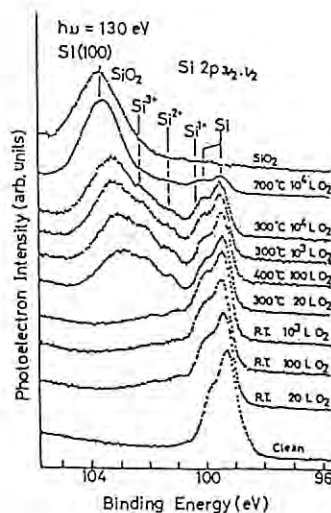


Fig. 2. Si 2p photoelectron spectra for the Si(100) surface exposed to oxygen.

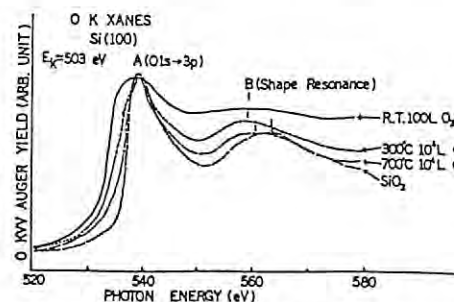


Fig. 3. Oxygen K-XANES spectra.



## ANGLE-RESOLVED PHOTOEMISSION STUDY OF THE Pd(110) CLEAN SURFACE

Kazutoshi YAGI, Kazuyuki HIGASHIYAMA, Satoru YAMAZAKI, Hiroyuki YANASHIMA, Hitoshi OHNUKI, Hirohito FUKUTANI and Hiroo KATO\*

Institute of Physics, University of Tsukuba, Tsukuba, Ibaraki 305

\*Photon Factory, National Laboratory for High Energy Physics, Tsukuba, Ibaraki 305

The electronic structure of palladium has been an interesting subject in experimental and theoretical point of views, because of its catalytic reactivity. In this work, we have made the polarization-dependent angle-resolved photoemission study of the Pd(110) clean surface. Especially, the normal emission study has been made in the photon energy range of 23~88 eV. Most of the features in the spectra can be understood in the bulk direct transition model. The energy band dispersion along the  $\Gamma$ -K-X direction in the B.Z. has been determined, by assuming the possible free-electron final state with the adjusted inner potential.

The data were taken with the CDM monochromator and 150° spherical analyzer at BL-11D station. The Pd(110) surface was cleaned in situ by several cycles of Ar<sup>+</sup>-sputtering and annealing (~600°C). The cleanliness of surface was judged by AES and LEED. The normal emission spectra were easily degraded in about an hour even in the low 10<sup>-10</sup> Torr range, presumably because of the adsorption of hydrogen contained in the ambient vacuum. Therefore, the sample was cleaned by mild annealings (~250°C) every one hour during measurements. The plane of polarization was chosen to be either parallel to the (001) or the (110) mirror plane, i.e., A<sub>||</sub> along the <110> or the <001> direction, respectively.

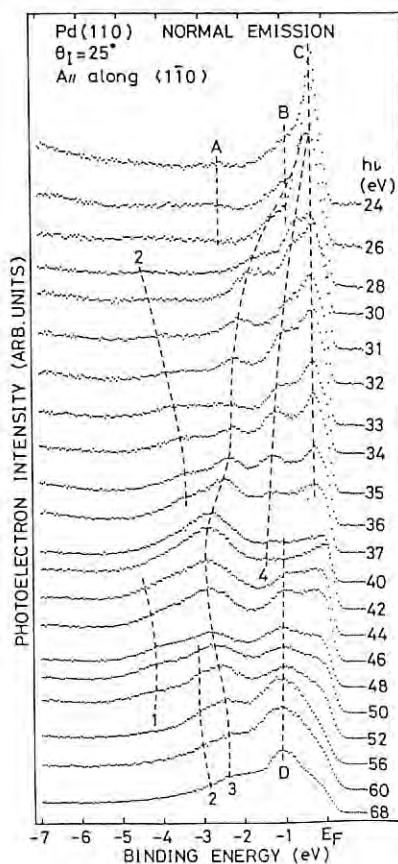


Fig.1

Figure 1 shows the change of normal emission spectra of the Pd(110) clean surface as a function of photon energy with A<sub>||</sub> along the <110> direction. Four dispersive bands (labelled 1~4) and four structures with no dispersion (labelled A~D) are observed in the spectra. Since the spin-orbit interaction in palladium is weak (~0.3 eV), the hybridization of bands will be small except for the band-crossing region. So, we can expect the single-group character of the observed bands. By using the ordinary dipole selection rule, we assign the bands 1, 2, 3 and 4 in fig.1 to the  $\Sigma_1$ ,  $\Sigma_1$ ,  $\Sigma_3$  and  $\Sigma_4$  bands, respectively. In order to convert the spectra in fig.1, as well as the ones in other experimental geometries (not shown) into E<sub>f</sub> vs k<sub>||</sub> relation, we assume a free-electron final band with an adjusted inner potential. The resulted dispersions are compared in fig.2 with the RAPW calculation by Christensen. In general, the agreement between experiment and theory is good for the bands 1~4 except for the zone boundary, in which the assumed free-electron final state is incorrect. As for the structures A~D, there are no counterparts in the theory. We tentatively assign the weak structures A and B to the Umklapp structures which originate from the  $\Sigma_1$  bands at the  $\Gamma$  point. A constant initial energy spectrum for the structure C shows two maxima at hν=24 and 32 eV. We ascribe the first maximum to the direct transition from the X<sub>2</sub> critical point to the s-like  $\Sigma_1$  final band, and the second one to the direct transition from the X<sub>2</sub> point to the flat f-like  $\Sigma_1$  band. A coupling to the evanescent final state may also occur because the adsorption of oxygen and hydrogen on the Pd(110) surface caused the drastic reduction in intensity of the structure C. There is no explanation to the structure D at present.

In conclusion, we have measured the normal photoemission spectra of the Pd(110) clean surface and analyzed within the framework of the one-electron band picture. Good agreement between experiment and theory has been obtained as for the  $\Sigma_1$ ,  $\Sigma_3$  and  $\Sigma_4$  bands although some features in the spectra remain unsolved.

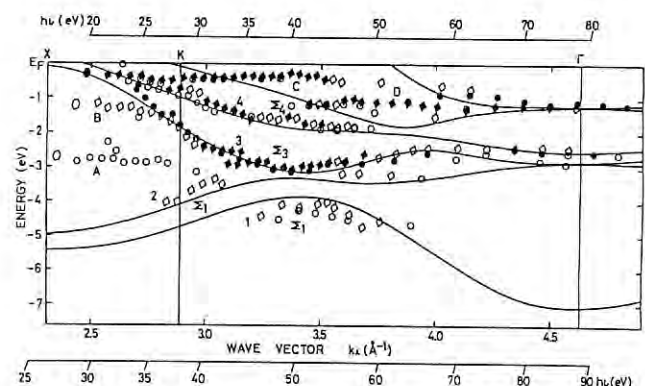


Fig.2

# AUTHOR INDEX

A			
Abe, O.	30	Endo, H.	53,205
Abe, S.	164,166	Endo, O.	162,205,206
Abe, T.	104	Endo, S.	152
Abe, Y.	256	Endoh, M.	119
Aiura, Y.	248,251,252,253,266	Endoh, Y.	210
Akai, T.	82,83	Endow, T.	260
Akimoto, K.	219,220,221	Esaki, N.	23
Akisada, M.	169,224	Eyring, E.M.	195
Akiyama, M.	121		
Amemiya, Y.	109,111,118,119,120,121,122		F
	123,124,125,126,127,128,129	Fuchizaki, K.	204
	130,131,132,133,134,167,189	Fujieda, S.	220
	190,194,195,208,213	Fujihira, Y.	208
Ando, H.	43,44	Fujii, K.	217,218
Ando, M.	149,150,151,152,183,189,190	Fujii, Y.	160
	191,194,195,198,211,224	Fujii, Y.	167,208
	227,267	Fujimoto, K.	105
Annaka, S.	187	Fujimoto, T.	56,73
Anno, I.	169	Fujisaki, H.	268
Anzai, H.	193	Fujisawa, T.	113
Aoki, H.	52,68	Fujita, K.	18,22
Aoki, S.	137,138,144,227	Fujita, N.	131
Aoshima, A.	185	Fujiwara, S.	267
Arai, A.	235,236	Fukagawa, H.	224
Arai, H.	256	Fukamachi, T.	165
Arakawa, H.	132	Fukuda, K.	240
Arashi, H.	85	Fukuda, M.	96,98
Asakura, K.	16,29,40,41,42,49,50,65,69,70	Fukumoto, N.	159
	71,75	Fukunaga, T.	21,61
Asanuma, H.	42	Fukuoka, A.	36,56,73
Ashida, T.	140	Fukushima, T.	39
		Fukutani, H.	248,250,251,281
	B	Fukuyama, K.	104,116
Bamba N.	35,52,68	Funabashi, M.	74,241,242,243,244,245
Bando, K.	40	Funabiki, T.	31,51,72
Bando, Y.	266	Funaki, M.	209
Bohlen, K.von	100	Furusawa, Y.	90,91,96,98
		Furuya, M.	110
	C	Futemma, T.	248
Cao, J.	235,236		G
Chiba, H.	263	Gohshi, Y.	142,143,144,145,151
Chiba, R.	258,261,262	Goto, A.	193
Chikaishi, K.	213	Goto, M.	159
Cho, T.	137,138	Goto, T.	267
Claverie, P.	17	Gotoh, S.	76,77
			H
	D	Hachiya, S.	115
Domen, K.	50	Hagiya, K.	154,173
		Hama, Y.	115
	E	Hamanaka, T.	124,128,129
Edagawa, K.	25	Hamaya, N.	160,204
Edamatsu, K.	240	Hanada, S.	222
Edamoto, K.	251,252,253,254,255	Harada, H.	139
Edamura, T.	30	Harada, J.	161,172,222
Egawa, T.	186	Harada, M.	42
Ehara, K.	165	Harada, M.	267,269
Ejima, Y.	95	Hasegawa, K.	223
Emura, S.	81	Hasegawa, S.	224
		Hashimoto, S.	238
		Hashizume, H.	185,196
		Hashizume, H.	203
		Hatano, Y.	257,258,261,262
		Hatta, I.	121

Hayahara, R.	38	Inoue, T.	51, 72
Hayaishi, T.	231, 232, 233, 234, 237	Inoue, Y.	34
260		Inui, M.	53
Hayakawa, K.	165	Inukai, J.	16, 71
Hayakawa, S.	144, 148	Irie, T.	152
Hayase, S.	161	Irikura, M.	197
Hayashi, C.	147	Ishida, H.	249
Hayashi, S.	136	Ishigame, M.	85
Hibino, T.	58	Ishihama, A.	131
Hida, M.	33	Ishii, T.	148
Hidaka, O.	146	Ishii, Y.	196
Hidaka, Y.	277	Ishikawa, M.	148
Hieda, K.	90, 91, 93, 95, 96, 98, 114	Ishikawa, T.	171, 180, 186, 187, 188, 214
Higashi, Y.	211	Ishiwari, H.	77
Higashiyama, K.	281	Isoda, S.	135, 182
Higuchi, T.	63	Itikawa, Y.	237
Higuchi, Y.	105, 106	Ito, A.	92, 99
Hikita, T.	50	Ito, E.	203
Hiragi, Y.	23, 107, 108, 109, 135, 182	Ito, K.	259, 260, 263, 264
Hirai, M.	136	Ito, M.	190
Hirai, T.	136	Ito, T.	90, 91, 95, 96, 98
Hirano, K.	187	Ito, T.	270
Hirano, T.	37, 60	Ito, Y.	257, 258, 261
Hirano, T.	209	Ito, Y.	262
Hirata, K.	266	Itoh, F.	21, 61, 189
Hirata, M.	138	Itoh, K.	158
Hirobe, M.	63	Itoh, M.	271
Hirosawa, I.	210, 219, 220, 221	Itoh, Y.	237
Hirose, K.	219	Iwamoto, H.	126, 127, 128
Hirose, Y.	32	Iwamoto, Y.	52
Hisatsugu, T.	76, 77	Iwasa, I.	199
Hohkawa,	278	Iwasaki, H.	161, 176
Homma, Y.	275	Iwasawa, Y.	16, 29, 40, 41, 42, 49, 65, 69, 70, 71
Honda, K.	63, 159	75	
Hondoh, T.	193	Iwata, J.	217
Honma, S.	94	Izumi, F.	153
Hori, M.	271	Izumi, K.	187, 188
Horiuti, K.	120, 123	Izumi, Y.	41, 71
Hosaka, R.	224	Izumi, Y.	109, 178, 179
Hoshi, R.	193		
Hoshi, S.	50		K
Hoshino, H.	53		
Hoshiya, H.	197	Kagawa, N.	203
Hosokawa, S.	53	Kageyama, H.	59
Hu, Z.	65	Kageyama, Y.	83
Hyodo, K.	224, 227	Kagoshima, Y.	227
	I	Kaji, H.	184, 192
		Kajita, A.	133, 134
Ichikawa, M.	36, 56, 73	Kajiwara, K.	108, 135, 182
Igarashi, Y.	133, 134	Kakahi, T.	51
Iguchi, Y.	228	Kakuchi, M.	227
Iida, A.	94, 141, 142, 144, 145, 146, 147	Kameta, K.	257, 258, 261, 262
	148, 149, 150, 151, 152, 215	Kamigaki, K.	161, 164, 166
Iida, S.	200	Kamihata, K.	45
Iijima, K.	266	Kamijo, N.	59
Ikai, A.	132	Kamimatsuse, H.	154
Ikeda, T.	150, 183	Kamon, K.	33, 54
Imafuku, M.	212	Kamosaki, T.	257, 258
Imai, H.	149, 150, 183, 194, 195	Kanai, H.	20, 24
Imai, K.	153	Kanamaru, F.	34
Imai, M.	205, 206	Kanayama, S.	247
Imamura, Y.	96, 98	Kaneda, K.	267
Imura, T.	66, 67	Kaneko, T.	83
Inagawa, K.	147	Kaneko, T.	164, 166
Ino, H.	25	Kasaya, M.	256
Inoko, Y.	111, 112, 113	Kashiwase, Y.	171
Inoue, H.	135	Katakura, H.	249
		Kataoka, M.	107, 108, 109, 110, 111, 112, 113

	118,149,183	Komano, H.	271
Katayama, Y.	53	Komeda, T.	252,253,266
Kato, H.	248,249,250,251,252,253,254	Konaka, S.	186
	255,256,266,270,281	Kondoh, N.	18,22
Kato, K.	159,181	Kondoh, T.	137,138
Kato, M.	222	Konishi, H.	160
Kato, N.	147	Koshiba, S.	191,198
Kato, S.	121	Kosuge, K.	202
Katsube, Y.	106	Kosugi, N.	36,48,56,73
Katsui, A.	87,88,89	Koto, K.	34,81
Katsura, T.	195,203	Kouno, E.	217
Kawado, S.	214	Koyama, A.	38,149,150
Kawaguchi, A.	182	Koyano, I.	232,233,234
Kawai, S.	83	Koyano, T.	216
Kawamoto, Y.	62	Kubo, H.	259
Kawamura, H.	162	Kubota, M.	226
Kawamura, T.	165	Kudo, A.	50
Kawamura, T.	188,272,273,274,275	Kudo, E.	210
	276,277,278	Kunimori, K.	65
Kawase, R.	193	Kuno, K.	80
Kawase, S.	280	Kurahashi, M.	159
Kawase, Y.	217	Kurihara, H.	103
Kawashima, T.	37,60,94,142,153	Kuroda, H.	17,36,39,48,56,73,74,218,230
Kawata, H.	149,150,151,152,183,189,190		241,242,243,244,245
	191,194,195,196,198,200	Kuroda, Y.	35
	201,211	Kuroiwa, Y.	160,216
Kihara, H.	131,132,133,134	Kuwabara, R.	29,69
Kihara, K.	140	Kuwano, N.	26
Kihara, N.	268	Kuwasawa, Y.	38
Kikegawa, T.	162,202,203,204,206,208,225	Kyushiki, H.	132
Kikuchi, S.	92		
Kikuchi, Y.	271		M
Kikuta, S.	180,187,188,214		
Kim, E.	108,135,182	Maeda, F.	277
Kimoto, S.	57	Maeda, H.	23,33,35,52,54,59,68
Kimura, H.	235,236	Maeda, K.	264
Kimura, K.	133,134	Maeda, S.	17
Kimura, T.	36,56,73	Maehama, S.	254,255
Kimura, T.	83	Maekawa, T.	55
Kinjo, Y.	92	Maeyama, S.	86,87,88,89,276,278
Kino, T.	201	Maezawa, H.	92,137,138,227,228,259,265,267
Kishimoto, S.	161	Maezawa, H.	90,91,93,95,96,98,114
Kita, E.	216	Makida, S.	157
Kitajima, Y.	74,241,242,243,244,245	Makihara, H.	150,183
Kitano, T.	79	Mao, O.	189,190
Kitazume, T.	256	Marumo, F.	19,117,158
Kito, Y.	124	Maruo, T.	275
Klabunde, K.J.	20	Maruo, Y.Y.	272,273,274
Klauser, R.	226	Maruyama, H.	52,68
Kobayashi, K.	90,91,92,93,95,96,98,99,107	Maruyama, K.	53
	108,111,112,113,114,178	Maruyama, T.	266
	183,195	Mashiyama, H.	161
Kobayashi, S.	267	Masujima, T.	149,150,151,152,183,194,195
Kobayashi, T.	126,127,128	Matsubara, E.	163,168
Kobayashi, Y.	38	Matsubara, I.	119,120,122,123
Kobayashi, Y.	159	Matsubayashi, N.	48,246
Kogiso, M.	171	Matsuda, M.	210
Kohra, K.	147	Matsui, J.	79,210,219,220,221
Koide, T.	239	Matsui, M.	140
Koide, Y.	259	Matsumoto, N.	96,98
Koike, Y.	82,83	Matsumoto, T.	43,44,140
Koizumi, A.	35,52,68	Matsumoto, T.	260
Koizumi, H.	257,258	Matsumoto, Y.	79,220
Koizumi, M.	17,229	Matsumoto, Y.	220
Koizumi, T.	230,237	Matsumuro, A.	203
Kojima, I.	63,159	Matsuo, T.	178,179
Kojima, S.	214	Matsuo, T.	230,237
Kojima, T.	213	Matsuoka, S.	121



Matsushima, N. 178  
 Matsushita, T. 21, 38, 167, 208  
 Matsuyoshi, S. 249  
 Mazumder, M.K. 249  
 Metoki, N. 167  
 Minato, I. 196  
 Mino, M. 52, 68  
 Minoura, M. 171  
 Mitomi, O. 144  
 Mitsuhashi, T. 186  
 Mitsui, T. 128, 129  
 Mitsui, Y. 103  
 Mitsuishi, T. 256  
 Mitsuya, M. 240  
 Miura, H. 85  
 Miura, K. 82  
 Miyahara, T. 248, 256, 268, 276, 278  
 Miyake, Y. 178, 179  
 Miyamoto, N. 249  
 Miyane, Y. 202  
 Miyazaki, E. 254, 255  
 Miyoshi, N. 96, 98  
 Miyoshi, S. 138  
 Mizuide, T. 235, 236  
 Mizuki, J. 210, 219, 220, 221  
 Mizuno, K. 201  
 Mizutani, H. 31, 51, 72  
 Mochiki, K. 223  
 Mochizuki, A. 142  
 Mochizuki, Y. 220  
 Mori, I. 271  
 Mori, K. 228  
 Mori, M. 171  
 Mori, T. 90, 91  
 Morigami, M. 267, 269  
 Moriguchi, S. 135, 182  
 Morikawa, H. 19, 62, 117, 158  
 Morimoto, T. 35  
 Morimoto, Y. 105  
 Morinaga, M. 222  
 Morioka, Y. 231, 260  
 Morisada, I. 238, 240  
 Moriwaki, H. 35  
 Motoyama, T. 43, 44, 140  
 Mōri, N. 202  
 Mukoyama, T. 184, 192, 230  
 Munakata, N. 114  
 Murakami, E. 231  
 Murakami, Y. 58  
 Murakami, Y. 167  
 Muramatsu, Y. 265  
 Murata, T. 23  
 Murata, Y. 226  
 Murayama, C. 202  
 Murofushi, Y. 80  
 Muroga, Y. 109

# N

Nadahara, S. 271  
 Nagano, M. 218  
 Nagaoka, S. 232, 233, 234  
 Nagata, H. 268  
 Nagata, T. 209, 232, 233, 237  
 Nagoshi, C. 151  
 Nakae, H. 140  
 Nakagawa, A. 104, 106  
 Nakagawa, M. 186

Nakagiri, N. 268  
 Nakahara, H. 240  
 Nakahata, T. 185  
 Nakai, I. 37, 60, 94, 141, 142, 153  
 Nakaishi, M. 78  
 Nakajima, T. 162, 164, 165, 166, 169, 184, 192  
 199  
 Nakamura, E. 247  
 Nakamura, K. 103  
 Nakamura, N. 49  
 Nakamura, Y. 32  
 Nakanishi, H. 152  
 Nakano, A. 30  
 Nakano, K. 115  
 Nakano, S. 38  
 Nakasako, M. 107, 110, 118  
 Nakashima, A. 85  
 Nakayama, S. 235, 236  
 Nakazawa, M. 280  
 Namba, H. 17, 229  
 Namikawa, K. 228  
 Namioka, T. 235, 236, 263, 264  
 Nanao, S. 190, 191, 198  
 Nara, Y. 270  
 Nasu, H. 157  
 Nihei, Y. 247  
 Nishi, F. 165  
 Nishida, S. 125  
 Nishihata, Y. 161  
 Nishijima, A. 48, 246  
 Nishimura, K. 125  
 Nishimura, K. 224  
 Nishimura, Y. 24, 51, 72  
 Nishino, J. 267, 269  
 Nishino, N. 259  
 Nishitani, S. 170, 175  
 Nitani, S. 112  
 Nittono, O. 197  
 Niwa, M. 58  
 Niwano, M. 249  
 Noda, C. 224  
 Noda, Y. 33, 54  
 Nojima, S. 111  
 Nokawa, M. 249  
 Nomachi, I. 37, 60  
 Nomura, E. 217  
 Nomura, H. 213  
 Nomura, M. 18, 21, 22, 25, 28, 45, 46, 47, 53  
 137, 138, 149, 150  
 Noriki, S. 96, 98  
 Nukui, A. 155, 158

# O

Oda, K. 18, 22, 25  
 Oda, T. 108  
 Ogasawara, S. 39  
 Ogata, K. 30  
 Ogura, K. 33, 54  
 Ohba, T. 174  
 Ohgaki, M. 117  
 Ohishi, Y. 167, 208  
 Ohmachi, Y. 188  
 Ohmasa, M. 154  
 Ohno, K. 139  
 Ohnuki, H. 281  
 Ohshima, K. 161, 172, 216, 222  
 Ohsumi, K. 139, 153, 154, 155, 158, 159, 176

Ohta, M. 104  
Ohta, T. 57, 74, 238, 241, 242, 243, 244, 245  
246  
Ohtaki, M. 42  
Ohtani, E. 203  
Ohtsuka, Y. 27  
Ohya, N. 249  
Oikawa, T. 23  
Oka, Y. 52  
Okada, K. 130  
Okada, K. 217, 218  
Okajima, H. 172  
Okamoto, N. 180  
Okamura, S. 76, 77  
Oki, K. 26  
Okudera, H. 43, 44, 140  
Okuno, M. 43, 44, 140  
Okuno, M. 270  
Okuyama, K. 162  
Onchi, M. 252, 253, 266  
Onishi, T. 50  
Ono, T. 193  
Onodera, A. 203  
Onuki, T. 144  
Osaka, Y. 66, 67  
Oshima, M. 86, 87, 88, 89, 188, 272, 273, 274  
275, 276, 277, 278  
Otsuka, K. 174  
Owari, M. 247  
Oyanagi, H. 53  
Ozawa, H. 155, 158, 159  
Ozutsumi, K. 37, 60

R

Ryuta, J. 173

S

Saegusa, N. 216  
Saeki, Y. 119, 122  
Saigusa, S. 95  
Saito, J. 146  
Saito, S. 173  
Saito, T. 186  
Saito, Y. 26  
Saitoh, K. 147  
Saitoh, N. 143  
Sakai, J. 110  
Sakai, N. 189, 190  
Sakaki, H. 198  
Sakanaka, T. 118  
Sakasai, A. 259  
Sakata, O. 185, 196  
Sakisaka, Y. 251, 252, 253, 266  
Sakuma, H. 185  
Sakuma, T. 163, 168  
Sakurai, H. 23, 145, 151  
Sakurai, M. 21, 61  
Sakurai, Y. 190, 191, 198  
Salama, T.M. 64  
Sano, M. 58  
Sano, T. 149, 183  
Sano, Y. 108, 135  
Sasaki, M.S. 95  
Sasaki, S. 170, 171, 172, 173, 174, 175, 176  
212, 222  
Sato, H. 146

Sato, N. 84  
Sato, S. 239  
Sato, S. 250  
Sato, T. 48, 246  
Sato, Y. 232, 233, 234, 237, 263  
Satoh, E. 215  
Satoh, N. 111  
Satoh, Y. 116  
Satow, Y. 75, 86, 87, 88, 89, 117, 137  
Sawada, H. 176  
Sawamoto, H. 203  
Seidou, M. 124  
Seki, K. 238, 240  
Sekine, T. 192  
Sekine, T. 225  
Sekiuchi, T. 61  
Sekiyama, H. 280  
Shi, J. 52, 68  
Shiba, S. 162  
Shibata, H. 230  
Shibata, K. 18, 22  
Shidara, T. 239  
Shigemasa, E. 231, 232, 233, 234  
Shima, K. 230  
Shimada, H. 48, 246  
Shimizu, K. 52, 68  
Shimizu, R. 267  
Shimizu, S. 197  
Shimizu, Y. 19, 158  
Shimojou, N. 94  
Shimomura, O. 85, 162, 202, 203, 205, 206, 207  
208, 225  
Shimomura, S. 160  
Shin, S. 85  
Shingaki, N. 160  
Shingu, H. 170, 175  
Shinohara, K. 92, 99  
Shinsaka, K. 257, 258, 261, 262  
Shiotani, N. 189, 190  
Shiozaki, I. 152  
Shirai, M. 16, 40, 41, 69, 70  
Shirodani, I. 162  
Shiwaku, H. 149, 150, 151, 152, 183, 194, 195  
Soda, K. 23  
Sone, T. 24  
Sorensen, Y.S. 207  
Suematsu, H. 167  
Sugahara, H. 86  
Sugawa, T. 189  
Sugawara, H. 165  
Sugawara, H. 256  
Sugawara, T. 25  
Sugaya, H. 43, 44, 140  
Sugi, H. 126, 127, 128  
Sugie, T. 259  
Sugishima, T. 66, 67  
Sugita, Y. 200  
Sugita, Y. 270  
Sugitani, Y. 181  
Sugiyama, H. 197  
Sugiyama, K. 156, 163, 168  
Suito, K. 203  
Sumiyama, K. 32  
Susaki, J. 202  
Suzuki, H. 199  
Suzuki, K. 21, 61, 189  
Suzuki, K. 90  
Suzuki, K. 217

Suzuki, S. 252,253  
 Suzuki, S. 267,269  
 Suzuki, T. 143  
 Suzuki, T. 228  
 Suzuki, Y. 141  
 Suzuki, Y. 224

T

Tabira, Y. 19  
 Tagawa, H. 109  
 Taguchi, I. 209  
 Taguchi, M. 38  
 Taguchi, T. 76,77  
 Tajima, Y. 130  
 Takada, Y. 243  
 Takagi, Y. 212  
 Takahashi, H. 202  
 Takahashi, H. 223  
 Takahashi, J. 279  
 Takahashi, K. 104  
 Takahashi, M. 145,151  
 Takahashi, T. 180,214  
 Takakura, K. 93  
 Takakuwa, Y. 249  
 Takano, M. 31  
 Takaoka, H. 196  
 Takata, Y. 240,242  
 Takeda, H. 146  
 Takeda, T. 169  
 Takei, F. 117  
 Takemori, S. 120,123  
 Takemura, K. 32  
 Takemura, K. 208  
 Takenaka, A. 102  
 Takenaka, E. 224  
 Takenaka, H. 196  
 Takenaka, Y. 117  
 Takeno, H. 200  
 Takesue, N. 222  
 Takeuchi, H. 186  
 Takeuchi, H. 259  
 Takeuchi, Y. 103  
 Takizawa, Y. 237  
 Takyu, T. 215  
 Tamura, A. 165  
 Tamura, K. 53  
 Tan, B. J. 20  
 Tanabe, K. 64  
 Tanaka, H. 23  
 Tanaka, H. 125,128  
 Tanaka, H. 238,240  
 Tanaka, K. 17,239,257,258,259,260,261  
 262,269,270,271  
 Tanaka, K. 117,201  
 Tanaka, S. 203  
 Tanaka, T. 20,24,31,51,64,72  
 Tanaka, Y. 190,191  
 Tanaka, Y. 217  
 Taniguchi, M. 238,240  
 Tanno, M. 64  
 Tasaki, A. 216  
 Tawara, H. 230  
 Terakado, S. 267,269  
 Terashima, T. 266  
 Terauchi, H. 33,54,161  
 Togaya, M. 203  
 Tohji, K. 62,177

Tokunaga, F. 107,110,118  
 Tokushige, M. 108  
 Tokutomi, S. 110  
 Tomiki, T. 248  
 Tomita, A. 27  
 Tomita, I. 153  
 Tonuma, T. 230  
 Toshima, N. 42  
 Toyoda, K. 146  
 Toyoda, T. 149,150,152,183,194  
 Toyofuku, F. 224  
 Tsuburaya, K. 162  
 Tsuchiya, J. 82  
 Tsuda, O. 191,198  
 Tsuji, K. 162,205,206  
 Tsukihara, T. 104,116  
 Tsunetomo, K. 66,67  
 Tsuruta, H. 131,132,133,134  
 Tuneiki, O. 38

U

Uchijima, T. 65  
 Udagawa, Y. 177  
 Ueda, K. 169  
 Ueda, K. 232,233,234,263  
 Ueda, Y. 202  
 Ueki, T. 107,108,109,111,112,113,135  
 136,178,179  
 Ueyama, K. 17,229  
 Ukai, M. 257,258,261,262  
 Umazume, Y. 120,123  
 Umetani, K. 169  
 Umetani, Y. 62  
 Uno, R. 155,158,159  
 Urakawa, H. 108,135,182  
 Urisu, T. 279  
 Uruga, T. 129  
 Usami, K. 209  
 Usami, T. 238  
 Ushida, K. 171  
 Ushikubo, T. 82,83  
 Usuda, K. 211  
 Utsumi, W. 203  
 Utsumi, Y. 279  
 Uzu, S. 63

W

Wada, K. 83  
 Waho, T. 273,274  
 Wakabayashi, K. 124,125,126,127,128,129,132  
 Wakita, H. 26,28,45,46,47  
 Wakita, M. 178  
 Wang, E.-Z. 128  
 Wang, Z.-X. 133  
 Waseda, Y. 163,168  
 Watanabe, H. 79  
 Watanabe, M. 92  
 Watanabe, M. 120,123  
 Watanabe, Y. 191,198  
 Wittmann, H.G. 100

X

Xu, Q. 55

Y

Yagi, K. 281  
 Yagi, N. 119, 120, 122, 123  
 Yagi, T. 106  
 Yagi, T. 203, 207, 225  
 Yagishita, A. 228, 230, 231, 232, 233, 234, 237  
 239  
 Yagou, Y. 200  
 Yamada, K. 210  
 Yamada, M. 78  
 Yamada, T. 95  
 Yamada, Y. 276, 278  
 Yamagata, T. 139  
 Yamaguchi, C. 169  
 Yamaguchi, H. 30  
 Yamaguchi, N. 137, 138, 259  
 Yamaguchi, T. 26, 28, 45, 46, 47  
 Yamaguchi, T. 64  
 Yamaji, A. 277  
 Yamakoshi, H. 150  
 Yamamoto, A. 170, 175  
 Yamamoto, K. 266  
 Yamamoto, M. 235, 236  
 Yamamoto, Y. 215  
 Yamamura, T. 49  
 Yamanaka, T. 140, 155, 156  
 Yamane, M. 19  
 Yamashita, H. 27  
 Yamashita, S. 26  
 Yamashita, Y. 77  
 Yamazaki, H. 52, 68  
 Yamazaki, M. 139  
 Yamazaki, S. 19, 158  
 Yamazaki, S. 281  
 Yanagihara, M. 235, 236  
 Yanashima, H. 266, 281  
 Yao, M. 53  
 Yaoita, K. 205, 206  
 Yasuami, S. 211  
 Yasuda, H. 32  
 Yasui, H. 164, 166  
 Yasuoka, N. 105, 106  
 Yata, O. 46, 47  
 Yatagai, F. 115  
 Yokokawa, T. 55  
 Yokomizo, H. 259  
 Yokota, Y. 104  
 Yokoyama, T. 39, 57, 74, 238, 240, 241, 242, 243  
 244, 245  
 Yonath, A. 100  
 Yoneda, A. 203  
 Yonenaga, I. 199  
 Yonezawa, T. 42  
 Yoshiasa, A. 34, 81  
 Yoshida, H. 149, 150, 151, 183, 194, 195  
 Yoshida, H. 164, 166  
 Yoshida, O. 130  
 Yoshida, S. 20, 24, 27, 31, 51, 72  
 Yoshihara, K. 184, 192  
 Yoshikawa, S. 104  
 Yoshiki, M. 240  
 Yoshimura, J. 50  
 Yoshimura, Y. 48, 246  
 Yoshino, H. 178  
 Yoshino, M. 237  
 Yoshitake, H. 29  
 Yoshizawa, M. 165  
 Yukawa, N. 222

## Subject Index

2-3-butanedione-2-monoxime 120, 123  
 3-Isopropylmalate dehydrogenase 102  
 $^{103}\text{mRh}$  192  
 $\alpha$ -AlCOH 173  
 Absolute calibration 259  
 Absorption edge shift 143  
 Actin filament 125  
 Active intermediates 63  
 ADL 217  
 Adsorption 17, 252  
 253, 255  
 Ag 50  
 $\text{Ag}_3\text{AsS}_3$  43  
 $\text{Ag}_3\text{AsS}_3$  glass 44  
 $\text{Ag}_3\text{SbS}_3$  43  
 $\text{AgBr-Ag}_2\text{O-GeO}_2$  glasses 19  
 Aggregation 135  
 Al-Mn alloy 170, 175  
 Al-Mn-Ru-Si 191  
 Alcohol 36  
 Aldolase 112  
 Alkali halide 226  
 Alloying elements 18, 22  
 Alpha-2-macroglobulin 132  
 Aluminum 201  
 Amorphous 61, 66, 67  
 Amorphous silicon 223  
 Amylopectin 136  
 Amylose 136  
 Analytical chemistry 60  
 Angle-resolved photoemission 281  
 Angle-resolved photoemission spectroscopy 252, 253  
 266  
 Animal experiment 169  
 Anomalous dispersion 106, 116  
 Anomalous scattering 158, 191  
 212  
 Anomalous transmission 171  
 Anomalous X-ray scattering 163, 168  
 Antiferromagnetic compounds 164, 166  
 Archaeology 142  
 ARPES 251, 254  
 255  
 Art 142  
 Asymmetric reflection 145  
 Atomic configuration 25  
 Atomic model 25  
 Attached catalyst 69  
 Au 278  
 $\text{Au-47.5at\%Cd}$  174  
 $\text{Au-Fe}$  alloy 172  
 Auger effect 90, 91, 93  
 Auger enhancement 99  
 Auger process 231  
 Austenitic steels 18, 22  
 Autoionization 263, 264  
 Background 184  
 Bacteria 90



Bacteriorhodopsin	107,129	Copper complex	23
Band structure	266	Core-excitation	232,233
Barium	89		234
Be	217	Coronary artery	169
Bi-Sr-Ca-Cu-O	277	Correlation	181
Bi-Zn-Fe-O glass	21	Critical exponent	179
Bi <sub>2</sub> O <sub>3</sub>	81	Cross-bridge	122
Bimetal	73	Cryo temperature	100,101
Bimetallic	36,42	Crystal	43,104
Bimetallic catalysts	20		116,176
Biology	94		211
Bisite	73	Crystal structure	60,153
Black phosphorus	162		175
Br-dUMP	93	Crystal structure analysis	105
Bragg reflection	267	Crystallization	182
Bragg-case	187	CT	209
Bragg-reflector	196	Cu oxide	143
Branched polyethylene	179	Cucumber green mottle mosaic virus	135
BrdU	96	CuInSe <sub>2</sub>	152
Broken Rodlike Chain	109	CVD	58,220
Bromide	47	CVD method	24
C-IC phase transitions	160	Cytochrome oxidase	104
C <sub>2</sub> H <sub>2</sub>	261	Cytochrome P-450	63
Ca-Ni-Mo	83	Damaged and fragile sites	98
CaF <sub>2</sub>	272,273	Debye-Waller factor	52
	274	Deformation	18,22
Calcium	263	Degree of order	26
Calcium binding	178	Dehydration	173
Calcium-binding protein	113	Demagnification	267
Calmodulin	178	Deposition	270
Carbon contamination	239	Depth profiling	149,194
Carbonyl	73		195
Catalyst	16,27	Detection of DNA damage	96
	29,36	Devil's staircase	160
	42,48	Diacetylene	240
	56,64	Diamond	177
	71,80	Diamond anvil cell	208
	83,246	Diffraction	176
Catechol	72	Diffuse scattering	222
Ca <sub>x</sub> Y <sub>1-x</sub> Ba <sub>2</sub> Cu <sub>3</sub> O <sub>7-y</sub>	82	Diffusion	79
CCD camera	224	Diffusion coefficient	193
Cell killing	99	Dimethylether	257
Ceramics	59	Direct observation system	247
Cerium alloy	26	Dislocation	199,201
Chalcohalide glass	157		211
Changes in local structure	39	Disordered material	168
Charge density	186	DMPC	121
Chemical analysis	94	Double Crystal Monochromator	30
Chemical state analysis	143	Doubly-excited states	263
Chemisorption	39	Dry cleaning	278
Chlorine gas	269	Dynamical theory	188
Chromosom	98	Dynamical X-ray diffraction	185
Chromosom aberration	95	Effect of stretch	126
Cl	241,242	Electron	260
Cluster	36,73	Electronic structure	240
Co-Mn/Al <sub>2</sub> O <sub>3</sub>	20	Encapsulation	56
Coal	27	Energy dispersive	156
Coincidence	260	Energy subtraction angiography	169
Colloid	42	Enzyme model	56
Complex	28	Equatorial reflection	126,127
Composite oxide	31	Etching	269,279
Composition	211	Eu	237
Compton	189	EUV region	257
Computer tomography	151	EXAFS	16,19
Contrant variation	110		20,21,22,24,25,27,28,29,30,31,32,33
Coordination	55		37,38,40,41,43,44,45,46,47,48,49,50
Copper (II) Chloride	28		51,52,53,55,57,58,59,60,62,63,64,66
Copper	87		67,69,71,75,79,80,81,82,83,86,87,88

	89, 149, 150, 157, 177, 183, 223		88, 89
Extinction	117		210
$\phi$ phase	170, 175	High-order reflection	200
F <sup>-</sup> ion conduction	62	High-pressure	225
Far ultra violet	259	Hopeite film	84
Fatty acid synthetase	132	Hydrated human nuclei	92
FCV	217	Hydrogenase	49, 105
Fe-Ag	32	Hydrogenation	83
Fe-Cu	32	Ice crystal dislocation climb	193
Fe-Cu-Ag	32	Icosahedral phase	25, 191
Fe-K edge	72	Imaging	94, 141
Fe-Mn/Al <sub>2</sub> O <sub>3</sub>	20		142, 151
Fe/MgO	216		194
Ferredoxin	116	Imaging plate	124, 125
Fibonacci lattice	161		134, 208
Film lattice mismatch	197	Imaging reconstruction technique	145
First order phase transition	167	Impurity	79
Fluorescence detection	243	In situ cleaning	239
Fluorescence excitation spectra	261, 262	Inactivation	114
Fluorescence X-ray detector	74	InAlAs/InP	197
Fluorescence yield	241	Inhibitor	103
Fluorescent EXAFS	28	InP	220
Fluorozirconate glass	62	Interface	221, 276
Focus	196	Interfacial superstructure	219
Focusing element	147	Intermediate	118
Fourier transformation	84	Intermediate valence	26
Fragmentation	232, 233	Iodine complex	136
	234	Iodine K-edge	169
$\gamma'$ phase	139	Ion	260
Ga(CH <sub>3</sub> ) <sub>3</sub>	234	Ion exchange	35
GaAs	17, 79	Ionic conductor	59, 81
	188, 211	Ionization	260, 275
	220, 269	Ionization chamber	258
	272, 273	Iron	27, 246
	274	Iron base alloys	68
GaAs/AlAs	198	Iron phthalocyanin	56
Gallium(III) Chloride	47	K-edge subtraction	224
Gas sensor	31	Killing effect	90, 91
Gas X-ray diffraction	186	Kinetics	156, 167
Gasification	27	Krypton	264
GeO <sub>2</sub>	156	La K-edge EXAFS	75
GeO <sub>2</sub> -P <sub>2</sub> O <sub>5</sub> glass	158	La <sub>2</sub> O <sub>3</sub> catalyst	75
Germanium oxide	58	Laser irradiation	214
Glass	45, 46, 47	Lattice misfit	139
Glasses	55	Lattice parameter	211
Gold	235	Laue method	154
Gold photocathodes	138	Layered material	181
Graphite intercalation compounds	167	Layered structure	50
Grazing incidence	185	Lipoamide dehydrogenase	102
Grazing incidence X-ray diffraction	219, 220	Liquid	45, 46
	221		53
Growth interruption	198	Liquid metal	205, 206
H <sup>+</sup> desorption	249	Liquid state	81
H <sub>2</sub> O	186, 229	Lithium	189
Hard X-ray	147	Lithography	217, 218
Heart muscle	119, 122		267
Helium gas scattering	76	Local atomic order	172
Helix-to-coil transition	109	Local structure	21
Hemocyanin	133	Long-period structure	204
Hemoglobin	134	Low temperature and high pressure	162
Hetero-interface	198	Low temperature X-ray diffraction	118
High pressure	156, 204	MAD method	106
	205	Magnetic glass	21
	206, 207	Magnetic lattice distortion	166
	208	Mammalian cells	91, 95
High resolution Compton profile	190		99
High T <sub>c</sub> Superconductor	52, 87	Martensite	33
		Mask membrane	78

Mastoparan	178	Optical elements	239
MAX80	203	Optical fiber	223
MBE	219,221	Optical materials	215
Mechanical alloying	61	Oscillating mirror	218
Medical diagnosis	224	Oxidation	212,240
Medium angle X-ray diffraction	130		255,280
Metal clusters	57	Oxide	59
Metal particle	50	Oxygen fugacity	225
Metallothionein	23	Oxygenation	72
Meteorite	146,209	Palladium	42
Methanol	73	Pendellösung fringe	165
Microbeam	144	Perfect crystal	201
Microchannel plate	137	Perovskite	34
Micrometer-size	154	PFPD	159
Mineral	146	Phase plate	187
Mineralogy	141	Phase separation	213
MIS	273,274	Phase transition	54,68
MISFET	220		121,162
Mixed conductor	85		202,205
Mixed oxide	65		206
Moderate-angle scattering	112	Phosphor Bronze	152
Modulated structure	160	Phosphorus	114
Molecular shape	110	Phosphorus K-edge	90,91
Molecule distortion	54	Photo-catalysis	51
Molluscan smooth muscle	130	Photoabsorption cross section	264
Molybdenum	48	Photoacoustic	181
Mono-X-ray	96,98	Photoacoustic spectra	152
Monochromatic X-rays	95	Photoacoustic spectroscopy	149,150
Monochromatized-X-ray	148		151,183
Monochromator	265		194,195
Multi-charged ions	230	Photochemical reaction	17,279
Multi-wavelength anomalous dispersion method	106	Photoelectron spectroscopy	256,272
Multichannel spectrometer	259	Photoemission	273,274
Multilayer	147,196	Photoemission Spectroscopy	17
	212	Photoionization	230,231
Multilayer filter	236		232,233
Multilayered film	216		234
Multiple anvil	203	Photoionization quantum yield	257,258
Multiple-photoionization	237		261
Multiply charged ion	231	Photopolymerization	240
Muscle	120,123	Phytochrome	110
Muscle contraction	125,128	Piezorefectivity	250
Mutation	95,115	Plasma diagnostics	137
N <sub>2</sub>	262	Platinum	42
Nb dimer	69	PMMA	77
Nb <sub>2</sub> O <sub>5</sub>	65	Polarization	87,88
Nb <sub>2</sub> O <sub>5</sub> /SiO <sub>2</sub>	51		89,187
NbC	38,254	Polaron	85
	255	Poly(glutamic acid)	109
Ni(100)	242,243	Poly(vinyl alcohol)	182
Ni(111)	241,244	Polycarbonates	215
	245	Polyethylene	238
Ni <sup>2+</sup> ions	55	Polymer blend	213
Ni <sup>3+</sup>	49	Position-sensitive detector	223
Nickel thiolate	49	Powder diffraction	140,153
Nickel-base superalloy	139		159
Nitrogen	86	Powder diffractometer	155
NiZr	61	Precipitate	60
NMR	93	Pressure	202
Non-crystalline material	30	Profile analysis	173
Nonequilibrium alloy	32	Promotion	36
Nuclear excitation	184,192	Protective carbon coat	268
O <sub>2</sub>	262	Protein crystallography	103,106
Oligomeric protein	112	PSD	229,249
Omega phase	222	PTFE	238
One-atomic layer Rh catalyst	70	Pulse method	195
Optical constant	235,268	Purple membrane	118,129

PVDF	238	Small angle X-ray scattering	109,110
Quantum efficiency	138	Small crystal	175
Quarternary structure	108	Small-angle scattering	111,113
Quasi-crystal	25,170	Small-angle X-ray diffraction	129
	190	Small-angle X-ray scattering	108
Radial distribution function	163,168	SMSI	65
Radiation damage	119,236	Sn K-edge	31
	271	Sn(CH <sub>3</sub> ) <sub>4</sub>	232,233
Radical scavenger	99	Soft X-ray	76,115
Rare earth compound	164,166		228,235
	256		236,268
Rare earths	204	Soft X-ray microscope	227
Rare-earth atom	237	Sol-Gel transition	179
RDF	157,158	Solid helium	199
Real time analysis	272	Solid solution	34,43
Reflectance measurement	268	Solution	37
Reflectivity profile	185	Solution X-ray scattering	112
Resist	218	Solvated metal atom dispersed	20
Resistivity	38	catalysts	
Resonance photoemission	277	SOXS	178
Rh <sub>2</sub> /SiO <sub>2</sub>	40	Spin state	34
RhNbO <sub>4</sub>	65	Spin-glass	172
Rhodium	39,65	Spontaneous distortion	164
	80	Spore	114
Ribosome	100,101	Sputtering	38,196
	131	Squid retina	124
Rietveld analysis	153	SR	224
Ripple structure	121	SR lithography	78
Ru K-edge	191	SR topography	193
Rubber-like	174	SrCo <sub>1-x</sub> Mn <sub>x</sub> O <sub>3</sub>	34
Rubidium	53	SRPES	226,276
Rydberg series	263		278
Sagittal focusing	145	SRT	193
Satellite	173	St.Séverin	209
Scale	148	State analysis	141
Scanning	148	Static Debye-Waller factor	200
Scattering Function	109	Stepper	217
Schottky barrier	219	Stopped-flow	131,133
Se-Rh/SiO <sub>2</sub>	41		134
Secondary electron conversion	138	Strengthening	18,22
efficiency		Structure	37,45
Section topography	200		46,47
Segmental length clamp	127		53,176
Selenium	37,53		205,206
Selenocysteine	23	Structural change	113,132
Selenometallothionein	23	Structural phase transition	210
Semiconductor	226	Structure analysis	140
Semiconductor process	279	Structure refinement	117
Short wavelength	117	Stuhrmann plot	110
Si	180,188	Subtilisin	103
	276	Subzero temperature	131
Si(100)	229	Sulf	246
Si(100) surface	280	sulfate-reducing bacteria	105,106
Si(Li) detector	76	Sulfur	243,244
Sialon	154		245
Silicon	200,214	Superconductivity	38
	270	Superconductor	82,202
Silicon sensor	223		266,276
Silicon surface	249		279
Silicon telluride	67	Superexcited states	257,258
Simple organic molecules	258		261,262
SIMS	275	Superstructure	140
Sintered diamond	203	Superthin film	235
Sinusoidal length change	128	Surface	221,226
SiO <sub>2</sub>	279		254,255
Si K-edge	30		279
Skeletal muscle	126,127	Surface EXAFS	74,241
Sm	237		242



Surface reaction	270	X-ray fluorescence spectroscopy	146
Surface reconstruction	242,245	X-ray goniometry	197
Surface relaxation	244	X-ray inelastic scattering	228
Surface structure	180,243	X-ray lithography	77,219
Surface transition of structure	71		271
Synchrotron	170,189	X-ray photoelectron diffraction	247
Synchrotron radiation	30,169	X-ray Raman scattering	177
	275	X-ray resonant scattering	165
Synchrotron X-rays	175	X-ray scattering	131,133
Tb	85		134
Telluride	66	X-ray small angle scattering	126,127
Temperature dependence	57	X-ray solution scattering	107
Temperature jump kinetics	135	X-ray spectrum	184
Thermal diffuse scattering	171	X-ray standing wave	74,185
Three dimensional structure	100,101		188,241
Threshold electron	231		242,243
Time-resolved measurement	126,127		244,245
	214	X-ray topography	197,199
Time-resolved SAXS	213	XAFS	68,82
TMG	17		85
Tobacco necrosis virus	104	XANES	18,26
Total reflection mirror	144		37,49
Toxicology	94		50,60
Trace element analysis	215		61,84
Trace element	146,148		238,240
Transformation	115		246,280
Transition	156	Xe	230
Transition metals	215	Yb	237
Tridymite	140	YBa <sub>2</sub> Cu <sub>3</sub> O <sub>7-x</sub>	266
Troponin-C	113	YBa <sub>2</sub> Cu <sub>3</sub> O <sub>y</sub>	87,88
Tryptophanase	108		89
Tungsten	86	YTTRIUM	88
UHV	74	Zeolite	35,56
Undulator	265	Zinc phosphating	84
Uniaxial stress	207	Zinc(II) Chloride	46
Uvarovite	176	Zinc(II) Iodide	45
V <sub>2</sub> O <sub>5</sub>	16	Zirconia	85
V <sub>2</sub> O <sub>5</sub> /SiO <sub>2</sub>	24	Zirconium	64
Vacancy source	201	Zone plate	147
Valence band	277	ZrO <sub>2</sub>	64
Valence excitation	229		
VUV	259,261		
	262,269		
	270,279		
VUV fluorescence	257		
VUV spectra of $\alpha$ -Al <sub>2</sub> O <sub>3</sub>	248		
$\omega$ -phase	33		
Weissenberg camera	103,159		
Wiggler beam	192		
Wiggler source	185		
Wustite	225		
X-ray	93,104		
	152,176		
	188,209		
X-ray contact microscopy	92		
X-ray detector	137		
X-ray diffraction	122,124		
	125,128		
	161,170		
	180,199		
	205,206		
	216,225		
X-ray fluorescence	94,141		
	142,143		
	144		
X-ray fluorescence	215		
X-ray fluorescence analysis	145		

# LIST OF PUBLISHED PAPERS

(Continued from the publication list in Photon Factory Activity Report 1987)

1987

Y.Amemiya, N.Kamiya, Y.Satow, T.Matsushita, J.Chikawa K.Wakabayashi, H.Tanaka and J.Miyahara  
A New Area Detector (Imaging Plate) and Its Application to Diffraction Studies at the Photon Factory  
Spri. Series Bio., 2 (1987) 61.

S.Aoki, Y.Gohshi and A.Iida  
A 10keV X-ray Microprobe with Grazing Incidence Mirrors  
X-ray Microscopy, (1987) 254.

A.Araki, I.Honjo, M.Katoh, Y.Kamiya and M.Kihara  
Survey and Alignment of Photon Factory Storage Ring at KEK  
Proceedings of the 1987 IEEE Particle Accelerator Conference, (1987) 1777.

Y.Fukushima and T.Okamoto  
Extended X-ray Absorption Fine Structure Study of Cobalt-exchanged Sepiolite  
Proc. Int. Cray Conf., (1987) 9.

N.Hamaya, Y.Kuroiwa and Y.Fujii  
A Unique High Pressure Apparatus for X-ray Diffraction Studies of Phase Transitions up to 5 kbars  
Nucl. Instr. Meth. B, 29 (1987) 537.

T.Hondoh, K.Azuma and A.Higashi  
Self-Interstitials in Ice  
J. de Phys. (France) Colloque C1, 48 (1987) 183.

I.Honjo, M.Katoh, A.Araki, Y.Kamiya and M.Kihara  
Measurement of Betatron Function at the Photon Factory  
Proceedings of the 1987 IEEE Particle Accelerator Conference, (1987) 1272.

Y.Inagaki, K.Shima and H.Maezawa  
Response Function of Si(Li) Detector for 1.3-4.0 keV Monochromatic Photons  
Nucl. Instr. Meth., B27 (1987) 353.

T.Ishii, K.Soda, K.Naito, T.Miyahara, H.Kato, S.Sato, T.Mori, M.Taniguchi, A.Kakizaki, Y.Onuki and T.Komatsubara  
VUV Studies on the 4f Partial States in Lanthanide-copper Compounds  
Physica Scripta, 35 (1987) 603.

H.Iwasaki  
Research Activity of the Photon Factory  
Proc. Jpn.-China Joint Symp. on Accelerators for Nuclear Sci. and Their Applications, (1987)

M.Izawa, Y.Takiyama, S.Tokumoto, S.Sakanaka, M.Kobayashi and H.Kobayakawa  
Quick Recovery to UHV by Using Dry Nitrogen Ventilation System  
KEK Report 87-8, (1987) 55.

Y.Kamiya and M.Katoh  
Sideband Spectra of a Longitudinal Instability

Observed in Photon Factory Storage Ring  
Proceedings of the 1987 IEEE Particle Accelerator Conference, (1987) 1313.

Y.Kamiya, M.Katoh, I.Honjo, A.Araki and M.Kihara  
Low Emittance Optics of Photon Factory Storage Ring at KEK  
Proceedings of the 1987 IEEE Particle Accelerator Conference, (1987) 455.

Y.Kamiya, M.Katoh and I.Honjo  
Sextupole Correction for a Ring with Large Chromaticity and the Influence of Magnetic Errors on its Parameters  
Proceedings of the 1987 IEEE Particle Accelerator Conference, (1987) 1310.

N.Kashiwagura, Y.Kashihara, M.Sakata, J.Harada, S.W.Wilkins and A.W.Stevenson  
High Resolution Investigation of the Rod-Shaped Scattering from a (111) Si Surface by a Synchrotron Radiation Source  
Jpn. J. Appl. Phys., 26 (1987) L2026.

M.Kataoka  
Information of Protein Inner Structure Derived by Small-Angle X-ray Scattering  
Biophysics, 27 (1987) 50. (in Japanese).

M.Katoh and Y.Kamiya  
Effect of Insertion Devices on Beam Parameters  
Proceedings of the 1987 IEEE Particle Accelerator Conference, (1987) 437.

M.Katoh, I.Honjo and Y.Kamiya  
Lattice Design for 8GeV Synchrotron Radiation Source  
Proceedings of the 1987 IEEE Particle Accelerator Conference, (1987) 452.

T.Katsura, Y.Kamiya, K.Haga and T.Mitsuhashi  
A Beam Position Feedback System for Beam Lines at the Photon Factory  
Proceedings of the 1987 IEEE Particle Accelerator Conference, (1987) 538.

N.Kondo, K.Shibata, K.Oda, K.Fujita and M.Nomura  
Effect of Solute C, N Atoms and Low Cyclic Fatigue Behavior on X-Ray Absorption Near Edge Fine Structure of Austenitic Stainless Steels  
Sos. Materials Sci., Jpn., (1987) 94. (in Japanese).

H.Maeda  
Accurate Bond Length Determination by EXAFS Method  
J.Phys. Soc. Jpn., 56 (1987) 2777.

H.Maeda, N.Bamba, A.Koizumi, Y.Yoshikawa, T.Ishii, H.Maruyama, M.Hida Y.Kuroda, H.Yamazaki and T.Morimoto  
EXAFS Study on  $Y_{1-x}Ba_xCuO_{3-d}$  Superconductors  
J. Phys. Soc. Jpn., 56 (1987) 3413.

T.Mitsuhashi, K.Haga and T.Katsura  
Construction of a Synchrotron Radiation(SR) Position Monitor by Means of X-ray Photoemission  
Proceedings of 1987 IEEE Particle Accelerator Conference, (1987) 576.

T.Mitsuhashi, T.Urano, T.Katsura, K.Haga, A.Enomoto, H.Hanaki and S.Ohsawa

- Energy Spectra of Electron Beam at the KEK 2.5GeV Linac  
Proceedings of the 12th Linear Accelerator Meeting in Japan, (1987) 129.
- T.Mitsui, K.Wakabayashi, H.Tanaka, T.Kobayashi, Y.Ueno, Y.Amemiya, H.Iwamoto, T.Hamanaka and H.Sugi  
Sinusoidal Length Change Study of Muscle Contraction and Self-Induced Translation Model of Myosin Motion  
Bio. Syn. Rad., (1987) 295.
- M.Nagura, T.Ueki, Y.Hiragi, H.Tagawa, M.Kataoka, Y.Izumi, Y.Muroga and Y.Amemiya  
Microsegregated Structure in the Regenerated Silk Fibroin Film from Bombyx mori  
J. Polymer Science: Part B, 25 (1987) 2567.
- I.Nakai, J.Akimoto, M.Imafuku, R.Miyawaki, Y.Sugitani and K.Koto  
Characterization of the Amorphous State in Metamict Silicates and Niobates by EXAFS and SANES Analyses  
Phys. Chem. Minerals, 15 (1987) 113.
- S.Nakai, T.Mitsuishi, H.Sugawara, H.Maezawa, T.Matsukawa, S.Mitani, K. Yamasaki and T. Fujikawa  
Oxygen K X-Ray-Absorption Near-Edge Structure of Alkaline-Earth-Metal and 3d-Transition-Metal Oxides  
Phys. Rev. B, 36 (1987) 9241.
- M.Nishimura, K.Asakura and Y.Iwasawa  
Carbon Monoxide Hydrogenation on SiO<sub>2</sub>-, Al<sub>2</sub>O<sub>3</sub>-or TiO<sub>2</sub>-Attached Nb-Monomer Catalysts  
Chem. Lett., (1987) 573.
- T.Ohta, K.Seki, I.Morisada, N.Kosugi, T.Usami and S.Hashimoto  
Polarized C K-XANES Spectra of Oriented Polyethylene and poly(vinylidene difluoride) Films  
New Opportunities Chem., (1987) C-8.
- Y.Sakisaka, T.Komeda, M.Onchi, H.Kato, S.Masuda and K.Yagi  
Photoemission Study of the Valence-band Satellite of Ni(110)  
Phys. Rev. B, 36 (1987) 6383.
- Y.Shimizugawa, H.Morikawa, F.Marumo, A.Nakajima, K.Urabe and M.Nomura  
Local Structures Around Ce Atoms in CeO<sub>2</sub>-stabilized Tetragonal ZrO<sub>2</sub>  
Yogyo-Kyokai-Shi, 95 (1987) 1131. (in Japanese).
- K.Sugiyama and Y.Waseda  
The Characteristic Features of Perovskite-type Oxide Structures and the Latest Topics on the Perovskite Derivative Structures  
Bull. Jpn. Inst. Metals, 26 (1987) 771.
- T.Takahashi, H.Ohsawa, N.Gunasekara, H.Ishii, T.Kinoshita, T.Sagawa, H.Kato, T.Miyahara and K.Shindo  
Angle-Resolved Photoemission Study of Rhombohedral Arsenic  
Physica Scripta, 36 (1987) 187.
- T.Takahashi, H.Ohsawa, N.Gunasekara, H.Ishii, T.Kinoshita, T.Sagawa, H.Kato, T.Miyahara and K.Shindo  
Electronic Band Structure of Rhombohedral Arsenic Studies by Angle-resolved Photoemission with Synchrotron Radiation  
Phys. Rev. B, 35 (1987) 4089.
- K.Tohji and Y.Udagawa  
Novel Approach for Structural Analysis by X-Ray Raman scattering  
Phys. Rev. B, 36 (1987) 9410.
- T.Urisu and H.Kyuragi  
Synchrotron Radiation-Excited Chemical-Vapor Deposition and Etching  
J. Vac. Sci. Technol., B5 (1987) 1436.
- T.Urisu and H.Kyuragi  
Synchrotron Radiation Excited Semiconductor Processes  
Oyo-Butsuri, 56 (1987) 1035. (in Japanese).
- S.Watanabe, M.Akisada, K.Hyodo and T.Takeda  
Fundamental Studies on Boundary Estimation of Low SNR Arteriogram by "Minimum Difference of Density Method"  
Med. Imaging Technol., 5 (1987) 267. (in Japanese).
- 1988
- S.Arai, T.Kamosaki, M.Ukai, K.Shinsaka, Y.Hatano, Y.Ito, H.Koizumi, A.Yagishita, K.Ito and K.Tanaka  
Lyman- $\alpha$ , Lyman- $\alpha$  Coincidence Detection in the Photodissociation of Doubly Excited Molecular Hydrogen into Two H(2p)  
J. Chem. Phys., 88 (1988) 3016.
- K.Edamoto, S.Maehama, E.Miyazaki, T.Miyahara and H.Kato  
Angle-resolved Photoemission Study of NO Chemisorption on Ag(111) Surface  
Surface Sci., 204 (1988) L744.
- H.Endo, M.Inui, M.Yao, K.Tamura, H.Hoshino, Y.Katayama and K.Maruyama  
Structure of Isolated Selenium Chain in the Channels of Mordenite  
Z. Phys. Chem., 156 (1988) 507.
- K.Fujii and K.Okada  
Temperature Measurement of Be Windows Irradiated by Synchrotron Radiation  
Jpn. J. Appl. Phys., 27 (1988) L1980.
- K.Fujii, K.Okada, M.Nagano and H.Kuroda  
An X-ray Stepper for Synchrotron Radiation Lithography  
J. Vac. Sci. Technol., B6 (1988) 2135.
- K.Fujii, K.Okada, M.Nagano and H.Kuroda  
Precisely Controlled Oscillating Mirror System for Highly Uniform Exposure in Synchrotron Radiation Lithography  
J. Vac. Sci. Technol., B6 (1988) 2128.
- A.Fujimori, T.Miyahara, T.Koide, T.Shidara, H.Kato, H.Fukutani and S.Sato  
4f-derived Photoemission and 4f-ligand Hybridization in Light Rare-earth Halides

- Phys. Rev., 38 (1988) 7789.
- Y.Gohshi, S.Aoki, A.Iida, S.Hayakawa, H.Yamaji and K.Sakurai  
A Scanning X-ray Fluorescence Microprobe with Synchrotron Radiation  
Advances X-Ray Anal., 31 (1988) 495.
- Y.Hatano  
Dissociation Dynamics of Superexcited Molecules  
Radiochimica Acta, 43 (1988) 119.
- T.Hayaishi, E.Murakami, A.Yagishita, F.Koike, Y.Morioka and J.E.Hansen  
Photoion Spectra in Coincidence with Threshold Electrons near the Ar 2p Ionisation Limits  
J. Phys. B, 21 (1988) 3203.
- Y.Hiragi, H.Nakatani, K.Kajiwarra, H.Inoue, H.Sano and M.Kataoka  
Temperature-Jump Apparatus and Measuring System for Synchrotron Solution X-Ray Scattering Experiments  
Rev. Sci. Instr., 59 (1988) 64.
- M.Ichikawa, A.Fukuoka and T.Kimura  
Selective CO Hydrogenation to C<sub>1</sub>-C<sub>2</sub> Fe-containing Rh, Pt, and Pd Bimetal Carbonyl Cluster-derived Catalysts  
Proc. 9th Intl. Cong. Catal., 2 (1988) 569.
- A.Iida, K.Sakurai and Y.Gohshi  
Near-surface Analysis of Semiconductor Using Grazing Incidence X-ray Fluorescence  
Adv. in X-ray Anal., 31 (1988) 487.
- A.Iida, K.Sakurai, Y.Gohshi and S.Komiya  
Analysis of Contamination Layer of InP During LPE Process by Synchrotron Radiation-Excited X-Ray Fluorescence  
Jpn. J. Appl. Phys., 27 (1988) L1825.
- M.Inui, M.Yao and H.Endo  
EXAFS Study on Selenium-Tellurium Mixed Chains  
J. Phys. Soc. Jpn., 57 (1988) 553.
- T.Ishikawa  
Measurement of the Coherence Length of Highly Collimated X-Rays from the Visibility of Equal-Thickness Fringes  
Acta Crystallogr., A44 (1988) 496.
- T.Ishikawa  
Observation of Minute Strain Fields in Silicon Single Crystals by X-Ray Topography  
Oyo Butsuri, 57 (1988) 1496. (in Japanese).
- T.Ishikawa  
Contrast of Defect Images  
X-Ray Diffraction, edited by K.Kohra, Kyoritsu Shuppan (Tokyo), (1988) 453. (in Japanese).
- T.Ishikawa  
Applications of Extremely Collimated X-Rays  
Houshakou, 1 (1988) 65. (in Japanese).
- M.Ito and N.Kanaya  
Pascal  
Sci.-Pub. Co. Tokyo, (1988) (in Japanese).
- K.Ito, K.Ueda, T.Namioka, K.Yoshino and Y.Morioka  
High-resolution Absorption Spectrum of Ne I in the Region of 565- 595 Å  
J. Opt. Soc. of America B, 5 (1988) 2006.
- F.Itoh, T.Sekiuchi, M.Sakurai, T.Fukunaga and K.Suzuki  
A Structural Study on Solid State Amorphization of Ni-Zr Alloys by Ball Milling  
Suppl. Trans. JIM, 29 (1988) 127.
- T.Itoh, Y.Iwabuchi and M.Kataoka  
Study on the Size and Shape of CuCl Microcrystals Embedded in Alkali-Chloride Matrices and Their Correlation with Exciton Confinement  
Phys. Stat. Sol. b, 145 (1988) 567.
- M.Izawa, H.Kobayakawa, S.Sakanaka and S.Tokumoto  
Suppression of Cavity-induced Coupled-bunch Instabilities  
KEK Internal 88-7, (1988) (in Japanese).
- N.Kanaya, S.Sato and S.Asaoka  
Distributed Control System for Synchrotron Radiation Beam Channel  
KEK-Report 87-25, (1988) 49.
- Y.Kashiwase, M.Mori, M.Kogiso, M.Minoura and S.Sasaki  
Diffraction Pattern Caused by X-ray Thermal Diffuse Scattering in Absorbing Perfect Crystal  
J. Phys. Soc. Jpn., 57 (1988) 524.
- K.Kato, Y.Sugitani  
Correlation Photoacoustic Measurement by Excitation with Synchrotron Radiation  
Anal. Sci., 4 (1988) 59.
- T.Katsura  
Quieting of the Photon Beam Motion in the Photon Factory Storage Ring  
Proc. of Int. Workshop on Constructing 1-2 GeV Synchrotron Radiation Facilities, (1988)
- Y.Kawase, J.Mizuki, K.Akimoto, T.Kitano, J.Matsui, S.Sato and Y.Satow  
Developing a Multipurpose SR Beam Line Highly Efficient in Material Characterization  
Nucl. Instrum. and Methods, A266 (1988) 238.
- T.Kitano, H.Watanabe and J.Matsui  
Fluorescence EXAFS Study of Zn-Doped LEC InP Crystal  
Jpn. J. Appl. Phys., 27 (1988) L9.
- T.Kitano, Y.Matsumoto and J.Matsui  
Local Structure Around Zn Atoms Diffused into the GaAs Crystal  
Appl. Phys. Lett., 53 (1988) 1390.
- M.Kobayashi  
Gas Load, Pressure Distribution and Pumping of a Synchrotron Radiation Source  
AIP Conference Proceedings, 171 (1988) 155.
- T.Koide, T.Shidara, M.Yanagihara and S.Sato  
Resuscitation of Carbon-contaminated Mirrors and Gratings by Oxygen Discharge Cleaning. 2: Efficiency Recovery in the 100-1000-eV Range  
Appl. Opt., 27 (1988) 4305.
- H.Koizumi, K.Shinsaka, T.Yoshimi, K.Hironaka,



- S.Arai, M.Ukai, M.Morita, H.Nakazawa, A.Kimura, Y.Hatano, Y.Ito, Y.Zhang, A.Yagishita, K.Ito and K.Tanaka  
Ionization Efficiencies of  $C_3H_6$ ,  $C_4H_8$ ,  $C_6H_{12}$ ,  $C_2H_6O$ , and  $C_3H_8O$  Isomers  
*Radiat. Phys. Chem.*, 32 (1988) 111.
- S.Kojima, S.Kawado, T.Ishikawa, T.Takahashi and S.Kikuta  
Time-Resolved X-Ray Diffraction from a Silicon Crystal Irradiated by a Q-Switched Nd:YAG Laser  
*Jpn. J. Appl. Phys.*, 27 (1988) L1377.
- T.Komeda, Y.Sakisaka, M.Onchi, H.Kato, S.Suzuki, K.Edamoto and Y.Aiura  
Angle-Resolved Photoemission Study of the Hydrogen-adsorbed Cr(110) Surface at 80 K  
*Phys. Rev. B*, 38 (1988) 7349.
- T.Komeda, Y.Sakisaka, M.Onchi, H.Kato, S.Suzuki, K.Edamoto and Y.Aiura  
Angle-resolved Photoemission Study of Oxygen-Adsorbed Cr(110)  
*Phys. Rev. B*, 38 (1988) 7345.
- T.Kondoh, N.Yamaguchi, T.Cho, M.Hirata, S.Miyoshi, S.Aoki, H.Maezawa and M.Nomura  
Current Response Characteristics of Microchannel Plates X-Ray Detector Using Synchrotron Radiation (0.6-2keV and 5-20keV)  
*Rev. Sci. Instr.*, 59 (1988) 252.
- H.Kubo, T.Sugie, A.Sakasai, Y.Koide, N.Nishino, H.Yokomizo, H.Takeuchi, K.Tanaka, H.Maezawa and N.Yamaguchi  
Multichordal spectroscopy on JT-60  
*Rev. Sci. Instrum.*, 59 (1988) 1515.
- H.Maeda, A.Koizumi, N.Bamba, E.T.Muromachi, F.Izumi, M.Onoda, Y.Kuroda, H.Maruyama, Y.Yoshikawa, T.Ishii, M.Hida and H.Yamazaki  
EXAFS Study on the Local Structure of a New High-Tc Superconductor in the Bi-Sr-Ca-Cu-O System  
*Jpn. J. Appl. Phys.*, 27 (1988) L807.
- H.Maeda, T.Fukunaga, K.Suzuki, K.Osamura, M.Hida, H.Terauchi and N.Kamijo  
EXAFS Studies of Amorphous Nickel-Zirconium Alloys  
*Jpn. J. Appl. Phys.*, 27 (1988) L938.
- H.Maeda, T.Fukunaga, K.Suzuki, K.Osamura, M.Hida, H.Terauchi and N.Kamijo  
EXAFS Studies of Amorphous Nickel-zirconium Alloys  
*Jpn. J. Appl. Phys.*, 27 (1988) L938.
- S.Maeyama, Y.Satow, M.Oshima and A.Katsui  
Polarized Extended X-ray Absorption Fine Structure of High- $T_c$  Superconducting Single-crystal  $YBa_2Cu_3O_y$   
*Jpn. J. Appl. Phys.*, 27 (1988) L1657.
- H.Maezawa, K.Hieda, K.Kobayashi, Y.Furusawa, T.Mori, K.Suzuki, and T. Ito  
Effects of Monoenergetic X-Rays with Resonance Energy of Bromine K-Absorption Edge on Bromouracil-Labelled E. Coli Cells  
*Int. J. Rad. Biol.*, 53 (1988) 301.
- H.Maezawa, K.Hieda, K.Kobayashi and T.Ito  
Effects of Auger Cascades of Bromine Induced by K-shell Photoionization on Plasmid DNA, Bacteriophages, E.coli and Yeast Cells.  
DNA Damage by Auger Emitters, (1988) 135.
- S.Masuda, Y.Harada, H.Kato, K.Yagi, T.Komeda, T.Miyano, M.Onchi, and Y.Sakisaka  
Angle-Resolved Photoemission Study of a Thin FeO(111) Layer Formed on Fe (110)  
*Phys. Rev. B*, 37 (1988) 8088.
- S.Masuda, Y.Harada, H.Kato, K.Yagi, T.Komeda, T.Miyano, M.Onchi and Y.Sakisaka  
Angle-resolved Photoemission Study of a Thin FeO(111) Layer Formed on Fe(110)  
*Phys. Rev. B*, 37 (1988) 8088.
- T.Masujima  
Photoacoustic X-ray Absorption Spectroscopy  
*Spr. Series Opt. Sci.*, 58 (1988) 19.
- E.Matsubara, K.Harada, Y.Waseda and M.Iwase  
Anomalous X-ray Scattering Study of  $GeO_2$  Glass  
*Z. Naturforsch. A*, 43a (1988) 181.
- E.Matsubara, Y.Waseda and H.Itozaki  
Method for the Quantitative Structural Analysis of Amorphous Ge Thin Film by X-rays  
*Transactions Jpn. Inst. Metals*, 28 (1988) 1.
- Y.Matsuo, K.Ohshima, H.Iwasaki, Y.Kuroiwa, H.Maeta and K.Haruna  
X-ray Diffuse Scattering from  $\beta'$ -AgZn Alloy  
*J. Phys. F*, 18 (1988) 2505.
- T.Mitsubishi, M.Katoh and S.Ohsawa  
Optics Matching between Beam Transport Line of Photon Factory Storage Ring and KEK 2.5GeV Linac  
Proceedings of the 13th Linear Accelerator Meeting in Japan, (1988) 31.
- T.Mitsui, K.Wakabayashi, H.Tanaka, T.Kobayashi, Y.Amemiya, H.Iwamoto, E-Z.Wang, T.Hamanaka and H.Sugi  
A Self-Induced Translation Model of Myosin Head Motion Along Thin Filament in Muscle Contraction  
Molecular Mechanism Muscle Contr., (1988) 405.
- T.Miyanaga, N.Matsubayashi, T.Fukumoto, K.Yokoi, I.Watanabe, K.Murata and S. Ikeda  
EXAFS Study on Polynuclear Molybdenum and Tungsten Compounds  
*Chem. Lett.*, (1988) 487.
- T.Miyanaga, N.Matsubayashi, I.Watanabe and S.Ikeda  
EXAFS and XANES of Titanium (III), (IV) and the Mixed Valence Complex in Aqueous Solution  
*Advances X-ray Chem. Anal. Jpn.*, 19 (1988) 119.
- T.Miyanaga, I.Watanabe and S.Ikeda  
Amplitude in EXAFS and Ligand Exchange Reaction of Hydrated 3d Transition Metal Complexes  
*Chem. Lett.*, (1988) 1073.
- T.Miyanaga, I.Watanabe, S.Ikeda and T.Fujikawa  
XANES of Aqua Complexes of 3d Transition Metals in Solid and Solution  
*Bull. Chem. Soc. Jpn.*, 61 (1988) 3199.
- J.Mizuki, K.Akimoto, I.Hirosawa, K.Hirose, T.Mizutani and J.Matsui  
Observation of the Superstructure at the

- Al-GaAs(001) Interface by Synchrotron X-ray Diffraction  
J. Vac. Sci. & Technol., B6 (1988) 31.
- Y.Morioka, K.Maeda, K.Ito and T.Namioka  
Linear State of H<sub>2</sub>O Found from a VUV Absorption Band  
J. Phys. B, 21 (1988) L121.
- Y.Morioka, K.Maeda, K.Ito and T.Namioka  
Linear State of H<sub>2</sub>O Found from a VUV Absorption Band  
J. Phys., B21 (1988) L121.
- Y.Muroga, H.Tagawa, Y.Hiragi, T.Ueki, M.Kataoka, Y.Izumi and Y.Amemiya  
Conformational Analysis of Broken Rodlike Chains. 2. Conformational Analysis of Poly(D-glutamic acid) in Aqueous Solution by Small Angle X-ray Scattering  
Macromolecules, 21 (1988) 2756.
- S.Nakai, A.Kawata, M.Ohashi, M.Kitamura, C.Sugiura, T.Mitsuishi and H. Maezawa  
Core-Exciton Absorption in the FK Absorption Spectra of 3d Transition-Metal Fluorides  
Phys. Rev. B, 37 (1988) 10895.
- N.Nakamura, K.Haga, Y.Kamiya and T.Katsura  
The Improved Beam Orbit Measurement and its Operating System  
KEK Internal 88-14, (1988)
- N.Nakayama, I.Moritani, T.Shinjo, Y.Fujii and S.Sasaki  
Anomalous X-ray Scattering Study of Composition Profile in Fe/Mn Superlattice Films  
J. Phys. F: Metal Physics, 18 (1988) 429.
- T.Namioka and K.Ito  
Modern Developments in VUV Spectroscopic Instrumentation  
Phys. Scr., 37 (1988) 673.
- T.Nasu, K.Nagaoka, M.Sakurai, T.Fukunaga, F.Itoh and K. Suzuki  
EXAFS Study Mechanical Deformation for Pd-Si Amorphous Alloy  
Materials Sci. Engineering, 98 (1988) 553.
- M.Nishimura, K.Asakura and Y.Iwasawa  
Silver(I) Solvation in Some N-donor Solvents from Ag K-edge EXAFS  
J. Chem. Soc., Chem. Comm., (1988) 433.
- M.Niwano, S.Sato, T.Koide, T.Shidara, A.Fujimori, H.Fukutani, S.Shin and M.Ishigame  
Optical Properties of CeO<sub>2</sub> Crystal in the Photon Energy Range of 2.5-40 eV  
J. Phys. Soc. Jpn., 57 (1988) 1489.
- M.Nomura  
Application of Synchrotron Radiation to Catalysts  
Shokubai, 30 (1988) 15. (in Japanese).
- M.Nomura and T.Yamaguchi  
Concentration Dependence of Extended X-ray Absorption Fine Structure and X-ray Near-edge Structure of Copper(II) Perchlorate Aqueous Solution: Comparison of Solute Structure in Liquid and Glassy State  
J. Phys. Chem., 92 (1988) 6157.
- S.-J.Oh, S.Suga, A.Kakizaki, M.Taniguchi, T. Ishii, J.-S.Kang, J. W.Allen, O.Gunnarsson, N.Christensen, A.Fujimori, T.Suzuki, T.Kasuya, T.Miyahara, H.Kato, K.Sch nhammer, M.S.Torikachvili and M.B.Maple  
Observation of Kondo Resonance in YbAl<sub>3</sub>  
Phys. Rev. B, 37 (1988) 2861.
- K.Ohshima, J.Harada, M.Morinaga, P.Georgopoulos and J.B.Cohen  
Distortion-Induced Scattering due to Vacancies in NbCo<sub>72</sub>  
Acta Cryst., A44 (1988) 167.
- K.Okada, K.Fujii, Y.Kawase and M.Nagano  
Development of Highly Reliable Synchrotron Radiation Lithography Beamline  
J. Vac. Sci. Technol., B6 (1988) 191.
- H.Oyanagi, T.Sakamoto, K.Sakamoto, T.Matsushita, T.Yao and T.Ishiguro  
Si/Ge/Si Monolayer Heterostructure on Si(100) Studied by Surface-Sensitive EXAFS  
J. Phys. Soc. Jpn., 57 (1988) 2086.
- L.Rao, A.Fukuoka and M.Ichikawa  
Selective Formation of Lower Alkenes and Alcohols in CO +H<sub>2</sub> Reaction Catalysed on NaY Zeorite-encapsulated Rh<sub>6</sub> and RhFe Bimetallic Cluster-derived Catalysts  
J. Chem. Soc., Chem. Comm., (1988) 458.
- K.Saitoh, K.Inagawa, K.Kohra, C.Hayashi, A.Iida and N.Kato  
Fabrication and Characterization of Multilayer Zone Plate for Hard X-rays  
Jpn. J. Appl. Phys., 27 (1988) L2131.
- K.Sakamoto, Y.Suzuki, T.Hirano and K.Usami  
Improvement of Spatial Resolution of Monochromatic X-ray CT Using Synchrotron Radiation  
Jpn. J. Appl. Phys., 27 (1988) 127.
- S.Sakanaka, M.Izawa, H.Kobayakawa and M.Kobayashi  
Observation of Ion-trapping in Single Bunch Operation at the Photon Factory Storage Ring  
Jpn. J. Appl. Phys., 27 (1988) 1031.
- Y.Sakisaka, T.Komeda, M.Onchi, H.Kato, S.Suzuki, K.Edamoto and Y.Aiura  
Angle-resolved Photoemission from Cr(110): Observation of a Bulk Magnetic Phase Transition  
Phys. Rev. B, 38 (1988) 1131.
- K.Sakurai, A.Iida, M.Takahashi and Y.Gohshi  
Chemical State Mapping by X-Ray Fluorescence Using Absorption Edge Shifts  
Jpn. J. Appl. Phys., 27 (1988) L1768.
- K.Sakurai, A.Iida and Y.Gohshi  
Analysis of Signal to Background Ratio in Synchrotron Radiation X-Ray Fluorescence  
Anal. Sciences, 4 (1988) 3.
- K.Sakurai, A.Iida and Y.Gohshi  
Chemical State Analysis by X-Ray Fluorescence Using Shifts of Iron K Absorption Edge  
Anal. Science, 4 (1988) 37.

- K.Sakurai, A.Iida and Y.Gohshi  
Chemical State Analysis by X-Ray Fluorescence  
Using Absorption Edge Shifts 19 (1988) 57.
- T.Sakurai, S.Suzuki and M.Sano  
X-ray Absorption Study on the Type II  
Copper-depleted Cucumber Ascorbate Oxidase  
Inorganica Chimica Acta, 152 (1988) 3.
- M.Sano  
The Change of X-ray Absorption Near Edge Structure  
in Solid and Solution  
Chem. Phys. Lett., 148 (1988) 331.
- M.Sano and T.Matsubara  
Structural Change in the One-electron  
Oxidation-reduction at the Copper site in Nitrite  
Reductase. Evidence from EXAFS  
Inorganic Chimica Acta, 152 (1988) 53.
- M.Sano, T.Maruo and H.Yamatera  
Structural Determination of Solvated Copper  
Species in Formamide Solution by EXAFS  
J. Chem. Phys., 89 (1988) 1185.
- T.Sato, T.Murakami, Y.Amemiya, H.Hashizume and  
T.Takahashi  
Determination of Structure and Formation Kinetics  
of Early Stage GPZones in an Al-1.7at.%Cu Alloy  
by Small-Angle X-ray Scattering of Synchrotron  
Radiation  
Acta Metal., 36 (1988) 1335.
- Y.Suzuki, K.Usami, K.Sakamoto, H.Kozaka,  
T.Hirano, H.Shiono and H.Kohno  
X-ray Computerized Tomography Using Monochromated  
Synchrotron Radiation  
Jpn. J. Appl. Phys., 27 (1988) L461.
- K.Takemura, O.Shimomura, K.Hase and T.Kikegawa  
The High Pressure Equation of State of  $\alpha$ -Mn to  
42 GPa  
J. Phys. F, 18 (1988) 197.
- B.Tan, K.Klabunde, T.Tanaka, H.Kanai and S.Yoshida  
An EXAFS Study of Co-Mn/SiO<sub>2</sub> Bimetallic Solvated  
Metal Atom Dispersed (SMAD) Catalysts  
J. Amer. Chem. Soc., 110 (1988) 5951.
- S.Tokutomi, M.Kataoka, J.Sakai, M.Nakasako,  
F.Tokunaga M.Tasumi and M. Furuya  
Small-Angle X-Ray Scattering Studies on the  
Macromolecular Structure of the  
Red-Light-Absorbing Form of 121 kDa pea  
phytochrome and Its 114 kDa Chromopeptide  
Biochimica et Biophysica Acta, 953 (1988) 297.
- T.Tonuma, T.Mukoyama, T.Koizumi, T.Matsuo,  
H.Shibata, K.Shima, H.Tawara and A.Yagishita  
Multiple photoionization of Xe in the vicinity of  
L edges  
Proc. Inter. Seminar Atomic Molecular Phys.,  
(1988) 26.
- K.Tsuji, O.Shimomura, K.Tamura and H.Endo  
Structure of Liquid Se under High Pressure  
Z. Phys. Chem. Neue Folge, 156 (1988) 495.
- K.Wakabayashi, Y.Amemiya and H.Tanaka  
Synchrotron X-Ray Diffraction Studies on  
Structural Changes of ThinFilaments during an  
Isometric Contraction of Frog Skeletal Muscle  
Ener. Trans. ATPASES, (1988) 21.
- K.Wakabayashi  
Fast X-Ray Diffraction Pattern during Muscle  
Contraction by Synchrotron Radiation  
ELAN, (1988) 22.
- K.Wakabayashi, Y.Ueno, Y.Amemiya and H.Tanaka  
Intensity Changes of Actin-Based layer Lines From  
Frog Skeletal Muscles During An Isometric  
Contraction  
Mol. Mechanism Muscle Contr., (1988) 353.
- K.Wakabayashi, H.Tanaka, H.Iwamoto, E-Z.Wang,  
T.Kobayashi, Y.Amemiya, H.Sugi and T.Mitsui  
Intensity changes of the 7.2-nm myosin meridional  
reflection from tetanized frog skeletal muscles  
during sinusoidal length changes  
J. Muscle Res. Cell Motility, 9 (1988) 275.
- Y.Waseda, E.Matsubara and K.Sugiyama  
Anomalous X-ray Scattering Facility for Structural  
Characterization of Materials using Synchrotron  
Radiation  
Sci. Rep. Res. Inst., 34A (1988) 1.
- K.Yagi, M.Miyabe, A.Yamada, Y.Aiura, H.Fukutani,  
M.Yuri, H.Kato, T.Koide and T.Shidara  
Piezoreflectance of Rubidium Chloride in the  
Vacuum Ultraviolet Region from 6 to 30eV  
J. Phys. Soc. Jpn., 57 (1988) 1478.
- T.Yamaguchi, M.Nomura, H.Wakita and H.Ohtani  
An Extended X-ray Absorption Fine Structure Study  
of Aqueous Rare Earth Perchlorate Solutions in  
Liquid and Glassy States  
J. Chem. Phys., 89 (1988) 5153.
- M.Yanagihara, Y.Kondo, T.Hanyu and S.Yamaguchi  
Intrinsic Luminescence Excitation Spectra near  
the K and Cl 1s Edges in KCl and KBr  
Solid State Commun., 68 (1988) 345.
- M.Yanagihara, M.Niwano, T.Yamada, S.Yamaguchi  
Soft X-Ray Reflection from Silicon and Quartz  
Mirrors  
Appl. Optics, 27 (1988) 563.
- M.Yanagihara, M.Niwano, T.Koide and S.Sato  
Soft X-Ray Optical Constants: Pt, Ag, and Cu  
Jpn. J. Appl. Phys., 27 (1988) 666.
- A.Yoshiasa, F.Kanamaru S.Emura and K.Koto  
Variations of Ag Bonding Distances in the AgBr I  
Solid-Solution with Rock-Salt Type Structure by  
X-ray and EXAFS Analyses  
Sol. State Ionics, 27 (1988) 267.
- A.Yoshiasa, F.Kanamaru and K.Koto  
Local Structure of the Superionic Conducting -AgI  
Type AgI Br Solid-Solution  
Sol. State Ionics, 27 (1988) 275.
- K.Yoshino, G.Stark, P.L.Smith, W.H.Parkinson and  
K.Ito  
Higher-resolution Spectra and Photoabsorption  
Coefficients for Carbon Monoxide Absorption Bands  
between 94.0 nm and 100.4 nm  
J. Physique, 49 (1988) C1-37.











